

**Early evolution of environments and metabolism: insights from
nitrogen, selenium and sulfur isotopes**

Eva E. Stüeken

A dissertation

submitted in partial fulfillment of the
requirements for the degree of

Doctor of Philosophy

University of Washington

2014

Reading committee:

Roger Buick, Chair

John A. Baross

David C. Catling

Program authorized to offer degree:

Earth & Space Sciences

©Copyright 2014

Eva E. Stüeken

Acknowledgments

My work and I have been funded by various agencies over the years, including the UW Royalty Research Fund, the National Science Foundation, the UW Astrobiology Program, the Earth & Space Science Department, and a GSA Graduate Student Research grant. I owe special thanks to Vikki Meadows for funding parts of my field work. I further thank Andy Schauer, Kyle Samek, Joy Layback, Scott Kuehner and Dave McDougall for technical support, and Julien Foriel for training me and making me a better geochemist during the first two years. I thank Zach Adam for introducing me to the Belt Supergroup in western Montana and for helping me plan my sample collection. Additional samples were provided by Roger Buick, Simon Poulton, Gerald Zieg, Bradley Guy, Boswell Wing, Ariel Anbar, Andrew Knoll, Linda Kah, Hans Machel, Shane Schoepfer and Isabel Montanez. I also thank Charlotte Schreiber for establishing contacts to some of her colleagues and for sharing thoughts on sedimentology and environmental evolution. I thank John Baross, David Catling and David Stahl for serving on my advisory committee, especially John for many inspiring conversations over lunch about life as such and its origins in particular. I want to thank Rika Anderson, Zoë Harold, Sanjoy Som, Marcela Ewert-Sarmiento, Billy Brazelton, Anthony Adler and Clara Fuchsman for friendship, dinners and board game nights, and my family for support over the long distance.

But none of this would have been possible – and it certainly would have ended a lot sooner – without support and encouragement from the best PhD advisor I could have asked for. Roger, I thank you for being an academic father in every sense of the word.

University of Washington

Abstract

Early evolution of environments and metabolism: insights from nitrogen, selenium and sulfur isotopes

Eva Elisabeth Stueeken

Chair of the Supervisory Committee:
Dr. Roger Buick
Department of Earth & Space Sciences

The evolution of planet Earth and its biosphere are tightly linked through global biogeochemical cycles, and this dissertation seeks to explore this linkage during the Precambrian with new strategies and geochemical techniques. The first chapter is the result of a group project in which we propose that multiple environments and processes were involved in prebiotic chemistry. We conclude that the origin of life can be more plausibly explained if the various building blocks of living cells slowly emerged from global geochemical cycles. In the second part of my thesis (Chapters 2-3), I explore how microorganisms exploited and modified these cycles, in particular the global sulfur cycle. Statistical analyses of sulfur concentrations and isotopic ratios in marine mudrocks support an early Archean origin of microbial sulfate reduction and late Archean enhancement of biological pyrite oxidation on land, leading to increasing fluxes of sulfate and other nutrients to the ocean. In the third part (Chapters 4-7), I further test this hypothesis through analyses of selenium isotopes and abundances. After establishing a new

analytical technique, I show that selenium was mobilized by oxidative weathering in the late Archean, concurrently with sulfur. Because of selenium's high redox potential, these results confirm the antiquity of oxygenic photosynthesis. A compilation of selenium data through time further indicates oxygenation of the deep ocean in the Neoproterozoic or mid-Paleozoic, which may have facilitated the rise of metazoans. The late Permian mass extinction, however, was apparently not directly linked to an episode of ocean anoxia. The third part of this work (Chapters 8-10) focuses on nitrogen isotopes as a proxy for nitrogen speciation in the water column. Results show that biological nitrogen fixation using Mo-nitrogenase dates back to at least the mid-Archean and was the dominant nitrogen source at that time. Marine nitrate concentrations were also low in the mid-Proterozoic, which may have restricted the radiation of eukaryotic life. Lastly, I use nitrogen isotopes in lacustrine sediments as a proxy for alkalinity and show that alkaline lakes may have been common on Archean continents, making them potentially important environments for the origin and early evolution of life.

Table of Contents

Introduction	9
Chapter 1: Did life originate from a global chemical reactor?	12
Abstract.....	12
1.1. Introduction.....	13
1.2. Prerequisites for the origin of life.....	16
1.3. Hadean micro-environments and their potential role in the origin of life.....	23
1.4. Global transport and concentration processes on the Hadean Earth.....	39
1.5. Merging bioinformatics with geochemistry.....	48
1.6. Future research directions.....	52
1.7. Conclusion.....	55
Tables.....	58
Figures.....	61
References.....	67
Appendix to Chapter 1.....	82
Chapter 2: Contributions to Late Archaean sulphur cycling by life on land	88
Abstract.....	88
2.1. Introduction.....	89
2.2. Method.....	89
2.3. Results.....	91
2.4. Discussion and conclusion.....	91
Tables.....	96
Figures.....	97
References.....	100
Appendix to Chapter 2.....	102
Chapter 3: Evolution of the Archean sulfur cycle revealed by quadruple sulfur isotopes	135
Abstract.....	135
3.1. Introduction.....	136
3.2. Methods.....	138
3.3. Results.....	139
3.4. Discussion.....	140
3.5. Conclusion.....	146
Tables.....	149
Figures.....	150
References.....	154
Appendix to Chapter 3.....	157
Chapter 4: Selenium isotope analysis of organic-rich shales: advances in sample preparation and isobaric interference correction	160
Abstract.....	160
4.1. Introduction.....	161
4.2. Methods.....	163
4.3. Results.....	173
4.4. Discussion.....	180
4.5. Conclusion.....	184
Tables.....	187
Figures.....	193

References.....	207
Chapter 5: Selenium in the latest Archean: a longer whiff but no MIF.....	210
Abstract.....	210
5.1. Introduction.....	210
5.2. Materials and methods.....	212
5.3. Results.....	213
5.4. Discussion.....	214
5.5. Conclusion.....	219
Figures.....	220
References.....	222
Appendix to Chapter 5.....	224
Chapter 6: Deep-time trends in selenium isotopic geochemistry supporting secular redox changes in the ocean and atmosphere.....	236
Abstract.....	236
6.1. Introduction.....	237
6.2. Methods.....	240
6.3. Results.....	242
6.4. Discussion.....	249
6.5. Conclusions.....	257
Tables.....	260
Figures.....	262
References.....	269
Appendix to Chapter 6.....	273
Chapter 7: Depression and collapse: Selenium isotope ratios and biological productivity in the late Permian.....	282
Abstract.....	282
7.1. Introduction.....	283
7.2. Geologic Setting.....	286
7.3. Methods.....	287
7.4. Results.....	292
7.5. Discussion.....	294
7.6. Conclusion.....	303
Tables.....	305
Figures.....	308
References.....	312
Chapter 8: A test of the nitrogen-limitation hypothesis for retarded eukaryote radiation: nitrogen isotopes across a Mesoproterozoic basinal profile.....	316
Abstract.....	316
8.1. Introduction.....	317
8.2. Geological setting.....	320
8.3. Sampling.....	322
8.4. Analytical methods.....	323
8.5. Results.....	326
8.6. Discussion.....	331
8.7. Conclusion.....	345
Tables.....	348

Figures.....	351
References.....	359
Chapter 9: Isotopic evidence for biological N₂ fixation by Mo-nitrogenase since 3.2 Gyr	367
Abstract.....	367
9.1. Introduction.....	368
9.2. Results.....	370
9.3. Discussion.....	370
9.4. Conclusion.....	373
Tables.....	375
Figures.....	376
References.....	378
Appendix to Chapter 9.....	380
Chapter 10: Nitrogen isotope evidence for alkaline lakes on late Archean continents	407
Abstract.....	407
10.1. Introduction.....	408
10.2. Results.....	411
10.3. Discussion.....	413
10.4. Conclusion.....	421
Tables.....	423
Figures.....	425
References.....	430
Appendix to Chapter 10.....	434
Conclusion	467

Introduction

Studying the history of life on Earth is an important task for astrobiologists, because the answers to the questions of how life started and radiated on this planet, how it evolved, and why it survived for about four billion years may also apply to other worlds. Recent advances in planetary science and astronomy, including the recent Kepler mission, have revealed that terrestrial planets are relatively common in the galaxy and that the major volatiles that contribute to life as we know it, *i.e.* H₂O, CO₂ and others, are widespread in planetary atmospheres. It is therefore conceivable that other biospheres exist that are carbon-based and use water as a solvent. If so, then the strategy of using redox chemistry to gain energy from the environment for growth may also be widespread. All life on Earth uses some type of redox reactions in its metabolism. Unlike other forms of energy, redox chemistry has the advantage that through catalysis it can be focused at a molecular level for the formation or breakage of particular chemical bonds. Many major elements are redox active within the stability field of liquid water, including sulfur, nitrogen, carbon, and iron. Furthermore, redox gradients can be created by fundamental planetary processes such as volcanism and solar radiation, making it almost certain that this form of energy is common on other planets. Hence if life exists elsewhere, then it seems plausible that its metabolism would be based on redox reactions between substrates provided from the environment. A planet's fluxes of electron donors and acceptors may thus place important constraints on the success of its biosphere. The Earth's surface has undergone major transformations in its redox state over the past four billion years, including irreversible changes and temporary fluctuations, with significant implications for the course of biological evolution. This makes the Earth an ideal target for astrobiologists to investigate how life exploits planetary redox gradients, how it modifies them, and how redox states can control the expansion of the

biosphere. In this study, I use new and established geochemical tools address the following general questions pertaining to redox-powered life:

1. Which forms of metabolism were present in early organisms when the planet was largely anoxic?

In Chapter 3, I use sulfur isotopes compiled from the literature to test if microbial sulfate reduction was widespread in the early Archean, long before the onset of oxidative weathering. In Chapter 9, I present new nitrogen isotope data from rocks of mid-Archean age to assess the possibility of Mo-catalyzed biological N₂ fixation long before marine Mo concentrations reached modern levels.

2. Did non-marine environments represent important habitats in early evolution?

Using a simple box model and sulfur concentrations in marine sediments as a proxy for the flux of sulfate into the ocean (Chapter 2), I attempt to reconstruct the expansion of microbial pyrite oxidation on land. The hypotheses developed in this work are further tested with new selenium isotope and abundance data from the mid-Archean to the modern (Chapters 4, 5 and 6). In Chapter 10, I present new nitrogen isotope measurements from lacustrine sediments and discuss the hypothesis that alkaline lakes may have been relatively common on Archean land surfaces, potentially providing important niches for prebiotic chemistry and early metabolism.

3. Did marine anoxia limit the radiation of complex life in the ocean or cause major mass extinctions?

I use nitrogen isotopes across a basinal profile in the Belt Supergroup to determine if nitrogen was a limiting nutrient in the Mesoproterozoic ocean that could have restricted the radiation of eukaryotic life (Chapter 8). The selenium data in Chapter 6 are used as an additional proxy for the oxygenation of the deep ocean between the Neoproterozoic and mid-Paleozoic. Furthermore,

I present selenium isotope data across the Permian-Triassic mass extinction to test if it coincided with an episode of marine anoxia or not (Chapter 7).

Chapters are organized by element from sulfur (Chapter 2 and 3) to selenium (Chapters 4, 5, 6 and 7) to nitrogen (Chapters 8, 9 and 10). If they are published, citations are provided in footnotes on the first page and author contributions listed at the end. While sulfur and nitrogen isotopes are established biogeochemical proxies, selenium isotopes are a relatively recent addition to the toolbox. The selenium-related chapters in my dissertation are thus more exploratory in nature with the goal of establishing which biotic and environmental parameters affect selenium isotopes in natural environments.

Overall, the results support early origins for major metabolic strategies, including sulfate reduction, nitrogen fixation, and possibly oxygenic photosynthesis, and they strengthen current views of major redox transitions in the Earth's atmosphere and ocean. This also corroborates the idea that non-marine habitats were significant for the early evolution of life and biogeochemical cycles. But before moving on to discussing my own geochemical analyses, I present the outcomes of a group project in Chapter 1. We discuss the origin of life on Earth in its global context as a template for assessing the possibility of independent origins elsewhere.

Chapter 1: Did life originate from a global chemical reactor?¹

Abstract

Many decades of experimental and theoretical research on the origin of life have yielded important discoveries regarding the chemical and physical conditions under which organic compounds can be synthesized and polymerized. However, such conditions often seem mutually exclusive, because they are rarely encountered in a single environmental setting. As such, no convincing models explain how living cells formed from abiotic constituents. Here, we propose a new approach that considers the origin of life within the global context of the Hadean Earth. We review previous ideas and synthesize them in four central hypotheses: (1) Multiple microenvironments contributed to the building blocks of life, and these niches were not necessarily inhabitable by the first organisms; (2) Mineral catalysts were the backbone of prebiotic reaction networks that led to modern metabolism; (3) Multiple local and global transport processes were essential for linking reactions occurring in separate locations; (4) Global diversity and local selection of reactants and products provided mechanisms for the generation of most of the diverse building blocks necessary for life.

We conclude that no single environmental setting can offer enough chemical and physical diversity for life to originate. Instead, any plausible model for the origin of life must acknowledge the geological complexity and diversity of the Hadean Earth. Future research may therefore benefit from identifying further linkages between organic precursors, minerals, and fluids in various environmental contexts.

¹ Co-authors: Rika E. Anderson, Jeff S. Bowman, William J. Brazelton, Jesse Colangelo-Lillis, Aaron D. Goldman, Sanjoy M. Som, John A. Baross. Published in: *Geobiology* (2013) v. 11 (2), pp. 101-126. All authors contributed equally to this work.

1.1. Introduction

The settings for the origin of life are unknown and greatly debated. Historically, these debates have revolved around what requirements for the origin of life are met – or not met – by a particular environmental setting. In particular, disagreements over which environmental factors are best suited for the synthesis of individual organic polymers have dominated origin of life research. This focus on synthesis has been wildly successful in terms of discovering properties of biochemical molecules, but it offers little insight into the conditions necessary to achieve all of the properties essential to a self-replicating entity that is capable of Darwinian evolution.

A wide chasm exists between what is known about the mechanisms involved in the synthesis of organic compounds and an understanding of the sequence of reactions leading to a proto-metabolic network or to replicating macromolecules, a situation exemplified by the RNA world hypothesis. One probable root cause of this disconnect is the notion, originally promulgated by Darwin and Haldane, that life arose in a single location – a “primordial soup” – which hosted a suite of different organic compounds. Modifications to this model include periods of evaporation to facilitate organic polymerization and the periodic input of high-energy processes such as lightning discharge, bolide impacts, radioactive decay and/or ultraviolet radiation. Although much useful information has resulted from this approach, including a broader understanding of mechanisms leading to the abiotic synthesis and polymerization of organic compounds, most research within the primordial soup model has been limited to laboratory experiments that do not yield sufficient insight into how natural processes on the early Earth would have resulted in the emergence of life.

As a way forward, we propose that environmental complexity was a necessary requirement for the origin of biological complexity. A large number of steps must have been

required to produce a living entity from organic precursors, suggesting that a wide range of environmental conditions must have been involved in the origin of life. Furthermore, life may not have been the product of a highly unlikely sequence of events, but instead the gradual outcome of a number of frequently occurring and inter-related processes. We illustrate our proposition by examining eight broad categories of possible environmental settings of the Hadean Earth (3.8 – 4.5 Ga) that could have contributed one or more of the “reaction-steps” leading to life. Although our limited knowledge of the Hadean Earth is a clear impediment to this line of research, there are enough features of the Hadean that are known or can be inferred to provide useful constraints to the origin of life. We also take advantage of the extensive literature that delineates the range of physical and chemical conditions that can result in the synthesis of organic precursors; these include conditions outside of the bounds for life as we know it. We thus uncouple the conditions that may have led to the origin of life from life itself. Four central hypotheses, derived from a synthesis of previous ideas, permeate our argument and are developed throughout the text:

Hypothesis 1: The various settings that contributed to the origin of life were not necessarily coupled in time or space to the settings that supported the growth of the earliest microbial communities.

Hypothesis 2: Mineral catalysis provided high concentrations of organic compounds important for the synthesis of macromolecules and high-energy compounds, such as acetyl-CoA, through “proto-metabolic” networks that necessitated catalysis by multiple minerals.

Hypothesis 3: Dynamic surface and subsurface circulation systems were necessary to transport various organic compounds synthesized under specific sets of conditions to other environments for further reactions. This resulted in a greater diversity of organic compounds and prebiotic reaction networks. Included in these different environmental settings was a narrow subset of environmental conditions that spawned and maintained early life forms.

Hypothesis 4: Global diversity and local scarcity of reactants and products were key for prebiotic chemistry. Each unique environmental setting in the Hadean would have favored the production of a few important compounds, and mixing processes on large and small scales allowed the products of each setting to interact with each other (Figure 1.1). Thus on a global scale, the great variety of ingredients required for life could be generated and combined in biochemically more productive ways than it would be possible in a primordial soup at one location.

One advantage of a single setting for the origin of life may be the close spatial proximity of different reactions. However, the possibility of dilution does not make it implausible to envision the origin of life as a global phenomenon. Firstly, under anoxic conditions and prior to the evolution of heterotrophy organic matter would presumably have had a much longer lifetime in the ocean, allowing compounds to accumulate to high concentrations (e.g. Lasaga *et al.*, 1971; Bada, 2004). Secondly, numerous mechanisms in many environmental settings, in particular adsorption and encapsulation (Section 1.2.4), would have concentrated molecules from diluted fluids in a range of local environments. The characteristic sorption and diffusion properties of different molecules could have led to chemical selection (Sections 1.4.2 and 1.4.3), such that specific compounds may have become concentrated from a diverse mixture. Lastly, we argue

that the origin of life was a natural outgrowth of fundamental geological processes. Instead of constructing specialized scenarios that circumvent the risk of dilution for specific important compounds, it may therefore be more fruitful to identify how such compounds could have been generated from the most important geochemical processes on the early Earth.

We are not attempting to provide an answer to the question of which environment served as the setting in which the first living organism formed and thrived. Rather, we propose that future research in this field should consider the larger context of individual settings by treating them as potentially linked components of a global chemical reactor. To this end, this review paper seeks to synthesize previous work on potential Hadean environments in which important prebiotic reactions may have occurred in order to place the origin of life within a global context, with the aim of presenting a fresh perspective on the origin of life and, moreover, evaluating the possibility of a second independent origin of life on another planetary body.

1.2. Prerequisites for the origin of life

While there is active debate regarding the precise requirements for the existence of life, it is generally agreed that the prerequisites for the origin of life include a source of energy, a source of carbon, and a means of concentration and catalysis. What follows is a necessarily brief overview of each of these prerequisites and how they might have been provided on the Hadean Earth. For more exhaustive discussions of these topics, see Hazen (2012), Deamer (2011), Hazen (2005), Morowitz (2004), Lahav (1999), and De Duve (1995).

1.2.1. Energy

We define energy as a collective term for all the drivers of physical and chemical processes that were necessary for prebiotic chemical reactions to proceed (e.g. Deamer (2007) and Deamer & Weber (2010)) Of the various forms of energy that were required for the origin of life, metabolic energy is the only *internal* energy source (Deamer (2007)); *i.e.* it is electrochemical energy carried within high-energy molecules like ATP that can be stored inside a cell. Modern life harnesses electrochemical energy by coupling reduced and oxidized chemicals obtained from the environment, and it may be expected that the precursors to modern metabolic cycles operated on the same principle. We therefore expect that a redox gradient would have been important in an origin of life setting to establish proto-metabolism (Section 1.4.3). Maintaining a redox gradient over geologically significant periods of time requires continuous sources of *external* energy, and the two largest and most ubiquitous sources of energy on Earth are solar radiation and geothermal heat.

Solar energy can create species useful for modern life and potentially also for prebiotic chemistry by photolysis of atmospheric constituents. For example, UV photolysis of volcanogenic SO₂ and H₂S is thought to have produced a mixture of SO₂, H₂S, S⁰ and H₂SO₄ (Farquhar *et al.*, 2001; Ono *et al.*, 2003), which could have acted as important oxidation or reduction species for protometabolisms. Another photolytic product may have been Fe³⁺ produced from Fe²⁺ in the surface ocean (Anbar & Holland, 1992). Nitrate (NO₃⁻) may have been produced during lightning events (reviewed in Ducluzeau *et al.*, 2008) and served as an electron acceptor or as a source of fixed nitrogen.

Geothermal energy, which drives mantle convection, plate tectonics, and hydrothermal circulation of water through the crust, can also be translated into electrochemical energy because the process of planetary differentiation has set up a redox gradient between water and ferrous

iron contained in oceanic crust. Consequently, aqueous alteration of oceanic crust results in the production of molecular hydrogen (H_2) and oxidized (ferric) iron (McCammon, 2005; Hellevang, 2008). H_2 can in turn serve as an electron donor to volcanogenic CO_2 or to other oxidants produced by photolysis or lightning. A type of aqueous alteration of oceanic crust known as serpentinization can provide extremely high concentrations of H_2 in hydrothermal fluids (Section 1.3.7). The extent to which H_2 in the Hadean would have vented from chimney-like structures with highly focused flow (resulting in high local H_2 concentrations), versus venting from diffuse flow systems (H_2 distributed over a larger area, resulting in lower local concentrations), remains poorly constrained. Massive quantities of H_2 (up to 50 bars) were also generated during the moon-forming impact at 4.5 Ga by oxidation of ferrous iron (Fe^{2+}) and platinum group elements in the mantle (Sleep *et al.*, 2004). After the moon-forming impact, global atmospheric H_2 levels decreased due to loss to space, but the timing and rates of this process are unclear (Tian *et al.*, 2005; Catling, 2006; Tian *et al.*, 2006). On the anoxic Hadean Earth, H_2 presumably had a significantly longer lifetime and was therefore probably ubiquitous in most environments.

Protometabolic cycles and early metabolisms would have depended upon the presence of a continuously produced redox couple. While photolysis and lightning could have produced locally high concentrations of reactive compounds that fueled important reactions in environmental niches, geothermally produced H_2 and volcanogenic CO_2 in particular may have been the drivers of many prebiotic and early biotic reactions on a global scale. One advantage of the $H_2 + CO_2$ redox couple as a source of electrochemical energy is that both species are volatile, sufficiently water-soluble, and can easily diffuse into organic or inorganic compartments because they are uncharged. Consequently, this source of electrochemical energy would likely have been abundant in most or all environmental settings on the Hadean Earth.

1.2.2. Synthesis of organic carbon compounds

Initial stages in the origin of life likely required a continuous source of organic compounds to act as precursors to important biological polymers. Those prebiotic monomers had to be activated, *e.g.* by loss of water molecules or by addition of phosphate, for polymerization to be thermodynamically feasible (Deamer & Weber, 2010). Broadly speaking, three prebiotic sources of organic compounds are most commonly described: electrical discharge or ultraviolet radiation; input from meteorites, particularly carbonaceous chondrites; and reactions associated with sites of active serpentinization at hydrothermal vents (Charlou *et al.*, 1998).

The basic building blocks of life as we know it consist primarily of nucleotides, peptides, lipids, and carbohydrates. Mechanisms have been found that can produce subsets of all those basic building blocks (Table 1.1). There is no consensus on how prevalent those mechanisms would have been on the Hadean Earth, but, as discussed below, they do not mutually exclude each other on a global scale. It is therefore plausible that many of the building blocks formed through different mechanisms, and interacted with each other in prebiotic reaction networks.

One often-discussed and potential source of organic compounds is meteorites, including interplanetary dust, which may have delivered organic material (Chyba & Sagan, 1992; Pizzarello & Shock, 2010; Schmitt-Kopplin *et al.*, 2010) and phosphorus (Pasek & Lauretta, 2005) or produced HCN in the atmosphere by shock heating (Chyba & Sagan, 1992). Experimental work suggests that under UV radiation, biological co-factors (Meierhenrich *et al.*, 2005) and non-racemic amino acids (de Marcellus *et al.*, 2011) can be produced in interstellar ices, which may have been delivered to Earth through comet impacts.

Given the pervasiveness of H₂ and CO₂ on the Hadean Earth (Section 1.2.1), reactions between these two compounds may have occurred in multiple environmental settings and produced myriads of organic compounds. So far, this process has mostly been studied in the context of serpentinization-driven hydrothermal systems, where H₂ is most abundant today (Proskurowski *et al.*, 2008). The power of H₂ to drive biochemical synthesis (Morita, 1999; Nealson *et al.*, 2005) is most evident in the persistence of dense biofilm communities around modern sites of active H₂-production such as the Lost City vent field. However, H₂ also plays an important role in other modern ecosystems because H₂-transfer is at the heart of almost every biochemical reduction or oxidation reaction (Nealson *et al.*, 2005). It is therefore conceivable that H₂ fueled many prebiotic synthesis reactions by coupling not only with CO₂ but also with organic substrates.

1.2.3. Catalysis

Catalysts increase the rate of chemical reactions by reducing the activation energy of chemical reactions, and can serve as a means of “selecting” favored products over others (Copley *et al.*, 2007). While proteins serve as the primary catalysts in modern biochemistry (enzymes), coding for complex proteins would not have been available in prebiotic chemistry. Instead, minerals are commonly invoked as non-biological catalysts for life’s origin. The abundance of specific minerals in the Hadean was controlled by geological processes and the redox state of the Earth’s surface (Figure 1.2; see Hazen *et al.* (2008) and Papineau (2010) for a more detailed review on this topic). A diversity of micro-environments with different physicochemical characteristics and mineral assemblages likely increased the diversity of catalyzed primordial reactions.

We can infer which minerals are the most likely to have been important catalysts in the prebiotic Earth through both top-down and bottom-up approaches. For example, the only carbon fixation pathway that is present in both archaea and anaerobic bacteria, the reductive acetyl-CoA, or Wood-Ljungdahl, pathway (Berg *et al.*, 2010) (Figure 1.3), involves enzymes with catalytic centers that are remarkably similar to metal sulfide minerals (Russell & Martin, 2004). The minerals alone, without the organic components, can successfully catalyze at least some of the steps in the reductive acetyl-CoA pathway (Huber & Wächtershäuser, 1997; Cody *et al.*, 2000; Cody *et al.*, 2004). This pathway has also been proposed as the most ancient carbon fixation pathway because of its simplicity (Fuchs & Stupperich, 1985; Berg *et al.*, 2010; Fuchs, 2011) and the phylogeny of its proteins (Peretó *et al.*, 1999). Most organisms that utilize this pathway today are fueled by the $H_2 + CO_2$ redox couple, and the exceptions almost certainly represent later evolutionary innovations (Baptiste *et al.*, 2005). Hydrogenases, which catalyze the uptake and production of H_2 , also contain iron and/or nickel at their catalytic sites. Both iron and nickel are commonly associated with serpentinites (Sleep *et al.*, 2004). Hence, this is consistent with the idea that early biochemical pathways were driven by H_2 , and that the first biochemical pathways evolved as mimicry of already operating geochemical reactions (Cody & Scott, 2007). The distribution and availability of certain mineral catalysts within different environments (Section 1.3) may thus help constrain the extent to which different environmental settings may have contributed to certain steps in the origin of life (further discussed in Section 1.5).

1.2.4. Concentration

Mechanisms of concentration increase the overall rates of chemical reactions. Moreover, concentration of selected compounds also increases the probability of such reactions that are

otherwise unreactive in dilute media. Concentration mechanisms in pore spaces, on mineral surfaces, or within non-biogenic lipid membranes could also have acted as prebiotic forms of encapsulation which prevented the diffusion of biochemically useful products or even provided the grounds for genetic heredity (Maynard-Smith & Szathmary, 1997; Sowerby *et al.*, 2001; Sowerby *et al.*, 2002).

Modern life utilizes lipid membranes as encapsulation mechanisms to prevent diffusion of cellular components, to generate concentration gradients, and to maintain a unit of heredity. Many researchers have focused on possible mechanisms for the formation of early lipid membranes, such as micelles (Deamer *et al.*, 2002). There is dispute, however, regarding how early such encapsulating membranes would have played a role in the evolution of life; some argue that encapsulating membranes must have been an early feature of life, while others argue that it would have been a much later development. The latter point of view suggests that the earliest stages of life's formation may have involved encapsulation through inorganic micro-compartments such as fluid inclusions, vesicles, porous sediments and hydrothermal chimneys or sea ice brine pockets (Section 1.3). If inorganic micro-compartments served as concentration points for prebiotic molecules, then it is possible that lipid membranes only became important at later stages in the origin and evolution of biochemicals (Koonin & Martin, 2005). However, it is also conceivable that non-biological lipid membranes played a more active role by transporting prebiotic compounds between different environmental settings.

Our current state of knowledge does not allow us to constrain the prerequisites for the origin of life well enough to identify a single environmental setting as the location where life originated. This may change with further experimental research, but it may also indicate that more than one setting was necessary to provide all the energy sources, organic precursors,

catalysts and concentration mechanisms. If so, then life was only able to originate on the Hadean Earth because the unique physical, geological and chemical attributes of individual micro-environments allowed for a greater diversity of reactions to occur simultaneously (Figure 1.1). Through global mixing processes, these elements were able to interact and create each of the successive stages for life's origin.

1.3. Hadean micro-environments and their potential role in the origin of life

It is almost certain that a great number of inter-connected micro-environments existed on the Hadean Earth soon after the formation of oceans. The age and extent of oceans on Earth are unknown, but Hadean zircons provide geochemical evidence for liquid water near the Earth's surface since 4.4 Ga (Mojzsis *et al.*, 2001; Wilde *et al.*, 2001; Hoskin, 2005). Geological evidence for life extends back to 3.5 billion years (Ga), possibly 3.8 Ga (reviewed in Buick, 2007); hence the origin of life most likely happened in the early Archean (3.5-3.8 Ga) or Hadean (3.8-4.5 Ga) eon. Although the scarcity of direct evidence preserved in the rock record makes it challenging to draw detailed conclusions about the micro-environments present at that time, careful extrapolations and modeling results allow us to identify eight broad categories of settings (Figure 1.4) that may have existed and played a role in the origin of life. For a more detailed review of Hadean and Archean geology refer to Rollinson (2007) and references therein.

1.3.1. The atmosphere

The Earth's atmosphere (Figure 1.4a) has been prescribed a pivotal role in the creation of life's building blocks since the experiments of Urey and Miller reported in 1953. The experiments demonstrated the production of biologically important organic compounds

(including amino acids) by passing electric charge through a mixture of gases which were at the time considered to be the components of Earth's early, reducing atmosphere (H_2O , CH_4 , H_2 and NH_3) (Miller, 1953). However, the redox state of the Hadean atmosphere is not well constrained, as it depends (among other factors) on the escape rate of hydrogen, which remains uncertain. Results of more recent models of the early atmosphere range from highly reducing with as much as 30% H_2 (Tian *et al.*, 2005; but see also Catling, 2006; Tian *et al.*, 2006) to nearly neutral, dominated by N_2 , CO_2 , CO , and H_2O , with lesser amounts of H_2 , SO_2 , CH_4 and H_2S (Kasting & Catling, 2003). Under neutral conditions the synthesis of organic compounds by electric discharge is much less efficient (Schlesinger & Miller, 1983). Nevertheless, even in a neutral atmosphere a wide array of amino acids could still have been produced by lightning in volcanic eruption clouds (Johnson *et al.*, 2008), which may have been frequent on the Hadean Earth.

The Hadean atmosphere could also have hosted particulate matter with catalytic surfaces. On the modern Earth, natural dust particles are largely derived from continental erosion. On the early Earth that fraction may have been smaller if dry land masses were less extensive. Instead, volcanic ash particles may have been more abundant relative to modern Earth. As today, wind churning the ocean surface would have created seawater aerosols. Marine aerosols, volcanic ash, and dust particles could have acted as a continually recycled population of reaction chambers and catalytic surfaces, experiencing variable degrees of radiation, temperature and water activity during vertical and horizontal atmospheric transport (Dobson *et al.*, 2000; Tuck, 2002). In particular, dehydration of amino acids during atmospheric transport has been suggested as a mechanism for activation and polymerization (Tuck, 2002). Additionally, amphiphiles (organic molecules with both hydrophilic and lipophilic properties) including stearic and oleic acids have been shown to form exterior films on marine aerosols that could have served as proto-

membranes in prebiotic chemistry (Tervahattu *et al.*, 2002; Donaldson *et al.*, 2004). The source alkanes for these amphiphiles on the early Earth may have been derived from the reaction of water with iron carbide derived from Earth's interior or perhaps from iron-rich meteorites where such carbides exist (Marquez *et al.*, 1996). Thus, the Hadean atmosphere likely created a large number of concentration points for potential prebiotic organic synthesis reactions.

Another important role of the modern atmosphere is to protect life in surface environments from solar UV radiation. In the Hadean, the Sun's output in the extreme UV range was stronger than it is today (Cockell, 2000), while at the same time the Earth was lacking a protective ozone layer (reviewed in Catling & Kasting, 2007). It is possible that a hydrocarbon haze acted as a UV shield transparent to visible light (Wolf & Toon, 2010), but in the absence of a UV shield, solar UV radiation could have had both positive and negative impacts on prebiotic chemical reactions in the lower atmosphere and in surface-exposed settings, through either activating or destroying prebiotic molecules

1.3.2. Water bodies on land

Continental crust may have appeared as early as 4.35 Ga, as suggested by isotopic evidence from detrital zircons (Harrison *et al.*, 2008), but this interpretation is still debated (e.g. Pietranik *et al.*, 2008; Kemp *et al.*, 2010). Models for the evolution of continental crust volume show a possible range from > 50 % of today's volume at 3.8 Ga (e.g. Brown, 1979; Armstrong, 1981) to < 5 % (e.g. Veizer & Jansen, 1979; McLennan & Taylor, 1982). Most authors favor the idea that continental crust was not widespread during the Hadean; however, that does not preclude the presence of land masses exposed to the atmosphere. Islands could have been created by hotspot volcanism, by crustal expansion during water-rock interaction (serpentinization,

Section 1.3.7) or by tectonic uplift. Hence non-marine water bodies including lakes, pore waters in vesicular volcanic rocks or in sediments, and groundwater contained in subsurface aquifers (Figure 1.4b) were almost certainly available to host prebiotic reactions that required salt-free conditions.

Due to the great variety of factors influencing the chemistry and hydrology of terrestrial water bodies, it is difficult to assign them a general role in the origin of life. Cyclical evaporation of fluids exposed to the atmosphere could have concentrated the water content and perhaps facilitated dehydration, activation and polymerization of organic monomers (e.g. Rode *et al.*, 1999, Section 1.2.2); . Terrestrial hot springs may have created strong gradients in temperature, metal availability, and other chemical parameters (Mulkidjanian *et al.*, 2012). Atmospheric reaction products in particular would have been concentrated in these exposed environments on land where they could have undergone further reactions. Furthermore, clay minerals produced during weathering of the crust could have provided sites for adsorption and polymerization of organic monomers (Meng *et al.*, 2004; Ferris, 2005a). Continental groundwater would have differed from fluids circulating through oceanic crust (Section 1.3.8) because Hadean protocontinents likely harbored a greater variety of minerals created by felsic and mafic magmatism and metamorphic processes (Figure 1.2), thus perhaps allowing a wider range of mineral-catalyzed prebiotic reactions to occur. The maximum depth of groundwater flow systems is mostly controlled by the topography of land masses, but it can also be limited by subsurface brines (Phillips & Castro, 2004). The interface between such brines and meteoric groundwater could have established strong gradients in salinity and pH with possibly important implications for prebiotic chemistry (Section 1.4.3). Similarly, discharge of groundwater along continental

margins would have mixed any prebiotic reactants and products contained in groundwater with those contained in coastal and marine waters.

1.3.3. Beaches

The location of beaches (Figure 1.4c) at the interface between land, seawater, and air may have given them a prominent role in the origin of life because it would have allowed them to concentrate and process a huge variety of reactants transported by rivers, the ocean and the atmosphere. Furthermore, beaches have four characteristics advantageous for prebiotic organic synthesis: accumulation of heavy detrital minerals, evaporation-concentration cycles, a gradient in water activity, and high porosity.

In the Hadean beach sand around volcanic islands may have been rich in mafic minerals such as olivine or pyroxene. Along the shores of proto-continent heavy detrital minerals could have included uraninite and monazite (Rasmussen & Buick, 1999). Radioactive radiation of detrital uraninite has been proposed as a source of heat and as a catalyst of organic reactions through the formation of radicals (Parnell, 2004; Adam, 2007). It may also have liberated phosphate through bombardment of detrital monazite (Adam, 2007).

Evaporation-concentration cycles in tidal pools on beaches would have promoted dehydration reactions leading to biomolecule polymerization. Furthermore, evaporation of seawater would have led to the precipitation of evaporite minerals, especially if the salinity of the ocean was higher than it is today (Knauth, 2005). Evaporites could have included halite, carbonate or nahcolite and possibly gypsum (although prebiotic sulfate was likely rare) (Boulter & Glover, 1986; Buick & Dunlop, 1990; Lowe & Worrell, 1999; Sugitani *et al.*, 2003), and they may have offered a unique set of catalytic surfaces or concentration points within fluid

inclusions. Interestingly, calcite has crystallographic features that could have led to chiral selection (Hazen *et al.*, 2001; Hazen & Sholl, 2003). Beaches may also have been a site of accumulation of evaporitic borate minerals, for which there is tentative isotopic evidence back to the Archean (Grew *et al.*, 2011). Borate is known to stabilize ribose, the backbone of RNA, but it is not clear whether the tectonic processes necessary for accumulation of boron would have been active early enough to play an important role in prebiotic chemistry (Benner *et al.*, 2010; Grew *et al.*, 2011).

The high porosity of beaches enables fluid exchange between the permanently flooded (phreatic) zone and the overlying (vadose) zone and creates a gradient in moisture, temperature and light intensity. Fluid exchange along those gradients by convection (Section 1.4.1.4) and chromatographic separation of compounds (discussed by Cleaves *et al.*, 2012) could have promoted a greater variety of prebiotic reaction products.

1.3.4. Sea-ice

Although the young Sun was 25-35% fainter in the early history of the Solar System (Gough, 1981), a number of mechanisms have been suggested that could have led to a globally warm climate (Kasting, 2010). Other models, however, suggest that early oceans may have been covered by thin ice, at least locally (reviewed in Zahnle *et al.*, 2010), and especially if latitudinal temperature gradients were stronger (Bada *et al.*, 1994) (Section 1.4.1.1). Modern sea ice commonly incorporates organic compounds, either sorbed to particles entrained in the ice matrix, sorbed to the ice itself, or in solution (Pfirman *et al.*, 1995; Wania *et al.*, 1998). Today, those compounds include formaldehyde (Barret *et al.*, 2009), methane, and various biogenic sulfur species (Thomas & Dieckmann, 2002). In an abiotic Hadean ocean, sea ice would have captured

volatiles and organics produced on the seafloor or in the atmosphere and encapsulated them for reaction with other chemical species (Figure 1.4d).

As ice freezes, it partitions into a solid and liquid phase with salt and other solutes being rejected from the solid into the liquid phase. The volume fraction of the liquid phase relative to the solid phase is a function of temperature and bulk salinity of the ice matrix (Cox & Weeks, 1983; Pringle *et al.*, 2009). Lowering the salinity or temperature will increase the proportion of solid ice crystals relative to liquid brine - a process called *eutectic freezing*. The effect of eutectic freezing on solutes, including organics, contained within ice brines is to increase their concentration as temperatures decrease. Because of this concentrating effect and because the low temperature of sea-ice environments slows down the degradation of reaction products, ice environments have been cited as a potentially significant site for the production of prebiotic molecules (Levy *et al.*, 2000; Kanavarioti *et al.*, 2001; Miyakawa *et al.*, 2002a; Miyakawa *et al.*, 2002b; Price, 2007; Pierre-Alain & Hans, 2008; Price, 2009) (Supplementary Table A1.1).

Furthermore, ice provides spatial and temporal gradients of pH, water activity, and temperature. As these parameters strongly affect the behavior of organic and inorganic chemical species, the presence of gradients will increase the number of potential chemical reactions, some of which could be important for the origin of life. For example, the precipitation of calcite (CaCO_3) at -2.1°C will result in the loss of the carbon buffering system in seawater and a decrease in pH. In a similar manner, salts have an effect on water activity; salts with low eutectic points interact more strongly with water molecules and impart a stronger influence on water activity. It is difficult to model or empirically derive the precipitation of specific salts as the exact starting composition of Hadean seawater is unknown. However, temperature variations over diurnal or seasonal cycles would have led to changes in brine composition over time, thus

creating a variety of chemical micro-environments within the ice. Additionally, temperature also controls horizontal and vertical gradients in pH and water activity within ice. A vertical gradient is created due to the difference in temperature between the upper (atmospheric) and lower (seawater) interfaces. Horizontal temperature gradients can be established by the presence of low albedo material such as volcanic ash or cryoconite (windblown dust) deposited on the surface (Wharton *et al.*, 1985). Under exposure to sunlight this detrital material emits in the infrared, warming the surrounding ice, and in extreme cases, creating melt ponds. On the contemporary Earth, cryoconite holes host distinct microbial ecosystems (Christner *et al.*, 2003); on the prebiotic Earth they were likely to have hosted distinct chemical environments.

1.3.5. Sea-surface microlayer

The sea surface microlayer (SSML, Figure 1.4e) describes the interface between the ocean and the atmosphere, and is operationally defined as the upper 1000 μm of the ocean (Liss & Duce, 1997). The SSML may have been a crucial setting for prebiotic synthesis or polymerization reactions due to an abundance of both organic material and external energy sources. Attenuation of UV light in the water column results in a comparatively high abundance of photons at the SSML, and while often associated with its destructive potential for biomolecules, a variety of biochemically useful molecules have been synthesized under UV light, including deoxyribose, ribose, amino acids, aldehydes, and uracil (Shigemasa *et al.*, 1977; Folsome *et al.*, 1983; Pestunova *et al.*, 2005; Nuevo *et al.*, 2009), perhaps creating an oil slick at the sea surface (Lasaga *et al.*, 1971; Nilson, 2002). The SSML is rich in organic and inorganic materials collected from both the atmosphere and ocean, held in place by buoyancy, electrostatic attraction, physical or chemical adsorption, and surface tension (Hunter & Liss, 1977; Sieburth,

1983; Liss & Duce, 1997). Material from the water column is transported to the sea surface via a number of processes including diffusion, turbulent mixing, bubble and particle transport, and large scale circulation driven by wind (Langmuir circulation), tidal forces, and internal waves (Frew, 1997).

In addition to dissolved molecules, suspended particulates composed of volcanic ash or pumice could have accumulated in slick zones within the SSML (Section 1.4.1.2) (cf. Brasier *et al.*, 2011). Volcanic ash alters to zeolite, which has hydrophobic surfaces that provide protected sorption sites for the polymerization of water-insoluble organic monomers. Pumice and volcanic ash can release phosphorus (Timperley, 1983; Frogner *et al.*, 2001), one of the cardinal elements required for life. Furthermore, the high porosity of pumice allows it to entrain and concentrate organic material, and because it floats, pumice is conducive to distribution by ocean currents. Annual contemporary production of pumice is estimated at billions of cubic meters of drift pumice (Jokiel & Cox, 2003) from a variety of locales (Timperley, 1983; Timperley & Vigor-Brown, 1985; Felitsyn & Kirianov, 2002; Jokiel & Cox, 2003)

Products and reactants from the SSML would thus have been connected on timescales of seconds to days with the deep ocean via particle settling and with the atmosphere via ejection of bubbles and aerosols (Wallace Jr. & Duce, 1978).

1.3.6. Marine sediments

Organic and inorganic material produced at the surface of the ocean, on land or in the atmosphere eventually sinks down to the ocean floor. On the modern Earth, clay minerals with a high affinity for adsorption are responsible for 80% of organic net export from the surface ocean to the deep ocean (Kennedy *et al.*, 2002). On the prebiotic Earth, this mechanism probably

provided an efficient shuttle of monomers and polymers to deep marine sediments (Figure 1.4f). Modern marine pelagic sediments are largely dominated by biogenic minerals such as carbonates and silica (Li & Schoonmaker, 2003). In the absence of biogenic material and due to more volcanic activity in the Hadean, prebiotic marine sediments would have contained a larger proportion of metal-rich phases, mafic minerals, volcanic ash, pumice and their alteration products, in particular zeolites and smectite clays. A common constituent of parts of the Archean (3.5 – 3.8 Ga) marine sedimentary rock record are banded iron formations (BIFs) composed of iron oxides and silica (chert) (Nutman *et al.*, 1997). Although biological formation processes for BIFs are thought to be more plausible (Konhauser *et al.*, 2007), abiotic oxidation of ferrous iron by photolysis (Cairns-Smith, 1978; Braterman *et al.*, 1983; François, 1986) could have occurred on a smaller scale prior to life's origin. Iron oxides can act as catalysts for the formation of nucleobases (Shanker *et al.*, 2011).

Burial and diagenesis of sediment packages would have led to progressively increasing temperatures, as well as changes in pore fluid salinity and pH. This process may have created a great variety of prebiotic reactors enclosed in pore spaces with different physicochemical characteristics. However, fluid exchange across sediment packages would have been slow during quiescent periods, as clays and abiotically precipitated silica likely formed impermeable layers (Hofmann & Bolhar, 2007). Nonetheless, flow paths could have been created during catastrophic events (Section 1.4.1.5) or mud volcanism (Mazzini, 2009) associated with methane gas production by serpentinization in the underlying oceanic crust (Section 1.3.7). Evidence for such activity in the Archean was recently discovered at Isua, Greenland (Pons *et al.*, 2011) Like terrestrial beach sediments, marine sediments may have concentrated organic compounds from a variety of environments, but the fluid residence time in marine sediment packages was likely

much greater. Hence, kinetically-inhibited reactions that can proceed in the absence of light and in saltwater may have occurred in this setting.

1.3.7. Hydrothermal systems

Marine hydrothermal systems (Figure 1.4g), generally found at mid-ocean ridges and along ridge flanks, occur where seawater interacts with crustal rock, creating strong gradients in temperature and chemical composition, while the altered crust becomes enriched in chemical precipitates and metamorphic minerals. The temperature of the early Earth's mantle was higher than it is today (Turcotte, 1980; Richter, 1988), and that extra heat was probably dissipated by longer mid-ocean ridges, or faster spreading, or a combination of both (e.g. Hargraves, 1986). Thus, hydrothermally active sites almost certainly existed in the Hadean ocean, and may have been a more common feature than they are today.

Today, known hydrothermal vent systems can be broadly classified into magma-driven, basalt-hosted systems and serpentinization-driven, peridotite-hosted systems. Some fields, such as Rainbow hydrothermal field on the Mid-Atlantic Ridge, which is magma-driven but peridotite-hosted, display characteristics of both (see below). Found at spreading centers or at seamounts where water is heated by rising magma, contemporary magma-driven systems have fluids reaching temperatures up to 400°C and acidities as low as pH 2. They are enriched in transition metals, sulfide, CO₂, methane and hydrogen, but depleted in magnesium relative to seawater (von Damm, 1990). In the Hadean, magma-driven hydrothermal systems may have contained more Fe²⁺ and H₂ than today due to the lack of oxidizing sulfate in anoxic seawater (Kump & Seyfried Jr, 2005). When hydrothermal fluid rises buoyantly through porous oceanic crust and mixes with cold alkaline seawater, minerals precipitate to form chimney structures.

Pyrite (FeS_2), a principal component of these vent structures, has been suggested as a catalyst for the production of several organic precursors for the origin of life because it can facilitate the fixation of CO or CO_2 to form simple organic molecules (Wächterhäuser, 1988a; Wächterhäuser, 1988b; Wächterhäuser, 1990; Cody, 2004).

In the absence of oxidative weathering on land, magma-driven hydrothermal vent systems were likely the major source of transition metals to the Hadean ocean. Transition metals, many of which are important components of enzymes (e.g. Schoepp-Cothenet *et al.*, 2012b), are easily scavenged by dissolved sulfide (Zerkle *et al.*, 2005); however, their solubility can be enhanced if they become complexed with organic molecules. On the modern Earth, organically complexed Fe and Cu derived from hydrothermal vents account for 9 % and 14 % of the deep-ocean reservoir of total Fe and Cu, respectively (Sander & Koschinsky, 2011). Hence, dissolved metals liberated in magma-driven hydrothermal vents in the Hadean could have been distributed around the globe as organic complexes.

In serpentinization-driven hydrothermal systems, in contrast – a geochemical reaction between seawater and olivine leading to the formation of magnetite and serpentine (serpentinization) – can alter fluid chemistry and provide heat for circulation even in the absence of magmatic heating. Serpentinization-driven hydrothermal systems are exemplified by the Lost City hydrothermal field (Kelley *et al.*, 2001; Kelley *et al.*, 2005). Hydrothermal fluids venting from Lost City chimneys do not exceed $\sim 90^\circ\text{C}$, and can reach a pH of 11, resulting in the precipitation of carbonate minerals.

Most significantly for the origin of life, serpentinization-associated Fischer-Tropsch type reactions also generate organic compounds (Holm & Charlou, 2001; McCollom & Seewald, 2007), including high levels of formate, (Lang *et al.*, 2010), methane (Proskurowski *et al.*, 2008),

hydrogen cyanide (Holm & Neubeck, 2009), and organic sulfur compounds (Heinen & Lauwers, 1996). Larger hydrocarbons containing at least four carbon atoms have been detected as well (Proskurowski *et al.*, 2008). If organic matter from other sources (Table 1.1) were introduced and concentrated in a serpentinizing environment, the highly reducing conditions could promote synthesis of longer carbon chains. In addition to organic carbon, hydrothermal vents may also have provided a source of fixed nitrogen (Brandes *et al.*, 2008; Holm & Neubeck, 2009) and phosphorus (Yamagata *et al.*, 1991) for the origin of life. Hennessey *et al.* (1992) showed that amino acids are produced in laboratory conditions meant to simulate hydrothermally altered submarine crust, producing a similar variety to those produced in Miller's electric spark experiments, but in significantly greater quantities (Hennessey *et al.*, 1992).

Perhaps more so than the presence of essential elements or polymerization, the greatest contribution of both magma-driven and serpentinization-driven hydrothermal systems to the origin of life may have been the formation of geological, physical, and chemical gradients as a result of the dynamic mixing and mineral formation associated with hydrothermal systems (Baross & Hoffman, 1985). Mixing of hydrothermal fluids with seawater both above and below the seafloor creates gradients in temperature, pH, chemical composition and redox state which may have allowed many important prebiotic reactions to occur in tandem (Koonin & Martin, 2005; Martin & Russell, 2007; Martin *et al.*, 2008; Lane *et al.*, 2010) before interacting and integrating into a larger reaction network. Moreover, phase separation into brine and vapor phases could contribute to the number of microenvironments in which reactions can occur, and perhaps allow prebiotic dehydration reactions to proceed within the brine phase.

It has been suggested that in the early Archean, hydrothermal fluids were overall more alkaline than today (Shibuya *et al.*, 2010). However, both hydrothermal sulfides (Vearncombe *et*

al., 1995; Huston *et al.*, 2002) and serpentinites (Blais & Auvray, 1990) have been detected in the Archean rock record, so both magma-driven and serpentinization-driven systems probably co-occurred during the Hadean. As mentioned above, the modern Rainbow hydrothermal field on the Mid-Atlantic Ridge has magmatically-heated, acidic hydrothermal fluids that circulate through ultramafic rocks and are enriched in both H₂ and various metals (Charlou *et al.*, 2002; Douville *et al.*, 2002). These mixing systems may have been ideal for prebiotic chemistry (Russell *et al.*, 2010).

1.3.8. Oceanic crust

Fluid circulation through oceanic crust is most vigorous near hydrothermal systems at mid-ocean ridge axes where the fluid residence time ranges from days to years (Johnson *et al.*, 2010). Although the volume of fluid flux dissipates with distance from the ridge axis, fluids continue to be exchanged in the upper crust for many millions of years, even where typical hydrothermal vent features have long disappeared, which creates a separate unique environment for prebiotic chemical reactions (Figure 1.4h). Overall, it has been estimated that at least 60% of the oceanic crust is hydrologically active (Edwards *et al.*, 2011). Recharge seems to occur at point sources such as unsedimented seamounts, and flow velocities are on the order of tens to hundreds of meters per year (Fisher & Becker, 2000; Spinelli & Fisher, 2004; Bekins *et al.*, 2007; Hutnak & Fisher, 2007; Hutnak *et al.*, 2008). Seamounts are abundant features on the modern Earth and may have been more prevalent in the Hadean. It therefore seems likely that this hydrological dynamism was an important feature of the ocean crust. While the Precambrian ocean was probably saturated with silica (Siever, 1992; Hofmann, 2011) and possibly carbonate, which may have lowered the porosity of the crust by precipitation, stronger tidal interaction and

more vigorous tectonism could have opened up fractures and thus sustained permeability. Today, the subsurface fluid flow connects mid-plate regions over a distance of many kilometers. On a more hydrothermally active Hadean planet, these flow paths could have allowed fluids from very different chemical and mineralogical regimes to mix and exchange reactants and products of prebiotic reactions.

Intra-crustal fluids are characterized by long residence times in contact with crustal minerals and by moderately warm temperatures, which today range from 10-30°C at the bottom of the marine sediment layer to 20-40°C at the bottom of the crustal high-porosity zone (Johnson & Pruis, 2003). Hence, these fluids are much warmer than the modern deep ocean (~2°C), allow more time for mineral-catalyzed reactions than vent systems, and are well protected from radiation compared to surface environments.

The minerals of greatest interest for the origin of life in the ocean crust may have been the alteration products of mafic minerals and basaltic glass, particularly clays and zeolites. Fluid flux through the crust occurs preferentially through connected channels, such as around breccia zones and pillow and flow boundaries (Fisher & Becker, 2000), so these regions would have been exposed to the greatest alteration. Experiments with basalt alteration reactions under elevated CO₂ concentrations, as might be expected in the Hadean, produced Ca-Mg-Fe carbonates, Fe-hydroxides, and Ca-Mg-Fe clays (Gysi & Stefansson, 2012), which could have participated in prebiotic synthesis or polymerization reactions. Moreover, the region for potential catalysis and polymerization in the deep subsurface is extensive, as evidenced by the presence of cryptoendolythic microbial communities supported by serpentinization by-products at depth (Hazen *et al.*, 2012; Menez *et al.*, 2012). Thus, the potential reaction space for prebiotic chemistry within the ocean crust is vast, hydrologically dynamic, and interconnected globally.

1.3.9. Where did life originate?

Table 1.2 compares the different settings based on their ability to fulfill the requirements for life (Section 1.2). Although some settings appear to have similar characteristics, they may differ markedly in their mineralogy and hydrology, and they have the potential to produce unique sets of organic compounds. Consequently, Table 1.2 does not show which single setting was best for the origin of life. On the contrary, it highlights that multiple settings were probably needed to satisfy all of the requirements. It is therefore unreasonable to favor a single setting for all steps in the origin of life.

A more parsimonious scenario is that the Hadean Earth hosted a diverse array of settings, each of which provided specific constraints for different chemical reactions (Figure 1.1). Only physical interaction and exchange of reactants and products among this variety of settings would have provided all the necessary ingredients for life.

The importance of mixing processes, however, does not imply that all of the important prebiotic reactions occurred in an “organic soup”, in which the biochemically productive reactions comprised only a tiny subset of all the reactions occurring. In contrast, we argue that the diversity of settings in the Hadean would have allowed different reactions to occur in different settings, and each setting would have provided constrained parameters to nurture sparse reaction networks that could conceivably generate specific modules of modern biochemistry (Morowitz & Smith, 2007; Trefil *et al.*, 2009). Thus, life was not a highly improbable outcome of a single experiment in an organic soup, but instead a gradual emergence from successful interactions among globally distributed, simultaneously forming reaction products.

1.4. Global transport and concentration processes on the Hadean Earth

If the origin of life was a global phenomenon that involved multiple environmental settings, then transport processes would have been critical for the exchange of prebiotic reactants and products. Here, we consider major mixing mechanisms on the Hadean Earth that may have served to connect crustal, sedimentary, marine, terrestrial and atmospheric sites where relevant prebiotic reactions could have occurred (Figure 1.5).

1.4.1. Local and global mixing processes

1.4.1.1. Atmospheric transport

The combination of incoming solar radiation coupled with planetary rotation governs atmospheric circulation. This results in atmospheric longitudinal bands (the Hadley, Ferrel, and polar cells) that dictate the transport of air masses and heat. Today, an air mass can circulate around the globe in two weeks (Jacob, 1999). Regional differences in air pressure further mix the atmosphere by causing winds and turbulence.

In the Hadean, the rotation period of the planet was most likely faster than it is today (Wahr, 1988; Williams, 2000). Extrapolating from Mid-Precambrian geological evidence (Williams, 2000) to about 4 Ga yields a Hadean rotation period of approximately 14 hours. Williams and Holloway (1982) predict that a doubling of today's rotation rate reduces the latitudinal extent of the Hadley cell from 30° to approximately 18°, while at the same time increases the number of longitudinal bands from three to four. Longitudinal winds would probably become more vigorous. Hence, if the Hadean Earth was rotating at nearly twice the modern rate, then the products of Miller-Urey-type reactions (Section 1.3.1) and liquid or particulate aerosols would have been efficiently transported around the planet in a direction

parallel to the equator. A faster rotation would also have led to a stronger Coriolis effect and thus limited the transport of air masses and material across lines of latitude. An additional consequence might have been a steeper latitudinal temperature gradient in the Hadean (Williams & Holloway, 1982), which may have led to a greater variety of environmental settings.

1.4.1.2. Ocean circulation

Atmospheric circulation cells coupled with landmass distribution are the dominant factor in surface ocean circulation. Wind, directionally controlled by the parameters of Hadley cell formation, imparts a stress on the sea surface. Coriolis forces and friction shift the direction of transport away from this stress. The speed of water transport at the sea surface is inversely proportional to the Coriolis force, and therefore to Earth's angular momentum (Ekman, 1905). On the contemporary Earth, this mechanism concentrates material floating on the sea surface within subtropical gyres, which have become infamous as "garbage patches" (Moore *et al.*, 2001). With a stronger Coriolis force (Section 1.4.1.1) this effect would probably have been even more pronounced in the Hadean ocean, thus allowing ice, pumice, organics within the SSML, and other debris floating in the Hadean surface ocean to become concentrated in small eddies. Large ocean gyres, however, were probably weaker, resulting in reduced latitudinal transport of water masses (Hunt, 1979).

The volume of continental mass present in the Hadean is still subject to debate (see Section 1.3.2), and these intervening landmasses would have had a strong influence on the nature of ocean circulation. Pope *et al.* (2012) recently estimated ocean volume in the early Archean to be up to 26% more voluminous than modern oceans. This may have effectively reduced the amount of terrestrial landmass available. If, however, continental crust was less extensive, a

more voluminous ocean may not necessarily have been deeper. It is therefore likely that volcanic islands were common and led to the formation of eddies and regional water mixing. Small eddies are so efficient at transport that the water parcels they contain maintain an identifiable heat signature weeks after formation, and marine organisms can be transported hundreds of kilometers (Olson & Backus, 1985). Furthermore, Adams *et al.* (2011) demonstrated that deep-reaching eddies can entrain material from deep-sea hydrothermal vents and transport it over several kilometers. Combined with stronger tidal pumping resulting from a much closer Moon, ocean currents may thus have efficiently transported materials along regional environmental gradients.

1.4.1.3. River runoff

Fluvial networks in the Hadean would have played the same central role as modern rivers in eroding and transporting continental material to the ocean. Rivers are also a medium for aqueous chemistry between material transported along the river bed and atmospheric constituents, brought into contact through turbulent mixing. The oxidation of soluble ferrous iron into insoluble ferric iron by entrained atmospheric oxygen is a modern example. However, a critical difference in the Hadean was the lack of vegetation, which likely led to fundamentally different river forms and dynamics compared with modern vegetated analogs. Most importantly, vegetation perturbs near-bank flow and binds sediments, which increases bank stability. Hence, it limits shear-stress and thus erosion of the bank walls (Miller, 2000). Field observations (Mackin, 1956), theoretical arguments (Miller, 2000) and flume experiments (Gran & Paola, 2001) consistently show that unvegetated channels are typically braided (exhibiting multiple channels that are separated by erodible bars), and the individual channels migrate laterally at

higher rates. This leads to a higher width-to-depth ratio in unvegetated river systems. It can therefore be assumed that Hadean terrain was scoured by rivers more frequently compared with modern floodplains. Atmospheric reaction products deposited on Hadean land surfaces thus had a higher probability of being transported to the ocean.

1.4.1.4. Convection in air and water masses

Convection caused by thermal or compositional gradients between fluids can contribute to mixing on a local or regional scale. Gradients are ubiquitous within and between many environmental settings on Earth, and buoyancy-driven convection results as long as the time-scales of gradient dissipation by diffusion are comparatively longer.

In prebiotic chemistry, convective transport may have played an important role because the cyclical nature of convection implies that compounds contained in convecting fluids are repeatedly exposed to various physicochemical conditions. This could have led to chemical selection and maturation of specific reaction products. Furthermore, small, closed convection cells within thin films of fluid may have encapsulated organic compounds that were dissolved in fluids or adsorbed to suspended solids. This concentrating mechanism may have been able to speed up the rate of chemical reactions.

The Hadean Earth probably had a variety of environments where convection occurred. For example, where tides transport seawater inland, the seawater will quickly sink into fresh-water saturated sediments. Convection driven by the density gradient between salt water and fresh water makes this mixing process more efficient than diffusion alone. Dissolved constituents can thus be exchanged rapidly between sediment packages protected from radiation and exposed tide pools (Smetacek *et al.*, 1976). Environments with thermal gradients could have produced

Rayleigh-Bénard convection cells (convection caused by temperature-dependent density gradients). Examples of such environments include the geothermal gradient in permeable oceanic crust and sediments, the interface between hydrothermal fluids and seawater, or diurnally heated air masses. Temperature may also facilitate convection in fluids by changing surface tension (Bénard-Marangoni convection).

Convection at the microscale can have a concentrating impact as well. Baaske *et al.* (2007) simulated molecular transport of nucleotides in elongated hydrothermal pores, and found that thermal convection along the pore combined with thermodiffusion across the pore resulted in accumulation of nucleotides. Budin *et al.* (2009) experimentally tested this concept with microcapillary diffusion columns, and experimentally verified accumulation of nucleotides, oligonucleotides, as well as fatty acids. Moreover, they observed that accumulation of fatty acids resulted in self-assembly of large vesicles containing encapsulated DNA, a potentially crucial first step in the origin of life.

1.4.1.5. Catastrophic events

Large-scale mixing of fluids and minerals likely occurred during catastrophic events such as asteroid and comet impacts, volcanic eruptions, or earthquakes, all of which may have resulted in slope failure (turbidites), tsunamis and crustal deformation.

The Earth was subject to heavy meteorite bombardment in the late Hadean up to 3.8 Ga (Kring & Cohen, 2002). Large impacts may have sterilized the planet (Sleep *et al.*, 1989) or restricted habitable environments to the deep subsurface (Abramov & Mojzsis, 2009). However, it is not certain whether life originated before, during, or after the time of potentially sterilizing impacts, or whether sterilizing impacts ever even occurred on Earth (Ryder, 2003). Smaller,

non-sterilizing impacts would have likely enhanced the exchange of material between sites by triggering ocean-wide tsunamis, crustal faulting and exposure of subsurface settings (Grieve, 1987; Pickering *et al.*, 1991; Dypvik & Jansa, 2003; Glikson, 2004).

Volcanic eruptions were probably more common on the Hadean Earth due to higher geothermal heat flux (Martin *et al.*, 2007). Subaerial explosive eruptions deliver ash particles and gases into the upper atmosphere, from where they are distributed around the globe (Section 1.4.1.1). After rainout, fine ash particles and vesicular material such as pumice can remain suspended in the ocean water column for long periods of time (Section 1.4.2). Hadean volcanoes therefore provided large amounts of material with catalytic surfaces to various environmental settings.

With frequently erupting volcanoes (Martin *et al.*, 2007) and with more tectonic activity (Hargraves, 1986), submarine seismic events were perhaps also more common in the Hadean than today. It has been hypothesized that seismicity could have supplied an entire subsurface ecosystem on the early Earth with enough nutrients for millions or billions of years (Sleep & Zoback, 2007). Moreover, micro-earthquakes, caused by tidal interaction between the Earth and the Moon (Tolstoy *et al.*, 2002), were probably stronger when the Moon was significantly closer than it is today (Williams, 2000). Hence, eruptions, seismicity and tides together would have caused frequent crustal fracturing and faulting, opening up new flow paths for fluid circulation into the subsurface. Even today lunar effects on hydrothermal flow patterns are measurable (Aliani *et al.*, 2004), and on a more volcanically and hydrothermally active early Earth, the Moon could have acted as an important pump for reagents and products traveling through crust and sediment packages.

1.4.2. Particles as stabilizing agents for transport

Some of the previously described settings naturally occurred in close spatial proximity such that degradation and dilution of reactants and products during transport from one setting to another would not have been significant. Other far apart settings interacted as a result of large-scale mixing processes as described above. In the anoxic Hadean ocean, oxidative degradation of organics during transport, the primary cause of organic destabilization today (Keil *et al.*, 2004), would have been negligible. Nevertheless, reactants and products were probably transported more efficiently and altered minimally between sites if they were either encapsulated in membranes, contained within porous particles, or adsorbed onto mineral surfaces. Many minerals such as smectite clays, feldspars, and iron oxides have been shown to stabilize numerous organic molecules, including organic acids, sugars, proteins and lipids, by adsorption (Sansone *et al.*, 1987; Ding & Henrichs, 2002; Keil *et al.*, 2004). In the modern ocean, these minerals are present on scales of milligrams per kg of seawater, and transported in enormous quantities, in the range of tens of megatons per yr (Mackenzie *et al.*, 1979; Summons, 1993; Li, 2000; Syvitski *et al.*, 2003). The surface area of erodible land masses in the Hadean is uncertain, but even if the flux of land-derived mineral grains to the ocean was smaller, it was perhaps compensated by larger quantities of volcanic ejecta. Sulfide particles produced by submarine hydrothermal processes (Trochine & Trefry, 1988) would also have been more stable in the anoxic Hadean ocean. Suspended particles that eventually settle on the seafloor or that become re-suspended during strong tidal or catastrophic events (Section 1.4.1.5) would thus have created a vertical shuttle of adsorbed material between the atmosphere, land masses, the sea surface, and the deep ocean. Lateral transport may also have been important in connecting different environments. In the

modern ocean, fine-grained particles can be transported laterally for hundreds of kilometers by ocean currents (Mollenhauer *et al.*, 2006).

Overall, the particulate load suspended in the atmosphere and ocean, in combination with mixing and transport processes could have served as important vectors for transport of prebiotic organic molecules and mineral catalysts between environmental settings.

1.4.3. The benefits of gradients in prebiotic chemistry

As discussed above, chemical and physical gradients likely stimulated fluid convection and exchange of material with important implications for prebiotic chemistry. However, gradients in temperature, pH, redox potential, light intensity, salinity, pressure, density, and chemical composition could also have played a more direct role in the production of complex biomolecules. The interaction of substrates and/or fluids far from equilibrium with each other is necessary to provide energy for organic synthesis (Shock & Schulte, 1998). Furthermore, the energy that is made available during convective mixing can be exploited by a greater diversity of reactions, including reaction networks, if gradients in multiple parameters are present. One excellent example of this multiplicity of gradients is found in mid-ocean ridge flanks (Section 1.3.7), where hydrothermal fluids mix with ambient seawater to create gradients of temperature, pH, redox potential, and concentrations of many inorganic and organic species (Baross & Hoffman, 1985; Shock & Schulte, 1998). Other examples include beaches, where meteoric fresh water mixes with seawater and where water activity decreases from the bottom towards the top of a sediment layer (Section 1.3.3); or sea ice, where seawater undergoes changes in salinity, pH and temperature during eutectic freezing (Section 1.3.4). In all cases, physical and chemical

gradients can progressively impact the thermodynamics of synthesis reactions and increase the number of possible reactants and products.

Redox gradients, which are exploited for metabolism in modern organisms, were likely particularly important in establishing proto-metabolism (Section 1.2.1). It seems plausible that living cells adopted this strategy from natural gradients that were harnessed by prebiotic chemistry (cf. Martin & Russell (2007)).

Pressure gradients are an understudied subject in prebiotic chemistry. Models suggest that at high pressure, such as in the deep ocean or within the ocean crust, the polarity of H₂O molecules decreases, which lowers the stability of ionic species in solution but increases the solubility of apolar organic molecules or gases (Shock, 1992; Bassez, 2003). High-pressure environments may therefore be conducive to otherwise thermodynamically unfeasible reactions.

Gradients could also have played an important role in mineral catalysis. The charge of both mineral surfaces and organic monomers changes as a function of pH (Stumm & Morgan, 1996; Williams & Frasca, 1999; Munsch *et al.*, 2001): low pH leads to more positive overall charge, but the pH creating a zero charge is specific to each organic compound and to each crystallographic face of a mineral. Consequently, mineral grains that are exposed to variable pH conditions, such as during convective or advective transport, could potentially adsorb and desorb different amino acids (Churchill *et al.*, 2004) or nucleotides (Ferris, 2005b) over time. This process could in turn have diversified organic polymers in prebiotic chemistry.

Once complex organic polymers had formed, transport along gradients could have affected their secondary and tertiary fold structure, allowing them to undergo a greater set of further reactions. For example, RNA in modern organisms requires specific concentrations of Mg or Ca ions in order to obtain a three-dimensional structure that makes it biochemically useful

(e.g. Dann *et al.*, 2007). In particular Mg has been shown to stabilize phosphate groups of nucleotides (Holm, 2012). If ionic concentrations change, the organic polymer rearranges into a different configuration. Some proteins change their fold structure with temperature and pressure (Heremans & Smeller, 1998; Serganov & Patel, 2007). Hence convective transport of organic polymers within or between different environments on the Hadean Earth would have caused those changes to occur repeatedly.

1.5. Merging bioinformatics with geochemistry

Embracing the immense diversity of niches and microenvironments is clearly important for a bottom-up approach to the origin of life. However, certain key processes are likely to have selectively produced some of the most important elements for the origin of life. One means by which we can identify those important processes is through a top-down perspective: those geochemical processes that have left an imprint in modern biochemistry must clearly have played a prominent role in prebiotic reaction networks.

Traditional top-down approaches to the origin of life often begin with the phylogenetic tree of all extant organisms. Universal phylogenetic analyses of conserved genes demonstrate that all known organisms evolved from a single ancestor or genetically continuous community (Cairns-Smith, 2003; Theobald, 2010) resulting in the “unity of biochemistry” of all extant organisms (Kluyver & Donker, 1959). By identifying the root of the phylogenetic tree, such studies also suggest that this Last Universal Common Ancestor (LUCA) lived in a hot environment (Schwartzmann & Lineweaver, 2004; Gaucher *et al.*, 2008), and had an autotrophic metabolism (Pace, 1997; Berg *et al.*, 2010). LUCA is now understood to have been a complex “organism” with a sophisticated genetic system (Harris *et al.*, 2003; Goldman *et al.*, 2010)

perhaps composed of an RNA genome (Glansdorff *et al.*, 2008) and metabolism (Caetano-Anolles *et al.*, 2007; Srinivasan & Morowitz, 2009). However, any extrapolation from these features of LUCA to a geochemical environment will only reflect the final stages in the origin of life, because the prebiotic world and modern world are separated by extensive geological and biological evolution. As such, no direct evidence linking modern life to any single prebiotic chemistry regime or origin of life setting currently exists. The development of LUCA probably took place well after the origin of life, and thus under completely different circumstances. Some have suggested that LUCA or the bacterial and archaeal last common ancestors were survivors of hot conditions, such as an impact event (Gogarten-Boekels *et al.*, 1995; Nisbet & Sleep, 2001). Therefore, traditional genome phylogeny can only give us limited information about the origin of life itself.

Nonetheless, prebiotic chemistry is thought to have left a distinct imprint on molecular biology, particularly in the form of metalloenzymes. Metalloenzymes are proteins that bind metal or metal compounds and coordinate the metal's regular catalysis (Karlin, 1993). The metal ion cofactors are known to greatly enhance enzyme catalytic potential and protein stability (Cvetkovic *et al.*, 2010). Of all characterized modern proteins, about a third require a metal cofactor for function (Rosenzweig, 2002). However, the evidence indicates that almost 50% of metalloproteins in *Pyrococcus furiosus* are uncharacterized and include metals not observed in characterized proteins from *P. furiosus* (Cvetkovic *et al.*, 2010). The importance of metal cofactors in modern biochemistry may thus be even greater than previously thought. A survey of metal usage in modern enzymes is summarized in Table 1.3. These enzymes are grouped in broad categories as designated by the Enzyme Commission. Oxidoreductases catalyze the transfer of hydrogen or oxygen atoms or electrons from one substance to another; transferases

transfer functional groups from one substance to another; hydrolases cleave chemical bonds through the formation of water; lyases add or remove functional groups without hydrolysis; isomerases bring about intramolecular rearrangement; and ligases use ATP to bring together new molecules. Interestingly, oxidoreductases, which catalyze key energy-generating reactions, exhibit the broadest range of metal cofactors. Although it is possible that some of these cofactors were later evolutionary innovations, perhaps triggered by the onset of oxidative weathering in the late Archean (e.g. Boyd *et al.*, 2011), the ability of metals to catalyze biochemically useful reactions suggests that they may also have played a prominent role in prebiotic chemistry (cf. Section 1.2.3, Figure 1.3). A model for the origin of life will therefore be more convincing if it includes geological processes that constantly replenish the supply of transition metals.

The results of protein evolution studies indicate that iron-, manganese-, cobalt-, nickel-, molybdenum-, and tungsten-containing proteins are ancient and probably existed at the time of LUCA (Dupont *et al.*, 2010; Schoepp-Cothenet *et al.*, 2012a; Schoepp-Cothenet *et al.*, 2012b). Members of the “Complex-Iron-Sulfur-Molybdoenzyme” (CISM) family have received particular attention since they appear to have been involved in the harvest of energy at the earliest stages of life (Schoepp-Cothenet *et al.*, 2012b). Tungsten can substitute for molybdenum in CISM (Schoepp-Cothenet *et al.*, 2012b) and is more soluble under reducing conditions (Schoepp-Cothenet *et al.*, 2012a). But because tungsten is much rarer than molybdenum in the Earth’s crust and mantle, the importance of CISM-like catalysts in prebiotic chemistry may indicate that at least some components of early metabolism evolved in geological settings that were particularly enriched in metals above crustal background, such as acidic hydrothermal systems (Section 1.3.7)

Enzymes other than oxidoreductases mostly involve major elements (Table 1.3) that could have been ubiquitous in all environmental settings. Cobalt is exceptional in that it seems to be the only minor element that is used in four of the six enzyme categories. Concentrations of cobalt are highest in primitive meteorites, moderately high in mafic rocks and relative low in felsic rocks (Carr & Turekian, 1961), which further indicates that leaching and complexation of metals from oceanic crust and perhaps also meteoritic sources were crucial processes for the origin and evolution of enzymes. It is thought that the earliest enzymes mimicked slow abiotic reactions that were already taking place (Lazcano & Miller, 1999). An example from laboratory experiments is the demonstration that Fe/Ni sulfides can catalyze the reduction of CO₂ to acetyl thioesters (Huber & Wächtershäuser, 1997). Thus, some metalloenzymes and their catalytic mechanisms may have originated during the transition from prebiotic chemistry to genetically-directed metabolism (van der Gulik *et al.*, 2009; Schoepp-Cothenet *et al.*, 2012a). As the primitive genetic system took metabolic control of its chemical context, prebiotic reactions catalyzed by metal ions or mineral surfaces may have been replaced by their enzymatic counterparts. However, the potential catalytic reactions of most transition metal minerals are unknown, particularly their reactions under different pH, temperature and pressure conditions (Section 1.6). More information of this kind, in particular about the types of organic metal complexes that could have formed under prebiotic conditions (cf. Sander & Koschinsky, 2011), about the distribution of particulate mineral grains at the Earth's surface, and about the metal requirements of the most ancient enzyme sub-categories may thus further elucidate the relative importance of different environmental settings for certain steps in the origin of life.

If transition-metal minerals catalyzed the important reaction steps that eventually resulted in metabolic pathways, then an unavoidable conclusion is that some of the earliest steps leading

to life occurred on mineral surfaces. If it can be demonstrated that other minerals such as clays were essential for the formation of certain ligands or for polymerization of monomers, then this may be evidence for a physical linkage between different geological settings (e.g. metal-rich hydrothermal settings or meteorite debris linked with marine or lacustrine sediments) during the origin of life.

1.6. Future research directions

One appeal of a single setting for the origin of life is the possibility to artificially recreate most relevant prebiotic processes in the laboratory. If, however, the origin of life were indeed a global or at least regional phenomenon, it will clearly make experimental research under plausible environmental conditions more challenging. Nevertheless, progress towards testing the hypothesis of a global chemical reactor can still be made by further exploring the effects of geochemical gradients and by better constraining the catalytic potential of diverse mineral surfaces and solutes under different conditions.

1.6.1. Exploring geochemical gradients

As discussed above (Section 1.4.3), the physicochemical properties of many mineral surfaces and organic compounds can change with temperature, pressure, pH, or fluid composition. The importance of collecting more data of this kind has been widely appreciated only recently by experimentalists. For example, the use of geochemically-relevant buffers is relatively new to origin of life experiments (Shock, 1990; Holm & Andersson, 2005; McCollom & Seewald, 2007; Powner *et al.*, 2009), and the behavior of biochemical reactions in disequilibrium environments or in flow-through systems is completely unexplored (Shock &

Schulte, 1998). The few studies that have been conducted in plausible prebiotic conditions were performed in closed systems with one potential catalyst, and only one possible reaction was assayed (McCollom & Seewald, 2007).

Future experiments could benefit from exploring a wider range of conditions that represent the expected diversity of settings in the Hadean (Hazen & Sverjensky, 2010). For example, it would be useful to test how the products of a Urey-Miller type reaction behave and react when exposed to evapo-concentration processes on a beach or to alkaline or acidic and metal-rich fluids in a hydrothermal vent (such as with a setup similar to that used by Mielke *et al.*, 2010). Furthermore, it is known that at the extreme ends of salinity, pH and temperature gradients, biomolecules can decompose (Demirjian *et al.*, 2001; Tenchov *et al.*, 2006), but these stability limits need to be further explored in an environmental context.

1.6.2. Wider reaction space

Recent experimental studies have measured the ability of individual minerals to catalyze organic synthesis reactions (Cody *et al.*, 2004; Foustoukos & Seyfried, 2004; Schoonen *et al.*, 2004), but not all reactions require the same minerals. The Hadean Earth hosted a plethora of mineral species (Hazen *et al.*, 2008; Hazen & Ferry, 2010; Papineau, 2010) whose substrates and products were frequently exchanged by various mixing processes. Clearly, the next generation of prebiotic chemistry experiments would benefit from exploring a wider range of potential mineral catalysts. Moreover, as has been noted before (Hazen & Sverjensky, 2010), the incorporation of realistic physical and chemical conditions, in which complex combinations of compounds interacted within gradients and fluid fluxes, could move prebiotic synthesis experiments beyond the synthesis of simple building blocks.

As for biological enzymes, mineral catalysis for any given reaction has an optimum suite of environmental conditions which will determine the efficiency of the reaction. Expanding the experimental reaction space of mineral catalysis would complement the already significant body of literature on mineral catalysis produced in recent decades (summarized in Figure 1.6 and in Table A1.2. Because the Hadean Earth was composed of innumerable environmental micro-niches hosting chemical disequilibria capable of facilitating mineral-catalyzed prebiotic synthesis, added scientific value would result from constraining the limits of pressure (P), temperature (T) and pH for specific reactions. This knowledge could then be used to place constraints on the extent of plausible synthesis reactions taking place on the Hadean Earth, but also on asteroids and comets that delivered extraterrestrial organic precursors. Parts of the P/T/pH space (in particular very high temperatures) are precluded from interest by predicted organic chemistry. However, given the multiple parameter-space involved in these reactions, constraining this unexplored space may reveal heretofore unanticipated products under conditions potentially relevant to the origin of life. More specific suggestions regarding potential experiments in mineral surfaces research are discussed in Hazen & Sverjensky (2010).

1.6.3. Homogeneous catalysis

The role of minerals in heterogeneous catalysis has been emphasized repeatedly above; however, metals in solution might be more accessible catalysts in aqueous environments. Recent advances in structural inorganic chemistry allow the investigation of their importance in the origin of life (Morowitz *et al.*, 2010).

Transition metals are most abundant in sulfide phases, and before the rise of oxygen, hydrothermal alteration of oceanic crust would have been their major source to the ocean

(Section 1.3.7). In addition to water-rock interactions at the seafloor, impacts of meteorites, some of which are more metal-rich than the Earth's crust, could have led to temporary enrichments of metals on the Hadean surface. Hence, different geological processes would have established gradients of transition metals in the ocean and in crustal settings.

The involvement of dissolved metals in prebiotic chemistry is an understudied subject (Morowitz *et al.*, 2010), although the rules of chemistry and physics governing those reactions are the same as in modern life forms as they were in the Hadean. For example, the compact, divalent zinc ion with a high affinity for oxygen is commonly used in extant organisms for rapid ligand-exchange reactions (Frausto da Silva & Williams, 1991; Shriver & Atkins, 1999). The multiple possible redox states of copper and iron, on the other hand, are the basis of many electron transfer reactions (Frausto da Silva & Williams, 1991; Shriver & Atkins, 1999). Different metals have different preferences for ligands and molecular geometries, and life exploits those preferences for its own chemical machinery. Based on these data, it seems plausible that dissolved metals could have played a significant catalytic role in prebiotic chemistry, and future experiments would benefit from exploring this possibility.

1.7. Conclusion

We propose that investigations into the origin of life must account for the geochemical complexity of the early Earth system. The origin of life was a complex process that resulted in a global transformation of our planet; it is only reasonable to conclude that it required complex interactions among many processes and settings on a global scale.

Envisioning the origin of life in a global context is advantageous because it makes prebiotic chemistry more plausible and because the global context is an inescapable reality.

Origin of life research is often discussed in terms of a dichotomy: productive chemical reactions vs. environmental relevance. We have argued that thinking about prebiotic processes in a global context eliminates the dichotomy and opens the possibility that the relevant chemical reactions are also the most productive.

How can we use this information in our search for life elsewhere? Life as we know it could probably not have originated without active geological processes (*e.g.* rock and hydrological cycles) and the environmental conditions that result from these processes. As a corollary, any rocky planetary body with water and active geological cycles may have the potential for a *de novo* origin of Earth-like life. As such, it may be more important for astrobiologists to understand the dynamic geological properties of a planetary body than to understand how exactly life originated on Earth.

Of course, a tremendous amount of laboratory and field-based research is required to demonstrate how natural reactions involving a variety of energy sources, catalysts and organic and inorganic compounds can lead to reaction networks and biological systems. Much insight can be gained from highly focused experiments with one kind of molecule under one set of conditions. However, if one views the origin of life as a complex network of reactions occurring in multiple sets of conditions over extended periods of time and space, then this complexity should be reflected in the design of future experimental studies. This paper has not attempted to solve the problem of the origin of life, but rather to describe an approach that may prove useful for a field that is still in its beginning stages.

Acknowledgments

Funding was provided by an NSF Interdisciplinary Graduate Education and Research Training (IGERT) grant and a NASA Astrobiology Institute grant through Cooperative Agreement NNA04CC09A to the Geophysical Laboratory at the Carnegie Institution for Science. We thank Roger Buick for helpful comments on an earlier version of this manuscript, as well as Bob Hazen and two anonymous reviewers whose input greatly improved the paper.

Tables

Table 1.1: Summary of compounds found universally in modern life, and settings that have been proposed for their prebiotic synthesis

Biological component	Setting	Energy source	Selected References
Amino acids	atmosphere/ocean, continents, terrestrial volcanoes, extraterrestrial synthesis (meteors), hydrothermal vents	Lightning, impact shock, heat	(Miller, 1953; Chyba & Sagan, 1992; Tingle & Hochella Jr., 1993)
Nucleotides	evaporating pond, extraterrestrial synthesis (meteors)	evaporation, heat, UV	(Kvenvolden <i>et al.</i> , 1970; Orgel, 1998; Zubay & Mui, 2001; Powner <i>et al.</i> , 2009)
Lipids	peridotite-hosted hydrothermal vents, extraterrestrial synthesis (meteors)	serpentinization (Fischer-Tropsch-type reactions), heat	(Deamer, 2007)
Carbohydrates	extraterrestrial synthesis (meteors), peridotite-hosted hydrothermal vents, atmosphere/ocean, alkaline streams	serpentinization (Fischer-Tropsch-type reactions), lightning, heat	(Deamer, 2007; Benner <i>et al.</i> , 2010)

Table 1.2: Summary of chemical and physical properties of distinct environmental settings.

Intensity of parameters is rated from near absent (-) to very high (+++).

parameter environment	precursors	concentration		energy and gradients			catalysis	fluid residence time
	organic synthesis	encapsulation	dehydration	light energy	pH gradient	temperature gradient	catalytic minerals	
atmospheric gases and particulates	+++	++	+	+++	-	-	-	days to weeks
exposed lakes	+	-	+	++	-	-	++	months to years
continental Groundwater	+	++	-	-	++	+	++	years to Ma
beach settings	++	+++	+++	++	-	+	++	hours to days
sea-ice	+	+++	++	++	+	+	+	months
sea-surface microlayer	+	-	-	+++	-	-	+	seconds
hydrothermal vents	+++	++	++	-	+++	+++	+++	days to weeks
upper oceanic crust	+	+	-	-	+	++	++	years to ka
marine sediments	-	+	-	-	-	+	+++	years to Ma

Table 1.3: Metal cofactor usage, indicated by ‘x’ if present, in the six major categories of enzymes as defined by the Enzyme Commission (Webb, 1992). Metal usage is surveyed from the Kyoto Encyclopedia of Enzyme Genes and Genomes database (Kanehisa *et al.*, 2006).

	Cd	Ca	Co	Cu	Fe	Fe-S	Mn	Mg	Mo	Ni	K	Se	W	Zn
oxidoreductases $A^- + B \rightarrow A + B^-$		X	X	X	X		X		X		X	X	X	X
transferases $A-X + B \rightarrow A + B-X$	X	X			X	X	X	X						
hydrolases $A-X + H_2O \rightarrow A-OH + B-H$		X	X		X		X	X		X	X			X
lyases $A-B-X \rightarrow A=B + X$		X	X	X	X		X	X						X
isomerases $A-B \rightarrow B-A$			X		X		X							X
ligases $A-X + B \rightarrow A-B + X$								X						

Figures

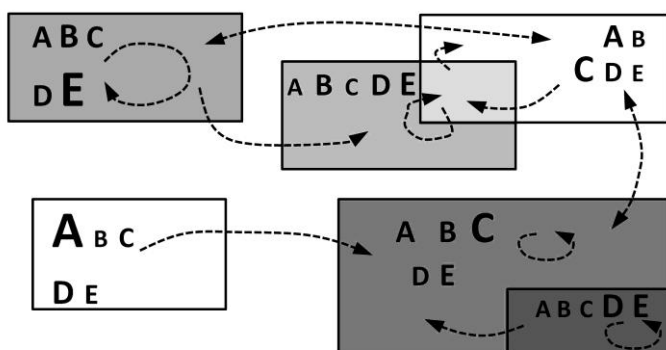


Figure 1.1. Abstract illustration of how the abundance of compounds A to E differs between settings with different physicochemical conditions (boxes) and selective transport processes (arrows)

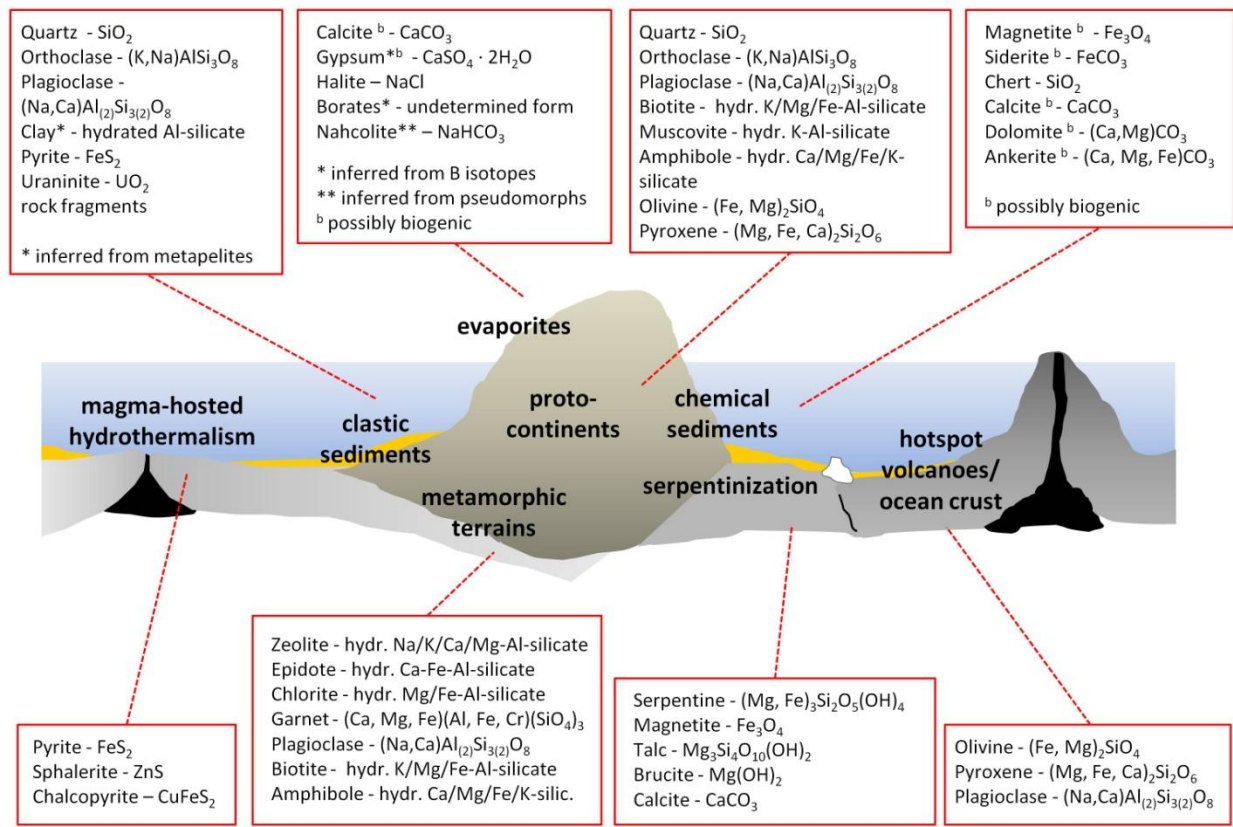


Figure 1.2. Major and some important minor minerals present on the Archean Earth as inferred from the geologic record, listed in no particular order. While all biogenic minerals for which no non-biological mechanism can be invoked would have been absent during the Hadean prior to the origin of life, the primary mineral phases of solidifying magma and their secondary alteration products were probably similarly common. (For references see text).

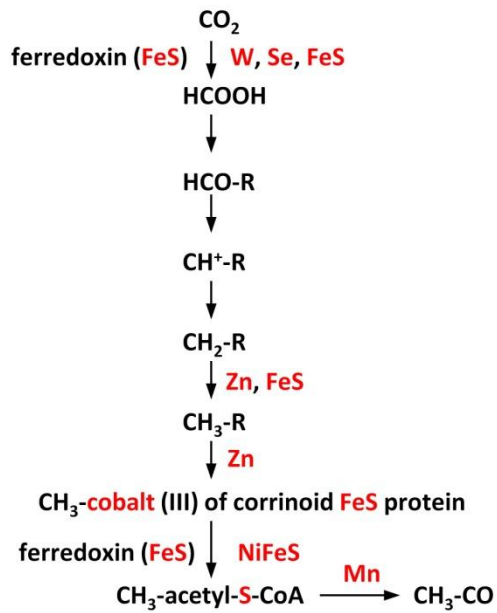


Figure 1.3. The reductive acetyl-CoA pathway of carbon fixation (as employed by methanogens), annotated to highlight steps that involve metals and sulfur, all of which are common in hydrothermal systems. Metals and sulfur found in the corresponding enzymes for each step are shown at the right, and metal-sulfur clusters in ferredoxin cofactors are shown at the left. The atomic structure of the FeNiS complex associated with the acetyl-CoA-generating step is remarkably similar to that of the mineral greigite (Russell & Martin, 2004). Other information compiled from (Ragsdale, 1991) and (Ljungdahl, 1986).

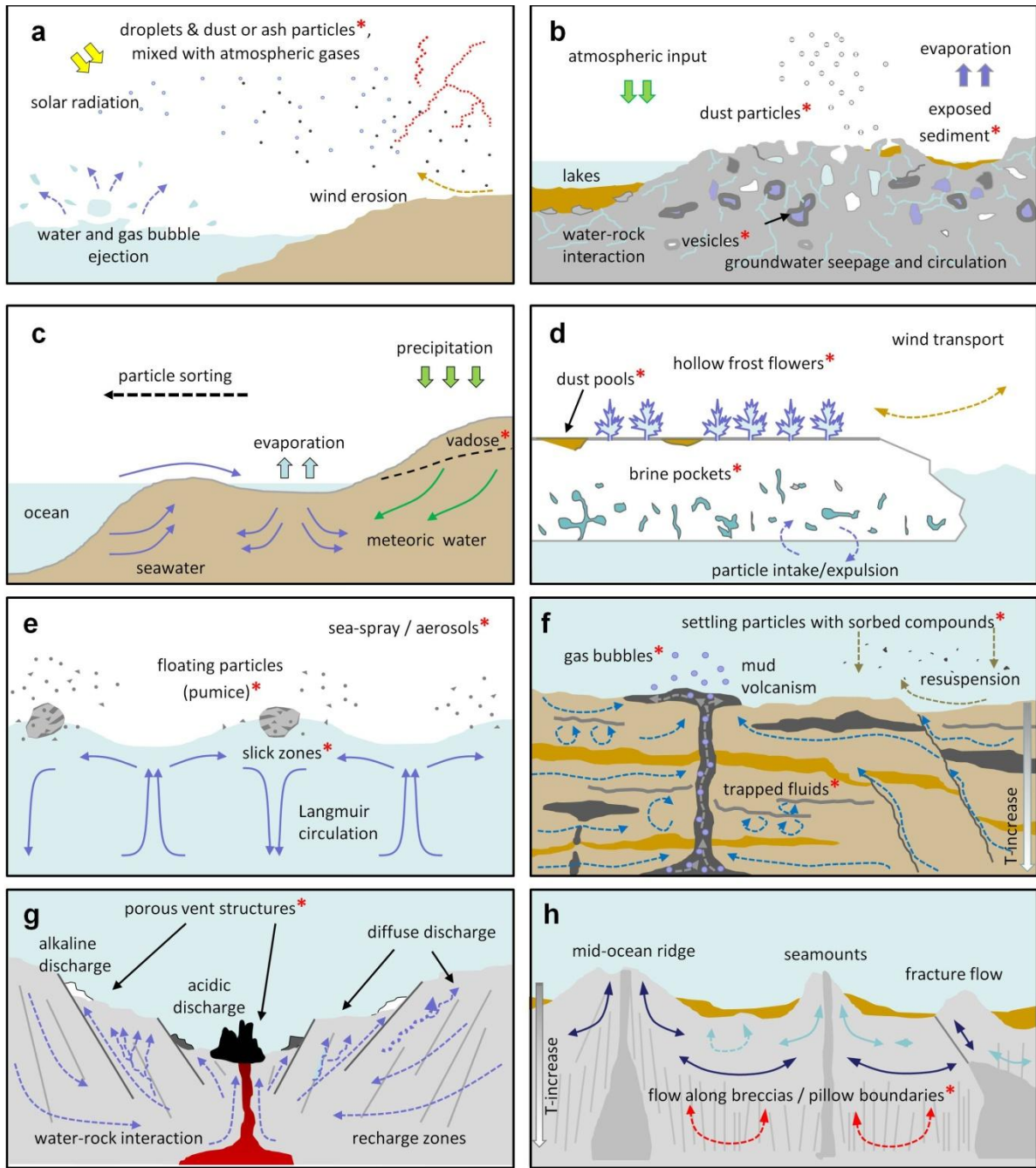


Figure 1.4. Examples of micro-environments on the Hadean Earth and their major physicochemical properties relevant to the origin of life. Micro-compartments that can concentrate reagents are marked with red asterisks.

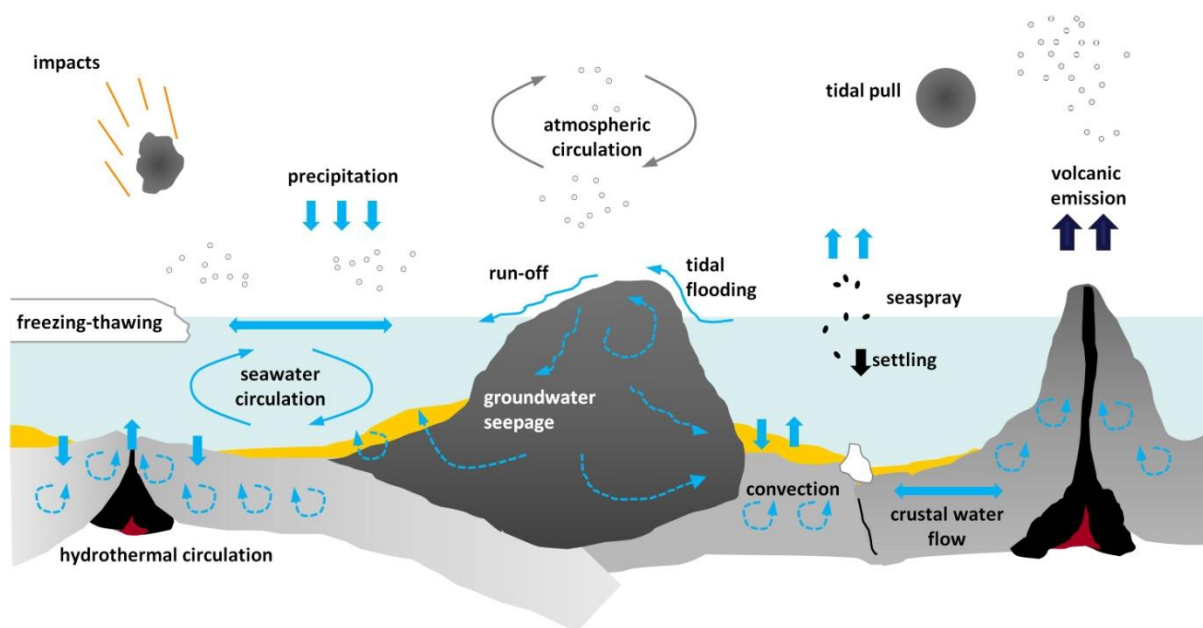


Figure 1.5. Overview of mixing processes that may have linked different sites on the Hadean Earth and facilitated reactions between a greater variety of compounds.

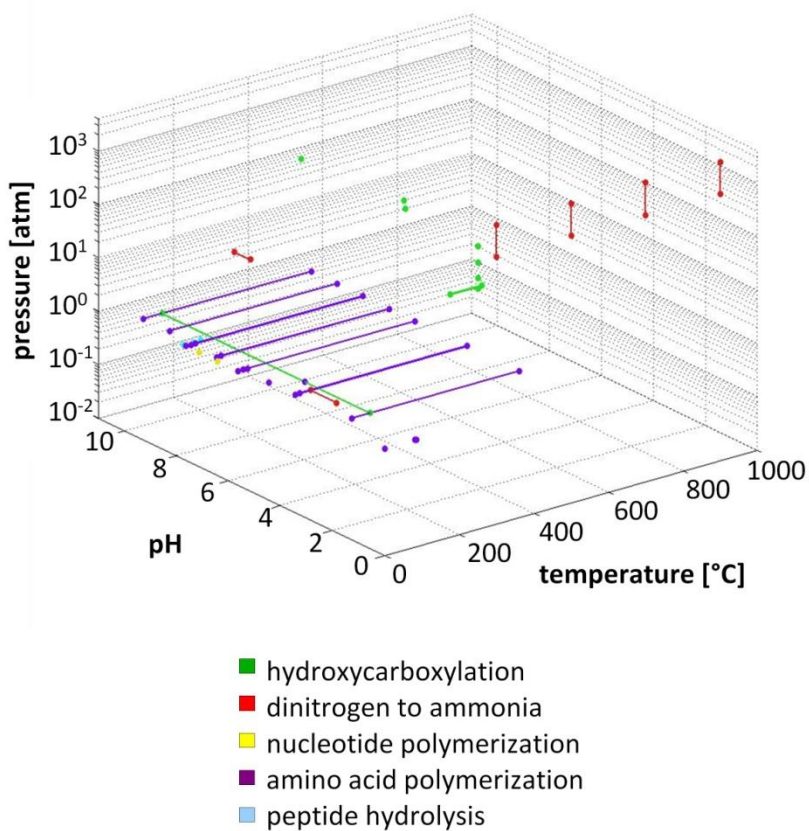


Figure 1.6. Charted above is the chemical reaction space (temperature, pressure, pH) examined for a number of potentially relevant mineral-catalyzed prebiotic reactions. The figure does *not* include all mineral-catalyzed reaction studied do far, but a selection of the reactions most commonly discussed in the literature. The space examined does not indicate successful production, only the space which has been investigated. Values not reported are plotted as a 0 value on the respective axis. Not included in the plot are reactant suites and the time of reaction. For references see Supplementary Table A1.2.

References

- Abramov O, Mojzsis SJ (2009) Microbial habitability of the Hadean Earth during the late heavy bombardment. *Nature*, **459**, 419-422.
- Adam Z (2007) Actinides and the Origin of Life. *Astrobiology*, **7**, 852-872.
- Adams DK, McGillicuddy Jr. DJ, Zaamudio L, Thurnherr AM, Liang X, Rouxel O, German CR, Mullineaux LS (2011) Surface-generated mesoscale eddies transport deep-sea products from hydrothermal vents. *Science*, **332**, 580-583.
- Aliani S, Meloni R, Dando PR (2004) Periodicities in sediment temperature time-series at a marine shallow water hydrothermal vent in Milos Island (Aegean Volcanic arc, Eastern Mediterranean). *Journal of Marine Systems*, **46**, 109-119.
- Anbar A, Holland HD (1992) The photochemistry of manganese and the origin of banded iron formations. *Geochimica et Cosmochimica Acta*, **56**, 2595-2603.
- Armstrong RL (1981) Radiogenic isotopes: the case for crustal recycling on a near-steady-state no-continental-growth Earth. *Philosophical Transactions of the Royal Society of London A*, **301**, 443-472.
- Baaske P, Weinert FM, Duhr S, Lemke KH, Russell MJ, Braun D (2007) Extreme accumulation of nucleotides in simulated hydrothermal pore systems. *Proceedings of the National Academy of Sciences*, **104**, 9346-9351.
- Bada JL (2004) How life began on Earth: a status report. *Earth and Planetary Science Letters*, **226**, 1-15.
- Bada JL, Bigham C, Miller SL (1994) Impact melting of frozen oceans on the early Earth: Implications for the origin of life. *Proceedings of the National Academy of Sciences*, **91**, 1248-1250.
- Baptiste E, Brochier C, Boucher Y (2005) Higher-level classification of the Archaea: Evolution of methanogenesis and methanogens. *Archaea*, **1**, 353-363.
- Baross J, Hoffman SE (1985) Submarine hydrothermal vents and associated gradient environments as sites for the origin and evolution of life. *Origins of Life and Evolution of Biospheres*, **15**, 327-345.
- Barret M, Houdier S, Gallet J-C, Domine F, Beine H, Jacobi H-W, Weibring P, Walega J, Fried A, Richter D (2009) Aldehydes in Arctic snow at Barrow (AK) during the Barrow 2009 field campaign. *Eos*, **90**.
- Bassez M-P (2003) Is high-pressure water the cradle of life? *Journal of Physics: Condensed Matter*, **15**, L353-L361.
- Bekins BA, Spivack AJ, Davis EE, Mayer LA (2007) Dissolution of biogenic ooze over basement edifices in the equatorial Pacific with implications for hydrothermal ventilation of the oceanic crust. *Geology*, **35**, 679-682.
- Benner SA, Kim H-J, Kim M-J, Ricardo A (2010) Planetary organic chemistry and the origins of biomolecules. In: *The Origins of Life* (eds Deamer D, Shostak JW). Cold Spring Harbor Laboratory Press, New York.
- Berg IA, Kockelkorn D, Ramos-Vera WH, Say RF, Zarzycki J, Hugler M, Alber BE, Fuchs G (2010) Autotrophic carbon fixation in archaea. *Nature Reviews Microbiology*, **8**, 447-460.
- Blais S, Auvray B (1990) Serpentinization in the Archean komatiitic rocks of the Kuhmo greenstone belt, eastern Finland. *Canadian Mineralogist*, **28**, 55-66.

- Boulter CA, Glover JE (1986) Chert with relict hopper moulds from Rocklea Dome, Pilbara craton, Western Australia: an Archaean halite-bearing evaporite. *Geology*, **14**, 128-131.
- Boyd ES, Anbar A, Miller SL, Hamilton TL, Lavin M, Peters JW (2011) A late methanogen origin for molybdenum-dependent nitrogenase. *Geobiology*, **9**, 221-232.
- Brandes JA, Hazen RM, Yoder Jr HS (2008) Inorganic nitrogen reduction and stability under simulated hydrothermal conditions. *Astrobiology*, **8**, 1113-1126.
- Brasier MD, Matthewman R, McMahon S, Wacey D (2011) Pumice as a remarkable substrate for the origin of life. *Astrobiology*, **11**, 725-735.
- Braterman PS, Cairns-Smith AG, Sloper RW (1983) Photo-oxidation of hydrated Fe²⁺ - Significance for banded iron formations. *Nature*, **303**, 163-164.
- Brown GC (1979) The changing pattern of batholith emplacement during earth history. In: *Origin of Granite Batholiths* (eds Atherton MP, Tarney J), Nantwich, Shiva, pp. 106-115.
- Budin I, Bruckner RJ, Szostak JW (2009) Formation of protocell-like vesicles in a thermal diffusion column. *Journal of the American Chemical Society*, **131**, 9628-9629.
- Buick R (2007) The earliest records of life on Earth. In: *Planets and Life: The Emerging Science of Astrobiology* (eds Sullivan III. WT, Baross JA). Cambridge University Press.
- Buick R, Dunlop JSR (1990) Evaporitic sediments of Early Archaean age from the Warrawoona Group, North Pole, Western Australia. *Sedimentology*, **37**, 247-277.
- Caetano-Anolles G, Kim H-S, Mittenthal JE (2007) The origins of modern metabolic networks inferred from phylogenomic analysis of protein architecture. *Proceedings of the National Academy of Sciences*, **104**, 9358-9363.
- Cairns-Smith AG (1978) Precambrian solution photochemistry, inverse segregation, and banded iron formations. *Nature*, **76**, 807-808.
- Cairns-Smith G (2003) Fine-tuning in living systems: early evolution and the unity of biochemistry. *International Journal of Astrobiology*, **2**, 87-90.
- Carr MH, Turekian KK (1961) The geochemistry of cobalt. *Geochimica et Cosmochimica Acta*, **28**, 9-60.
- Catling DC (2006) Comment on "A hydrogen-rich early Earth atmosphere. *Science*, **311**, 38a.
- Catling DC, Kasting JF (2007) Planetary atmospheres and life. In: *Planets and Life: The Emerging Science of Astrobiology* (eds Sullivan III. WT, Baross J). Cambridge University Press, Cambridge.
- Charlou JL, Donval JP, Fouquet Y, Jean-Baptiste P, Holm N (2002) Geochemistry of high H₂ and CH₄ vent fluids issuing from ultramafic rocks at the Rainbow hydrothermal field (36°14'N, MAR). *Chemical Geology* **191**, 345-359.
- Charlou JL, Fouquet Y, Bougault H, Donval JP, Etoubleau J, Jean-Baptiste P, Dapigny A, Appriou P, Rona PA (1998) Intense CH₄ plumes generated by serpentinization of ultramafic rocks at the intersection of the 15°20'N fracture zone and the Mid-Atlantic Ridge. *Geochimica et Cosmochimica Acta*, **62**, 2323-2333.
- Christner BC, Kvitko BH, Reeve JN (2003) Molecular identification of Bacteria and Eukarya inhabiting an Antarctic cryoconite hole. *Extremophiles*, **7**, 177-183.
- Churchill H, Teng H, Hazen RM (2004) Correlation of pH-dependent surface interaction forces to amino acid adsorption: Implications for the origin of life. *American Mineralogist*, **89**, 1048-1055.
- Chyba C, Sagan C (1992) Endogenous production, exogenous delivery and impact-shock synthesis of organic molecules: an inventory for the origins of life. *Nature*, **355**, 125-132.

- Cleaves HJ, Scott AM, Hill FC, Leszczynski J, Sahai N, Hazen RM (2012) Mineral-organic interfacial processes: potential roles in the origins of life. *Chemical Society Reviews*, **41**, 5365-5568.
- Cockell CS (2000) The ultraviolet history of the terrestrial planets - implications for biological evolution. *Planetary and Space Science*, **48**, 203-214.
- Cody GD (2004) Transition metal sulfides and the origins of metabolism. *Annual Review of Earth and Planetary Sciences*, **32**, 569-599.
- Cody GD, Boctor NZ, Brandes JA, Filley TR, Hazen RM, Yoder HS (2004) Assaying the catalytic potential of transition metal sulfides for abiotic carbon fixation. *Geochimica et Cosmochimica Acta*, **68**, 2185-2196.
- Cody GD, Boctor NZ, Filley TR, Hazen RM, Scott JH, Sharma A, Yoder Jr. HS (2000) Primordial carbonylated iron-sulfur compounds and the synthesis of pyruvate. *Science*, **289**, 1337-1340.
- Cody GD, Scott JH (2007) The roots of metabolism. In: *Planets and Life: The Emerging Science of Astrobiology* (eds Sullivan III. WT, Baross J). Cambridge University Press.
- Copley SD, Smith E, Morowitz HJ (2007) The origin of the RNA world: Co-evolution of genes and metabolism. *Bioorganic Chemistry*, **35**, 430-443.
- Cox GFN, Weeks WF (1983) Equations for determining the gas and brine volumes in sea-ice samples. *Journal of Glaciology*, **29**, 306-316.
- Cvetkovic A, Menon AL, Thorgersen MP, Scott JW, Poole II FL, Jenney Jr FE, Lancaster WA, Praissman JL, Shannukh S, Vaccaro BJ, Trauger SA, Kalisiak E, Apon JV, Siuzdak G, Yannone SM, Trainer JA, Adams MWW (2010) Microbial metalloproteomes are largely uncharacterized. *Nature* **466**, 779-782.
- Dann CE, Wakeman CA, Sieling CL, Baker SC, Irnov I, Winkler WC (2007) Structure and mechanism of a metal-sensing regulatory RNA. *Cell*, **130**, 878-892.
- De Duve C (1995) *Vital dust: the origin and evolution of life on Earth*, BasicBooks, New York.
- de Marcellus P, Meinert C, Nuevo M, Filippi J-J, Danger G, Deboffe D, Nahon L, Le Sergeant d'Hendecourt L, Meierhenrich UJ (2011) Non-racemic amino acid production by ultraviolet irradiation of achiral interstellar ice analogs with circularly-polarized light. *The Astrophysical Journal Letters*, **727:L27**.
- Deamer D (2011) *First life: discovering the connections between stars, cells, and how life began*, University of California Press, Berkeley.
- Deamer D, Dworkin JP, Sandford SA, Bernstein MP, Allamandola LJ (2002) The first cell membranes. *Astrobiology*, **2**, 371-381.
- Deamer D, Weber AL (2010) Bioenergetics and life's origin. In: *The Origins of Life* (eds Deamer D, Shostak JW). Cold Spring Harbor Laboratory Press, New York.
- Deamer DW (2007) The origin of cellular life. In: *Planets and Life: The Emerging Science of Astrobiology* (eds Sullivan III. WT, Baross J). Cambridge University Press, Cambridge.
- Demirjian DC, Moris-Varas F, Cassidy CS (2001) Enzymes from extremophiles. *Current Opinion in Chemical Biology*, **5**, 144-151.
- Ding X, Henrichs SM (2002) Adsorption and desorption of proteins and polyamino acids by clay minerals and marine sediment. *Marine Chemistry*, **77**, 225-237.
- Dobson CM, Ellison GB, Tuck AF, Vaida V (2000) Atmospheric aerosols as prebiotic chemical reactors. *Proceedings of the National Academy of Sciences*, **97**, 11864-11868.
- Donaldson DJ, Tervahattu H, Tuck AF, Vaida V (2004) Organic aerosols and the origin of life: a hypothesis. *Origins of Life and Evolution of Biospheres*, **34**, 57-67.

- Douville E, Charlou JL, Oelkers EH, Bienvenu P, Jove Colon CF, Donval JP, Fouquet Y, Prieur D, Appriou P (2002) The rainbow vent fluids (36°14'N, MAR): the influence of ultramafic rocks and phase separation on trace metal content in Mid-Atlantic Ridge hydrothermal fluids. *Chemical Geology*, **184**, 37-48.
- Ducluzeau A-L, van Lis R, Duval S, Schoepp-Cothenet B, Russel MJ, Nitschke W (2008) Was nitric oxide the first deep electron sink? *TRENDS in Biochemical Sciences*, **34**, 9-15.
- Dupont CL, Butcher A, Valas RE, Bourne PE, Caetano-Anolles G (2010) History of biological metal utilization inferred through phylogenomic analysis of protein structure. *Proceedings of the National Academy of Sciences*, **107**, 10567-10572.
- Dypvik H, Jansa LF (2003) Sedimentary signatures and processes during marine bolide impacts: a review. *Sedimentary Geology*, **161**, 309-337.
- Ekman VW (1905) On the influence of the Earth's rotation on ocean-currents. *Arkiv. Mat. Astr. Fysik.*, **2**.
- Farquhar J, Savarino J, Airieau S, Thiemens MH (2001) Observation of the wavelength-sensitive mass-dependent sulfur isotope effects during SO₂-photolysis: Implications for the early atmosphere. *Journal of Geophysical Research*, **106**, 32829-32839.
- Felitsyn S, Kirianov V (2002) Mobility of phosphorus during weathering of volcanic ashes. *Lithology and Mineral Resources*, **37**, 275-278.
- Ferris JP (2005a) Catalysis and Prebiotic Synthesis. *Reviews in Mineralogy and Geochemistry*, **59**, 187-210.
- Ferris JP (2005b) Mineral catalysis and prebiotic synthesis: montmorillonite-catalyzed formation of RNA. *Elements*, **1**, 145-149.
- Fisher AT, Becker K (2000) Channelized fluid flow in oceanic crust reconciles heat-flow and permeability data. *Nature*, **403**, 71-74.
- Folsome C, Brittain A, Zelko M (1983) Photochemical synthesis of biomolecules under anoxic conditions. *Origins of Life and Evolution of Biospheres*, **13**, 49-55.
- Foustoukos DI, Seyfried WE (2004) Hydrocarbons in hydrothermal vent fluids: the role of chromium-bearing catalysts. *Science*, **304**, 1002-1005.
- François LM (1986) Extensive deposition of banded iron formations was possible without photosynthesis. *Nature*, **320**, 352-354.
- Frausto da Silva JJR, Williams RJP (1991) *The Biological Chemistry of the Elements - The Inorganic Chemistry of Life*, Oxford University Press, New York.
- Frew NM (1997) The role of organic films in air-sea gas exchange. In: *The sea surface and global change* (eds Liss PS, Duce RA). Cambridge University Press, Cambridge, pp. 121-171.
- Frogner P, Gislason SR, Oskarsson N (2001) Fertilizing potential of volcanic ash in ocean surface water. *Geology*, **29**, 487-490.
- Fuchs G (2011) Alternative pathways of carbon dioxide fixation: Insights into the early evolution of life? *Annual Reviews of Microbiology*, **65**, 631-658.
- Fuchs G, Stupperich E (1985) Evolution of autotrophic CO₂ fixation. In: *Evolution of Prokaryotes FEMS Symposium* (ed Schleier SE). Academic Press, London, pp. 235-251.
- Gaucher EA, Govindarajan S, Ganesh OK (2008) Palaeotemperature trend for Precambrian life inferred from resurrected proteins. *Nature*, **451**, 704-708.
- Glansdorff N, Xu Y, Labendan B (2008) The last universal common ancestor: emergence, constitution and genetic legacy of an elusive forerunner. *Biology Direct*, **3**.

- Glikson A (2004) Early Precambrian asteroid impact-triggered tsunamis: excavated seabed, debris flows, exotic boulders, and turbulence features associated with 3.47-2.47 Ga-old asteroid impact fallout units, Pilbara craton, western Australia. *Astrobiology*, **4**, 19-50.
- Gogarten-Boekels M, Hilario E, Gogarten JP (1995) The effects of heavy meteorite bombardment on the early evolution - The emergence of the three Domains of Life. *Origins of Life and Evolution of Biospheres*, **25**, 251-264.
- Goldman AD, Samudrala R, Baross JA (2010) The evolution and functional repertoire of translation proteins following the origin of life. *Biology Direct*, **5**.
- Gough DO (1981) Solar interior structure and luminosity variations. *Solar Physics*, **74**, 21-34.
- Gran KB, Paola C (2001) Riparian vegetation controls on braided stream dynamics. *Water Resources Research*, **37**, 3275-3283.
- Grew ES, Bada JL, Hazen RM (2011) Borate minerals and origin of the RNA world. *Origins of Life and Evolution of Biospheres*, **41**, 307-316.
- Grieve RAF (1987) Terrestrial impact structures. *Annual Review of Earth and Planetary Sciences*, **15**, 245-270.
- Gysi AP, Stefansson A (2012) Mineralogical aspects of CO₂ sequestration during hydrothermal basalt alteration - An experimental study at 75 to 250 C and elevated pCO₂. *Chemical Geology*, **306-307**, 146-159.
- Hargraves RB (1986) Faster spreading or greater ridge length in the Archean? *Geology*, **14**, 750-752.
- Harris JK, Kelley ST, Spiegelman GB, Pace NR (2003) The genetic core of the universal ancestor. *Genome Research*, **13**, 407-412.
- Harrison TM, Schmitt AK, McCulloch MT, Lovera OM (2008) Early (>4.5 Ga) formation of terrestrial crust: Lu-Hf, $\delta^{18}\text{O}$, and Ti thermometry results for Hadean zircons. *Earth and Planetary Science Letters*, **268**, 476-486.
- Hazen RM (2005) *Genesis: the scientific quest for life's origin*, Joseph Henry Press, Washington D.C.
- Hazen RM (2012) Geochemical origins of life. In: *Fundamentals of Geobiology* (eds Knoll AH, Canfield DE, Konhauser KO). Wiley-Blackwell Oxford, UK, pp. 315-332.
- Hazen RM, Ferry JM (2010) Mineral evolution: Mineralogy in the fourth dimension. *Elements*, **6**, 9-12.
- Hazen RM, Filley TR, Goodfriend GA (2001) Selective adsorption of L- and D-amino acids on calcite: Implications for biochemical homochirality. *Proceedings of the National Academy of Sciences*, **98**, 5487-5490.
- Hazen RM, Hemley RJ, Mangum AJ (2012) Carbon in Earth's interior: storage, cycling, and life. *EoS Transactions of the American Geophysical Union*, **93**, 17-28.
- Hazen RM, Papineau D, Bleeker W, Downs RT, Ferry JM, McCoy TJ, Sverjensky DA, Yang H (2008) Mineral evolution. *American Mineralogist*, **93**, 1693-1720.
- Hazen RM, Sholl DS (2003) Chiral selection on inorganic crystalline surfaces. *Nature Materials*, **2**, 367-374.
- Hazen RM, Sverjensky DA (2010) Mineral surfaces, geochemical complexities and the origin of life. In: *The origins of life. A subject collection from Cold Spring Harbor Perspectives in Biology* (eds Deamer D, Szostak JW). Cold Spring Harbor Laboratory Press, Cold Spring Harbor, NY.

- Heinen W, Lauwers AM (1996) Organic sulfur compounds resulting from the interaction of iron sulfide, hydrogen sulfide and carbon dioxide in an anaerobic aqueous environment. *Origins of Life and Evolution of the Biosphere*, **26**, 131-150.
- Hellevang H (2008) On the forcing mechanism for the H₂-driven deep biosphere. *International Journal of Astrobiology*, **7**, 157-167.
- Hennet RJC, Holm N, Engel MH (1992) Abiotic synthesis of amino acids under hydrothermal conditions and the origin of life: a perpetual phenomenon? *Naturwissenschaften*, **79**, 361-365.
- Heremans K, Smeller L (1998) Protein structure and dynamics at high pressure. *Biochimica et Biophysica Acta (BBA) - Protein Structure and Molecular Enzymology*, **1386**, 353-370.
- Hofmann A (2011) Archean hydrothermal systems in the Barberton Greenstone Belt and their significance as a habitat for early life. In: *Earliest life on Earth: habitats, environments and methods of detection* (eds Golding SD, Glikson M). Springer Science and Business Media B.V.
- Hofmann A, Bolhar R (2007) Carbonaceous cherts in the Barberton Greenstone Belt and their significance for the study of early life in the Archean record. *Astrobiology*, **7**, 355-388.
- Holm N, Charlou JL (2001) Initial indications of abiotic formation of hydrocarbons in the Rainbow ultramafic hydrothermal system, Mid-Atlantic Ridge. *Earth and Planetary Science Letters*, **191**, 1-8.
- Holm NG (2012) The significance of Mg in prebiotic geochemistry *Geobiology*, **10**, 269-279.
- Holm NG, Andersson E (2005) Hydrothermal simulation experiments as a tool for studies of the origin of life on earth and other terrestrial planets: a review. *Astrobiology*, **5**, 444-460.
- Holm NG, Neubeck A (2009) Reduction of nitrogen compounds in oceanic basement and its implications for HCN formation and abiotic organic synthesis. *Geochemical Transactions*, **10**, 1-11.
- Hoskin PWO (2005) Trace-element composition of hydrothermal zircon and the alteration of Hadean zircon from the Jack Hills, Australia. *Geochimica et Cosmochimica Acta*, **69**, 637-648.
- Huber C, Wächtershäuser G (1997) Activated acetic acid by carbon fixation on (Fe,Ni)S under primordial conditions. *Science*, **276**, 245-247.
- Hunt BG (1979) The effects of past variations of the Earth's rotation rate on climate. *Nature*, **281**, 188-191.
- Hunter KA, Liss PS (1977) The input of organic material to the oceans: air sea interactions and the chemical composition of the sea surface. *Marine Chemistry*, **5**, 361-379.
- Huston D, Sun S-S, Blewett R, Hickman AH, Van Kranendonk M, Phillips D (2002) The Timing of Mineralization in the Archean North Pilbara Terrain, Western Australia *Economic Geology*, **97**, 733-755.
- Hutnak M, Fisher AT (2007) Influence of sedimentation, local and regional hydrothermal circulation, and thermal rebound on measurements of seafloor heat flux. *Journal of Geophysical Research*, **112**.
- Hutnak M, Fisher AT, Harris R, Stein C, Wang K, Spinelli G, Schindler M, Villinger H, Silver E (2008) Large heat and fluid fluxes driven through mid-plate outcrops on ocean crust. *Nature Geoscience*, 1-4.
- Jacob D (1999) *Introduction to Atmospheric Chemistry*.
- Johnson AP, Cleaves HJ, Dworkin JP, Glavin DP, Lazcano A, Bada JL (2008) The Miller volcanic spark discharge experiment *Science*, **322**, 404.

- Johnson HP, Pruis MJ (2003) Fluxes of fluid and heat from the oceanic crustal reservoir. *Earth and Planetary Science Letters*, **216**, 564-574.
- Jokiel P, Cox F (2003) Drift pumice at Christmas Island and Hawaii: evidence of oceanic dispersal patterns. *Marine Geology*, **202**, 121-133.
- Kanavarioti A, Monnard P-A, Deamer DW (2001) Eutectic phases in ice facilitate nonenzymatic nucleic acid synthesis. *Astrobiology*, **1**, 271-281.
- Kanehisa M, Goto S, Hattori M, Aoki-Kinoshita KF, Itoh M, Kawashima S, Katayama T, Araki M, Hirakawa M (2006) From genomics to chemical genomics: new developments in KEGG. *Nucleic Acids Research*, **34**, D354-D357.
- Karlin KD (1993) Metalloenzymes, structural motifs, and inorganic models. *Science*, **261**, 701-708.
- Kasting JF (2010) Faint young Sun redux. *Nature*, **464**, 687-689.
- Kasting JF, Catling DC (2003) Evolution of a habitable planet. *Annual Reviews in Astronomy and Astrophysics*, **41**, 429-463.
- Keil RG, Dickens AF, Arnason R, Nunn BL, Devol AH (2004) What is the oxygen exposure time of laterally transported organic matter along the Washington margin? *Marine Chemistry*, **92**, 157-165.
- Kelley D, Karson JA, Blackman DK, Frueh-Green GL, Butterfield DA, Lilley MD, Olson EJ, Schrenk MO, Roe KK, Lebon GT, Rivizzigno P (2001) An off-axis hydrothermal vent field near the Mid-Atlantic Ridge at 30°N. *Nature*, **412**, 145-149.
- Kelley D, Karson JA, Frueh-Green GL, Yoerger DR, Shank TM, Butterfield DA, Hayes JM, Schrenk MO, Olson EJ, Proskurowski G, Jakuba M, Bradley A, Larson B, Ludwig K, Glickson D, Buckman K, Bradley AS, Brazelton WJ, Roe K, Elend MJ, Delacour A, Bernasconi SM, Lilley MD, Baross J, Summons RE, Sylva SP (2005) A Serpentinite-Hosted Ecosystem: The Lost City Hydrothermal Field *Science*, **307**, 1428-1434.
- Kemp AIS, Wilde SA, Hawkesworth CJ, Coath CD, Nemchin A, Pidgeon RT, Vervoort JD, DuFrane SA (2010) Hadean crustal evolution revisited: New constraints from Pb-Hf isotope systematics of the Jack Hills zircons. *Earth and Planetary Science Letters*, **296**, 45-56.
- Kennedy MJ, Pevear DR, Hill RJ (2002) Mineral surface control of organic carbon in black shale. *Science*, **295**, 657-660.
- Kluyver AJ, Donker HJ (1959) Die Einheit in der Biochemie. In: *Albert Jan Kluyver, his life and work* (eds Kamp AF, La Riviere JWM, Verhoeven W). North-Holland Publishing, Amsterdam, pp. 211-267.
- Knauth LP (2005) Temperature and salinity history of the Precambrian ocean: implications for the course of microbial evolution. *Palaeogeography, Palaeoclimatology, Palaeoecology*, **219**, 53-69.
- Konhauser KO, Amskold L, Lalonde SV, Posth NR, Kappler A, Anbar A (2007) Decoupling photochemical Fe(II) oxidation from shallow-water BIF deposition. *Earth and Planetary Science Letters*, **258**, 87-100.
- Koonin EV, Martin W (2005) On the origin of genomes and cells within inorganic compartments. *TRENDS in Genetics*, **21**, 648-654.
- Kring DA, Cohen BA (2002) Cataclysmic bombardment throughout the inner solar system 3.9-4.0 Ga. *Journal of Geophysical Research*, **107**.

- Kump LR, Seyfried Jr WE (2005) Hydrothermal Fe fluxes during the Precambrian: Effect of low oceanic sulfate concentrations and low hydrostatic pressure on the composition of black smokers. *Earth and Planetary Science Letters*, **235**, 654-662.
- Kvenvolden K, Lawless J, Pering K, Peterson E, Flores J, Ponnampereuma C, Kaplan IR, Moore C (1970) Evidence for extraterrestrial amino acids and hydrocarbons in the Murchison Meteorite. *Nature*, **228**, 923-928.
- Lahav N (1999) *Theories of life's origin*, Oxford University Press, New York.
- Lane N, Allen JF, Martin W (2010) How did LUCA make a living? Chemiosmosis in the origin of life. *Bioessays*, **32**, 271-280.
- Lang SQ, Butterfield DA, Schulte M, Kelley DS, Lilley MD (2010) Elevated concentrations of formate, acetate and dissolved organic carbon found at the Lost City hydrothermal field. *Geochimica et Cosmochimica Acta*, **74**, 941-952.
- Lasaga AC, Holland HD, Dwyer MJ (1971) Primordial oil slick. *Science*, **174**.
- Lazcano A, Miller SL (1999) On the origin of metabolic pathways. *Journal of Molecular Biology*, **49**, 424-431.
- Levy M, Miller SL, Brinton K, Bada JL (2000) Prebiotic Synthesis of Adenine and Amino Acids Under Europa-like Conditions. *Icarus*, **145**, 609-613.
- Li Y-H (2000) *A compendium of geochemistry*, Princeton University Press.
- Li Y-H, Schoonmaker JE (2003) Chemical composition and mineralogy of marine sediments. In: *Sediments, Diagenesis and Sedimentary Rocks* (ed Mackenzie FT). Elsevier-Pergamon, Oxford, pp. 1-35.
- Liss PS, Duce RA (1997) *The sea surface and global change*, Cambridge University Press, Cambridge.
- Ljungdahl (1986) The autotrophic pathway of acetate synthesis in acetogenic bacteria. *Annual Reviv of Microbiology*, **40**, 415-450.
- Lowe DR, Worrell GF (1999) Sedimentology, mineralogy, and implications of silicified evaporites in the Kromberg Formation, Barberton Greenstone Belt, South Africa. *Geological Society of America Special Papers*, **329**, 167-188.
- Mackenzie FT, Lantzy RJ, Paterson V (1979) Global trace metal cycles and predictions. *Mathematical Geology*, **11**, 99-142.
- Mackin JH (1956) Cause of braiding by a graded river. *Geological Society of America Bulletin*, **67**, 1717-1718.
- Marquez C, Lazcano A, Miller SL, Oro J (1996) Fully deuterated aliphatic hydrocarbons obtained from iron carbide treated with dcl and D₂O. *Origins of Life and Evolution of Biospheres*, **26**, 450-451.
- Martin RS, Mather TA, Pyle DM (2007) Volcanic emissions and the early Earth atmosphere. *Geochimica et Cosmochimica Acta*, **71**, 3673-3685.
- Martin W, Baross J, Kelley D, Russell MJ (2008) Hydrothermal vents and the origin of life. *Nature Reviews Microbiology*.
- Martin W, Russell MJ (2007) On the origin of biochemistry at an alkaline hydrothermal vent. *Philosophical Transactions of the Royal Society of London B*, **362**, 1887-1925.
- Maynard-Smith J, Szathmary E (1997) *The major transition in evolution*, Oxford University Press, New York.
- Mazzini A (2009) Mud volcanism: Processes and implications. *Marine and Petroleum Geology*, **26**, 1677-1680.
- McCammon C (2005) The Paradox of Mantle Redox *Science*, **308**, 807-808.

- McCollom TM, Seewald JS (2007) Abiotic synthesis of organic compounds in deep-sea hydrothermal environments. *Chemical Reviews*, **107**, 382-401.
- McLennan SM, Taylor SR (1982) Geochemical constraints on the growth of the continental crust. *Journal of Geology*, **90**, 347-361.
- Meierhenrich UJ, Munoz-Caro GM, Schutte WA, Thiemann WH-P, Barbier B, Brack A (2005) Precursors of biological cofactors from ultraviolet irradiation of circumstellar/interstellar ice analogues. *Chemistry - A European Journal*, **11**, 4895-4900.
- Menez B, Pasini V, Brunelli D (2012) Life in the hydrated suboceanic mantle. *Nature Geoscience*.
- Meng M, Stievano L, Lambert J-F (2004) Adsorption and thermal condensation mechanisms of amino acids on oxide supports. 1. Glycine on Silica. *Langmuir*, **20**, 914-923.
- Mielke RE, Russell MJ, Wilson PR, McGlynn SE, Coleman M, Kidd R, Kanik I (2010) Design, fabrication, and test of a hydrothermal reactor for origin-of-life experiments. *Astrobiology*, **10**, 799-810.
- Miller RG (2000) Influence of bank vegetation on alluvial channel patterns. *Water Resources Research*, **34**, 1109-1118.
- Miller SL (1953) A production of amino acids under possible primitive Earth conditions. *Science*, **117**, 528-529.
- Miyakawa S, Cleaves HJ, Miller S (2002a) The cold origin of life: B. Implications based on pyrimidines and purines produced from frozen ammonium cyanide solutions. *Origins of Life and Evolution of Biospheres*, **32**, 209-218.
- Miyakawa S, James Cleaves H, Miller S (2002b) The cold origin of life: A. Implications based on the hydrolytic stabilities of hydrogen cyanide and formamide. *Origins of Life and Evolution of Biospheres*, **32**, 195-208.
- Mojzsis SJ, Harrison TM, Pidgeon RT (2001) Oxygen-isotope evidence from ancient zircons for liquid water at the Earth's surface 4,300 Myr ago. *Nature*, **409**, 178-181.
- Mollenhauer G, McManus JF, Benthien A, Mueller PJ, Eglinton TI (2006) Rapid lateral particle transport in the Argentine Basin: Molecular ^{14}C and ^{230}Th s evidence *Deep Sea Research I*, **53**, 1224-1243.
- Moore CJ, Moore SL, Leecaster MK, Weisberg SB (2001) A Comparison of Plastic and Plankton in the North Pacific Central Gyre. *Marine Pollution Bulletin*, **42**, 1297-1300.
- Morita R (1999) Is H_2 the Universal Energy Source for Long-Term Survival? *Microbial Ecology*, **38**, 307-320.
- Morowitz H (2004) *Beginnings of cellular life: metabolism recapitulates biogenesis*, Yale University Press, New Haven.
- Morowitz H, Smith E (2007) Energy flow and the organization of life. *Complexity*, **13**, 51-59.
- Morowitz HJ, Srinivasan V, Smith E (2010) Ligand Field Theory and the Origin of Life as an Emergent Feature of the Periodic Table of Elements. *Biological Bulletin*, **219**, 1-6.
- Mulkidjanian AY, Bychkov AY, Dibrova DA, Galperin MY, Koonin EV (2012) Origin of the first cells at terrestrial, anoxic geothermal fields. *Proceedings of the National Academy of Sciences* **109**, 821-840.
- Munsch S, Hartmann M, Ernst S (2001) Adsorption and separation of amino acids from aqueous solutions on zeolites. *Chem. Commun.*, 1978-1979.
- Nealson KH, Inagaki F, Takai K (2005) Hydrogen-driven subsurface lithoautotrophic microbial ecosystems (SLiMEs): do they exist and why should we care? *TRENDS in Microbiology*, **13**, 405-410.

- Nilson FPR (2002) Possible impact of a primordial oil slick on atmospheric and chemical evolution. *Origins of Life and Evolution of the Biosphere*, **32**, 247-253.
- Nisbet EG, Sleep NH (2001) The habitat and nature of early life. *Nature*, **409**, 1083-1091.
- Nuevo M, Milam SN, Sandford SA, Elsila JE, Dworkin JP (2009) Formation of Uracil from the Ultraviolet Photo-Irradiation of Pyrimidine in Pure H₂O Ices. *Astrobiology*, **9**, 683-695.
- Nutman AP, Mojzsis SJ, Friend CRL (1997) Recognition of ≥ 3850 Ma water-lain sediments in West Greenland and their significance for the early Archaean Earth. *Geochimica et Cosmochimica Acta*, **61**, 2475-2484.
- Olson DB, Backus RH (1985) The concentrating of organisms at fronts: A cold-water fish and a warm-core Gulf Stream ring. *Journal of Marine Research*, **43**, 113-137.
- Ono S, Eigenbrode JL, Pavlov AA, Kharecha P, Rumble III D, Kasting JF, Freeman KH (2003) New insights into Archean sulfur cycle from mass-independent sulfur isotope records from the Hamersley Basin, Australia. *Earth and Planetary Science Letters*, **213**, 15-30.
- Orgel LE (1998) The origin of life - a review of facts and speculations. *TRENDS in Biochemical Sciences*, **23**, 491-495.
- Pace NR (1997) A molecular view of microbial diversity and the biosphere. *Science*, **276**, 734-740.
- Papineau D (2010) Mineral environments on the earliest Earth. *Elements*, **6**, 25-30.
- Parnell J (2004) Mineral radioactivity in sands as a mechanism for fixation of organic carbon on the early Earth. *Origins of Life and Evolution of the Biosphere*, **34**, 533-547.
- Pasek MA, Lauretta DS (2005) Aqueous Corrosion of Phosphide Minerals from Iron Meteorites: A Highly Reactive Source of Prebiotic Phosphorus on the Surface of the Early Earth. *Astrobiology*, **5**, 515-535.
- Peretó JG, Velasco AM, Becerra A, Lazcano A (1999) Comparative biochemistry of CO₂ fixation and the evolution of autotrophy. *International microbiology: the official journal of the Spanish Society for Microbiology*, **2**, 3.
- Pestunova O, Simonov A, Snytnikov V, Stoyanovsky V, Parmon V (2005) Putative mechanism of the sugar formation on prebiotic Earth initiated by UV-radiation. *Advances in Space Research*, **36**, 214-219.
- Pfirman SL, Eicken H, Bauch D, Weeks WF (1995) The potential transport of pollutants by Arctic sea ice. *Science of the Total Environment*, **159**, 129-146.
- Phillips FM, Castro MC (2004) Groundwater dating and residence-time measurements. In: *Surface and Ground Water, Weathering, and Soils* (eds Holland HD, Turekian KK). Elsevier-Pergamon, Oxford.
- Pickering KT, Soh W, Taira A (1991) Scale of tsunami-generated sedimentary structures in deep water. *Journal of the Geological Society, London*, **148**, 211-214.
- Pierre-Alain M, Hans Z (2008) Eutectic Phase in Water-Ice: A Self-Assembled Environment Conducive to Metal-Catalyzed Non-Enzymatic RNA Polymerization. *Chemistry & Biodiversity*, **5**, 1521-1539.
- Pietranik AB, Hawkesworth CJ, Storey CD, Kemp AIS, Sircombe KN, Whitehouse MJ, Bleeker W (2008) Episodic, mafic crust formation from 4.5 to 2.8 Ga: New evidence from detrital zircons, Slave craton, Canada. *Geology*, **36**, 875-878.
- Pizzarello S, Shock E (2010) The organic composition of carbonaceous meteorites: The evolutionary story ahead of biochemistry. *Cold Spring Harbor Perspectives in Biology*.

- Pons M-L, Quitte G, Fujii T, Rosing MT, Reynard B, Moynier F, Douchet C, Albarede F (2011) Early Archean serpentine mud volcanoes at Isua, Greenland, as a niche for early life. *Proceedings of the National Academy of Sciences*, **108**, 17639-17643.
- Pope EC, Bird DK, Rosing M (2012) Isotope composition and volume of Earth's early oceans. *Proceedings of the National Academy of Sciences*.
- Powner MW, Gerland B, Sutherland JD (2009) Synthesis of activated pyrimidine ribonucleotides in prebiotically plausible conditions. *Nature*, **459**, 239-242.
- Price PB (2007) Microbial life in glacial ice and implications for a cold origin of life. *FEMS Microbiology Ecology*, **59**, 217-231.
- Price PB (2009) Microbial genesis, life and death in glacial ice. *Canadian Journal of Microbiology*, **55**, 1-11.
- Pringle DJ, Miner JE, Eicken H, Golden KM (2009) Pore space percolation in sea ice single crystals. *Journal of Geophysical Research*, **114**, C12017.
- Proskurowski G, Lilley MD, Seewald JS, Fruh-Green GL, Olson EJ, Lupton JE, Sylva SP, Kelley DS (2008) Abiogenic hydrocarbon production at lost city hydrothermal field. *Science*, **319**, 604-607.
- Ragsdale (1991) Enzymology of the acetyl-CoA pathway of CO₂ fixation. *Critical Reviews in Biochemistry and Molecular Biology*, **26**, 261-300.
- Rasmussen B, Buick R (1999) Redox state of the Archean atmosphere: Evidence from detrital heavy minerals in ca. 3250-2750 Ma sandstones from the Pilbara Craton, Australia. *Geology*, **27**, 115-118.
- Richter FM (1988) A major change in the thermal state of the Earth at the Archaean-Proterozoic boundary: consequences for the nature and preservation of continental lithosphere. *Journal of Petrology*, 39-52.
- Rode BM, Son HL, Suwannachot Y (1999) The combination of salt induced peptide formation reaction and clay catalysis: a way to higher peptides under primitive Earth conditions. *Origins of Life and Evolution of the Biosphere*, **29**, 273-286.
- Rollinson H (2007) *Early Earth systems*, Blackwell Publishing, Oxford, UK.
- Rosenzweig AC (2002) Metallochaperones: Bind and deliver. *Chemistry and Biology*, **9**, 673-677.
- Russell MJ, Hall AJ, Martin W (2010) Serpentinization as a source of energy at the origin of life. *Geobiology*.
- Russell MJ, Martin W (2004) The rocky roots of the acetyl-CoA pathway. *TRENDS in Biochemical Sciences*, **29**, 358-363.
- Ryder G (2003) Bombardment of the Hadean Earth: Wholesome or deleterious? . *Astrobiology*, **3** 3-6.
- Sander SG, Koschinsky A (2011) Metal flux from hydrothermal vents increased by organic complexation. *Nature Geoscience*, **4**, 145-150.
- Sansone FJ, Andrews CC, Okamoto MY (1987) Adsorption of short-chain organic acids onto nearshore marine sediments. *Geochimica et Cosmochimica Acta*, **51**, 1889-1896.
- Schlesinger G, Miller SL (1983) Prebiotic synthesis in atmospheres containing CH₄, CO and CO₂. I: Amino Acids. *Journal of Molecular Evolution*, **19**, 376-382.
- Schmitt-Kopplin P, Gabelica Z, Gougeon RD, Fekete A, Kanawati B, Harir M, Gebefuegi I, Eckel G, Hertkorn N (2010) High molecular diversity of extraterrestrial organic matter in Murchison meteorite revealed 40 years after its fall. *Proceedings of the National Academy of Sciences*, **107**, 2763-2768.

- Schoepp-Cothenet B, Van Lis R, Atteia A, Baymann F, Capowicz L, Ducluzeau A-L, Duval S, Brink FT, Russell MJ, Nitschke W (2012a) On the universal core of bioenergetics. *Biochimica et Biophysica Acta (BBA) - Bioenergetics*, **in press**.
- Schoepp-Cothenet B, van Lis R, Philippot P, Magalon A, Russell MJ, Nitschke W (2012b) The ineluctable requirement for the trans-iron elements molybdenum and/or tungsten in the origin of life. *Scientific Reports*, **2**, 1-5.
- Schoonen M, Smirnov A, Cohn C (2004) A perspective on the role of minerals in prebiotic synthesis. *AMBIO*, **33**, 539-551.
- Schwartzmann DW, Lineweaver CH (2004) The hyperthermophilic origin of life revisited. *Biochemical Society Transactions*, **32**.
- Serganov A, Patel DJ (2007) Ribozymes, riboswitches and beyond: regulation of gene expression without proteins. *Nature Reviews Genetics*, **8**, 776-790.
- Shanker U, Bhushan B, Bhattacharjee G, Kamaluddin (2011) Formation of nucleobases from formamide in the presence of iron oxides: implications in chemical evolution and origin of life. *Astrobiology*, **11**, 225-233.
- Shibuya R, Komiya T, Nakamura K, Takai K, Maruyama S (2010) Highly alkaline, high-temperature hydrothermal fluids in the early Archean ocean. *Precambrian Research*, **182**, 230-238.
- Shigemasa Y, Matsuda Y, Sakazawa C, Matsuura T (1977) Formose reactions. II. The photochemical formose reaction. *Bulletin of the Chemical Society of Japan*, **50**, 222-226.
- Shock E (1992) Chemical environments of submarine hydrothermal systems. *Origins of Life and Evolution of Biospheres*, **22**, 67-107.
- Shock EL (1990) Do amino acids equilibrate in hydrothermal fluids? *Geochimica et Cosmochimica Acta*, **54**, 1185-1189.
- Shock EL, Schulte MD (1998) Organic synthesis during fluid mixing in hydrothermal systems. *Journal of Geophysical Research*, **103**, 28513-28527.
- Shriver DF, Atkins PW (1999) *Inorganic Chemistry*, Oxford University Press.
- Sieburth J (1983) Microbiological and organic-chemical processes in the surface and mixed layer. In: *Air sea exchange of gases and particles* (eds Liss PS, Slinn WGN). D. Reidel Publishing Company, Dordrecht, pp. 121-172.
- Siever R (1992) The silica cycle in the Precambrian. *Geochimica et Cosmochimica Acta*, **56**, 3265-3272.
- Sleep NH, Meibom A, Fridriksson T, Coleman RG, Bird DK (2004) H₂-rich fluids from serpentinization: Geochemical and biotic implications. *Proceedings of the National Academy of Sciences*, **101**, 12818-12823.
- Sleep NH, Zahnle KJ, Kasting JF, Morowitz HJ (1989) Annihilation of ecosystems by large asteroid impacts on the early Earth. *Nature*, **342**, 139-142.
- Sleep NH, Zoback MD (2007) Did earthquakes keep the early crust habitable? *Astrobiology*, **7**, 1023-1032.
- Smetacek V, Bodungen B, Broeckel K, Zeitzschel B (1976) The plankton tower. II. Release of nutrients from sediments due to changes in the density of bottom water. *Marine Biology*, **34**, 373-378.
- Sowerby SJ, Cohn CA, Heckl WM, Holm N (2001) Differential adsorption of nucleic acid bases: relevance to the origin of life. *Proceedings of the National Academy of Sciences*, **98**, 820-822.

- Sowerby SJ, Petersen GB, Holm N (2002) Primordial coding of amino acids by adsorbed purine bases. *Origins of Life and Evolution of Biospheres*, **32**, 35-46.
- Spinelli G, Fisher AT (2004) Hydrothermal circulation within topographically rough basaltic basement on the Juan de Fuca Ridge flank. *Geochemistry, Geophysics, Geosystems*, **5**, 1-19.
- Srinivasan V, Morowitz HJ (2009) The canonical network of autotrophic intermediary metabolism: Minimal metabolome of a reductive chemoautotroph. *Biological Bulletin*, **216**, 126-130.
- Stumm NJ, Morgan JJ (1996) *Aquatic Chemistry*, John Wiley & Sons, Inc., New York.
- Sugitani K, Mimura K, Suzuki K, Nagamine K, Sugisaki R (2003) Stratigraphy and sedimentary petrology of an Archean volcanic-sedimentary succession at Mt. Goldsworthy in the Pilbara Block, Western Australia: implications of evaporite (nahcolite) and barite deposition. *Precambrian Research*, **120**, 55-79.
- Summons RE (1993) Biochemical cycles. A review of fundamental aspects of organic matter formation, preservation, and composition. In: *Organic geochemistry: principles and applications* (eds Engel MH, Macko SA). Plenum Press, New York, pp. 3.
- Syvitski JPM, Peckham SD, Hilberman R, Mulder T (2003) Predicting the terrestrial flux of sediment to the global ocean: A planetary perspective. *Sedimentary Geology*, **162**, 5-24.
- Tenchov B, Vescio EM, Sprott GD, Zeidel ML, Mathai JC (2006) Salt tolerance of Archeal extremely halophilic lipid membranes. *Journal of Biological Chemistry*, **281**, 10016-10023.
- Tervahattu H, Juhanoja J, Kupianinen K (2002) Identification of an organic coating on marine aerosol particles by TOF-SIMS. *Journal of Geophysical Research*, **107**, 10.1029/2001JD001403.
- Theobald DL (2010) A formal test of the theory of universal common ancestry. *Nature*, **465**, 219-222.
- Thomas DN, Dieckmann GS (2002) Antarctic sea ice - a habitat for extremophiles. *Science*, **295**, 641-644.
- Tian F, Toon OB, Pavlov AA (2006) Response to comment on "A hydrogen-rich early Earth atmosphere. *Science*, **311**, 38b.
- Tian F, Toon OB, Pavlov AA, De Sterck H (2005) A hydrogen-rich early Earth atmosphere. *Science*, **308**, 1014-1017.
- Timperley MH (1983) Phosphorus in spring waters of the Taupo Volcanic Zone, North Island, New Zealand. *Chemical Geology*, **38**, 287-306.
- Timperley MH, Vigor-Brown R (1985) Weathering of pumice in the sediments as a possible source of major ions for the waters of Lake Taupo, New Zealand. *Chemical Geology*, **49**, 43-52.
- Tingle TN, Hochella Jr. MF (1993) Formation of reduced carbonaceous matter in basalts and xenoliths: Reactions of C-O-H gases in olivine crack surfaces. *Geochimica et Cosmochimica Acta*, **57**, 3245-3249.
- Tolstoy M, Vernon FL, Orcutt JA, Wyatt FK (2002) Breathing of the seafloor: Tidal correlations of seismicity at Axial volcano. *Geology*, **30**, 503-506.
- Trefil J, Morowitz H, Smith E (2009) The origin of life: A case is made for the descent of electrons. *American Scientist*, **97**, 206-213.

- Trocine RP, Trefry JH (1988) Distribution and chemistry of suspended particles from an active hydrothermal vent site on the Mid-Atlantic Ridge at 26°N. *Earth and Planetary Science Letters*, **88**, 1-15.
- Tuck A (2002) The Role of Atmospheric Aerosols in the Origin Of Life. *Surveys in Geophysics*, **23**, 379-409.
- Turcotte DL (1980) On the thermal evolution of the Earth. *Earth and Planetary Science Letters*, **48**, 53-58.
- van der Gulik P, Masser S, Gilis D, Buhman H, Rooman M (2009) The first peptides: the evolutionary transition between prebiotic amino acids and early proteins. *Journal of Theoretical Biology*, **261**, 531-539.
- Vearncombe S, Barley ME, Groves DI, McNaughton NJ, Mikucki EJ, Vearncombe JR (1995) 3.26 Ga black smoker-type mineralization in the Stretney Belt, Pilbara Craton, Western Australia. *Journal of the Geological Society, London*, **152**, 587-590.
- Veizer J, Jansen SL (1979) Basement and sedimentary recycling and continental evolution. *Journal of Geology*, **87**, 341-370.
- von Damm KL (1990) Seafloor hydrothermal activity: black smoker chemistry and chimneys. *Annual Review of Earth and Planetary Sciences*, **18**.
- Wächterhäuser G (1988a) Before Enzymes and Templates: Theory of Surface Metabolism. *Microbiological Reviews*, **52**, 452-484.
- Wächterhäuser G (1988b) Pyrite formation, the first energy source for life: a hypothesis. *Synthetic and Applied Microbiology*, **10**, 207-210.
- Wächterhäuser G (1990) Evolution of the first metabolic cycles. *Proceedings of the National Academy of Sciences*, **87**, 200-204.
- Wahr JM (1988) The Earth's Rotation. *Annual Review of Earth and Planetary Sciences*, **16**, 231-249.
- Wallace Jr. GT, Duce RA (1978) Open-ocean transport of particulate trace metals by bubbles. *Deep Sea Research*, **25**, 827-835.
- Wania F, Hoff JT, Jia CQ, Mackay D (1998) The effects of snow and ice on the environmental behaviour of hydrophobic organic chemicals. *Environmental Pollution*, **102**, 25-41.
- Webb EC (1992) *Enzyme nomenclature 1992: recommendations of the Nomenclature Committee of the International Union of Biochemistry and Molecular Biology on the nomenclature and classification of enzymes*, Academic Press, San Diego.
- Wharton RA, Jr., McKay CP, Simmons GM, Jr., Parker BC (1985) Cryoconite holes on glaciers. *BioScience*, **35**, 499-503.
- Wilde SA, Valley JW, Peck WH, Graham CM (2001) Evidence from detrital zircons for the existence of continental crust and oceans on the Earth 4.4 Gyr ago. *Nature*, **409**, 175-178.
- Williams A, Frasca B (1999) Ion-exchange chromatography. In: *Current Protocols in Protein Science* (eds Coligan JE, Dunn BM, Speicher DW, Wingfield PT). John Wiley & Sons, New York.
- Williams G, Holloway J (1982) The range and unity of planetary circulations. *Nature*, **297**, 295-299.
- Williams GE (2000) Geological constraints on the Precambrian history of Earth's rotation and the Moon's orbit. *Reviews of Geophysics*, **38**, 37-59.
- Wolf ET, Toon OB (2010) Fractal organic haze provided an ultraviolet shield for early Earth. *Science*, **328**, 1266-1268.
- Yamagata Y, Watanabe H, Saitoh M, Namba T (1991) Volcanic production of polyphosphates and its relevance to prebiotic evolution. *Nature*, **352**, 516-519.

- Zahnle KJ, Schaefer L, Fegley B (2010) Earth's earliest atmospheres. In: *The Origins of Life* (eds Deamer D, Shostak JW). Cold Spring Harbor Laboratory Press, New York.
- Zerkle AL, House CH, Brantley SL (2005) Biogeochemical signatures through time as inferred from whole microbial genomes. *American Journal of Science*, **305**, 467-502.
- Zubay G, Mui T (2001) Prebiotic synthesis of nucleotides. *Origins of Life and Evolution of Biospheres*, **31**, 87-102.

Appendix to Chapter 1

Table A1.1. Organic synthesis reactions at low temperatures. Note: the formation of uracil from pyrimidine under UV light was tested under conditions similar to those on the moon Titan.

reaction	T [K]	P [atm]	pH	Reactants	Product	Catalyst	Time	References
Production of amino acids from tholins	253/293	1	nr	tholins, NH ₄ OH	asparagine, glutamine, histidine	none	1 yr	(Neish <i>et al.</i> , 2010)
Production of adenine and amino acids from NH ₄ CN	195/253	1	9.2	NH ₄ CN	adenine, glycine, various other amino acids	none	25 yr	(Levy <i>et al.</i> , 2000)
Peptides from amino acids	253	1	nr	B-glutamic acid, EDAC	peptides	none	48 hours	(Liu & Orgel, 1997)
UV mediated conversion of pyrimidine to uracil	20-30	10 ⁻¹¹	nr	H ₂ O, pyrimidine	uracil	none	22-23 hours	(Nuevo <i>et al.</i> , 2009)
Nucleic acids from uridine salts	255	1	6 - 8	uridine 5'-monophosphate imidazolide	oligouridylates	Mg ²⁺ , Pb ²⁺	31 days	(Kanavarioti <i>et al.</i> , 2001)
Pyrimidines and purines from HCN	195	1	nr	HCN and NH ₃	various purines and pyrimidines, to include adenine, guanine, uracil	none	27 yr	(Miyakawa <i>et al.</i> , 2002)

Table A1.2. Selected mineral-catalyzed organic synthesis reactions, plotted in Figure 1.8 with colors indicated in column 1. nr = not reported.

Reaction	T[C]	P [atm]	Ph	Reactants	Selected products	Mineral reactant/catalyst	time	References
carbon chain formation and carbon fixation (hydroxycarboxylation)	250	494, 987, 1974	nr	iron sulfide, alkyl(nonyl)thiol, formic acid	pyruvate C ₃ H ₄ O ₃	pyrite (Fe ₂ S)	6 hours	(Cody <i>et al.</i> , 2000)
[grouped as green]	250	1974	nr	iron sulfide, alkyl(nonyl)thiol, formic acid	see Table 2 within reference	nicek, cobalt, iron, copper, zinc sulfides	6 hours	(Cody <i>et al.</i> , 2004)
	400	494	5	formic acid, NiO, FeS, Hcl	C ₂ and C ₃ alkanes	(Fe ₂ Ni ₇)S ₈	3 days	(Fu <i>et al.</i> , 2008)
	100	1	2 – 10	methly thiol (CH ₃ SH), CO	Activated thioester (CH ₃ COSCH ₃), hydrolyzes to acetate	precipitated nickel and iron sulfide NiS FeS	7days	(Huber & Wächtershäuser, 1997)
	175-260	345	nr	H ₂ and C ¹³ labeled CO ₂ , HCO ₃ ⁻ , HCOOH	methane, thermal decomposition ethane and propane	NiFe-alloy, olivine, hematite and magnetite	250 to >6000 hours	(McCollom & Seewald, 2003)
	390	395	8.8; 4.8	C ¹³ labeled CO ₂ , HCO ₃ ⁻	ethane, propane	FeCr ₂ O ₄ and magnetite; just magnetite	774, 1062 hours	(Foustoukos & Seyfried, 2004)
	250	321	Nr	formic acid, powdered Fe	hydrocarbons	Magnetite	44hours	(McCollom & Seewald, 2006)
dinitrogen to ammonia in dilute H₂S, FeS catalyst	120	49	6.9 – 7.5	N ₂ , H ₂ S	NH ₃	FeS	Every 15 min, 2-7 days/24 hours	(Schoonen, Xu, Y.)
[grouped as red]	80	1	3 – 4	N ₂ , H ₂ S	NH ₃	FeS	7 days	(Dörr <i>et al.</i> , 2003)
	300, 500,700, 900	987-3948	nr	N ₂ , formic acid; NO ₂ ; NO ₃ ⁻	NH ₃	Fe ₃ O ₄ ; FeS	2 min, or 24 hours	(Brandes <i>et al.</i> , 1998)

montmorillonite catalyzed nucleotide polymerization	25	1	8	activated mononucleotides	RNA-like oligomers: 9-10 monomer units	Montmorillonite+alkyl ammonium cations	3-7 days	(Ertem <i>et al.</i> , 2010)
[grouped as yellow]	25	1	8	5'-phosphorimidazole of adenosine and uridine	RNA-like timer isomers	Na+-montmorillonite	7 days	(Ertem <i>et al.</i> , 2007)
	25	1	6.8, 7.5, 8	5'-phosphorimidazole of nucleosides (ImpNs)	RNA-like oligomers: up to 14 monomer units in length	Na+-montmorillonite	3-7 days	(Ertem, 2004)
	25	1	8	5'-phosphorimidazole of nucleosides (ImpNs)	oligomers with similar structures to short RNA fragments	Montmorillonite	7 days	(Ertem <i>et al.</i> , 2008)
	25	1	8	2'-d-5'-GMP, 2'-d-5'-AMP, 2'-d-5'-CMP, 2'-d-5'-TMP,	dinucleotides	Na+-montmorillonite	3-4 days	(Ferris <i>et al.</i> , 1990)
	25	1	8	phosphorimidazole of adenosine (ImpA)	oligomers up to 10 nucleotides in length	Na+-montmorillonite	3 days	(Ferris & Ertem, 1992)
	25	1	8	phosphorimidazole of adenosine (ImpA)	oligomers of adenylic acid up to 11 nucleotides in length	Na+-montmorillonite	3-7 days	(Ferris & Ertem, 1993)
amino acid polymerization by mineral surfaces	100	1	4.5	FeS, H ₂ S, mercaptoacetic acid, aniline, tyrosine	acetylamides	pyrite formation	2 days, 4 days	(Keller <i>et al.</i> , 1994)
[grouped as purple]	80	1	nr	glycine, L-alanine	peptide dimers	activated alumina (neutral, acidic, weakly acidic, basic), kaolinite	1-14 days	(Bujdak & Rode, 2001)
	85	1	nr	glycine, alanine, leucine, valine, proline	dipeptides, cyclic anhydrides	activated alumina	3 hours	(Bujdak & Rode, 2001; Bujdak & Rode, 2003)
	nr	1	nr	glutamic acid, aspartic acid, O-phospho-L-serine	45-unit oligomers	hydroxylapatite, illite	24 hours	(Hill <i>et al.</i> , 1998)

	50-500	1	2,4,6,7,8,9,10	glycine, lysine, glutamic acid, leucine, alanine	peptides	SiO ₂ , TiO ₂	nr	(Lambert, 2008)
	25	1	6, 8	1-ethyl-3-(3-dimethylaminopropyl) carbodiimide, aspartic acid, B-glutamic acid, arginine	oligopeptides of B-glutamic acid, tripeptide glu3, oligoarginines	hydroxylapatite, Fe ₂ S, illite, kaolinite, montmorillonite	3.5, 6, 24 hours	(Liu & Orgel, 1998)
	38	1	4,5,6,7,8	glycylglycine, trimetaphosphate, MgCl ₂	tetraglycine, hexaglycine	Mg	10 days	(Yamagata & Inomata, 1997).
degradation by mineral surfaces	25, 50, 70C	1	8.1	glycine, diglycine, diketopiperazine, triglycine	polymer degradation and hydrolysis products	calcite, hematite, montmorillonite, pyrite, rutile, amorphous silica	30, 60, 90, 120 hours	(Marshall-Bowman <i>et al.</i> , 2010)
[grouped as blue]	30	1	nr	RNA, lipids	biopolymer decomposition products	pyrite (Fe ₂ S)	up tp 200 hours	(Cohn <i>et al.</i> , 2004)
	25	1	7.2	Sugar-phosphate ester (p-nitrophenyl phosphate)	hydrolysis products	montmorillonite,	2 hours	(Baldwin <i>et al.</i> , 1995)

Supplementary references

- Baldwin DS, Beatti JK, Coleman M, Jones DR (1995) Phosphate ester hydrolysis facilitated by mineral phases. *Environmental Science and Technology*, **29**, 1706-1709.
- Brandes JA, Bocter NZ, Cody GD, Cooper BA, Hazen RM, Yoder Jr HS (1998) Abiotic nitrogen reduction on the early Earth. *Nature*, **395**, 365-367.
- Bujdak J, Rode BM (2001) Activated alumina as an energy source for peptide bond formation: Consequences for mineral-mediated prebiotic processes. *Amino Acids*, **21**, 281-291.
- Bujdak J, Rode BM (2003) Alumina catalyzed reactions of amino acids. *Journal of Thermal Analysis and Calorimetry*, **73**, 797-805.
- Cody GD, Bocter NZ, Brandes JA, Filley TR, Hazen RM, Yoder HS (2004) Assaying the catalytic potential of transition metal sulfides for abiotic carbon fixation. *Geochimica et Cosmochimica Acta*, **68**, 2185-2196.
- Cody GD, Bocter NZ, Filley TR, Hazen RM, Scott JH, Sharma A, Yoder Jr. HS (2000) Primordial carbonylated iron-sulfur compounds and the synthesis of pyruvate. *Science*, **289**, 1337-1340.
- Cohn CA, Borda MJ, Schoonen MAA (2004) RNA decomposition by pyrite-induced radicals and possible role of lipids during the emergence of life. *Earth and Planetary Science Letters*, **225**, 271-278.
- Dörr M, Kässbohrer J, Grunert R, Kreisel G, Brand WA, Werner RA, Geilmann H, Apfel C, Robl C, Weigand W (2003) A possible prebiotic formation of ammonia from dinitrogen on iron sulfide surfaces. *Angewandte Chemie International Edition*, **42**, 1540-1543.
- Ertem G (2004) Montmorillonite, Oligonucleotides, RNA and the Origin of Life. *Origins of Life and Evolution of Biospheres*, **34**, 549-570.
- Ertem G, Hazen RM, Dworkin JP (2007) Sequence Analysis of Trimer Isomers Formed by Montmorillonite Catalysis in the Reaction of Binary Monomer Mixtures. *Astrobiology*, **7**, 715-722.
- Ertem G, Snellinger-O'Brien AM, Ertem MC, Rogoff DA, Dworkin JP, Johnston MV, Hazen RM (2008) Abiotic formation of RNA-like oligomers by montmorillonite catalysis: part II. *International Journal of Astrobiology*, **7**, 1-7.
- Ertem G, Steudel A, Emmerich K, Lagaly G, Schuhmann R (2010) Correlation between the extent of catalytic activity and charge density of montmorillonite. *Astrobiology*, **10**, 743-749.
- Ferris JP, Ertem G (1992) Oligomerization of ribonucleotides on Montmorillonite: Reaction of the 5'-Phosphorimidazolide of adenosine. *Science*, **257**, 1387-1389.
- Ferris JP, Ertem G (1993) Montmorillonite Catalysis of RNA Oligomer Formation in Aqueous Solution. A model for the prebiotic Formation of RNA. *Journal of the American Chemical Society*, **115**, 12270-12275.
- Ferris JP, Kamaluddin, Ertem G (1990) Oligomerization reactions of deoxyribonucleotides on montmorillonite clay: the effect of mononucleotide structure, phosphate activation and montmorillonite composition on phosphodiester bond formation. *Origins of Life and Evolution of Biospheres*, **20**, 279-291.
- Foustoukos DI, Seyfried WE (2004) Hydrocarbons in hydrothermal vent fluids: the role of chromium-bearing catalysts. *Science*, **304**, 1002-1005.

- Fu Q, Foustoukos DI, Seyfried Jr WE (2008) Mineral catalyzed organic synthesis in hydrothermal systems: An experimental study using time-of-flight secondary ion mass spectrometry. *Geophysical Research Letters*, **35**.
- Hill AR, Böhler C, Orgel LE (1998) Polymerization on the rocks: negatively-charged α -amino acids. *Origins of Life and Evolution of Biospheres*, **28**, 235-243.
- Huber C, Wächtershäuser G (1997) Activated acetic acid by carbon fixation on (Fe,Ni)S under primordial conditions. *Science*, **276**, 245-247.
- Kanavarioti A, Monnard P-A, Deamer DW (2001) Eutectic phases in ice facilitate nonenzymatic nucleic acid synthesis. *Astrobiology*, **1**, 271-281.
- Keller M, Blöchl E, Wächtershäuser G, Stetter KO (1994) Formation of amide bonds without a condensation agent and implications for origin of life. *Nature*, **368**, 836-838.
- Lambert J-F (2008) Adsorption and polymerization of amino acids on mineral surfaces: a review. *Origins of Life and Evolution of Biospheres*, **38**, 211-242.
- Levy M, Miller SL, Brinton K, Bada JL (2000) Prebiotic Synthesis of Adenine and Amino Acids Under Europa-like Conditions. *Icarus*, **145**, 609-613.
- Liu R, Orgel LE (1997) Efficient oligomerization of negatively-charged β -amino acids at -20°C . *Journal of the American Chemical Society*, **119**, 4791-4792.
- Liu R, Orgel LE (1998) Polymerization on the rocks: beta-amino acids and arginine. *Origins of Life and Evolution of Biospheres*, **28**, 245-257.
- Marshall-Bowman K, Ohara S, Sverjensky DA, Hazen RM, Cleaves HJ (2010) Catalytic peptide hydrolysis by mineral surface: Implications for prebiotic chemistry. *Geochimica et Cosmochimica Acta*, **74**, 5852-5861.
- McCollom TM, Seewald JS (2003) Experimental constraints on the hydrothermal reactivity of organic acids and acid anions: I. Formic acid and formate. *Geochimica et Cosmochimica Acta*, **67**, 3625-3644.
- McCollom TM, Seewald JS (2006) Carbon isotope composition of organic compounds produced by abiotic synthesis under hydrothermal conditions. *Earth and Planetary Science Letters*, **243**, 74-84.
- Miyakawa S, Cleaves HJ, Miller S (2002) The cold origin of life: B. Implications based on pyrimidines and purines produced from frozen ammonium cyanide solutions. *Origins of Life and Evolution of Biospheres*, **32**, 209-218.
- Neish CD, Somogyi A, Smith MA (2010) Titan's primordial soup: formation of amino acids via low-temperature hydrolysis of tholins. *Astrobiology*, **10**, 337-347.
- Nuevo M, Milam SN, Sandford SA, Elsila JE, Dworkin JP (2009) Formation of Uracil from the Ultraviolet Photo-Irradiation of Pyrimidine in Pure H_2O Ices. *Astrobiology*, **9**, 683-695.
- Schoonen MAA (Xu, Y.) Nitrogen Reduction Under Hydrothermal Vent Conditions: Implications for the Prebiotic Synthesis of C-H-O-N Compounds. *Astrobiology*, **1**, 133-142.
- Yamagata Y, Inomata K (1997) Condensation of glycylglycine to oligoglycines with trimetaphosphate in aqueous solution. II: Catalytic Effect of Magnesium Ion. *Origins of Life and Evolution of Biospheres*, **27**, 339-344.

Chapter 2: Contributions to Late Archaean sulphur cycling by life on land²

Abstract

From evidence in palaeosols, life on land dates back to at least 2.76 billion years ago (Rye & Holland, 2000; Watanabe *et al.*, 2000). However, the biogeochemical effects of Archaean terrestrial life are thought to have been limited, due to the lack of a protective ozone shield from ultraviolet radiation before the rise of atmospheric oxygen several hundred million years later (Cockell, 2000). Records of chromium delivery from the continents suggest that microbial mineral oxidation began at least 2.48 billion years ago (Konhauser *et al.*, 2011) but do not indicate when the terrestrial biosphere began to dominate major biogeochemical cycles. Here we combine marine sulphur abundance data with a mass balance model of the sulphur cycle to estimate the effects of the Archaean and early Proterozoic terrestrial biosphere on sulphur cycling. We find that terrestrial oxidation of pyrite by microbes using oxygen has contributed a substantial fraction of the total sulphur weathering flux since at least 2.5 billion years ago, with probable evidence of such activity 2.7-2.8 billion years ago. The late Archaean onset of terrestrial sulphur cycling is supported by marine molybdenum abundance data and coincides with a shift to more sulphidic ocean conditions (Reinhard *et al.*, 2009). Thus, significant microbial land colonization evidently began by 2.7-2.8 billion years ago and the oxidation of pyrite at this time provides further evidence (Buick, 2008) for the appearance of molecular oxygen several hundred million years before the Great Oxidation Event.

² Co-authors: D. C. Catling, R. Buick. Published in Nature Geoscience (2012) v. 5 (10), pp. 722-725.

2.1. Introduction

We investigated sulphur abundances in marine sediments as a proxy for life on land, because the various mechanisms by which sulphur can be supplied or removed are understood well enough to detect biological contributions. Our database of ancient marine sedimentary sulphide concentrations (1194 samples from 70 Precambrian formations) in fine-grained clastic facies was compiled from the literature. These data show (Fig. A2.1) that significant increases in the relative abundance of sulphur occurred in the late Archaean and again after the ~2.5 Gyr rise of oxygen. Because of scatter in the data, we employed statistical tests to verify our inferred trends to 95% confidence levels or better. The enrichment of sulphur relative to the siliciclastic background implies a selective enhancement of the sulphur input, which could have been caused by biotic or abiotic weathering, volcanic degassing, or hydrothermal fluids. To evaluate the contributions of different sulphur sources, we constructed a sulphur cycle model.

2.2. Method

In our model, the steady state biogenic input of sulphur to the ocean ($F_{bioticw}$) is estimated as the difference between the total output (F_{out}) and the combined abiotic input fluxes after accounting for detrital sulphide deposition (Fig. A2.2). Before the advent of widespread sulphate-rich evaporites late in the Proterozoic, the major sink for continent-derived sulphur is assumed to be precipitation of sulphide minerals in continental shelf environments, as it is now. Therefore the total output flux for the earlier Precambrian (F_{out}) can be calculated as the product between the sedimentation rate on continental shelves (D) and the concentration of sulphide in shelf sediments ($[S]$). We assume a sedimentation rate similar to modern, noting that a lower rate due to smaller or more inundated Archaean continents does not alter our ultimate conclusions

(Sec. A2.3.3). Abiotic input fluxes considered in the model include volcanic emissions (F_{volc}) and abiotic oxidative weathering ($F_{abioticw}$). We ignore hydrothermal sulphur (Sec. A2.3.2) because it would have precipitated proximal to deep-sea vents under the anoxic conditions prevailing throughout the earlier Precambrian. Potential additions by detrital pyrite are accounted for by iteratively modifying the model based on the assumption that negligible detrital sulphide was deposited after atmospheric oxygenation. We emphasize that increased erosion responsible for enhanced fluxes of detrital pyrite (perhaps because of continental growth) would have raised the total supply of clastic sediments without increasing the relative concentration of sulphur. Selective continental weathering of sulphide minerals can thus be monitored by comparing the average total sulphur concentration ($[S]$) between different stages. The volcanic flux is calculated following previously published parameterizations (Canfield, 2004).

The model can be expressed through the following relationships:

$$F_{in} = F_{out} \Rightarrow F_{volc} + F_w = D \cdot [S] \Rightarrow F_{volc} + (F_{abioticw} + F_{bioticw}) = D \cdot [S] \quad (\text{Eq. 2.1})$$

A detailed description of the computation of these individual fluxes and sensitivities to assumptions is given in the supplementary material. In brief, the abiotic oxidative weathering flux ($F_{abioticw}$) is a function of atmospheric oxygen levels, pH and the surface area of exposed sulphide minerals (Williamson & Rimstidt, 1994) (Sec. A2.4.3). We assume 10^{-5} present atmospheric levels (PAL) of oxygen in the Archaean and 10^{-1} PAL in the Proterozoic (Catling & Claire, 2005 and citations therein). Weathering pH is set to 7 and the surface area of exposed sulphide is calculated for modern conditions and held constant throughout the Precambrian. If pH were more acid (from release of sulphuric acid) or the area of abiotically weathered sulphide minerals were smaller in the Precambrian, a greater biotic flux is required to account for the total weathering sulphur flux (Sec. A2.4.2). So the pH and area assumptions are conservative.

2.3. Results

The total continental sulphur weathering flux (F_w) through time inferred from the data is shown in Fig. 2.1. The dispersion in the fluxes at individual times likely arises from environmental differences between geological formations causing a spread in sulphur concentrations and from temporal or spatial variations in the sedimentation rate that are not accounted for by the model. To identify long-term changes in the weathering flux, we divide the dataset into two, stepping through 100 Myr increments (Section A2.5), and calculate the statistical significance of the difference between the two data blocks. Significant changes in the continental weathering flux of sulphur occur at 2.8 Gyr and 2.5 Gyr. Consequently, the sulphur weathering flux can be divided into three stages (Table 2.1). On average, $F_w(t)$ is required to increase by a factor of ~ 10.0 ($p_{\text{one-tailed}} = 0.003$) from the first Archaean stage (3.3-2.8 Gyr) to the second Archaean stage (2.8-2.5 Gyr), and then by a factor of ~ 2.3 ($p_{\text{one-tailed}} = 0.010$) from the second Archaean stage to the post-Archaean. If we compare the average $F_w(t)$ for all the Archaean data (> 2.5 Gyr) to the Proterozoic (2.5-1.0 Gyr), we observe an increase across the Archaean-Proterozoic boundary by a factor of ~ 3.5 ($p_{\text{one-tailed}} = 0.001$).

2.4. Discussion and conclusion

Abiotic weathering alone cannot explain the total observed weathering flux at any stage (Fig. 2.2). The difference between total weathering and abiotic weathering before 2.8 Gyr may be explained by detrital sulphur input (Holland, 1999; Rasmussen & Buick, 1999; England *et al.*, 2002), but this cannot explain the increase in total weathering in the late Archaean and across the Archaean-Proterozoic boundary because both steps are accompanied by statistically significant

increases in the total sulphur concentration in sediments (Table A2.3). Enhanced erosion of land masses adding detrital sulphur would also have increased the flux of siliciclastic sediments, which does not preferentially enrich sulphur. It is possible that abiotic pyrite oxidation or degassing of very sulphur-rich volcanic rocks such as komatiites temporarily led to a higher sulphur input into the ocean than is accounted for by the model. Both scenarios can be tested using a compilation of molybdenum concentrations in clastic marine sediments over time (Fig. 2.3) because unlike sulphur, Mo is not volatile and is uniformly distributed between ultramafic to felsic rocks (Taylor, 1964; Eggins *et al.*, 1997). After averaging data for each time point and then for different time periods, we see significant increases in sedimentary Mo concentrations around 2.7 Gyr by a factor of 2.1 ($p_{\text{one-tailed}} = 0.003$) and again around 2.5 Gyr by a factor of 5.7 ($p_{\text{one-tailed}} = 0.01$). A division of the Mo dataset at 2.8 Gyr is also statistically significant ($p_{\text{one-tailed}} = 0.02$). Therefore, the increases in the total sulphur weathering flux observed at those times can only be explained by oxidation of continental sulphides. Because abiotic weathering has already been accounted for, these results imply that biological oxidation ($F_{\text{bioticw}}(t)$) has dominated the flux of sulphur to continental shelves since 2.5 Gyr and probably 2.8 Gyr. The record of sulphur concentrations in clastic marine sediments thus provides strong evidence for an extensive terrestrial biosphere since the GOE and most probably earlier.

This conclusion is consistent with sulphur isotopes (Fig. A2.3) indicating oxidative weathering since ~2.8 Gyr or shortly thereafter (Strauss, 2002), as well as with authigenic Cr enrichments indicating a biogenic chromium flux from continents to the ocean at ~2.4 Gyr (Konhauser *et al.*, 2011, Fig. A2.10). The absence of Cr enrichments prior to 2.4 Gyr is likely due to the higher redox potential of Cr relative to S and hence a difference in sensitivity between the two proxies. Enhanced late Archaean continental weathering can also be reconciled with the

record of increasing mass-independent fractionation (MIF) of sulphur isotopes in the late Archaean (e.g. Farquhar *et al.*, 2007). Because MIF is produced by photolysis reactions, the MIF record suggests incorporation of atmospherically processed sulphur, which is usually considered to be volcanogenic SO₂ or H₂S. If, however, biotic continental weathering were more important than previously supposed and exceeded the volcanic input to shelf sediments (Fig. 2.2), then our results may be evidence that a greater flux of biogenic sulphur gases such as CS₂ or dimethyl sulphide to the late Archaean atmosphere contributed significantly to the preservation of MIF (cf. Zahnle *et al.*, 2006).

It is generally thought that the lack of an atmospheric ozone shield prior to the GOE resulted in lethal UV radiation on Earth's land surface, preventing the colonization of terrestrial habitats (e.g. Cockell, 2000). However, a Precambrian terrestrial biosphere may have thrived in endolithic habitats, such as those found in Antarctica today (Walker & Pace, 2007), and was clearly present in Archaean lakes such as those of the Tumbiana Formation by 2.72 Gyr (Buick, 1992). Alternatively, an organic haze derived from methane photolysis may have provided some ultraviolet shielding (Pavlov *et al.*, 2001; Wolf & Toon, 2010). If a terrestrial biota was already extensive in the late Archaean between 2.8 and 2.5 Gyr, then expansion out of local, protected habitats onto exposed land areas after the rise of oxygen and coincident establishment of an ozone shield could explain the stepwise increase in the biogenic sulphur weathering flux from the late Archaean to the Proterozoic (Fig. 2.2). The inferred lower weathering flux of sulphur during the Proterozoic of $\sim 1.3 \cdot 10^{12}$ mol yr⁻¹ compared to the modern $\sim 2.0 \cdot 10^{12}$ mol yr⁻¹ (Table 2.1) implies further expansion of terrestrial life in the late Neoproterozoic or Phanerozoic. Mid-Proterozoic atmospheric oxygen levels were probably between 1% to $\sim 10\%$ of present (Canfield, 2005), and under such conditions, biotic pyrite oxidation as well as aerobic heterotrophy may

have been less effective energy sources than today. Our results may therefore provide further evidence for a second rise of atmospheric oxygen in the Neoproterozoic. They are also consistent with carbon and oxygen isotope evidence for more efficient oxidation of terrestrial organic matter after 850 Myr (Knauth & Kennedy, 2009).

Colonization of land masses by pyrite-oxidizing bacteria would also have affected marine life. By increasing the supply of sulphate, life on land would have allowed the ancient (Shen *et al.*, 2001) but previously suppressed (Habicht *et al.*, 2002) metabolism of dissimilatory sulphate reduction to become ecologically prominent in the ocean. Thus the terrestrial biosphere would have been indirectly responsible for the widespread occurrence of euxinia along late Archaean and Proterozoic continental margins (Poulton & Canfield, 2011). If microbial sulphate reduction suppressed methanogenesis, then the biotic weathering flux may also have facilitated the rise of oxygen in the atmosphere (Catling & Claire, 2005).

The advent of terrestrial biotic sulphide oxidation apparent by 2.8 Gyr and certain by 2.5 Gyr implies that a significant source of oxidants was available, most likely biogenic O₂ (Sec. A2.4.3). The large biotic weathering flux derived in our model requires an O₂ source of similarly large magnitude, possibly in close spatial proximity. As only cyanobacteria are known to generate O₂ in large quantities during their metabolism, our results may provide indirect evidence for the Archaean evolution of these microbes and indicate that the appearance of oxygenic photosynthesis preceded the Great Oxidation Event by at least several hundred million years (contra Liang *et al.*, 2006). This joins several other lines of evidence supporting such a conclusion (Buick, 2008) and implies that atmospheric oxygenation was retarded by geological oxygen sinks.

We conclude that continents have been inhabited by microbial communities since at least 2.5 Gyr and probably 2.8 Gyr, and their metabolic activity played a significant role in the global biogeochemical cycles of redox-sensitive elements, particularly sulphur.

Acknowledgments

We thank Harald Strauss for sharing his sulphur database. This study was funded by NSF EAR-0921580. DCC also acknowledges support from NASA Astrobiology grant NNX10AQ90G.

Author contributions

EES and DCC designed and analysed the model, and all authors contributed to the collection of literature data and the composition of the manuscript.

Tables

Table 2.1: Average sulphur fluxes to continental shelves. Values are reported in mol yr⁻¹. See the text for definitions of F_{volc} , F_w , $F_{abioticw}$ and $F_{bioticw}$. Relative contributions of sulphur sources to continental shelf sediments are given in parentheses, noting that there are considerable inferred increases in the absolute total weathering fluxes in the Proterozoic and Phanerozoic.

	F_{volc}	F_w	$F_{abioticw}$	$F_{bioticw}$
3.3-2.8 Gyr	$1.3 \cdot 10^{11}$ (70.4%)	$5.5 \cdot 10^{10}$	$3.5 \cdot 10^9$ (1.9 %)	$5.2 \cdot 10^{10}$ (27.7 %)
2.8-2.5 Gyr	$1.2 \cdot 10^{11}$ (17.6 %)	$5.5 \cdot 10^{11}$	$3.5 \cdot 10^9$ (0.5 %)	$5.5 \cdot 10^{11}$ (81.9 %)
>2.5 Gyr	$1.2 \cdot 10^{11}$ (25.8 %)	$3.6 \cdot 10^{11}$	$3.5 \cdot 10^9$ (0.7 %)	$3.5 \cdot 10^{11}$ (73.4 %)
2.5-1.0 Gyr	$9.2 \cdot 10^{10}$ (6.9 %)	$1.3 \cdot 10^{12}$	$3.5 \cdot 10^{11}$ (26.0 %)	$9.0 \cdot 10^{11}$ (67.1 %)
Modern	$6.0 \cdot 10^{10}$ (2.9 %) ^(a)	$2.0 \cdot 10^{12}$ ^(b)	$1.1 \cdot 10^{12}$ (53.7 %)	$9.0 \cdot 10^{11}$ (43.4 %)

(a) from Canfield 2004 and references therein, scaled by 30 % to account for the fraction deposited on continental shelves (see main text).

(b) total river flux ($4.03 \cdot 10^{12}$ mol yr⁻¹ from Emerson & Hedges, 2008) scaled by 50 % to include natural pyrite-derived fraction only.

Figures

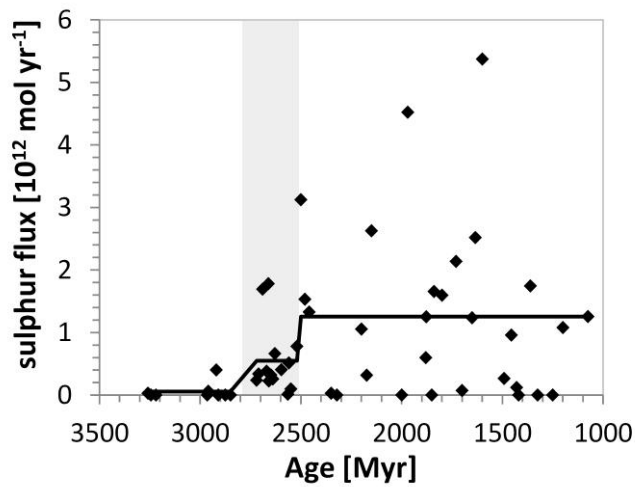


Fig. 2.1: Total inferred weathering flux F_w to continental margins over time. Values are calculated using Eq. (2.1). Each individual point at a given time is derived from averaged marine sulphur concentrations from one geologic formation or more if there are several formations of the same age. Calculated average fluxes for three temporal stages are shown as horizontal lines, where the stages are 2.5-1.0 Gyr, 2.8-2.5 Gyr, and 3.3-2.8 Gyr.

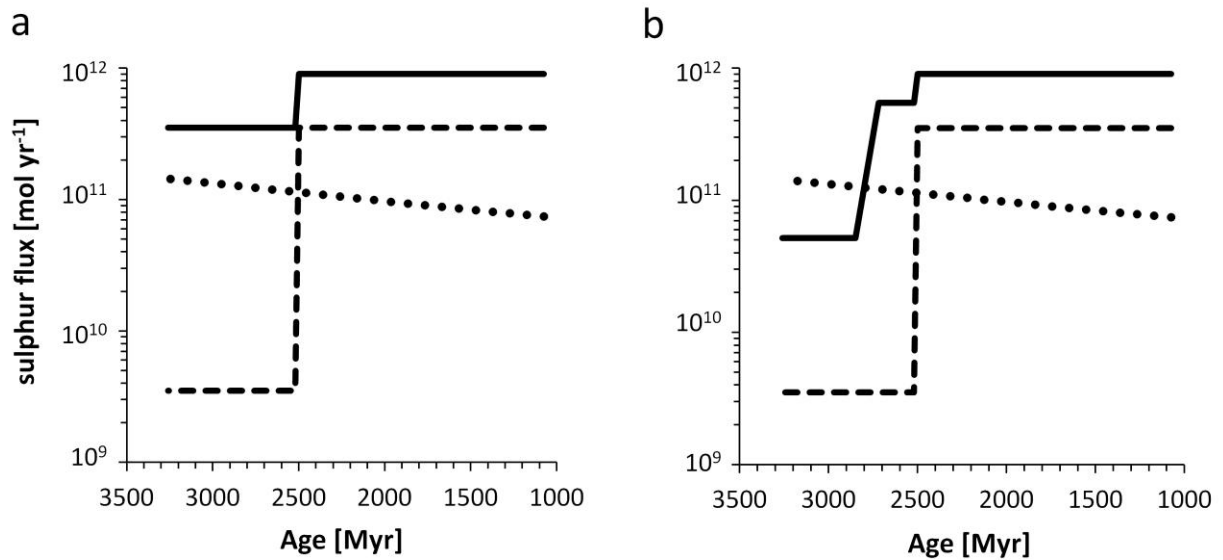


Fig. 2.2: Contribution of different sulphur sources to continental margin sediments. The two scenarios (a) and (b) are as follows: (a) the data contributing to the calculations have been divided up into two temporal stages of Archaean (>2.5 Gyr) and post-Archaean (2.5-1.0 Gyr); (b) the data have been divided up into three temporal stages: 3.3-2.8Gyr, 2.8-2.5 Gyr, and 2.5-1.0 Gyr. The solid line marks the biotic/detrital weathering flux, the dashed line marks the abiotic weathering flux, the dotted line marks the volcanic flux. It is evident that only a biotic weathering flux can account for the Proterozoic total weathering flux.

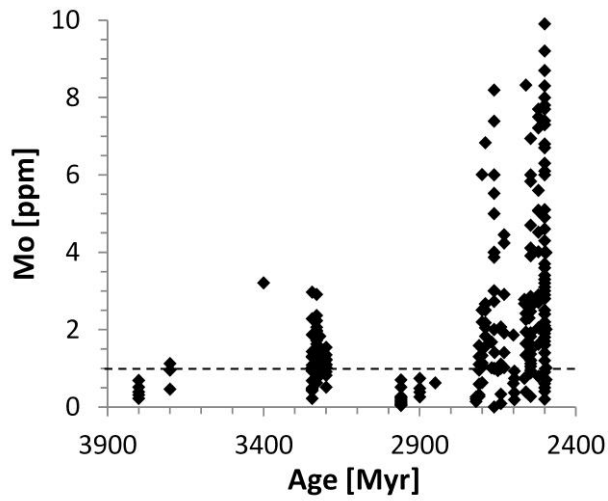


Fig. 2.3. Molybdenum concentrations in the late Archaean and early Proterozoic. The data show a step change around ~2.7 Gyr, which is significant to a 99 % confidence level. References and additional data are provided in the supplementary material (Sec. A2.6). Dashed black line marks crustal average. Data from the Mt. McRae Shale (2.5 Gyr) are cut off at 10 ppm.

References

- Buick R (1992) The antiquity of oxygenic photosynthesis: evidence from stromatolites in sulphate-deficient Archean lakes. *Science*, **255**, 74-77.
- Buick R (2008) When did oxygenic photosynthesis evolve? *Philosophical Transactions of the Royal Society B*, **363**, 2731-2743.
- Canfield DE (2004) The evolution of the Earth surface sulfur reservoir. *American Journal of Science*, **304**, 839-861.
- Canfield DE (2005) The early history of atmospheric oxygen: Homage to Robert M. Garrels. *Annual Review of Earth and Planetary Sciences*, **33**, 1-36.
- Catling DC, Claire MW (2005) How Earth's atmosphere evolved to an oxic state: a status report. *Earth and Planetary Science Letters*, **237**, 1-20.
- Cockell CS (2000) The ultraviolet history of the terrestrial planets - implications for biological evolution. *Planetary and Space Science*, **48**, 203-214.
- Eggins SM, Woodhead JD, Kinsley LPJ, Mortimer GE, Sylvester P, McCulloch MT, Hergt JM, Handler MR (1997) A simple method for precise determination of > 40 trace elements in geological samples by ICPMS using enriched isotope internal standardisation. *Chemical Geology*, **134**, 311-326.
- Emerson S, Hedges J (2008) *Chemical oceanography and the marine carbon cycle*, Cambridge University Press, Cambridge, UK.
- England GL, Rasmussen B, Krapez B, Groves DI (2002) Palaeoenvironmental significance of rounded pyrite in siliclastic sequences of the Late Archean Witwatersrand Basin: oxygen-deficient atmosphere or hydrothermal alteration? *Sedimentology*, **49**, 1133-1156.
- Farquhar J, Peters M, Johnston DT, Strauss H, Masterson AL, Wiechert U, Kaufman AJ (2007) Isotopic evidence for Mesoarchean anoxia and changing atmospheric sulphur chemistry. *Nature*, **449**, 706-709.
- Habicht KS, Gade M, Thamdrup B, Berg P, Canfield DE (2002) Calibration of sulfate levels in the Archean Ocean. *Science*, **298**, 2372-2374.
- Holland HD (1999) When did the Earth's atmosphere become oxic? A Reply. *The Geochemical News*, **100**, 20.
- Knauth LP, Kennedy MJ (2009) The late Precambrian greening of the Earth. *Nature*, **460**, 728-732.
- Konhauser KO, Lalonde SV, Planavsky NJ, Pecoits E, Lyons TW, Mojzsis SJ, Rouxel OJ, Barley ME, Rosiere C, Fralick PW, Kump LR, Bekker A (2011) Aerobic bacterial pyrite oxidation and acid rock drainage during the Great Oxidation Event. *Nature*, **478**, 369-373.
- Liang M-C, Hartman H, Kopp RE, Kirschvink JL, Yung YL (2006) Production of hydrogen peroxide in the atmosphere of a Snowball Earth and the origin of oxygenic photosynthesis. *Proceedings of the National Academy of Sciences*, **103**, 18896-18899.
- Pavlov AA, Brown LL, Kasting JF (2001) UV shielding of NH₃ and O₂ by organic hazes in the Archean atmosphere. *Journal of Geophysical Research*, **106**, 23267-23287.
- Poulton SW, Canfield DE (2011) Ferruginous conditions: A dominant feature of the ocean through Earth's history. *Elements*, **7**, 107-112.
- Rasmussen B, Buick R (1999) Redox state of the Archean atmosphere: evidence from detrital heavy minerals in ca. 3250-2750 Ma sandstones from the Pilbara Craton, Australia. *Geology*, **27**, 115-118.

- Reinhard CT, Raiswell R, Scott CT, Anbar A, Lyons TW (2009) A late Archean sulfidic sea stimulated by early oxidative weathering of the continents. *Science*, **326**, 713-716.
- Rye R, Holland HD (2000) Life associated with a 2.76 Ga ephemeral pond?: Evidence from Mount Roe #2 paleosol. *Geology*, **28**, 483-486.
- Shen Y, Buick R, Canfield DE (2001) Isotopic evidence for microbial sulphate reduction in the early Archean era. *Nature*, **410**, 77-81.
- Strauss H (2002) The isotopic composition of Precambrian sulphides - seawater chemistry and biological evolution. In: *Precambrian Sedimentary Environments: A Modern Approach to Ancient Depositional Systems* (eds Altermann W, Corcoran PL). Blackwell Science, Oxford.
- Taylor SR (1964) Abundance of chemical elements in the continental crust: a new table. *Geochimica et Cosmochimica Acta*, **28**, 1273-1285.
- Walker JJ, Pace NR (2007) Endolithic microbial ecosystems. *Annual Reviews in Microbiology*, **61**, 331-347.
- Watanabe Y, Martini JEJ, Ohmoto H (2000) Geochemical evidence for terrestrial ecosystems 2.6 billion years ago. *Nature*, **408**, 574-578.
- Williamson MA, Rimstidt JD (1994) The kinetics and electrochemical rate-determining step of aqueous pyrite oxidation. *Geochimica et Cosmochimica Acta*, **58**, 5443-5454.
- Wolf ET, Toon OB (2010) Fractal Organic Haze Provided an Ultraviolet Shield for Early Earth. *Science*, **328**, 1266-1268.
- Zahnle KJ, Claire MW, Catling DC (2006) The loss of mass-independent fractionation in sulfur due to a Palaeoproterozoic collapse of atmospheric methane. *Geobiology*, **4**, 271-283.

Appendix to Chapter 2

A2.1. Sulphur data sources

Data sources are shown in Table A2.1 where formation ages were revised where conflicts or discrepancies occurred. All data points are provided in a separate excel file. We used total sulphur concentrations, unless the total sulphide fraction was specifically reported, assuming that sulphate contributions are negligible or small throughout that part of the Precambrian considered here, prior to 1.0 Gyr.

For each age point, outliers defined as larger or smaller than the average \pm two standard deviations were removed from the dataset. It is possible that post-depositional effects led to addition or removal of sulphur in individual samples; however, this would apply to sediments of any age. Thus by taking long-term averages of many data points, effects of post-depositional alteration become minimal.

Table A2.1: Data sources for sulphur concentrations from Precambrian shales

Age [Myr]	Location	Author	Age revised after
1075	Nonesuch Shale	(Burnie <i>et al.</i> , 1972)	
1200	Borden Basin	(Scott <i>et al.</i> , 2008b)	
1250	Hongshuizhuang Fm	(Strauss & Moore, 1992)	
1325	Wumishan Fm	(Strauss & Moore, 1992)	
1361	Velkerri Fm	(Donnelly, 1988)	(Johnston <i>et al.</i> , 2008)
1361	Velkerri Fm	(Jackson & Raiswell, 1991)	(Johnston <i>et al.</i> , 2008)
1361	Velkerri Fm	(Scott <i>et al.</i> , 2008b)	(Johnston <i>et al.</i> , 2008)
1361	Lansen Creek Shale	(Strauss, 2002)	(Johnston <i>et al.</i> , 2008)
1361	Velkerri Fm	(Strauss, 2002)	(Johnston <i>et al.</i> , 2008)
1420	Greyson Fm	(Strauss & Moore, 1992)	
1429	McMinn Fm	(Strauss, 2002)	(ASUD, 2011)
1429	Corcoran Fm	(Strauss, 2002)	(ASUD, 2011)
1429	Mainoru Fm	(Strauss, 2002)	(ASUD, 2011)

1455	Newland Fm	(Lyons <i>et al.</i> , 2000)	
1455	Newland Fm	(Strauss & Moore, 1992)	
1455	Prichard Fm	(Strauss & Moore, 1992)	
1600	Bijaigarh Shale	(Banerjee <i>et al.</i> , 2006)	
1600	Rampur Shale	(Banerjee <i>et al.</i> , 2006)	
1635	Reward Fm	(Shen <i>et al.</i> , 2002)	(ASUD, 2011)
1650	Candlow Fm	(Strauss, 2002)	
1700	Deoland Fm	(Banerjee <i>et al.</i> , 2006)	
1700	Kajrahat Fm	(Banerjee <i>et al.</i> , 2006)	
1730	Wollogorang Fm	(Shen <i>et al.</i> , 2002)	
1700	Chuanlingguo Fm	(Strauss & Moore, 1992)	(Planavsky <i>et al.</i> , 2011)
1800	Temiscamie Fm	(Cameron & Garrels, 1980)	(Evangelatos <i>et al.</i> , 2009)
1800	Albanel Fm	(Cameron & Garrels, 1980)	(Evangelatos <i>et al.</i> , 2009)
1840	Rove Fm	(Poulton <i>et al.</i> , 2004)	
1840	Rove Fm	(Cameron & Garrels, 1980)	(Poulton <i>et al.</i> , 2004)
1850	Whitewater Fm	(Cameron & Garrels, 1980)	(Medvedev <i>et al.</i> , 2009)
1878	Gunflint Fm	(Cameron & Garrels, 1980)	(Johnston <i>et al.</i> , 2006)
1880	Menihok Fm	(Cameron & Garrels, 1980)	(Findlay <i>et al.</i> , 1995)
1880	Ruth Shale	(Cameron & Garrels, 1980)	(Zentmyer <i>et al.</i> , 2011)
1880	Fontano Fm	(Strauss & Moore, 1992)	(Hoffman <i>et al.</i> , 2011)
1880	Attikamagen Group	(Cameron & Garrels, 1980)	(Zentmyer <i>et al.</i> , 2011)
1970	Pilgularvi Fm	(Melezhik <i>et al.</i> , 1998)	(Kuznetsov <i>et al.</i> , 2011)
2000	Whites Fm	(Strauss, 2002)	
2150	Francevillian Series	(Scott <i>et al.</i> , 2008b)	
2150	Sengona Argillite Fm	(Scott <i>et al.</i> , 2008b)	
2150	Zaonezhskaya Fm	(Scott <i>et al.</i> , 2008b)	
2174	Silverton Fm	(Watanabe <i>et al.</i> , 1997)	(Guo <i>et al.</i> , 2009)
2200	Mapedi Shale	(Strauss & Beukes, 1996)	(Yamaguchi, 2002)
2200	Mapedi Shale	(Strauss, 2002)	(Yamaguchi, 2002)
2200	Mapedi Shale	(Yamaguchi, 2002)	
2322	Timeball Hill Fm	(Watanabe <i>et al.</i> , 1997)	(Bekker <i>et al.</i> , 2004)
2322	Timeball Hill Fm	(Yamaguchi, 2002)	(Bekker <i>et al.</i> , 2004)
2350	Gowganda Fm	(Cameron & Garrels, 1980)	(Papineau <i>et al.</i> , 2007)
2460	Malips Mbr, Penge Fm	(Cameron, 1983)	(Pickard, 2003)
2480	Dales Gorge Mbr	(Cameron, 1983)	(Simonson <i>et al.</i> , 2009)
2500	Mt McRae Shale	(Kaufman <i>et al.</i> , 2007)	
2500	Mt McRae Shale	(Ono <i>et al.</i> , 2003)	
2500	Mt McRae Shale	(Strauss, 2002)	
2520	Klein Naute Fm	(Ono <i>et al.</i> , 2009a)	(Simonson <i>et al.</i> , 2009)
2520	Gamohaam Fm	(Scott <i>et al.</i> , 2008b)	(Sumner & Beukes, 2009)
2550	Oak Tree Fm	(Yamaguchi, 2002)	(Bumby <i>et al.</i> , 2011)
2550	Reivilo Fm	(Strauss & Beukes, 1996)	(Bumby <i>et al.</i> , 2011)
2550	Reivilo Fm	(Strauss, 2002)	(Bumby <i>et al.</i> , 2011)
2560	Monteville Fm	(Ono <i>et al.</i> , 2009b)	(Bumby <i>et al.</i> , 2011)
2560	Monteville Fm	(Strauss & Beukes, 1996)	(Bumby <i>et al.</i> , 2011)
2560	Monteville Fm	(Strauss, 2002)	(Bumby <i>et al.</i> , 2011)

2565	Wittenoom Dolomite Fm	(Czaja <i>et al.</i> , 2010)	(Partridge <i>et al.</i> , 2008)
2565	Wittenoom Dolomite Fm	(Yamaguchi, 2002)	(Partridge <i>et al.</i> , 2008)
2597	Marra Mamba Iron Fm	(Czaja <i>et al.</i> , 2010)	(Partridge <i>et al.</i> , 2008)
2597	Marra Mamba Iron Fm	(Yamaguchi, 2002)	(Partridge <i>et al.</i> , 2008)
2630	Carawine Dolomite Fm	(Czaja <i>et al.</i> , 2010)	(Rasmussen <i>et al.</i> , 2005)
2630	Carawine Dolomite Fm	(Yamaguchi, 2002)	(ASUD, 2011)
2640	Black Reef Fm	(Strauss & Beukes, 1996)	(Yamaguchi, 2002)
2640	Black Reef Fm	(Strauss, 2002)	(Yamaguchi, 2002)
2640	Black Reef Fm	(Watanabe <i>et al.</i> , 1997)	(Yamaguchi, 2002)
2640	Black Reef Fm	(Yamaguchi, 2002)	
2650	Lokammona Fm	(Ono <i>et al.</i> , 2009b)	(Simonson <i>et al.</i> , 2009)
2650	Lokammona Fm	(Strauss & Beukes, 1996)	(Simonson <i>et al.</i> , 2009)
2650	Lokammona Fm	(Strauss, 2002)	(Simonson <i>et al.</i> , 2009)
2660	Boomplaas Fm	(Strauss & Beukes, 1996)	(Simonson <i>et al.</i> , 2009)
2660	Boomplaas Fm	(Strauss, 2002)	(Simonson <i>et al.</i> , 2009)
2662	Jeerinah Fm	(Czaja <i>et al.</i> , 2010)	(Scott <i>et al.</i> , 2008b)
2662	Jeerinah Fm	(Kakegawa <i>et al.</i> , 2000)	(Scott <i>et al.</i> , 2008b)
2662	Jeerinah Fm	(Ono <i>et al.</i> , 2003)	(Scott <i>et al.</i> , 2008b)
2662	Jeerinah Fm	(Scott <i>et al.</i> , 2008b)	
2662	Jeerinah Fm	(Scott <i>et al.</i> , 2011)	(Scott <i>et al.</i> , 2008b)
2662	Jeerinah Fm	(Strauss & Moore, 1992)	(Scott <i>et al.</i> , 2008b)
2662	Jeerinah Fm	(Strauss, 2002)	(Scott <i>et al.</i> , 2008b)
2662	Jeerinah Fm	(Yamaguchi, 2002)	(Scott <i>et al.</i> , 2008b)
2670	Vryburg Fm	(Ono <i>et al.</i> , 2009b)	(Simonson <i>et al.</i> , 2009)
2670	Vryburg Fm	(Strauss & Beukes, 1996)	(Simonson <i>et al.</i> , 2009)
2670	Vryburg Fm	(Strauss, 2002)	(Simonson <i>et al.</i> , 2009)
2690	Lewin Shale	(Strauss, 2002)	(Yamaguchi, 2002)
2690	Lewin Shale	(Yamaguchi, 2002)	
2710	Rietgat Fm	(Yamaguchi, 2002)	
2720	K-8	(Watanabe <i>et al.</i> , 1997)	
2720	Pillingini Tuff Fm	(Yamaguchi, 2002)	
2850	Upper Jeppestown Shale	(Strauss, 2002)	
2850	Lower Jeppestown Shale	(Strauss, 2002)	
2850	Upper Government Shale	(Strauss, 2002)	
2850	Middle Government Shale	(Strauss, 2002)	
2850	Government Magnetic Shale	(Strauss, 2002)	
2850	Lower Government Shale	(Strauss, 2002)	
2850	Upper Coronation Shale	(Strauss, 2002)	
2850	Middle Coronation Shale	(Strauss, 2002)	
2850	Lower Coronation Shale	(Strauss, 2002)	
2850	Observatory Shale	(Strauss, 2002)	
2875	Boosens Shale	(Strauss, 2002)	(Farquhar <i>et al.</i> , 2007)
2875	Boosens Shale	(Watanabe <i>et al.</i> , 1997)	(Farquhar <i>et al.</i> , 2007)

2910	Roodepoort	(Watanabe <i>et al.</i> , 1997)	
2920	Mosquito Creek Fm	(Ohmoto <i>et al.</i> , 2006)	
2960	Parktown Fm	(Yamaguchi, 2002)	
2965	Mozaan Gp	(Ono <i>et al.</i> , 2006)	
2965	Mozaan Gp	(Strauss, 2002)	(Ono <i>et al.</i> , 2006)
3245	Sheba Fm	(Holland, 1984)	
3245	Sheba Fm	(Strauss, 2002)	(Bao <i>et al.</i> , 2007)
3245	Sheba Fm	(Yamaguchi, 2002)	(Bao <i>et al.</i> , 2007)
3220	Moodies Gp	(Strauss, 2002)	(Javaux <i>et al.</i> , 2010)
3260	Swartkoppie Fm	(Strauss, 2002)	(Schopf <i>et al.</i> , 2007)

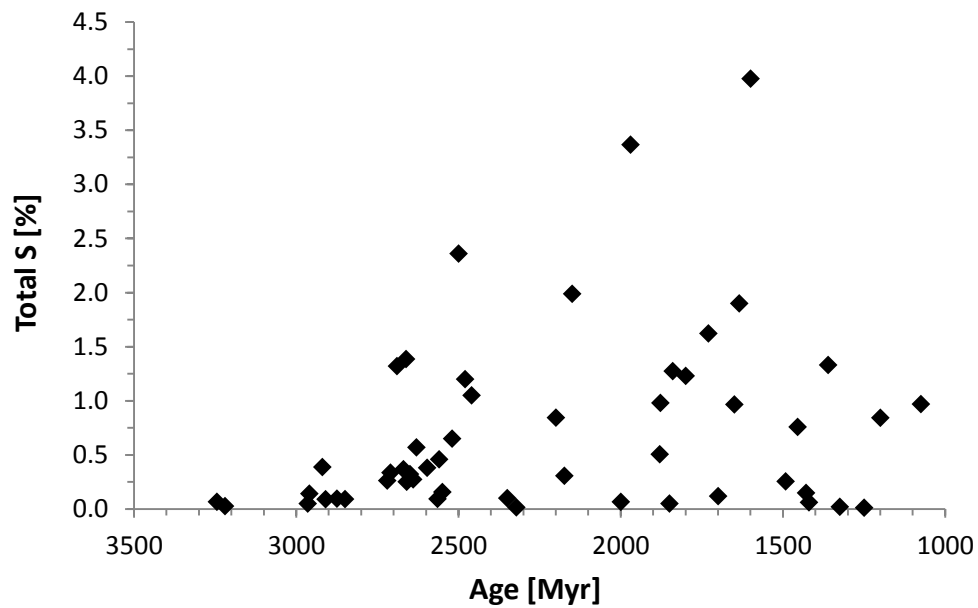


Fig. A2.1: Time-point average sulphur concentrations. For references see Table A2.1.

A2.2. Detailed Model Description

The major fluxes in and out of the ocean considered in the model are the total output flux F_{out} , and three input fluxes (Fig. A2.2): volcanic emission F_{volc} , abiotic oxidative weathering $F_{abioticw}$, and detrital + biological weathering $F_{bioticw}$. The sum of the latter two fluxes is the total weathering flux, F_w .

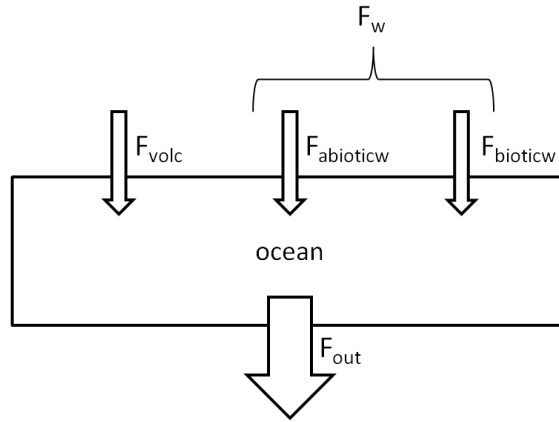


Fig. A2.2: A schematic diagram showing the basic sulphur fluxes considered in the model. See the text for definitions of the flux variables.

A2.2.1. Sulphur concentrations as a record of weathering fluxes

On timescales exceeding the residence time of sulphur, which would be shorter in the early ocean than today's 7.9 Myr (Holland *et al.*, 1986) because of lower marine sulphate concentrations, it is reasonable to assume that the ocean attains steady state with respect to sulphur sources (F_{in}) and sinks (F_{out}) at any time t . Thus,

$$F_{in}(t) = F_{out}(t) \quad (\text{Eq. A2.1})$$

Hereafter, we specify all fluxes in units of mol yr^{-1} .

A2.2.1.1. Sinks

On the modern Earth, shelf environments represent by far the largest sink for marine sulphur (Berner & Berner, 1987). Farquhar *et al.* (2010) estimated that throughout the Archaean

and Paleoproterozoic essentially all continent-derived sulphur was deposited on continental shelves. We therefore assume that shelf sediments accurately record changes in the sulphur weathering flux over time. This assumption is conservative because it may lead to an underestimation of the total weathering flux in the Mesoproterozoic, if sinks to the deep ocean became important at that time.

Today, sulphur is lost from the ocean in the form of either sulphate evaporites or sulphide minerals. Isotopic data show that marine sulphate concentrations were low until a second rise of oxygen in the Neoproterozoic (Canfield & Teske, 1996; Kah *et al.*, 2004) so that evaporite formation only became significant during that era (Canfield & Farquhar, 2009). However, the relative proportions of sulphide minerals and sulphate evaporites formed at any given time since then are poorly constrained. We therefore restrict our model to the Archaean, Paleo-, and Mesoproterozoic. During these times, the formation of sulphate evaporites can be neglected as a sink of sulphur from the ocean. This is also a conservative assumption because by neglecting sulphate evaporites as an additional sink we may underestimate the total weathering flux. But this simplification allows us to use sulphide concentrations of clastic shelf sediments to calculate the total sink, as follows:

$$F_{out}(t) = D \cdot [S](t) \quad (\text{Eq. A2.2})$$

Here, D is the average rate of sedimentation on continental margins. We take a nominal, uniformitarian value of $D = 4.4 \cdot 10^{15} \text{ g yr}^{-1}$, which is the average sedimentation rate on continental margins during the Phanerozoic (Gregor, 1985). Sensitivity studies show that lower values of D , possibly due to smaller continents in the past, do not affect our conclusions (Section A2.3.3 and A2.4.1). $[S](t)$ is the concentration of reduced sulphur in shelf sediments at time t . Sulphur concentrations are taken from an extensive database compiled from the literature of

1194 individual samples spread throughout 70 geologic formations (Section A2.2). Only marine shales and siltstones are considered, because those represent the major lithologies on continental shelves today and probably also in the past (Garrels & Mackenzie, 1971). Furthermore, coarser-grained facies are most likely to contain detrital sulphides that bypassed continental weathering (particularly prior to atmospheric oxygenation).

A2.2.1.2. Sources

Sulphur deposited on continental shelves is ultimately derived from either volcanic degassing ($F_{volc}(t)$) or continental weathering ($F_w(t)$) such that:

$$F_{in}(t) = F_{volc}(t) + F_w(t) \quad (\text{Eq. A2.3})$$

Contributions from hydrothermal vents can be neglected because evidence suggests that the Precambrian deep ocean was ferruginous (Poulton & Canfield, 2011) so that sulphur would have been locally removed as sulphide precipitates near the hydrothermal source (Section A2.3.2).

The volcanic sulphur flux is estimated by multiplying the modern flux ($F_{volc(mod)} = 2 \cdot 10^{11}$ mol yr⁻¹, Canfield (2004) and citations therein) by a factor Q which accounts for increased ancient volcanic activity. We take a parameterization of Q from Canfield (2004), where $Q(t) = 1.00 + 0.1217 \cdot t + 0.0942 \cdot t^2$. Here t is the age in billion years ago (Gyr) (Section A2.3.1). Thus:

$$F_{volc}(t) = F_{volc(mod)} \cdot Q(t) \cdot f_{cont} \quad (\text{Eq. A2.4})$$

where f_{cont} is the fraction of the Earth's surface area covered by continents. For example, if f_{cont} was similar in the Archaean to the modern value, only approximately 30 % of the volcanic sulphur would have been deposited on continental shelves at any given time, while the remaining 70 % would have been incorporated into deep-sea sediments. Therefore the volcanic flux of sulphur reaching shelf sediments would be scaled by a factor of $f_{cont} = 0.3$. The assumption of a

modern value for f_{cont} is conservative for our purposes because it leads to an underestimation if continents were smaller in the Precambrian (Eriksson, 1999).

The total continental weathering flux $F_w(t)$ is then calculated as the difference between the total sink (Eq. A2.2) and the volcanic flux (Eq. A2.4) (see the schematic in Fig. A2.2) such that:

$$F_w(t) = D \cdot [S](t) - F_{\text{volc}}(t) \quad (\text{Eq. A2.5})$$

Using sulphur concentration data $[S]$ from the literature (Table A2.1), we can calculate $F_w(t)$ using Eq. A2.5 (Fig. 2.1). If the product of D and $[S](t)$ is smaller than $F_{\text{volc}}(t)$ due to exceptionally small concentrations of sulphur in a particular formation, Eq. A2.5 gives the unrealistic result that the weathering flux $F_w(t)$ could be negative. We have excluded such unreasonable data points for a few very sulphur-poor formations by setting $F_w(t)$ in these cases to zero mol yr^{-1} .

Now that we have estimates of the flux of weathered sulphur from the continents, we assess whether this flux can be explained by purely abiotic weathering or must be explained by a larger biotic weathering flux.

A2.2.2. Weathering Sources

Sulphur liberated during continental weathering can have three source fluxes: abiotic oxidative weathering ($F_{\text{abioticw}}(t)$), mechanically weathered detrital pyrite, and biogenic weathering. We combine the last two fluxes into one variable ($F_{\text{bioticw}}(t)$) because they cannot be constrained independently. Hence,

$$F_w(t) = F_{\text{abioticw}}(t) + F_{\text{bioticw}}(t) \quad (\text{Eq. A2.6})$$

A2.2.2.1. Abiotic weathering

Williamson and Rimstidt (1994) experimentally determined a rate law for abiotic weathering of pyrite as a function of dissolved oxygen. In units of $\text{mol m}^{-2} \text{yr}^{-1}$, their abiotic pyrite oxidation rate (R_{pO_2}) as a function of pO_2 (in units of atm) is:

$$R_{pO_2} = 10^{-8.19(\pm 0.10)} \cdot ((pO_2 \cdot K_{O_2})^{0.5(\pm 0.04)}) / (m_{H^+}^{0.11(\pm 0.01)}) \cdot 31,536,000 \quad (\text{Eq. A2.7})$$

Here, K_{O_2} is the Henry's law constant for O_2 , which is $0.00126 \text{ mol L}^{-1} \text{ atm}^{-1}$ at 25°C (Stumm & Morgan, 1996), and 31,536,000 is a conversion factor from per second to per year. The molarity (mol L^{-1}) of protons is m_{H^+} , *i.e.* the abiotic oxidation rate increases with decreasing m_{H^+} , which is equivalent to increasing pH. In our model, we take a nominal pH of 7 for the weathering solution. Lower pH values might occur in pyrite-rich settings because of the generation of acidity during sulphide weathering (Rohwerde & Sand (2007), also reviewed by Konhauser *et al.* (2011)). Since our aim is to assess the relative importance of biotic versus abiotic weathering, we choose a conservative assumption (Section A2.4.3). The partial pressure of oxygen is set to 10^{-5} times the present atmospheric level (PAL, 0.21 atm) for the Archaean and 10^{-1} PAL for the Proterozoic based on geologic constraints (*e.g.* Catling & Claire (2005) and citations therein). The flux of abiotically weathered pyrite in units of mol-S yr^{-1} is then equal to the abiotic weathering rate (Eq. A2.7) multiplied by the total surface area of exposed pyrite (A_{py}):

$$F_{abioticw}(t) = A_{py} \cdot R_{pO_2}(t) \quad (\text{Eq. A2.8})$$

We estimate A_{py} for the modern Earth, assuming initially that all pyrite weathered today is oxidized abiotically (Section A2.3.2). This assumption is modified iteratively in subsequent steps (Section A2.2.2.2), when an estimate of the biotic flux is made. To start with, we use the modern flux of riverine sulphate to the ocean ($F_w(mod) = 4.025 \cdot 10^{12} \text{ mol yr}^{-1}$) (Emerson & Hedges, 2008) divided by R_{pO_2} at 1 PAL:

$$A_{py} = F_w(mod) \cdot 0.5 / R_{pO_2}(mod) \quad (\text{Eq. A2.9})$$

Berner and Berner (1987) estimated that today more than 40 % of riverine sulphate is anthropogenic. Of the naturally produced sulphate, two thirds are likely derived from the dissolution of evaporites and only one third from the oxidation of sulphide minerals, but these relative proportions are poorly constrained. We therefore scale the modern flux $F_w(mod)$ by a conservative factor of 0.5 (Eq. A2.9).

A2.2.2.2. Biotic and physical weathering

The detrital plus biogenic sulphur flux ($F_{bioticw}(t)$) to continental shelves is calculated as the difference between the total weathering flux ($F_w(t)$) and the abiotic flux ($F_{abioticw}(t)$):

$$F_{bioticw}(t) = D \cdot [S](t) - F_{volc}(t) - A_{py} \cdot R_{po2}(t) \quad (\text{Eq. A2.10})$$

Detrital pyrite largely disappears from the geologic record after 2.3 Gyr because it dissolves in oxygenated river waters (reviewed by Holland (1999)). Hence the post-Archaeon value for $F_{bioticw}(t)$ likely only comprises biogenic sulphur. The average Paleo- and Meso-Proterozoic biogenic sulphur flux are then subtracted from the modern flux ($F_w(mod)$) to obtain a more accurate estimate of the modern abiotic flux ($F_{abioticw}(mod)$). This value is then used iteratively to replace $F_w(mod)$ in Eq. A2.9 to calculate a new value for A_{py} . Convergence of Proterozoic $F_{bioticw}(t)$ to one decimal is achieved in five iterations. We then calculate long-term averages (Fig. 2), which is appropriate for two reasons. First, it is likely that the sedimentary sulphur concentrations reported in the literature represent a wide range of different environmental settings (*e.g.* Section A2.3). Second, the exact nature of the evolution curve for atmospheric pO_2 over time is not well resolved.

A2.3. Possible biases in the total weathering flux

Several factors that our model does not account for could theoretically affect the total weathering flux calculated as $F_w(t) = D \cdot [S](t) - F_{volc}(t)$.

A2.3.1. Volcanic degassing

It is likely that the volcanic sulphur flux was variable over time and did not follow the smooth pattern prescribed by the Q-factor (Eq. A2.4). Such variations may contribute to the scatter in $F_w(t)$ (Fig. 2.1). By averaging over several hundred million years, the effects of periods with exceptionally low or high volcanic sulphur fluxes are reduced. Furthermore, the volcanic flux is generally minor compared to the total weathering fluxes, especially in the late Archaean and Proterozoic (Fig. 2.2). Hence inaccuracies in our approximation of $F_{volc}(t)$ should not undermine the predominance of $F_w(t)$.

A2.3.2. Hydrothermal sulphur addition

We neglect hydrothermal addition to sedimentary sulphur because the very deep ocean was certainly ferruginous in the Archaean (Holland, 1984) and likely remained so until the end of the Mesoproterozoic (Planavsky *et al.*, 2011; Poulton & Canfield, 2011), thus removing sulphide generated in deep-sea hydrothermal vents via pyrite precipitation. Consequently, hydrothermal sulphides would not have reached continental shelves. If hydrothermal sulphides had played a significant role, this assumption would result in an overestimate of $F_w(t)$. But there are additional reasons why this can be discounted. Most sedimentary sulphides of Proterozoic and late Archaean age show non-zero $\delta^{34}\text{S}$ values (Fig. A2.3) and a wider spread (Fig. A2.4) suggestive of bacterial sulphate reduction and thus predominance of non-hydrothermal sulphide. We cannot rule out the possibility of hydrothermal addition before 3 Gyr when $\delta^{34}\text{S}$ shows much less variation, though this was probably due to low concentrations of sulphate in the water

column (Habicht *et al.*, 2002). However, lastly, the total hydrothermal flux of sulphur into the ocean is equal to only about one third of the volcanic flux (Canfield, 2004). Since the volcanic flux is overall small compared to $F_w(t)$ (Fig. 2.2), hydrothermal input would not, if present, significantly affect our calculations or conclusions.

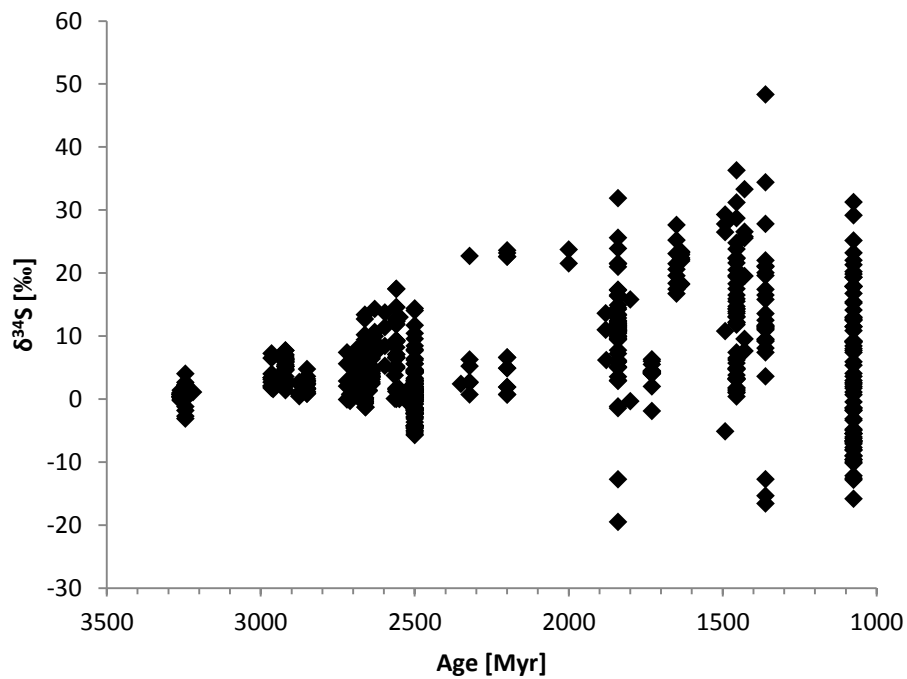


Fig. A2.3: Sulphur isotope compositions of data used in this model. See Table A2.1 for references. Note difference to Fig. A2.12 which includes data from other lithologies and environments not considered in this model.

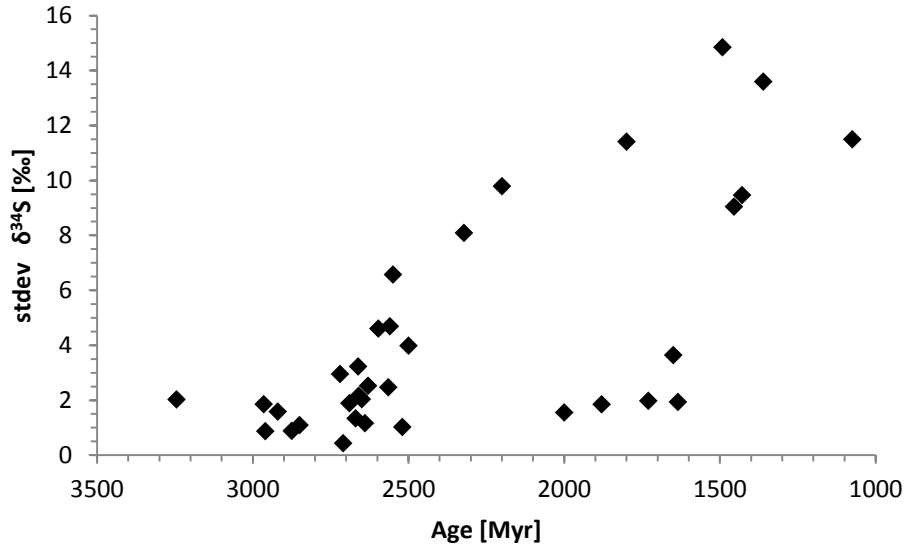


Fig. A2.4: Time-point standard deviation of $\delta^{34}\text{S}$ composition. See Table A2.1 for references.

A2.3.3. Deposition rate

The total weathering flux may be overestimated if the deposition rate D was smaller in the Precambrian than the Phanerozoic average used in the model. If continents increased in size over time, then this would mostly affect results for the mid Archaean. Thus by applying a constant, possibly too high, value for D throughout the Precambrian, the difference in $F_w(t)$ between the Archaean and the Proterozoic may in fact appear smaller than it actually was.

Most models of crustal growth (Eriksson, 1999) predict that continents had reached nearly 80 % of today's volume around the time of the GOE. Most recently, it was demonstrated using zircon data that 80 % of the present volume, as well as a modern style of crystal recycling, may already have been in place by 3 Gyr (Hawkesworth *et al.*, 2010; Dhuime *et al.*, 2012). It is thus unlikely that the long-term average deposition rate has changed drastically since the mid-Archaean. Furthermore, while using an adjusted deposition rate D changes the $F_w(t)/F_{volc}(t)$ ratio

slightly (Table A2.2), but it does not significantly lower the importance of continental weathering as a source of sulphur to continental shelves. For the second Archaean stage (2.8-2.5 Gyr), the calculated ratio $F_w(t)/F_{volc}(t)$ is greater than unity for a deposition rate D down to $1.6 \cdot 10^{15} \text{ g yr}^{-1}$, or 36 % of the average Phanerozoic value. Flament *et al.* (2008) estimated that until the end of the Archaean, continents were mostly submerged and only 2-3 % of the Earth's surface area were above sea level, based on a theoretical model. This scenario perhaps contradicts recent data (Dhuime *et al.*, 2012), but if correct it may have resulted in a significantly lower value for D and a relatively higher contribution of volcanic sulphur to continental shelves. However, it is unlikely that the observed increases in total sulphur concentration at 2.8 Gyr and 2.5 Gyr were due to continental emergence alone, because that would also have raised the erosion rate of silicate minerals and not led to a selective increase in sulphur abundance. And for total sulphur concentration to increase by ~ 400 % at 2.8 Gyr (Table A2.3) the sulphur weathering flux must have contributed a significant fraction to the total supply of sulphur to marine shelves. Hence even if the total weathering flux $F_w(t)$ were smaller in the Archaean than calculated with a constant value for D of $4.4 \cdot 10^{15} \text{ g yr}^{-1}$, the $F_w(t)/F_{volc}(t)$ was probably close to or greater than unity and weathering therefore an important source of sulphur to continental shelves.

It is likely that D varied regionally (Garrels & Mackenzie, 1971) and temporally over the course of supercontinent cycles, which probably explains part of the variations in $F_w(t)$ (Fig. 2.1). However, the value of $4.4 \cdot 10^{15} \text{ g yr}^{-1}$ calculated by Gregor (1985) is an average over the entire Phanerozoic, which also experienced large fluctuations in total shelf area as eustatic sea-level changed and as super-continent amalgamated and broke up. It is therefore reasonable to use this value to calculate averages over several hundred million years.

Table A2.2: Effect of changing D on F_w/F_{volc} ratio.

	$D = 3.5 \cdot 10^{15} \text{ g yr}^{-1}$	$D = 4.4 \cdot 10^{15} \text{ g yr}^{-1}$
3.3-2.8 Gyr	0.2	0.4
2.8-2.5 Gyr	3.5	4.7
>2.5 Gyr	2.1	2.9
2.5-1.0 Gyr	10.6	13.6

A2.3.4. Reactant availability

Sulphur produced by oxidative biological or abiotic weathering on continents would have been in the form of sulphate. Permanent storage of sulphate in marine sediments prior to the advent of major evaporite depositories requires reduction to sulphide, with organic carbon acting as the major reducing agent. Reaction with iron then forms iron sulphide minerals. Hence the increase in the total sulphur concentration of marine sediments over time (Fig. A2.1) could in theory also be controlled by an increase in the availability of organic carbon or reactive iron rather than an increase in the delivery of sulphate to the ocean.

Before the GOE, ferrous iron would have been delivered to the oceans by anoxic weathering of iron-rich rocks. This source would have been largely extinguished by atmospheric oxygenation. After the GOE, the major source of ferrous iron to the ocean was probably hydrothermal activity (Veizer *et al.*, 1982), which, similar to volcanic activity, probably decreased over time (e.g. Canfield, 2004). It is therefore unlikely that reactive iron became more abundant across the Archaean-Proterozoic boundary and it can therefore not serve as an explanation for increasing sulphur concentrations in marine sediments.

Total organic carbon in marine sediments increases together with total sulphur (Fig. A2.5, Table A2.3), and the change for each from the Archaean to the Proterozoic is statistically significant (Table A2.4). However, the average S/TOC ratio remains nearly constant (Fig. A2.6, Table A2.3), and variations in S/TOC between the Archaean and Proterozoic are not statistically significant (Table A2.4). Hence if the organic carbon availability increased, it may have resulted in increased sulphide deposition on continental shelves, even if the flux of sulphate to the ocean remained constant. Organic carbon concentrations in marine sediments are controlled by (i) the redox state of the water column and hence the rate of remineralization, (ii) the availability of nutrients driving productivity, and (iii) the sedimentation rate. We comment on these in turn:

(i) It is unlikely that the redox state of the water column became more reduced from the Archaean into the Proterozoic, as atmospheric oxygen levels increased (Catling & Claire, 2005).

(ii) Nutrients would have been introduced by hydrothermal activity or continental weathering. The former likely decreased over time (Section A2.2.2.), while the latter is in turn tied to the delivery of sulphate to the ocean. In other words, the total sulphur concentration of marine sediments probably did not increase just because of higher concentrations of organic matter, but instead, productivity was probably stimulated by increasing weathering fluxes of sulphate and associated trace metals, many of which are micronutrients.

(iii) see Section A2.2.3.

Table A2.3: Average total sulphur, total organic carbon (TOC) and S/TOC ratio.

	Total S [wt. %]	TOC [wt. %]	S/TOC
3.3-2.8 Gyr	0.12 ± 0.11	0.47 ± 0.67	1.11 ± 1.04
2.8-2.5 Gyr	0.49 ± 0.40	1.52 ± 1.33	1.14 ± 0.76
>2.5 Gyr	0.34 ± 0.36	1.11 ± 1.22	1.13 ± 0.85
2.5-1.0 Gyr	0.98 ± 1.00	2.07 ± 2.18	1.19 ± 1.30

Table A2.4: One-tailed p-values calculated with Student t-test, assuming unequal variance.

	Total sulphur	TOC	S/TOC
3.3-2.8 Gyr to 2.8-2.5 Gyr	0.002	0.011	0.474
2.8-2.5 Gyr to 2.5-1.0 Gyr	0.014	0.165	0.432
>2.5 Gyr to 2.5-1.0 Gyr	0.002	0.030	0.417

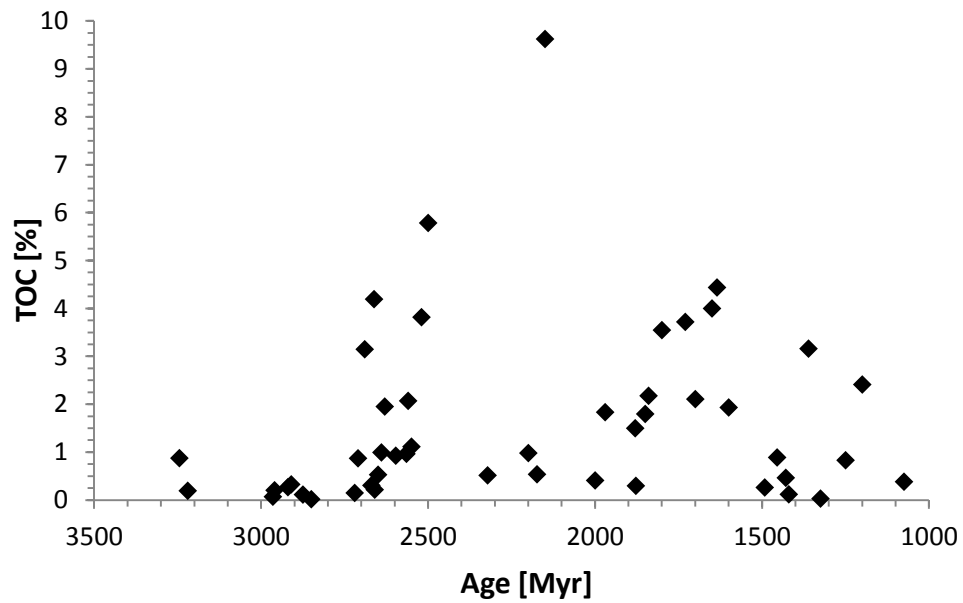


Fig. A2.5: Time-point average TOC concentrations. For references, see Table A2.1.

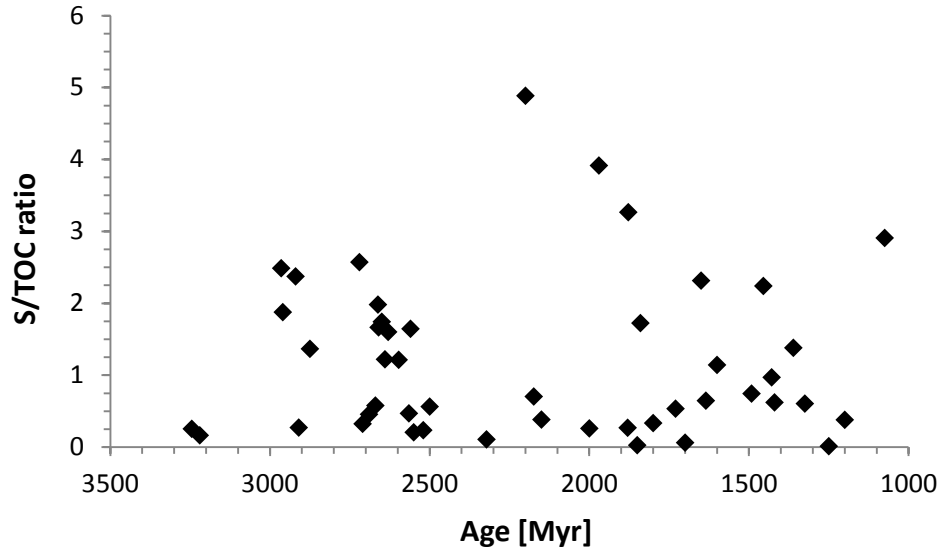


Fig. A2.6: Sulphur/TOC weight percent ratio over time. For references, see Table A2.1. (One outlier at 2850 Myr with an S/TOC ratio of 19.4 was removed. As can be seen from Figure A2.1 and A2.5 this outlier was most likely driven by an exceptionally low TOC concentration rather than a high total sulphur abundance).

A2.4. Possible biases in the biological and detrital flux

The calculated flux $F_{bioticw}(t) = F_w(t) - A_{py} \cdot R_{po2}$ could theoretically be biased by inaccuracies in each of the terms.

A2.4.1. Sensitivity to the total weathering flux

The biological and detrital flux $F_{bioticw}(t)$ may be overestimated if the calculated total weathering flux $F_w(t)$ is higher than in reality. As discussed above (Section A2.3) the most likely bias in $F_w(t)$ might arise from applying the Phanerozoic average sedimentation rate to the Precambrian. Reducing the average sedimentation rate D to 80 % of the modern value (*cf.* Section A2.3.3) while keeping all other parameters constant lowers the $F_{bioticw}(t)/F_{abioticw}(t)$ ratio (Table A2.5), but the abiotic weathering rate $F_{abioticw}(t)$ is still smaller for all time periods. If the

Precambrian deposition rate, D , was smaller due to smaller continents, the same should have been true for the fraction of volcanic sulphur being deposited on continents and shelves (Section A2.3.3) and for the total surface area of exposed pyrite, A_{py} . Hence the $F_{bioticw}(t)/F_{abioticw}(t)$ ratio would probably have been comparatively insensitive to continental area. As $F_{abioticw}(t)$ is perhaps more likely to be overestimated (see below), we conclude that even if D was smaller in the Precambrian and all other parameters remained constant, a detrital and/or biological sulphur flux would still have been necessary to explain the observed concentrations of sulphur in marine sediments.

Table A2.5: Effects of changes in D on the $F_{bioticw}(t)/F_{abioticw}(t)$ ratio.

	$D = 4.4 \cdot 10^{15} \text{ g yr}^{-1}$	$D = 3.5 \cdot 10^{15} \text{ g yr}^{-1}$
3.3-2.8 Gyr	14.7	5.7
2.5-2.8 Gyr	155.9	85.8
>2.5 Gyr	100.7	54.5
1.0-2.5 Gyr	2.6	1.1

A2.4.2. Total exposed surface area of pyrite

If the total surface area of pyrite exposed to weathering (A_{py}) is overestimated, then this would result in an underestimation of $F_{bioticw}(t)$, given the way that abiotic weathering depends on A_{py} . In our model, we initially assume that all of the pyrite weathered today is subject to abiotic weathering, because the proportions of biological and abiotic weathering are unknown. By subtracting the Proterozoic biogenic flux in five iterations (Section A2.3.2.2), this assumption is essentially modified to 55 % of today's pyrite being oxidized abiotically. That is equivalent to 27.5 % of the total modern river flux being caused by abiotic pyrite oxidation, 22.5 % being caused by biotic pyrite oxidation, and the remaining 50 % being caused by sulfate dissolution or

anthropogenic activity. These figures would imply that today the biological oxidation rate is nearly the same or somewhat smaller than the abiotic oxidation rate. However, experimental work has shown that especially under low pH conditions the biological pyrite oxidation rate is several orders of magnitude higher than the abiotic oxidation rate (reviewed by Roden, 2008). This is because oxidation of pyrite results in acidification of the weathering solution and the abiotic oxidation rate declines with decreasing pH (Rohwerder & Sand, 2007; Konhauser *et al.*, 2011). Our estimate of A_{py} is therefore more likely to be too high, meaning that abiotic oxidation (Eq. A2.8) is probably overestimated so that $F_{bioticw}(t)$ (Eq. A2.10) is underestimated, if anything, so that our conclusion of a late Archean biotic flux is unmodified. Table A2.6 shows how our calculated ratio of biotic to abiotic weathering in the Precambrian changes if the fraction of modern abiotic oxidation (K) is modified. Even if 50 % of the modern river flux were due to natural abiotic oxidation of pyrite, the biotic oxidation of pyrite would still have been of similar magnitude as abiotic oxidation in the Proterozoic, and biotic oxidation would be necessary to explain the late Archean weathering flux irrespective of K . A value greater than 50 % for K is unlikely not only because of the known effects of biological activity, but also because of the known contributions of sulfate dissolution and anthropogenic mining activities, which together make up more than 50 % of the total modern river flux (Berner & Berner, 1987).

Table A2.6: $F_{bioticw}/F_{abioticw}$ as a function of K . Here K is defined as the fraction of the modern river flux (Emerson & Hedges, 2008) that is caused by abiotic oxidation of pyrite.

K	10%	30%	50%	70%	90%	100%
2.5-1.0 Gyr	8.9	2.3	1.0	0.4	0.1	0.0
> 2.5 Gyr	279.4	92.5	55.1	39.1	30.2	27.0
3.3-2.8 Gyr	42.4	13.5	7.7	5.2	3.8	3.3
2.8-2.5 Gyr	431.7	143.2	85.5	60.8	47.1	42.3

A2.4.3. Oxidation rate

The oxidation rate determined by Williamson and Rimstidt (1994) is a function of pH (Fig. A2.7). We use pH = 7 as a conservative estimate in our model, but it is possible that the oxidation of pyrite occurred in more acidic environments, because atmospheric CO₂ concentrations were probably higher in the Precambrian resulting in more acidic rain water (Fabre *et al.* (2011) and references therein). Furthermore, acidity is generated during the oxidation itself (Rohwerder & Sand, 2007; Konhauser *et al.*, 2011). At pH 4, for example, the oxidation rate would be smaller by a factor of 2.1 compared to pH 7 (Fig. A2.7). If weathering fluids in the Precambrian were significantly more acidic than they are today, the calculated $F_{bioticw}/F_{abioticw}$ ratio would be higher. The values presented in Table A2.5 of $F_{bioticw}/F_{abioticw}$ are thus probably an underestimation.

Uncertainties in the exponents of the rate law (Eq. A2.7) could lower or raise the calculated abiotic oxidation rate by several percent (Fig. A2.8). In most cases, the errors in the exponents to pH and pO₂ have negligible effects, reaching 25 % only under low O₂ and neutral pH conditions. Uncertainties in the first factor of Eq. A2.7 can alone impart errors of up to 25 %. In the most extreme case this could result in a total uncertainty of up to 60 % for the abiotic weathering rate, but even then the biogenic or detrital weathering flux of sulphur would still be much larger (see Fig. 2.2).

It is possible that the rate law determined by Williamson and Rimstidt (1994) is not always applicable under natural conditions. For example, the presence of Fe³⁺_(aq) is known to increase the abiotic weathering rate (Williamson & Rimstidt, 1994). However, the scarcity of

ferric iron minerals in paleosols until ~2.4 Gyr and the stability of ferrous iron at the Earth's surface (Catling & Claire, 2005) suggest that $\text{Fe}^{3+}_{(\text{aq})}$ was probably not generated at large quantities to abiotically oxidize significant quantities of pyrite in the late Archaean. Furthermore, as discussed by Konhauser *et al.* (2011), the reaction between pyrite and $\text{Fe}^{3+}_{(\text{aq})}$ is not self-sustaining and will stop if $\text{Fe}^{3+}_{(\text{aq})}$ is not regenerated by oxidation of Fe^{2+} with O_2 . Another thermodynamically possible oxidant is Mn^{4+} (Bottrell *et al.*, 2008); however, due to its high redox potential the production of Mn^{4+} from Mn^{2+} is likely too slow (Konhauser *et al.*, 2011). Also NO_3^- can serve as an oxidant for sulphide (Bosch *et al.*, 2012); however, the modeled flux of NO_3^- from the atmosphere to the Earth's land surface in the late Archaean (Ducluzeau *et al.*, 2008) is one order of magnitude smaller than the total weathering flux of sulphur and therefore also abiotic NO_3^- alone could not have been the major oxidant. Pyrite oxidation is thus ultimately dependent on molecular oxygen and we therefore adopt the pO_2 -dependent rate law.

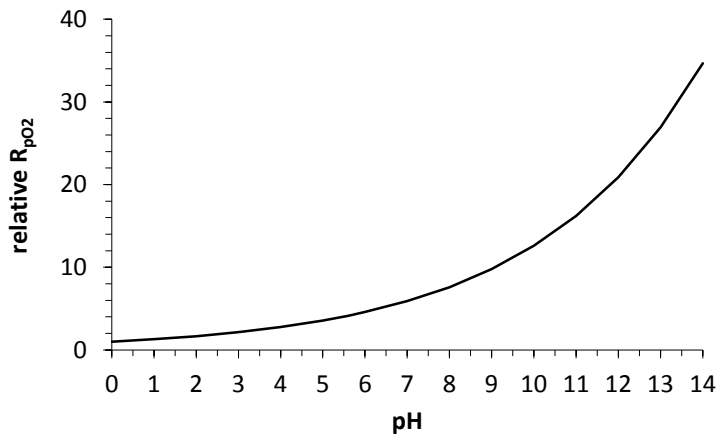


Fig. A2.7: Change in abiotic oxidation rate R_{pO_2} as a function of pH, relative to pH = 0 (Eq. A2.7).

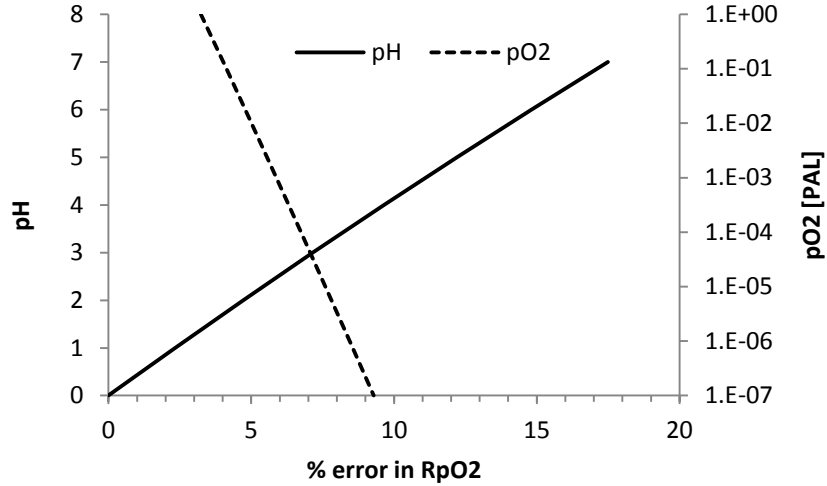


Fig. A2.8: Percent error in R_{pO_2} arising by reducing the exponent of either pH or pO_2 by 1 sigma (Eq. A2.7). (Results for addition of 1 sigma are within $\pm 1\%$ of these values).

A2.5. Analysis of bias in temporal subdivisions around 2.5 Gyr and 2.8 Gyr

The analysis of the data may be biased by *a priori* assumptions about major transitions in the redox state of the Earth's atmosphere. To test that, we divided the $F_w(t)$ data set (Fig. 1) at various time points and calculated the statistical significance of the difference in $F_w(t)$ between the resulting data blocks (Fig. A2.9). By far the lowest p-values were obtained for divisions at 2.8 Gyr ($p = 2.6 \cdot 10^{-6}$) and 2.7 Gyr ($p = 6.2 \cdot 10^{-6}$), which coincides with the time when a wider spread in $\delta^{34}\text{S}$ values of marine sedimentary sulphides indicates locally increased seawater sulphate concentrations (Strauss, 2002). The p-value exceeds 0.01 (*i.e.* the 99 % confidence limit is no longer met) for all divisions at ages younger than 2.5 Gyr and it generally increases with decreasing division ages (Fig. A2.9). Since 2.5 Gyr is roughly the beginning of the Great Oxidation Event, we conclude that the observed changes in the total weathering flux ($F_w(t)$, Fig. 2.1) are predominantly driven by global increases in atmospheric oxygen and that therefore our chosen boundaries at 2.8 Gyr and 2.5 Gyr are not arbitrary.

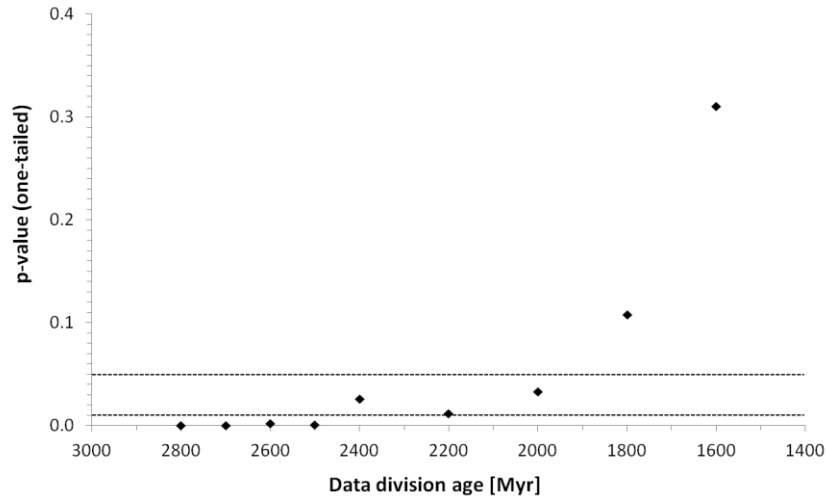


Fig. A2.9: Student t-test results for divisions of the data set at various ages. Dashed lines indicate 95 % and 99 % confidence levels.

A2.6. Agreement with other proxies

Our conclusion that oxidative weathering aided by microbial activity began in the late Archean is supported by other independent evidence. Konhauser *et al.* (2011) concluded that Cr abundances indicate oxidative weathering started during the GOE because the largest enrichment in Cr occurs between 2.48 and 2.32 Gyr (Fig. A2.10). However, Cr has a higher redox potential than sulphur, and hence their data are thus not inconsistent with late Archaean oxidative weathering commencing before 2.5 Gyr, but in fact support the second rise in S weathering observed around 2.5 Gyr.

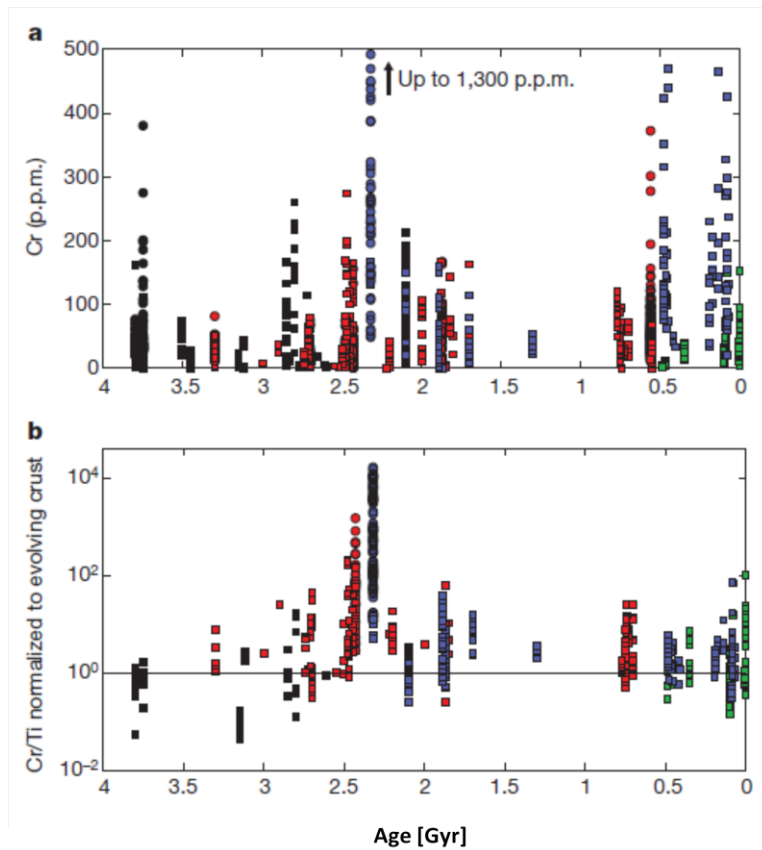


Fig. A2.10: Chromium abundances in marine iron oxide deposits over time (taken from Konhauser *et al.* (2011)). Black marks Algoma-type iron formations (may be subject to volcanic Cr-enrichment), red marks Superior-type iron formations (form on continental shelves), blue marks oolitic iron stones (shallow water), green marks Phanerozoic hydrothermal and exhalative iron formations.

Another commonly used proxy for oxidative weathering is the total concentration of molybdenum, or the Mo/TOC ratio. We have augmented the existing Mo database (Scott *et al.*, 2008b) with published data from the earlier Archaean (Fig. A2.11), and the results show that Mo concentrations in marine sediments began to increase in the 2.8-2.7 Gyr interval.

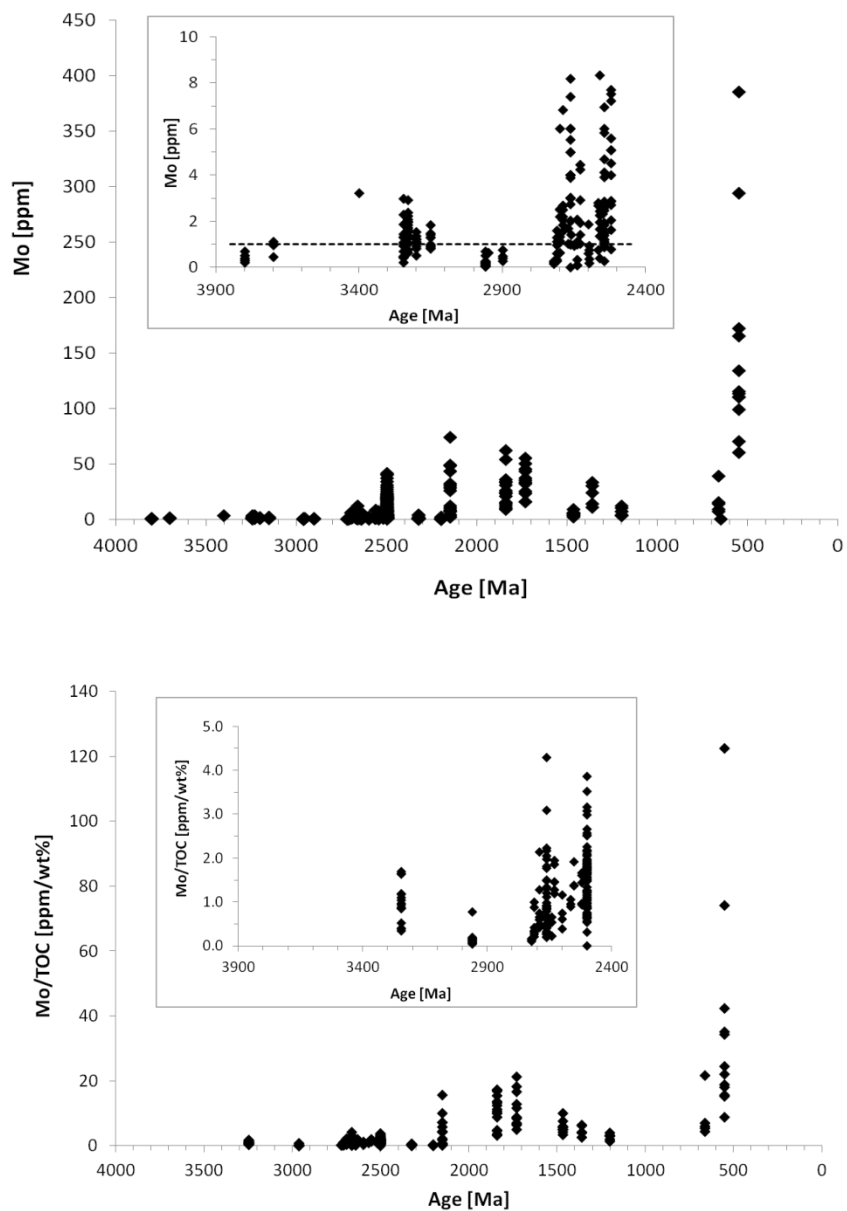


Fig. A2.11: Total Mo (top) and Mo/TOC ratios (bottom) in marine sediments (clastics and chert) through the Precambrian. Inserts show Archean data only, where the Mt. McRae Shale data (0.2-41.4 ppm Anbar *et al.* (2007)) is excluded from the insert in the top panel for better scale. Data are taken from McLennan *et al.* (1983a; 1983b; 1984), Yamaguchi (2002), Siebert *et al.*(2005), Anbar *et al.* (2007), Wille *et al.*(2007) and Scott *et al.*(2008a). Dashed line marks the modern crustal average (Wille *et al.*, 2007).

Lastly, the record of mass-dependent sulphur isotope fractionation (Fig. A2.12) is consistent with increasing levels of sulphate in the ocean starting between 2.8-2.7 Gyr (Strauss, 2002), when

values begin to show a broader spread and a significant difference between sulphides and sulphates at that time. Both features are indicative of bacterial sulphate reduction with marine sulphate concentrations larger than 1 % modern levels (Habicht *et al.*, 2002).

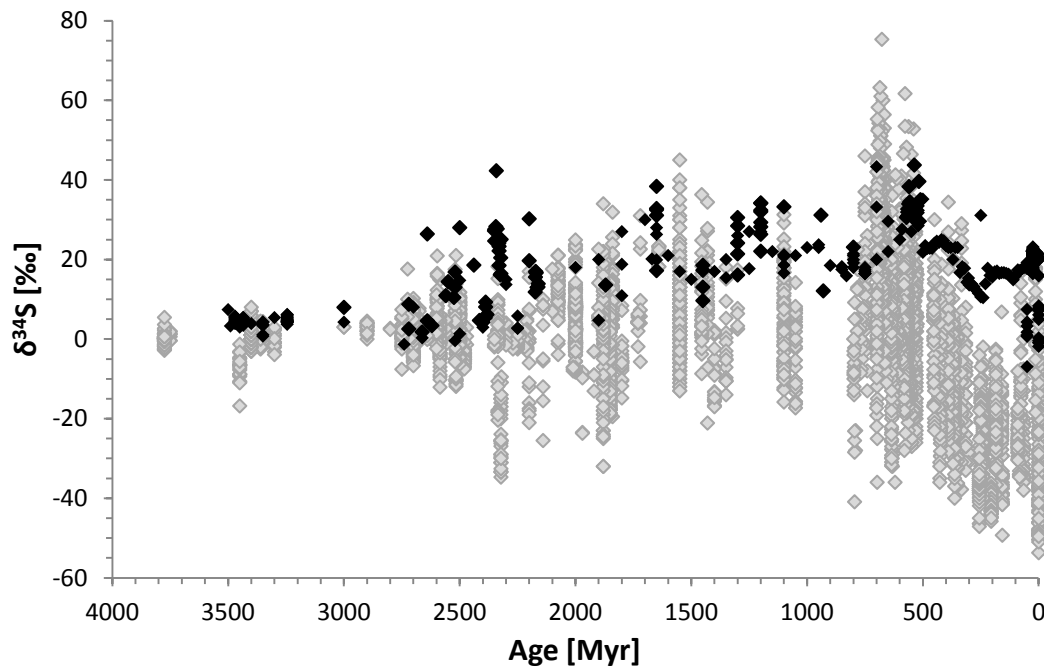


Fig. A2.12: Mass-dependent sulphur isotope record from marine sediments. Black diamonds are sulphates (Farquhar *et al.*, 2000; Farquhar *et al.*, 2002; Johnston *et al.*, 2005; Bao *et al.*, 2007; Philippot *et al.*, 2007; Domagal-Goldman *et al.*, 2008; Ueno *et al.*, 2008; Guo *et al.*, 2009; Shen *et al.*, 2009), gray diamonds are sulphides (Canfield & Farquhar, 2009).

Supplementary references

- Anbar A, Duan Y, Lyons TW, Arnold GL, Kendall B, Creaser RA, Kaufman AJ, Gordon GW, Scott CT, Garvin J, Buick R (2007) A whiff of oxygen before the Great Oxidation Event? *Science*, **317**, 1903-1906.
- ASUD (2011) Stratigraphic Units Database. Australian Government.
- Banerjee S, Dutta S, Paikaray S, Mann U (2006) Stratigraphy, sedimentology and bulk organic geochemistry of black shales from the Proterozoic Vindhyan Supergroups (central India). *Journal of Earth System Science*, **115**, 37-47.
- Bao H, Rumble III D, Lowe DR (2007) The five stable isotope compositions of Fig Tree barites: Implications on sulfur cycle in ca. 3.2 Ga oceans. *Geochimica et Cosmochimica Acta*, **71**, 4868-4879.
- Bekker A, Holland HD, Wang P-L, Rumble III D, Stein HJ, Hannah JL, Coetsee LL, Beukes NJ (2004) Dating the rise of atmospheric oxygen. *Nature*, **427**, 117-120.
- Berner EK, Berner RA (1987) *The global water cycle - geochemistry and environment*, Prentice-Hall, Inc., Englewood Cliffs, NJ.
- Bosch J, Lee K-Y, Jordan G, Kim K-W, Meckenstock RU (2012) Anaerobic, Nitrate-Dependent Oxidation of Pyrite Nanoparticles by *Thiobacillus denitrificans*. *Environmental Science and Technology*, **46**, 2095-2101.
- Bottrell SH, Boettcher ME, Schippers A, Parkes RJ, Jorgensen BB, Raiswell R, Telling J, Gehre M (2008) Abiotic sulfide oxidation via manganese fuels the deep biosphere: stable isotope evidence. In: *EGU General Assembly*. Geophysical Research Abstracts, pp. EGU2008-A-10613.
- Bumby AJ, Eriksson KA, Catuneanu O, Nelson DR, Rigby MJ (2011) Meso-Archaeon and Palaeo-Proterozoic sedimentary sequence stratigraphy of the Kaapvaal Craton. *Marine and Petroleum Geology*, (**in press**).
- Burnie SW, Schwarcz HP, Crocket JH (1972) A sulfur isotopic study of the Whie Pine Mine, Michigan. *Economic Geology*, **67**, 895-914.
- Cameron EM (1983) Genesis of Proterozoic iron-formation: sulphur isotope evidence. *Geochimica et Cosmochimica Acta*, **47**, 1069-1074.
- Cameron EM, Garrels RM (1980) Geochemical composition of some Precambrian shales from the Canadian Shield. *Chemical Geology*, **28**, 181-197.
- Canfield DE (2004) The Evolution of the Earth Surface Sulfur Reservoir. *American Journal of Science*, **304**, 839-861.
- Canfield DE, Farquhar J (2009) Animal evolution, bioturbation, and the sulfate concentration of the oceans. *Proceedings of the National Academy of Sciences*, **106**, 8123-8127.
- Canfield DE, Teske A (1996) Late Proterozoic rise in atmospheric oxygen concentration inferred from phylogenetic and sulphur-isotope studies. *Nature*, **382**, 127-132.
- Catling DC, Claire MW (2005) How Earth's atmosphere evolved to an oxic state: a status report. *Earth and Planetary Science Letters*, **237**, 1-20.
- Czaja AD, Johnson CM, Beard BL, Eigenbrode JL, Freeman KH, Yamaguchi KE (2010) Iron and carbon isotope evidence for ecosystem and environmental diversity in the ~2.7 to 2.5 Ga Hamersley Province, Western Australia. *Earth and Planetary Science Letters*, **292**, 170-180.

- Dhuime B, Hawkesworth CJ, Cawood PA, Storey CD (2012) A change in the geodynamics of continental growth 3 billion years ago. *Science*, **335**, 1334-1336.
- Domagal-Goldman SD, Kasting JF, Johnston DT, Farquhar J (2008) Organic haze, glaciations and multiple sulfur isotopes in the Mid-Archean Era. *Earth and Planetary Science Letters*, **269**, 29-40.
- Donnelly TH (1988) Depositional environment of the middle Proterozoic Velkerri Formation in northern Australia: geochemical evidence. *Precambrian Research*, **42**, 165-172.
- Ducluzeau A-L, van Lis R, Duval S, Schoepp-Cothenet B, Russel MJ, Nitschke W (2008) Was nitric oxide the first deep electron sink? *TRENDS in Biochemical Sciences*, **34**, 9-15.
- Emerson S, Hedges J (2008) *Chemical oceanography and the marine carbon cycle*, Cambridge University Press, Cambridge, UK.
- Eriksson PG (1999) Sea level changes and the continental freeboard concept: general principles and application to the Precambrian. *Precambrian Research*, **97**, 143-154.
- Evangelatos J, Butler K, Spray JG (2009) A marine magnetic study of a carbonate-hosted impact structure: Ile Rouleau, Canada. *Geophysical Journal International*, **179**, 171-181.
- Fabre S, Berger G, Nedelec A (2011) Modeling of continental weathering under high-CO₂ atmospheres during Precambrian times. *Geochemistry, Geophysics, Geosystems*, **12**, doi:10.1029/2010GC003444.
- Farquhar J, Bao H, Thiemens MH (2000) Atmospheric influence of Earth's earliest sulfur cycle. *Science*, **289**, 756-758.
- Farquhar J, Peters M, Johnston DT, Strauss H, Masterson AL, Wiechert U, Kaufman AJ (2007) Isotopic evidence for Mesoarchaeon anoxia and changing atmospheric sulphur chemistry. *Nature*, **449**, 706-709.
- Farquhar J, Wing B, McKeegan KD, Harris JW, Cartigny P, Thiemens MH (2002) Mass-Independent Sulfur of Inclusions in Diamond and Sulfur Recycling on Early Earth. *Science*, **298**, 2369-2372.
- Farquhar J, Wu N, Canfield DE, Oduro H (2010) Connections between sulfur cycle evolution, sulfur isotopes, sediments, and base metal sulfide deposits. *Economic Geology*, **105**, 509-533.
- Findlay JM, Parrish RR, Birkett TC, Watanabe DH (1995) U-Pb ages from the Nimish Formation and Montagnais glomeroporphyritic gabbro of the central New Quebec Orogen, Canada. *Canadian Journal of Earth Sciences*, **32**, 1208-1220.
- Flament N, Coltice N, Rey PF (2008) A case for late-Archean continental emergence from thermal evolution models and hypsometry. *Earth and Planetary Science Letters*, **275**, 326-336.
- Garrels RM, Mackenzie FT (1971) *Evolution of sedimentary rocks*, W. W. Norton & Company. Inc., New York.
- Gregor CB (1985) The mass-age distribution of Phanerozoic sediments. In: *The chronology of the geologic record* (ed Snelling NJ). The Geological Society of London, London, UK, pp. 284-289.
- Guo Q, Strauss H, Kaufman AJ, Schroeder S, Gutzmer J, Wing B, Baker MA, Bekker A, Jin Q, Kim S-T, Farquhar J (2009) Reconstructing Earth's surface oxidation across the Archean-Proterozoic transition. *Geology*, **37**, 399-402.
- Habicht KS, Gade M, Thamdrup B, Berg P, Canfield DE (2002) Calibration of sulfate levels in the Archean Ocean. *Science*, **298**, 2372-2374.

- Hawkesworth CJ, Dhuime B, Pietranik AB, Cawood PA, Kemp AIS, Storey CD (2010) The generation and evolution of the continental crust. *Journal of the Geological Society*, **167**, 229-248.
- Hoffman PF, Bowring SA, Buchwaldt R, Hildebrand RS (2011) Birthdate for the Coronation paleocean: age of initial rifting in Wopmay orogen, Canada. *Canadian Journal of Earth Sciences*, **48**, 281-293.
- Holland HD (1984) *The chemical evolution of the atmosphere and oceans*, Princeton University Press, Princeton, NJ.
- Holland HD (1999) When did the Earth's atmosphere become oxic? A Reply. *The Geochemical News*, **100**, 20.
- Holland HD, Lazar B, McCaffrey M (1986) Evolution of the atmosphere and oceans. *Nature*, **320**, 27-33.
- Jackson MJ, Raiswell R (1991) Sedimentology and carbon-sulphur geochemistry of the Velkerri Formation, a mid-Proterozoic potential oil source in northern Australia. *Precambrian Research*, **54**, 81-108.
- Javaux EJ, Marshall CP, Bekker A (2010) Organic-walled microfossils in 3.2-billion-year-old shallow-marine siliciclastic deposits. *Nature*, **463**, 934-938.
- Johnston DT, Farquhar J, Summons RE, Shen Y, Kaufman AJ, Masterson AL, Canfield DE (2008) Sulfur isotope biogeochemistry of the Proterozoic McArthur Basin. *Geochimica et Cosmochimica Acta*, **72**, 4278-4290.
- Johnston DT, Poulson SR, Fralick PW, Wing B, Canfield DE, Farquhar J (2006) Evolution of the oceanic sulfur cycle at the end of the Paleoproterozoic. *Geochimica et Cosmochimica Acta*, **70**, 5723-5739.
- Johnston DT, Wing B, Farquhar J, Kaufman AJ, Strauss H, Lyons TW, Kah LC, Canfield DE (2005) Active microbial sulfur disproportionation in the Mesoproterozoic. *Science*, **310**, 1477-1479.
- Kah LC, Lyons TW, Frank TD (2004) Low marine sulphate and protracted oxygenation of the Proterozoic biosphere. *Nature*, **431**, 834-838.
- Kakegawa T, Kasahara Y, Hayashi K-I, Ohmoto H (2000) Sulfur and carbon isotope analyses of the 2.7 Ga Jeerinah Formation, Fortescue Group, Australia. *Geochemical Journal*, **34**, 121-133.
- Kaufman AJ, Johnston DT, Farquhar J, Masterson AL, Lyons TW, Bates S, Anbar A, Arnold GL, Garvin J, Buick R (2007) Late Archean biospheric oxygenation and atmospheric evolution. *Science*, **317**, 1900-1903.
- Konhauser KO, Lalonde SV, Planavsky NJ, Pecoits E, Lyons TW, Mojzsis SJ, Rouxel OJ, Barley ME, Rosiere C, Fralick PW, Kump LR, Bekker A (2011) Aerobic bacterial pyrite oxidation and acid rock drainage during the Great Oxidation Event. *Nature*, **478**, 369-373.
- Kuznetsov AB, Gorokhov IM, Ovchinnikova GV, Melezhik VA, Vasil'eva IM, Gorokhovskii BM, Konstantinova GV, Mel'nikov NN (2011) Rb-Sr and U-Pb systematics of metasedimentary carbonate rocks: The Paleoproterozoic Kuetsjarvi Formation of the Pechenga Greenstone Belt, Kola Peninsula *Lithology and Mineral Resources*, **46**, 151-164.
- Lyons TW, Luepke JJ, Schreiber ME, Zieg GA (2000) Sulfur geochemical constraints on Mesoproterozoic restricted marine deposition: lower Belt Supergroup, northwestern United States. *Geochimica et Cosmochimica Acta*, **64**, 427-437.

- McLennan SM, Taylor SR, Eriksson KA (1983a) Geochemistry of Archean shales from the Pilbara Supergroup, Western Australia. *Geochimica et Cosmochimica Acta*, **47**, 1211-1222.
- McLennan SM, Taylor SR, Kroener A (1983b) Geochemical evolution of Archean shales from South Africa. I. The Swaziland and Pongola Supergroups. *Precambrian Research*, **22**, 93-124.
- McLennan SM, Taylor SR, McGregor VR (1984) Geochemistry of Archean metasedimentary rocks from West Greenland. *Geochimica et Cosmochimica Acta*, **48**, 1-13.
- Medvedev PV, Melezhik VA, Filippov MM (2009) Paleoproterozoic petrified oil field (Shunga Event). *Paleontological Journal*, **43**, 972-979.
- Melezhik VA, Grinenko LN, Fallick AE (1998) 2000-Ma sulphide concretions from the 'Productive' Formation of the Pechenga Greenstone Belt, NW Russia: genetic history based on morphological and isotopic evidence. *Chemical Geology*, **148**, 61-94.
- Ohmoto H, Watanabe Y, Ikemi H, Poulson SR, Taylor BE (2006) Sulphur isotope evidence for an oxic Archean atmosphere. *Nature*, **442**, 908-911.
- Ono S, Beukes NJ, Rumble III D (2009a) Origin of two distinct multiple-sulfur isotope compositions of pyrite in the 2.5 Ga Klein Naute Formation, Griqualand West Basin, South Africa. *Precambrian Research*, **169**, 48-57.
- Ono S, Beukes NJ, Rumble III D, Fogel ML (2006) Early evolution of atmospheric oxygen from multiple-sulfur and carbon isotope records of the 2.9 Ga Mozaan Group of the Pongola Supergroup, South Africa. *South African Journal of Geology*, **109**, 97-108.
- Ono S, Eigenbrode JL, Pavlov AA, Kharecha P, Rumble III D, Kasting JF, Freeman KH (2003) New insights into Archean sulfur cycle from mass-independent sulfur isotope records from the Hamersley Basin, Australia. *Earth and Planetary Science Letters*, **213**, 15-30.
- Ono S, Kaufman AJ, Farquhar J, Sumner DY, Beukes NJ (2009b) Lithofacies control on multiple-sulfur isotope records and Neoproterozoic sulfur cycles. *Precambrian Research*, **169**, 58-67.
- Papineau D, Mojzsis SJ, Schmitt AK (2007) Multiple sulfur isotopes from Paleoproterozoic Huronian interglacial sediments and the rise of atmospheric oxygen. *Earth and Planetary Science Letters*, **255**, 188-212.
- Partridge MA, Golding SD, Baublys KA, Young E (2008) Pyrite paragenesis and multiple sulfur isotope distribution in late Archean and early Paleoproterozoic Hamersley Basin sediments. *Earth and Planetary Science Letters*, **272**, 41-49.
- Philippot P, Van Zuilen M, Lepot K, Thomazo C, Farquhar J, Van Kranendonk MJ (2007) Early Archean microorganisms preferred elemental sulfur, not sulfate. *Science*, **317**, 1534-1537.
- Pickard AL (2003) SHRIMP U–Pb zircon ages for the Palaeoproterozoic Kuruman Iron Formation, Northern Cape Province, South Africa: evidence for simultaneous BIF deposition on Kaapvaal and Pilbara Cratons. *Precambrian Research*, **125**, 275-315.
- Planavsky NJ, McGoldrick P, Scott CT, Li C, Reinhard CT, Kelly AE, Chu X, Bekker A, Love GD, Lyons TW (2011) Widespread iron-rich conditions in the mid-Proterozoic ocean. *Nature*, **477**, 448-451.
- Poulton SW, Canfield DE (2011) Ferruginous conditions: A dominant feature of the ocean through Earth's history. *Elements*, **7**, 107-112.
- Poulton SW, Fralick PW, Canfield DE (2004) The transition to a sulphidic ocean ~1.84 billion years ago. *Nature*, **431**, 173-177.

- Rasmussen B, Blake TS, Fletcher IR (2005) U-Pb zircon age constraints on the Hamersley spherule beds: Evidence for a single 2.63 Ga Jeerinah-Carawine impact ejecta layer *Geology*, **33**, 725-728.
- Roden EE (2008) Microbiological controls on geochemical kinetics 2: Case study on microbial oxidation of metal sulfide minerals and future prospects. In: *Kinetics of water-rock interaction* (eds Brantley SL, Kubicki JD, White AF). Springer, pp. 417-467.
- Rohwerder T, Sand W (2007) Mechanisms and biochemical fundamentals of bacterial metal sulfide oxidation. In: *Microbial processing of metal sulfides* (eds Donati ER, Sand W). Springer, pp. 35-58.
- Schopf JW, Kudryavtsev AB, Czaja AD, Tripathi AB (2007) Evidence of Archean life: Stromatolites and microfossils. *Precambrian Research*, **158**, 141-155.
- Scott C, Lyons TW, Bekker A, Shen Y, Poulton SW, Chu X, Anbar AD (2008a) Tracing the stepwise oxygenation of the Proterozoic ocean. *Nature*, **452**, 456-459.
- Scott CT, Bekker A, Reinhard CT, Schnetger B, Krapez B, Rumble III D, Lyons TW (2011) Late Archean euxinic conditions before the rise of atmospheric oxygen. *Geology*, **39**, 119-122.
- Scott CT, Lyons TW, Bekker A, Shen Y, Poulton SW, Chu X, Anbar A (2008b) Tracing the stepwise oxygenation of the Proterozoic ocean. *Nature*, **452**, 456-459.
- Shen Y, Canfield DE, Knoll AH (2002) Middle Proterozoic ocean chemistry: Evidence from the McArthur Basin, Northern Australia. *American Journal of Science*, **302**, 81-109.
- Shen Y, Farquhar J, Masterson AL, Kaufman AJ, Buick R (2009) Evaluating the role of microbial sulfate reduction in the early Archean using quadruple isotope systematics. *Earth and Planetary Science Letters*, **279**, 383-391.
- Siebert C, Kramers JD, Meisel T, Morel P, Naegler TF (2005) PGE, Re-Os, and Mo isotope systematics in Archean and early Proterozoic sedimentary systems as proxies for redox conditions of early Earth. *Geochimica et Cosmochimica Acta*, **69**, 1787-1801.
- Simonson BM, Sumner DY, Beukes NJ, Johnson S, Gutzmer J (2009) Correlating multiple Neoproterozoic-Paleoproterozoic impact spherule layers between South Africa and Western Australia. *Precambrian Research*, **169**, 100-111.
- Strauss H (2002) The isotopic composition of Precambrian sulphides - seawater chemistry and biological evolution. In: *Precambrian Sedimentary Environments: A Modern Approach to Ancient Depositional Systems* (eds Altermann W, Corcoran PL). Blackwell Science, Oxford.
- Strauss H, Beukes NJ (1996) Carbon and sulfur isotopic compositions of organic carbon and pyrite in sediments from the Transvaal Supergroup, South Africa. *Precambrian Research*, **79**, 57-71.
- Strauss H, Moore TB (1992) Abundances and isotopic compositions of carbon and sulfur species in whole rock and kerogen samples. In: *The Proterozoic Biosphere - A Multidisciplinary Study* (eds Schopf JW, Klein C). Cambridge University Press, Cambridge.
- Stumm W, Morgan JJ (1996) *Aquatic Chemistry*, John Wiley & Sons Inc., New York.
- Sumner DY, Beukes NJ (2009) Sequence stratigraphic development of the Neoproterozoic Transvaal carbonate platform, Kaapvaal Craton, South Africa. *South African Journal of Geology*, **109**, 11-22.
- Ueno Y, Ono S, Rumble III D, Maruyama S (2008) Quadruple sulfur isotope analysis of ca. 3.5 Ga Dresser Formation: New evidence for microbial sulfate reduction in the early Archean. *Geochimica et Cosmochimica Acta*, **72**, 5675-5691.

- Veizer J, Compston W, Hoefs J, Nielsen H (1982) Mantle buffering of the early oceans. *Naturwissenschaften*, **69**, 173-180.
- Watanabe Y, Naraoka H, Wronkiewicz DJ, Condie KC, Ohmoto H (1997) Carbon, nitrogen, and sulfur geochemistry of Archean and Proterozoic shales from the Kaapvaal Craton, South Africa. *Geochimica et Cosmochimica Acta*, **61**, 3441-3459.
- Wille M, Kramers JD, Naegler TF, Beukes NJ, Schroeder S, Meisel T, Lacassie JP, Voegelin AR (2007) Evidence for a gradual rise of oxygen between 2.6 and 2.5 Ga from Mo isotopes and Re-PGE signatures in shales. *Geochimica et Cosmochimica Acta*, **71**, 2417-2435.
- Williamson MA, Rimstidt JD (1994) The kinetics and electrochemical rate-determining step of aqueous pyrite oxidation. *Geochimica et Cosmochimica Acta*, **58**, 5443-5454.
- Yamaguchi KE (2002) Geochemistry of Archean-Paleoproterozoic black shales: the early evolution of the atmosphere, oceans, and biosphere. In: *Department of Geosciences*. Pennsylvania State University, pp. 485.
- Zentmyer RA, Pufahl PK, James NP, Hiatt EE (2011) Dolomitization on an evaporitic Paleoproterozoic ramp: Widespread syndimentary dolomite in the Denault Formation, Labrador Trough, Canada. *Sedimentary Geology*, **238**, 116-131.

Chapter 3: Evolution of the Archean sulfur cycle revealed by quadruple sulfur isotopes

Abstract

Given the much lower redox potential of SO_4^{2-} compared to O_2 , it is conceivable that SO_4^{2-} was a stable ion with moderately high concentrations in the Archean ocean long before the Great Oxidation Event (GOE). Here we evaluate this hypothesis with statistical analyses of major and minor sulfur isotope ratios from Archean sediments, particularly $\Delta^{36}\text{S}$ offsets between sulfide and sulfate minerals. We find a persistent signature of partial microbial sulfate reduction in the form of a statistically significant $\Delta^{36}\text{S}$ offset before 3.2 billion years (Ga), which cannot be explained by abiotic processes. This offset is proportional to fractionations in $\delta^{34}\text{S}$, indicating that the latter are also the result of microbial rather than thermochemical SO_4^{2-} reduction. This finding argues for a conservative, uniform marine SO_4^{2-} reservoir in the early Archean ocean, possibly in the mM range. We propose that such high concentrations were sustained because microbial sulfate reduction was reductant-limited, as indicated by low levels of total organic carbon (TOC) in sediments of this age. Between 3.2 and 2.75 Ga, sulfate minerals are absent from the geologic record, but sulfides show a large negative $\Delta^{36}\text{S}$ offset, possibly indicating phototrophic sulfide oxidation. In the late Archean after 2.75 Ga, the $\Delta^{36}\text{S}$ offset in sulfides disappears, which, combined with the absence of sulfate deposits and high TOC levels, suggests a decline of marine SO_4^{2-} concentrations in response to incipient oxidative weathering of the continents, increased riverine nutrient fluxes, and high biological productivity in marine environments. We therefore conclude that seawater sulfate levels reached an all-time minimum shortly before the GOE.

3.1. Introduction

Multiple lines of evidence indicate that atmospheric oxygen levels increased in the late Archean to early Proterozoic (Farquhar *et al.*, 2014), and it is generally also assumed that the abundance of other electron acceptors such as ferric iron, nitrate and sulfate increased in surface environments in a more or less stepwise fashion around this time. The absence of red beds until ~2.3 Ga and the abundance of banded iron formations suggest that Fe^{2+} was more stable than Fe^{3+} except in shallow seawater, organic $\delta^{15}\text{N}$ values close to 0‰ show that the nitrogen cycle was anaerobic and dominated by N_2 fixation until at least 2.7 Ga (Beaumont & Robert, 1999; Garvin *et al.*, 2009; Godfrey & Falkowski, 2009), and detrital pyrite, uraninite and siderite are incompatible with high levels of O_2 or NO_3^- (Rasmussen & Buick, 1999; England *et al.*, 2002). However, these proxies do not rule out the possibility that SO_4^{2-} , which has a comparatively low redox potential, was a thermodynamically stable ion in the Archean ocean long before the rise of oxygen. Sulfate was continuously produced anaerobically by photolysis of volcanogenic SO_2 gas (e.g. Zahnle *et al.* 2006) and possibly also by phototrophic sulfide oxidation. Its major sinks would have been microbial reduction and evaporite precipitation. Hence if microbial reduction rates were muted, perhaps due to a limiting supply of electron donors, then marine sulfate concentrations could have built up to significant levels prior to the GOE. The idea of elevated Archean sulfate concentrations has previously been proposed based on occurrences of sulfate minerals in the early Archean rock record (Huston & Logan, 2004). Isotopic data indicative of moderate sulfate levels in those environments have, however, been interpreted as anomalous, resulting from localized hydrothermal processes (e.g. Johnston, 2011). Here we review the evolution of Archean sulfate levels with a statistical analysis of the quadruple sulfur isotope

record. The four stable isotopes of sulfur (^{32}S , ^{33}S , ^{34}S , and ^{36}S) were fractionated mass-independently throughout the Archean, presumably by photolysis of SO_2 in an anoxic atmosphere (Farquhar *et al.*, 2000). This effect is quantified as $\Delta^{33}\text{S}$ and $\Delta^{36}\text{S}^*$ in the two major reaction products SO_4^{2-} and S_8 (Farquhar *et al.*, 2000). Models suggest that organic sulfur compounds could also have been created (Halevy, 2013), but these predictions cannot be reconciled with the geologic record and will therefore not be considered in this discussion. SO_2 photolysis also causes mass-dependent fractionation in $\delta^{34}\text{S}$ with an empirical relationship of $\Delta^{33}\text{S} = 0.89 \cdot \delta^{34}\text{S}$ in sulfides and sulfates, termed the Archean reference array (ARA, Figure 3.1) (Kaufman *et al.*, 2007; Ono *et al.*, 2009). The $\Delta^{36}\text{S}/\Delta^{33}\text{S}$ ratio of photochemical reaction products was between -0.9 and -1.0 for most of the Archean (Farquhar *et al.*, 2000; Kaufman *et al.*, 2007; Ueno *et al.*, 2008; Roerdink *et al.*, 2012) with variations resulting from differences in atmospheric pressure or haze density (Masterson *et al.*, 2011; Zerkle *et al.*, 2012). In the ocean, SO_4^{2-} and S_8 eventually became incorporated into sulfate and sulfide minerals. Where microbial sulfate reduction occurs, it can impart an additional mass-dependent isotope fractionation of up to -66‰ in $\delta^{34}\text{S}$ (Sim *et al.*, 2011). Furthermore, molecular interactions associated with the microbial sulfate reduction pathway result in characteristic fractionation factors for $\Delta^{36}\text{S}$ and to a much lesser extent for $\Delta^{33}\text{S}$ that differ from those of equilibrated atomic masses (Farquhar *et al.*, 2003; Johnston *et al.*, 2005). This effect is also distinct from that of magnetic isotope effects associated with thermochemical sulfate reduction where $\Delta^{33}\text{S}$ is fractionated mass-independently with no corresponding change in $\Delta^{36}\text{S}$ (Oduro *et al.*, 2011). The $\Delta^{36}\text{S}/\Delta^{33}\text{S}$ slope of microbial sulfate reduction is around -7 with sulfide attaining more negative $\Delta^{36}\text{S}$ values and residual sulfate becoming increasingly positive (Ono *et al.*, 2006; Johnston *et al.*, 2007). When sulfides

* $\Delta^{33}\text{S} = \delta^{33}\text{S} - 1000 \cdot [(1 + \delta^{34}\text{S}/1000)^{0.515} - 1]$ and $\Delta^{36}\text{S} = \delta^{36}\text{S} - 1000 \cdot [(1 + \delta^{34}\text{S}/1000)^{1.89} - 1]$, where $\delta^{3x}\text{S} = [(\text{S}^{3x}/\text{S}^{32}\text{S})_{\text{spl}}/(\text{S}^{3x}/\text{S}^{32}\text{S})_{\text{std}} - 1] \cdot 1000$. Here ^{3x}S stands for ^{33}S , ^{34}S or ^{36}S .

derived by microbial reduction from sulfate with variable MIF are plotted on a $\Delta^{33}\text{S}$ (x-axis) versus $\Delta^{36}\text{S}$ (y-axis) scatter plot, the y-axis intercept of the regression line shifts away from $\sim 0\%$ in a negative direction while the slope stays constant. Phototrophic sulfide oxidation, in contrast, produces sulfate with a smaller negative offset in $\Delta^{36}\text{S}$ of up to 0.9% but negligible offsets in $\Delta^{33}\text{S}$ and $\delta^{34}\text{S}$ (Zerkle *et al.*, 2009). It is conceivable that atmospheric redox reactions cause shifts in $\Delta^{36}\text{S}$, but such reactions have so far not been described, and their importance will be further discussed below. Quadruple sulfur isotopes of sulfate and sulfide minerals have therefore been used to infer the presence of microbial sulfate reduction in the early Archean (Ueno *et al.*, 2008; Shen *et al.*, 2009; Roerdink *et al.*, 2013), but have not so far been subject to a statistical analysis through time, which has the potential to reveal global trends in the evolution of the sulfur cycle.

3.2. Methods

We compiled sulfur isotope data from sedimentary rocks reported in the literature (Appendix A3.1) and used standard statistical methods to identify trends in mass-dependent fractionation effects on major and minor isotopes through the Archean. Where analyses were conducted with *in-situ* techniques, we averaged the data for each sample to make them comparable to bulk rock studies. Effects on $\delta^{34}\text{S}$ are evaluated after correcting for MIF assuming the empirical ARA (Figure 3.1). Thus deviations in $\delta^{34}\text{S}$ from the crustal composition of 0% and shifts in the y-axis intercept on $\Delta^{33}\text{S}$ -vs- $\Delta^{36}\text{S}$ plots indicate microbial activity. Where the y-axis intercept and $\delta^{34}\text{S}$ mean differ significantly between sulfides and sulfates, sulfate consumption was incomplete, indicating a significant sulfate reservoir in the ocean. To investigate possible linkages between the sulfur cycle and biological productivity, we also compiled total organic carbon (TOC) concentrations through the Precambrian (Appendix A3.2).

3.3. Results

The results show that during the early Archean, $\Delta^{36}\text{S}$ of sulfate minerals (*i.e.* the y-intercept in a $\Delta^{33}\text{S}$ -vs- $\Delta^{36}\text{S}$ -plot) is offset from zero by $+0.23 \pm 0.10\text{‰}$ (1- σ , Figure 3.2, Table 3.1), while sulfides are shifted negative by $-0.11 \pm 0.07\text{‰}$. The difference between the two regression lines is statistically significant ($p_{\text{two-tailed}} = 0.0001$, Table 3.2) and consistent with comparatively large mass-dependent fractionations in $\delta^{34}\text{S}$ during this interval (Figure 3.3), suggesting that the two parameters were affected by the same process. MIF-corrected $\delta^{34}\text{S}$ values of all sulfides, including those for which $\Delta^{36}\text{S}$ is unknown, spread over a wide range (-18.3 to $+6.8\text{‰}$) but skew negative (mean $-3.6 \pm 5.8\text{‰}$), while sulfates are positive ($+5.6 \pm 1.3\text{‰}$). Data from clearly volcanogenic sulfides that fall along a distinct ‘felsic volcanic array’ with positive $\Delta^{33}\text{S}$ and negative $\delta^{34}\text{S}$ (Figure 3.1) (Philippot *et al.*, 2012) were excluded from the calculation. If $\delta^{34}\text{S}$ *in-situ* measurements of sulfides from microtubules in metabasaltic glass (McLoughlin *et al.*, 2012), for which $\Delta^{36}\text{S}$ was not reported, are included, the $\delta^{34}\text{S}_{\text{sulfide}}$ mean decreases to $-6.8 \pm 9.2\text{‰}$ and the minimum to -39.8‰ .

In the mid-Archean, sulfates are essentially absent, but $\Delta^{36}\text{S}_{\text{sulfide}}$ shows a large offset from zero of $-0.80 \pm 0.08\text{‰}$, while the slope is preserved (-0.87 ± 0.10). The range of MIF-corrected $\delta^{34}\text{S}$ is smaller than in the early Archean (-9.8‰ to $+16.8\text{‰}$) and shifted towards positive values (mean $+2.2 \pm 2.8\text{‰}$). TOC values during this interval are very low, averaging 0.3% .

The $\Delta^{36}\text{S}$ offset disappears in the late Archean (sulfide = $+0.09 \pm 0.05\text{‰}$, sulfate = $+0.15 \pm 0.34\text{‰}$) and becomes statistically insignificant ($p = 0.30$). MIF-corrected $\delta^{34}\text{S}$ values show a wide spread (-22.1‰ to $+35.8\text{‰}$), but are centered around a mean of $0.0 \pm 5.1\text{‰}$. The mean $\delta^{34}\text{S}$ of sulfates is $+7.1 \pm 8.7\text{‰}$. However, all sulfates reported from this interval are chemical extracts

of siliciclastic rocks or carbonates and may therefore have been contaminated by sulfide during sample preparation, which would make the comparison of the two phases invalid. The lack of $\Delta^{36}\text{S}_{\text{sulfide}}$ and mean $\delta^{34}\text{S}_{\text{sulfide}}$ offsets from 0‰ makes it unlikely that a large isotopically distinct sulfate reservoir existed during this time. TOC levels averaged over all lithologies increase significantly ($p = 0.002$) from 0.3% to 1.2% around 2.75 Ga (Figure 4, Table A3.2 and A3.3).

3.4. Discussion

These results support three unorthodox, but we believe robust, conclusions about the Archean sulfur cycle: (1) that microbial sulfate reduction was widespread and persistent throughout the Archean, *contra* interpretations derived from $\delta^{34}\text{S}$ alone (Canfield & Raiswell, 1999); (2) that marine sulfate accumulated to significant concentrations during the early Archean but concentrations declined in the late Archean, *contra* the standard interpretation of the $\delta^{34}\text{S}$ record (Habicht *et al.*, 2002); and (3) that in the early Archean sulfate with a photolytic origin had variable $\Delta^{33}\text{S}$ fractionations both positive and negative, *contra* the conventional model of mass-independent sulfur isotope fractionation (Farquhar *et al.*, 2001). The Archean sulfur cycle evidently evolved through three distinct phases, behaving differently during the early (>3.2 Ga), mid (3.2-2.75 Ga) and late (2.75-2.5 Ga) Archean intervals.

3.4.1. The early Archean

The significant negative $\Delta^{36}\text{S}$ offset between sulfides and sulfates in the early Archean can be explained by mass-dependent fractionation along a line with a slope of ~ -7 during reduction of sulfate that originally carried MIF with positive $\Delta^{36}\text{S}$. This interpretation is supported by *in-situ* and high-resolution bulk analyses of sulfide grains whose close association

with sulfate strongly suggests that they were derived from them and which plot along a -7 trend line (Shen *et al.*, 2009; Roerdink *et al.*, 2013). Additional support comes from the marked negative values in $\delta^{34}\text{S}$ in samples from four separate localities (Shen *et al.*, 2009; Wacey *et al.*, 2010; Bontognali *et al.*, 2012; McLoughlin *et al.*, 2012; Roerdink *et al.*, 2013), which are too extreme to be the result of abiotic thermochemical sulfate reduction. $\Delta^{36}\text{S}$ offsets are proportional to these $\delta^{34}\text{S}$ fractionations: The maximum range in $\delta^{34}\text{S}_{\text{MIF-corrected}}$, including *in-situ* measurements of both sulfur phases, is 50.1‰, while the maximum range in $\Delta^{36}\text{S}$ offsets is 3.5‰. Both are comparable to observations in modern cultures (Johnston *et al.*, 2007) and perhaps representative of maximum achievable fractionations before 3.2 Ga. Hence if the positive $\Delta^{36}\text{S}$ offset of early Archean sulfates was caused by partial microbial sulfate reduction, then a $\delta^{34}\text{S}_{\text{sulfate}}$ fractionation of 5.6‰, or 11% of the maximum range, should be associated with a $\Delta^{36}\text{S}$ offset of $+0.39 \pm 0.09\text{‰}$, which agrees well with the observed value of $+0.23 \pm 0.10\text{‰}$. For sulfides, the same calculation would predict an offset of $-0.23 \pm 0.37\text{‰}$, which is within error of the observed $-0.11 \pm 0.07\text{‰}$. This good match implies that microbial sulfate reduction alone can explain both the $\Delta^{36}\text{S}$ offsets and the mass-dependent fractionations in $\delta^{34}\text{S}$, making it unlikely that either one is the result of hydrothermal processes. It is also unlikely that either the $\Delta^{36}\text{S}$ offsets or the $\delta^{34}\text{S}$ fractionations were introduced by post-depositional alteration, because the mass balance of sulfides and sulfates is roughly the same in both parameters: Using MIF-corrected $\delta^{34}\text{S}$ values of samples for which a $\Delta^{36}\text{S}$ offsets were reported and assuming an initial composition of $\delta^{34}\text{S} = 0\text{‰}$, sulfides ($\delta^{34}\text{S} = -3.3 \pm 5.3\text{‰}$) make up 63% and sulfates ($\delta^{34}\text{S} = +5.6 \pm 1.3\text{‰}$) 37% of the total sulfur output in this sample set. A $\Delta^{36}\text{S}$ offsets of $+0.23 \pm 0.10\text{‰}$ in sulfates would thus require an offset of $-0.13 \pm 0.33\text{‰}$ in sulfides, which is nearly identical to the observation. Post-depositional alteration could not have preserved this mass balance. The $\Delta^{36}\text{S}$

offsets are therefore primary. They are seen consistently in sulfates, specifically barites, throughout the early Archean, from several different localities between 3.55 and 3.25 Ga, implying that microbial sulfate reduction was widespread during this interval. The remarkable homogeneity of major and minor sulfur isotope ratios in sulfates also argues against local production under hydrothermal conditions (cf. Johnston, 2011). Instead it is more likely that most sulfate minerals precipitated from the seawater SO_4^{2-} pool (Huston & Logan, 2004), sustained by volcanogenic input and slow biological consumption. Measurements of interfacial angles indicate that some early Archean barites are pseudomorphs after evaporative gypsum which precipitated in shallow waters (Buick & Dunlop, 1990). Silicified gypsum pseudomorphs are also common in many early Archean sediments, precipitating during earliest diagenesis (Buick & Barnes, 1984). Evidence for halite is absent. If gypsum precipitated before halite, and if early Archean seawater had similar concentrations of Ca^{2+} , Na^+ and Cl^- as in the Phanerozoic, then marine sulfate concentrations may have been between 0.7 and 2.8mM (Canfield & Farquhar, 2012). This range is consistent with concentrations of up to 8mM measured in marine fluid inclusions from the 3.48 Ga Dresser Fm (Foriel *et al.*, 2004).

Assuming an average volcanic sulfur flux of $5 \cdot 10^{11}$ mol yr⁻¹ between 3.55 and 3.2 Ga (Canfield, 2004) and a modern ocean volume of $1.35 \cdot 10^{21}$ L (Henderson & Henderson, 2009), then SO_4^{2-} with a concentration of 1mM would have had a residence time of 2.7 million years. This estimate increases if a significant fraction of volcanogenic sulfur was in the form of H_2S or S^0 . Hence SO_4^{2-} would have been a major conservative ion in early Archean seawater. This is further supported by geochemical and mineralogical evidence for seawater sulfate circulation through marine hydrothermal systems at this time (Huston *et al.*, 2001; Golding *et al.*, 2011).

We propose that relatively high sulfate levels were sustained by muted microbial consumption rates due to a limiting supply of reductants. Relatively low concentrations of organic carbon in sediments of this age (Figure 3.4) support this conclusion. Minimal oxidative weathering probably limited the flux of redox-sensitive nutrients into the ocean and restricted biological productivity, such that only a small fraction of all available sulfate was consumed. If partial microbial sulfate reduction was responsible for pushing the initial (MIF-corrected) composition of SO_4^{2-} from 0‰ to 5.65‰, as suggested by the complementary biogenic offset in $\Delta^{36}\text{S}$, and if the maximum achievable fractionation in $\delta^{34}\text{S}$ before 3.2Gyr was ~50‰, as suggested by the maximum observed range, then mass balance requires that microbial reduction only consumed ~11% of all available SO_4^{2-} (Figure 3.5). This contrasts with ~40% consumption in the modern ocean, where SO_4^{2-} is fractionated to +20‰ at a concentration of 28mM. Suppressed biological sulfate reduction implies that, on a global average, early Archean sulfide minerals should be depleted down to -44.35‰. This depleted reservoir may exist in deep marine sediments or oceanic basalts (e.g. (McLoughlin *et al.*, 2012)), especially if SO_4^{2-} behaved conservatively.

It is noteworthy that the $\Delta^{36}\text{S}/\Delta^{33}\text{S}$ ratios, *i.e.* the slopes of the regression lines, do not differ significantly between sulfates and sulfides in the early Archean (Table 3.1). If photolytic sulfate had exclusively negative $\Delta^{33}\text{S}$ while S_8 were positive, as generally assumed, then the mass-dependent effect of microbial sulfate reduction and subsequent mixing between reduced biogenic and atmospheric sulfur species should have led to a shallower slope for sulfide minerals. Many sulfides plot substantially below the sulfate regression line but have markedly positive $\Delta^{33}\text{S}$ values (Figure 3.2a, bottom right quadrant). The existence of abundant sulfides with both positive and negative $\Delta^{33}\text{S}$ fractionations that also display offset $\Delta^{36}\text{S}$ values and large

(> ±10%) $\delta^{34}\text{S}_{\text{sulfide}}$ fractionations suggests that they were produced by microbial reduction of a sulfate source that also displayed positive and negative $\Delta^{33}\text{S}$. Similar results have been produced in experiments using with a range of photolytic wavelengths (Ueno *et al.*, 2009). Hence the data may indicate that the sign of photolytic fractionations varied over time due to changing atmospheric opacity caused by the intermittent development of organic haze after photolysis of methane (Zerkle *et al.*, 2012). Although the marine SO_4^{2-} pool was probably fairly homogeneous on a global scale, as suggested by the relatively small isotopic spread in early Archean barite deposits, the effect of varying compositions in atmospheric SO_4^{2-} could have been preserved in sulfides forming in shallow waters close to the atmospheric source where dilution with the marine reservoir was minor. Alternatively or additionally, the magnitudes and signs of atmospheric exit channels for other MIF products may have varied depending on atmospheric sulfur, oxygen and methane concentrations (Zerkle *et al.*, 2012). Regardless of the cause, the evidence of $\Delta^{33}\text{S}_{\text{sulfate}}$ of varying sign argues for a more nuanced model of early Archean atmospheric chemistry.

3.4.2. The mid-Archean

The large negative $\Delta^{36}\text{S}$ offset in sulfides between 3.2 Ga and 2.75 Ga is a striking feature of the Archean quadruple sulfur isotope record. Unlike in the early Archean, it cannot easily be explained by microbial sulfate reduction, because $\delta^{34}\text{S}$ does not show correspondingly large negative fractionations. The isotopic enrichment in $\delta^{34}\text{S}$ of sulfides may be the result of sulfate reduction under closed-system conditions where the sulfate supply was limited, such as within sediment pore-spaces. However, this mechanism should have also resulted in a net positive shift in $\Delta^{36}\text{S}$ in sulfides, which is not observed. The two isotopic signatures can be

reconciled if a significant proportion of seawater sulfate was produced by phototrophic sulfide oxidation and thus obtained a negative $\Delta^{36}\text{S}$ offset (Zerkle *et al.*, 2009). This would then have been inherited by sulfide produced in pore waters during sulfate reduction. Mass balance requires one or more missing reservoirs with overall negative $\delta^{34}\text{S}$ and positive $\Delta^{36}\text{S}$ compositions, which may have been in non-marine sediments or subducted oceanic crust. The inferred relative predominance of phototrophic sulfide oxidation was perhaps due to a muted photolytic sulfate source under a hazy atmosphere at this time (Zerkle *et al.*, 2012). Alternatively, the large negative $\Delta^{36}\text{S}$ offset could be the result of a so far undescribed atmospheric reaction, perhaps involving organic sulfur compounds (DeWitt *et al.*, 2010; Oduro *et al.*, 2012; Halevy, 2013). However, the $\Delta^{36}\text{S}$ -vs- $\Delta^{33}\text{S}$ slope through all sulfides is statistically indistinguishable from that characteristic of photochemical reactions in the early and late Archean (Table 3.2), which makes it more likely that the negative $\Delta^{36}\text{S}$ offset is the result of a secondary process acting after atmospheric deposition.

3.4.3. The late Archean

The late Archean disappearance of the $\Delta^{36}\text{S}$ offset between sulfates and sulfides and the $\delta^{34}\text{S}_{\text{sulfide}}$ mean near the crustal average rule out the presence of a significant hidden reservoir. Nearly all sulfur that entered the ocean must have been deposited as sulfide; sulfate evaporites were likely trivial, consistent with the near absence of late Archean sulfate minerals in the rock record. Independent estimates of late Archean marine sulfate concentrations are low, around $80\mu\text{M}$, with a residence time of ~ 200 kyr (Jamieson *et al.*, 2013). The spread in $\delta^{34}\text{S}_{\text{sulfide}}$ shows that dissolved sulfate concentrations were locally high enough to allow mass-dependent fractionation to be expressed during sulfate reduction. However, rapid sulfate consumption and

mixing of resulting sulfide phases probably led to a net average of 0‰ for both $\delta^{34}\text{S}$ mean and $\Delta^{36}\text{S}$ offset in marine sediments (Figure 3.5); sulfate could not accumulate to precipitate as an isotopically distinct reservoir elsewhere. Elevated TOC concentrations (Figure 3.4) suggest that biological productivity increased in the late Archean, and hence microbial sulfate reduction may no longer have been limited by electron donors. Productivity may in turn have been stimulated by the onset of oxidative weathering and higher nutrient fluxes from land to sea (Stüeken *et al.*, 2012). If terrestrial environments were more oxidized than the ocean but anaerobic metabolisms relatively more abundant in seawater, then marine sulfate levels could have decreased despite increasing sulfate input. Concentrations were thus kept below the threshold of evaporitic gypsum precipitation by rapid microbial sulfate reduction coupled to oxidation of more abundant organic matter.

3.5. Conclusion

Consistent with the record of stratiform barite deposits (Huston & Logan, 2004), the secular trend in quadruple sulfur isotopes suggests that marine sulfate concentrations were moderately high in the early Archean and perhaps also in the mid-Archean, but then declined around 2.75 Ga, probably until after the GOE. Most early Archean barites carry a consistent signature of partial microbial sulfate reduction in the form of positive $\delta^{34}\text{S}$ fractionations and $\Delta^{36}\text{S}$ offsets relative to concurrent sulfides, making it unlikely they are the products of localized hydrothermal processes. The presence of a significant seawater SO_4^{2-} reservoir before 3.2 Ga, possibly in the mM-range, is not ruled out by the records of detrital minerals, MIF, BIF or $\delta^{15}\text{N}_{\text{org}}$, which indicate low levels of dissolved O_2 ($E_{\text{O}_2/\text{H}_2\text{O}} = 0.77\text{V}$ at 10^{-6}bar pO_2) and NO_3^- ($E_{\text{NO}_3^-/\text{N}_2} = 0.63\text{V}$ at pH7, 10^{-10}M NO_3^- , 1bar N_2) through almost all of the Archean (Farquhar *et*

al., 2014). However, these proxies do not constrain concentrations of SO_4^{2-} , which has a much lower redox potential ($E_{\text{H}_{\text{SO}_4^-/\text{H}_2\text{S}} = -0.22\text{V}$ at pH7) and is thermodynamically stable in the presence of reduced iron and ammonium.

We suggest that the major limiting factor upon sulfate reduction was organic carbon, whose production only increased in the late Archean in response to incipient oxidative weathering of the continents and a higher nutrient supply. Prior to that, marine sulfate concentrations and residence times could have been considerable due to suppressed rates of microbial sulfate reduction. Marine sulfate levels may thus have reached an all-time minimum shortly before the GOE.

We further note that there are abundant early Archean sulfides with both positive and negative $\Delta^{33}\text{S}$ fractionations that also display offset $\Delta^{36}\text{S}$ values and large ($> \pm 10\%$) $\delta^{34}\text{S}_{\text{sulfide}}$ fractionations. This suggests that they were produced by microbial reduction of a sulfate source that also displayed positive and negative $\Delta^{33}\text{S}$, in turn implying that MIF-inducing photolysis did not exclusively produce $\Delta^{33}\text{S}_{\text{sulfate}}$ of one sign only. Though the cause is currently unknown, varying atmospheric conditions are the most likely candidate, hinting that a more flexible model of early Archean atmospheric chemistry may be required.

Acknowledgments

This work was funded by National Science Foundation grant EAR-0921580 and the NASA Astrobiology Institute Virtual Planetary Laboratory. We thank Mark Claire for stimulating discussions.

Author contributions

E. Stüeken and R. Buick designed the study, E. Stüeken compiled the literature database, performed the statistical analyses and made the figures, E. Stüeken and R. Buick wrote the manuscript.

Tables

Table 3.1: Regression parameters. Errors are one standard deviation. Parameters for mid-Archean sulfates are missing because this category only contains one data point.

	3.9-3.2 Ga		3.2-2.75 Ga		2.75-2.45 Ga	
	sulfide	sulfate	sulfide	sulfate	sulfide	sulfate
slope	-0.79 ± 0.07	-0.83 ± 0.12	-0.87 ± 0.10	-	-0.99 ± 0.02	-0.82 ± 0.22
intercept	-0.11 ± 0.07	+0.23 ± 0.10	-0.80 ± 0.08	-	+0.09 ± 0.05	+0.15 ± 0.34

Table 3.2: Student t-test results. Two-tailed p-values for slope (top-right half) and intercept (bottom-left half) comparisons of $\Delta^{33}\text{S}$ -vs.- $\Delta^{36}\text{S}$ regression lines through sulfate and sulfide populations of different time intervals. Numbers of data points are shown in the diagonal.

	slope	3.9-3.2 Ga		3.2-2.75 Ga		2.75-2.45 Ga	
		Sulfide	sulfate	sulfide	sulfate	sulfide	sulfate
3.9-3.2 Ga	sulfide	n = 56	0.75	0.55	-	0.03	0.89
	sulfate	0.0001	n = 97	0.83	-	0.34	0.96
3.2-2.75 Ga	sulfide	< 0.0001	< 0.0001	n = 80	-	0.21	0.86
	sulfate	-	-	-	n = 1	-	-
2.75-2.45 Ga	sulfide	0.09	0.89	< 0.0001	-	n = 296	0.47
	sulfate	0.26	0.75	0.001	-	0.30	n = 8

Figures

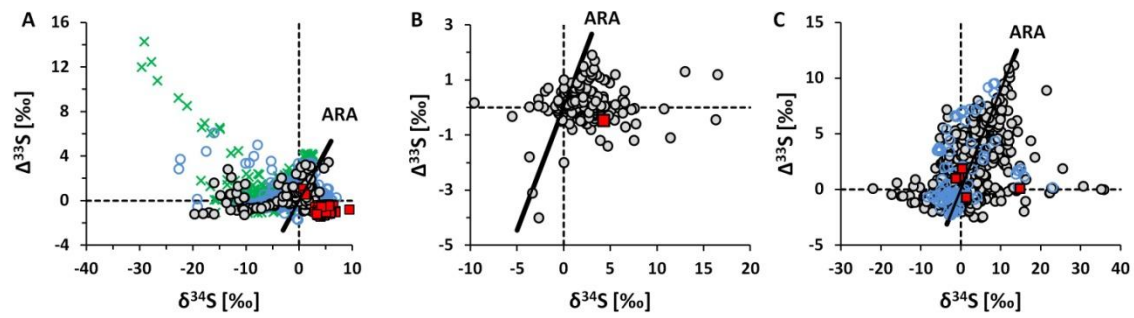


Figure 3.1: $\Delta^{33}\text{S}$ versus $\delta^{34}\text{S}$. Open black circles = bulk sulfides, blue circles = *in-situ* sulfides, red squares = sulfates, ARA = Archean reference array. A: early Archean, 3.9-3.2Ga. Green x = felsic volcanic array. B: mid-Archean, 3.2-2.75Ga. C: late Archean, 2.75-2.45Ga.

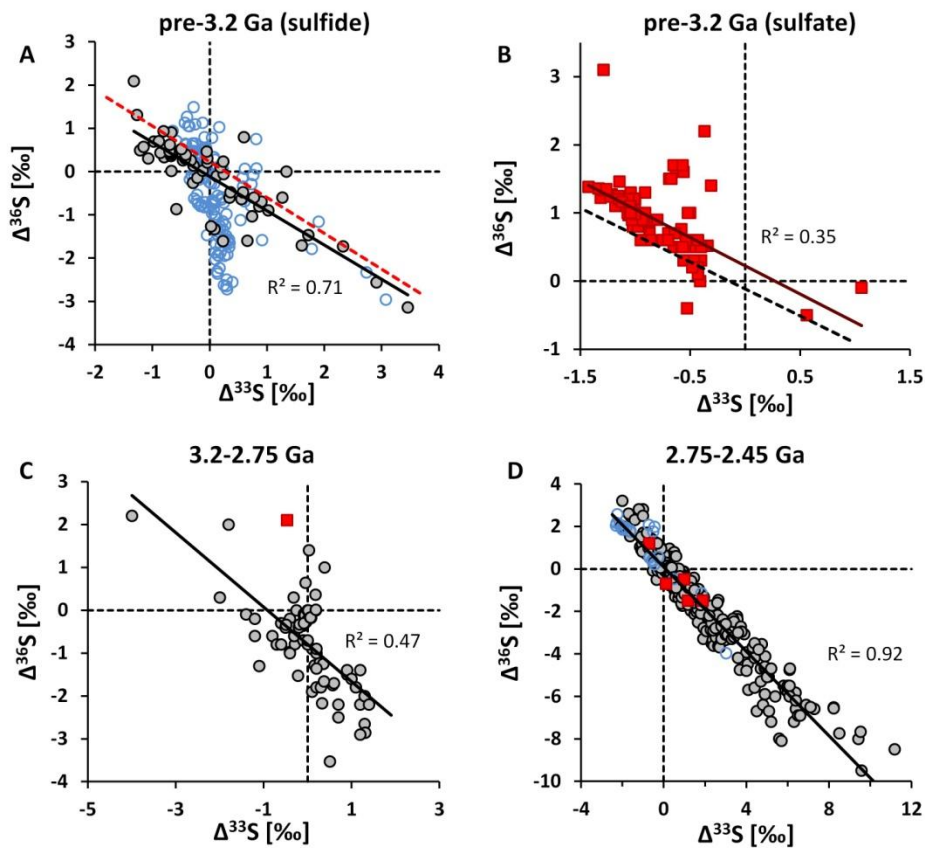


Figure 3.2: Quadruple sulfur isotope trends. $\Delta^{36}\text{S}$ versus $\Delta^{33}\text{S}$ in the early Archean (A and B), mid-Archean (C) and late Archean (D). Black solid lines in panel A, C, and D mark trend lines through sulfide data. In panel A, the trend of contemporaneous sulfates is shown in red, and in panel B, the trend of contemporaneous sulfides is shown in black. In-situ analyses (blue) are not included in the regressions.

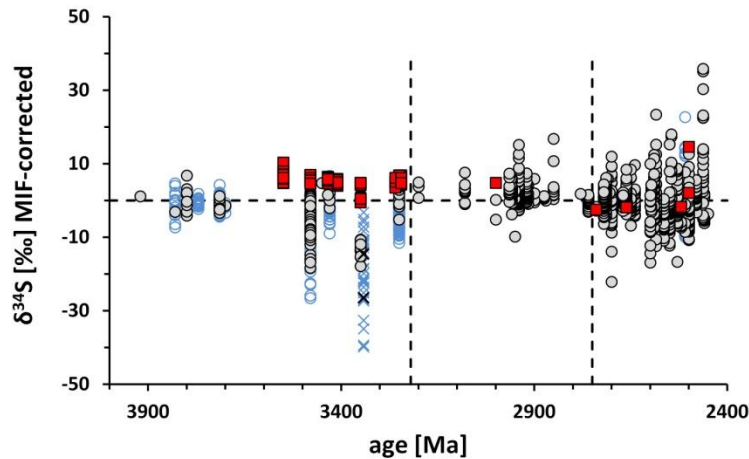


Figure 3.3: Mass-dependent $\delta^{34}\text{S}$ fractionation in the Archean. Values are corrected for MIF using the ARA. Open black circles = bulk rock sulfides; open blue circles = *in-situ* sulfides data; X = sulfides from Archean pillow basalts where $\Delta^{33}\text{S}$ was not reported but extreme negative $\delta^{34}\text{S}$ cannot be explained by photolysis along the ARA; red squares = bulk sulfates. The ‘felsic volcanic array’ is excluded.

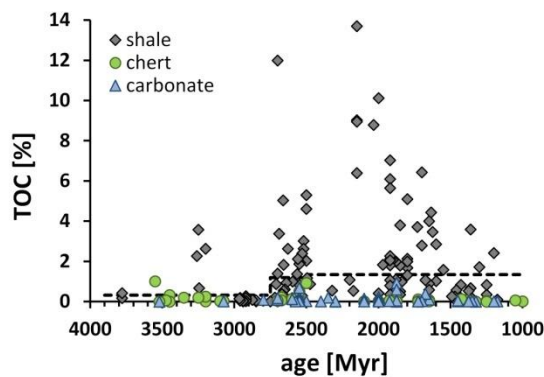


Figure 3.4: Marine TOC through time. Concentrations increase significantly in the late Archean, in particular in shales, indicating higher productivity. Dashed line = average of all formations and lithologies with subdivisions at 2.75 Ga and 2.5 Ga.

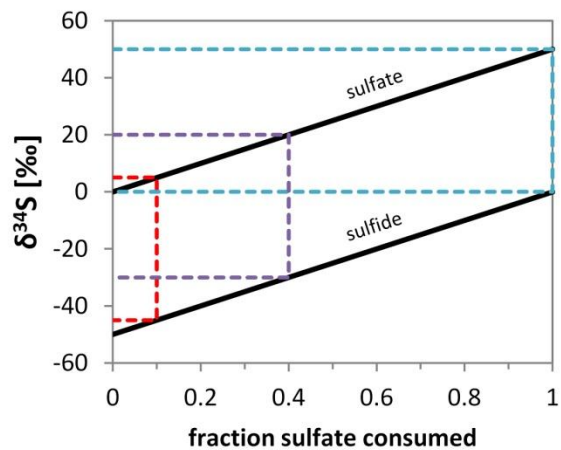


Figure 3.5: Global mean mass-dependent $\delta^{34}\text{S}$ fractionation in sulfides and sulfates as a function of sulfate consumption. Dashed lines represent scenarios for the early Archean (red), the late Archean (light blue) and the modern ocean (purple).

References

- Beaumont V, Robert F (1999) Nitrogen isotope ratios of kerogens in Precambrian cherts: a record of the evolution of atmosphere chemistry? *Precambrian Research*, **96**, 63-82.
- Bontognali TRR, Sessions AL, Allwood AC, Fischer W, Grotzinger JP, Summons RE, Eiler JM (2012) Sulfur isotopes of organic matter preserved in 3.45-billion-year-old stromatolites reveal microbial metabolism. *Proceedings of the National Academy of Sciences*, **109**, 15146-15151.
- Buick R, Barnes KR (1984) Cherts in the Warrawoona Group: early Archaean silicified sediments deposited in shallow water environments. *University of Western Australia, Geology Department & University Extension Special Publication*, **9**, 37-53.
- Buick R, Dunlop JSR (1990) Evaporitic sediments of early Archaean age from the Warrawoona Group, North Pole, Western Australia. *Sedimentology*, **37**, 247-277.
- Canfield DE (2004) The Evolution of the Earth Surface Sulfur Reservoir. *American Journal of Science*, **304**, 839-861.
- Canfield DE, Farquhar J (2012) The global sulfur cycle. In: *Fundamentals of Geobiology* (eds Knoll AH, Canfield DE, Konhauser KO). Blackwell Publishing Ltd.
- Canfield DE, Raiswell R (1999) The Evolution of the Sulfur Cycle. *American Journal of Science*, **299**, 697-723.
- DeWitt HL, Hasenkopf CA, Trainer MG, Farmer DK, Jimenez JL, McKay CP, Toon OB, Tolbert MA (2010) The formation of sulfate and elemental sulfur aerosols under varying laboratory conditions: implications for early earth. *Astrobiology*, **10**, 773-781.
- England GL, Rasmussen B, Krapez B, Groves DI (2002) Palaeoenvironmental significance of rounded pyrite in siliclastic sequences of the Late Archaean Witwatersrand Basin: oxygen-deficient atmosphere or hydrothermal alteration? *Sedimentology*, **49**, 1133-1156.
- Farquhar J, Bao H, Thieme MH (2000) Atmospheric influence of Earth's earliest sulfur cycle. *Science*, **289**, 756-758.
- Farquhar J, Johnston DT, Wing BA, Habicht KS, Canfield DE, Airieau S, Thieme MH (2003) Multiple sulphur isotopic interpretations of biosynthetic pathways: implications for biological signatures in the sulphur isotope record. *Geobiology*, **1**, 27-36.
- Farquhar J, Savarino J, Airieau S, Thieme MH (2001) Observation of wavelength-sensitive mass-independent sulfur isotope effects during SO₂ photolysis: Implications for the early atmosphere. *Journal of Geophysical Research*, **106**, 32829-32839.
- Farquhar J, Zerkle A, Bekker A (2014) Geologic and geochemical constraints on Earth's early atmosphere. *Treatise on Geochemistry*, **6**, 91-138.
- Foriel J, Philippot P, Rey P, Somogyi A, Banks D, Ménez B (2004) Biological control of Cl/Br and low sulfate concentration in a 3.5-Gyr-old seawater from North Pole, Western Australia. *Earth and Planetary Science Letters*, **228**, 451-463.
- Garvin J, Buick R, Anbar AD, Arnold GL, Kaufman AJ (2009) Isotopic evidence for an aerobic nitrogen cycle in the latest Archean. *Science*, **323**, 1045-1048.
- Godfrey LV, Falkowski PG (2009) The cycling and redox state of nitrogen in the Archaean ocean. *Nature Geoscience*, **2**, 725-729.
- Golding SD, Duck LJ, Young E, Baubllys KA, Glikson M, Kamber BS (2011) Earliest seafloor hydrothermal systems on Earth: comparison with modern analogues. In: *Earliest life on Earth: habitats, environments and methods of detection* (eds Golding SD, Glikson M). Springer Science+Business, pp. 15-49.

- Habicht KS, Gade M, Thamdrup B, Berg P, Canfield DE (2002) Calibration of sulfate levels in the Archean Ocean. *Science*, **298**, 2372-2374.
- Halevy I (2013) Production, preservation, and biological processing of mass-independent sulfur isotope fractionation in the Archean surface environment *Proceedings of the National Academy of Sciences*, **110**, 17644-17649.
- Henderson P, Henderson GM (2009) *The Cambridge Handbook of Earth Science Data*, Cambridge University Press, New York.
- Huston DL, Brauhart CW, Driberg SL, Davidson GJ, Groves DI (2001) Metal leaching and inorganic sulfate reduction in volcanic-hosted massive sulfide mineral systems: evidence from the paleo-Archean Panorama district, Western Australia. *Geology*, **29**, 687-690.
- Huston DL, Logan GA (2004) Barite, BIFs and bugs: evidence for the evolution of the Earth's early hydrosphere. *Earth and Planetary Science Letters*, **220**, 41-55.
- Jamieson JW, Wing BA, Farquhar J, Hannington M (2013) Neoproterozoic seawater sulphate concentrations from sulphur isotopes in massive sulphide ore. *Nature Geoscience*, **6**, 61-64.
- Johnston DT (2011) Multiple sulfur isotopes and the evolution of Earth's surface sulfur cycle. *Earth-Science Reviews*, **106**.
- Johnston DT, Farquhar J, Canfield DE (2007) Sulfur isotope insights into microbial sulfate reduction: when microbes meet models. *Geochimica et Cosmochimica Acta*, **71**, 3929-3947.
- Johnston DT, Farquhar J, Wing BA, Kaufman AJ, Canfield DE, Habicht KS (2005) Multiple sulfur isotope fractionations in biological systems: a case study with sulfate reducers and sulfur disproportionators. *American Journal of Science*, **305**, 645-660.
- Kaufman AJ, Johnston DT, Farquhar J, Masterson AL, Lyons TW, Bates S, Anbar A, Arnold GL, Garvin J, Buick R (2007) Late Archean biospheric oxygenation and atmospheric evolution. *Science*, **317**, 1900-1903.
- Masterson AL, Farquhar J, Wing B (2011) Sulfur mass-independent fractionation patterns in the broadband UV photolysis of sulfur dioxide: pressure and third body effects. *Earth and Planetary Science Letters*, **306**, 253-260.
- McLoughlin N, Grosch EG, Kilburn MR, Wacey D (2012) Sulfur isotope evidence for a Paleoproterozoic subseafloor biosphere, Barberton, South Africa. *Geology*, **40**, 1031-1034.
- Oduro H, Harms B, Sintim HO, Kaufman AJ, Cody G, Farquhar J (2011) Evidence of magnetic isotope effects during thermochemical sulfate reduction. *Proceedings of the National Academy of Sciences*, **108**, 17635-17638.
- Oduro H, Whitehill A, Farquhar J, Summons RE, Ono S (2012) Origin of anomalous isotope effects in photo- and thermo-chemical reactions of organosulfur compounds. In: *Goldschmidt Conference Abstract #2180*. Mineralogical Magazine.
- Ono S, Kaufman AJ, Farquhar J, Sumner DY, Beukes NJ (2009) Lithofacies control on multiple-sulfur isotope records and Neoproterozoic sulfur cycles. *Precambrian Research*, **169**, 58-67.
- Ono S, Wing B, Johnston DT, Farquhar J, Rumble D (2006) Mass-dependent fractionation of quadruple stable sulfur isotope system as a new tracer of sulfur biogeochemical cycles. *Geochimica et Cosmochimica Acta*, **70**, 2238-2252.
- Philippot P, van Zuilen M, Rollion-Bard C (2012) Variations in atmospheric sulphur chemistry on early Earth linked to volcanic activity. *Nature Geoscience*, **5**, 668-674.

- Rasmussen B, Buick R (1999) Redox state of the Archean atmosphere: Evidence from detrital heavy minerals in ca. 3250-2750 Ma sandstones from the Pilbara Craton, Australia. *Geology*, **27**, 115-118.
- Roerdink DL, Mason PRD, Farquhar J, Reimer T (2012) Multiple sulfur isotopes in Paleoarchean barites identify an important role for microbial sulfate reduction in the early marine environment. *Earth and Planetary Science Letters*, **331-332**, 177-186.
- Roerdink DL, Mason PRD, Whitehouse MJ, Reimer T (2013) High-resolution quadruple sulfur isotope analyses of 3.2 Ga pyrite from the Barberton Greenstone Belt in South Africa reveal distinct environmental controls on sulfide isotopic arrays. *Geochimica et Cosmochimica Acta*, **117**, 203-215.
- Shen Y, Farquhar J, Masterson AL, Kaufman AJ, Buick R (2009) Evaluating the role of microbial sulfate reduction in the early Archean using quadruple isotope systematics. *Earth and Planetary Science Letters*, **279**, 383-391.
- Sim MS, Bosak T, Ono S (2011) Large sulfur isotope fractionation does not require disproportionation. *Science*, **333**, 74-77.
- Stüeken EE, Catling DC, Buick R (2012) Contributions to late Archaean sulphur cycling by life on land. *Nature Geoscience*, **5**, 722-725.
- Ueno Y, Johnson MS, Danielache SO, Eskebjerg C, Pandey A, Yoshida N (2009) Geological sulfur isotopes indicate elevated OCS in the Archean atmosphere, solving faint young sun paradox. *Proceedings of the National Academy of Sciences*, **106**, 14784-14789.
- Ueno Y, Ono S, Rumble III D, Maruyama S (2008) Quadruple sulfur isotope analysis of ca. 3.5 Ga Dresser Formation: New evidence for microbial sulfate reduction in the early Archean. *Geochimica et Cosmochimica Acta*, **72**, 5675-5691.
- Wacey D, McLoughlin N, Whitehouse MJ, Kilburn MR (2010) Two coexisting sulfur metabolisms in a ca. 3400 Ma sandstone. *Geology*, **38**, 1115-1118.
- Zahnle, K., Claire, M., Catling, D. (2006). The loss of mass-independent fractionation in sulfur due to a Palaeoproterozoic collapse of atmospheric methane. *Geobiology*, **4**, 271-283.
- Zerkle AL, Claire MW, Domagal-Goldman SD, Farquhar J, Poulton SW (2012) A bistable organic-rich atmosphere on the Neoproterozoic Earth. *Nature Geoscience*, **5**, 359-363.
- Zerkle AL, Farquhar J, Johnston DT, Cox RP, Canfield DE (2009) Fractionation of multiple sulfur isotopes during phototrophic oxidation of sulfide and elemental sulfur by a green sulfur bacterium. *Geochimica et Cosmochimica Acta*, **73**, 291-306.

Appendix to Chapter 3

A3.1. Mid- to late Archean transition in MDF effects

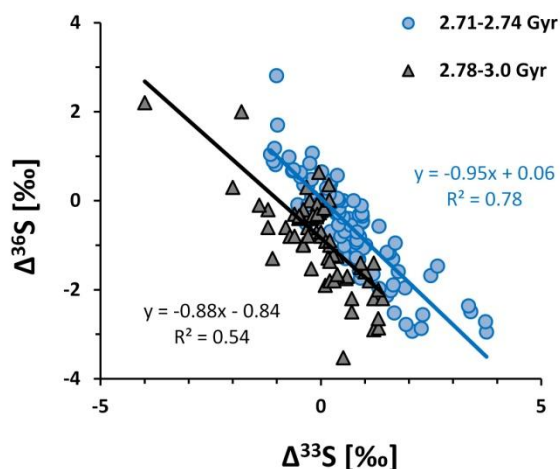


Figure A3.1: $\Delta^{36}\text{S}$ -offset transition. Sulphides from 2.78- 3.00 Gyr (black) show a marked negative offset in $\Delta^{36}\text{S}$ compared to sulphides from 2.71-2.74 Gyr (blue). No data are available between 2.74 and 2.78 Gyr. The transition likely occurred during that interval.

A3.2. TOC

Data sources for TOC are provided in an Excel file. For the early Archean, we generated new data from five samples of the Isua supracrustal belt in Greenland and seven samples of the Coonterunah Group in Western Australia. Samples were sequentially sonicated in hexane, methanol, and DI- H_2O (18 M Ω), finely powdered, and decarbonated with 6 N HCl at 65°C for three days. The acid was refreshed after one day. Washed and dried powders were weighed into

pre-combusted silver capsules (800°C over night) and then analyzed by flash combustion with an elemental analyzer (Costech ECS 4010) coupled to a mass spectrometer (Finnigan MAT253). All Pyrex vials and centrifuge tubes used during sample preparation were pre-combusted at 500°C overnight. The average relative precision, based on replicate analyses of rock samples, was ± 2.5 %.

Table A3.1: New total carbon data

sample	location	age [Myr]	lithology	TOC [%]
20053	Isua	3780	metapelite	0.316
20054	Isua	3780	metapelite	0.018
20055F	Isua	3780	metapelite	0.003
20058	Isua	3780	metapelite	0.007
20060	Isua	3780	metapelite	0.534
12001	Coonterunah Gp	3520	carbonate	0.004
12002	Coonterunah Gp	3520	carbonate	0.004
12003	Coonterunah Gp	3520	carbonate	0.003
12004	Coonterunah Gp	3520	metapelite	0.003
12005a	Coonterunah Gp	3520	chert	0.003
12005b	Coonterunah Gp	3520	chert	0.001
12005c	Coonterunah Gp	3520	carbonate	0.003

Data were averaged first by study and then by geological formation. Measurements of shales are more abundant and hence statistically more significant than those of carbonates and cherts (Table A3.2). However, some early Archean cherts may represent silicified mudrocks and carbonates may contain variable amounts of siliciclastic material. Averaging over all lithologies therefore provides the most conservative estimate of total TOC burial. Concentrations increase most significantly around 2.75 Gyr (Table A3.3).

Table A3.2: TOC averages (\bar{X}) and standard deviations (σ) for time intervals and lithologies. Values are in weight %. n = number of formations. Although error bars are large, differences between intervals relevant for this study are statistically significant (Table A3.3)

time interval		carbonate	chert	shale	all
3.9-3.2 Gyr	\bar{X}	0.003	0.233	1.038	0.551
	σ		0.316	1.358	0.959
	n	1	9	7	17
3.2-2.75 Gyr	\bar{X}	0.053	0.076	0.203	0.166
	σ	0.053	0.112	0.562	0.497
	n	2	4	21	27
3.9-2.75 Gyr	\bar{X}	0.036	0.185	0.404	0.314
	σ	0.047	0.275	0.884	0.727
	n	3	13	28	44
2.75-2.5 Gyr	\bar{X}	0.160	0.192	1.789	1.192
	σ	0.210	0.281	2.320	1.997
	n	9	11	34	54
2.5-1.0 Gyr	\bar{X}	0.092	0.039	2.388	1.311
	σ	0.187	0.042	2.658	2.260
	n	37	23	69	129

Table A3.3: Relevant one-tailed p-values for TOC comparisons, using all lithologies.

	3.2-2.75 Gyr	2.75-2.5 Gyr	2.5-1.0 Gyr
3.9-3.2 Gyr	0.070	0.039	
3.2-2.75 Gyr		0.0003	
3.9-2.75 Gyr		0.002	
2.75-2.5 Gyr			0.363

Chapter 4: Selenium isotope analysis of organic-rich shales: advances in sample preparation and isobaric interference correction³

Abstract

Selenium has a complex biogeochemical cycle with many similarities to that of sulfur. Fractionations of selenium isotopes induced in bacterial respiration reactions have been recognized as potential recorders of environmental oxidation states, opening up the possibility of further constraining bioproductivity and the redox evolution of the Earth's atmosphere and ocean over time. However, analyses of selenium isotopes are complicated by interferences with organic compounds as well as a number of isobaric interferences. Application of existing sample preparation protocols to geological samples replete with organic carbon can result in incomplete extraction yields and incomplete removal of isobarically interfering germanium and arsenic. We present measurements of three different organic-rich shales of varying ages prepared with eight different sample preparation protocols and identify a method with which high selenium yields are obtained for all three samples while the concentration of germanium is greatly reduced. We further investigate the quantitative importance of isobaric interferences and present new post-analytical data correction protocols. If selenium concentrations in standards and samples are matched to within 5 %, the ratios of five isotopes of selenium (⁷⁴Se, ⁷⁶Se, ⁷⁷Se, ⁷⁸Se and ⁸²Se) can be measured with precisions better than 0.2‰ for $\delta^{76/78}\text{Se}$, $\delta^{77/78}\text{Se}$ and $\delta^{82/78}\text{Se}$ and 0.5‰ for $\delta^{74/78}\text{Se}$, allowing analytical accuracy to be monitored with three-isotope diagrams and thus enabling the detection of any mass-independent isotopic fractionation.

³ Co-authors: J. Foriel, B. K. Nelson, R. Buick, D. C. Catling. Published in : Journal of Analytical Atomic Spectrometry (2013), v. 28 (11), pp. 1734-1749. Reproduced by permission of The Royal Society of Chemistry.

4.1. Introduction

Selenium is a non-metal with an average atomic mass of 78.96 and six stable isotopes ($^{74}\text{Se} = 0.889\%$, $^{76}\text{Se} = 9.366\%$, $^{77}\text{Se} = 7.635\%$, $^{78}\text{Se} = 23.772\%$, $^{80}\text{Se} = 49.607\%$, $^{82}\text{Se} = 8.731\%$). Like sulfur, its neighbor in group 16 of the periodic table, selenium exists in multiple redox states in nature (Johnson, 2004; Johnson & Bullen, 2004), it can be assimilated into proteins by organisms (reviewed in Gladyshev, 2012), and its isotopes fractionate during dissimilatory reduction of oxyanions (Herbel *et al.*, 2000; Ellis *et al.*, 2003). The isotopic composition of reduced selenium phases may, therefore, serve as a proxy for the bioavailability of selenium oxyanions in an overlying water body. A number of studies have demonstrated that selenium isotope fractionations are preserved in environmental and geological samples (Hagiwara, 2000; Rouxel *et al.*, 2002; Rouxel *et al.*, 2004; Layton-Matthews *et al.*, 2006; Wen *et al.*, 2007; Clark & Johnson, 2008; Clark & Johnson, 2010; Schilling *et al.*, 2011b; Wen & Carignan, 2011; Mitchell *et al.*, 2012). Therefore, it is conceivable that selenium isotope variations can be used to further constrain large-scale redox changes that occurred in Earth's atmosphere and oceans over geological time (reviewed in Catling & Claire, 2005). Sedimentary rocks, particularly shales, are the best recorders of past surface environmental conditions, but they commonly carry significant amounts of organic matter, arsenic and germanium, all of which may interfere with selenium isotope analyses. The impact of some of these and other interferences on the quality of selenium isotopic data have so far not been quantitatively documented. Although some studies report complete separation of selenium from germanium during sample preparation (Rouxel *et al.*, 2002; Layton-Matthews *et al.*, 2006), the lack of literature data on ^{74}Se , the isotope most strongly masked by Ge, suggests that problems arising from this interference are not entirely resolved. Similarly, isobaric interferences with $^{76}(\text{AsH})$ can

be minimized with a collision cell (Rouxel *et al.*, 2002), but this technique may not be readily available and therefore new correction methods need to be explored (e.g. Clark & Johnson, 2008). Lastly, reported values for rock standard SGR-1 diverge by a few tenths of a permil (see below, also noted by Mitchell *et al.* (2012), possibly due to differences in sample preparation, but reasons for this divergence have so far not been discussed.

This study investigates chemical preparation techniques for three shale samples, including SGR-1, with different amounts of arsenic and organic carbon of varying thermal maturity. We identify a method that yields nearly complete recovery of selenium and greatly lowers isobaric interferences by germanium isotopes. Further, we quantify the importance of isobarically interfering Ge, AsH, ArAr, ArCl, BrH, Kr, and SeH species and present a new protocol to correct for interferences by arsenic, germanium, and argon compounds formed from the carrier gas. This method can be used to independently analyze four (and with larger uncertainty five) of the six isotopes of selenium, which allows monitoring of analytical accuracy through three-isotope diagrams. It may also allow detection of mass-independent fractionation (MIF) of selenium isotopes, if it exists, which may be, by analogy to mass-independent fractionation of sulfur isotopes (Farquhar *et al.*, 2000), a valuable tool for detecting environmental redox changes in deep time.

For all experiments, selenium is separated from the sample matrix by chemical digestion and thiol-impregnated cotton fiber (TCF) column purification. Analyses are done with a multi-collector, inductively-coupled plasma mass spectrometer (MC-ICP-MS) where samples are introduced with a hydride generator (HG). Isotope compositions are expressed in δ -notation with NIST SRM 3149 serving as the reference standard (Carignan & Wen, 2007):

$$\delta^{x/y}\text{Se} = ([^x\text{Se}/^y\text{Se}]_{\text{sample}} / [^x\text{Se}/^y\text{Se}]_{\text{SRM3149}} - 1) \cdot 1000 \quad (\text{Eq. 4.1})$$

Results are mostly reported in terms of $\delta^{82/78}\text{Se}$. Samples are analyzed by standard-sample bracketing (SSB), which allows independent analysis of multiple isotopes and thus detection of potential MIF. The alternative use of a double-spike, where a solution artificially enriched in two selenium isotopes is added to samples to correct for mass fractionation induced during sample preparation, precludes analysis of the spiked isotopes in the original sample and may therefore hinder the possible discovery of MIF (further discussed in Section 4.4.4).

4.2. Methods

4.2.1. Reagents

We used mercaptoacetic acid (98 %), acetic anhydride (99.6 %), and sulfuric acid (98 %) of reagent grade in concentrated form for TCF preparation, along with oil-free cotton balls from Western Family®. Concentrated acetic acid glacial (99.9 %), hydrogen peroxide (30 %), hydrofluoric acid (48 %) and perchloric acid (70 %) used for sample preparation were trace metal grade. Reagent grade hydrochloric acid (38 %) and nitric acid (70%) were further purified with triple distillation. Hydrochloric acid and nitric acid used for dish washing were reagent grade. All acid dilutions were performed with RO-DI-H₂O. Sodium borohydride solution was prepared by dissolving pellets in 0.1 M sodium hydroxide; both were reagent grade. Argon gas used in the ICP-MS was of 99.998 % purity from Praxair.

4.2.2. Sample preparation

Sedimentary rocks can contain various selenium phases, including selenate (Se^{VI}) and selenite (Se^{IV}) adsorbed onto clay particles or iron oxide minerals, elemental selenium grains (Se^0), organic-bound selenide ($\text{Se}^{\text{-II}}_{\text{org}}$), and selenide substituting for sulfur in sulfide minerals

(Se^{-II}_{inorg}) (Kulp & Pratt, 2004; Fan *et al.*, 2011). The HG-MC-ICP-MS technique requires that all selenium is in an aqueous tetravalent state, isolated from interfering organic and inorganic compounds. The sample preparation protocol (Figure 4.1) was therefore designed to homogenize the various solid phases of selenium in solution, minimize the concentration of matrix elements, and control the redox state of bulk selenium at all times. Homogenization of the sample was achieved by complete dissolution and oxidation of all selenium phases. The selenium was then separated from the sample matrix and purified by filtration through a column of thiol-impregnated cotton fiber (TCF), followed by further chemical treatment of the sample after extraction of selenium from the column.

4.2.2.1. TCF preparation

TCF has been used widely for the chemical separation of selenium from complex sample matrices (Rouxel *et al.*, 2002; Yu *et al.*, 2002; Layton-Matthews *et al.*, 2006). It was prepared following published recipes (Yu *et al.*, 2001; Savard *et al.*, 2006). First, 53 ml of mercaptoacetic acid, 35 ml of acetic anhydride, 16 ml of glacial acetic acid, and 0.15 ml of concentrated sulfuric acid were mixed in a 300 ml Pyrex glass beaker. The addition of sulfuric acid to the mixture causes an exothermic reaction increasing the temperature up to 80 °C. After the temperature had dropped to 40 °C, 12 g of untreated, oil-free cotton balls were immersed in the solution. The beaker was then covered with aluminum foil and placed into a heated sand bath for five days at 40-45 °C. The TCF was stirred thoroughly every day until it transformed into a homogenous viscous liquid. After five days, the thiol-enriched cellulose fraction was separated from excess organic acids by vacuum filtration through a 1 µm-pore size filter and thorough washing with DI-water (~1.5 liters). The remaining solid was air-dried for three days on a watch glass. Once dry,

it was pulverized in a commercial coffee-grinder for ~20 seconds. TCF has been reported to degrade over the course of months (Yu *et al.*, 2001), but the implications for selenium isotope analyses are unknown. We tested this effect with different batches of TCF stored over several months in darkness.

4.2.2.2. Sample digestion

Powdered rock samples were weighed into 90 ml Savillex® Teflon beakers. Complete dissolution and oxidation of samples was achieved with a mixture of concentrated hydrofluoric acid (HF), concentrated perchloric acid (HClO₄) and 8 N nitric acid (HNO₃). The beakers were then capped tightly and placed into an aluminum heating block (Evapoclean®) set to 130 °C. After two days, excess acid was evaporated at 130 °C to incipient dryness. For kerogen-rich samples, an extra 10 ml of concentrated HClO₄ was added each day for 1-2 days, until the sample turned pale yellow. Concentrated hydrogen peroxide (H₂O₂) has been used instead of HClO₄ for the oxidation of organic compounds (Rouxel *et al.*, 2002; Savard *et al.*, 2006; Zhu *et al.*, 2008); however, we found that mature kerogen is more efficiently oxidized with HClO₄. Furthermore, without HClO₄ the sample must be evaporated at less than 80 °C to avoid loss of selenium by volatilization (e.g. Layton-Matthews *et al.*, 2006, and references therein). The use of HClO₄ greatly reduces the volatility of selenium; we tested evaporation of solutions at temperatures up to 150 °C without any measurable loss of selenium or isotopic fractionation (see below). A temperature of 130 °C was chosen for better control of the evaporation process since selenium loss does occur if the sample is dried to completion.

After digestion with strong oxidizers, selenium is likely in the form of aqueous Se^{VI} and/or Se^{IV}. TCF has a much higher adsorption affinity for selenium in the tetravalent state (Yu

et al., 2002). Reduction of Se^{VI} to Se^{IV} was achieved by adding 10 ml of 6 M hydrochloric acid to the sample and placing it in a boiling water bath for 30 minutes. The beaker was capped tightly to avoid selenium loss. Bye & Lund (1988) demonstrated that the reduction goes to completion even in the presence of 10 % HClO₄ by volume.

After cooling to room temperature, insoluble fluorides were removed by centrifugation (10 minutes; washed once with 10 ml of 0.6 M HCl) to avoid clogging of the filtration column in subsequent steps. Selenium fluorides are not solid at room temperature (Table 16 in Bagnall, 1966) and it is therefore unlikely that selenium is lost from the sample during this step.

4.2.2.3. Column filtration

Samples were passed through a vacuum filtration system with a 1 µm pore-sized filter paper and a TCF column attached to the fritted glass filter. TCF columns were made from 0.145 +/- 0.005 g of TCF powder (Zhu *et al.*, 2008) packed into a 1 ml pipette tip. Pipette tips were cut at the narrow end by ~4 mm to increase the surface area (~ 2 mm diameter) for more efficient suction. A small cotton ball (untreated) placed at the bottom of the tip prevented TCF powder from falling out. The pipette tip was attached to the glass filter with PVC tubing and zip-ties, rinsed with DI-water and replaced for each sample. For filtration, the flask was attached to a vacuum pump (Rocker 400). Untreated cotton and non-acid washed rubber tubing did not yield any detectable selenium contribution to procedural blanks.

Prior to sample filtration, the TCF was preconditioned with 10 ml of 0.6 N HCl, then 2 ml of 6 N HCl and then again with 10 ml of 0.6 N HCl (Savard *et al.*, 2006) in order to (i) clean the TCF of any residual HCl-soluble contaminants, (ii) adjust the acidity of the TCF to that of the sample solution, and (iii) have time to adjust the speed of the vacuum pump to approximately 1

ml per minute (Savard *et al.*, 2006). The sample was then diluted from 6 N to 0.6 N HCl, poured into the glass funnel and filtered through the TCF column, which takes up Se^{IV} from the solution by adsorption. Immediately following the sample, 2 ml of 6 N HCl and 2 ml of DI- H_2O were passed sequentially through the column to first remove interfering matrix elements adsorbed to the TCF (Yu *et al.*, 2002; Zhu *et al.*, 2008) and then to wash out excess HCl which could later interfere with selenium oxidation by HNO_3 .

4.2.2.4. Extraction

After filtration, the TCF was air-dried for a few minutes and then transferred from the pipette tip to a 15 ml centrifuge tube. We tested eight different methods (A-H; Table 4.1) of extracting selenium from the TCF. All extractions were done by oxidation with either HNO_3 or H_2O_2 for 30 minutes in a boiling water bath. The resulting solution was then separated from the TCF by centrifugation and transferred either by pouring or with a pipette into an open 30 ml Teflon beaker for evaporation on a 60°C hotplate (except in method A). After evaporation to 0.5 ml, the sample was mixed with 2 ml of 6 N HCl, transferred into a 30 ml screw-top Teflon beaker, capped tightly, and placed into a boiling water bath for 30 minutes to reduce any Se^{VI} produced during oxidation to Se^{IV} . After cooling to room temperature, the liquid was transferred into a PTFE bottle and diluted with 17.5 ml DI- H_2O . In method A, the 3 ml of sample extracted from the centrifuge tube (Table 4.1) were directly transferred to a LDPE bottle and mixed with 2 ml of concentrated HCl and 15 ml of DI- H_2O without any further heating.

We applied these methods listed in Table 4.1 to three organic-rich shales of varying age (Table 4.2). SGR-1 is an aliquot of the U.S. Geological Survey shale standard from the Eocene Green River Formation, USA, (e.g. Sweeney *et al.*, 1987), UW-McRae is a late Archean shale

from the Mount McRae Shale, Australia (e.g. Anbar *et al.*, 2007), and OCB+2.5 is a late-Permian shale from the Sulphur Mountain Formation, Opal Creek, Canada (Henderson, 1997). All three materials are moderately selenium-rich but show marked variations in their arsenic and total organic carbon (TOC) content (Table 4.2).

A NIST 3149 Se standard solution processed through the entire chemical protocol with method C was unfractionated ($\delta^{82/78}\text{Se} = -0.07 \pm 0.11 \text{ ‰}$) relative to unprocessed standard (internal precision $0.08 \pm 0.05 \text{ ‰}$, 1σ), and shows complete selenium recovery. We did not test other methods with pure Se solutions, but focused on rock standards to assess variability associated with chemical sample preparation. Because Se separation yields, isobaric interferences, and matrix effects are critical, relying only on a pure Se standard to test methodology does not provide an adequate representation of precision or accuracy.

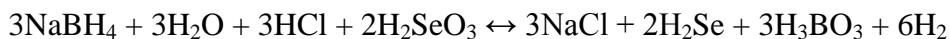
All sample containers were acid-washed with 8 N HNO_3 (reagent grade) and 6 N HCl (reagent grade) overnight and then rinsed five times with DI- H_2O . We analyzed procedural blanks processed with method D, which requires the most acid, as well as with method E, and did not detect any selenium signal above background (~ 0.1 ppb, equivalent to ~ 2 ng of selenium).

4.2.3. HG-MC-ICP-MS Analysis

4.2.3.1. Instrument Configuration and Operating Parameters

Isotopic measurements were performed with a Nu Plasma HR multi-collector, inductively-coupled plasma mass spectrometer. The sample was introduced in the form of H_2Se gas, which was continuously produced in a cold vapor hydride generator (HGX-200, Cetac Technologies) (Table 4.3). Sodium borohydride (NaBH_4 , 1 wt. % in 0.1 M NaOH) acted as a

reducing agent in the hydride generator (HG), catalyzing the reduction of Se^{IV} to Se^{-II} with the oxidation of H⁻ (in NaBH₄) to H⁰ (as H₂) (chapter 2 in Dědina & Tsalev, 1995 and references therein):



The reaction resulted in the formation of a very soluble white crystalline precipitate, possibly NaCl or borate salts, in the HG around the gas-liquid separator; however, this precipitate did not compromise analytical quality. NaBH₄ is known to degrade over the course of days by surface-catalyzed H₂-production (chapter 4 in Dědina & Tsalev, 1995 and references therein) and therefore must be refreshed daily.

Lens voltage potentials, the plasma torch position, and the flow rate of the argon carrier gas were adjusted daily to optimize the stability and intensity of the selenium signal. Most tuning was done by monitoring mass 78, which provides a strong signal (24 % of total Se) and minor interferences.

4.2.3.2. Analytical protocol

Samples were analyzed by sample-standard-bracketing (SSB) (Rouxel *et al.*, 2002; Mason *et al.*, 2004; Rouxel *et al.*, 2004; Layton-Matthews *et al.*, 2006), using Se NIST SRM 3149 solution as the bracketing standard. The concentration of samples and bracketing standards was matched to within 5 % to minimize the impact of isobaric interferences (see below). We assumed an exponential law for instrumental mass bias of selenium isotopes in the ICP-MS to calculate the fractionation exponent β defined as (Russell *et al.*, 1978; Albarède *et al.*, 2004; Clark & Johnson, 2008):

$$\beta = \ln([\text{}^{82}\text{Se}/\text{}^{78}\text{Se}]_{\text{MEAS}} / [\text{}^{82}\text{Se}/\text{}^{78}\text{Se}]_{\text{TRUE}}) / \ln(m_{82}/m_{78}), \quad (\text{Eq. 4.2})$$

where ${}^{78}\text{Se}$ and ${}^{82}\text{Se}$ are the abundances of the two isotopes, m_{82} and m_{78} their atomic masses (81.917 u and 77.917 u, Fernandez-Marinez & Charlet, 2009), and the subscripts ‘MEAS’ and ‘TRUE’ denote measured and natural abundances, respectively. The exponent β was calculated after isobaric ArAr and Kr interferences were subtracted from the standards. The Kr-correction was done in two iterations, using ${}^{84}\text{Kr}$ and the β -value of selenium, as discussed below. The ArAr-correction in the bracketing standards, however, deviated from the protocol used for samples. We first assumed that the measured ${}^{82}\text{Se}/{}^{78}\text{Se}$ ratio was not affected by interferences to calculate an initial value of β . This assumption was modified in two iterations after calculating ${}^{80}\text{Se}/{}^{78}\text{Se}$ from ${}^{82}\text{Se}/{}^{78}\text{Se}$, using the β value, and assuming that any difference between the calculated and measured ${}^{80}\text{Se}/{}^{78}\text{Se}$ ratio was due to argon interferences on mass 80 and 78. The ${}^{80}(\text{ArAr})/{}^{78}(\text{ArAr})$ ratio that we used in this calculation was determined in a separate experiment (see below). After two iterations of the Kr and ArAr-correction, this procedure led to a new value of β that accurately reflected instrumental mass bias. The average β -value of the two bracketing standards was then used to correct for instrumental mass bias in the sample.

In a second step, we subtracted the average NIST 3149 composition of the two bracketing standards in delta-notation from the sample values. This step minimized isobaric interferences in the sample associated with the carrier gas, NaBH_4 and HCl . In Table 4.3, this correction method is referred to as ‘SSB’. Residual interferences due to mismatches in the Se concentration of standards and samples or resulting from the sample matrix were corrected subsequently with methods described below (‘manual’ in Table 4.3). Because the isotopic composition of the NIST 3149 standard is 0‰ by definition (Equation 4.1), the sample-to-NIST 3149 comparison directly

provided the isotopic composition of the sample. It could also be used to estimate the concentration of selenium, because the correlation between concentration and measured voltage was linear with a small background subtraction of typically 0.01-0.03 V, which was determined at the beginning of each analytical session. This blank included contributions from argon and krypton interferences and traces of selenium contained in the carrier gas and acid. The blank was stable over several months, and replicate measurements of our in-house rock standard UW-McRae over a range of concentrations from 100 to 1000 times above background did not show any trend ($R^2 = 0.03$) that would indicate a significant effect of the blank on measured isotopic ratios. Sample-to-background ratios were typically above 100.

Accurate correction of the great number of isobaric interferences (Table 4.3) can only be achieved by analyzing additional signals of masses other than those of the six selenium isotopes. Here we analyzed all ions beams from mass 71 to 84 for standards and samples. In this range the Nu instrument is only capable of capturing a span of eight mass units at once. Analyses were therefore broken up into two separate cycles corresponding to different optical settings (Table 4.4). The first cycle recorded masses 76 to 84, which includes most of the selenium isotopes, krypton isotopes and Ar-dimers (Table 4.3). The second cycle recorded masses 71 to 79, which encompasses most isotopes of germanium, three isotopes of selenium, arsenic and arsenic hydrides (Table 4.3).

4.2.4. Isobaric interference correction

All six isotopes of selenium are subject to isobaric interferences from other elements or compounds. The mass resolution of the MC-ICP-MS does not allow resolution of the selenium signals from those of the interfering species (Table 4.3). If those isobaric interferences are not

taken into account, measured selenium isotope ratios deviate from the theoretical mass-dependent fractionation (MDF) line in three-isotope diagrams, which may prohibit accurate quantification of isotopically fractionating processes in the environment. Furthermore, for the detection of natural mass-independent fractionation (MIF) inherent to the sample as well as to validate the absence of natural MIF, it is necessary to correct for isobaric interferences without assuming a strict MDF behavior for the isotopes of selenium. In theory, interferences arising from the carrier gas or the reagents (ArAr, ArCl, Kr, BrH) could be subtracted by standard-sample bracketing or on-peak background subtraction. In practice, however, minor differences in the selenium concentration and fluctuations in the gas flow rate inherent to the HG can lead to errors. For that reason, ^{80}Se , which overlaps with a strong $^{80}(\text{ArAr})$ signal, cannot be resolved and typically is not reported. But the magnitude of this and other interferences have not been reported quantitatively. Here we quantified interferences with Kr, ArAr, Ge, AsH, SeH, ArCl and BrH and investigated new correction methods. Unlike previous studies, we used half-mass zeros instead of on-peak blank subtraction; however, standard-sample bracketing, *i.e.* subtraction of a mass-bias corrected averaged NIST 3149 composition, ultimately has the same effect as on-peak zeros, and errors arising from this method are negligible if concentrations of samples and standards are matched to within a few percent (see below).

Minor species include doubly-charged rare earth elements, rare argon dimers (masses 74 and 72) or ArCl compounds (masses 71 and 73), hydrides of germanium (masses 71, 73, 74, and 77), and transition metal oxides ($^{74, 76}\text{NiO}$, $^{79, 81}\text{CuO}$, ^{75}CoO , $^{80, 82, 84}\text{ZnO}$, $^{72, 73, 74}\text{FeO}$). We did not detect any significant signals at half-masses, which would be the case if doubly-charged rare earth elements were present. GeH can be monitored at mass 71, but the measured intensities were sufficiently low to ignore the GeH interferences with Se isotopes. The contribution from

transition metal oxides was tested with pure 1 ppm standard solutions of Ni, Cu, Co, Zn and Fe and no signal above background was detected, which demonstrates that no transition metal oxides form in the hydride generator or in the plasma.

4.3. Results

4.3.1. TCF extraction

From the eight extraction methods tested, only methods C, E, and F resulted in consistently high selenium yields for all three sample types (Table 4.5). Comparison of the selenium yield for SGR-1 processed with methods C, E and F (3.40-3.47 ppm) with published results (3.51 ± 0.25 ppm, Table 4.2) further suggests that these protocols result in nearly complete recovery (97-99%) of sample selenium. Partial loss of selenium occurred in methods A (only one centrifugation, 86% recovery), B (only two centrifugations, 94%), G (oxidation with H_2O_2 , 89%) and in method D for sample OCB+2.5 (more HNO_3 for oxidation, 95% recovery compared to the highest yield in method F). With the addition of 2 ml of concentrated H_2O_2 to the evaporation step (method H), nearly all selenium was lost, so method H is not included in Table 4.5.

Isotopic ratios for the USGS reference material SGR-1 obtained with methods A and H are closest to values reported by Layton-Matthews *et al.* (2006) and Rouxel *et al.* (2002) (Table 4.6), but both methods resulted in suppressed yields. Methods B and E agree best with the value reported by Schilling *et al.* (2011b) and methods C and F are close to the results from Mitchell *et al.* (2012). The average SGR-1 value of the three methods (C, E, F) that provide consistently high yields for all samples ($\delta^{82/78}\text{Se} = -0.06 \pm 0.18$ ‰) also provides closest agreement with the value reported by Mitchell *et al.* (2012).

Unlike the other seven methods, method E provides substantially improved separation of Ge from Se (Figure 4.2), presumably due to volatilization during evaporation with aqua regia. Because selenium was retained, Ge/Se ratios in samples processed with method E are nearly two orders of magnitude lower compared to other protocols. Arsenic concentrations were not affected.

4.3.2. TCF degradation

Storage of TCF over one year did not result in any detectable loss in precision or accuracy (Figure 4.3). Both Se isotope ratios and total yields are within error of UW-McRae aliquots processed with fresh TCF that was kept in use for four weeks.

4.3.3. Isobaric interferences

Kr: Krypton is present in trace amounts in the argon carrier gas or dissolved in sample and reagent solutions (Clark & Johnson, 2008). We monitored it at mass 84 and calculated the abundance of other Kr isotopes assuming the same instrumental mass bias as calculated for Se isotopes (Equation 4.2). The importance of Kr interferences was quantified with an array of NIST 3149 solutions of varying Se concentrations and hence different Kr/Se ratios, normalized to a bracketing solution with 40 ppb Se. The results show that subtraction of Kr contributions to measured signals on masses 82, 80, and 78 has a significant effect on $\delta^{82/78}\text{Se}$, $\delta^{82/77}\text{Se}$, and $\delta^{82/76}\text{Se}$ at low selenium concentrations (Figure 4.4). $\delta^{80/78}\text{Se}$ was altered by only 0.01 ‰ or less over the tested range from 0.5 to 60.0 ppb. Over typical signal intensities of 10 to 20 V for total Se, small differences of around 5 % in Se concentrations between two solutions, such as

standards and samples, resulted in only minor variations in Kr-induced isotopic anomalies of around 0.01-0.02 ‰ for all isotopic ratios. The Kr correction (when using 99.998% Ar gas) was therefore only important when selenium concentrations in samples and standards were not well matched; otherwise, the effect was negligible.

Ge: Germanium is a minor constituent in silicate rocks. Although most Ge can be removed during sample preparation (see below), residual traces may significantly affect the measured values of ^{74}Se and ^{76}Se . We quantified the importance of Ge-induced anomalies as a function of the Ge/Se ratio in the rock with a simple model calibrated with SGR-1 (processed with method C) and mixed Se-Ge-solutions. The average TCF-efficiency and HG-efficiency of germanium relative to selenium were found to be 0.014 ± 0.011 and 0.62 ± 0.11 , respectively, which allowed us to estimate the concentrations of Ge in UW-McRae and OCB+2.5 (Table 4.2), albeit with large uncertainty. The calculated Ge/Se ratios are comparatively small in the three samples tested; Li & Schoonmaker (2004) report Ge/Se of 2.7 for an average Se-poor shale. Hence germanium interferences can induce errors of several hundred ‰ in $\delta^{74/78}\text{Se}$ and several ten ‰ in $\delta^{82/76}\text{Se}$ for natural samples processed with method C. Because germanium is in the sample matrix, standard-sample bracketing and on-peak blank subtraction are do not correct for these interferences.

If samples are prepared with method E (Table 4.1), then Ge-levels can be suppressed enough so that interference on ^{76}Se is negligible, and even $\delta^{74/78}\text{Se}$ can be determined (Figure 4.6). For all other methods, errors have to be corrected manually. In previous studies, this was done using measured intensities of ^{72}Ge and ^{73}Ge (Rouxel *et al.*, 2002; Layton-Matthews *et al.*, 2006), but we found that the correction is more precise if Ge interferences are quantified directly

by calculating the deviation of selenium isotope ratios from expected values. For this new method, any non-zero value in $\delta^{74/78}\text{Se}$ was assumed to be due to the addition of ^{74}Ge to the signal at mass 74. Applying this assumption to Equation (4.1) led to the following expression (Equation 3):

$$\delta^{74/78}\text{Se}_{\text{measured}} = ([^{74}\text{Se}+^{74}\text{Ge})/^{78}\text{Se}]_{\text{sample}} / [^{74}\text{Se}/^{78}\text{Se}]_{\text{SRM3149}} - 1) \cdot 1000 \quad (\text{Eq. 4.3})$$

where ^{74}Se , ^{78}Se and ^{74}Ge were mass-bias corrected abundances, and abundances in the sample were identical to that of the standard. We then used the *MS Excel Solver* function to calculate the $^{74}\text{Ge}/^{74}\text{Se}$ ratio of the solution that was required to explain the measured $\delta^{74/78}\text{Se}$ value. The calculated $^{74}\text{Ge}/^{74}\text{Se}$ ratio was converted to the corresponding $^{76}\text{Ge}/^{76}\text{Se}$ ratio, assuming that instrumental mass bias of Ge isotopes was the same as for Se isotopes and that it dominated over any Ge isotopic fractionation induced by environmental processes or sample preparation. We then used the $^{76}\text{Ge}/^{76}\text{Se}$ ratio to determine and subtract the contribution of ^{76}Ge to the measured $\delta^{82/76}\text{Se}$ value. Hence, $\delta^{74/78}\text{Se}$ was sacrificed (by assuming $\delta^{74/78}\text{Se} = 0\text{‰}$), but $\delta^{82/76}\text{Se}$ could be resurrected with high precision for samples whose natural fractionation fell within the range of a few ‰ (Table 4.7).

ArAr: Argon has 3 stable isotopes of mass 36 (0.34%), 38 (0.063%) and 40 (99.6%) (Lee *et al.*, 2006) that form ArAr dimers in the plasma of the ICP-MS (Table 4.3). We quantified the effect of argon interferences with a series of NIST 3149 solutions of varying Se concentrations. Results showed that interference of $^{80}(\text{ArAr})$ on ^{80}Se was severe and in practice cannot be corrected by standard-sample bracketing because even minor mismatches in Se concentrations of a few percent can lead to errors in $\delta^{80/78}\text{Se}$ of several permil (Figure 4.7A and B). Errors in $\delta^{82/78}\text{Se}$ and $\delta^{82/76}\text{Se}$ due to interferences with $^{78}(\text{ArAr})$ and $^{76}(\text{ArAr})$ were less than 0.2 ‰ and 0.5 ‰,

respectively, for sample-standard concentrations matched to within 5 %. They were thus small but not negligible.

We investigated a new method of correction, comparable to the approach presented by Clark & Johnson (2008) and Elwaer & Hinterlmann (Elwaer & Hintelmann, 2008). Similar to the Ge correction, any non-zero values in $\delta^{80/78}\text{Se}$ were assumed to be due to $^{80}(\text{ArAr})$ differences between sample and standards (Equation 4):

$$\delta^{80/78}\text{Se}_{\text{measured}} = ([(^{80}\text{Se}+^{80}\text{ArAr})/(^{78}\text{Se}+^{78}\text{ArAr})]_{\text{sample}} / [^{80}\text{Se}/^{78}\text{Se}]_{\text{SRM3149}} - 1) \cdot 1000 \quad (\text{Eq. 4.4})$$

where, as in Equation 3, abundances were mass-bias corrected and identical between sample and standard. We then calculated the required $^{80}(\text{ArAr})/^{80}\text{Se}$ ratio using the *MS Excel Solver* function and subtracted corresponding contributions of $^{76}(\text{ArAr})$ and $^{78}(\text{ArAr})$ from the measured signals on mass 76 and 78. As for the Ge-correction, the initial assumption introduced an error for samples that are naturally fractionated. However, within the range of values typically reported for sedimentary rocks (-2 to +2 ‰, (Rouxel *et al.*, 2002; Shore, 2010; Mitchell *et al.*, 2012)) this error was at most 0.07 ‰ for $\delta^{82/76}\text{Se}$ and less than 0.01 ‰ for $\delta^{82/78}\text{Se}$ and $\delta^{82/74}\text{Se}$ (Table 4.8).

The instrumental mass bias for argon dimers that we used in these calculations was determined by optimization (Figure 4.8). The smallest deviations from 0‰ for a series of NIST 3149 solutions (1 – 15 ppb) were obtained with a $^{76}(\text{ArAr})/^{80}(\text{ArAr})$ ratio of 0.006679 ± 0.000065 (1σ) and a $^{78}(\text{ArAr})/^{80}(\text{ArAr})$ ratio of 0.01311 ± 0.00148 (1σ). Within error, these values overlapped with the natural ratios of 0.006636 and 0.001257 (Lee *et al.*, 2006). The optimized ratios correlated slightly with Se concentrations (Figure 4.8C and D), which may indicate instrumental mass fractionation relative to the more concentrated reference standard, or alternatively, incomplete removal of other interferences such as SeH or Kr. However, the difference in the correction effect between the optimized value + 1σ and the optimized value - 1σ

was less than 0.03 ‰ for the $\delta^{80/78}\text{Se}$ anomalies (of up to ± 20 ‰) that were typically observed (Figure 4.9). Within the range of uncertainty, our new argon correction technique is thus not very sensitive to variability in instrumental mass bias for Ar dimers.

AsH: Arsenic is typically present in sulfide- and organic-rich rocks. It has only one isotope at mass 75, but can form AsH in the plasma of the ICP-MS. As for germanium, we measured the relative TCF-efficiency (0.019 ± 0.004) and HG-efficiency (0.47 ± 0.01) of arsenic and constructed a simple model of As-induced errors in Se-isotope ratios as a function of As/Se in the rock (Figure 4.12). The model was calibrated with SGR-1 and mixed Se-As-solutions, assuming that selenium isotopes in this rock standard had no MIF (Rouxel *et al.*, 2002; Layton-Matthews *et al.*, 2006). Li & Schoonmaker (2004) reported an average As concentration of 13 ppm and an average As/Se ratio of 22 for shales. Although the As/Se ratio was lowered significantly during chemical preparation of the sample, and the AsH formation efficiency was approximately half that of SeH formation, isobaric interference by ^{76}AsH may still induce significant errors in $\delta^{82/76}\text{Se}$. The As/Se ratio in OCB+2.5 (calibrated against SGR-1) was small enough that AsH interferences were insignificant. For SGR-1 and UW-McRae, however, interference effects of a few tenths of a ‰ were commonly observed. This error could be corrected by measuring the ^{75}As signal and calculating the $^{76}\text{AsH}/^{75}\text{As}$ ratio based on the SGR-1 calibration. Data for the UW-McRae standard processed with method E showed significant improvement (Figure 4.11). Similar results have been achieved with other As-bearing samples.

SeH: Like arsenic, selenium can form hydrides in the plasma, but it is uncertain to what extent selenium hydrides affect measured isotopic compositions. We used a series of NIST 3149

solutions bracketed with a 40 ppb NIST 3149 to determine the SeH/Se ratio at various concentrations, using Kr-corrected signals at mass 83 and 82 (Elwaer & Hintelmann, 2008). Assuming that all selenium isotopes produced selenium hydrides with the same efficiency, we then calculated the relative difference in delta values between the 40 ppb bracketing standard and other selenium concentrations. This test allowed us to assess how closely samples and standards have to be matched to minimize the effect of SeH interferences. Results showed that the efficiency of SeH formation (measured as the SeH/Se ratio) increased from 0.2 % to about 2 % with decreasing selenium abundance (Figure 4.12), but errors in isotopic ratios were small (Figure 4.13) and negligible as long as the concentrations of standards and samples were matched to within 20%.

ArCl and BrH: Bromine is present as BrH in trace amounts in HCl and ArCl can form in the plasma of the ICP-MS, but in particular, the importance of ArCl is unknown. Here we used the comparison of variations in $\delta^{78/77}\text{Se}$ (subject to ArCl interference) and $\delta^{82/77}\text{Se}$ (subject to ArCl and BrH interferences) in a series of NIST 3149 solutions to test for interferences on mass 77 and 82 after ArAr and Kr interferences were subtracted. If ArCl and BrH interferences were absent, then $\delta^{82/77}\text{Se}$ and $\delta^{78/77}\text{Se}$ values should be 0 ‰. Non-zero values that exceeded errors introduced by SeH formation (see above) indicated the presence of an additional interference such as ArCl or BrH. Results showed that $\delta^{78/77}\text{Se}$ and $\delta^{82/77}\text{Se}$ deviated significantly from 0 ‰ (Figure 4.14a and 4.14b). The values were nearly identical in magnitude, suggesting that they were subject to a common interference on mass 77. We then assumed that any non-zero values in $\delta^{78/77}\text{Se}$ were caused by an interference on ^{77}Se and calculated theoretical values for $\delta^{82/77}\text{Se}$ with that same interference. The theoretical $\delta^{82/77}\text{Se}$ values nearly matched the measured values

(Figure 4.14c), which confirmed that the interference with mass 77 was dominating and that $\delta^{82/77}\text{Se}$ was not perturbed significantly by BrH on mass 82. The most plausible explanation for the interference on mass 77 was ArCl, which can be corrected by standard-sample bracketing if Se concentrations in standards and samples are matched to within 5% (Figure 4.14d). Alternatively, the interference on mass 77 could be ArArH, but this is perhaps unlikely given the relatively low abundance of SeH.

4.4. Discussion

4.4.1. Sample preparation

Overall, the eight TCF extraction protocols do not differ markedly in their results (except method H) and error bars mostly overlap, but they show trends that may explain some of the variability in isotopic compositions of SGR-1 reported in the literature (Table 4.6).

The partial loss of selenium with method A and B is most likely due to incomplete desorption of selenium from the TCF. Furthermore, it is possible that partial evaporation of the sample after extraction from the TCF leads to oxidation and destruction of organic compounds carried over from the TCF or from the sample. The addition of aqua regia (method E) probably further enhances that process. Therefore, the absence of evaporation in method A may result in a large residual fraction of organic molecules, which can potentially bind selenium and hinder the formation of H_2Se gas in the hydride generator (chapter 4 in Dědina & Tsalev, 1995). A combination of incomplete recovery and residual organic compounds may thus explain why the $\delta^{82/78}\text{Se}$ value for SGR-1 reported by Rouxel *et al.* (2002), whose approach is reproduced in method A, was slightly higher than found in more recent studies (Table 4.6). In method D, the large amount of HNO_3 used for extraction from the TCF may lead to partial decomposition of the

TCF itself and release additional TCF-organic compounds into solution. We are uncertain why samples SGR-1 and OCB+2.5 show different responses to this method, but this lack of consistency may indicate that the relatively high $\delta^{82/78}\text{Se}$ value reported by Layton-Matthews *et al.* (2006), whose protocol is most similar to method D, was also affected by organic residues. With the addition of 2 ml of H_2O_2 to the evaporation step (method H), the resulting selenium yield is so reduced that it was close to the detection limit, probably due to either volatilization or interference of residual H_2O_2 with subsequent reduction steps to Se^{II} . The partial loss of selenium in method G, which uses small amounts of H_2O_2 , could therefore be explained by the same mechanism not going to completion. Hence the use of hydrogen peroxide after TCF extraction can be detrimental and should be avoided.

The measured isotopic composition of SGR-1 is most sensitive to the method of extraction, whereas the values obtained for UW-McRae are all within analytical error regardless of extraction method. This difference in sensitivity to the method of extraction correlates with the thermal maturity and age of organic matter in the different samples (Table 4.2), suggesting that immature, reactive organic hydrocarbon molecules have the greatest potential to interfere with selenium analysis in the HG-MC-ICP-MS system. Using small amounts of concentrated nitric acid and repeating the extraction three times improves the total selenium yield compared to protocols relying on larger amounts of nitric acid or a single extraction (Elwaer & Hintelmann, 2008).

The use of aqua regia during the final evaporation step (method E) significantly decreases the concentration of Ge in the sample solution and is a significant improvement over other protocols.

4.4.2. Data reduction

TCF chemistry alone may not provide adequate removal of As and possibly Ge if aqua regia is not applied. The presence of even relatively small amounts of Ge and As results in interferences that can make accurate measurement of ^{74}Se and ^{76}Se impossible. Our post-analytical interference correction procedure reduces the effects of As and Ge interferences, allowing reproducible measurement of $\delta^{76/78}\text{Se}$ and $\delta^{82/76}\text{Se}$.

Similar to published protocols for argon dimer correction, which use on-peak blank subtraction, we are not able to correct for interference on ^{80}Se , but our approach represents an improvement because it is less reliant on argon flow stability. As long as concentrations between samples and bracketing standards are matched to within a few percent, such that Ar-induced shifts in $\delta^{80/78}\text{Se}$ are less than 20 ‰, the error introduced by our protocol is almost negligible.

We demonstrate that interferences with ArCl on mass 77 and presumably on mass 75 exist and can be significant; however, as for selenium hydrides, close matching of concentrations between standards and samples provides adequate correction. Interferences with BrH are probably minor and any contributions that may be present can be corrected by keeping Se concentrations and solution acidity constant throughout the analytical session.

4.4.3. Data precision

Results on three organic-rich shales showed that we were able to achieve an average precision of 0.14 ‰ (1σ) for $\delta^{82/78}\text{Se}$ (Figure 4.15). It seems likely that most of the residual error was due to small losses of selenium during sample preparation or to slight variances in the efficiency of the hydride generation system. In the case of the UW-McRae in-house standard, which we have measured most often, the average standard deviation of replicate analyses of the

same solution was slightly larger (0.11 ‰ for $\delta^{82/78}\text{Se}$) than the standard deviation of averaged replicate analyses of separate digests (0.09 ‰ for $\delta^{82/78}\text{Se}$), suggesting that variances in the hydride generation process dominated over subtle differences in sample preparation. In Table 4.5 we therefore report the standard deviation of all analyses, irrespective of the number of digests.

Herbel *et al.* (2000) demonstrated that in pure-culture experiments, microbial dissimilatory reduction of selenium oxyanions can induce isotopic fractionations of up to 7 ‰. The range of reported isotopic variations in geological samples preserving biogenic fractionations is typically on the order of 1-2 ‰ (Herbel *et al.*, 2002; Rouxel *et al.*, 2002; Clark & Johnson, 2010; Shore, 2010; Mitchell *et al.*, 2012), with extreme variations of up to 13 ‰ in altered sediments or hydrothermal deposits (Hagiwara, 2000; Rouxel *et al.*, 2004; Wen *et al.*, 2007; Wen & Carignan, 2011). Hence the natural variation of $\delta^{82/78}\text{Se}$ is significantly larger than our analytical precision. The described protocol is therefore useful for the application of multiple selenium isotope pairs as a paleo-redox proxy.

4.4.4. Standard-sample bracketing (SSB) vs. selenium double spike

Alternative methods for determining selenium isotope compositions of geological and environmental samples employ a double spike enriched in ^{74}Se and ^{82}Se or ^{74}Se and ^{77}Se to correct for mass fractionation induced during sample preparation and mass spectrometry (Hagiwara, 2000; Herbel *et al.*, 2000; Johnson *et al.*, 2000; Clark & Johnson, 2008; Elwaer & Hintelmann, 2008; Zhu *et al.*, 2008; Clark & Johnson, 2010; Shore, 2010; Schilling *et al.*, 2011b; Schilling *et al.*, 2011a; Schilling & Wilcke, 2011; Mitchell *et al.*, 2012). The major disadvantage of SSB compared to the double spike technique is that it requires more involved chemical preparation to ensure complete recovery of sample selenium. Furthermore, routine analyses are

more cumbersome because the results are sensitive to mismatches in the selenium concentration between samples and bracketing standards. Lastly, analytical precision is somewhat better with a double spike, allowing detection of smaller fractionation effects. The advantages of SSB are that it avoids the high costs and time associated with developing a double spike, and most importantly it allows analysis of five of the six Se isotopes, which in turn allows monitoring of analytical accuracy on three-isotope diagrams. Furthermore, SSB allows better monitoring of multiple isotopes of potentially interfering species, and therefore can be used to analyze samples with complex matrices rich in As and Ge. Finally, because Se-MDF is not assumed during data processing to correct for isobaric interferences, the SSB approach also leaves open the possibility of detecting natural mass-independent fractionation. By analogy to sulfur or mercury (reviewed by Farquhar *et al.*, 2007; Gosh *et al.*, 2008), the least abundant (^{74}Se) and the only odd-numbered (^{77}Se) isotopes may hold specific information about MIF processes in the selenium isotope system and so should not be sacrificed in a double-spike if searching for this unusual but potentially highly informative fractionation style.

4.5. Conclusion

Organic-rich shales are probably the most important hosts of reduced selenium phases, whose isotopic composition can potentially serve as a proxy for surface redox conditions and bioproductivity over the course of Earth's history (e.g. Mitchell *et al.*, 2012). Analyses may be complicated by the complex matrix of such shales due to interferences with organic compounds, arsenic hydrides and germanium. Organic-rich samples of low thermal maturity appear to be particularly sensitive to the preparation method, suggesting that immature organic matter interacts or interferes more severely with selenium during sample preparation or analysis than

mature kerogen. However, our results also show that selenium isotope measurements can be reliably obtained from organic-rich geological matrices replete with interfering elements. Based on our experiments, we recommend the addition of the following steps to the published TCF selenium extraction methods for the analysis of organic-rich sediments:

- rock powder digestion step using perchloric acid at high temperature (130 °C) for a more complete removal of organic compounds;
- triple extraction of the post-TCF solution with small amounts of concentrated nitric acid; and
- aqua regia treatment after TCF column extraction, which greatly lowers the concentration of germanium and probably that of organic compounds while ensuring nearly complete selenium recovery.

The preferred TCF extraction method is therefore method E. Residual interferences with Ge and AsH, as well as interferences with ArAr and related species can be corrected by SSB and post-analytical data processing if selenium concentrations in standards and samples are matched to within 5 %. This method thus allows analysis of five of the six stable isotopes of selenium and therefore has the potential to detect mass-independent fractionation, if it exists.

Acknowledgements

This work was funded by the NSF grant EAR 0921580, the NASA Astrobiology Institute grant to the Virtual Planetary Laboratory team, and the University of Washington RRF. We thank Joy Laydbak, Scott Kuehner, Paul Bédard and Dany Savard for technical advice and assistance. Philip Pogge von Strandmann and Kristen Mitchell are thanked for helpful discussions.

Author contributions

RB supervised the project and collected the UW-McRae sample, JF collected the OCB+2.5 sample, JF and EES developed the analytical method, EES carried out the experiments presented in this paper and wrote the manuscript, BKN owned the mass spectrometer, DCC had the idea of MIF-Se.

Tables

Table 4.1: TCF extraction methods.

Method	oxidizing agent ^e	# ext. ^a	transfer	evaporation conditions	references
A	0.2 ml 8N HNO ₃ + 3.3 ml DI-H ₂ O	1	3.0 out of 3.5 ml pipetted, final quantity corrected by factor 1.17	no evaporation	Rouxel <i>et al.</i> 2002
B	0.2 ml 8N HNO ₃ + 3.3 ml DI-H ₂ O	2	solution poured	HNO ₃ evaporated to 0.5 ml	
C	0.2 ml 16N HNO ₃ + 3.3 ml DI-H ₂ O	3	solution poured	HNO ₃ evaporated to 0.5 ml	
D^b	1 ml 8N HNO ₃ + 4ml DI-H ₂ O	3	pipetted 4, 5, and 5 ml	HNO ₃ evaporated to 0.5 ml	Layton- Matthews <i>et al.</i> 2006
E	0.2 ml 16N HNO ₃ + 3.3 ml DI-H ₂ O	3	solution poured	HNO ₃ evaporated to 0.5 ml, addition of aqua regia ^c , re- evaporated to 0.5 ml	
F^d	0.2 ml 16N HNO ₃ + 3.3 ml DI-H ₂ O	3	solution poured	HNO ₃ evaporated to 0.5 ml	
G	0.2 ml H ₂ O ₂ + 0.5 ml 16N HNO ₃ + 3.8 ml DI-H ₂ O	2	solution poured	evaporated to 0.08ml, 1 ml 16N HNO ₃ added once and 0.05 ml H ₂ O ₂ , + 0.01 ml 16N HNO ₃ added three times and re-evaporated to 0.05 ml	Zhu <i>et al.</i> 2008
H	0.2ml 16N HNO ₃ + 3.3 ml DI-H ₂ O	3	solution poured	HNO ₃ evaporated to 0.5ml, added 2 ml H ₂ O ₂ , re- evaporated to 0.1 ml	

a - # ext = number of extractions by centrifugation where oxidizing agent is added each time.

b - used 0.2 mg ± 5 % TCF instead of 0.145 mg

c - aqua regia in method E is made from concentrated HCl and HNO₃ in a 3:1 ratio.

d - sample digested at 150°C instead of 130°C

e - in all methods, DI-H₂O is added after the TCF has been boiled with the oxidizer.

Table 4.2: Description of samples analyzed with methods A through H.

	SGR-1	UW-McRae	OCB+2.5
age	45 Ma	2500 Ma	250 Ma
TOC	25 % ^c	8 % ^d	1 % ^d
sample type	thermally immature oil shale	thermally overmature black shale	thermally mature gray shale
Se content	3.51 ± 0.26 ppm ^a	3.13 ± 0.09 ppm ^b	4.35 ± 0.06 ppm ^b
As content	67 ± 5 ppm ^c	143 ± 31 ppm ^e	2.6 ± 0.5 ppm ^e
Ge content	1.59 ppm ^f	1.73 ± 1.40 ppm ^g	1.00 ± 0.81 ppm ^g
As/Se ratio	19 ± 2	46 ± 10	0.6 ± 0.1
Ge/Se ratio	0.45 ± 0.03	0.56 ± 0.45	0.23 ± 0.19
δ^{82/78}Se^h	+0.19 ± 0.24 ‰	+0.90 ± 0.15 ‰	-1.27 ± 0.17 ‰

a - average value of a compilation of literature values by Savard *et al.* (2009).

b - maximum average value determined in this study, *i.e.* method E for UW-McRae, method F for OCB+2.5.

c - U.S. Geological Survey (Dennen *et al.*, 2006).

d - measured in the UW-Isolab, using the same facilities and methods as described by Stüeken (2013)

e - tentative values; calibrated using As in SGR-1 and approximate estimates of the TCF and HG efficiency of As from pure solutions.

f - Mortlock and Frohlich (1987).

g - tentative values; calibrated using Ge in SGR-1 and approximate estimates of the TCF and HG efficiency of Ge from pure solutions.

h - for UW-McRae and OCB+2.5, this is the average value of all individual analyses in methods C, E, and F (see below). For SGR-1, this is the average of the four published values (Table 4.6)

Table 4.3: Fractional abundances of the major species interfering with Se in the 72-84 mass range.

Mass	species	Source	natural abundance	correction method
72	⁷² Ge	sample	0.2731	used to monitor Ge
73	⁷³ Ge	sample	0.0776	used to monitor Ge
74	⁷⁴ Ge	sample	0.3672	used to correct ⁷⁶ Ge
75	⁷⁵ As	sample	1	used to correct ⁷⁶ AsH
	⁷⁵ (SeH)	sample, NaBH ₄	0.00889	
	⁷⁵ (ArCl)	carrier gas, acid	0.754749	
76	⁷⁶ (ArAr)	carrier gas	0.006646	manual, using ⁸⁰ ArAr
	⁷⁶ Ge	sample	0.0783	manual, using ⁷⁴ Ge
	⁷⁶ (AsH)	sample, NaBH ₄	1	manual, using ⁷⁵ As, ⁸³ SeH
77	⁷⁷ (SeH)	sample, NaBH ₄	0.09366	SSB
	⁷⁷ (ArArH)	carrier gas, NaBH ₄	0.006646	SSB
	⁷⁷ (ArCl)	carrier gas, acid	0.241439	SSB
78	⁷⁸ (ArAr)	carrier gas	0.001253	manual, using ⁸⁰ ArAr
	⁷⁸ (SeH)	sample, NaBH ₄	0.07635	SSB
	⁷⁸ Kr	carrier gas	0.00355	manual, using ⁸⁴ Kr
79	⁷⁹ (ArArH)	carrier gas, NaBH ₄	0.001253	
	⁷⁹ Br	acid	0.5069	
	⁷⁹ (SeH)	sample, NaBH ₄	0.23772	
80	⁸⁰ (ArAr)	carrier gas	0.992086	used to correct ^{76,78} ArAr
	⁸⁰ Kr	carrier gas	0.02286	manual, using ⁸⁴ Kr
	⁸⁰ (BrH)	acid, NaBH ₄	0.5069	SSB
81	⁸¹ (ArArH)	carrier gas, NaBH ₄	0.992086	
	⁸¹ Br	acid	0.4931	
	⁸¹ (SeH)	sample, NaBH ₄	0.49607	
82	⁸² Kr	carrier gas	0.11593	manual, using ⁸⁴ Kr
	⁸² (BrH)	acid, NaBH ₄	0.4931	SSB
83	⁸³ (SeH)	sample, NaBH ₄	0.08731	used to monitor SeH/Se
	⁸³ Kr	carrier gas	0.11500	
84	⁸⁴ Kr	carrier gas	0.56987	used to monitor ⁷⁸⁻⁸² Kr

Masses directly overlapping with selenium isotopes are marked by grey shading. See text for reference to correction methods. SSB = standard-sample bracketing.

Table 4.4: Operating parameters of the HG-MC-ICP-MS system.

ICP-MS:															
RF power	1300 W														
sample cone	nickel														
skimmer cone	nickel														
Ar flow rates:															
cooling	15.0 L/min														
auxiliary	0.80 L/min														
Fassel type torch	position adjusted daily														
Hydride Generator:															
Ar flow rates ^a :															
sample carrier I	~ 0.15 L/min (adjusted daily)														
sample carrier II	~ 1.25 L/min (adjusted daily)														
solution uptake rates:															
sample/standard	0.74 mL/min														
NaBH ₄	0.74 mL/min														
solution compositions:															
NaBH ₄	1 % (wt.) NaBH ₄ in 0.01M NaOH, refreshed daily														
sample acidity	0.6N HCl														
standard acidity	0.6N HCl														
washing solution	0.6N HCl														
Analysis:															
Faraday cup separation	½ mass separation between cups														
delay time between cycles	3 seconds														
number of repeats	50, in 5 blocks of 10														
integration time	8 seconds														
zeros	half-mass zeros, each block														
sample transfer time	200 seconds														
sample washout time	240 seconds														
MC-ICP-MS cup configuration:															
cup:	H6	H5	H4	H3	H2	H1	Ax	L1	L2	IC0	L3	IC1	L4	IC2	L5
1 st cycle:	84	83	82		81		80		79		78		77		76
2 nd cycle:	79	78	77		76		75		74		73		72		71

a - the hydride generator contains a Teflon membrane to minimize water vapor in the plasma. Ar carrier line I enters the HG below the membrane, Ar carrier line II enters above the membrane.

Table 4.5: Comparison of different methods for extracting selenium from the TCF column.

method	sample	SGR-1	UW-McRae	OCB+2.5
A	Se [ppm]	3.02 ± 0.32	2.50 ± 0.06	3.45 ± 0.02
	$\delta^{82/78}\text{Se}$ [‰]	+0.18 ± 0.22	+0.83 ± 0.11	-1.04 ± 0.09
	n	15	5	2
B	Se [ppm]	3.29 ± 0.03	2.99 ± 0.01	4.31 ± 0.03
	$\delta^{82/78}\text{Se}$ [‰]	+0.03 ± 0.06	+0.82 ± 0.12	-1.29 ± 0.25
	n	3	3	2
C	Se [ppm]	3.46 ± 0.05	3.11 ± 0.05	4.31 ± 0.04
	$\delta^{82/78}\text{Se}$ [‰]	-0.11 ± 0.17	+0.92 ± 0.14	-1.27 ± 0.08
	n	15	8	3
D	Se [ppm]	3.46 ± 0.06	not analyzed	4.13 ± 0.14
	$\delta^{82/78}\text{Se}$ [‰]	-0.38 ± 0.22	not analyzed	-1.04 ± 0.19
	n	9	-	7
E	Se [ppm]	3.40 ± 0.06	3.13 ± 0.09	4.28 ± 0.09
	$\delta^{82/78}\text{Se}$ [‰]	+0.05 ± 0.18	+0.87 ± 0.13	-1.31 ± 0.23
	n	9	81	6
F	Se [ppm]	3.47 ± 0.16	3.07 ± 0.02	4.35 ± 0.06
	$\delta^{82/78}\text{Se}$ [‰]	-0.10 ± 0.08	+0.93 ± 0.11	-1.20 ± 0.14
	n	2	5	3
G	Se [ppm]	3.13 ± 0.03	not analyzed	not analyzed
	$\delta^{82/78}\text{Se}$ [‰]	+0.21 ± 0.08	not analyzed	not analyzed
	n	4	-	-

Shown are averages over replicate analyses of multiple digests, $\pm 1\sigma$. n = number of analyses. Preferred methods with consistently high yields are shaded. Compare Se [ppm] in Table 4.2.

Table 4.6: Interlaboratory comparison expressed in terms of $\delta^{82/78}\text{Se}$.

[‰]	this study (average of method C, E, F)	Rouxel <i>et al.</i> , 2002	Layton- Matthews <i>et al.</i> , 2006	Mitchell <i>et al.</i> , 2012	Schilling <i>et al.</i> , 2011a	Johnson 2011 (pers. com.)
SGR-1	-0.06 ± 0.18 (n = 26)	$+0.35 \pm 0.24^{\text{a}}$ (n not rep.)	$+0.40 \pm 0.21^{\text{b}}$ (n = 3)	$-0.13 \pm 0.03^{\text{c}}$ (n = 11)	$+0.13 \pm 0.06^{\text{c}}$ (n = 4)	
UW-McRae	$+0.88 \pm 0.14$ (n = 94)					$+0.73 \pm 0.04$ (n = 4)
OCB+2.5	-1.27 ± 0.17 (n = 12)					-1.15 ± 0.03 (n = 2)

Measured isotopic compositions of shale samples, expressed in terms of $\delta^{82/78}\text{Se}$, $\pm 1\sigma$. Analyses by Mitchell *et al.* (2012), Schilling *et al.* (2011a) and Johnson (2011, pers. com.) were done with a selenium double-spike. n = number of measurements. pers. com. = personal communication; not rep. = not reported.

a – conversion from MERCK to NIST scale after Carignan and Wen (2007).

b – conversion from MERCK to NIST scale after Layton-Matthews *et al.* (2006).

c – calculated from reported value for $\delta^{82/76}\text{Se}$.

Table 4.7: Ge-correction error.

natural $\delta^{74/78}\text{Se}$ [‰]	+0.50	+1.00	+2.00	+5.00	+10.00
error in $\delta^{76/78}\text{Se}$ [‰]	-0.01	-0.02	-0.04	-0.10	-0.20
error in $\delta^{82/76}\text{Se}$ [‰]	+0.01	+0.02	+0.04	+0.10	+0.20

Table 4.8: ArAr-correction error.

natural $\delta^{80/78}\text{Se}$ [‰]:	+0.50	+1.00	+2.00	+5.00	+10.00
error in $\delta^{74/78}\text{Se}$ [‰]	0.00	0.00	0.00	+0.01	0.03
error in $\delta^{76/78}\text{Se}$ [‰]	-0.02	-0.03	-0.07	-0.17	-0.33
error in $\delta^{77/78}\text{Se}$ [‰]	0.00	0.00	0.00	+0.01	+0.03
error in $\delta^{82/78}\text{Se}$ [‰]	0.00	0.00	0.00	+0.01	+0.03
error in $\delta^{82/76}\text{Se}$ [‰]	+0.02	+0.04	+0.07	+0.18	+0.36

Figures

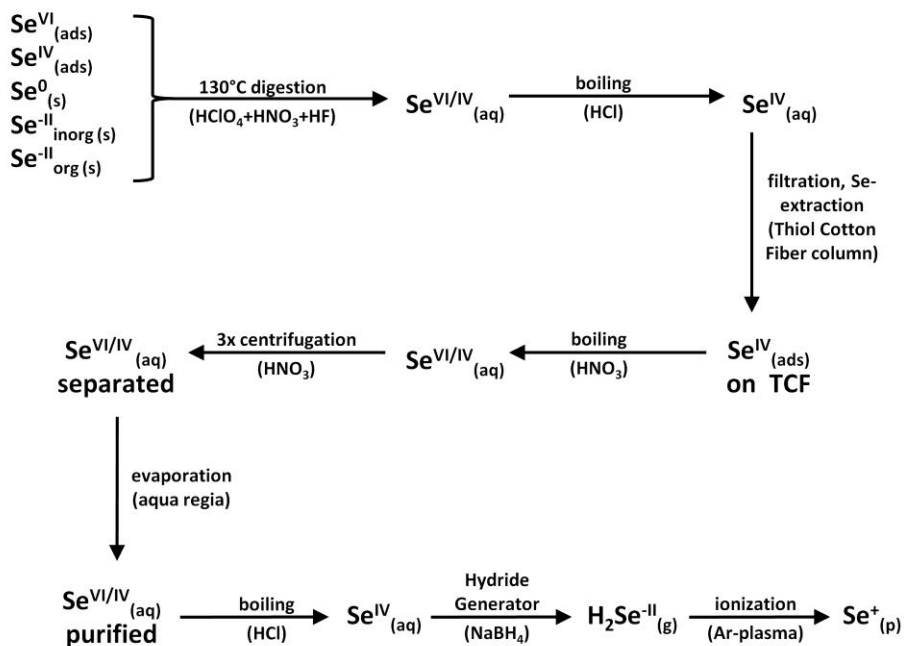


Figure 4.1: Sample preparation flowchart. Some deviations from this protocol were tested and are discussed in the text. $\text{Se}^{\text{VI/IV}}$ indicates that both redox states may be present; s = solid; aq = aqueous; ads = adsorbed; g = gas, p = plasma.

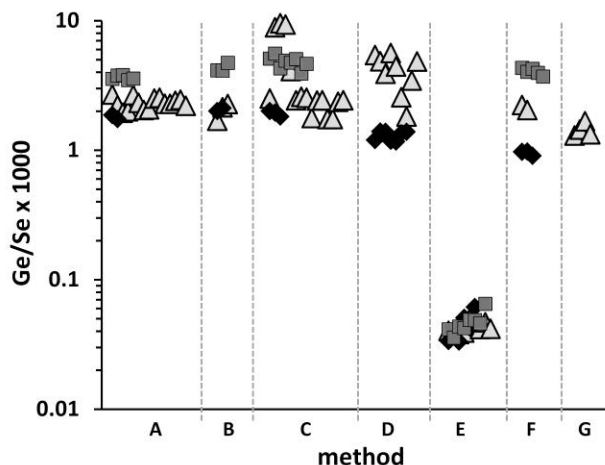


Figure 4.2: Aqua regia effect. The Ge/Se ratio of sample solutions, expressed as the total voltage of all isotopes, is decreased by nearly two orders of magnitude for samples processed by method E. Diamonds = OCB+2.5; triangles = SGR-1; squares = UW-McRae. Each point marks one individual measurement, plotted in no specific order.

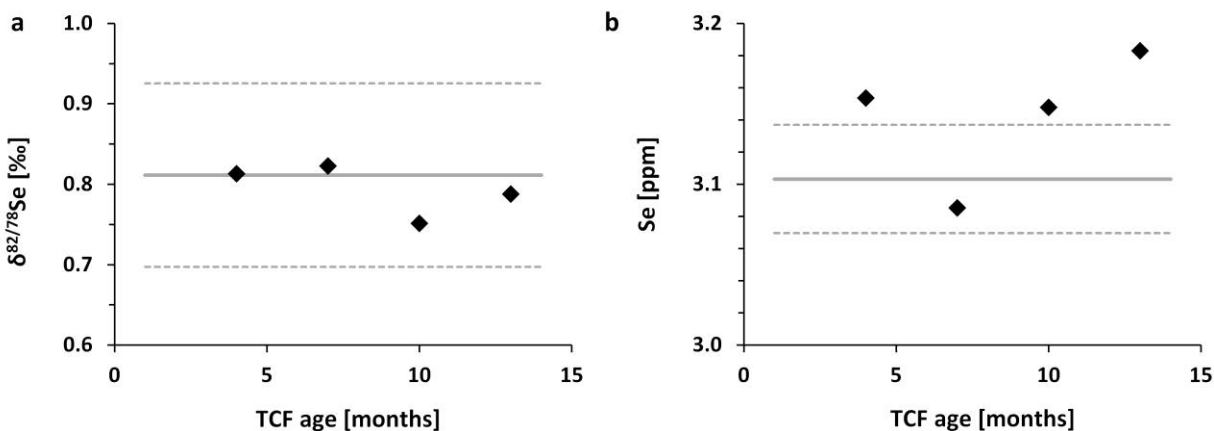


Figure 4.3: TCF long-term stability. Black diamonds = individual measurements of UW-McRae, processed with method E and different age batches of TCF. All data were obtained during a single analytical session. Thick grey line = average of UW-McRae aliquots analyzed in the same session, processed with method E and fresh TCF; dashed grey lines = \pm one standard deviation from the average. **a:** isotopic composition; **b:** total Se yield.

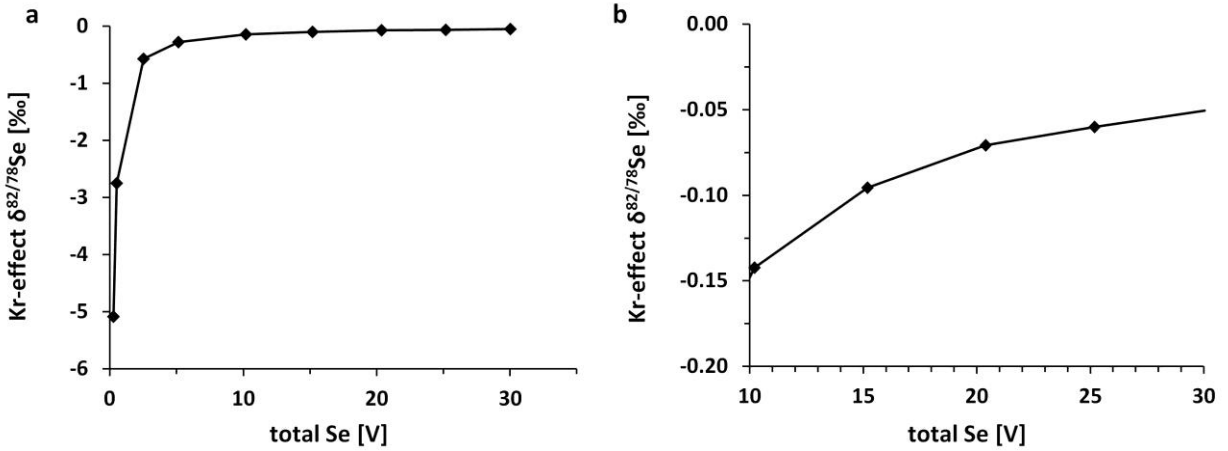


Figure 4.4: Kr interference effect. Change in $\delta^{82/78}\text{Se}$ after Kr interferences have been removed from signals at masses 78 and 82. **a:** full range; **b:** detailed view of typical analytical range. Total Se is the sum of all isotopes in volts.

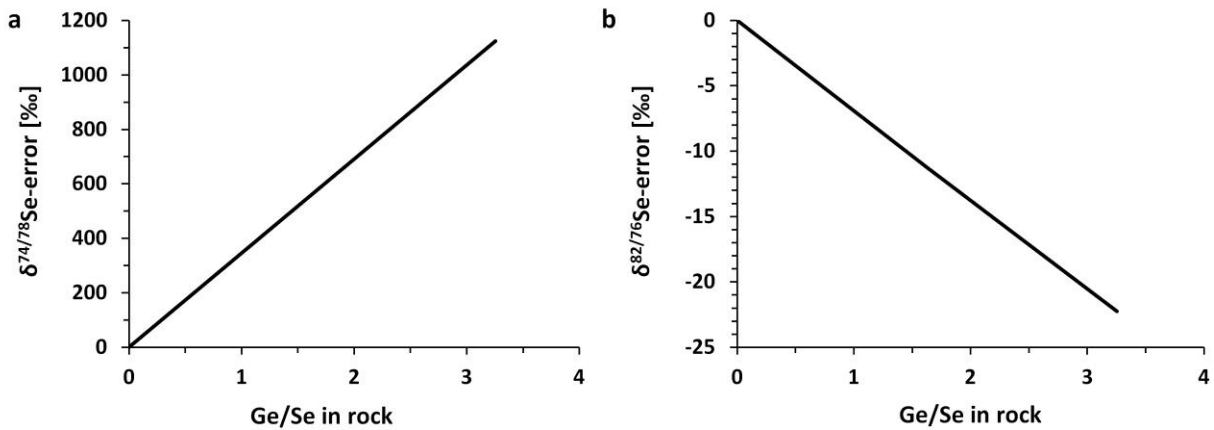


Figure 4.5: Ge-induced errors. Curves are calibrated with pure Se-Ge-solutions and SGR-1.

Anomalies refer to deviations from predicted isotopic ratios assuming mass-dependent fractionation. **a:** effect on $\delta^{74/78}\text{Se}$; **b:** effect on $\delta^{82/76}\text{Se}$, which is nearly equivalent in magnitude to the effect on $\delta^{78/76}\text{Se}$.

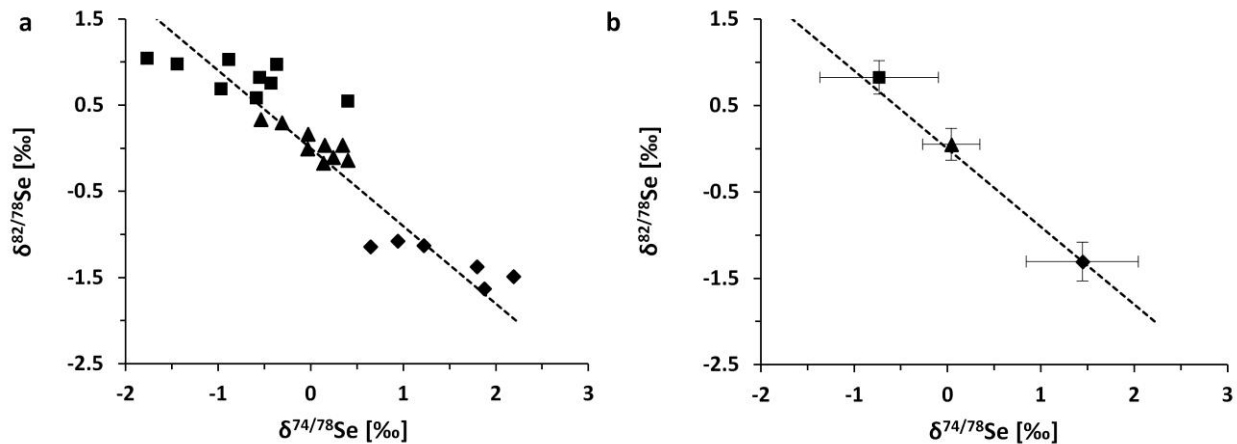


Figure 4.6: $\delta^{74/78}\text{Se}$ versus $\delta^{82/78}\text{Se}$. Demonstrates the precision in $\delta^{74/78}\text{Se}$ possible using protocol E with enhanced Ge separation. Squares = UW-McRae; triangles = SGR-1; diamonds = OCB+2.5. Results are from sample aliquots processed with method E. **a:** individual measurements; **b:** average $\pm 1\sigma$. Dashed line = theoretical mass dependent fractionation.

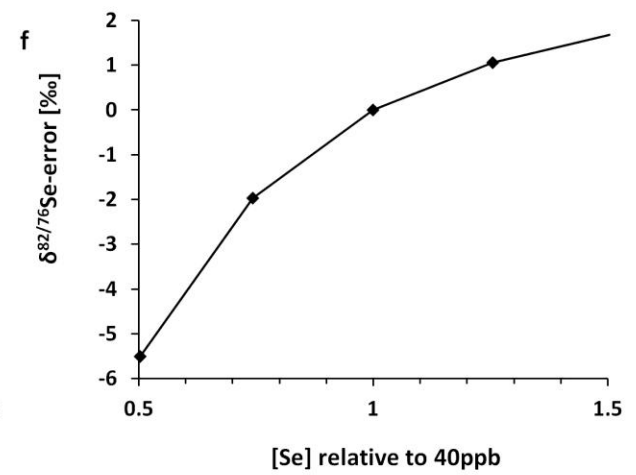
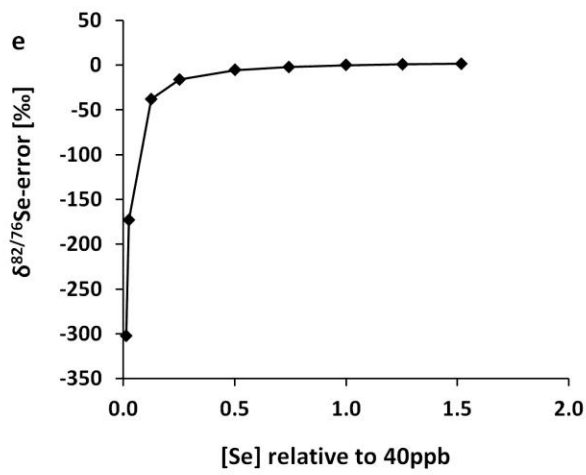
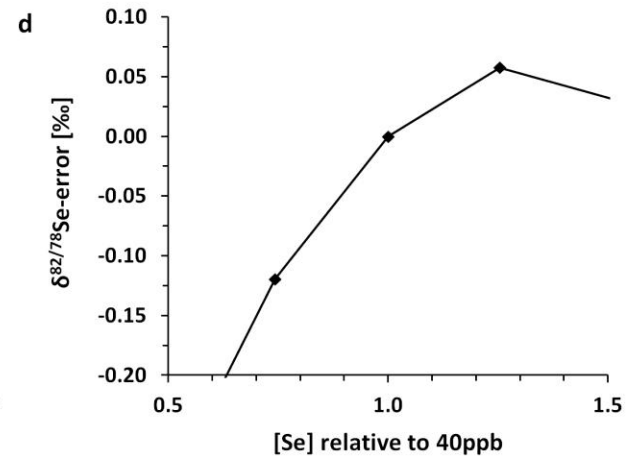
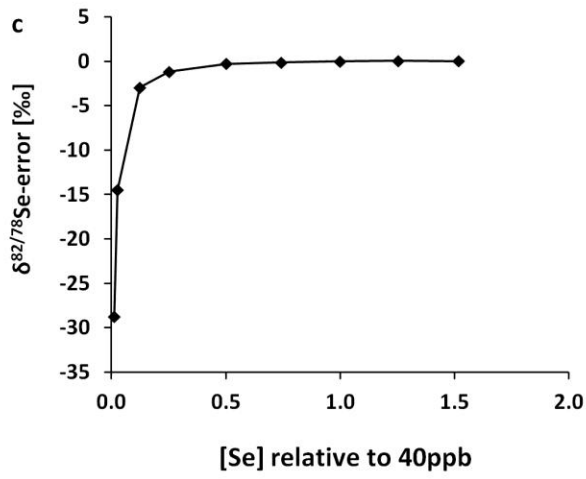
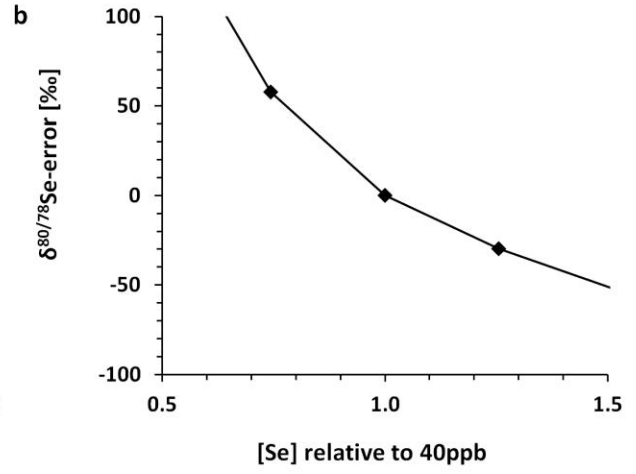
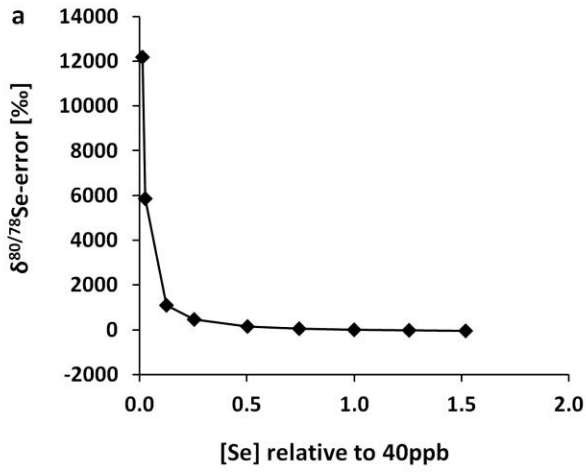


Figure 4.7: Ar-induced errors. Error refers to deviation of selenium isotope ratios from expected mass dependent fractionation. In the case of NIST 3149 this anomaly is equal to any non-zero value. Se concentrations on x-axis are plotted as signal intensity relative to a 40 ppb solution, which was used as the bracketing standard in this experiment. **a, b:** effect on $\delta^{80/78}\text{Se}$; **c, d:** effect on $\delta^{82/78}\text{Se}$; **e, f:** effect on $\delta^{82/76}\text{Se}$. Panels a, c, and e show full concentration range; panels b, d, and f show range where Se concentrations are within 50 % of the bracketing standard.

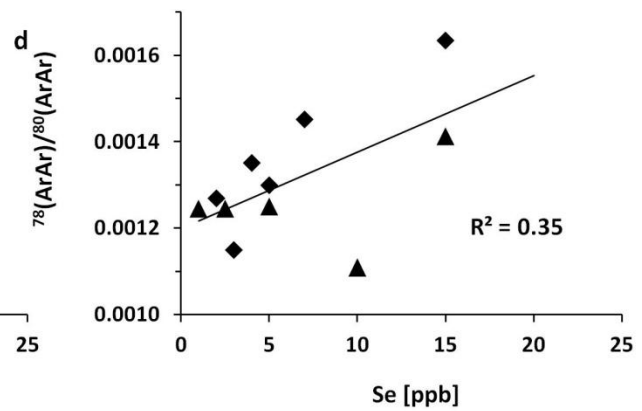
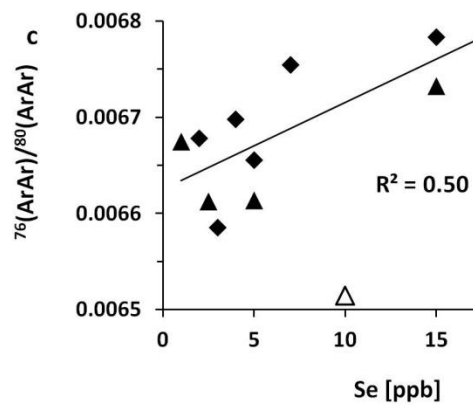
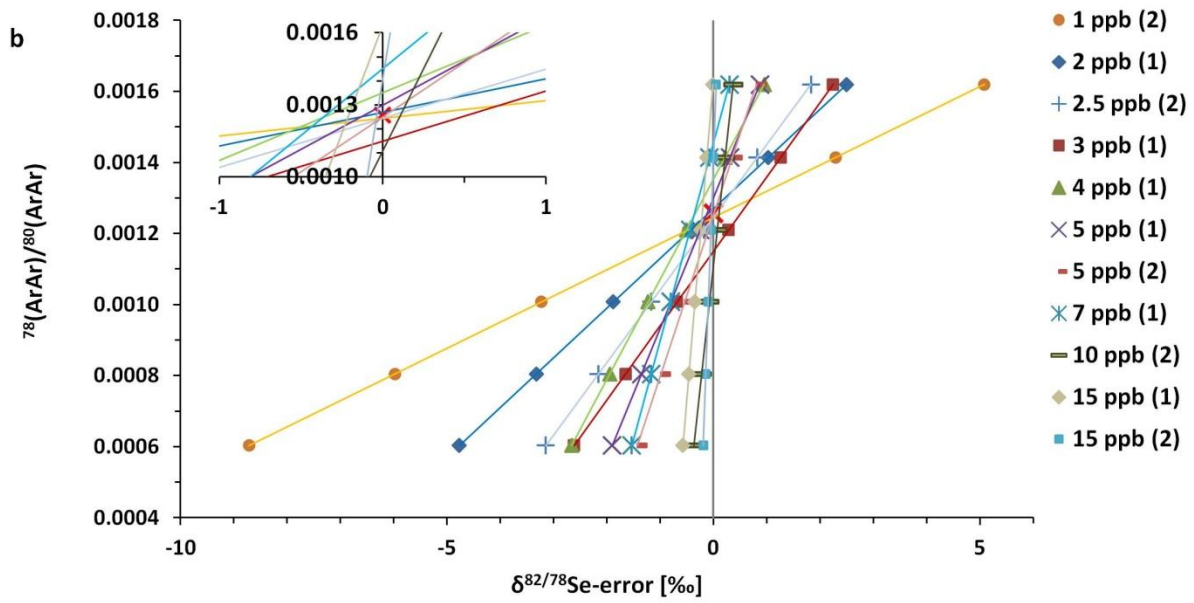
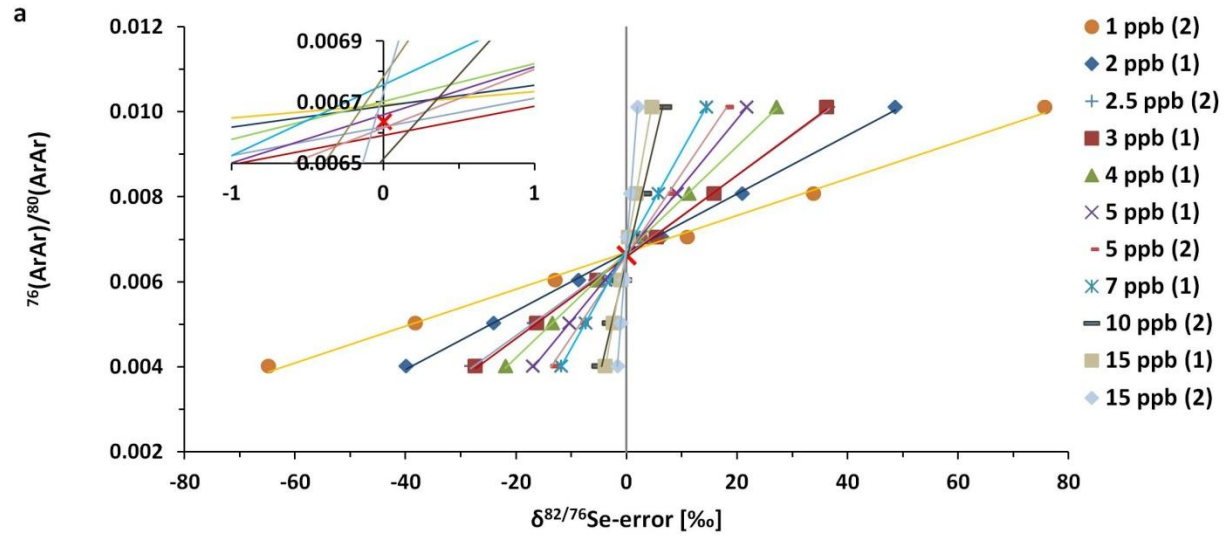


Figure 4.8: Mass bias optimization for argon dimers. Aliquots of NIST 3149 were analyzed at various concentrations and referenced to a solution at 20 ppb. The optimized $^{76}(\text{ArAr})/^{80}(\text{ArAr})$ (panel **a**) and $^{78}(\text{ArAr})/^{80}(\text{ArAr})$ (panel **b**) ratios were determined by applying a range of ratios (y-axes) and calculating the 0 ‰-intercept of the residual error in $\delta^{82/76}\text{Se}$ and $\delta^{82/78}\text{Se}$, respectively (x-axes). Ratios were previously corrected for trace AsH and Ge. Measurements were done in two sessions (1) and (2), separated by nine months. Inserts show detail of zone of intercepts. Red x = natural ratios in air (Lee *et al.*, 2006). **c**: optimized $^{76}(\text{ArAr})/^{80}(\text{ArAr})$ ratio versus Se concentration. Value at 10 ppb was found to be an outlier. **d**: optimized $^{78}(\text{ArAr})/^{80}(\text{ArAr})$ ratio versus Se concentration. Black diamonds = session 1, black triangles = session 2.

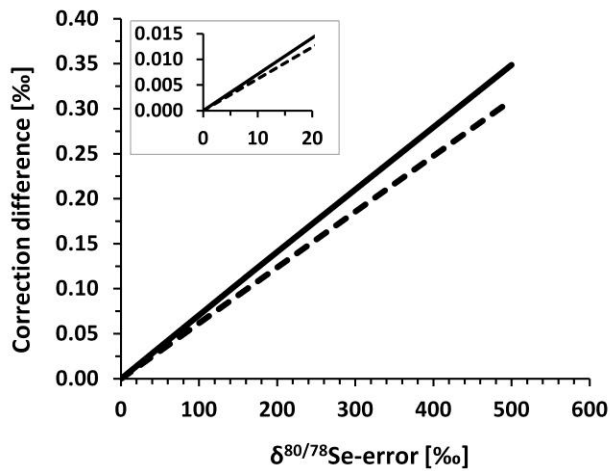


Figure 4.9: Ar correction uncertainty. The x-axis shows errors in $\delta^{80/78}\text{Se}$, which are here defined as non-zero values and assumed to be due to argon dimer interferences. The y-axis shows the difference in permil between an argon dimer correction using the optimized argon dimer mass bias $+1\sigma$ and the optimized argon dimer mass bias -1σ . Solid line = effect on $\delta^{82/78}\text{Se}$, and optimized mass bias referring to $^{78}(\text{ArAr})/^{80}(\text{ArAr})$ ratio (Figure 4.8a); dashed line = effect on $\delta^{82/76}\text{Se}$, and optimized mass bias referring to $^{76}(\text{ArAr})/^{80}(\text{ArAr})$ ratio (Figure 4.8b). Typical $\delta^{80/78}\text{Se}$ errors in samples whose Se concentrations are matched with that of the bracketing standard to within a few percent are in the range of up to 20 ‰ (insert).

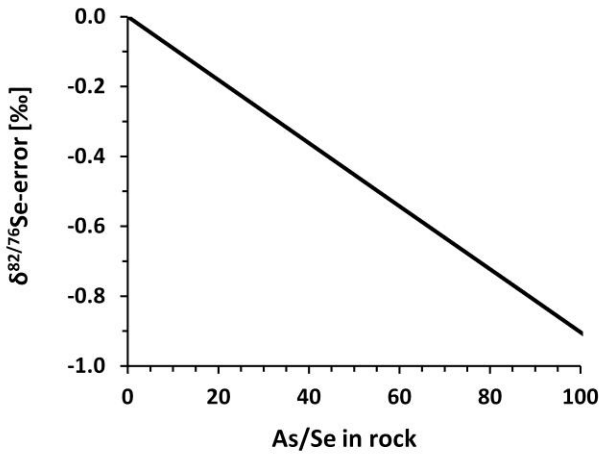


Figure 4.10: AsH-induced errors. Curves are calibrated with pure Se-As-solutions and SGR-1. Error refers to deviations from predicted isotopic ratios assuming mass-dependent fractionation. The effect on $\delta^{82/76}\text{Se}$ is nearly equivalent in size to the effect on $\delta^{78/76}\text{Se}$.

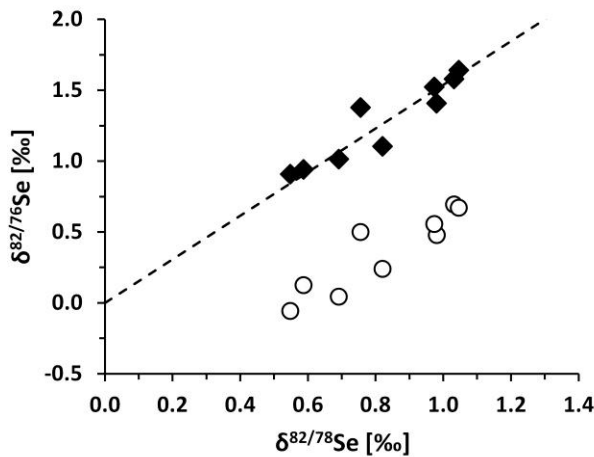


Figure 4.11: AsH correction. Each point represents one measurement of an aliquot of UW-McRae processed with method E. Open circles = not corrected for AsH interferences on mass 76; filled diamonds = corrected for AsH interferences by calibration of the AsH/As ratio with SGR-1. Dashed line = theoretical mass dependent fractionation.

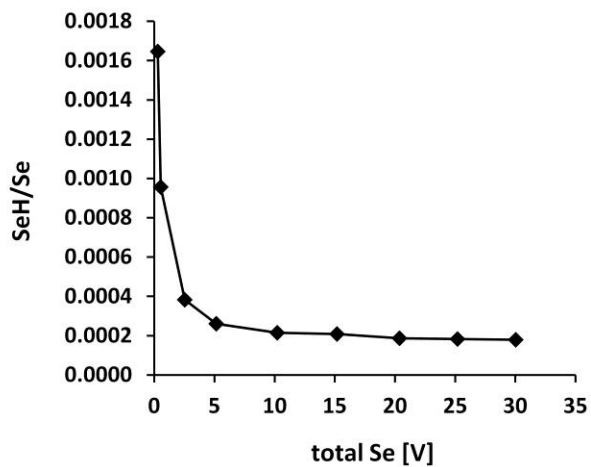


Figure 4.12: SeH/Se ratio. Total selenium voltage is the sum of all Se isotopes. SeH/Se ratios were calculated from signals at mass 83 (SeH) and 82 (Se) after corrections for Kr interference.

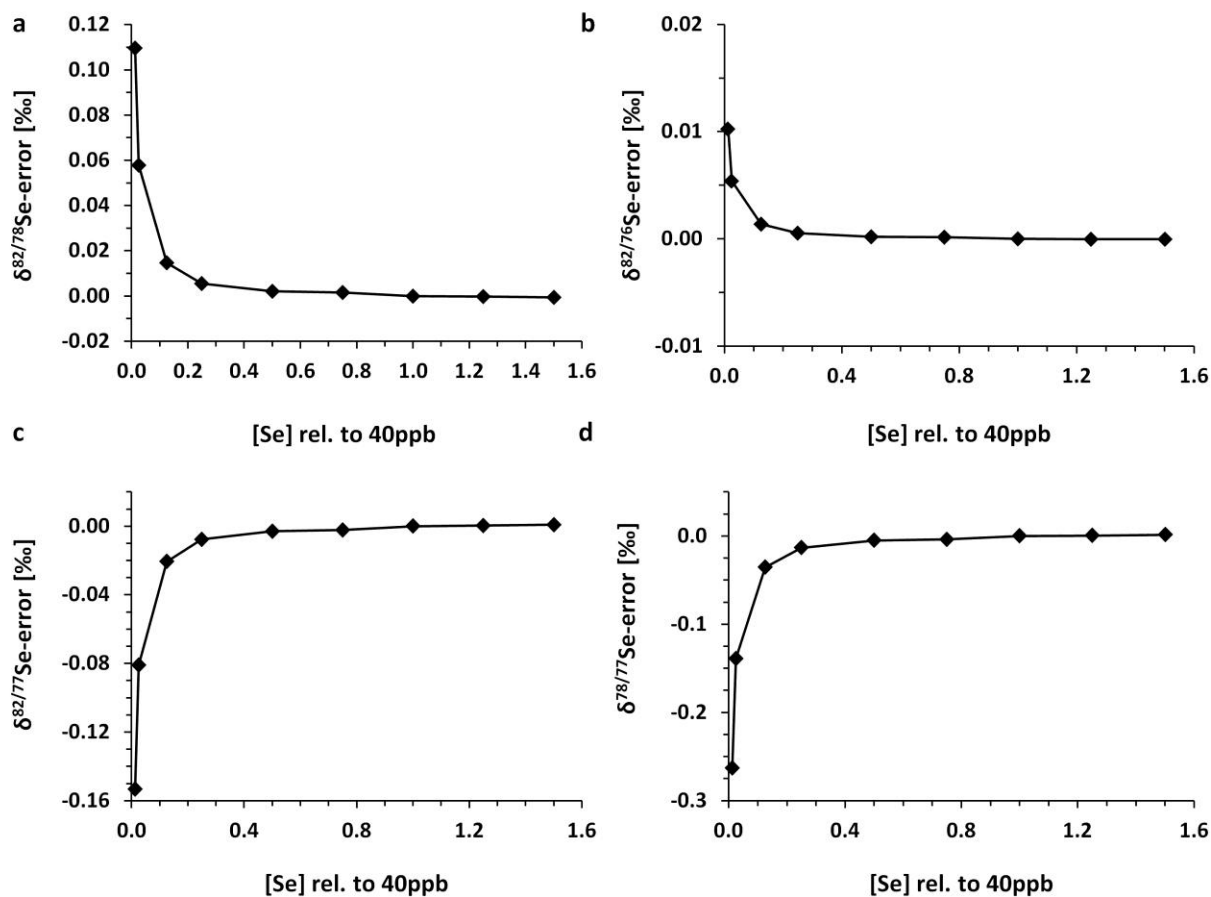


Figure 4.13: SeH induced errors. The y-axes show by how much SeH-formation offsets measured isotopic ratios from theoretical values free of interferences. These errors were calculated from SeH/Se ratios shown in Figure 4.12. Concentrations on the x-axis are signal intensity relative to 40 ppb solution, which was used as bracketing standard. **a:** effect on $\delta^{82/78}\text{Se}$; **b:** effect on $\delta^{82/76}\text{Se}$; **c:** effect on $\delta^{82/77}\text{Se}$; **d:** effect on $\delta^{78/77}\text{Se}$.

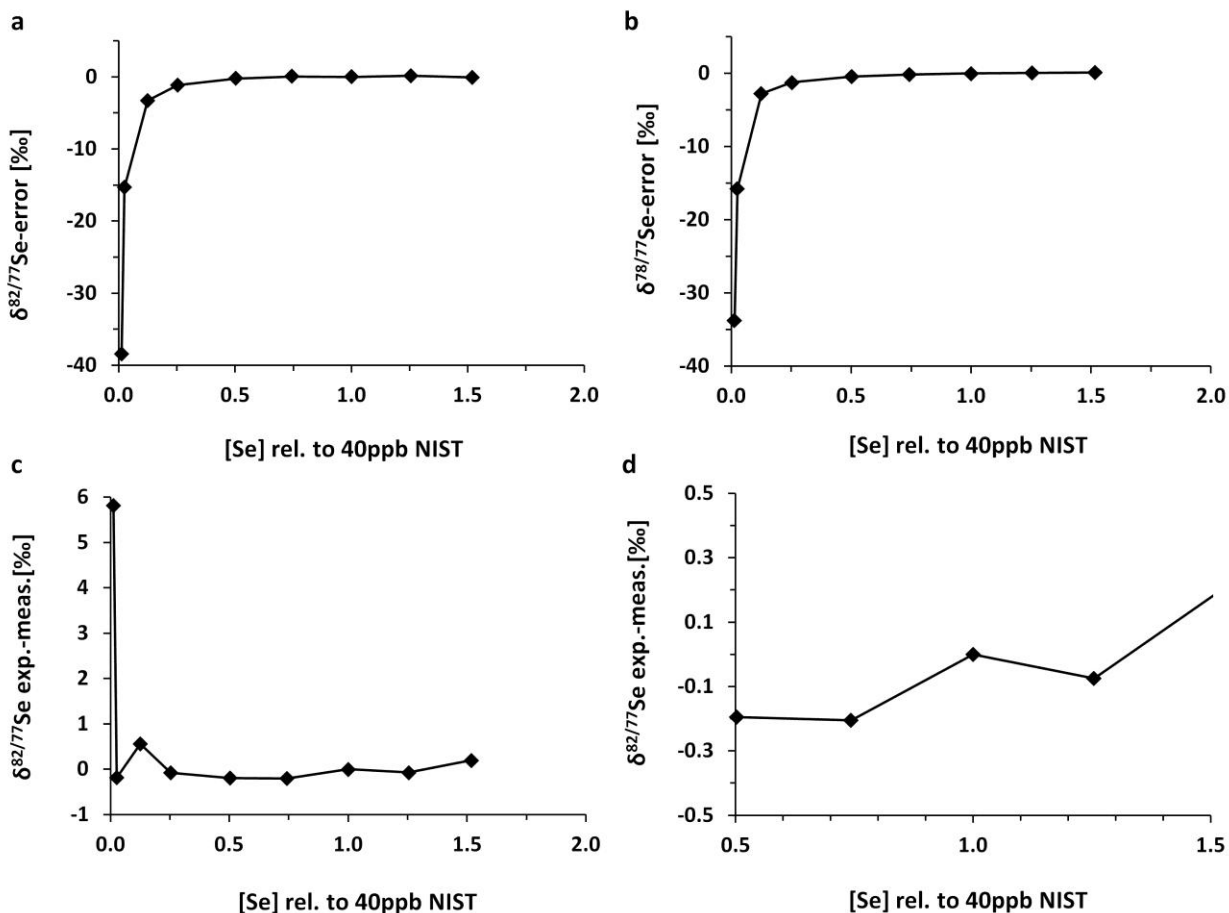


Figure 4.14: ArCl interference. **a:** measured error in $\delta^{82/77}\text{Se}$ versus concentration relative to the 40 ppb bracketing standard **b:** measured error in $\delta^{78/77}\text{Se}$ versus concentration relative to the 40 ppb bracketing standard. Results have been corrected for interferences by Ar-dimers, Kr, AsH, and Ge. **c:** Difference between the expected and measured value for $\delta^{82/77}\text{Se}$, where the expected values are calculated by assuming an interference on mass 77 that would explain the observed error in $\delta^{78/77}\text{Se}$. This interference is most likely $^{77}(\text{ArCl})$. **d:** same as panel c, focusing on region where concentrations match the bracketing standard to within 50 %.

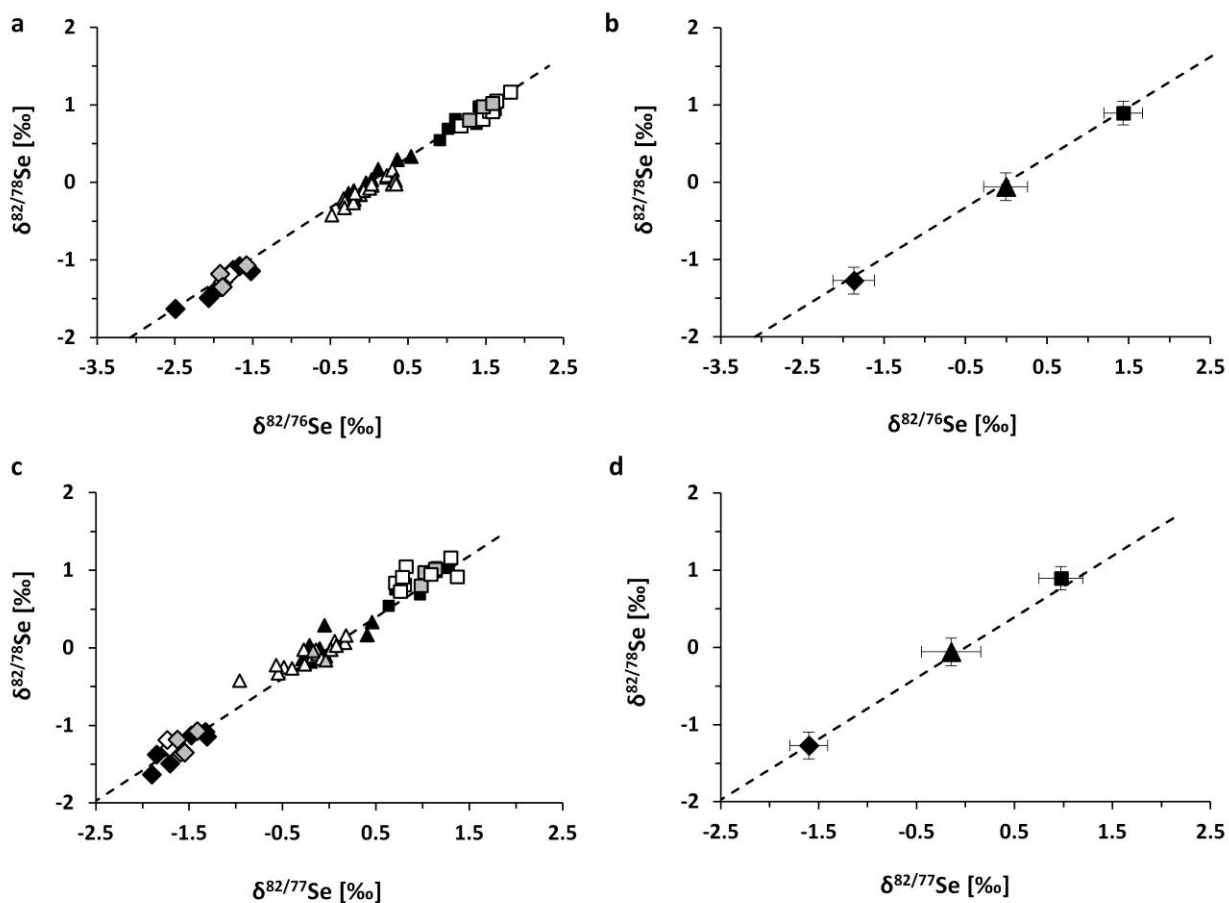


Figure 4.15: Standard measurements. Results for OCB+2.5 (diamonds), SGR-1 (triangles) and UW-McRae (squares) processed with the three most consistent methods E (black), F (grey) and C (white). **a, b:** $\delta^{82/78}\text{Se}$ versus $\delta^{82/76}\text{Se}$; **c, d:** $\delta^{82/78}\text{Se}$ versus $\delta^{82/77}\text{Se}$. Each value in panel (a) and (c) is one measurement, panel (b) and (d) show averages of individual measurements from all three methods, $\pm 1\sigma$. Dashed line = theoretical mass dependent fractionation. Selected data points for UW-McRae, method E, are those that were prepared and analyzed in the same batch as aliquots of other methods.

References

- Albarède F, Télouk P, Blichert-Toft J, Boyet M, Agranier A, Nelson BK (2004) Precise and accurate isotopic measurements using multiple-collector ICPMS. *Geochimica et Cosmochimica Acta*, **68**.
- Anbar AD, Duan Y, Lyons TW, Arnold GL, Kendall B, Creaser RA, Kaufmann AJ, Gordon GW, Scott C, Garvin J, Buick R (2007) A whiff of oxygen before the Great Oxidation Event? *Science*, **317**, 1903-1906.
- Bagnall KW (1966) The chemistry of selenium, tellurium and polonium. In: *Topics in inorganic and general chemistry* (ed Robinson PL). Elsevier Publishing Company, Amsterdam.
- Bye R, Lund W (1988) Optimal conditions for the reduction of selenate to selenite by hydrochloric acid. *Fresenius Zeitschrift fuer Analytische Chemie*, **332**, 242-244.
- Carignan J, Wen H (2007) Scaling NIST SRM 3149 for Se isotope analysis and isotopic variations of natural samples. *Chemical Geology*, **242**, 347-350.
- Catling DC, Claire MW (2005) How Earth's atmosphere evolved to an oxic state: A status report. *Earth and Planetary Science Letters*, **237**, 1-20.
- Clark SK, Johnson TM (2008) Effective isotopic fractionation factors for solute removal by reactive sediments: a laboratory microcosm and slurry study. *Environmental Science and Technology*, **42**.
- Clark SK, Johnson TM (2010) Selenium stable isotope investigation into selenium biogeochemical cycling in a lacustrine environment: Sweitzer Lake, Colorado. *Journal of Environmental Quality*, **39**, 2200-2210.
- Dědina J, Tsalev DL (1995) *Hydride Generation Atomic Absorption Spectrometry*, John Wiley & Sons Ltd, West Sussex, UK.
- Dennen KO, Johnson CA, Otter ML, Silva SR, Wandless GA (2006) $\delta^{15}\text{N}$ and non-carbonate $\delta^{13}\text{C}$ values for two petroleum source rock reference materials and a marine sediment reference material. U.S. Geological Survey, Open File Report 2006-1071.
- Ellis AS, Johnson TM, Herbel MJ, Bullen T (2003) Stable isotope fractionation of selenium by natural microbial consortia. *Chemical Geology*, **195**, 119-129.
- Elwaer N, Hintelmann H (2008) Selective separation of selenium (IV) by thiol cellulose powder and subsequent selenium isotope ratio determination using multicollector inductively coupled plasma mass spectrometry. *Journal of Analytical Atomic Spectrometry*, **23**, 733-743.
- Fan HF, Wen H, Hu M, Zhao H (2011) Selenium speciation in Lower Cambrian Se-enriched strata in South China and its geological implications. *Geochimica et Cosmochimica Acta*, **75**, 7725-7740.
- Farquhar J, Bao H, Thiemens M (2000) Atmospheric influence on Earth's earliest sulfur cycle. *Science*, **289**, 756-758.
- Farquhar J, Peters M, Johnston DT, Strauss H, Masterson A, Wiechert U, Kaufman AJ (2007) Isotopic evidence for Mesoarchean anoxia and changing atmospheric sulphur chemistry. *Nature*, **449**, 706-709.
- Fernandez-Marinez A, Charlet L (2009) Selenium environmental cycling and bioavailability: a structural chemist point of view. *Reviews in Environmental Science and Biotechnology*, **8**, 81-110.

- Gladyshev VN (2012) Selenoproteins and selenoproteomes. In: *Selenium: Its molecular biology and role in human health* (eds Hatfield DL, Berry MJ, Gladyshev VN). Springer Science + Business Media, pp. 109-123.
- Gosh S, Xu Y, Humayun M, Odom L (2008) Mass-dependent fractionation of mercury isotopes in the environment. *Geochemistry Geophysics Geosystems*, **9**, doi:10.1029/2007GC001827.
- Hagiwara Y (2000) Selenium isotope ratios in marine sediments and algae: A reconnaissance study. University of Illinois at Urbana-Champaign, Urbana, IL, pp. 62.
- Henderson CM (1997) Uppermost Permian conodonts and the Permian–Triassic boundary in the Western Canada Sedimentary Basin. *Bulletin of Canadian Petroleum Geology*, **45**, 693-707.
- Herbel MJ, Johnson TM, Oremland RS, Bullen T (2000) Fractionation of selenium isotopes during bacterial respiratory reduction of selenium oxyanions. *Geochimica et Cosmochimica Acta*, **64**, 3701-3709.
- Herbel MJ, Johnson TM, Tanji KK, Gao S, Bullen TD (2002) Selenium stable isotope ratios in California agricultural drainage water management system. *Journal of Environmental Quality*, **31**, 1146-1156.
- Johnson TM (2004) A review of mass-dependent fractionation of selenium isotopes and implications for other heavy stable isotopes. *Chemical Geology*, **204**, 201-214.
- Johnson TM, Bullen T (2004) Mass-dependent fractionation of selenium and chromium isotopes in low-temperature environments. *Reviews in Mineralogy and Geochemistry*, **55**, 289-317.
- Johnson TM, Bullen T, Zawislanski PT (2000) Selenium stable isotope ratios as indicators of sources and cycling of selenium: results from the northern reach of san francisco. *Environmental Science and Technology*, **34**, 2075-2079.
- Kulp TR, Pratt LM (2004) Speciation and weathering of selenium in Upper Cretaceous chalk and shale from South Dakota and Wyoming, USA. *Geochimica et Cosmochimica Acta*, **68**, 3687-3701.
- Layton-Matthews D, Leybourne MI, Peter JM, Scott SD (2006) Determination of selenium isotopic ratios by continuous-hydride-generation dynamic-reaction-cell inductively coupled plasma-mass spectrometry. *Journal of Analytical Atomic Spectrometry*, **21**, 41-49.
- Lee J-Y, Marti K, Severinghaus JP, Kawamura K, Yoo H-S, Lee JB, Kim JS (2006) A redetermination of the isotopic abundances of atmospheric Ar. *Geochimica et Cosmochimica Acta*, **70**, 4507-4512.
- Li Y-H, Schoonmaker JE (2004) Chemical composition and mineralogy of marine sediments. In: *Sediments, Diagenesis, and Sedimentary Rocks* (eds Holland HD, Turekian KK). Elsevier-Pergamon, Oxford, UK.
- Mason TFD, Weiss DJ, Horstwood M, Parrish RR, Russell SS, Mullane E, Coles BJ (2004) High-precision Cu and Zn isotope analysis by plasma source mass spectrometry: Part 2. Correcting for mass discrimination effects. *Journal of Analytical Atomic Spectrometry*, **19**, 218-226.
- Mitchell K, Mason PRD, Van Cappellen P, Johnson TM, Gill BC, Owens JD, Ingall ED, Reichart G-J, Lyons TW (2012) Selenium as paleo-oceanographic proxy: A first assessment. *Geochimica et Cosmochimica Acta*, **89**, 302-317.

- Mortlock RA, Frohlich PN (1987) Continental weathering of germanium: Ge/Si in the global river discharge. *Geochimica et Cosmochimica Acta*, **51**, 2075-2082.
- Rouxel O, Fouquet Y, Ludden JN (2004) Subsurface processes at the Lucky Strike hydrothermal field, Mid-Atlantic Ridge: evidence from sulfur, selenium, and iron isotopes. *Geochimica et Cosmochimica Acta*, **68**, 2295-2311.
- Rouxel O, Ludden J, Carignan J, Marin L, Fouquet Y (2002) Natural variations of Se isotopic composition determined by hydride generation multiple collector inductively coupled plasma mass spectrometry. *Geochimica et Cosmochimica Acta*, **66**, 3191-3199.
- Russell WA, Papanastassiou DA, Tombrello TA (1978) Ca isotope fractionation on the Earth and other solar system materials. *Geochimica et Cosmochimica Acta*, **42**, 1075-1090.
- Savard D, Bedard LP, Barnes S-J (2006) TCF selenium preconcentration in geological materials for determination at sub-ug g⁻¹ with INAA (Se/TCF-INAA). *Talanta*, **70**, 566-571.
- Savard D, Bedard LP, Barnes S-J (2009) Selenium concentrations in twenty-six geological reference materials: New determinations and proposed values. *Geostandards and Geoanalytical Research*, **33**, 249-259.
- Schilling K, Johnson TM, Wilcke W (2011a) Isotope fractionation of selenium during fungal biomethylation by *Alternaria alternata*. *Environmental Science and Technology*, **45**, 2670-2676.
- Schilling K, Johnson TM, Wilcke W (2011b) Selenium partitioning and stable isotope ratios in urban topsoil. *Soil Science Society of America Journal*, **75**, 1354-1364.
- Schilling K, Wilcke W (2011) A method to quantitatively trap volatilized organoselenides for stable selenium isotope analysis. *Journal of Environmental Quality*, **40**, 1021-1027.
- Shore AJT (2010) Selenium geochemistry and isotopic composition of sediments from the Cariaco Basin and the Bermuda Rise: a comparison between a restricted basin and the open ocean over the last 500 ka. In: *Department of Geology*. University of Leicester, Leicester, pp. 307.
- Stüeken EE (2013) A test of the nitrogen-limitation hypothesis for retarded eukaryote radiation: Nitrogen isotopes across a Mesoproterozoic basinal profile. *Geochimica et Cosmochimica Acta*, **120**, 121-139.
- Sweeney JJ, Burnham AK, Braun RL (1987) A model of hydrocarbon generation from type I. kerogen: Application to Uinta Basin, Utah. *AAPG Bulletin*, **71**, 967-985.
- Wen H, Carignan J (2011) Selenium isotopes trace the source and redox processes in the black shale-hosted Se-rich deposits in China. *Geochimica et Cosmochimica Acta*, **75**, 1411-1427.
- Wen H, Carignan J, Hu RZ, Fan HF, Chang B, Yang GS (2007) Large selenium isotopic variations and its implications in the Yutangba Se deposit, Hubei Province, China. *Chinese Science Bulletin*, **52**, 2443-2447.
- Yu M, Sun D, Tian W, Wang G, Shen W, Xu N (2002) Systematic studies on adsorption of trace elements Pt, Pd, Au, Se, Te, As, Hg, Sb on thiol cotton fiber. *Analytica Chimica Acta*, **456**, 147-155.
- Yu M, Tian W, Sun D, Shen W, Wang G, Xu N (2001) Systematic studies on adsorption of 11 trace heavy metals on thiol cotton fiber. *Analytica Chimica Acta*, **428**, 209-218.
- Zhu J-M, Johnson TM, Clark SK, Zhu X-K (2008) High precision measurement of selenium isotopic composition by hydride generation multiple collector inductively coupled plasma mass spectrometry with a ⁷⁴Se-⁷⁷Se double spike. *Chinese Journal of Analytical Chemistry*, **36**, 1385-1390.

Chapter 5: Selenium in the latest Archean: a longer whiff but no MIF

Abstract

Selenium undergoes redox transformations and isotopic fractionations at relatively high redox potentials and could therefore provide additional insight into changes in oceanic and atmospheric O₂ levels over Earth's history. Furthermore, by analogy to S, it is conceivable that Se isotopes express mass-independent fractionation (MIF) and may thus provide additional insights into atmospheric oxygenation. We test these ideas with Se data from the 2.5 Gyr Mt. McRae Shale, which records some of the highest MIF in S isotopes, followed by evidence for a 'whiff of oxygen' in the Earth's atmosphere. We observe a significant positive excursion in Se concentrations and isotopic ratios, overlapping but not quite coincident with excursions in Mo and N isotopes and abundances. All Se isotope fractionations are mass-dependent within error. Together, these data discount the possibility of a later metasomatic alteration of the Mt. McRae Shale, strengthen the inference of a temporary spike in atmospheric O₂, and suggest that this whiff may have been more prolonged than previously thought. This is the first report of a Se isotope excursion in the Precambrian rock record and it verifies that Se isotopes can serve as a powerful redox proxy in deep time.

5.1. Introduction

The rise of atmospheric oxygen had profound effects on the evolution of life and biogeochemical cycles, because it provided new sources of metabolic energy and mobilized important nutrients by oxidative weathering. It is now clear that the atmosphere became oxygenated long before the deep ocean, but the timing, magnitude, and extent of the first

appearance of free O₂ remain subjects of debate (Lyons *et al.*, 2014). The distinctive redox properties of Se and its isotopes may help resolve these uncertainties. First, the oxyanions biselenite, selenite (both Se^{IV}) and selenate (Se^{VI}) are soluble only under suboxic to oxic conditions, at a higher Eh than is the case for sulfate (Fig. 5.1) (Johnson, 2004). Evidence of Se mobility in surface environments should therefore indicate a relatively high oxidation state. Second, reaction with O₂ is the most plausible way to generate significant Se^{IV} and Se^{VI}, because, unlike S or Fe, no photosynthetic metabolism is known that can directly oxidize reduced Se phases (Se⁰ or Se^{-II} in sulfides). Further, while NO₃⁻ or MnO₂ are theoretically strong enough oxidizers to form Se oxyanions, it is hard to construct a credible scenario whereby they themselves are produced in significant quantities without free O₂. Se may thus be a more direct proxy for increasing atmospheric oxygen levels. Third, the six stable isotopes of Se are fractionated by several permil during oxyanion reduction under suboxic conditions (Fig. 5.1) (Johnson, 2004), concurrently with denitrification (Oremland, 1990). Se isotopes should therefore have been particularly sensitive to the extent of suboxia along Precambrian continental margins. Lastly, Se gases such as H₂Se or biogenic methyl-selenides (Wen & Carignan, 2007) should have been longer lived in the anoxic Archean atmosphere, which raises the possibility that Se isotopes in the sedimentary record might show the photochemical imprint of mass-independent fractionation (MIF-Se), comparable to MIF-S (Farquhar *et al.*, 2000).

We test these hypotheses with samples from the Mt. McRae Shale, an outer shelf deposit from the Archean-Proterozoic boundary. This formation records some of the highest MIF-S values (Kaufman *et al.*, 2007), followed by the first marked increase in Mo concentrations, indicating a pulse of oxidative weathering of terrestrial sulfide minerals (Anbar *et al.*, 2007). Deeper marine waters on the outer shelf continued to be anoxic during this interval (Reinhard *et*

al., 2009), leading to nearly quantitative Mo sequestration (Anbar *et al.*, 2007). This pattern is consistent with a ‘whiff of oxygen’ in the atmosphere and a strong redox gradient from terrestrial to deep marine environments. However, existing data are relatively insensitive to the extent of suboxia between the two redox end-members, and they cannot unambiguously rule out the possibility that oxidation was driven by electron acceptors other than O₂. Here we use Se isotope and abundance data to further substantiate that conclusion and to test for MIF-Se in the late Archean

5.2. Materials and methods

The Mt. McRae Shale (2.5 Gyr) was deposited along the southern margin of the Pilbara craton, Western Australia (Blake & Barley, 1992), in a deep subtidal environment, possibly by hemipelagic sedimentation (Krapez *et al.*, 2003). We obtained 41 fresh samples from a 100m section of the ABDP-9 drill core (Fig. 5.2) that has previously been analyzed for S, Fe, C, N, and some trace metals (Anbar *et al.*, 2007; Kaufman *et al.*, 2007; Garvin *et al.*, 2009; Reinhard *et al.*, 2009; Duan *et al.*, 2010; Kendall *et al.*, 2013). In addition, we analyzed a 16cm section of the core (124.06-123.91m) at ~1cm resolution to constrain background variability of Se at short timescales during an environmentally stable interval. Methods for sample preparation and analysis are summarized in the appendix and described in detail by Stüeken *et al.* (2013). In brief, rock powders were dissolved in HF, HNO₃ and HClO₄, Se was extracted with a thiol-cotton fiber column, and analyses were carried out with a hydride-generator multi-collector inductively-coupled plasma mass-spectrometer. Measurements were normalized by standard-sample bracketing. Unless otherwise noted, results are expressed in delta notation as $\delta^{82/78}\text{Se}$ relative to NIST SRM 3149. As for other trace elements (e.g. Anbar *et al.*, 2007), Se mobility

was estimated from total Se concentrations normalized to crustal background, expressed as enrichment factors EF (Appendix A5.4).

5.3. Results

Se EF show three distinct stages (Fig. 5.2). Below 150m, they are relatively low (mean 19 ± 17), but display a spike up to 60 at 169.47m, coincident with the largest $\Delta^{33}\text{S}$ values in the section. Between 150 m and 133 m, enrichments are consistently above 30 (max. 208, mean 68 ± 49), concurrent with marked enrichments in Mo ($R^2 = 0.46$), total organic carbon ($R^2 = 0.39$), and a minor enrichment in S concentrations ($R^2 = 0.20$). In the upper part of the section, Se EF return to low values (mean 12 ± 6).

Se isotopes show considerable variability over the entire 100 meters (-0.2‰ to $+1.4\text{‰}$, mean $+0.5 \pm 0.4\text{‰}$ (1σ)). The maximum $\delta^{82/78}\text{Se}$ value coincides with the highest Se concentration, but the two parameters are not correlated ($R^2 = 0.26$ for all samples, or 0.06 without the most Se-rich sample). When the isotopic data are binned using the same subdivisions as for Se enrichments, they show an increase from $+0.4 \pm 0.3\text{‰}$ (190-150 m) to $+0.9 \pm 0.4\text{‰}$ (150-133m), followed by a decline back to $+0.3 \pm 0.4\text{‰}$ (133-100m). Both changes are statistically significant ($p_{\text{one-tailed}} < 10^{-3}$ for both), whereas the two intervals before and after the excursion are statistically indistinguishable ($p_{\text{one-tailed}} = 0.21$). However, the isotopic excursion ends slightly earlier than the abundance excursion (Fig. 5.2). Overall, this excursion pattern is comparable to the $\delta^{98/95}\text{Mo}$ record (Fig. 5.2). In the high-resolution section from 124.06-123.91 m, $\delta^{82/78}\text{Se}$ values are comparatively stable (-0.3‰ to $+0.1\text{‰}$), despite a 34-fold increase in total S content across a pyrite lamina at 123.99m (Fig. 5.2, Table A5.2).

Three-isotope diagrams (Fig. 5.3) show that no samples significantly deviate from the mass-dependant fractionation line for any of the isotopes compared. Thus, there is no evidence for MIF-Se in this sample set.

5.4. Discussion

5.4.1. Evidence against a metasomatic alteration

The regional metamorphic grade of these rocks is very low (prehnite-pumpellyite facies, <300°C, Smith *et al.*, 1982), but it has been argued that they were locally altered around bedding-parallel chlorite veins by metasomatic fluids at temperatures up to 450°C (Kirschvink *et al.*, 2012; Fischer *et al.*, 2014) and thus that the elemental and isotopic excursions are secondary. However, like previous authors (Anbar *et al.*, 2007; Kendall *et al.*, 2013), we conclude that metasomatic overprinting cannot explain the geochemical excursions. First, the Se and Mo isotopic excursions end earlier than the longer tails in Se and Mo abundances (Fig. 5.2). The various excursions generally decay at differing rates upwards and aren't symmetrical around their peaks, unlike the pattern expected of alteration around a later concordant vein or vein set. To produce this metasomatically would require multiple pulses of fluids from discrete sources with distinct compositions infiltrating at different stratigraphic levels, which is not likely. Second, the positive excursion in $\delta^{15}\text{N}$, indicative of aerobic conditions in surface waters, peaks well above the metal enrichments, inconsistent with metasomatism emanating from a fracture many meters below. Third, it is very difficult to conceive of metasomatic processes that would reset the Se, N and Mo isotopic systems but not S and Os isotopes across such a short stratigraphic interval (Kendall *et al.*, 2013). If these metasomatic fluids also introduced kerogen (to explain the spike in TOC during the excursion interval), then C/N ratios and $\delta^{13}\text{C}_{\text{org}}$ values should also have been perturbed (Fig. A5.2). Lastly,

chlorite veins are present in samples at the base of the section and at the very top of the Se excursion (Fig. A5.4), but are not observed in our most Se-rich sample, indicating that there is no relationship between the intensity of metasomatic veining and excursions in redox-sensitive elements and their isotopes. Thus, the excursions appear to be primary and indigenous, not secondary and metasomatic as proposed by Kirschvink and colleagues (2012).

5.4.2. Se weathering with free O₂

Sedimentary Se can be derived from three sources, including hydrothermal fluids, volcanic ejecta, and crustal weathering. A sudden spike in Se enrichment factor to ~60 around 169.5 m coincident with high $\Delta^{33}\text{S}$ suggests that the volcanic flux was non-trivial at this time, if MIF-S was produced in reactions involving volcanogenic SO₂ (Farquhar *et al.*, 2000). However, the major Se enrichment in the middle section is associated with low $\Delta^{33}\text{S}$, making a volcanogenic source of Se for this part of the section improbable. Furthermore, this mechanism cannot explain the coincident enrichment in Mo and Re, and the correlation between these three element's abundances suggests that they were introduced by the same process.

A hydrothermal source for either Se or Mo can be discounted because Fe and Mn, which are typically associated with hydrothermal deposits, are relatively scarce in this interval (Anbar *et al.*, 2007). This leaves as the remaining hypothesis that the Se and Mo excess in the 150-130m interval was caused by a pulse in continental oxidative weathering (Anbar *et al.*, 2007), possibly enhanced by microbial activity (Stüeken *et al.*, 2012).

We cannot rule out that volcanism was responsible for the persistent enrichments above crustal background before and after the whiff. However, we note that also Mo is slightly enriched and N isotopes are somewhat elevated throughout the section (Fig 5.2), consistent with

a low but non-zero extent of oxidative weathering throughout the late Archean (Stüeken *et al.*, 2012). Furthermore, unlike Mo, Se does not require euxinia to be scavenged from the water column, because it can be reduced to Se^0 or incorporated into organic matter, as indicated by its nutrient-type profile in the modern ocean (Cutter & Cutter, 2001). The predominance of ferruginous rather than euxinic conditions before and after the whiff (Reinhard *et al.*, 2009) could thus explain why Se is generally more enriched than Mo during those intervals. Given the high redox potential of Se oxyanions (Fig. 5.1), it is conceivable that very low levels of O_2 in the weathering environment would only produce Se^0 , which can be transported to the ocean as suspended particulates (Doblin *et al.*, 2006). However, redox reactions involving Se^0 do not impart isotopic fractionations (Johnson, 2004). The isotopic variability in the Mt. McRae Shale therefore indicates that Se was oxidized to either Se^{IV} or Se^{VI} prior to reductive fractionation. This interpretation is supported by N isotope evidence for the presence of nitrate in surface waters at this time (Garvin *et al.*, 2009), because nitrate is stable at similar Eh-pH conditions to Se^{VI} (Brookins, 1988).

Though sulfide can be oxidized by anoxygenic photosynthetic microbes, this metabolism is so far unknown for Se, making it unlikely as the source for Se oxyanions. Alternatively, Se could have been oxidized by NO_3^- and MnO_2 , but these would themselves most plausibly require free O_2 for their own formation. Our Se data thus strengthen the conclusion of a brief but substantial rise in O_2 (Anbar *et al.*, 2007).

5.4.3. Mass-dependent isotope fractionation under suboxia

The strictly mass-dependent behavior of Se isotopes in this study (Fig. 5.3), even during the interval of highest MIF-S, suggests that photochemical reactions involving Se gases were

insignificant. MIF-S occurs during photolysis of SO₂ but is unlikely for the much less volatile SeO₂. Organic Se gases and H₂Se are suitably volatile (Wen & Carignan, 2007), but their production in the late Archean may have been too small. Alternatively, relevant photons may have been absorbed by other atmospheric constituents, or Se gases may simply not acquire MIF during photochemistry.

The mass-dependent fractionations in the Mt. McRae Shale exceed the range seen in meteorites ($\delta^{82/78}\text{Se} = -0.2\text{‰}$ to $+0.6\text{‰}$, average $+0.1 \pm 0.3\text{‰}$) and Phanerozoic upper crust (-0.3‰ to $+0.6\text{‰}$, average $0.0 \pm 0.5\text{‰}$) (Rouxel *et al.*, 2002) and therefore cannot be explained by changes in crustal source rock alone. It is also unlikely that the fractionation occurred during weathering, because Se isotopes are not fractionated during oxidation (Johnson, 2004). Furthermore, weathering fractionation should result in a consistent unidirectional shift of all isotopic values relative to average crust, which is not observed. Lastly, the low variability in the high-resolution section suggests that isotopic differences are not simply the result of varying pyrite content. It is thus most likely that the isotopic fractionation, in particular the positive excursion during the O₂ whiff, was caused by an aqueous process that operated at a site between weathering and deposition.

The isotopic stability at high stratigraphic resolution further indicates that fractionation resulted from a significant environmental perturbation rather than the random minor fluctuations inherent to stable natural systems. During the whiff, this fractionating process must have preferentially removed isotopically light Se from the water column, such that only the residual heavy phase remained to be sequestered on the outer shelf. A similar model with onshore fractionation and offshore sequestration has been proposed for the Mo isotope record (Duan *et al.*, 2010). In the Mo system, the isotopically fractionating reaction is thought to have been

adsorption of molybdate to Mn-oxides forming in coastal waters. Likewise, Se^{IV} can adsorb to Fe-Mn-oxides (Balistreri & Chao, 1990), but the isotopic effect of 0.6 ‰ is too small to explain the observed $\delta^{82/78}\text{Se}$ values of up to +1.4 ‰ (Johnson, 2004). Similarly, the small isotopic effect of Se assimilation into biomass (0.6‰) (Clark & Johnson, 2010) implies that a large amount of organic Se would have had to be removed from the system for the residue to become as heavy as +1.4 ‰. Some degree of Se assimilation likely occurred in all settings, muting the size of the excursion. However, the very high Se concentrations in the 150-130m interval suggest that a large fraction of the fluvial Se flux reached the outer shelf and only a small amount was removed during transport.

The most likely explanation for the isotopic enrichment in the sampled offshore sediments is thus partial reduction of Se oxyanions under suboxic conditions further onshore (Fig. 5.4). Both biotic and abiotic processes are conceivable. The main mechanism of Se draw-down in the euxinic waters offshore was probably assimilation into biomass, indicated by correlated $\delta^{82/78}\text{Se}$ and TOC ($R^2 = 0.54$) and comparable to Phanerozoic anoxic basins (Cutter, 1982; Mitchell *et al.*, 2012). Combined with the N isotope record, which shows a positive excursion somewhat later than the metal enrichment peaks (Garvin *et al.*, 2009), our data further suggest that the establishment of euxinia during the O_2 whiff was succeeded by an expansion of suboxic conditions to the outer shelf rather than a direct return to ferruginous anoxia. Lower $\delta^{15}\text{N}$ values during the start of the whiff indicate that N_2 -fixation was still the major N source, whereas the later positive excursion shows that nitrate became stable after the euxinic period. The same could have been true for Se^{VI} given its similar redox potential. The moderately high Se EF and fairly low to slightly negative $\delta^{82/78}\text{Se}$ values after the positive $\delta^{82/78}\text{Se}$ excursion coincide with

high $\delta^{15}\text{N}$, which may be the result of non-quantitative Se oxyanion reduction on a suboxic outer shelf. If so, then the O_2 whiff may have been more prolonged than previously thought.

5.5. Conclusion

We present the first report of a Se isotopic excursion in the Precambrian rock record. It occurs over a short stratigraphic interval near the Archean-Proterozoic boundary, showing that Se has the potential to record information about biogeochemical processes in deep time. Combined with other geochemical proxies, it further strengthens the idea that oxygen was produced in surface environments long before the Great Oxidation Event.

Acknowledgements

This work was funded by NSF grant EAR 0921580 to RB. We thank the UW Isotope Geochemistry Lab for technical support.

Figures

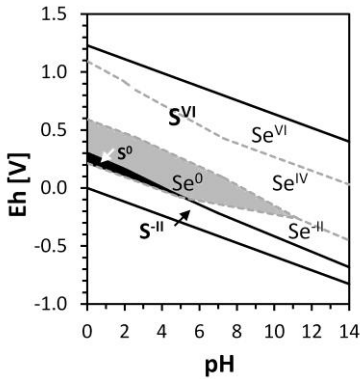


Figure 5.1: Eh-pH diagram. Gray dashed lines mark boundaries for Se (assuming $[Se] = 10^{-10}M$), black solid lines mark boundaries for S (assuming $[S] = 10^{-3}M$).

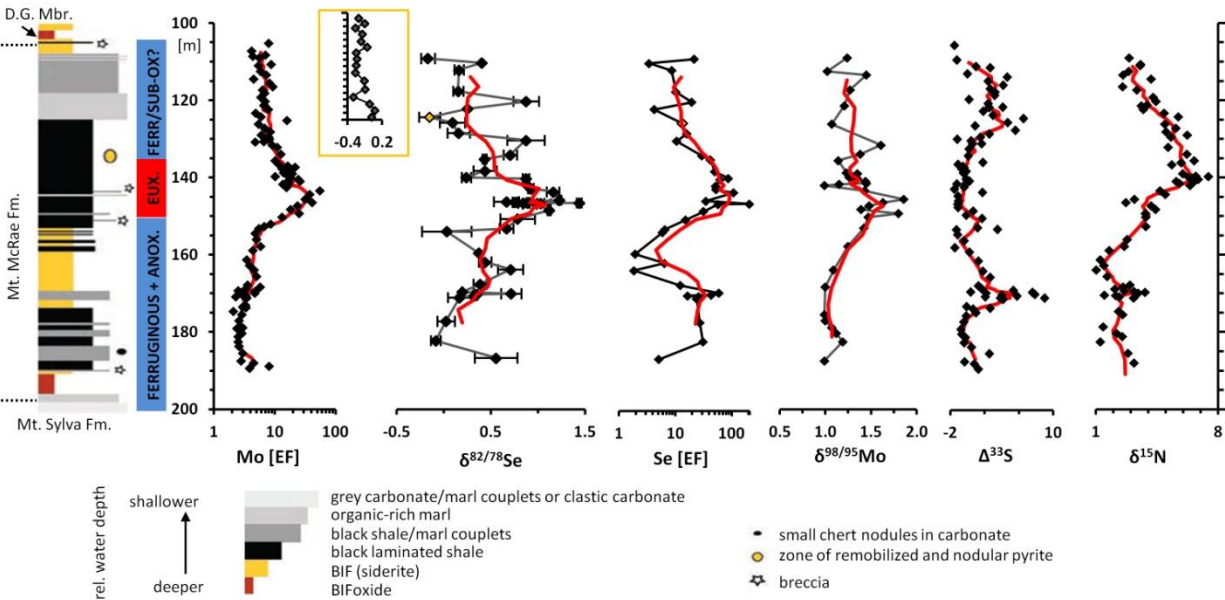


Figure 5.2: Stratigraphic section of ABDP-9. Se data are plotted as averages $\pm 1\sigma$. EF = enrichment factor in log scale. Red line = 5-point running mean. Insert shows $\delta^{82/78}Se$ at high resolution over 16cm from 124.06-123.91m (y-axis tick marks at 1cm-spacing, average = orange data point). Water-column redox state inferred from iron speciation is indicated on the left, where blue = ferruginous, red = euxinic.

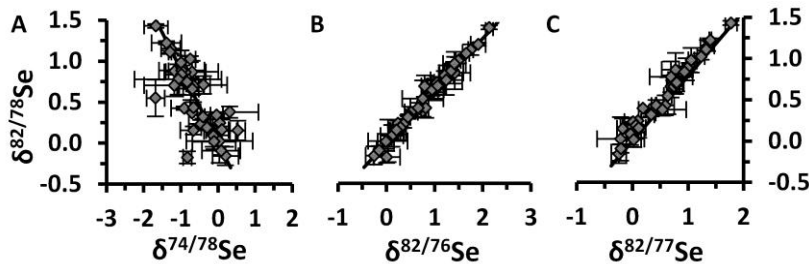


Figure 5.3: Three-isotope diagrams. Symbols mark average values in permil $\pm 1\sigma$. Solid black line = theoretical mass-dependent fractionation.

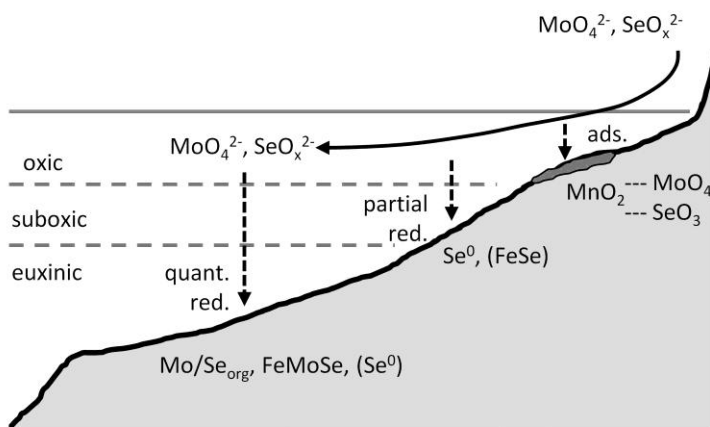


Figure 5.4: Proposed selenium cycle. Oxidative weathering produces molybdate (MoO_4^{2-}) and selenate (SeO_4^{2-}) or selenite (SeO_3^{2-}), here denoted SeO_x^{2-} . Adsorbed Se in nearshore sediments will experience slight negative isotopic fractionation. Farther offshore, in suboxic conditions, partial reduction of Se oxyanions to pyrite-bound selenide (FeSe or $\text{Se}^{-\text{II}}$) or elemental Se (Se^0) in sediments should induce negative isotopic fractionation in the sedimentary phases. In euxinic waters, selenium will be captured by sulfides during quantitative reduction (denoted “quant. red.”) as well as by organic selenide (Se_{org}). Euxinic sediments should thus record the isotopic composition of seawater Se oxyanions.

References

- Anbar AD, Duan Y, Lyons TW, Arnold GL, Kendall B, Creaser RA, Kaufmann AJ, Gordon GW, Scott C, Garvin J, Buick R (2007) A whiff of oxygen before the Great Oxidation Event? *Science*, **317**, 1903-1906.
- Balistrieri LS, Chao TT (1990) Adsorption of selenium by amorphous iron oxyhydroxide and manganese dioxide. *Geochimica et Cosmochimica Acta*, **54**, 739-751.
- Blake TS, Barley ME (1992) Tectonic evolution of the late Archean to early Proterozoic Mount Bruce Megasequence set, Western Australia. *Tectonics*, **11**, 1415-1425.
- Brookins DG (1988) *Eh-pH Diagrams for Geochemistry*, Springer-Verlag, New York.
- Clark SK, Johnson TM (2010) Selenium stable isotope investigation into selenium biogeochemical cycling in a lacustrine environment: Sweitzer Lake, Colorado. *Journal of Environmental Quality*, **39**, 2200-2210.
- Cutter GA (1982) Selenium in reducing waters. *Science*, **217**, 829-831.
- Cutter GA, Cutter LS (2001) Sources and cycling of selenium in the western and equatorial Atlantic Ocean. *Deep-Sea Research II*, **48**, 2917-2931.
- Doblin MA, Baines SB, Cutter LS, Cutter GA (2006) Sources and biogeochemical cycling of particulate selenium in the San Francisco Bay estuary. *Estuarine, Coastal and Shelf Science*, **67**, 681-694.
- Duan Y, Anbar AD, Arnold GL, Lyons TW, Gordon GW, Kendall B (2010) Molybdenum isotope evidence for mild environmental oxygenation before the Great Oxidation Event. *Geochimica et Cosmochimica Acta*, **74**, 6655-6668.
- Farquhar J, Bao H, Thiemens M (2000) Atmospheric influence on Earth's earliest sulfur cycle. *Science*, **289**, 756-758.
- Fischer WW, Slotznick S, Johnson JE, Webb SM, Rasmussen B, Raub TD, Kirschvink JL (2014) Archean 'whiffs of oxygen' tied to post-depositional processes. In: *Goldschmidt Conference Abstracts # 3504*, Sacramento, USA.
- Garvin J, Buick R, Anbar AD, Arnold GL, Kaufman AJ (2009) Isotopic evidence for an aerobic nitrogen cycle in the latest Archean. *Science*, **323**, 1045-1048.
- Johnson TM (2004) A review of mass-dependent fractionation of selenium isotopes and implications for other heavy stable isotopes. *Chemical Geology*, **204**, 201-214.
- Kaufman AJ, Johnston DT, Farquhar J, Masterson AL, Lyons TW, Bates S, Anbar AD, Arnold GL, Garvin J, Buick R (2007) Late Archean biospheric oxygenation and atmospheric evolution. *Science*, **317**, 1900-1903.
- Kendall B, Brennecke GA, Weyer S, Anbar AD (2013) Uranium isotope fractionation suggests oxidative uranium mobilization at 2.50 Ga. *Chemical Geology*, **362**, 105-114.
- Kirschvink JL, Raub TD, Fischer W (2012) Archean "whiffs of oxygen" go poof! In: *Goldschmidt Conference Abstracts*, Montreal, Quebec, Canada, pp. 1943.
- Krapez B, Barley ME, Pickard AL (2003) Hydrothermal and resedimented origins of the precursor sediments to banded iron formation: sedimentological evidence from the early Palaeoproterozoic Brockman Supersequence of Western Australia. *Sedimentology*, **50**, 979-1011.
- Lyons TW, Reinhard CT, Planavsky NJ (2014) The rise of oxygen in Earth's early ocean and atmosphere. *Nature*, **506**, 307-315.

- Mitchell K, Mason PRD, Van Cappellen P, Johnson TM, Gill BC, Owens JD, Ingall ED, Reichart G-J, Lyons TW (2012) Selenium as paleo-oceanographic proxy: A first assessment. *Geochimica et Cosmochimica Acta*, **89**, 302-317.
- Oremland RS (1990) Measurement of in situ rates of selenate removal by dissimilatory bacterial reduction in sediments. *Environmental Science and Technology*, **24**, 1157-1164.
- Reinhard CT, Raiswell R, Scott C, Anbar AD, Lyons TW (2009) A late Archean sulfidic sea stimulated by early oxidative weathering of the continents. *Science*, **326**, 713-716.
- Rouxel O, Ludden J, Carignan J, Marin L, Fouquet Y (2002) Natural variations of Se isotopic composition determined by hydride generation multiple collector inductively coupled plasma mass spectrometry. *Geochimica et Cosmochimica Acta*, **66**, 3191-3199.
- Smith R, Perdrix JL, Parks TC (1982) Burial metamorphism in the Hamersley basin, western Australia. *Journal of Petrology*, **23**, 75-102.
- Stüeken EE, Catling DC, Buick R (2012) Contributions to late Archaean sulphur cycling by life on land. *Nature Geoscience*, **5**, 722-725.
- Stüeken EE, Foriel J, Nelson BK, Buick R, Catling DC (2013) Selenium isotope analysis of organic-rich shales: advances in sample preparation and isobaric interference correction. *Journal of Analytical Atomic Spectrometry*, **28**, 1734-1749.
- Wen H, Carignan J (2007) Reviews on atmospheric selenium: Emissions, speciation and fate. *Atmospheric Environment*, **41**, 7151-7165.

Appendix to Chapter 5

A5. 1. Sample preparation

Sample preparation and analytical protocols are described in more detail by Stüeken *et al.* (2013, method 'E' therein). One to two grams of rock powder were digested in 10 ml of each concentrated HF and HClO₄ and 8N HNO₃ at 130°C in a screw-top Teflon beaker for two days. Excess acid was partially evaporated and HClO₄ was refreshed for an additional 2-4 days. After evaporation to incipient dryness at 130°C, the sample was boiled with 10 ml of 6N HCl for 30 minutes, centrifuged for 20 minutes, diluted with 90 ml DI-H₂O and then passed through a thiol cotton fiber (TCF) column to separate the selenium from the sample matrix (Yu *et al.*, 2002). The column was then washed with 2 ml of 6N HCl and 2 ml of DI-H₂O. The air-dried TCF with adsorbed selenium was transferred into a 15 ml centrifuge tube and boiled with 0.2 ml of 16 N HNO₃ for 30 minutes. Then 3.3 ml of DI-H₂O were added, the tube was shaken vigorously, and solid fibers were separated from the solution by centrifugation for 20 minutes. The supernatant was decanted into an open Teflon beaker. Addition of 0.2 ml 16N HNO₃ + 3.3 ml DI-H₂O and centrifugation were repeated two more times. The final 10.5 ml of sample solution were evaporated in the Teflon beaker to 0.5 ml at 60°C, then 5 ml of aqua regia (HCl:HNO₃ = 3:1) were added and re-evaporated to 0.5 ml. After that, the sample was transferred together with 2 ml of 6N HCl into a screw-top Teflon beaker and boiled for 20 minutes. After cooling to room temperature, the sample was mixed with 17.5 ml DI-H₂O and contained in a PTFE bottle.

A5. 2. Isotopic analyses

Analyses were conducted with a Nu Instruments multi-collector inductively-coupled-plasma mass spectrometer, attached to a cold-vapor hydride generator (Cetac HGX-200). Samples were analyzed by standard-sample bracketing, where NIST SRM 3149 served as the bracketing standard (Rouxel *et al.*, 2002; Layton-Matthews *et al.*, 2006). The known concentration of NIST SRM 3149 solutions was also used to calculate Se concentrations in the sample, assuming a linear relationship between concentration and measured voltage. Results are reported in delta notation in terms of $\delta^{82/78}\text{Se}$, relative to NIST SRM 3149 (Carignan and Wen, 2007) as follows:

$$\delta^{82/78}\text{Se} = \left[\frac{(^{82}\text{Se}/^{78}\text{Se})_{\text{spl}}}{(^{82}\text{Se}/^{78}\text{Se})_{\text{std}}} - 1 \right] \cdot 1000$$

Selenium concentrations in standards and samples were matched to within 5 % to minimize isobaric interferences with ArCl, BrH and SeH. Interferences with ArAr, Kr, Ge and AsH were corrected post-analytically as described by Stüeken *et al.* (2013). Our final results plot along the theoretical mass dependent fractionation line in three-isotope diagrams (Figure 5.2 and A5.1). Analyses of ^{74}Se , the least abundant selenium isotope, are readily compromised by ^{74}Ge , the most abundant isotope of germanium, which explains the high degree of scatter in $\delta^{74/78}\text{Se}$. Analyses of ^{77}Se in sample 108.79 were not reproducible, which we attribute to the rare formation of $(\text{AsH}_2)^+$ in the plasma, because this sample had by far the highest As/Se ratio. Formation of $(\text{AsH}_2)^+$ probably also explains why many measurements have slightly lower $\delta^{82/77}\text{Se}$ values than predicted from mass-dependent fractionation from $\delta^{82/78}\text{Se}$. Given this possibility, and the fact that average $\delta^{82/77}\text{Se}$ values fall within error along the MDF line (Figure 5.3 in the main text), we conclude that MIF is absent in our data. (Note that we cannot constrain As concentrations with high accuracy, because our protocols are optimized for Se, but the As/Se

ratio in this sample was ~6 times higher than the average of all other samples prepared with the same protocol. Approximate As concentrations in Table A5.1 are calculated by calibration of As/Se ratios against rock standard SGR-1). Apart from these outliers, our data suggest natural mass-independent fractionation (*cf.* Farquhar *et al.*, 2000) is absent in the Mt. McRae shale and that isobaric interferences have been properly corrected.

A5.3. Data accuracy and precision

The USGS reference material SGR-1 prepared and analyzed with the same protocol yields an isotopic composition of $+0.05 \pm 0.18$ ‰ (1σ , $n = 9$) for $\delta^{82/78}\text{Se}$. This value falls in between the most recently published values of -0.13 ± 0.03 ‰ (Mitchell *et al.*, 2012) and $+0.13 \pm 0.06$ ‰ (Schilling *et al.*, 2011) and overlaps within error with previous estimates of $+0.35 \pm 0.24$ ‰ (Rouxel *et al.*, 2002) and $+0.40 \pm 0.21$ ‰ (Layton-Matthews *et al.*, 2006). Our measured Se concentration of 3.40 ± 0.06 ppm is within 97 % of the nominal value of 3.51 ± 0.26 ppm (Savard *et al.*, 2009). The analytical precision in $\delta^{82/78}\text{Se}$ for replicate analyses of the same solution is 0.08 ‰ on average. Replicate digestions, tested with one sample (119.94m) and an in-house standard from the same formation, have a precision of 0.09 ‰.

A5.4. Enrichment factors

To account for variations in mineralogy, we calculated selenium enrichment factors (EF), defined as $[\text{Se}/\text{Al}]_{\text{sample}}/[\text{Se}/\text{Al}]_{\text{crust}}$, where $[\text{Se}/\text{Al}]_{\text{crust}} = 0.017$ ppm/%. The average Al concentration of upper continental crust (8.04 wt. %) was taken from Taylor & McLennan (1995), but the selenium concentration (0.14 ppm) was taken from Li & Schoonmaker (2004) because the Se value reported by Taylor & McLennan (1995) is unrealistically high (50 ppm)

compared to more recent compilations of concentrations in various rock types (Rouxel *et al.*, 2002; Savard *et al.*, 2009).

A5.5. Distribution of chlorite veins

Kirschvink *et al.* (2012) and Fischer *et al.* (2014) proposed that the geochemical excursions observed in the middle part of the Mt. McRae Shale, previously attributed to the effects of a syn-sedimentary “whiff” of oxygen (Anbar *et al.*, 2007), were caused instead by post-depositional alteration by hot metasomatic fluids periodically injected into bedding-parallel fractures over an interval of about 1 billion years after sediment deposition. Chlorite-filled veins visible in the drill core were cited as evidence for this process. We examined hand samples and thin sections of a subset of our samples and found chlorite-filled veins at the base of the section (182.14m, Figure A5.2) and in one sample at the end of the whiff interval (134.94m), but not in samples that capture the most extreme trace-metal enrichments (146.34m, 140.04m, Figure A5.2). Hence we conclude that while metasomatic fluids did penetrate the rock, they appear to have been rare and relatively metal-poor and therefore cannot be responsible for the metal enrichments and isotopic excursions between 150 and 130m.

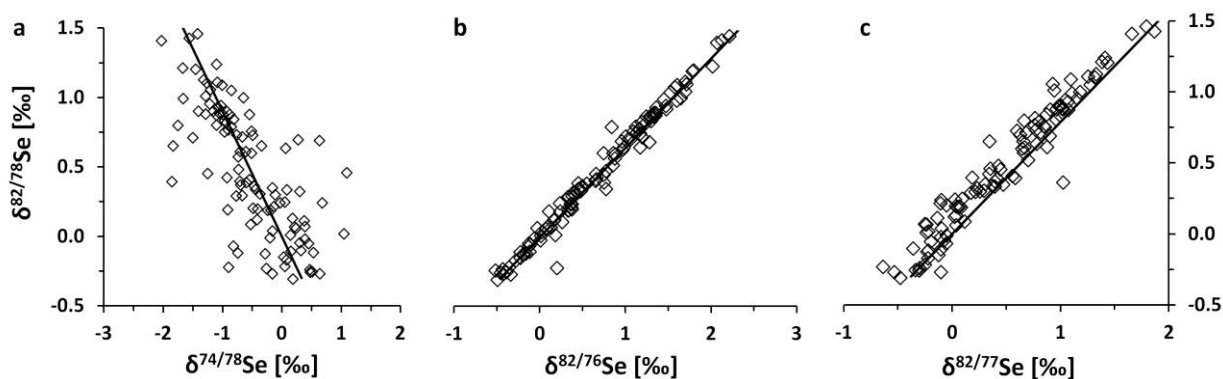


Figure A5.1: Three-isotope diagrams of individual analyses. As in Figure 5.2, solid lines mark theoretical mass-dependent fractionation.

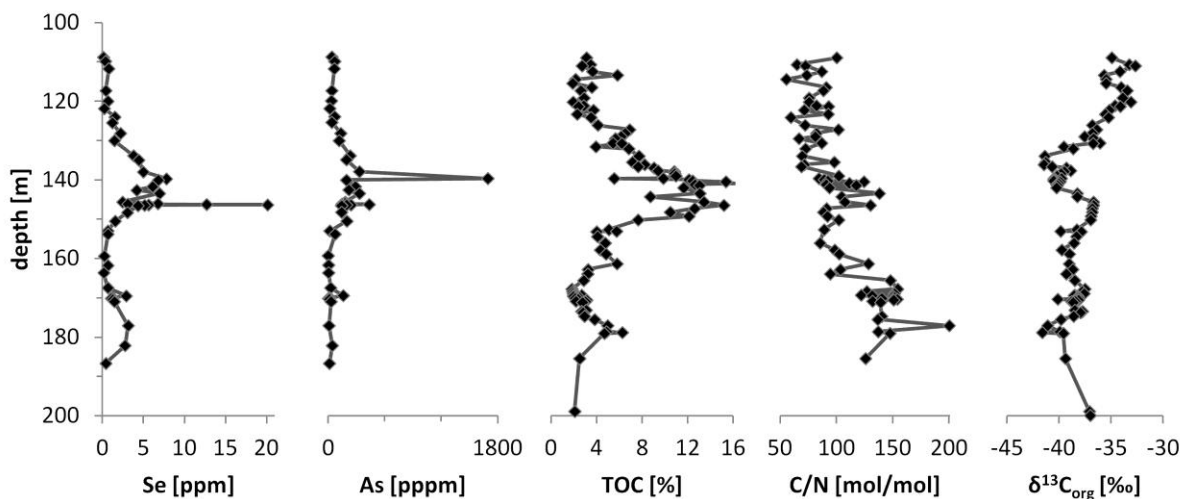


Figure A5.2: Elemental abundances and organic carbon isotopes. Showing no significant perturbation in $\delta^{13}\text{C}_{\text{org}}$ and C/N ratios correlating with the whiff interval despite large enrichments in TOC. Arsenic shows an enrichment pattern similar to Se, with no enrichment at 182.14m where chlorite veins are present (note that As concentrations are only approximate).

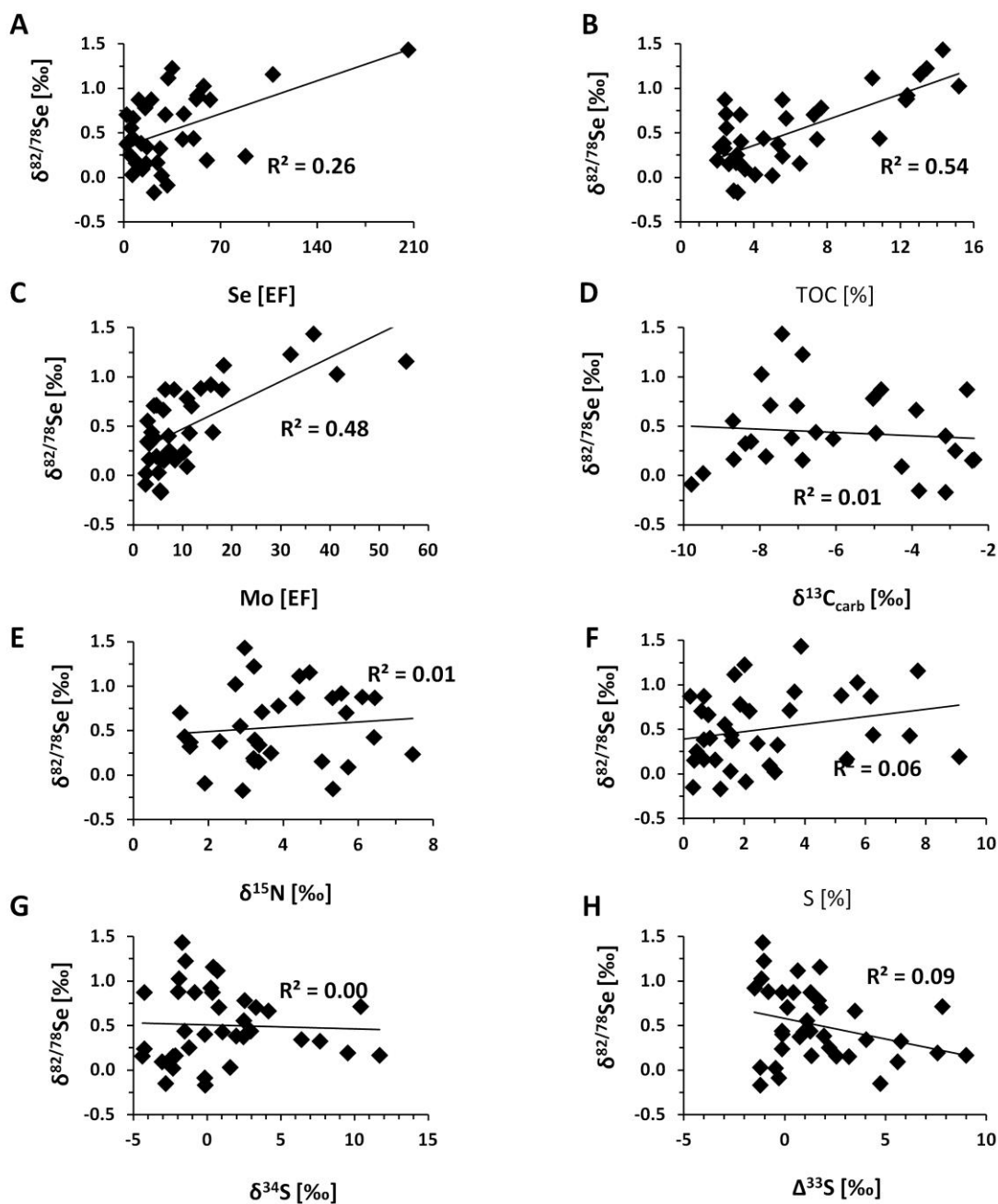


Figure A5.3: Correlations between Se isotopes and other geochemical parameters. The most significant correlation is observed between $\delta^{82/78}\text{Se}$ and TOC (panel B), which highlights the importance of productivity on the selenium cycle. Absence of correlations with $\delta^{34}\text{S}$ (panel G) and $\Delta^{33}\text{S}$ (panel H) show that selenium is not a geochemical twin of sulfur. The lack of correlation between lighter $\delta^{13}\text{C}_{\text{carb}}$ and $\delta^{82/78}\text{Se}$ (panel D) suggests that diagenetic overprinting had insignificant effects on selenium isotopes.

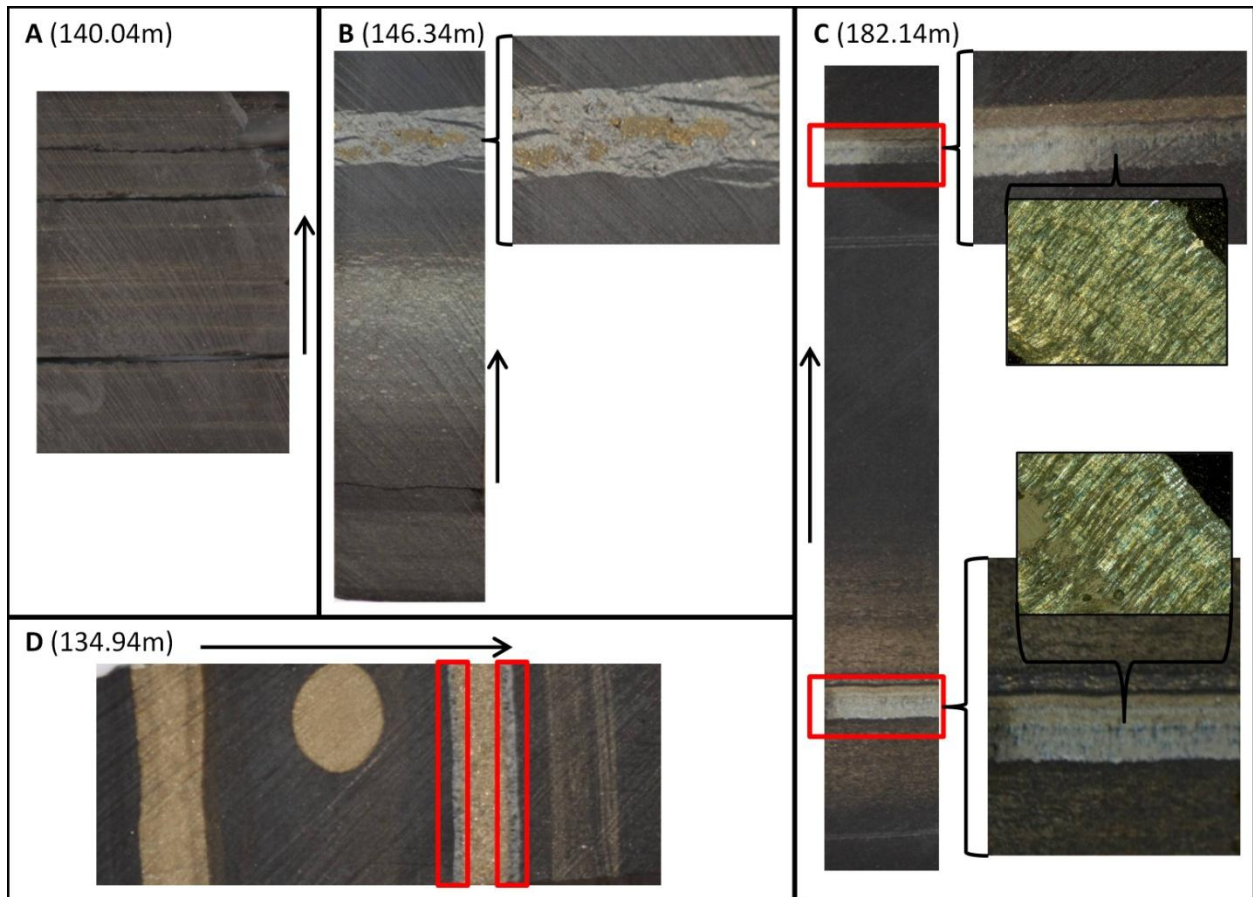


Figure A5.4: Photographs of selected samples analyzed in this study. A: sample 140.04m; typical representative of the whiff interval that is free of veins. B: sample 146.34m; marks the Se enrichment peak; contains a carbonate vein with pyrite (close-up), but not chlorite. C: sample 182.14m; well below the whiff interval; contains two chlorite veins (red boxes) shown in close-up and in photomicrographs under crossed polars highlighting fibrous texture. D: sample 134.94m; marks the end of the whiff; contains two thin fibrous chlorite veins (red boxes). Arrows mark stratigraphic 'up' direction and 1cm length.

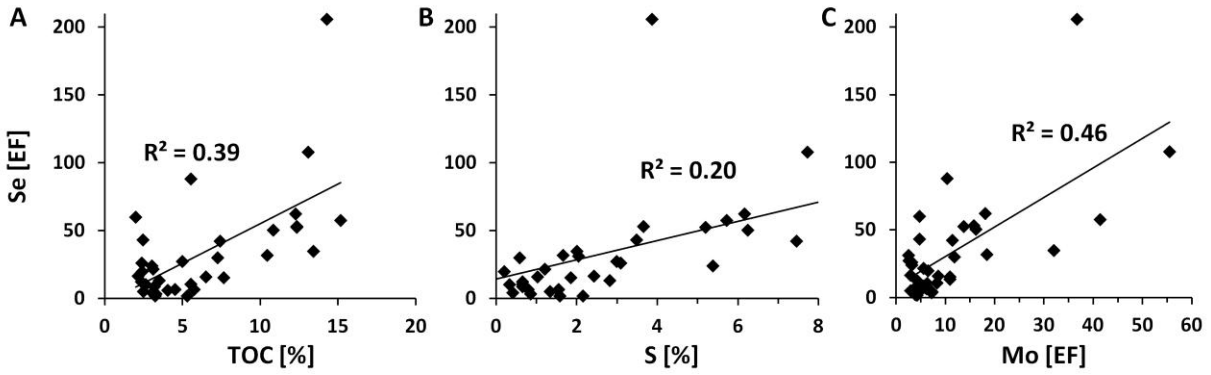


Figure A5.5: Correlations between Se enrichments and other elemental abundances. The slightly better correlation with TOC (panel A) compared to S (panel B) suggests that most Se is organic-bound rather than pyrite-hosted in these samples. The correlation with Mo (panel C) suggests that Se and Mo had similar depositional and diagenetic histories.

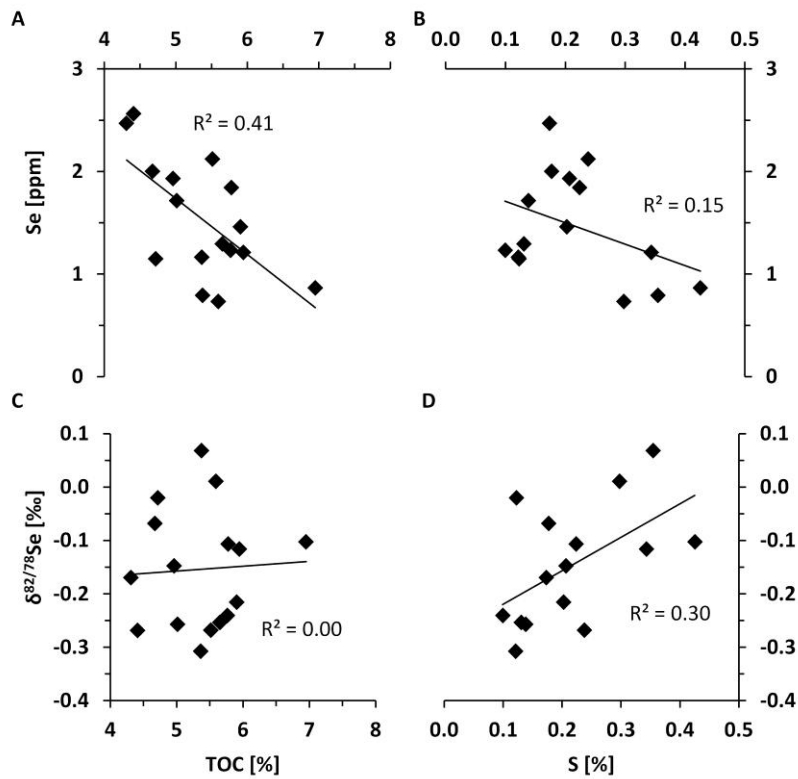


Figure A5.6: Correlations in high stratigraphic resolution samples. $n = 16$; samples extending to 8cm on either direction of 123.98m. In panels b and d, the data point with 7.4% sulfur ($\delta^{82/78}\text{Se} = -0.3$, $[\text{Se}] = 2.6\text{ppm}$) was excluded. Otherwise, $R^2_{\text{panel b}} = 0.21$ and $R^2_{\text{panel d}} = 0.06$.

Table A5.1: Data set. Aluminum data used to calculate enrichment factors (EF) are taken from Anbar *et al.* (2007). Where samples did not match, we used the Al percentage of the two nearest bracketing samples. n = number of replicate selenium measurements. Where enrichment factors are missing, Al data were not available. Sample 123.98 is the average of the 16 high-resolution analyses (Table A5.2). Note that As concentrations are not well calibrated and only serve as a rough guide.

sample [m]	n	Se [ppm]	σ [ppm]	Se [EF]	σ	$\delta 82/78\text{Se}$ [‰]	σ [‰]	$\delta 82/76\text{Se}$ [‰]	σ [‰]	$\delta 82/77\text{Se}$ [‰]	σ [‰]	$\delta 74/78\text{Se}$ [‰]	σ [‰]	As [ppm]	σ [ppm]
108.79	2	0.11	0.00	21.68	0.00	-0.17	0.07	0.00	0.28			-0.83	0.11	41.23	2.83
109.9	1	0.40	0.00	3.46	0.00	0.40		0.75		0.19		-0.71		70.56	3.56
111.76	2	0.79	0.00	8.69	0.00	0.16	0.05	0.25	0.12	0.05	0.03	-0.67	0.35	68.39	3.37
117.31	2	0.43	0.02	10.35	0.01	0.15	0.05	0.18	0.11	-0.04	0.13	0.06	0.44	40.01	0.98
119.94	6	0.69	0.02	19.78	0.01	0.87	0.14	1.39	0.20	0.96	0.12	-0.70	0.71	37.85	6.83
121.86	1	0.25		4.24		0.25		0.23		0.09		0.04		20.22	
123.98*	16	1.53	0.58			-0.15	0.11	-0.26	0.18	-0.25	0.14	0.20	0.35	72.63	45.85
125.45	3	1.22	0.08	13.36	0.02	0.09	0.13	0.11	0.23	-0.04	0.06	-0.14	0.09	39.26	2.69
128.17	2	2.20	0.01	15.99	0.00	0.16	0.12	0.24	0.16	-0.18	0.11	0.53	0.21	137.66	1.33
130.06	2	1.45	0.03	10.65	0.00	0.87	0.20	1.42	0.32	0.77	0.25	-0.89	0.56	118.57	2.89
133.85	2	3.81	0.04	29.94	0.01	0.70	0.07	1.07	0.13	0.76	0.14	-0.66	0.44	234.92	36.21
134.94	3	4.43	0.04	42.36	0.01	0.43	0.02	0.68	0.05	0.45	0.11	-0.91	0.35	197.51	30.84
137.96	2	4.99	0.22	50.28	0.04	0.44	0.12	0.81	0.06	0.59	0.16		1.85	335.75	23.01
139.71	2	7.81	0.11	87.98	0.02	0.24	0.05	0.35	0.02	0.01	0.15	-0.47	0.32	1695.37	13.27
140.04	3	6.82	0.09	62.19	0.01	0.87	0.03	1.27	0.07	1.02	0.05	-1.08	0.10	194.09	9.76
141.72	2	6.11	0.04	52.39	0.01	0.88	0.00	1.32	0.04	1.02	0.01	-1.17	0.17	292.36	6.39
142.6	2	4.16	0.04	53.14	0.01	0.92	0.03	1.35	0.00	1.02	0.03	-0.98	0.07	222.83	3.85
143.45	2	6.95	0.00	107.87	0.00	1.16	0.07	1.75	0.05	1.34	0.13	-1.28	0.26	335.12	57.16
145.61	2	2.46	0.00	34.91	0.00	1.23	0.02	1.90	0.16	1.40	0.02	-1.39	0.40	183.96	7.13
146.02	3	6.75	0.26			0.66	0.13	0.99	0.20	0.69	0.06	-0.73	0.21	177.49	5.33
146.17	2	3.08	0.11			0.75	0.02	1.05	0.06	0.77	0.01	-0.84	0.10	148.91	3.09
146.26	2	12.70	0.42			0.89	0.02	1.34	0.01	0.99	0.03	-0.98	0.61	438.84	12.53
146.34	3	20.06	0.18	205.76	0.03	1.43	0.02	2.13	0.07	1.77	0.11	-1.68	0.32	244.39	7.46

146.39	2	5.63	0.21			0.84	0.05	1.20	0.12	0.93	0.04	-0.99	0.16	194.67	6.55
146.45	2	5.12	0.02	57.64	0.00	1.03	0.04	1.49	0.05	1.23	0.07	-0.75	0.14	142.75	0.38
146.58	2	4.35	0.15			0.98	0.15	1.41	0.23	1.06	0.06	-1.00	0.01	142.14	3.38
148.27	2	3.06	0.01	31.90	0.00	1.12	0.02	1.65	0.07	1.32	0.01	-1.30	0.04	142.25	2.52
150.49	3	1.57	0.01	15.25	0.00	0.78	0.18	1.24	0.33	0.69	0.39	-1.08	1.17	202.15	6.95
153	2	0.68	0.01	6.57	0.00	0.66	0.07	0.94	0.13	0.74	0.10	-0.69	0.02	18.68	0.29
153.77	3	0.70	0.01	5.91	0.00	0.03	0.26	0.03	0.41	-0.21	0.43	0.03	0.89	73.67	2.48
159.34	1	0.24		1.95		0.37		0.49		0.39		-0.70		2.98	
161.71	2	0.70	0.04	6.51	0.01	0.44	0.07	0.66	0.16	0.42	0.01	-0.67	0.09	7.35	0.37
163.63	2	0.18	0.01	1.87	0.00	0.71	0.13	0.79	0.07	0.77	0.15	-1.18	0.81	6.88	0.39
167.47	3	0.67	0.01	12.35	0.00	0.38	0.07	0.51	0.14	0.54	0.43	0.31	0.78	27.25	0.92
169.47	2	2.92	0.06	59.93	0.02	0.19	0.01	0.28	0.07	0.06	0.04	-0.30	0.16	163.39	0.68
169.94	2	1.21	0.01	43.29	0.01	0.71	0.11	1.06	0.14	0.79	0.02	-0.40	0.64	16.57	0.37
170.17	2	1.09	0.02	16.55	0.01	0.34	0.01	0.46	0.01	0.35	0.06	-0.04	0.17	8.18	0.10
170.39	2	1.27	0.00	25.96	0.00	0.32	0.02	0.45	0.05	0.33	0.06	-0.41	0.05	15.12	0.02
170.94	3	1.47	0.03	24.10	0.01	0.16	0.12	0.20	0.16	0.11	0.13	0.10	0.19	33.08	0.58
177.1	2	3.13	0.03	27.19	0.00	0.02	0.09	-0.01	0.17	0.02	0.13	-0.11	0.58	9.03	0.06
182.14	2	2.78	0.04	31.27	0.01	-0.09	0.05	-0.15	0.05	-0.21	0.02	0.08	0.52	47.22	7.39
186.64	2	0.42	0.00	5.15	0.00	0.55	0.23	0.75	0.43	0.63	0.07	-1.68	0.25	15.47	0.39

Table A5.2. High resolution data. Aluminum concentrations were not available for these samples. All samples were measured only once.

sample [m]	Se [ppm]	$\delta 82/78\text{Se}$ [‰]	$\delta 82/76\text{Se}$ [‰]	$\delta 82/77\text{Se}$ [‰]	$\delta 74/78\text{Se}$ [‰]	TOC [%]	TS [%]	As [ppm]
124.06	0.73	0.01	0.01	-0.24	0.14	5.59	0.30	57.48
124.05	0.79	0.07	-0.03	-0.24	0.21	5.38	0.35	72.64
124.04	1.15	-0.02	0.01	-0.10	0.38	4.72	0.12	60.87
124.03	1.16	-0.31	-0.50	-0.48	0.18	5.36	0.12	56.60
124.01	0.87	-0.10	-0.12	-0.36	0.32	6.95	0.43	74.04
124.00	1.21	-0.12	-0.16	-0.22	0.53	5.95	0.34	49.33
123.99	2.56	-0.27	-0.34	-0.53	0.64	4.41	7.38	235.60
123.98	1.29	-0.25	-0.39	-0.34	0.50	5.65	0.13	39.17
123.97	1.23	-0.24	-0.52	-0.30	0.47	5.77	0.10	42.68
123.96	1.71	-0.26	-0.46	-0.30	0.47	5.01	0.14	70.66
123.95	2.00	-0.07	-0.13	-0.06	-0.82	4.67	0.18	77.52
123.94	2.47	-0.17	-0.29	-0.22	0.07	4.31	0.17	97.86
123.93	1.93	-0.15	-0.23	-0.12	0.03	4.96	0.21	55.53
123.92	2.12	-0.27	-0.43	-0.10	-0.16	5.51	0.24	55.10
123.92	1.84	-0.11	-0.23	-0.10	0.15	5.78	0.22	50.61
123.91	1.46	-0.22	-0.36	-0.25	0.05	5.90	0.20	66.46

Supplementary references

- Anbar, A.D., Duan, Y., Lyons, T.W., Arnold, G.L., Kendall, B., Creaser, R.A., Kaufmann, A.J., Gordon, G.W., Scott, C., Garvin, J., and Buick, R., 2007, A whiff of oxygen before the Great Oxidation Event?: *Science*, v. 317, p. 1903-1906.
- Carignan, J., and Wen, H., 2007, Scaling NIST SRM 3149 for Se isotope analysis and isotopic variations of natural samples: *Chemical Geology*, v. 242, p. 347-350.
- Farquhar, J., Bao, H., and Thiemens, M., 2000, Atmospheric influence on Earth's earliest sulfur cycle: *Science*, v. 289, p. 756-758.
- Fischer, W.W., Slotznick, S., Johnson, J.E., Webb, S.M., Rasmussen, B., Raub, T.D., and Kirschvink, J.L., 2014, Archean 'whiffs of oxygen' tied to post-depositional processes, *Goldschmidt Conference Abstracts # 3504*: Sacramento, USA.
- Kirschvink, J.L., Raub, T.D., and Fischer, W., 2012, Archean "whiffs of oxygen" go Poof!, *Goldschmidt Conference Abstracts*: Montreal, Quebec, Canada, p. 1943.
- Layton-Matthews, D., Leybourne, M.I., Peter, J.M., and Scott, S.D., 2006, Determination of selenium isotopic ratios by continuous-hydride-generation dynamic-reaction-cell inductively coupled plasma-mass spectrometry: *Journal of Analytical Atomic Spectrometry*, v. 21, p. 41-49.
- Li, Y.-H., and Schoonmaker, J.E., 2004, Chemical composition and mineralogy of marine sediments, *in* Holland, H.D., and Turekian, K.K., eds., *Sediments, Diagenesis, and Sedimentary Rocks, Volume 7: Treatise on Geochemistry*: Oxford, UK, Elsevier-Pergamon.
- Mitchell, K., Mason, P.R.D., Van Cappellen, P., Johnson, T.M., Gill, B.C., Owens, J.D., Ingall, E.D., Reichart, G.-J., and Lyons, T.W., 2012, Selenium as paleo-oceanographic proxy: A first assessment: *Geochimica et Cosmochimica Acta*, v. 89, p. 302-317.
- Rouxel, O., Ludden, J., Carignan, J., Marin, L., and Fouquet, Y., 2002, Natural variations of Se isotopic composition determined by hydride generation multiple collector inductively coupled plasma mass spectrometry: *Geochimica et Cosmochimica Acta*, v. 66, p. 3191-3199.
- Savard, D., Bedard, L.P., and Barnes, S.-J., 2009, Selenium concentrations in twenty-six geological reference materials: New determinations and proposed values: *Geostandards and Geoanalytical Research*, v. 33, p. 249-259.
- Schilling, K., Johnson, T.M., and Wilcke, W., 2011, Selenium partitioning and stable isotope ratios in urban topsoil: *Soil Science Society of America Journal*, v. 75, p. 1354-1364.
- Stüeken, E.E., Foriel, J., Nelson, B.K., Buick, R., and Catling, D.C., 2013, Selenium isotope analysis of organic-rich shales: advances in sample preparation and isobaric interference correction: *Journal of Analytical Atomic Spectrometry*, v. 28, p. 1734-1749.
- Taylor, S.R., and McLennan, S.M., 1995, The geochemical evolution of the continental crust: *Reviews in Geophysics*, v. 33, p. 241-265.
- Yu, M., Sun, D., Tian, W., Wang, G., Shen, W., and Xu, N., 2002, Systematic studies on adsorption of trace elements Pt, Pd, Au, Se, Te, As, Hg, Sb on thiol cotton fiber: *Analytica Chimica Acta*, v. 456, p. 147-155.

Chapter 6: Deep-time trends in selenium isotopic geochemistry supporting secular redox changes in the ocean and atmosphere

Abstract

It has been proposed that selenium isotopes, like those of the geochemically similar element sulfur, might monitor the global redox state of the Earth's surface over time. If so, then major changes to the oxygen status of the ocean and atmosphere should be manifest as points of inflection in secular trends of marine selenium isotopes or elemental concentrations. Here we test that proposition by analysis of marine and non-marine mudrocks through time from ~3.2 Gyr old onwards. $\delta^{82/78}\text{Se}$ shows small fractionations of mostly less than 2‰ throughout Earth's history. All fractionations are mass-dependent within error. In the Archean, especially after 2.7 Gyr, we find a significant heavy isotopic enrichment from non-marine ($-0.28 \pm 0.67\text{‰}$) to marine samples ($+0.37 \pm 0.27\text{‰}$). Together with increasing selenium concentrations from the mid-Archean to the late Archean, this trend supports the onset of oxidative weathering on land with partial reduction of selenium oxyanions during fluvial transport. The Paleoproterozoic Great Oxidation Event (GOE) is not reflected in the marine $\delta^{82/78}\text{Se}$ record. However, there is a major inflection in the secular $\delta^{82/78}\text{Se}$ curve during the Neoproterozoic or early Paleozoic, from a Precambrian mean of $+0.42 \pm 0.45\text{‰}$ to a post-Precambrian mean of $-0.02 \pm 0.42\text{‰}$. This probably reflects a major restructuring of the Earth's surface redox state, with the oceans becoming more oxic and thus allowing selenium oxyanions to be stable throughout the water column. Since then selenium oxyanion reduction has probably been restricted to anoxic basins and diagenetic environments in sediments. The transition in the selenium cycle confirms the Neoproterozoic to mid-Paleozoic

“Second Rise of Oxygen” hypothesis, setting the stage for the evolution of marine metazoans and ultimately for terrestrial complex life.

6.1. Introduction

Selenium is an essential micronutrient for life (e.g. Mayland, 1994; Gladyshev, 2012). In natural environments, it can be found in four different redox states as Se^{VI} (SeO_4^{2-}), Se^{IV} (SeO_3^{2-} or HSeO_3^-), Se^0 , and organic and inorganic $\text{Se}^{-\text{II}}$. In the modern ocean, the oxyanions Se^{VI} and Se^{IV} are most abundant and show typical nutrient abundance profiles, with depletion in the photic zone and constant concentration in the deep ocean (Cutter & Cutter, 2001). Organic $\text{Se}^{-\text{II}}$ is common in surface waters but it is almost entirely re-oxidized at depth. This trend is reversed in anoxic water columns, which are dominated by organic $\text{Se}^{-\text{II}}$ phases (Cutter, 1982; Cutter, 1992). Sediments that formed in anoxic environments therefore mostly contain reduced phases including Se^0 and organic and pyrite-bound $\text{Se}^{-\text{II}}$ (Kulp & Pratt, 2004; Fan *et al.*, 2011).

The six stable isotopes of selenium (masses 82, 80, 78, 77, 76, 74) are strongly fractionated kinetically in favor of the lighter masses during biotic or abiotic reduction reactions of oxyanions to Se^0 or inorganic $\text{Se}^{-\text{II}}$. In laboratory experiments, abiotic reduction ($\epsilon_{\text{max}} = 25\%$, where $\epsilon = \delta^{82/78}\text{Se}_{\text{reactant}} - \delta^{82/78}\text{Se}_{\text{product}}$) can impart larger negative fractionations than biotic reduction ($\epsilon_{\text{max}} = 14 \%$) (Johnson *et al.*, 1999; Herbel *et al.*, 2000; Ellis *et al.*, 2003; Johnson & Bullen, 2003), but in natural systems, abiotic reduction is kinetically inhibited and biological fractionation dominates (Johnson & Bullen, 2004). Large fractionations can also occur during equilibration of Se species with different redox states, where, as in kinetic isotope fractionation, the more oxidized forms can become isotopically enriched by up to 33‰ (Li & Liu, 2011), but it has so far not been demonstrated if equilibrium processes are significant in natural environments.

Other isotopic systems like sulfur and carbon are dominated by kinetic fractionation. Moderate negative fractionations from 0.6‰ to 2.6‰ have been reported for Se^{VI} assimilation into biomass (Johnson *et al.*, 1999; Hagiwara, 2000; Clark & Johnson, 2010), but the highest values have been questioned (Johnson & Bullen, 2004). Hence isotopic fractionation associated with this process is probably on the order of 0.6‰ and thus minor. Similarly, Se^{IV} adsorption on iron oxides and volatilization of organic Se^{II} from incubated soils both result in small negative fractionations of less than 0.6‰ (Johnson *et al.*, 1999). Consequently, it appears that selenium isotope fractionations preserved in geological samples are largely controlled by biological reduction of Se oxyanions, but fractionations in natural environments may be smaller than those measured in cultures where the supply of substrates is much higher (Johnson & Bullen, 2004). This raises the possibility of using selenium isotopes as an independent tool for reconstructing redox changes in surface environments over Earth's history (Mitchell *et al.*, 2012) (Chapter 5). Because of its relatively low abundance, multiple redox states and high redox potential (Fig. 6.1), selenium may be more sensitive to redox and productivity changes than other proxies, such as sulfur and perhaps molybdenum.

In this study, we take two steps towards establishing selenium isotopes as a redox proxy. First, we compile recent marine selenium isotope data from the literature and create a working model for how selenium isotopes behave on a global scale in the modern ocean under known redox conditions. This will provide a platform for interpreting selenium isotope data in deep time. Second, we present new data from kerogenous mudrocks through time with particular focus on the Precambrian and environmental gradients in the late Archean and Mesoproterozoic. Combined with existing datasets, this provides us with a record spanning the last 3.2 billion years, *i.e.* across the proposed Paleoproterozoic and Neoproterozoic oxidation events. Both of

these events could have affected the selenium biogeochemical cycle, and hence the sedimentary selenium record may provide independent evidence or additional information on them. More specifically, we test the following hypotheses: (1) Because the most mobile selenium species Se^{IV} and in particular Se^{VI} are only stable under oxic conditions, we would expect that the marine selenium cycle changed profoundly with the oxygenation of the deep ocean in the Neoproterozoic (Canfield & Teske, 1996; Sahoo *et al.*, 2012). Se^{VI} and Se^{IV} should have become more stable ions in the water column, *i.e.* they should no longer have been subject to quantitative reduction, leading to larger net isotopic fractionations preserved in sediments. Hence, we expect to see a systematic difference in isotopic values before and after the Neoproterozoic oxidation event. (2) The high redox potential of selenium oxyanions ($\text{Se}^{\text{IV}/\text{VI}}$) compared to sulfate (S^{VI}) may also have delayed the onset of the selenium weathering flux from land into the ocean. Total sulfur (TS) abundances in marine sediments increased in the late Archean, suggesting incipient oxidative weathering of sulfide minerals, enhanced by microbial activity (Stüeken *et al.*, 2012). If conditions were not oxidizing enough for selenium, then TS/TSe ratios in sediments should have been elevated for some time interval afterwards, perhaps until the Paleoproterozoic or Neoproterozoic oxidation events, when atmospheric oxygen levels rose globally. If, however, microbial activity led to locally high redox states sufficient for selenium oxidation, then the Se^{IV} and/or Se^{VI} flux to the ocean may have increased concurrently with the S^{VI} flux and TS/TSe ratios should be constant through time. Hence marine TS/TSe ratios may serve as an indirect proxy for non-marine redox processes. We would further expect to see isotopic differences between non-marine, shallow marine and deeper marine sediments if $\text{Se}^{\text{IV}/\text{VI}}$ stability and abundance decreased from oxic terrestrial habitats to anoxic seawater.

6.2. Methods

6.2.1. Compilation of recent data

To better understand the modern selenium cycle, we compiled data from the literature representing the last 500 kyr during which the ocean redox state is relatively well constrained. Included are data from the mid-Atlantic (Johnson & Bullen, 2004), the Bermuda Rise (Shore, 2010), the Cariaco Basin (Shore, 2010), the Arabian Sea (Mitchell *et al.*, 2012) and the Black Sea (Johnson & Bullen, 2004; Mitchell *et al.*, 2012). The data set was divided into two categories: open oxic ocean and restricted anoxic basins. Data from the mid-Atlantic, the Bermuda Rise, the Arabian Sea, and from the glacial oxygenated stages of the Cariaco Basin (Shore, 2010) were included in the oxic ocean category. Samples from the Arabian Sea include sediments that formed below an oxygen minimum zone (Mitchell *et al.*, 2012), but because the Arabian Sea rapidly exchanges water masses with the open ocean by upwelling and therefore likely has a high supply of selenium oxyanions, it is more similar to an oxic ocean. The restricted anoxic basin category includes data from the interglacial Cariaco Basin (Shore, 2010) and the Black Sea. Although some samples from the Black Sea have been described as oxic (Mitchell *et al.*, 2012), euxinic conditions in the deeper water column probably result in low selenium oxyanion concentrations and a short residence time throughout the basin (Cutter, 1992). Therefore, we assigned all Black Sea samples to the anoxic restricted basin category.

6.2.2. New analyses of ancient rocks

Our new analyses focused on whole-rock analyses of kerogenous mudrocks (Table 1), because they are relatively abundant and selenium-rich. This approach has the disadvantage that mudrocks can contain multiple isotopically-distinct selenium phases including elemental Se⁰, Se⁻

^{II} bound to organic matter or substituting for S^{-II} in sulfide minerals, and Se^{IV} adsorbed to mineral surfaces or kerogen. Combining these phases probably reduces the measured isotopic range and might make it more difficult to discern patterns. In some ways, this is analogous to measuring trends in carbon isotopes without separating organic carbon from carbonate. However, separation techniques for differing selenium phases in rocks are only beginning to be developed (Kulp & Pratt, 2004; Fan *et al.*, 2011; Schilling *et al.*, 2014b), and it is uncertain if they are useful for ancient samples where isotopic ratios may have re-equilibrated. An alternative approach may be to analyze banded iron formations that primarily contain just one phase, *i.e.* adsorbed Se^{IV} (Schilling *et al.*, 2014a; Schirmer *et al.*, 2014). However, the selenium concentrations in such rocks are very low, presenting analytical difficulties, and BIF or equivalent deep-marine iron oxides are not available from all time periods or from all environments. Hence by analyzing mudrocks we are able to compile a large database spanning most of Earth's history and covering environmental gradients, and by also monitoring their total organic carbon (TOC) and total sulfur (TS) concentrations, we can at least qualitatively assess the importance of redox changes and productivity at any given time.

Our sample preparation methods and analytical protocols for selenium isotopes are described in much more detail in Stüeken *et al.* (Stüeken *et al.*, 2013). In brief, rock powders were digested with HF, HNO₃ and HClO₄, the selenium was extracted by column filtration through thiol cotton fibers and further purified with aqua regia. Analyses were carried out with a hydride-generator (HGX-200) coupled to a multi-collector inductively-coupled plasma mass spectrometer (Nu Instruments). Instrumental mass bias was corrected by standard sample bracketing. Isobaric interferences, most importantly by argon dimers, arsenic hydrides and germanium, were corrected post-analytically (Stüeken *et al.*, 2013). Results are reported in

standard delta notation relative to NIST SRM 3149. Unless noted otherwise, we used the

$^{82}\text{Se}/^{78}\text{Se}$ ratio:

$$\delta^{82/78}\text{Se} = [({}^{82}\text{Se}/{}^{78}\text{Se})_{\text{sample}}/({}^{82}\text{Se}/{}^{78}\text{Se})_{\text{SRM3149}} - 1] \cdot 1000 \quad (\text{Eq. 6.1}),$$

because with our method this particular isotope pair yields the most accurate and precise measurements. For conversion to $\delta^{82/76}\text{Se}$, which has been used by other laboratories, values have to be multiplied by 1.54. We analyzed a total of 202 samples and 127 of those in replicates. The average precision (1σ) was 0.10‰ for $\delta^{82/78}\text{Se}$ and 1.6% (relative error) for Se concentrations. Our result for the international reference material SGR-1, processed with the same method, was $+0.05 \pm 0.18$ ‰ (1σ , $n = 9$), which is in good agreement with recently published values (Schilling *et al.*, 2011; Mitchell *et al.*, 2012).

Total organic carbon and total sulfur were analyzed with established methods used routinely in the UW Isolab (Schoepfer *et al.*, 2013; Stüeken, 2013) with precisions of 1% and 10%, respectively. For TOC, powders were decarbonated with HCl. Sulfur was analyzed on untreated samples. Analyses were carried out by flash combustion with an elemental analyzer coupled to a continuous-flow isotope-ratio mass spectrometer (Finnigan MAT 253).

6.3. Results

6.3.1. Trends in the modern ocean

The compilation of published selenium isotope data from marine sediment deposited over the last 500 kyr (Fig. 6.2) shows that sediments deposited under an oxic water column generally have a somewhat lighter isotopic composition ($\delta^{82/78}\text{Se}_{\text{avg}} = -0.10 \pm 0.21$ ‰, range -0.90 ‰ to +0.41 ‰) than sediments formed under anoxic water in restricted basins ($+0.07 \pm 0.24$ ‰, range -0.41 ‰ to +0.59 ‰; $p_{\text{one-tailed}} < 10^{-4}$). Anoxic basins thus tend to be closer in composition to

selenium oxyanions ($\text{Se}^{\text{IV}/\text{VI}}$) dissolved in the open ocean ($\sim+0.3$ ‰, (Rouxel *et al.*, 2004; Mitchell *et al.*, 2012)). The composition of Se^{VI} and Se^{IV} dissolved in seawater has not yet been measured directly, but it is probably captured by Se^{IV} adsorbed onto Fe-Mn nodules ($+0.32$ ‰, $n = 1$) (Rouxel *et al.*, 2004) and by phytoplankton that quantitatively assimilates Se^{VI} , Se^{IV} and organic $\text{Se}^{\text{-II}}$ in the photic zone ($+0.27$ ‰, $n = 1$) (Mitchell *et al.*, 2012). The close agreement in $\delta^{82/78}\text{Se}$ between Se^{IV} adsorbed on Mn-nodules and bulk phytoplankton, which assimilates a combination of Se^{VI} , Se^{IV} and organic $\text{Se}^{\text{-II}}$ (Fernandez-Marinez & Charlet, 2009), suggests these dissolved selenium species are isotopically homogenized, probably through the processes of biological assimilation and remineralization which do not impart net isotopic fractionations (Johnson & Bullen, 2004).

Today, under a fully oxic atmosphere, the input of selenium to the ocean from crustal weathering and volcanism probably has an average composition equivalent to that of the crust at $+0.01 \pm 0.49$ ‰ (Rouxel *et al.*, 2002). The close match with total average marine $\delta^{82/78}\text{Se}$ values in the Phanerozoic supports this hypothesis (Section 6.3.2). As meteorites show approximately the same value ($+0.11 \pm 0.34$ ‰) (Rouxel *et al.*, 2002), it is unlikely that on a global scale the selenium isotope composition of the upper crust has changed much throughout Earth's history. If so, then sediments from the modern oxic ocean are systematically depleted relative to the crustal source, dissolved $\text{Se}^{\text{IV}/\text{VI}}$ is enriched, and sediments from anoxic basins have a tendency to preserve that enrichment.

6.3.2. New data from ancient sedimentary rocks

All our new selenium isotope data plot within error along the theoretical mass-dependent fractionation line (Fig. 6.3), indicating that isobaric interferences occurring in the mass

spectrometer have been properly corrected. $\delta^{82/76}\text{Se}$ is the second most stable ratio after $\delta^{82/78}\text{Se}$ (Fig. 6.3a). $\delta^{82/77}\text{Se}$ (Fig. 6.3b) can be compromised by interferences with $^{77}(\text{ArCl})$ and possibly $^{77}(\text{AsH}_2)$ that are more difficult to monitor and to subtract (Stüeken *et al.*, 2013), which probably explains the enhanced scatter in our measurements of this isotopic ratio. $\delta^{78/74}\text{Se}$ (Fig. 6.3c) suffers from interferences with ^{74}Ge , magnified by the low abundance of ^{74}Se . Occasional outliers in $\delta^{78/74}\text{Se}$ are thus likely due to improperly corrected residual ^{74}Ge . So overall we do not see any evidence of mass-independent fractionation (MIF) at any time in the rock record, in stark contrast to the isotopic records of sulfur (Farquhar *et al.*, 2000). Photochemical reactions involving selenium were either not conducive to MIF, or volatile selenium compounds were insignificant in relative abundance. It is worth noting that eukaryotic algae, plants and fungi are significant contributors of the major selenium gases today, *i.e.* methylated Se^{II} (e.g. Chasteen & Bentley, 2003), and hence the flux of these gases may have been trivial in the earlier Precambrian prior to the radiation of eukaryotic life.

Combined with published selenium isotope data from the late Archean Mt. McRae Shale (Chapter 5) and several Phanerozoic basins (Johnson & Bullen, 2004; Shore, 2010; Mitchell *et al.*, 2012), our results show that throughout Earth's history (Fig. 6.4a) the range of mass-dependent selenium isotope fractionation recorded in mudrocks (-1.9‰ to +2.9‰) is significantly smaller than the 15-25‰ measured in oxyanion reduction experiments in the laboratory (Johnson *et al.*, 1999; Herbel *et al.*, 2000; Ellis *et al.*, 2003; Johnson & Bullen, 2003), but during most time intervals it exceeds the 0.6‰ expected for FeMn-oxide adsorption and assimilation into biomass (Johnson *et al.*, 1999; Clark & Johnson, 2010). Hence biotic or abiotic reduction reactions probably played an important role in the global biogeochemical selenium cycle since at least the Mesoarchean. As discussed above, the relatively small range in bulk

sediments is probably in part due to mixing of multiple selenium phases exhibiting differing isotopic fractionations, but it may also reflect a smaller magnitude in isotopic fractionation under natural, selenium -poor conditions.

The total average of all new and published data is $+0.19 \pm 0.49\text{‰}$ ($n = 469$) with a geometric average total selenium (TSe) concentration of $10^{0.06 \pm 0.65}$ ppm ($= 1.1 +4.0/-0.9$ ppm). We use geometric averages because of the wide range over several orders of magnitude. In the marine record (Table 6.2), isotopic ratios decrease slightly from the mid-Archean (here 3.19-2.87 Gyr; $+0.62 \pm 0.27\text{‰}$, $n = 23$, removing one outlier of $+1.43\text{‰}$ and 2.23 ppm TSe) to the late Archean (2.71-2.50 Gyr; $+0.35 \pm 0.39\text{‰}$, $n = 110$) ($p_{\text{one-tailed}} = 10^{-4}$) but show no major change from the late Archean to the Proterozoic (2.49-1.10 Gyr; $+0.45 \pm 0.55\text{‰}$, $n = 59$; $p_{\text{one-tailed}} = 0.12$). The most significant change in selenium isotopes occurs between the Proterozoic and the Phanerozoic (0.54 Gyr to modern; $-0.02 \pm 0.42\text{‰}$, $n = 182$; $p_{\text{one-tailed}} = 10^{-16}$). Hence Phanerozoic data tend to be close to the average composition of the crust ($+0.01 \pm 0.49 \text{‰}$) (Rouxel *et al.*, 2002), while Precambrian data are systematically enriched. Although we do not any data between 1.10 Gyr and 0.54 Gyr, it is plausible that this isotopic transition coincides with the purported “second rise of oxygen” and the oxygenation of the deep ocean in the late Neoproterozoic (Sahoo *et al.*, 2012).

In this compilation, we excluded Phanerozoic basins known to be restricted (modern Cariaco Basin and Black Sea, 380 Myr New Albany Shale, 180 Myr Posidonia Shale; total average $\delta^{82/78}\text{Se} = +0.23 \pm 0.40\text{‰}$, $n = 66$) (Johnson & Bullen, 2004; Shore, 2010; Mitchell *et al.*, 2012). These basins show distinctively higher TS/TSe ratios ($10^{0.26 \pm 0.44}$ [%/ppm], $n = 37$) than most other Phanerozoic basins ($10^{-0.57 \pm 0.56}$ [%/ppm], $n = 130$; $p_{\text{one-tailed}} = 10^{-14}$; Fig. 6.4c) due to higher TS concentrations. This is probably the result of local euxinia, and it supports our

decision to exclude these basins from the normal marine record. In the Precambrian, the distinction between restricted and open marine basins is uncertain. All basins sampled for this study have been argued to be in open exchange to the ocean, perhaps with the exception of the Belt Basin. But, as discussed in Section 6.4.1, the contrast between open and restricted environments should be most important in the Phanerozoic. We therefore treat all our Precambrian data as representative of normal marine conditions, but discuss environmental differences in more detail below.

A highly significant transition in selenium concentrations occurs between the mid-Archean ($10^{-0.76 \pm 0.21}$ ppm = 0.17 +0.11/-0.07 ppm) and the late Archean ($10^{-0.16 \pm 0.46}$ ppm = 0.69 +1.30/-0.45 ppm; $p_{\text{one-tailed}} = 10^{-23}$). This step coincides with the onset of low levels of oxidative weathering on land (Stüeken *et al.*, 2012). Concentrations then decrease slightly from the late Archean to the Proterozoic ($10^{-0.13 \pm 0.78}$ ppm = 0.74 +3.73/-0.62 ppm; $p_{\text{one-tailed}} = 0.005$) and increase again from the Proterozoic to the Phanerozoic ($10^{0.11 \pm 0.70}$ ppm = 1.29 +5.17/-1.03 ppm; $p_{\text{one-tailed}} = 0.02$).

Marine TS/TSe ratios [%/ppm] only show relatively subtle changes through time. They increase from $10^{-0.35 \pm 0.36}$ before 2.71 Gyr to $10^{-0.11 \pm 0.55}$ between 2.71 Gyr and 1.1 Gyr ($p_{\text{one-tailed}} = 0.04$) with no significant change between the late Archean and the Proterozoic ($p_{\text{one-tailed}} = 0.42$) and decrease again to $10^{-0.56 \pm 0.56}$ in the Phanerozoic ($p_{\text{one-tailed}} = 10^{-9}$).

A few selected sites further show environmental gradients in selenium isotopes:

- In the mid-Archean Witwatersrand Supergroup (Fig. 6.5a) in South Africa (2.96-2.87 Gyr), all samples are isotopically positive, but fluvial samples are slightly lighter ($\delta^{82/78}\text{Se} = +0.30 \pm 0.19\text{‰}$, n = 5) than proximal marine samples ($\delta^{82/78}\text{Se} = +0.74 \pm 0.28\text{‰}$, n = 8) ($p_{\text{one-tailed}} < 0.01$). Distal marine samples are variable ($\delta^{82/78}\text{Se} = +0.63 \pm 0.51\text{‰}$, n = 5). In general, marine shelf

samples from the Witwatersrand Supergroup agree well with upper continental slope samples from the Soanesville Group in Western Australia (3.2 Gyr; $\delta^{82/78}\text{Se} = +0.64 \pm 0.18\text{‰}$, $n = 9$).

- In the late Archean Fortescue Group (Fig. 6.5b) in Western Australia (2.75-2.65 Gyr), we find a significant contrast between marine environments ($\delta^{82/78}\text{Se} = +0.37 \pm 0.27\text{‰}$, $n = 28$) and non-marine environments ($\delta^{82/78}\text{Se} = -0.28 \pm 0.67\text{‰}$, $n = 19$) ($p_{\text{one-tailed}} < 0.001$). Shallow marine samples from the Carawine Formation ($\delta^{82/78}\text{Se} = +0.32 \pm 0.12\text{‰}$, $n = 7$) are on average the same as deeper marine samples from the Jeerinah Formation ($\delta^{82/78}\text{Se} = +0.38 \pm 0.30\text{‰}$, $n = 21$) but less variable. Both agree well with marine samples from the Ghaap Group in South Africa (2.56-2.52 Gyr; $\delta^{82/78}\text{Se} = +0.41 \pm 0.33\text{‰}$, $n = 15$).

- Volcanogenic massive sulfides (VMS) from the late Archean Kidd Creek Basin (2.7 Gyr; $\delta^{82/78}\text{Se} = +0.28 \pm 0.24\text{‰}$, $n = 5$) are statistically indistinguishable from associated marine black shales ($\delta^{82/78}\text{Se} = +0.07 \pm 0.22\text{‰}$, $n = 5$) ($p_{\text{one-tailed}} = 0.10$), but show a markedly smaller range and an isotopic enrichment compared to modern hydrothermal sulfides from the Mid-Atlantic Ridge ($\delta^{82/78}\text{Se} = -0.98 \pm 0.81\text{‰}$, $n = 51$, (Rouxel *et al.*, 2004)) and late Devonian VMS deposits from northwestern Canada ($\delta^{82/78}\text{Se} = -1.88 \pm 2.33\text{‰}$, $n = 23$; (Layton-Matthews *et al.*, 2013)).

- In the Mesoproterozoic Belt Supergroup (1.47 Gyr, Fig. 6.5c), isotopically light values ($\delta^{82/78}\text{Se} = -0.07 \pm 0.43\text{‰}$, $n = 7$) primarily occur in offshore facies in the west, whereas onshore facies from the eastern basin margin tend to be relatively enriched ($\delta^{82/78}\text{Se} = +0.73 \pm 0.33\text{‰}$, $n = 8$). Here, the offshore sites are located closer to the opening of the basin towards the ocean and also closer to the proposed major riverine inflow from the unsampled western basin margin (Ross & Villeneuve, 2003).

Deep basinal facies from the roughly coeval Roper Basin (1.36 Gyr; $\delta^{82/78}\text{Se} = +0.53 \pm 0.20\text{‰}$, $n = 7$) and samples of intermediate water depth from the Taoudeni Basin (1.1 Gyr; $\delta^{82/78}\text{Se} = +0.45$

$\pm 0.52\%$, $n = 5$) are generally positive. If these sediments were deposited distal to the most significant riverine water inflow, then all three Mesoproterozoic basins may show relative isotopic enrichment with increasing distance from the major selenium source.

- Our results for coastal Atlantic samples from the Cretaceous Ocean Anoxic Event I (OAE I) are all negative (120 Myr; $\delta^{82/78}\text{Se} = -0.41 \pm 0.23\%$, $n = 8$, Fig. 6.5f), whereas Mitchell *et al.* (Mitchell *et al.*, 2012) found primarily positive values (93 Myr; $\delta^{82/78}\text{Se} = +0.19 \pm 0.25\%$, $n = 27$) in deep-marine Atlantic samples from OAE II. Hence, taken together, the Atlantic Ocean may have displayed a basinal gradient during anoxic stages.

When all marine data points are combined, $\delta^{82/78}\text{Se}$ is not correlated with $\delta^{34}\text{S}$ ($r^2 = 0.002$), $\delta^{13}\text{C}_{\text{org}}$ ($r^2 = 0.07$), TS ($r^2 = 0.05$), TOC ($r^2 = 0.001$) or TSe ($r^2 = 0.03$). TSe shows a significant correlation with TS and TOC in logarithmic space ($r^2 = 0.48$ and 0.55 , respectively, Fig. 6.6), but much less so in linear space ($r^2 = 0.21$ and 0.24). It is possible that the logarithmic correlation is partly a result of lithology and sedimentation rate, *i.e.* fine-grained black shales with low sedimentation rates tending to accumulate much more reduced selenium, sulfides and organic carbon than siltstones or more rapidly accumulating sediments, regardless of whether the three elements are biogeochemically related. Based on the relatively weak correlations in linear space, we therefore conclude that selenium does not strictly follow either sulfur or organic matter under all conditions. However, we do see moderate correlations between $\delta^{82/78}\text{Se}$ and TOC in a few individual basins, in particular the Ghaap Group ($r^2 = 0.64$, $n = 15$, Fig. 6.5e) and the Belt Supergroup ($r^2 = 0.41$, $n = 15$, Fig. 6.5d). In both cases, $\delta^{82/78}\text{Se}$ values decrease with increasing TOC, but TSe is not correlated with TOC or TS. TOC data are not available for the marine Fortescue Group. None of the other basins for which we have more than 10 data points show significant correlations.

6.4. Discussion

We will first discuss the modern marine selenium cycle to establish a working model for how selenium operates under known redox conditions. Then we will step through the rock record and describe trends from the Archean through the Phanerozoic.

6.4.1. Proposed modern selenium cycle

The relatively low $\delta^{82/78}\text{Se}$ values preserved in sediment deposited in open marine conditions are likely the result of partial Se^{VI} or Se^{IV} reduction to Se^0 or inorganic $\text{Se}^{-\text{II}}$ under suboxic diagenetic conditions (Fig. 6.7) (Shore, 2010). This process would explain why residual Se^{VI} and Se^{IV} dissolved in seawater are relatively enriched. Addition of small amounts of isotopically heavy adsorbed Se^{IV} or organic $\text{Se}^{-\text{II}}$ to Se^0 and inorganic $\text{Se}^{-\text{II}}$ in open marine sediments may explain why bulk $\delta^{82/78}\text{Se}$ values are not as negative as one might expect given the fairly large fractionations associated with reduction reactions observed in laboratory simulations (Johnson *et al.*, 1999). Sequential extraction experiments indeed show that sediments and soils commonly contain multiple selenium phases with distinct isotopic compositions (Kulp & Pratt, 2004; Schilling *et al.*, 2014b). Sequential extractions have so far not been carried out on open marine sediments deposited under an oxic water column, but we would predict a mixture of isotopically light inorganic $\text{Se}^{-\text{II}}$ and/or Se^0 and small amounts of isotopically heavy Se^{IV} and/or organic $\text{Se}^{-\text{II}}$.

In the carbon and sulfur cycle, the isotopically heavy reservoirs complementary to isotopically light, reduced phases (organic matter and sulfide, respectively) are carbonate and sulfate minerals. In the case of selenium, however, the most oxidized species Se^{VI} does not form

major mineral deposits and incorporation into carbonate or sulfate minerals is probably minor. Adsorbed Se^{IV} on FeMn-oxides may be a significant isotopically heavy reservoir, complementary to the relatively light siliciclastic sediments from the open ocean; more data will be needed to test this possibility. Based on our data compilation, we propose that sediments from restricted anoxic basins, which tend to be isotopically heavy, represent a complementary positive repository to the isotopically lighter sediments from the global oxic ocean (Fig. 6.7). Under anoxic conditions, selenium assimilated into biomass is not recycled by oxidation (Cutter, 1982; Shore, 2010; Mitchell *et al.*, 2012). Furthermore, dissolved Se^{IV/VI} may be scavenged from the water column by quantitative reduction. Neither biological assimilation nor quantitative scavenging of residual selenium imparts a significant net isotope fractionation. Therefore, sediments formed under highly anoxic conditions are likely to capture the composition of marine Se^{IV/VI}. Hence the biogeochemical Se cycle shares similarities with the biogeochemical cycles of U and Mo, where open and restricted basins are also isotopically complementary to each other (*e.g.* (Anbar, 2004; Brennecke *et al.*, 2011)). If so, then the marine selenium cycle should have evolved markedly through time as the global ocean evolved from an anoxic to an oxic state.

6.4.2. Archean

Throughout the Archean, the global ocean was generally anoxic (Poulton & Canfield, 2011), but oxygenic photosynthesis may have created local oxygen oases since at least 3.0 Gyr (Crowe *et al.*, 2013; Planavsky *et al.*, 2014). Moreover, relatively high levels of TOC in the absence of iron or sulfur mineralization in the 3.2 Gyr Soanvesville Group have been interpreted as potential indirect evidence of even older cyanobacterial oxygenic photosynthetic activity (Buick, 2008). However, the low concentrations of selenium in mid-Archean sediments suggest

that there was no significant selenium flux into the ocean. It is important to note that, unlike molybdenum for example, selenium does not require euxinia to become enriched in anoxic sediments, because it can be immobilized by reduction to solid Se^0 . Hence the absence of H_2S alone cannot explain low TSe concentrations in mid-Archean sediments. Instead it is more likely that atmospheric pO_2 was too low for a significant oxidative weathering flux of selenium into the ocean; any O_2 that was biologically produced at this time was probably rapidly consumed by reductants with lower redox potentials. Mid-Archean marine sediments have TSe concentrations (0.20 ± 0.13 ppm, removing one outlier of 2.2 ppm from the Parktown Fm) only slightly above that of the upper crust (0.09 ppm) (Rudnick & Gao, 2014), but they are isotopically heavier by $0.65 \pm 0.58\%$. Given that fluvial samples from the Witwatersrand Supergroup are slightly lighter ($+0.30 \pm 0.19\%$, Fig. 6.5a), it is possible that there was a small but non-trivial flux of $\text{Se}^{\text{IV/VI}}$ from O_2 oases on land into the anoxic ocean, and partial reduction occurred during fluvial transport, rendering residual dissolved $\text{Se}^{\text{IV/VI}}$ isotopically enriched. Sulfur isotope data from the Witwatersrand Basin are also consistent with a small oxidative weathering source (Guy *et al.*, 2012). But we cannot rule out that the Se is instead of hydrothermal or volcanic origin and that isotopic fractionation occurred in the deep ocean or in volcanic eruptions. If so, then the range of TSe concentrations and $\delta^{82/78}\text{Se}$ values found in the mid-Archean provides a constraint on the volcanic and hydrothermal background supply to Archean sediments.

The marked increase in TSe concentrations in the late Archean (Fig. 6.4b), concurrent with an increase in TS concentrations (Stüeken *et al.*, 2012), must be due to either unusually high volcanic or hydrothermal activity or the onset of oxidative selenium weathering on land. The significant isotopic difference between non-marine and marine samples in the Fortescue Group (Fig. 6.5a) and the correlation between $\delta^{82/78}\text{Se}$ and TOC in the Ghaap Group (Fig. 6.5e) support

the latter. $\delta^{82/78}\text{Se}$ down to -1.88‰ in fluvio-lacustrine sediments can only be explained by partial Se^{VI} and/or Se^{IV} reduction during transport of selenium oxyanions to the ocean. The residual isotopically enriched selenium was then deposited in marine sediments following quantitative reduction or assimilation into biomass. It is likely that a large fraction of selenium dissolved in river water was organically complexed, even more so than in modern rivers (Doblin *et al.*, 2006), and did therefore not undergo reduction reactions. This would explain why marine sediments are not unusually enriched in $\delta^{82/78}\text{Se}$. However, the anti-correlation between $\delta^{82/78}\text{Se}$ and TOC in the late Archean Ghaap Group (Fig. 6.5e) might indicate that at least some of the selenium dissolved in seawater was in the form of oxyanions, which underwent further partial reduction under reducing, TOC-rich conditions. Hence isotopically heavy, TOC-poor samples probably mostly contain organic-bound Se (adsorbed Se^{IV} or organic $\text{Se}^{\text{-II}}$), whereas isotopically light, TOC-rich samples may contain an additional component of Se^0 or sulfide-bound $\text{Se}^{\text{-II}}$. Speciation analyses would be required to test this hypothesis. However, if selenium oxyanions were present in seawater, they were likely restricted to the upper water column. Otherwise hydrothermal sulfide minerals from the Kidd Creek Basin should show more negative $\delta^{82/78}\text{Se}$ values similar to Devonian VMS deposits (Layton-Matthews *et al.*, 2013) or modern black smokers, where Se^{IV} and Se^{VI} are continuously supplied by inflow of oxic seawater (Rouxel *et al.*, 2004). The much smaller range of fractionations in the Kidd Creek VMS deposits compared to fluvio-lacustrine sediments of similar age shows that the major source of selenium oxyanions to the late-Archean ocean was oxidative weathering rather than hydrothermal activity.

Oxidative selenium weathering is not inconsistent with occurrences of detrital pyrite and siderite in the same fluvial strata (Rasmussen & Buick, 1999), because selenium oxidation could have occurred in localized micro-environments, perhaps under O_2 -producing microbial mats,

while rivers well-mixed with the global atmosphere were generally O₂-depleted (cf. Johnson *et al.*, 2014)). The high redox potential of Se^{IV} and Se^{VI}, combined with the apparent absence of phototrophic Se-oxidizing microbes, implies that oxidation was driven by O₂ because other oxidants are either not strong enough (*e.g.* S^{VI}, Fe^{III}) or require O₂ themselves (*e.g.* Mn^{IV}, N^V) (Chapter 5). Our results thus provide further evidence for the early evolution of oxygenic photosynthesis long before the Paleoproterozoic GOE.

TS/TSe ratios in marine sediments further support the conclusion that terrestrial habitats were locally oxic in the late Archean, because if sulfur and selenium had been decoupled, then TS/TSe ratios should have increased markedly. The total sulfur weathering flux increased by an order of magnitude between 2.8 Gyr and 2.7 Gyr (Stüeken *et al.*, 2012), and if selenium had been unaffected because of its high redox potential, then TS/TSe ratios should have increased by the same factor. The very small observed increase by a factor of 1.5 ($p_{\text{one-tailed}} = 0.04$) instead suggests that selenium was mobilized together with sulfur, perhaps with a slightly larger fraction of dissolved selenium being retained in rivers and estuaries. Hence terrestrial habitats were evidently locally oxidizing enough for Se^{IV} and/or Se^{VI} to be stable.

6.4.3. Paleo- and Mesoproterozoic

Selenium isotopes and concentrations in marine mudrocks do not change markedly from the late Archean to the Paleo- and Mesoproterozoic. We found temporary $\delta^{82/78}\text{Se}$ enrichments up to +2.01‰ in the 2.32 Gyr Pretoria Group immediately after the Paleoproterozoic glaciation events, which may be a result of the proposed atmospheric O₂ overshoot between 2.35 and 2.05 Gyr (Bekker & Holland, 2012). Moderately high atmospheric pO₂ could have led to a greater proportion of selenium oxyanions in rivers relative to organically complexed selenium, and if a

significant fraction of those oxyanions were reduced, then the residual would have been pushed to high positive $\delta^{82/78}\text{Se}$ values. Alternatively, positive values could be explained by the opposite effect, i.e. a smaller amount of Se oxyanions in rivers subject to a relatively larger degree of partial reduction and hence more positive values in the residual dissolved fraction that reaches the ocean. However, in that case, large positive values up to 2‰ should be relatively more common in the Precambrian. Furthermore, initial reports of selenium isotopes in Se^{IV} adsorbed to banded iron formation of similar age show very negative values (Schilling *et al.*, 2014a), consistent with partial reduction of Se^{VI} to Se^{IV} in seawater on the outer shelf and suggesting that, unlike in the late Archean, partial reduction may have shifted from rivers to the ocean. Hence the Se oxyanions flux into the ocean was probably higher in the Paleoproterozoic than in the late Archean. The high $\delta^{82/78}\text{Se}$ values at 2.32 Gyr may thus be a more enhanced version of the ‘whiff of oxygen’ around 2.5 Gyr (Chapter 5). But this situation still contrasts with the modern ocean where marine Se^{IV} is derived from organic- Se^{II} oxidation rather than Se^{VI} reduction (Cutter & Bruland, 1984). Hence the BIF data may be further evidence for a chemocline within the Paleoproterozoic water column. Light Se^{IV} probably adsorbed to Fe-oxide particles in the photic zone and subsequently settled on the seafloor. Kerogenous shales, as analyzed in this study, could have preserved the composition of the residual heavy Se^{VI} by quantitative reduction.

Late Paleoproterozoic and Mesoproterozoic selenium data do not show any enrichments above +1.1‰ (Fig. 6.4a) and are generally similar to the late Archean. However, data along a basinal profile in the Belt Basin, where we found more negative $\delta^{82/78}\text{Se}$ closer to the major river inflow and positive values along the restricted basin margin (Fig. 6.5c), suggest that, as in the earlier Paleoproterozoic, partial $\text{Se}^{\text{IV}/\text{VI}}$ reduction may have occurred in the ocean rather than in

rivers. The correlation between $\delta^{82/78}\text{Se}$ and TOC (Fig. 6.5d) probably reflects a similar process as in the Ghaap Group, *i.e.* in the more reducing basin interior (Planavsky *et al.*, 2011; Stüeken, 2013), where TOC was high, partial reduction led to the formation of Se^0 or inorganic $\text{Se}^{-\text{II}}$, whereas along the oxidized basin margin, distal to the selenium inflow, the selenium oxyanion supply was scarce, and most of the preserved selenium in sediments was probably organic-bound. The correlation thus further supports the conclusion that dissolved selenium oxyanions were present in the upper water column of the Proterozoic ocean. However, the generally positive $\delta^{82/78}\text{Se}$ values in most Proterozoic mudrocks (Fig. 6.4a) suggest that partial reduction of selenium oxyanions occurred close to their source, perhaps near river deltas such as in the Belt Basin. Alternatively, or in addition, partial reduction could have occurred in unsampled regions far away from epicontinental basins. The preliminary BIF data from the Paleoproterozoic (Schilling *et al.*, 2014a) may support the latter, if BIF formed in an outer shelf environment. In either case, compared to the late Archean, partial $\text{Se}^{\text{IV/VI}}$ reduction during the Proterozoic may have moved further towards the ocean, likely because land surfaces and rivers became fully oxidized. However, selenium oxyanions were probably not as well-mixed throughout the water column as they are today and perhaps more rapidly consumed on a regional scale.

6.4.4. Phanerozoic

For most of the Phanerozoic, the marine selenium cycle was probably similar to what it is today (Section 6.4.1), as indicated by the more frequent occurrence of negative $\delta^{82/78}\text{Se}$ values in marine sediments. Hence selenium oxyanions were probably more abundant throughout the water column, except in restricted anoxic basins. The drop in TS/TSe ratios by a factor of 2.8 (Fig. 6.3c) in open marine sediments suggests an increase in the total selenium flux into the

ocean. It could also be an indication that selenium was well-mixed throughout the ocean and not sequestered proximal to its source. However, during anoxic events, such as in the Cretaceous, the selenium cycle probably reverted to its Precambrian state, as shown by the gradient between negative $\delta^{82/78}\text{Se}$ values from coastal samples during OAE-I and positive $\delta^{82/78}\text{Se}$ values from deep marine samples during OAE-II (Mitchell *et al.*, 2012), assuming Se sources were comparable during the events.

Large *et al.* (2014) recently reported a significant increase of selenium concentration in pyrite isolates across the Precambrian-Cambrian boundary, which is not reflected in our data from bulk sediments. It is conceivable that the difference between the two datasets is evidence for a change in Se-speciation rather than total supply. In the Precambrian, most sedimentary selenium was probably organic-bound, whereas in the Phanerozoic the greater abundance of selenium oxyanions in an oxic water column may have allowed for more dissimilatory reduction and incorporation of inorganic $\text{Se}^{-\text{II}}$ into sulfide minerals. If so, then the contrast between our whole-rock abundance data and that of the pyrite isolates presented by Large *et al.* (2014) is perhaps further evidence for total ocean oxygenation in the Neoproterozoic or Paleozoic.

We are not able to pin down the exact transition point from a mostly anoxic to a mostly oxic marine selenium cycle, because we have no data in the Neoproterozoic. Cambrian $\delta^{82/78}\text{Se}$ values from the Stephens Formation (+0.96‰) and from the Alum Shale (+0.21 ± 0.20‰, n= 15) (Mitchell *et al.*, 2012) are mostly positive, similar to the Proterozoic (Fig. 6.4a); the first negative $\delta^{82/78}\text{Se}$ values occur in the late Devonian, both in marine mudrocks (Fig. 6.4a) as well as in VMS deposits (Layton-Matthews *et al.*, 2013). Hence it is possible that the oxic Se cycle was only established as late as the mid-Paleozoic when the ocean became fully oxygenated to modern levels (Dahl *et al.*, 2010).

6.5. Conclusions

Our data support several conclusions about the evolution of the Earth's redox state and the global biogeochemical selenium cycle:

1. Concurrently rising Archean TS and TSe between 2.8 Gyr and 2.7 Gyr and the significant isotopic contrast between marine and non-marine samples in the late Archean indicate an early onset of oxidative selenium weathering in locally oxygenated terrestrial habitats long before the Paleoproterozoic global rise of atmospheric pO₂ levels. selenium oxyanions produced during weathering were partially reduced during fluvial transport to the ocean.
2. The GOE itself (~2.4-2.3Gyr) did not have a marked imprint on the selenium isotopic or abundance record, except for perhaps a small enrichment in $\delta^{82/78}\text{Se}$ during the proposed O₂ overshoot between 2.35Gyr and 2.05Gyr (Bekker & Holland, 2012). This may be because oxidative weathering prior to the GOE was already widespread. Furthermore, organic complexation of selenium during fluvial transport and in the ocean likely reduced the maximum observed fractionation in sediments.
3. A relatively greater proportion of selenium oxyanions may have reached the ocean in the Proterozoic, but reduction probably occurred along the chemocline, perhaps in the vicinity of river deltas. However, our lack of data from truly open marine settings, *i.e.* outside of epicontinental basins, makes it impossible to assess how selenium behaved in the oligotrophic ocean. If significant portions of the deep ocean were oxic (Reinhard *et al.*, 2013; Ader *et al.*, 2014), then partial Se^{IV/VI} reduction and isotopic fractionation could also have occurred offshore, similar to today.

4. In the modern ocean, selenium isotopes share some similarity with molybdenum isotopes, where sediments from restricted, anoxic basins form a complementary (positive) reservoir to isotopically negative sediments deposited in the open, oxic ocean (Fig. 6.7). The transition between the Proterozoic and modern selenium cycle may have occurred during the oxygenation of the deep ocean in the Neoproterozoic (Sahoo *et al.*, 2012), but given our present data set we cannot rule out the possibility that it took place as late as the mid-Paleozoic. In fact, the latter case is supported by the high redox potential of selenium (Fig. 6.1) and the evidence that atmospheric and marine oxygen levels increased to modern levels during the Devonian (Dahl *et al.*, 2010). Hence selenium may have been one of the last redox sensitive elements to adopt a fully oxic biogeochemical cycle in the ocean.

In summary, bulk selenium isotope ratios in mudrocks are consistent with the general view of Earth's redox evolution (Lyons *et al.*, 2014), but they have relatively limited utility as a paleoredox proxy for two major reasons. First, whole rock analyses are likely to represent mixtures of heterogeneous selenium phases, and in many siliciclastic samples, organic Se^{-II} is probably always one of the major phases. If organic Se^{-II} captures the composition of seawater (Section 6.4.1), then it will mask any negative fractionations carried by inorganic Se^{-II} or Se⁰. Second, selenium isotopes appear to have been fractionated during transport to the ocean or along ocean margins for most of Earth's history, except perhaps in the Phanerozoic where the total average of marine $\delta^{82/78}\text{Se}$ values is close to average crust, indicating quantitative transfer between reservoirs. Without spatial resolution it will thus be impossible to know the source composition of selenium entering a specific ocean basin. Results from a single site can therefore not readily be extrapolated to the global ocean. However, large datasets, such as the one

presented in this paper, have the potential to reveal trends. Our results thus further support the onset of oxidative weathering in the late Archean and ocean oxygenation in the Neoproterozoic through the mid-Paleozoic.

Acknowledgments

This project was financially supported by the University of Washington Royalty Research Fund and the National Science Foundation grant EAR0921580 to RB, as well as by the Virtual Planetary Laboratory at the University of Washington. We thank the UW Isotope Geochemistry Lab and the UW Isolab for technical support.

Author contributions

R. Buick supervised the project and provided samples, S. Poulton, B. Guy, B. Wing, L. Kah, A. Knoll, H. Machel, S. Schoepfer, J. Foriel and I. Montanez provided additional samples, E. Stüeken collected samples, carried out the analyses, interpreted the data and wrote the manuscript with advice and contributions from R. Buick.

Tables

Table 6.1: Major stratigraphic units analyzed in this study. Uncertainties are reported as 1σ

Unit	Location	Age [Gyr]	Setting	n	$\delta^{82/78}\text{Se}$ [‰]	log(TSe) [ppm]	log(S/Se) [%/ppm]
Soanesville Gp.	Australia	3.19	upper slope, open marine	9	$+0.64 \pm 0.18$	-0.89 ± 0.10	-0.55 ± 0.14
		2.94-2.92	fluvial	5	$+0.30 \pm 0.19$	-0.59 ± 0.22	$+0.10 \pm 0.37$
Witwatersrand Spgp.	S. Africa	2.96-2.87	proximal marine, possibly restricted epeiric sea	8	$+0.74 \pm 0.28$	-0.66 ± 0.26	-0.22 ± 0.45
		2.96-2.94	distal marine, epeiric sea, open to the ocean	5	$+0.63 \pm 0.51$	-0.46 ± 0.49	-0.34 ± 0.45
Pongola Spgp.	S. Africa	2.90	epeiric sea connected to the ocean, possibly restricted	2	$+0.41 \pm 0.44$	-0.76 ± 0.09	$+0.05 \pm 0.04$
Kidd Creek deposit	Canada	2.71	open marine shelf	5	$+0.07 \pm 0.22$	$+0.55 \pm 0.35$	
			volcanogenic massive sulfide deposit (VMS)	5	$+0.28 \pm 0.24$	$+2.73 \pm 0.78$	
Fortescue Gp.	Australia	2.78-2.72	fluvio-lacustrine	19	-0.28 ± 0.67	$+0.07 \pm 0.58$	-0.78 ± 0.67
		2.65	open marine shelf, onshore	7	$+0.32 \pm 0.12$	-0.23 ± 0.21	
		2.65	open marine shelf, offshore	21	$+0.38 \pm 0.30$	-0.02 ± 0.40	$+0.27 \pm 0.14$
Ghaap Gp.	S. Africa	2.56-2.52	open marine shelf	15	$+0.41 \pm 0.33$	$+0.23 \pm 0.51$	-0.08 ± 0.63
Hamersley Gp.	Australia	2.49	open marine shelf	3	$+0.46 \pm 0.66$	$+0.16 \pm 0.47$	
Pretoria Gp.	S. Africa	2.32	epeiric sea, open to the ocean	8	$+1.13 \pm 0.56$	$+0.43 \pm 0.78$	-0.33 ± 0.51
Namoon Gp.	Australia	1.9	intracontinental rift basin, possibly restricted	8	-0.07 ± 0.13	$+0.47 \pm 0.68$	-0.07 ± 0.13
Animikie Gp.	Canada	1.87-1.84	epeiric sea, open to the ocean	13	$+0.40 \pm 0.46$	-0.28 ± 0.44	$+0.23 \pm 0.42$
Belt Spgp.	USA	1.47	intracontinental rift basin, possibly restricted, onshore	8	$+0.73 \pm 0.33$	-1.09 ± 0.34	-0.34 ± 0.49
			intracontinental rift basin, possibly restricted, offshore	7	-0.07 ± 0.43	-0.75 ± 0.39	-0.49 ± 0.62
Roper Gp.	Australia	1.36	epeiric sea, open to the ocean, offshore	7	$+0.53 \pm 0.20$	-0.13 ± 0.71	-0.01 ± 0.14
El Mreiti Gp.	Mauritania	1.10	epeiric sea, open to the ocean, intermediate depth	5	$+0.45 \pm 0.52$	$+0.58 \pm 0.69$	-0.14 ± 0.70
Stephen Fm.	Canada	0.54	open marine shelf, submarine fan	1	+0.96	-1.11	+0.23
Woodbend Gp.	Canada	0.36	epeiric sea, open to the ocean	5	$+0.04 \pm 0.47$	-0.27 ± 0.86	$+0.21 \pm 0.46$
Wocklum Limestone	Germany	0.34	epeiric sea, open to the ocean	2	-0.72 ± 0.28	-1.46 ± 0.14	
Phosphoria Fm.	USA	0.26	epeiric sea, open to the ocean	3	$+0.01 \pm 0.74$	-0.66 ± 0.23	
Peril/Sandilands Fm.	Canada	0.20	open marine shelf	12	$+0.23 \pm 0.34$	$+0.64 \pm 0.45$	-0.79 ± 0.48
Fidalgo Complex	USA	0.16	deep open basin, turbidite (preserved as ophiolite)	1	-0.29	-0.36	-0.50
Morrison Fm.	USA	0.15	interior seaway, possibly restricted	1	-1.20	-1.05	
North Atlantic	Portugal	0.12	open marine margin, submarine fan	8	-0.41 ± 0.23	$+0.01 \pm 0.26$	-0.58 ± 0.30
Nanaimo Gp.	USA	0.08	open marine shelf, turbidite	1	+0.43	-0.31	-0.63
Mowry/Eagle/Cody Fm.	USA	0.10-0.07	interior seaway, possibly restricted	4	-0.44 ± 0.65	-0.53 ± 0.22	-1.20 ± 0.13
Hell Creek/Tullock Fm.	USA	0.065	fluvio-lacustrine	4	$+0.25 \pm 0.57$	-0.06 ± 0.36	

Table 2: Long-term averages of individual data points from open marine basins.

	$\delta^{82/78}\text{Se}$ [‰]	TSe [ppm]	S/Se [wt%/ppm]
mid-Archean (3.19-2.87Gyr)	+0.62 ± 0.27	$10^{-0.76 \pm 0.21}$	$10^{-0.31 \pm 0.36}$
late Archean (2.71-2.50Gyr)	+0.35 ± 0.39	$10^{0.16 \pm 0.46}$	$10^{-0.12 \pm 0.59}$
Proterozoic (2.49-1.10Gyr)	+0.45 ± 0.55	$10^{-0.13 \pm 0.78}$	$10^{-0.10 \pm 0.48}$
Phanerozoic (0.54Gyr to modern)	-0.02 ± 0.42	$10^{0.11 \pm 0.70}$	$10^{-0.56 \pm 0.56}$

Figures

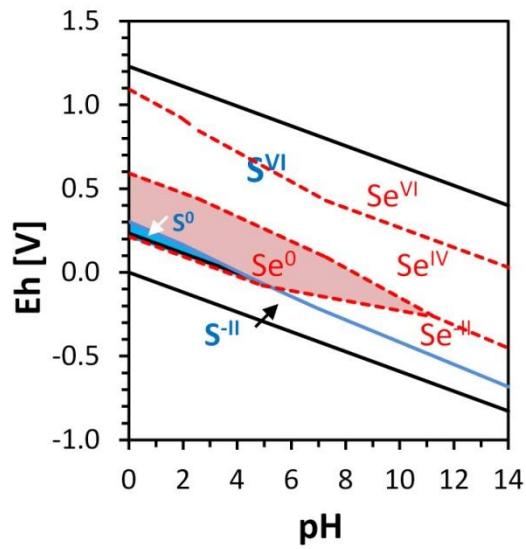


Figure 6.1: Eh-pH diagram of sulfur (10^{-3} M) and selenium (10^{-10} M). Black lines mark the stability field of H₂O and apply to both elements, blue lines are for sulfur species, red dashed lines are for selenium species.

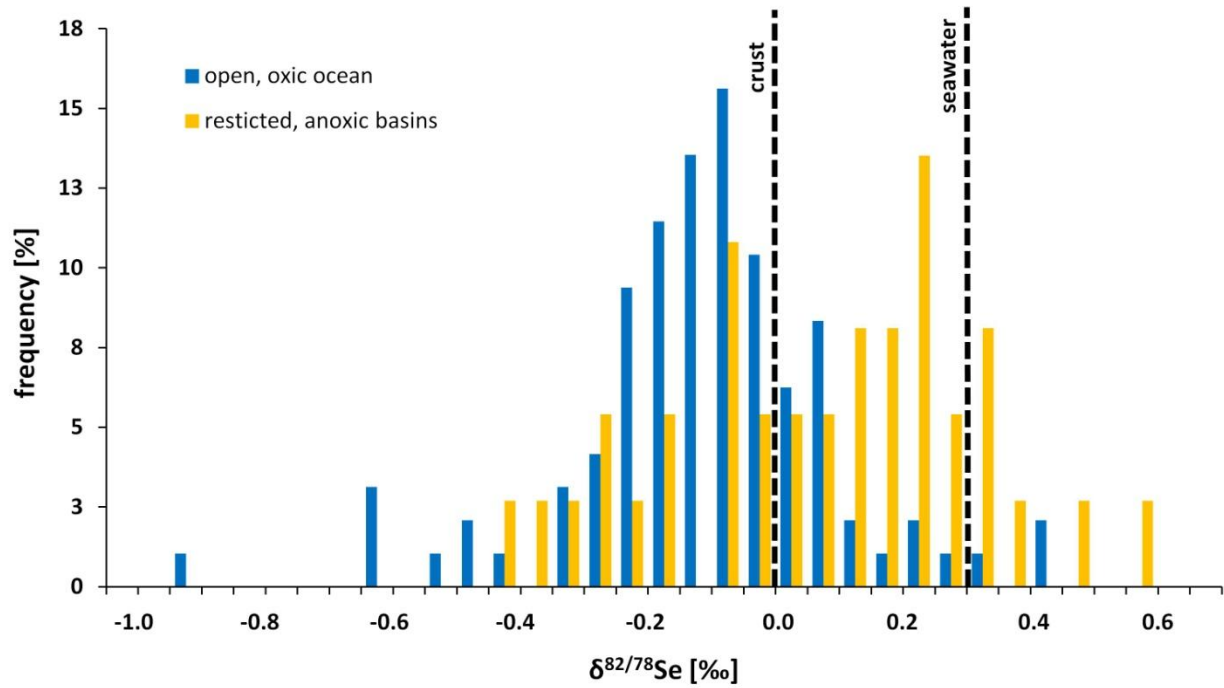


Figure 6.2: Selenium isotopes in open and restricted marine basins over the last 500 kyr. The compositions of the crust and seawater $\text{Se}^{\text{IV/VI}}$ are shown for reference (dashed black lines). Open marine sediments are systematically depleted whereas restricted basins tend to preserve the composition of $\text{Se}^{\text{IV/VI}}$, probably due to more quantitative reduction. See text for references.

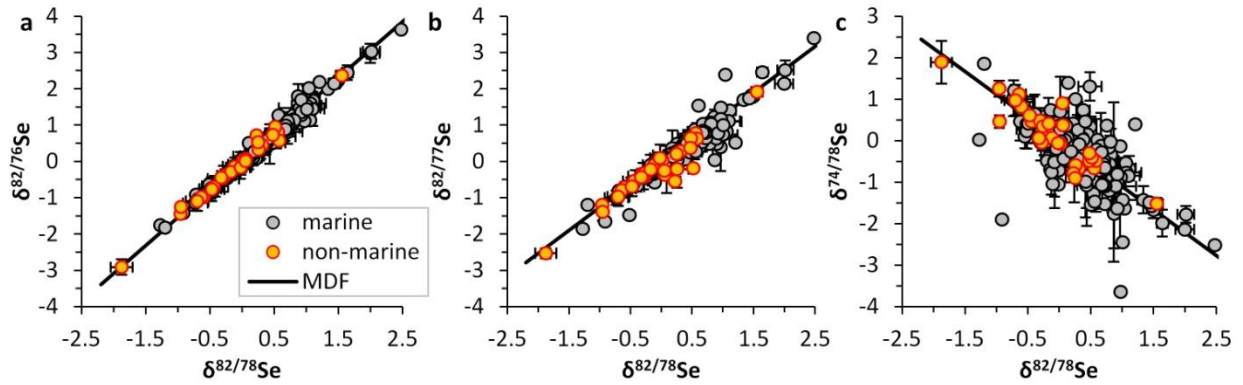


Figure 6.3: Mass-dependent fractionation in selenium isotopes. a: $\delta^{82/76}\text{Se}$ versus $\delta^{82/78}\text{Se}$; b: $\delta^{82/77}\text{Se}$ versus $\delta^{82/78}\text{Se}$; c: $\delta^{82/78}\text{Se}$ versus $\delta^{78/74}\text{Se}$. One outlier with $\delta^{78/74}\text{Se} = +13.7\text{‰}$ is not shown. Residual interferences are the most likely explanation for outliers in panel b and c. We therefore conclude that all four isotope pairs display mass-dependent fractionation. Errors are 1σ .

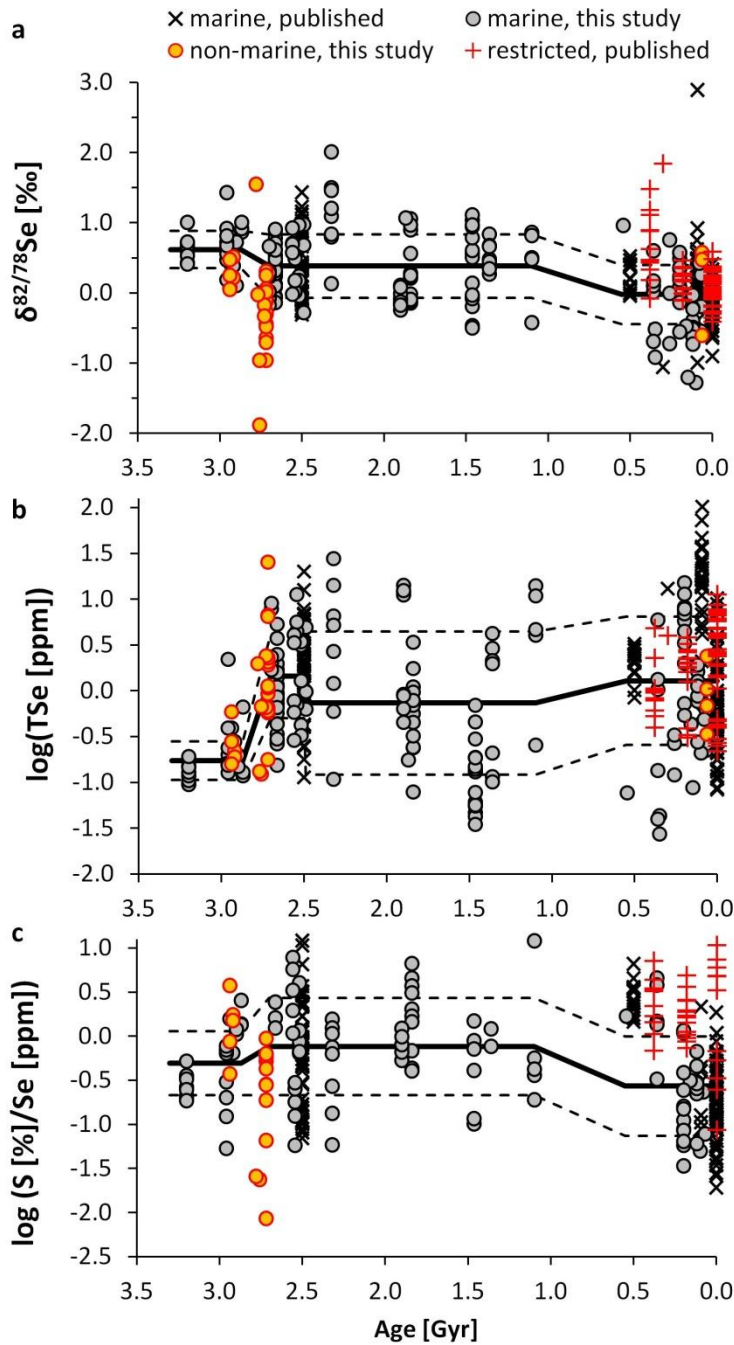


Figure 6.4: Bulk selenium isotope (a), abundances (b), and TS/TSe ratios (c) in mudrocks through time. Horizontal lines mark the total marine average (solid) $\pm 1\sigma$ (dashed) of new and published data.

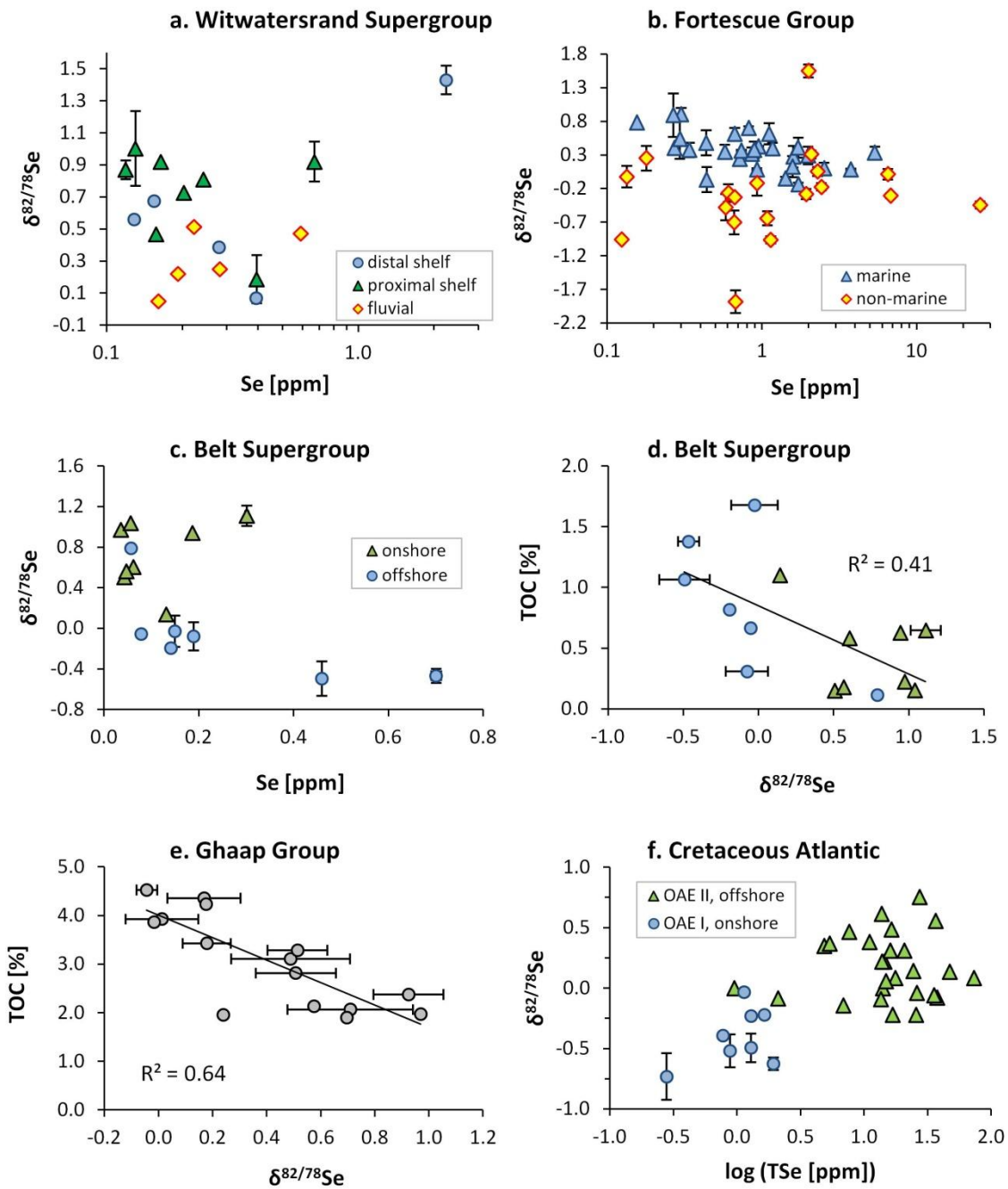


Figure 6.5: Selenium in selected basins. a: Witwatersrand Supergroup; b: Fortescue Group; c and d: Belt Supergroup; e: Ghaap Group; f: Cretaceous Atlantic Ocean, where data from OAE-II are from Mitchell *et al.* (2012). Error bars are 1σ .

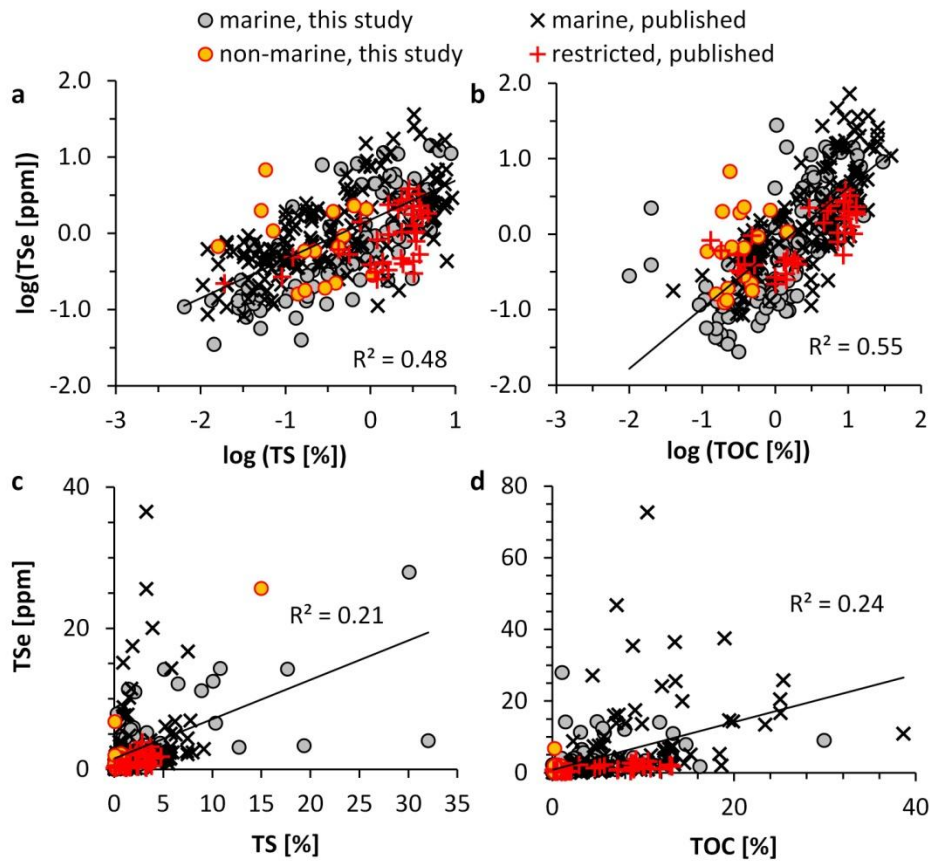


Figure 6.6: Total selenium (TSe) versus total sulfur (TS) and total organic carbon (TOC).

Correlations are significant in logarithmic scale (panel a and b) but not in linear scale (panel c and d).

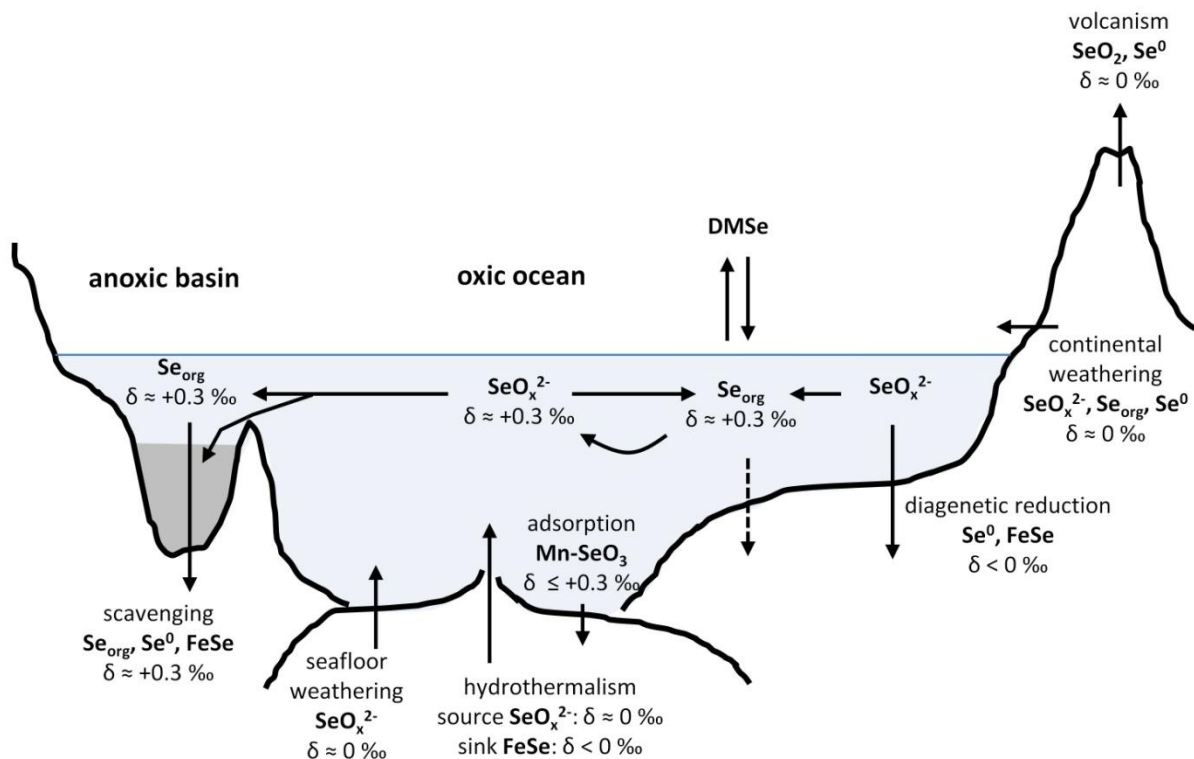


Figure 6.7: Proposed modern marine selenium cycle. Sources to the ocean include continental and seafloor weathering, volcanic emissions and hydrothermal fluids with isotopic composition probably similar to that of the crust. Selenium oxyanions (SeO_x^{2-} , where $x = 3$ for Se^{IV} or 4 for Se^{VI}) sourced from weathering can be partially reduced to Se^0 or inorganic $\text{Se}^{\text{-II}}$ (FeSe) during diagenesis, leading to negative $\delta^{82/78}\text{Se}$ values in sediments under an oxic water column. These negative values may be diluted with isotopically positive organic $\text{Se}^{\text{-II}}$ or adsorbed Se^{IV} , in particular to Mn-oxides (Mn-SeO_3). Reduction and/or assimilation into biomass are quantitative in restricted anoxic basins. Emissions of dimethyl selenide (DMSe) are negligible over geologic timescales. See text for references.

References

- Ader M, Sansjofre P, Halverson GP, Busigny V, Trindade RI, Kunzmann M, Nogueira AC (2014) Ocean redox structure across the Late Neoproterozoic Oxygenation Event: A nitrogen isotope perspective. *Earth and Planetary Science Letters*, **396**, 1-13.
- Anbar AD (2004) Molybdenum stable isotopes: observations, interpretations and directions. *Reviews in Mineralogy and Geochemistry*, **55**, 429-454.
- Bekker A, Holland HD (2012) Oxygen overshoot and recovery during the early Paleoproterozoic. *Earth and Planetary Science Letters*, **317**, 295-304.
- Brenneka GA, Herrmann AD, Algeo TJ, Anbar AD (2011) Rapid expansion of oceanic anoxia immediately before the end-Permian mass extinction. *Proceedings of the National Academy of Sciences*, **108**, 17631-17634.
- Buick R (2008) When did oxygenic photosynthesis evolve? *Philosophical Transactions of the Royal Society B: Biological Sciences*, **363**, 2731-2743.
- Canfield DE, Teske A (1996) Late Proterozoic rise in atmospheric oxygen concentration inferred from phylogenetic and sulphur-isotope studies. *Nature*, **382**, 127-132.
- Chasteen TG, Bentley R (2003) Biomethylation of selenium and tellurium: microorganisms and plants. *Chemical Reviews*, **103**, 1-26.
- Clark SK, Johnson TM (2010) Selenium stable isotope investigation into selenium biogeochemical cycling in a lacustrine environment: Sweitzer Lake, Colorado. *Journal of Environmental Quality*, **39**, 2200-2210.
- Crowe SA, Døssing LN, Beukes NJ, Bau M, Kruger SJ, Frei R, Canfield DE (2013) Atmospheric oxygenation three billion years ago. *Nature*, **501**, 535-538.
- Cutter GA (1982) Selenium in reducing waters. *Science*, **217**, 829-831.
- Cutter GA (1992) Kinetic controls on metalloid speciation in seawater. *Marine Chemistry*, **40**, 65-80.
- Cutter GA, Bruland KW (1984) The marine biogeochemistry of selenium: a re-evaluation. *Limnology and Oceanography*, **29**, 1179-1192.
- Cutter GA, Cutter LS (2001) Sources and cycling of selenium in the western and equatorial Atlantic Ocean. *Deep-Sea Research II*, **48**, 2917-2931.
- Dahl TW, Hammarlund EU, Anbar AD, Bond DP, Gill BC, Gordon GW, Knoll AH, Nielsen AT, Schovsbo NH, Canfield DE (2010) Devonian rise in atmospheric oxygen correlated to the radiations of terrestrial plants and large predatory fish. *Proceedings of the National Academy of Sciences*, **107**, 17911-17915.
- Doblin MA, Baines SB, Cutter LS, Cutter GA (2006) Sources and biogeochemical cycling of particulate selenium in the San Francisco Bay estuary. *Estuarine, Coastal and Shelf Science*, **67**, 681-694.
- Ellis AS, Johnson TM, Herbel MJ, Bullen T (2003) Stable isotope fractionation of selenium by natural microbial consortia. *Chemical Geology*, **195**, 119-129.
- Fan HF, Wen H, Hu M, Zhao H (2011) Selenium speciation in Lower Cambrian Se-enriched strata in South China and its geological implications. *Geochimica et Cosmochimica Acta*, **75**, 7725-7740.
- Farquhar J, Bao H, Thiemens M (2000) Atmospheric influence on Earth's earliest sulfur cycle. *Science*, **289**, 756-758.

- Fernandez-Marinez A, Charlet L (2009) Selenium environmental cycling and bioavailability: a structural chemist point of view. *Reviews in Environmental Science and Biotechnology*, **8**, 81-110.
- Gladyshev VN (2012) Selenoproteins and selenoproteomes. In: *Selenium: Its molecular biology and role in human health* (eds Hatfield DL, Berry MJ, Gladyshev VN). Springer Science + Business Media, pp. 109-123.
- Guy BM, Ono S, Gutzmer J, Kaufman AJ, Lin Y, Fogel ML, Beukes NJ (2012) A multiple sulfur and organic carbon isotope record from non-conglomeratic sedimentary rocks of the Mesoarchean Witwatersrand Supergroup, South Africa. *Precambrian Research*, **216**, 208-231.
- Hagiwara Y (2000) Selenium isotope ratios in marine sediments and algae: A reconnaissance study. University of Illinois at Urbana-Champaign, Urbana, IL, pp. 62.
- Herbel MJ, Johnson TM, Oremland RS, Bullen T (2000) Fractionation of selenium isotopes during bacterial respiratory reduction of selenium oxyanions. *Geochimica et Cosmochimica Acta*, **64**, 3701-3709.
- Johnson JE, Gerpheide A, Lamb MP, Fischer WW (2014) O₂ constraints from Paleoproterozoic detrital pyrite and uraninite. *Geological Society of America Bulletin*, **126**, 813-830.
- Johnson TM, Bullen T (2003) Selenium isotope fractionation during reduction by Fe(II)-Fe(III) hydroxide-sulfate (green rust). *Geochimica et Cosmochimica Acta*, **67**, 413-419.
- Johnson TM, Bullen T (2004) Mass-dependent fractionation of selenium and chromium isotopes in low-temperature environments. *Reviews in Mineralogy and Geochemistry*, **55**, 289-317.
- Johnson TM, Herbel MJ, Bullen TD, Zawislanski PT (1999) Selenium isotope ratios as indicators of selenium sources and oxyanion reduction. *Geochimica et Cosmochimica Acta*, **63**, 2775-2783.
- Kulp TR, Pratt LM (2004) Speciation and weathering of selenium in Upper Cretaceous chalk and shale from South Dakota and Wyoming, USA. *Geochimica et Cosmochimica Acta*, **68**, 3687-3701.
- Large RR, Halpin JA, Danyushevsky LV, Maslennikov VV, Bull SW, Long JA, Gregory DD, Lounejeva E, Lyons TW, Sack PJ, McGoldrick P, Calver CR (2014) Trace element content of sedimentary pyrite as a new proxy for deep-time ocean-atmosphere evolution. *Earth and Planetary Science Letters*, **389**, 209-220.
- Layton-Matthews D, Leybourne MI, Peter JM, Scott SD, Cousens B, Eglinton B (2013) Multiple sources of selenium in ancient seafloor hydrothermal systems: compositional and Se, S and Pb isotopic evidence from volcanic-hosted and volcanic-sediment-hosted massive sulfide deposits of the Finlayson Lake District, Yukon, Canada. *Geochimica et Cosmochimica Acta*, **117**, 313-331.
- Li X, Liu Y (2011) Equilibrium Se isotope fractionation parameters: A first principle study. *Earth and Planetary Science Letters*, **304**, 113-120.
- Lyons TW, Reinhard CT, Planavsky NJ (2014) The rise of oxygen in Earth's early ocean and atmosphere. *Nature*, **506**, 307-315.
- Mayland HF (1994) Selenium in plant and animal nutrition. In: *Selenium in the environment* (eds Frankenberger Jr. WT, Benson S). Marcel Dekker, Inc., New York.
- Mitchell K, Mason PRD, Van Cappellen P, Johnson TM, Gill BC, Owens JD, Ingall ED, Reichart G-J, Lyons TW (2012) Selenium as paleo-oceanographic proxy: A first assessment. *Geochimica et Cosmochimica Acta*, **89**, 302-317.

- Planavsky NJ, Asael D, Hofmann A, Reinhard CT, Lalonde SV, Knudsen A, Wang X, Ossa Ossa F, Pecoits E, Smith AJB, Beukes NJ, Bekker A, Johnson TM, Konhauser KO, Lyons TW, Rouxel OJ (2014) Evidence for oxygenic photosynthesis half a billion years before the Great Oxidation Event. *Nature Geoscience*, **7**, 283-286.
- Planavsky NJ, McGoldrick P, Scott CT, Li C, Reinhard CT, Kelly AE, Chu X, Bekker A, Love GD, Lyons TW (2011) Widespread iron-rich conditions in the mid-Proterozoic ocean. *Nature*, **477**, 448-451.
- Poulton SW, Canfield DE (2011) Ferruginous conditions: a dominant feature of the ocean through Earth's history. *Elements*, **7**, 107-112.
- Rasmussen B, Buick R (1999) Redox state of the Archean atmosphere: Evidence from detrital heavy minerals in ca. 3250-2750 Ma sandstones from the Pilbara Craton, Australia. *Geology*, **27**, 115-118.
- Reinhard CT, Planavsky NJ, Robbins LJ, Partin CA, Gill BC, Lalonde SV, Bekker A, Konhauser KO, Lyons TW (2013) Proterozoic ocean redox and biogeochemical stasis. *Proceedings of the National Academy of Sciences*, **110**, 5357-5362.
- Ross GM, Villeneuve M (2003) Provenance of the Mesoproterozoic (1.45 Ga) Belt basin (western North America): another piece in the pre-Rodinia paleogeographic puzzle. *Geological Society of America Bulletin*, **115**, 1191-1217.
- Rouxel O, Fouquet Y, Ludden JN (2004) Subsurface processes at the Lucky Strike hydrothermal field, Mid-Atlantic Ridge: evidence from sulfur, selenium, and iron isotopes. *Geochimica et Cosmochimica Acta*, **68**, 2295-2311.
- Rouxel O, Ludden J, Carignan J, Marin L, Fouquet Y (2002) Natural variations of Se isotopic composition determined by hydride generation multiple collector inductively coupled plasma mass spectrometry. *Geochimica et Cosmochimica Acta*, **66**, 3191-3199.
- Rudnick RL, Gao S (2014) Composition of the continental crust. *Treatise on Geochemistry*, **4**, 1-51.
- Sahoo SK, Planavsky NJ, Kendall B, Wang X, Shi X, Scott C, Anbar AD, Lyons TW, Jiang G (2012) Ocean oxygenation in the wake of the Marinoan glaciation. *Nature*, **489**, 546-549.
- Schilling K, Basu A, Johnson TM, Mason PRD, Tsikos H, Mondal SK (2014a) Se isotope signature of Paleoproterozoic banded iron formations. In: *Goldschmidt Conference Abstract # 2207*, Sacramento, CA, USA.
- Schilling K, Johnson TM, Mason PRD (2014b) A sequential extraction technique for mass-balanced stable selenium isotope analysis of soil samples. *Chemical Geology*, doi: 10.1016/j.chemgeo.2014.1004.1014.
- Schilling K, Johnson TM, Wilcke W (2011) Selenium partitioning and stable isotope ratios in urban topsoil. *Soil Science Society of America Journal*, **75**, 1354-1364.
- Schirmer T, Koschinsky A, Bau M (2014) The ratio of tellurium and selenium in geological material as a possible paleo-redox proxy. *Chemical Geology*, doi: 10.1016/j.chemgeo.2014.1003.1005.
- Schoepfer SD, Henderson CM, Garrison GH, Foriel J, Ward PD, Selby D, Hower JC, Algeo TJ, Shen Y (2013) Termination of a continent-margin upwelling system at the Permian-Triassic boundary (Opal Creek, Alberta, Canada). *Global and Planetary Change*, **105**, 21-35.
- Shore AJT (2010) Selenium geochemistry and isotopic composition of sediments from the Cariaco Basin and the Bermuda Rise: a comparison between a restricted basin and the

- open ocean over the last 500 ka. In: *Department of Geology*. University of Leicester, Leicester, pp. 307.
- Stüeken EE (2013) A test of the nitrogen-limitation hypothesis for retarded eukaryote radiation: Nitrogen isotopes across a Mesoproterozoic basinal profile. *Geochimica et Cosmochimica Acta*, **120**, 121-139.
- Stüeken EE, Catling DC, Buick R (2012) Contributions to late Archaean sulphur cycling by life on land. *Nature Geoscience*, **5**, 722-725.
- Stüeken EE, Foriel J, Nelson BK, Buick R, Catling DC (2013) Selenium isotope analysis of organic-rich shales: advances in sample preparation and isobaric interference correction. *Journal of Analytical Atomic Spectrometry*, **28**, 1734-1749.

Appendix to Chapter 6

Table A6.1: New selenium isotopic and abundance data presented in this study. Where standard deviations are missing, samples were only analyzed once.

sample ID	unit	Age [Myr]	TSe [ppm]	σ [ppm]	$\delta^{82/78}\text{Se}$ [‰]	σ [‰]	$\delta^{82/76}\text{Se}$ [‰]	σ [‰]	$\delta^{82/77}\text{Se}$ [‰]	σ [‰]	$\delta^{74/78}\text{Se}$ [‰]	σ [‰]
marine samples:												
Kcl 120702-6	Clagget Fm	70	0.26		0.26		0.45		0.49		1.00	
Kc 120702-4	Cody Fm	70	0.63	0.00	-0.55	0.13	-0.84	0.23	-0.74	0.11	0.28	0.47
Ke 120702-5	Eagle Fm	70	0.22		-0.19		-0.32		-0.37		0.59	
Sucialsland_111029A	Nanaimo Gp	80	0.49	0.00	0.43	0.16	0.48	0.55	0.69	0.18	-0.98	0.65
Kmfr 120701-1	Mowry Fm	100	0.21		-1.28		-1.75		-1.85		0.03	
DSDP398_1555.17m	North Atlantic	120	1.93	0.05	-0.63	0.05	-0.93	0.05	-0.81	0.02	0.47	0.47
DSDP398_1555.79m	North Atlantic	120	1.28		-0.23		-0.45		-0.35		0.59	
DSDP398_1560.18-1560.15m	North Atlantic	120	0.88	0.00	-0.52	0.14	-0.85	0.16	-0.68	0.13	0.41	0.60
DSDP398_1560.24m	North Atlantic	120	1.28	0.01	-0.49	0.12	-0.76	0.16	-0.63	0.19	0.68	0.07
DSDP398_1535.29m	North Atlantic	120	0.28	0.00	-0.73	0.19	-1.14	0.21	-1.00	0.20	1.03	0.43
DSDP398_1535.74m	North Atlantic	120	1.13	0.02	-0.03	0.01	-0.07	0.01	-0.13	0.01	-0.33	0.51
DSDP398_1583.27m	North Atlantic	120	0.77	0.00	-0.39	0.02	-0.69	0.00	-0.67	0.04	0.64	0.47
DSDP398_1585.69m	North Atlantic	120	1.64	0.00	-0.22	0.00	-0.39	0.03	-0.35	0.01	0.48	0.24
Jm 120630-3	Morrison Fm	150	0.09		-1.20		-1.82		-1.19		1.85	
Rosario 120708-1	Fidalgo Complex	160	0.43	0.02	-0.29	0.24	-0.47	0.36	-0.40	0.36	-0.05	0.42
QCI_J-12.5	Peril Fm	200	15.17		0.34		0.48		0.43		0.01	
QCI_J-19.4	Peril Fm	200	3.35		0.57		0.83		0.70		-0.08	
QCI_J-52.7	Peril Fm	200	0.73		-0.02		0.01		-0.06		-1.05	
QCI_J-78.7	Peril Fm	200	2.01		0.57		0.85		0.66		-1.12	
QCI_J-87.4	Peril Fm	200	0.54		0.09		0.06		0.02		0.41	
QCI_J-116	Sandilands Fm	200	5.84		-0.14		-0.17		-0.13		0.74	
QCI_J-129.7	Sandilands Fm	200	7.61		0.49		0.75		0.57		0.34	
QCI_J-144	Sandilands Fm	200	11.48		0.24		0.34		0.29		-0.69	
QCI_J-175	Sandilands Fm	200	8.19		-0.55		-0.85		-0.71		0.10	
QCI_J-211	Sandilands Fm	200	6.99		0.19		0.23		0.18		0.27	
QCI_J-226	Sandilands Fm	200	7.91		0.58		0.91		0.71		-0.22	
QCI_J-250	Sandilands Fm	200	4.48		0.36		0.53		0.45		-0.16	
Phos-2 Schoepfer	Phosphoria Fm	260	0.27		0.75		1.13		1.01		0.37	
Phos-3 Schoepfer	Phosphoria Fm	260	0.33		-0.01		-0.11		-0.15		-0.71	
Phos-4 Schoepfer	Phosphoria Fm	260	0.12		-0.72		-0.91		-1.00		1.21	
Wocklum_111218-5	Wocklum Limestone	350	0.03		-0.52		-0.63		-1.47		0.23	
Wocklum_111221-5	Wocklum Limestone	350	0.04		-0.91		-1.42		-1.65		-1.89	
Cynthia_10170ft	Woodbend Gp	360	0.04		0.60		1.24		0.57		-0.02	

Duverney CCS-89	Woodbend Gp	360	1.34	0.01	0.17	0.05	0.25	0.07	0.13	0.04	-0.09	0.31
L-Duverney 11331 ft	Woodbend Gp	360	0.14		0.01		0.11		-0.04		-0.02	
CCS-22	Woodbend Gp	360	1.04	0.01	-0.69	0.03	-1.04	0.05	-0.80	0.06	0.92	0.30
MajeonLake CCS-98b	Woodbend Gp	360	5.96	0.07	0.10	0.24	0.15	0.36	0.17	0.25	-0.27	0.73
BurgessShale_99004	Stephen's Fm	545	0.08	0.00	0.96	0.07	1.44	0.24	0.40	0.67	-1.49	0.98
F4-29	El Mreiti Gp, Tourist Fm	1100	0.26	0.00	0.86	0.02	1.29	0.06	1.22	0.20	-0.99	1.92
Fe-60	El Mreiti Gp, Tourist Fm	1100	4.09	0.10	-0.42	0.20	-0.68	0.28	-0.53	0.29	0.51	0.56
F4-51	El Mreiti Gp, Tourist Fm	1100	14.18	0.07	0.50	0.01	0.76	0.00	0.64	0.06	-0.06	0.65
F4-34	El Mreiti Gp, Tourist Fm	1100	11.00	0.09	0.48	0.13	0.66	0.15	0.60	0.16	-0.14	0.01
F4-45	El Mreiti Gp, Tourist Fm	1100	4.71	0.04	0.82	0.00	1.18	0.04	1.04	0.00	-0.33	0.62
K99_BR1_244.7m	Roper Gp, Maironu Fm	1361	0.12		0.45		0.66		0.25		0.15	
K99_GG1_53.2m	Roper Gp, Velkerri Fm	1361	0.10		0.27		0.57		0.11		-0.82	
K99_U4_82.25m	Roper Gp, Velkerri Fm	1361	0.21		0.48		0.66		0.49		-0.41	
CS-11	Roper Gp, Velkerri Fm	1361	2.93	0.04	0.35	0.11	0.45	0.20	0.46	0.31	-0.27	0.05
CS-6	Roper Gp, Velkerri Fm	1361	4.25	0.08	0.67	0.12	1.01	0.25	0.78	0.13	-0.67	0.13
CS-7	Roper Gp, Velkerri Fm	1361	1.98	0.03	0.66	0.24	0.92	0.35	0.83	0.30	-0.53	0.17
CS-9	Roper Gp, Velkerri Fm	1361	2.15	0.01	0.84	0.02	1.19	0.02	0.84	0.00	-0.70	0.25
Belt_110720-69	Belt Spgp, Chamberlain Fm, onshore	1465	0.04		0.97		1.44		0.81		-3.64	
Belt_110720-51	Belt Spgp, Chamberlain Fm, onshore	1465	0.19		0.94		1.41		1.13		-1.54	
Belt_110715-7	Belt Spgp, Chamberlain Fm, onshore	1465	0.06		0.61		1.10		1.54		0.02	
Belt_110715-13	Belt Spgp, Chamberlain Fm, onshore	1465	0.04		0.51		0.80		0.62		-1.54	
Belt_120701-11	Belt Spgp, Chamberlain Fm, onshore	1465	0.13		0.14		0.17		0.17		1.40	
Belt_110715-14	Belt Spgp, Newland Fm, onshore	1465	0.05		0.56		1.27		0.40		-0.59	
Belt_110720-1	Belt Spgp, Newland Fm, onshore	1465	0.30	0.00	1.11	0.10	1.68	0.19	1.41	0.04	-0.66	0.29
Belt_110717-4	Belt Spgp, Newland Fm, onshore	1465	0.06		1.04		2.02		2.39		-1.63	
Belt_110723-19	Belt Spgp, Greyson Fm, offshore	1465	0.14		-0.19		-0.29		-0.28		-0.48	
Belt_110722-23	Belt Spgp, Newland Fm, offshore	1465	0.06		0.79		1.28		0.92		-1.20	
Belt_110723-1	Belt Spgp, Newland Fm, offshore	1465	0.70	0.01	-0.47	0.07	-0.72	0.16	-0.65	0.07	0.55	0.22
Belt_110723-4	Belt Spgp, Newland Fm, offshore	1465	0.08		-0.05		-0.18		-0.01		-0.39	
Belt_110723-6	Belt Spgp, Newland Fm, offshore	1465	0.19	0.00	-0.08	0.14	-0.07	0.18	-0.09	0.11	-0.49	0.85
Belt_110723-11	Belt Spgp, Newland Fm, offshore	1465	0.46	0.01	-0.49	0.17	-0.75	0.28	-0.70	0.16	0.42	0.37
Belt_110723-12	Belt Spgp, Newland Fm, offshore	1465	0.15	0.00	-0.03	0.15	-0.11	0.37	0.08	0.17	0.44	0.08
98-1_05-01	Animikie Gp, Rove Fm	1840	0.79		0.97		1.27		1.49		-0.79	
98-1_05-8	Animikie Gp, Rove Fm	1840	3.42	0.06	0.56	0.05	0.86	0.06	0.79	0.15	-0.63	0.19
98-1_05-10	Animikie Gp, Rove Fm	1840	1.77	0.04	0.29	0.12	0.30	0.23	0.24	0.39	-0.01	0.64
98-1_05-19	Animikie Gp, Rove Fm	1840	0.32		0.25		0.32		0.10		-0.29	
98-1_05-25	Animikie Gp, Rove Fm	1840	0.08		0.90		1.06		0.49		13.70	
98-1_05-27	Animikie Gp, Rove Fm	1840	0.24		-0.14		-0.27		-0.30		-0.69	
89-MC-1_05-50	Animikie Gp, Rove Fm	1840	0.24		-0.11		-0.18		-0.57		-1.05	
89-MC-1_05-60	Animikie Gp, Rove Fm	1840	0.70		0.24		0.36		0.30		-0.53	
89-MC-1_05-65	Animikie Gp, Rove Fm	1840	0.45	0.00	-0.02	0.01	-0.04	0.01	-0.13	0.06	-0.12	0.02
89-MC-1_05-57	Animikie Gp, Rove Fm	1840	1.11		0.22		0.08		0.04		0.42	
89-MC-1_05-59	Animikie Gp, Rove Fm	1840	0.98		-0.09		-0.23		-0.21		-0.14	

89-MC-1_05-61	Animikie Gp, Rove Fm	1840	0.57		1.06		1.13		0.82		-0.54	
120727-16	Animikie Gp, Gunflint Fm	1870	0.18	0.01	1.07	0.24	1.60	0.33	1.10	0.25	-0.76	
PC_39_60.5	Nanooma Gp	1900	0.92	0.02	-0.01	0.10	0.00	0.17	-0.24	0.03	0.00	0.22
PC_40_63	Nanooma Gp	1900	0.46	0.00	-0.13	0.04	-0.12	0.01	-0.33	0.08	-0.75	0.54
PC_43_72	Nanooma Gp	1900	0.64	0.00	-0.24	0.04	-0.38	0.03	-0.45	0.11	0.10	0.45
PC_57_454	Nanooma Gp	1900	11.17	0.13	-0.16	0.00	-0.23	0.01	-0.32	0.05	-0.01	0.26
PC_59_457	Nanooma Gp	1900	14.31	0.32	-0.08	0.00	-0.11	0.02	-0.19	0.11	0.02	0.12
PC_63_466	Nanooma Gp	1900	12.15	0.22	0.11	0.03	0.17	0.11	0.09	0.09	-0.12	0.14
PC44-73	Nanooma Gp	1900	0.89	0.03	0.09	0.08	-0.01	0.11	-0.22	0.65	0.36	0.68
PC58-456	Nanooma Gp	1900	12.50	0.25	-0.18	0.13	-0.29	0.21	-0.09	0.28	0.46	0.06
EBA2_1335.4/1336.5_T	Pretoria Gp, Rooihoogte Fm	2322	6.58	0.06	0.13	0.08	0.16	0.17	0.09	0.10	-0.32	0.14
EBA2_1335.4/1336.5_L	Pretoria Gp, Rooihoogte Fm	2322	2.69	0.04	1.50	0.03	2.24	0.07	1.80	0.10	-1.67	0.20
EBA2_1335.4/1336.5_I	Pretoria Gp, Rooihoogte Fm	2322	5.23	0.01	1.46	0.01	2.17	0.05	1.82	0.02	-1.57	0.13
EBA2_1335.4-1336.5E	Pretoria Gp, Rooihoogte Fm	2322	27.97	0.38	2.01	0.13	3.04	0.21	2.52	0.27	-1.77	0.20
EBA-2#4_1337.5	Pretoria Gp, Rooihoogte Fm	2322	1.22	0.02	1.10	0.18	1.45	0.47	1.12	0.08	-0.84	0.01
EBA-2_1338.3G	Pretoria Gp, Rooihoogte Fm	2322	14.25	0.10	0.80	0.13	1.17	0.16	1.07	0.16	-0.56	0.69
EBA2#4_833.5	Pretoria Gp, Timeball Hill Fm	2322	0.11		1.21		2.19		0.52		0.40	
EBA2_1332.1D	Pretoria Gp, Timeball Hill Fm	2322	0.60		0.84		1.15		0.96		-0.92	
DalesGorge_99067	Hamersley Gp, Dales Gorge Mmb	2490	0.63	0.02	0.68	0.20	1.06	0.30	0.67	0.16	-0.64	0.21
DalesGorge_99068	Hamersley Gp, Dales Gorge Mmb	2490	4.97	0.07	-0.28	0.02	-0.47	0.01	-0.43	0.02	0.45	0.02
DalesGorge_99059	Hamersley Gp, Dales Gorge Mmb	2490	0.99	0.03	0.98	0.01	1.49	0.01	1.09	0.09	-0.88	0.48
GKF01_258.8	Ghaap Gp, Klein Naute Fm	2520	0.43		0.97		1.12		1.17		-0.13	
GKF01_264	Ghaap Gp, Klein Naute Fm	2520	3.45	0.05	-0.04	0.04	-0.20	0.01	-0.08	0.09	0.31	0.15
GKF01_265.1	Ghaap Gp, Klein Naute Fm	2520	3.16	0.07	0.17	0.14	0.11	0.21	0.19	0.07	-0.16	0.16
GKF01_290	Ghaap Gp, Klein Naute Fm	2520	1.30	0.03	0.18	0.01	0.12	0.03	0.37	0.49	0.13	0.31
GKF01_291.0	Ghaap Gp, Klein Naute Fm	2520	0.33		0.24		0.31		0.16		-0.44	
GKF01_447.5	Ghaap Gp, Nauga Fm	2545	5.67	0.08	0.18	0.09	0.24	0.11	0.24	0.13	0.09	0.13
GKF01_448.5	Ghaap Gp, Nauga Fm	2545	4.48	0.10	0.51	0.11	0.69	0.11	0.60	0.02	-0.45	0.09
GKF01_452.3	Ghaap Gp, Nauga Fm	2545	4.37	0.07	0.51	0.15	0.78	0.19	0.26	0.33	-0.31	0.03
GKF01_457.1	Ghaap Gp, Nauga Fm	2545	11.38	0.13	0.49	0.22	0.73	0.29	0.71	0.13	-0.38	0.14
GKF01_467.6	Ghaap Gp, Nauga Fm	2545	0.71	0.02	0.01	0.13	-0.09	0.01	-0.11	0.17	0.70	0.85
GKF01_1344.3	Ghaap Gp, Monteville Fm	2560	0.59		-0.02		-0.15		-0.11		0.36	
GKF01_1354.9	Ghaap Gp, Monteville Fm	2560	0.78	0.01	0.71	0.23	0.82	0.34	0.86	0.12	-0.47	0.25
GKF01_1422.1	Ghaap Gp, Monteville Fm	2560	4.10	0.05	0.92	0.13	1.29	0.10	0.83	0.16	-1.00	0.01
GKF01_1425	Ghaap Gp, Monteville Fm	2560	3.36	0.06	0.57	0.00	0.84	0.06	0.61	0.44	-0.70	0.31
GKF01_1353.3	Ghaap Gp, Monteville Fm	2560	0.29		0.70		0.80		0.81		-0.23	
AIDP2_141.53	Fortescue Gp, Carawine Fm	2665	0.27		0.41		0.70		0.24		0.52	
AIDP2_143.25	Fortescue Gp, Carawine Fm	2665	0.34	0.01	0.38	0.11	0.52	0.11	0.15	0.05	0.75	0.07
AIDP2_198.63	Fortescue Gp, Carawine Fm	2665	0.72	0.00	0.24	0.04	0.33	0.11	0.27	0.08	-0.12	0.04
AIDP2_198.70	Fortescue Gp, Carawine Fm	2665	0.95	0.01	0.43	0.01	0.65	0.09	0.47	0.00	-0.50	0.21
AIDP2_203.07	Fortescue Gp, Carawine Fm	2665	0.57	0.01	0.35	0.10	0.41	0.12	0.19	0.09	-0.04	0.52
AIDP2_245.95	Fortescue Gp, Carawine Fm	2665	0.73	0.01	0.37	0.01	0.53	0.06	0.37	0.02	0.07	0.15
AIDP2_254.26	Fortescue Gp, Carawine Fm	2665	0.93	0.01	0.09	0.01	0.11	0.00	0.05	0.03	-0.21	0.00

AIDP3_68.59	Fortescue Gp, Jeerinah Fm	2665	0.82	0.00	0.71	0.03	0.98	0.08	0.72	0.05	-0.57	0.35
AIDP3_79.78	Fortescue Gp, Jeerinah Fm	2665	1.98	0.03	0.30	0.13	0.41	0.22	0.28	0.23	0.26	0.67
AIDP3_85.4	Fortescue Gp, Jeerinah Fm	2665	2.52	0.03	0.10	0.08	0.13	0.10	0.08	0.09	-0.48	0.06
AIDP3_92.83	Fortescue Gp, Jeerinah Fm	2665	1.59	0.01	0.28	0.16	0.36	0.19	0.22	0.18	-0.31	0.40
AIDP3_106.82	Fortescue Gp, Jeerinah Fm	2665	0.86	0.01	0.32	0.10	0.46	0.19	0.31	0.12	-0.19	0.47
AIDP3_121.47	Fortescue Gp, Jeerinah Fm	2665	0.30	0.01	0.90	0.10	1.39	0.07	0.88	0.04	-0.76	0.51
AIDP3_138.99	Fortescue Gp, Jeerinah Fm	2665	0.44	0.01	0.49	0.19	0.52	0.10	0.32	0.24	1.31	0.35
AIDP3_160.88	Fortescue Gp, Jeerinah Fm	2665	0.67	0.00	0.61	0.09	0.97	0.03	0.39	0.01	-0.33	0.17
AIDP2_299.24	Fortescue Gp, Jeerinah Fm	2665	0.44	0.00	-0.07	0.19	-0.16	0.15	-0.18	0.27	0.11	0.36
AIDP2_310.51	Fortescue Gp, Jeerinah Fm	2665	1.58	0.02	0.13	0.16	0.16	0.20	0.04	0.18	0.08	0.41
AIDP2_321.01	Fortescue Gp, Jeerinah Fm	2665	0.16		0.78		1.05		0.49		-0.16	
AIDP2_344.18	Fortescue Gp, Jeerinah Fm	2665	1.71	0.02	-0.14	0.03	-0.22	0.05	-0.19	0.07	0.06	0.62
AIDP2_352.82	Fortescue Gp, Jeerinah Fm	2665	1.71	0.02	0.41	0.15	0.63	0.15	0.44	0.21	0.47	0.22
AIDP2_363.04	Fortescue Gp, Jeerinah Fm	2665	5.36	0.07	0.34	0.09	0.49	0.11	0.38	0.10	-0.23	0.17
AIDP2_371.8	Fortescue Gp, Jeerinah Fm	2665	1.11	0.01	0.62	0.16	0.95	0.17	0.66	0.23	-0.71	0.45
AIDP2_419.59	Fortescue Gp, Jeerinah Fm	2665	0.29	0.01	0.54	0.29	0.69	0.32	0.34	0.27	-0.95	0.52
AIDP2_430.19	Fortescue Gp, Jeerinah Fm	2665	0.27	0.01	0.89	0.32	1.48	0.44	0.63	0.15	-1.09	0.64
Jeerinah_99019	Fortescue Gp, Jeerinah Fm	2665	1.17	0.02	0.40	0.08	0.57	0.10	0.47	0.01	-0.54	0.04
Jeerinah_99021	Fortescue Gp, Jeerinah Fm	2665	3.75	0.02	0.09	0.01	0.10	0.01	0.06	0.05	0.01	0.17
Jeerinah_99022	Fortescue Gp, Jeerinah Fm	2665	1.42	0.00	-0.05	0.03	-0.14	0.08	-0.21	0.16	-0.19	0.11
Jeerinah_99018	Fortescue Gp, Jeerinah Fm	2665	0.89	0.01	0.38	0.12	0.54	0.18	0.07	0.16	0.02	0.49
KC8_py_vial1_1.8A	Kidd Creek deposit	2700		41.93	0.24	0.01	0.29	0.02	-0.03	0.39	-0.47	1.02
KC29B_po_0.1A	Kidd Creek deposit	2700		2.02	0.23	0.04	0.34	0.11	0.24	0.09	-0.14	0.21
KC48_py_vial1_1.8A	Kidd Creek deposit	2700		3.38	-0.01	0.02	-0.06	0.04	-0.08	0.10	0.21	0.32
KC83A_py_1.8A	Kidd Creek deposit	2700		1.10	0.66	0.01	0.91	0.01	0.54	0.26	-0.12	0.79
KC93_po_vial2_0.1A	Kidd Creek deposit	2700		3.27	0.26	0.13	0.31	0.13	0.05	0.10	-0.66	0.14
Z-80-2-68.5	Kidd Creek deposit	2700	2.04	0.02	0.31	0.02	0.44	0.04	0.29	0.03	-0.08	0.11
Z-80-2-84.7	Kidd Creek deposit	2700	1.70	0.09	-0.08	0.14	-0.16	0.19	-0.19	0.19	-0.51	1.11
Z-80-2-94.4	Kidd Creek deposit	2700	2.34	0.01	0.02	0.09	0.00	0.10	-0.05	0.10	-0.01	0.43
Z-80-2-107.1	Kidd Creek deposit	2700	7.90	0.04	-0.17	0.06	-0.25	0.14	-0.26	0.05	0.20	0.24
KL0039-119.5	Kidd Creek deposit	2700	9.10	0.11	0.29	0.05	0.41	0.07	0.21	0.00	-0.42	0.01
TW6-1749.9m	Witwatersrand Spgp, Booyens Fm	2870	0.12	0.01	0.87	0.06	1.80	0.33	0.04	0.05	-1.76	0.83
TW6-1750.2m	Witwatersrand Spgp, Booyens Fm	2870	0.13	0.01	1.00	0.23	1.54	0.54	0.74	0.13	-1.42	0.02
TW6-1750.9m	Witwatersrand Spgp, Booyens Fm	2870	0.67	0.01	0.92	0.13	1.36	0.13	0.88	0.11	-0.80	0.02
KWA11	Pongola Spgp	2900	0.15		0.72		1.11		0.65		-1.52	
KWA2	Pongola Spgp	2900	0.20		0.11		0.52		-0.01		0.36	
AMI_3343	Witwatersrand Spgp, Roodepoort Fm	2920	0.28		0.39		0.63		0.55		-0.85	
AMI_6821	Witwatersrand Spgp, Afrikander Fm	2940	0.39		0.07		0.13		-0.01		-0.44	
TF1_3035	Witwatersrand Spgp, Brixton Fm	2960	0.20		0.73		0.96		0.83		-1.09	
TF1_3670	Witwatersrand Spgp, Parktown Fm	2960	0.16		0.47		0.71		0.25		-0.84	
TF1_710	Witwatersrand Spgp, Parktown Fm	2960	0.13		0.56		0.81		0.28		-1.46	
TFI_3780	Witwatersrand Spgp, Parktown Fm	2960	0.15		0.68		0.86		1.03		-0.64	
TF1_3790	Witwatersrand Spgp, Parktown Fm	2960	2.23	0.02	1.43	0.09	2.15	0.14	1.75	0.03	-1.48	

TFI_4400	Witwatersrand Spgp, Parktown Fm	2960	0.24		0.81		1.14		1.04			-0.02	
TF1_09_4410	Witwatersrand Spgp, Parktown Fm	2960	0.16		0.92		1.70		0.78				-1.63
TF1_09_4430	Witwatersrand Spgp, Parktown Fm	2960	0.39	0.00	0.19	0.15	0.28	0.21	0.13	0.22			-0.26
Soanesville_97SSD32-06	Soanesville Gp, Paddy Market Fm	3200	0.10		1.01		1.45		1.01				-2.44
Soanesville_97SSD32-21	Soanesville Gp, Paddy Market Fm	3200	0.19	0.00	0.72	0.12	1.01	0.17	0.80	0.08			-0.65 0.57
Soanesville_97SSD51-03	Soanesville Gp, Paddy Market Fm	3200	0.10		0.71		1.11		0.80				-1.06
Soanesville_96049	Soanesville Gp, Paddy Market Fm	3200	0.15	0.00	0.43	0.15	0.64	0.28	0.52	0.12			-1.07 0.98
Soanesville_96050	Soanesville Gp, Paddy Market Fm	3200	0.10	0.00	0.68	0.04	0.99	0.08	0.85	0.06			-1.06 0.57
Soanesville_96051	Soanesville Gp, Paddy Market Fm	3200	0.12	0.00	0.59	0.11	0.87	0.16	0.73	0.09			-0.21 0.73
Soanesville_96052	Soanesville Gp, Paddy Market Fm	3200	0.13	0.00	0.67	0.04	0.89	0.11	0.80	0.08			-0.28 0.06
Soanesville_96055	Soanesville Gp, Paddy Market Fm	3200	0.15	0.00	0.53	0.05	0.75	0.07	0.64	0.06			-0.57 0.33
Soanesville_96056	Soanesville Gp, Paddy Market Fm	3200	0.15	0.00	0.42	0.03	0.63	0.12	0.50	0.03			-0.98 0.86
non-marine data:													
AB-KT-10	Hell Creek Fm	65	1.05		-0.60		-0.97		-0.71				0.82
AB-KT-4	Hell Creek Fm	65	0.34		0.56		0.82		0.78				-0.66
AB-KT-5	Hell Creek Fm	65	0.69		0.58		0.57		0.64				-0.49
AB-KT-6	Hell Creek Fm	65	2.40		0.48		0.75		0.65				-0.49
99042_Se	Fortescue Gp,Tumbiana Fm	2720	0.93	0.02	-0.12	0.18	-0.14	0.24	-0.10	0.17			0.08 0.45
99044_Se	Fortescue Gp,Tumbiana Fm	2720	25.69	0.87	-0.44	0.05	-0.70	0.06	-0.53	0.05			0.47 0.25
Tumbiana_99037	Fortescue Gp,Tumbiana Fm	2720	1.93	0.00	-0.28	0.08	-0.39	0.11	-0.41	0.02			-0.04 0.20
Tumbiana_99045	Fortescue Gp,Tumbiana Fm	2720	2.08	0.02	0.31	0.06	0.45	0.13	0.29	0.05			-0.67 0.21
Tumbiana_99046	Fortescue Gp,Tumbiana Fm	2720	1.08	0.01	-0.64	0.11	-0.98	0.15	-0.79	0.12			1.13 0.08
Tumbiana_99024	Fortescue Gp,Tumbiana Fm	2720	6.77	0.05	-0.30	0.04	-0.45	0.05	-0.33	0.00			0.49 0.30
Tumbiana_99038	Fortescue Gp,Tumbiana Fm	2720	0.66	0.02	-0.70	0.18	-1.09	0.27	-0.96	0.26			0.98 0.37
Tumbiana_99039	Fortescue Gp,Tumbiana Fm	2720	0.58	0.01	-0.48	0.20	-0.76	0.33	-0.69	0.26			0.62 0.32
Tumbiana_99040	Fortescue Gp,Tumbiana Fm	2720	2.29	0.03	0.06	0.06	0.08	0.11	-0.36	0.09			0.38 0.16
Tumbiana_99043	Fortescue Gp,Tumbiana Fm	2720	0.18	0.01	0.25	0.19	0.33	0.29	-0.21	0.51			-0.58 0.13
Tumbiana_130707-8	Fortescue Gp,Tumbiana Fm	2720	1.14	0.00	-0.96	0.05	-1.43	0.10	-1.20	0.07			1.26 0.19
Tumbiana_130712-4	Fortescue Gp,Tumbiana Fm	2720	0.60	0.01	-0.26	0.13	-0.38	0.15	-0.32	0.06			0.35 0.20
Tumbiana_130712-5	Fortescue Gp,Tumbiana Fm	2720	6.50	0.00	0.02	0.08	0.03	0.10	0.03	0.06			-0.07 0.25
Kylena_130708-6	Fortescue Gp, Kylena Fm	2730	2.42	0.02	-0.17	0.05	-0.28	0.07	-0.21	0.02			0.42 0.62
Kylena_130708-7	Fortescue Gp, Kylena Fm	2730	0.66	0.01	-0.33	0.04	-0.45	0.07	-0.43	0.04			0.07 0.04
Hardey_96039	Fortescue Gp, Hardey Fm	2760	0.12	0.01	-0.96	0.02	-1.25	0.04	-1.38	0.24			0.46 0.15
Hardey_96041	Fortescue Gp, Hardey Fm	2760	0.67	0.02	-1.88	0.17	-2.91	0.21	-2.53	0.14			1.89 0.51
MtRoeTuffAmygdale_81044	Fortescue Gp, MtRoe Fm	2770	0.13	0.01	-0.02	0.16	-0.15	0.20	0.10	0.37			-0.05 0.14
sub-MtRoe_21003	Fortescue Gp, Belary Fm	2780	1.99	0.00	1.55	0.09	2.37	0.13	1.92	0.11			-1.52 0.14
Wits_376_BABI	Witwatersrand Spgp, Rietkuil Fm	2920	0.22		0.52		0.96		-0.18				-0.41
Wits_411_BABI	Witwatersrand Spgp, Rietkuil Fm	2920	0.19		0.22		0.72		-0.54				-0.78
Wits_3323_BABI	Witwatersrand Spgp, Coronation Fm	2940	0.28		0.25		0.54		0.21				-0.89
Wits_3672_BABI	Witwatersrand Spgp, Promise Fm	2940	0.16		0.05		0.02		-0.25				0.91
Wits_3796_BABI	Witwatersrand Spgp, Promise Fm	2940	0.59		0.47		0.74		0.38				-0.29

Table A6.2: Auxiliary data. Total arsenic (TAs) concentrations are not well calibrated and should only be used as an approximation.

sample ID	TAs [ppm]	σ [ppm]	TS [%]	$\delta^{34}\text{S}$ [‰]	TOC [%]	$\delta^{13}\text{C}$ [‰]
marine samples:						
Kcl 120702-6	12.88				0.32	-24.90
Kc 120702-4	15.25	0.53	0.05	-18.01	0.68	-25.77
Ke 120702-5	7.37				0.31	-25.09
Sucialsland_111029A	5.34	0.17	0.11	0.05	0.63	-23.00
Kmfr 120701-1	19.02		0.01	0.03	0.90	-24.84
DSDP398_1555.17m	9.25	0.25	0.49	-22.84	1.11	-25.93
DSDP398_1555.79m	23.05		0.59	-13.82	1.11	-25.93
DSDP398_1560.18-1560.15m	4.88	0.14	0.20	-17.37	0.74	-27.10
DSDP398_1560.24m	15.18	0.64	0.86	-17.32	0.64	-27.29
DSDP398_1535.29m	3.55	0.02	0.08	-29.22	0.56	-23.05
DSDP398_1535.74m	23.50	0.20	0.34	-26.60	0.50	-23.05
DSDP398_1583.27m	5.92	0.24	0.21	-31.35	1.11	-25.47
DSDP398_1585.69m	4.51	0.22	0.10	-24.82	1.23	-25.53
Jm 120630-3	2.52				0.30	-19.81
Rosario 120708-1	5.27	0.11	0.14	-7.39	0.90	-26.78
QCI_J-12.5	19.47		0.88	-33.00		
QCI_J-19.4	9.75		0.54	-27.00		
QCI_J-52.7	5.32		0.80	-23.00		
QCI_J-78.7	8.06		0.78	-32.00		
QCI_J-87.4	4.33		0.63	-34.00		
QCI_J-116	2.94		0.52	-28.00		
QCI_J-129.7	6.23		0.85	-20.00		
QCI_J-144	9.40		1.72	-8.00		
QCI_J-175	3.12		0.70	-32.00		
QCI_J-211	2.01		0.45	-34.00		
QCI_J-226	6.33		0.27	-20.00		
QCI_J-250	3.38		1.10	-34.00		
Phos-2 Schoepfer	1.89					
Phos-3 Schoepfer	2.06					
Phos-4 Schoepfer	0.74					
Wocklum_111218-5	3.77				0.32	-24.22
Wocklum_111221-5	6.66				0.24	-22.77
Cynthia_10170ft	6.25		0.15	10.55	0.19	-26.07
Duverney CCS-89	6.77	0.21	1.81	10.06	1.46	-29.52
L-Duverney 11331 ft	10.17		0.62	-0.47	0.11	-27.09
CCS-22	10.35	0.39	1.53	-6.48	1.39	-29.21
MajeaneLake CCS-98b	11.95	0.91	1.94	2.99	5.08	-28.38
BurgessShale_99004	5.02	0.09	0.13	23.46	0.17	-26.32
F4-29	3.82	0.08	3.10	4.60	1.00	
Fe-60	22.06	1.26	2.30	13.70	1.00	
F4-51	46.00	3.61	5.10	-11.20	11.80	
F4-34	61.63	4.93	2.10	-14.70	13.30	
F4-45	8.93	0.68	2.00	-22.00	13.10	
K99_BR1_244.7m	0.76				0.09	-29.46
K99_GG1_53.2m	0.72				0.24	-31.69
K99_U4_82.25m	1.07				0.51	-32.03
CS-11	15.85	0.08	2.25	10.64	5.11	
CS-6	28.41	1.92			8.92	
CS-7	17.35	0.65			3.27	
CS-9	24.94	0.54	2.62	22.81	3.72	
Belt_110720-69	0.75		0.01	8.31	0.22	-32.48
Belt_110720-51	1.14		0.13	2.82	0.63	-31.45

Belt_110715-7	2.22			0.58	-34.22	
Belt_110715-13	2.49			0.15	-32.38	
Belt_120701-11	6.67		0.01	5.57	1.10	-33.13
Belt_110715-14	8.08				0.18	-32.40
Belt_110720-1	1.71	0.07	0.45	15.18	0.65	-32.23
Belt_110717-4	14.18				0.16	-32.56
Belt_110723-19	5.73				0.82	-28.04
Belt_110722-23	7.13		0.05	10.63	0.12	-19.74
Belt_110723-1	12.01	3.12	0.08	7.66	1.38	-23.61
Belt_110723-4	7.54				0.67	-25.44
Belt_110723-6	4.92	0.02			0.31	-25.31
Belt_110723-11	7.35	0.55			1.07	-25.03
Belt_110723-12	3.29	0.05			1.68	-27.42
98-1_05-01	9.45		0.55	6.77	1.88	
98-1_05-8	45.81	0.59	1.38	4.51	10.22	
98-1_05-10	36.00	1.74	2.98	3.33	16.26	
98-1_05-19	11.46		0.47	11.61	0.44	
98-1_05-25	21.70		0.03	15.21	0.23	
98-1_05-27	4.00		1.60	24.12	0.39	
89-MC-1_05-50	6.85		0.76	20.23	1.06	
89-MC-1_05-60	25.76			13.58	0.98	
89-MC-1_05-65	10.62	0.08	0.92	17.36		
89-MC-1_05-57	25.26		5.07	18.61	0.73	
89-MC-1_05-59	8.68			25.06	1.67	
89-MC-1_05-61	17.04		2.13	21.40	1.31	
120727-16	2.25	0.19			0.88	-33.65
PC_39_60.5	19.81	1.59	1.13	-4.30	2.21	
PC_40_63	17.27	0.18	0.56	-2.58	1.11	
PC_43_72	17.82	0.09	0.43	2.69	2.12	
PC_57_454	71.90	5.66	8.90	2.35	5.72	
PC_59_457	12.98	0.87	10.81	2.91	4.92	
PC_63_466	22.75	1.49	6.50	2.75	7.95	
PC44-73	30.18	1.76	0.88	0.26	1.82	
PC58-456	32.62	0.69	10.07	2.00	5.55	
EBA2_1335.4/1336.5_T	99.22	7.84	10.31	-26.84	3.22	
EBA2_1335.4/1336.5_L	39.30	2.77	2.03	-27.38	2.24	
EBA2_1335.4/1336.5_I	76.00	4.80	3.30	-26.90	2.87	
EBA2_1335.4-1336.5E	283.27	13.40	30.07	-26.34	1.05	
EBA-2#4_1337.5	28.38	0.27	0.33	10.31	1.01	
EBA-2_1338.3G	393.89	13.80	17.67	-27.61	1.43	
EBA2#4_833.5	29.51		0.01	1.02	0.19	
EBA2_1332.1D	35.17		0.08	-3.45	1.17	
DalesGorge_99067	6.66	0.19				
DalesGorge_99068	8.38	0.04				
DalesGorge_99059	0.98	0.00				
GKF01_258.8	7.22		0.37	-3.45	1.98	
GKF01_264	329.32	10.29	4.01	-1.53	4.53	
GKF01_265.1	100.19	2.08	12.70	-1.33	4.36	
GKF01_290	5.19	0.31	0.87	5.15	4.24	
GKF01_291.0	3.20		0.21	7.58	1.96	
GKF01_447.5	39.10	2.02	1.68	-3.73	3.43	
GKF01_448.5	14.56	0.40	1.14	-4.84	3.29	
GKF01_452.3	14.64	0.54	0.78	-2.85	2.82	
GKF01_457.1	15.72	0.23	1.42	12.98	3.11	
GKF01_467.6	13.03	0.55	0.04	-1.93	3.93	
GKF01_1344.3	5.08		1.16	4.99	3.87	
GKF01_1354.9	8.23	0.43	2.58	7.26	2.07	
GKF01_1422.1	349.95	12.59	32.02	0.24	2.38	
GKF01_1425	41.84	0.99	19.36	-2.66	2.14	

GKF01_1353.3	2.77		0.31	6.02	1.90	
AIDP2_141.53	10.94					
AIDP2_143.25	10.20	0.13				
AIDP2_198.63	9.34	0.07				
AIDP2_198.70	12.95	0.55				
AIDP2_203.07	19.47	0.36				
AIDP2_245.95	10.35	0.15				
AIDP2_254.26	15.87	0.18				
AIDP3_68.59	9.14	0.10				
AIDP3_79.78	6.18	0.29				
AIDP3_85.4	8.64	0.43				
AIDP3_92.83	4.92	0.14				
AIDP3_106.82	6.90	0.08				
AIDP3_121.47	3.87	0.08				
AIDP3_138.99	6.65	0.13				
AIDP3_160.88	42.95	0.53				
AIDP2_299.24	6.73	0.01				
AIDP2_310.51	10.88	0.41				
AIDP2_321.01	1.54					
AIDP2_344.18	7.28	0.19				
AIDP2_352.82	23.25	0.96				
AIDP2_363.04	8.97	0.42				
AIDP2_371.8	12.90	0.40				
AIDP2_419.59	1.66	0.02				
AIDP2_430.19	7.48	0.06				
Jeerinah_99019	9.87	0.22	1.88	-3.67	3.87	-40.29
Jeerinah_99021	10.33	0.09	4.68	2.28	7.22	-42.46
Jeerinah_99022	49.14	0.17	3.44	3.15	5.04	-41.56
Jeerinah_99018	2.84	0.13	2.16	4.79	7.01	-41.36
KC8_py_vial1_1.8A		114.91		-0.53		
KC29B_po_0.1A		49.22		0.73		
KC48_py_vial1_1.8A		4.40		-0.27		
KC83A_py_1.8A		6.24		0.24		
KC93_po_vial2_0.1A		107.40		0.16		
Z-80-2-68.5	65.90	1.69			2.33	
Z-80-2-84.7	77.67	1.68			3.33	
Z-80-2-94.4	43.81	0.51			3.48	
Z-80-2-107.1	168.84	1.54			14.70	
KL0039-119.5	328.15	0.94			29.91	
TW6-1749.9m	38.14	0.39	0.30	-0.92	0.33	-37.85
TW6-1750.2m	22.06	0.20	0.17	-1.84	0.56	-38.63
TW6-1750.9m	61.50	1.35	0.92	-1.04	0.75	-39.06
KWA11	3.79		0.18	3.61		
KWA2	0.30		0.21	2.19		
AMI_3343	6.44		0.18	1.90	0.01	-25.30
AMI_6821	8.47		0.62	0.70	0.02	-25.20
TF1_3035	19.31		0.13	1.90	0.11	-27.28
TF1_3670	11.59		0.11	5.40	0.20	-27.70
TF1_710	12.39		0.10	5.60	0.16	-27.10
TFI_3780	0.44					
TF1_3790	38.15	1.15	0.12	4.90	0.02	-25.60
TFI_4400	0.38		0.03	3.00	1.49	-27.77
TF1_09_4410	32.12		0.05	2.80	0.60	-27.50
TF1_09_4430	11.75	1.26	0.08	5.20	0.23	-28.10
Soanesville_97SSD32-06	19.79		0.05	0.79	1.55	-30.72
Soanesville_97SSD32-21	0.47	0.09	0.04	-0.56	1.20	-31.39
Soanesville_97SSD51-03	4.03		0.03	1.94	1.42	-30.58
Soanesville_96049	2.98	0.04	0.03	2.07	1.20	-31.39
Soanesville_96050	1.97	0.01	0.03	1.12	0.76	-31.29

Soanesville_96051	2.85	0.04	0.04	0.65	1.11	-31.10
Soanesville_96052	2.20	0.06	0.03	1.91	0.85	-30.84
Soanesville_96055	3.31	0.04	0.05	0.50	1.98	-30.58
Soanesville_96056	2.63	0.03	0.04	1.66	0.96	-30.84
non-marine samples:						
AB-KT-10	20.56					
AB-KT-4	2.75					
AB-KT-5	5.79					
AB-KT-6	12.50					
99042_Se	4.09	0.38	0.48	-1.45	0.59	-45.54
99044_Se	16.55	2.30	14.98	0.18		
Tumbiana_99037	6.99	1.74	0.36	2.59	0.33	-48.73
Tumbiana_99045	0.65	0.24	0.89	2.72	0.86	-45.05
Tumbiana_99046	1.53	0.30	0.07	2.33	1.47	-48.31
Tumbiana_99024	3.79	0.01	0.06	-0.23	0.24	-44.72
Tumbiana_99038	7.36	0.34	0.42	0.69	0.37	-49.03
Tumbiana_99039	2.06	0.11	0.17	0.82	0.18	-47.17
Tumbiana_99040	4.19	0.02	0.64	-0.58	0.37	-45.72
Tumbiana_99043	2.14	0.03	0.17	-0.38	0.49	-44.63
Tumbiana_130707-8	10.63	0.09				
Tumbiana_130712-4	0.46	0.04				
Tumbiana_130712-5	0.99	0.21				
Kylena_130708-6	4.56	0.06				
Kylena_130708-7	2.57	0.00				
Hardey_96039	17.97	0.65			0.20	-39.90
Hardey_96041	18.43	0.27	0.02	4.04	0.26	-41.18
MtRoeTuffAmygdale_81044	0.73	0.02			0.22	-41.84
sub-MtRoe_21003	20.74	0.34	0.05	4.13	0.19	-39.14
Wits_376_BABI	45.40		0.39	2.90	0.47	-47.37
Wits_411_BABI	43.60		0.29	6.60	0.22	-45.98
Wits_3323_BABI	22.89		1.06	0.40	0.37	-47.06
Wits_3672_BABI	16.10		0.14	2.80	0.16	-45.84
Wits_3796_BABI	32.94		0.22	2.40	0.12	-45.66

Chapter 7: Depression and collapse: Selenium isotope ratios and biological productivity in the late Permian

Abstract

The causes of the greatest known mass extinction in Earth's history in the latest Permian are actively debated. Here we use Se isotopes and abundances in marine mudrocks from an outer-shelf environment to test one of the most commonly quoted hypotheses about the collapse of the biosphere, *i.e.* widespread euxinia in the open ocean. Our data show the most negative excursion in the marine Se isotope record over the past 3.2Gyr, with a minimum of -1.8‰, immediately preceding the major mass extinction horizon. A net fractionation of this magnitude likely resulted from partial reduction of Se oxyanions dissolved in the water column. Due to their low abundance, Se oxyanions are rapidly scavenged in anoxic basins or regions of high biological productivity. The uniquely negative fractionations in this section are therefore a strong indicator for relatively oxygenated conditions at the time when biological productivity declined. The offset between the peak excursion and the major extinction horizon likely reflects a slow-down in ocean circulation, leading to nutrient limitation, which may thus have prohibited a rapid recovery of the biosphere in the early Triassic. Our data are thus consistent with the newly emerging view that euxinia was restricted to ocean margins and probably not responsible for the extinction event.

7.1. Introduction

The late Permian (~250 Myr) featured the largest known mass extinction in Earth's history, yet the causes and consequences are still not well understood (e.g. Erwin *et al.*, 2002; White, 2002). For example, it remains uncertain if the ocean was anoxic before, during or after the extinction, and if net biological productivity actually declined, and if so, if it was a gradual or abrupt change. Perturbations in sulfur isotopes (e.g. Kajiwara *et al.*, 1994; Luo *et al.*, 2010) and widespread occurrences of pyritic black shale (reviewed by White, 2002) have been interpreted as evidence for euxinia (anoxia with abundant dissolved S^{II} in the water column), but new data from transition element abundances and isotopes (Algeo *et al.*, 2010; Algeo *et al.*, 2011; Brennecka *et al.*, 2011; Proemse *et al.*, 2013) suggest that euxinia was localized along marine margins while the global ocean remained oxic. It is therefore uncertain if euxinia was indeed the major kill mechanism (cf. Grice *et al.*, 2005; Kump *et al.*, 2005). Regarding biological productivity, carbon isotopes in carbonates are generally used as a proxy, and the record shows a prominent negative excursion during the extinction interval (reviewed by Korte & Kozur, 2010). This excursion could be a reflection of net productivity decline; however, it could also have been caused by injection of light carbon into the ocean, in particular CH_4 . Despite paleontological evidence of a mass extinction, *i.e.* the disappearance of over 90% of all living marine species, we thus have no independent indication for a decline of biological activity at this time, other than theoretical models of total carbon fluxes (Algeo *et al.*, 2013). Se isotope data may help fill these gaps.

In the modern oxic ocean, Se is mainly present as oxyanions (both Se^{IV} and Se^{VI}), and it shows a nutrient-type profile in the water column with lowest concentrations in the surface layer and nearly constant levels below (Cutter & Cutter, 2001). This behavior reflects the importance

of Se uptake into biomass in the photic zone, forming organic $\text{Se}^{-\text{II}}$, and reoxidation of organic $\text{Se}^{-\text{II}}$ at depth (Cutter & Bruland, 1984). In sediments, especially under anoxic conditions, organic $\text{Se}^{-\text{II}}$ is usually a major component, in addition to Se^0 , inorganic $\text{Se}^{-\text{II}}$ and adsorbed Se^{IV} (Kulp & Pratt, 2004; Fan *et al.*, 2011). In anoxic basins, the organic $\text{Se}^{-\text{II}}$ component is likely enhanced because remineralization of organic matter is suppressed (Cutter, 1982; Cutter, 1992).

Se isotopes are fractionated by up to 25‰ during Se^{VI} and Se^{IV} reduction to Se^0 or inorganic $\text{Se}^{-\text{II}}$ where the residual oxyanions become isotopically enriched (Johnson *et al.*, 1999; Herbel *et al.*, 2000; Ellis *et al.*, 2003; Johnson & Bullen, 2003). It is possible that fractionations are smaller in natural marine environments where the range of observed $\delta^{82/78}\text{Se}$ values is $\sim 5\%$ over all of Earth's history (Chapter 6) and where the supply of Se oxyanions and reductants may be lower. Fractionations associated with assimilation into biomass and Se^{IV} adsorption are minor, up to 0.6‰ (Johnson *et al.*, 1999; Clark & Johnson, 2010). Biomass forming in the photic zone, where Se is quantitatively consumed, may thus record the composition of Se^{IV} and Se^{VI} in seawater, around +0.3‰ (Rouxel *et al.*, 2004; Mitchell *et al.*, 2012). Hence sediments in which organic $\text{Se}^{-\text{II}}$ is dominant would be expected to be isotopically heavier than sediments dominated by Se^0 and/or inorganic $\text{Se}^{-\text{II}}$, provided that the reduced inorganic phases formed in an environment where the supply of Se^{IV} and/or Se^{VI} was not limiting. This is probably the case in the modern open ocean, where sediments are on average 0.4‰ lighter than seawater (Chapter 6). Hence these sediments probably contain a relatively smaller amount of heavy organic $\text{Se}^{-\text{II}}$ and a larger proportion of Se^0 and/or inorganic $\text{Se}^{-\text{II}}$ formed by $\text{Se}^{\text{IV}/\text{VI}}$ reduction during diagenesis. Predominantly heavy sediments from modern and ancient anoxic basins (Mitchell *et al.*, 2012) (Chapter 6), on the other hand, likely contain a larger percentage of organic $\text{Se}^{-\text{II}}$; any inorganic

reduced Se present in those samples probably formed under limited $\text{Se}^{\text{IV/VI}}$ supply, resulting in quantitative reduction with no net negative fractionation.

Hence Se isotopes in bulk sediments alone probably cannot distinguish between high productivity (mostly organic $\text{Se}^{-\text{II}}$ production) and anoxia due to other causes (quantitative $\text{Se}^{\text{IV/VI}}$ reduction), because both scenarios would lead to heavy isotopic values. However, large negative Se isotope fractionations should be limited to mostly oxic environments with an oxic-suboxic interface and with low biological productivity, because in that case (a) the supply of Se oxyanions should be high, leading to non-quantitative reduction with larger net fractionations, and (b) assimilation of Se into biomass should be low, leading to minimal dilution of isotopically light Se^0 or inorganic $\text{Se}^{-\text{II}}$ with heavy organic $\text{Se}^{-\text{II}}$ in sediments. Se isotopes therefore have the potential to test the validity of the newly emerging picture of the latest Permian mass extinction, *i.e.* the collapse of biological productivity under relatively oxic conditions.

In this study, we present whole-rock Se isotope and abundance data from a marine stratigraphic section across the latest Permian extinction horizon. In addition, as a proof of concept, we sequentially extracted different Se phases from one sample and show that they are isotopically distinct, consistent with our interpretation of the bulk data. Sequential extraction analyses thus have the potential to provide additional information and should be revisited in future studies, but we emphasize that the focus of this study is on bulk rocks. Here we show that bulk Se isotopes can be a valuable new biogeochemical proxy in deep time, with a large negative excursion revealing productivity decline in oxygenated ocean waters.

7.2. Geologic Setting

Our samples are from outcrops of the Ranger Canyon and the unconformably overlying Sulphur Mountain Formations in the Western Canada Basin at Opal Creek, Kananaskis Valley, southwest Alberta (Henderson, 1997; Farley *et al.*, 2005; Schoepfer *et al.*, 2012). The unconformity represents a time gap of 5-7 Myr (Schoepfer *et al.*, 2012). The rocks have been only moderately deformed and mildly metamorphosed. Due to erosion during the last ice age, chemical weathering is limited to a thin surface layer, which could be removed with a rock saw. We are therefore confident that our measured isotope ratios are not affected by alteration (cf. Zhu *et al.*, 2014). Lithologies include organic-rich and variably sulfidic shale, siltstone and chert (Fig. 7.1).

The marine sediments were originally deposited in an outer shelf setting along the eastern margin of the Panthalassic Ocean (Henderson, 1997). Nitrogen isotopes and trace metal concentrations suggest that during the mid-Permian this site was located in a zone of coastal upwelling, with moderately high productivity and an oxygen-minimum zone (Schoepfer *et al.*, 2012; Schoepfer *et al.*, 2013). Productivity peaked in the late Permian, resulting in a brief episode of euxinia. Upwelling is then thought to have slowed as the ocean warmed under a CO₂-enriched atmosphere (Schoepfer *et al.*, 2012; Schoepfer *et al.*, 2013). The samples we analyzed span the time interval from when coastal upwelling was still active in the late Permian until recovery in the early Triassic after the mass-extinction event. The extinction event itself is marked by the abrupt disappearance of benthic fauna and bioturbation ~44 cm above the Ranger Canyon-Sulphur Mountain unconformity (Schoepfer *et al.*, 2012) (labeled 'EXT' in Fig. 7.1) whereas the biostratigraphic Permian-Triassic boundary occurs ~1 m above the extinction horizon. Assuming an average sedimentation rate of 2 cm kyr⁻¹ for this section (Farley *et al.*,

2005), the time span between the unconformity and the extinction horizon is approximately 20 kyr, which is close to the residence time of selenium in the modern ocean (26 kyr, Broecker & Peng, 1982).

7.3. Methods

7.3.1. Bulk sample preparation

A detailed description of our sample preparation and analytical protocol is given in Stüeken *et al.* (2013). We used two slightly different preparation procedures (methods D and E in Stüeken *et al.* (2013)) for this sample set, because method development was still in progress during the initial stages of this study. All samples were digested with HF, HClO₄, and HNO₃ and Se was separated from the matrix by filtration through a column of thiol cotton fibers (TCF). The Se was then desorbed with HNO₃, partially evaporated and redissolved in HCl for analysis. The two preparation procedures differ in that some samples were treated with aqua regia after column filtration to further minimize Ge concentrations (method E), whereas most samples were not (method D). But as shown in Table 7.1, we do not observe any systematic differences between the two methods.

7.3.2. Sequential extraction of selenium phases

One sample (position -40 cm) was treated with a sequential extraction protocol to separate three different selenium phases (Fig. 7.2): first adsorbed Se^{IV}, second inorganic Se^{-II} bound to pyrite and possibly Se⁰, and third refractory organic Se^{-II} and residual Se⁰. Traces of Se⁰ may be contained in both fraction two and three because we could not extract it separately. The stratigraphic level of -40 cm was chosen because that part of the section is before any isotopic excursions and so represents background conditions. The protocol was adapted from Kulp &

Pratt (2004) and carried out on four sample aliquots. Initial tests showed that acetic-acid-soluble, phosphate-exchangeable and water-soluble Se (e.g. Martens & Suarez, 1997; Wright *et al.*, 2003; Kulp & Pratt, 2004) were below detection limit (<0.1ppb) and thus were ignored in the final protocol.

* **NaOH-soluble selenium:** Se^{IV} strongly adsorbed to oxides and clay minerals as well as labile organic Se^{-II} compounds are soluble in NaOH (Martens & Suarez, 1997; Kulp & Pratt, 2004).

For extraction of this phase, 5g of rock powder were weighed into 50 ml polypropylene centrifuge tubes and mixed with 50ml of 0.1M NaOH for 2 h in a 90 °C water bath. The powder was kept in suspension with a magnetic stir bar. After cooling to room temperature, the solution containing the desorbed Se was separated by centrifugation for 20 minutes. The residual powder was washed with 20ml DI-H₂O, which was added to the NaOH solution. This solution was then filtered twice through a 0.2µm pore-size filter to remove colloidal particles, acidified with 8.86 ml of 6N HCl, and then passed through a TCF column. All subsequent steps followed the bulk sample protocol (using the method without aqua regia). Because the sample was not subject to oxidation during or after NaOH leaching, any labile organic Se^{-II} extracted by NaOH should not have been captured by the TCF, which is optimized for Se^{IV} (Yu *et al.*, 2002). However, we cannot exclude the possibility that O₂ dissolved in the NaOH or HCl oxidized some of the labile organic Se^{-II} or inorganic reduced Se phases. This fraction will therefore be referred to simply as the NaOH-extract. The residual sample powder was dried in a 60 °C oven over night.

* **Cr-reducible selenium:** Chromium reduction is commonly used to extract inorganic sulfides from bulk rocks (Canfield *et al.*, 1986) and thus would extract inorganic Se^{-II} contained in sulfide minerals. This step may also mobilize Se⁰ as documented for S⁰ (e.g. Gröger *et al.*, 2009). We used a diffusion process adapted from Burton *et al.* (2008), Ulrich *et al.* (1997) and Hsieh &

Shieh (1997). Two grams of rock powder were weighed into a 200ml serum bottle and wetted with a few drops of DI-H₂O. Three 5ml-pyrex test tubes were added to the bottle and filled by a syringe with 4ml of N₂-purged Zn-acetate solution (10% by weight) under a constant stream of N₂-gas. The bottle was then capped with a vacuum-tight rubber septum and evacuated and purged with N₂ three times through a needle. Then 15ml of 12N HCl and 15ml of 2M CrCl₂ were added sequentially through the needle with a syringe. Both solutions were previously purged with N₂-gas for two hours. The CrCl₂-solution was prepared from CrCl₃ by reduction with mossy zinc in 0.5M HCl (Hsieh & Yang, 1989; Hsieh & Shieh, 1997). After addition of all reagents, the serum bottles were sonicated for 20 minutes and placed on an orbital shaker for two days. Sonication was repeated on the second day. Zinc sulfide and ZnSe that precipitated in the Zn-acetate traps were transferred together with residual Zn acetate into a 90ml Teflon beaker and mixed with 10ml HClO₄ and 10ml concentrated HNO₃. The beaker was capped tightly and left at 130°C overnight. Subsequent extraction of selenium with TCF followed the bulk sample protocol. Residual rock powder was transferred from the serum bottle into a centrifuge tube, washed three times with DI-H₂O, and dried at 60 °C overnight.

* **Total residual selenium:** The residual powder contained refractory organic Se^{-II} and residual Se⁰. All rock powder remaining from the Cr-reduction was transferred into a 90 ml Teflon beaker and digested following the same protocol as for bulk samples.

Selenium abundances in each phase were calculated relative to the initial bulk sample, assuming that the total mass loss associated with NaOH desorption is negligible. This assumption is not required for Cr-reduction, because here the remaining rock powder is transferred quantitatively to the subsequent step.

7.3.3. Isotopic analyses

Analyses were carried out by multi-collector inductively-coupled plasma mass-spectrometry (Nu Instruments), where Se was introduced as H₂Se through a cold-vapor hydride generator (Cetac HGX-200). Analytical parameters are described in more detail in Stüeken *et al.* (2013). Instrumental mass bias was corrected by standard-sample bracketing. Interferences with ^{74,76,78}(ArAr), ⁷⁶(AsH) and ^{74,76}Ge were corrected post-analytically (Stüeken *et al.*, 2013). Unless otherwise noted, all results are reported in terms of ⁸²Se/⁷⁸Se relative to NIST SRM 3149:

$$\delta^{82/78}\text{Se} [\text{‰}] = \left(\frac{(^{82}\text{Se}/^{78}\text{Se})_{\text{sample}}}{(^{82}\text{Se}/^{78}\text{Se})_{\text{SRM3149}}} - 1 \right) \cdot 1000 \quad (\text{Eq. 7.1}),$$

because this is the most precise ratio using our protocol. For conversion to the more commonly used ratio $\delta^{82/76}\text{Se}$, $\delta^{82/78}\text{Se}$ values should be multiplied by 1.54. Three-isotope diagrams (Fig. 7.3) show that within error our data plot along the predicted mass-dependent fractionation line, indicating that all major interferences have been corrected and that mass-independent fractionation is absent. Our average precision for $\delta^{82/78}\text{Se}$ was 0.16‰, and the average relative error for total Se concentrations was 7%.

7.3.4. Carbon and sulfur isotope analyses

Data of organic C and total S abundances and isotopes are mostly taken from Schoepfer *et al.* (2013). We added a few additional analyses (at -40, -21, +3, +4, +5, +6 and +8cm) to increase stratigraphic resolution. Sample preparation and analyses were carried out with the same protocol and facilities as described by Stüeken (2013) and Schoepfer *et al.* (2013). For TOC, the average relative error (RE) was 15%, and the average standard deviation for $\delta^{13}\text{C}_{\text{org}}$ was 0.3‰. For total sulfur, the average RE was 7%, and the average standard deviation for $\delta^{34}\text{S}$ was 0.5‰.

7.3.5. Fractionation model description

We used a standard mass balance model of isotope fractionation to provide a framework for a quantitative evaluation of the isotope data. The isotopic composition of complementary oxidized ($\delta^{82/78}\text{Se}^{\text{VI}}$) and reduced ($\delta^{82/78}\text{Se}^{\text{red}}$) selenium phases is a function of the fraction (f) of oxidized Se remaining in the system and the fractionation factor (α) of the reduction reaction (cf. Canfield, 2001). The fractionation factor is related to the maximum fractionation ($\varepsilon \approx \delta^{82/78}\text{Se}^{\text{VI}} - \delta^{82/78}\text{Se}^{\text{red}}$) via the following approximation which is accurate for deltas of a few permil:

$$\varepsilon \approx 1000 \cdot (\alpha - 1) \quad (\text{Eq. 7.2})$$

In an open, steady-state system with progressive reduction, the composition of residual Se^{VI} ($\delta^{82/78}\text{Se}^{\text{VI}}_{\text{res}}$) evolves from its initial value ($\delta^{82/78}\text{Se}^{\text{VI}}_{\text{in}}$) as follows:

$$\delta^{82/78}\text{Se}^{\text{VI}}_{\text{res}} = ((\delta^{82/78}\text{Se}^{\text{VI}}_{\text{in}} / (1-f)) + ((\alpha-1) / \alpha) \cdot 10^3) / ((1/\alpha) + f / (1-f)) \quad (\text{Eq. 7.3})$$

In a closed system, where the Se demand exceeds the supply, isotopic fractionation is described by Rayleigh fractionation:

$$\delta^{82/78}\text{Se}^{\text{VI}}_{\text{res}} = (\delta^{82/78}\text{Se}^{\text{VI}}_{\text{in}} + 1000) \cdot f^{(1-\alpha)} - 1000 \quad (\text{Eq. 7.4})$$

In both systems, the composition of cumulative reduced Se ($\delta^{82/78}\text{Se}^{\text{red}}$) can be obtained by mass balance:

$$\delta^{82/78}\text{Se}^{\text{red}} = (\delta^{82/78}\text{Se}^{\text{VI}}_{\text{in}} - \delta^{82/78}\text{Se}^{\text{VI}}_{\text{res}} \cdot f) / (1-f) \quad (\text{Eq. 7.5})$$

The initial composition of Se^{VI} entering the ocean ($\delta^{82/78}\text{Se}^{\text{VI}}_{\text{in}}$) is assumed to be 0‰, *i.e.* equal to that of bulk Earth (Rouxel et al. 2002, converted to NIST scale after Carignan & Wen, 2007).

The maximum fractionation associated with biotic reduction of Se oxyanions to Se^0 is 14‰ (Johnson & Bullen, 2004), but because unaltered sediments display $\delta^{82/78}\text{Se}$ values within a small range of -2‰ to +2‰ (Johnson & Bullen, 2004; Shore, 2010, this study; Mitchell *et al.*, 2012) (Chapters 6 and 7), it is unknown if fractionations of this magnitude occur under natural marine

conditions with low Se supply. We therefore use 2‰ and 14‰ as the two end-members to calculate typical and extreme values for f (Fig. 7.4).

7.4. Results

7.4.1. Bulk selenium isotope data

Our results show a brief positive and a large negative isotopic excursion leading up to the main extinction horizon (Fig. 7.1, Table 7.2). We divide our dataset into four stages, capturing the time before the positive excursion (-40 to +3.5cm, stage I), the positive excursion itself (+4 to +9cm, stage II), the negative excursion (+10.5 to +46cm, stage III) and the return to stability (+49.9 to 1684cm, stage IV). In stage I, $\delta^{82/78}\text{Se}$ averages $+0.05 \pm 0.31\text{‰}$ ($n = 6$), which is similar to the mean composition of the crust ($+0.01 \pm 0.49\text{‰}$ (Rouxel *et al.*, 2002)). After excluding the data point at +1.5 cm as an outlier (because it lies outside the 2σ -uncertainty range of the other five data points) stage I has a slightly negative average of $-0.07 \pm 0.06\text{‰}$. Apart from this outlier, the $\delta^{82/78}\text{Se}$ record in stage I does not show a pronounced discontinuity across the unconformity. In stage II, $\delta^{82/78}\text{Se}$ increases to $+0.55 \pm 0.21\text{‰}$ ($n = 5$). This small but statistically significant ($p_{\text{one-tailed}} = 0.01$) positive excursion coincides with a pyrite-rich bed and a positive excursion in organic carbon isotopes (Schoepfer *et al.*, 2013). Above the pyrite bed and extending up to the main extinction horizon (stage IV), $\delta^{82/78}\text{Se}$ decreases to a minimum of $-1.8 \pm 0.3\text{‰}$ followed by a steady recovery back to $\sim -0.5\text{‰}$ by the time of peak metazoan extinction. This large negative excursion coincides with declines in $\delta^{34}\text{S}$, $\delta^{13}\text{C}_{\text{org}}$ and total organic carbon (TOC) during this stage (Schoepfer *et al.*, 2012; Schoepfer *et al.*, 2013). In stage IV, $\delta^{82/78}\text{Se}$ gradually increases to around $+0.3\text{‰}$ at the Permian-Triassic boundary (100cm), which is similar to the proposed composition of modern seawater Se^{IV} and Se^{VI} (Rouxel *et al.*, 2004; Mitchell *et*

al., 2012). Both $\delta^{34}\text{S}$ and $\delta^{13}\text{C}_{\text{org}}$ remain low, and TOC reaches values of up to 2%. The transition from stage III to stage IV is gradual and apparently not controlled by facies changes.

7.4.2. Sequential extraction experiment

The three Se extracts from one sample (-40 cm; Table 7.3) show distinct isotopic compositions and abundances (Fig. 7.5). The residual fraction, *i.e.* refractory organic $\text{Se}^{-\text{II}} (\pm \text{Se}^0)$ represents the major component, similar to samples analyzed in other studies (Kulp & Pratt, 2004; Fan *et al.*, 2011). Compared to the bulk sample, this fraction is isotopically slightly enriched by 0.20‰ in $\delta^{82/78}\text{Se}$. The next most abundant species is the Cr-reducible Se (inorganic $\text{Se}^{-\text{II}} (\pm \text{Se}^0)$) followed by NaOH-soluble Se (adsorbed Se^{IV} , possibly oxidized phases). Their relative abundances are comparable to those reported from Cretaceous (Kulp & Pratt, 2004) and Cambrian samples (Fan *et al.*, 2011). Both fractions are isotopically depleted relative to the bulk sample ($\delta^{82/78}\text{Se} = -0.17\text{‰}$) by 0.74‰ and 0.76‰, respectively.

Overall, nearly 92% of the total selenium was recovered by the sequential extraction protocol. The weighted mean of the three fractions has an isotopic composition of $-0.16 \pm 0.02\text{‰}$, *i.e.* only $0.01 \pm 0.11\text{‰}$ heavier than the bulk sample. This very close agreement suggests that the lost 8% belongs to the organic selenide $\pm \text{Se}^0$ fraction, which is so large that an additional 8% would have very little effect on the calculated weighted mean. If so, loss of organic selenides likely occurred during the treatment with NaOH, which has been shown to mobilize organic selenides from black shales and cherts of Cambrian age (Fan *et al.*, 2011). As mentioned above, most this labile organic $\text{Se}^{-\text{II}}$ fraction would have been lost during TCF filtration of the NaOH extract, unless it reacted with O_2 dissolved in the NaOH.

7.5. Discussion

The isotopic excursion in selenium isotopes associated with the latest Permian extinction is more negative than anything recorded so far from the sedimentary rock record over the past 3.2 Gyr (Rouxel *et al.*, 2002; Johnson & Bullen, 2004; Shore, 2010; Mitchell *et al.*, 2012)(Chapters 6 and 7). It is probably the result of a global event, because it coincides with carbon and sulfur isotope excursions that are regarded as global (e.g. Erwin *et al.*, 2002; White, 2002). As proposed in Section 7.1, our data thus indicate a brief interval around the latest Permian extinction event during which the supply of Se oxyanions exceeded the rate of reduction, and organic Se^{-II} production was minor. This finding supports the hypothesis that euxinia was not widespread in the open ocean at this time and that biological productivity temporarily collapsed. In more detail, and combined with other geochemical proxies, we interpret our data as a sequence of events represented by stages I to IV as follows.

7.5.1. Stage I: high-productivity upwelling zone

Stage I (Fig. 7.1) coincides with a period of regional coastal upwelling that caused moderately high productivity and the development of an oxygen minimum zone along the eastern margin of the Panthalassic ocean (Schoepfer *et al.*, 2012; Schoepfer *et al.*, 2013). Bulk $\delta^{34}\text{S}$ is relatively high in stage I, indicative of diagenetic sulfate reduction within the sediment as a closed system rather than in the open water column (Schoepfer *et al.*, 2013). Enrichment in trace elements (including Mo, U, V) however, suggests that the redox state of the water column was too reduced for efficient remineralization of organic matter and thus probably suboxic in parts (Schoepfer *et al.*, 2013). Se in sediments should thus include both organic Se^{-II} as well as inorganic reduced phases produced from a continuous supply of upwelled Se oxyanions. The organic fraction should be isotopically heavy, perhaps similar to modern marine biomass

(+0.3‰; (Mitchell *et al.*, 2012)), while the inorganic phases should be significantly lighter, especially if upwelling continuously replenished Se oxyanions and reduction was non-quantitative. Our results (averaging $-0.07 \pm 0.06\text{‰}$, as described in Section 7.4.1) are indeed consistent with a mixture of these two phases, and they agree well with samples from the upwelling zone of the modern Arabian Sea ($-0.07 \pm 0.08\text{‰}$, Mitchell *et al.*, 2012). A high local Se oxyanions supply is also supported by Se/TOC ratios that are more than one order of magnitude greater than those in modern phytoplankton (Fig. 7.6a). Se concentrations are also high relative to S (Fig. 7.6b), suggesting that Se oxyanions reduction was independent from sulfate reduction and proceeded under suboxic conditions.

The sequential extraction experiment conducted at the -40cm level from this part of the section confirms our interpretation. The Cr-reducible fraction (inorganic $\text{Se}^{\text{II}} \pm \text{Se}^0$; $-0.90 \pm 0.23\text{‰}$) is significantly lighter than the residual fraction (refractory organics $\pm \text{Se}^0$; $0.03 \pm 0.07\text{‰}$). If we had been able to extract Se^0 separately, the residual organic fraction would probably be slightly heavier and capture more accurately the composition of marine biomass. Hence inorganic reduced Se is evidently significantly depleted relative to organic Se^{II} and probably relative to dissolved $\text{Se}^{\text{IV/VI}}$, consistent with partial Se oxyanions reduction.

The isotopically light NaOH soluble fraction (adsorbed Se^{IV} or oxidized reduced phases; $-0.93 \pm 0.23\text{‰}$) is probably not derived from Se^{IV} dissolved in seawater; dissolved Se^{IV} is produced from organic matter remineralization (Cutter & Bruland, 1984), which does not fractionate isotopes (Johnson *et al.*, 1999). It should therefore be isotopically heavy. Instead, if it is adsorbed Se^{IV} , then it is likely derived from Se^{VI} reduction in sediments. In that case, the close agreement between Se^{IV} and inorganic Se^{II} and/or Se^0 would suggest that Se^{VI} -to- Se^{IV} reduction was not quantitative, perhaps because it occurred close to the sediment-water interface, but

further reduction to Se^0 or inorganic $\text{Se}^{-\text{II}}$ was, with the exception of Se^{IV} preserved by adsorption. Alternatively, the close match between the NaOH-extract and the Cr-reducible fraction may indicate that the NaOH extraction partially oxidized some inorganic reduced phases such as Se^0 or $\text{Se}^{-\text{II}}$.

7.5.2. Stage II: euxinia

The positive carbon isotope excursion during stage II (Fig. 7.1) likely marks a pulse in productivity, perhaps due to increased nutrient input by volcanism or (Schoepfer *et al.*, 2013). It coincides with a massive pyrite bed, which has been interpreted as either a result of water column euxinia (Schoepfer *et al.*, 2013) or hydrothermal sulfide addition to the sediment (Schoepfer *et al.*, 2012). Our new analyses show that the pyrite bed is slightly depleted in $\delta^{34}\text{S}$ compared to stage I, which would be consistent with a relatively higher contribution of syngenetic pyrite formed by microbial sulfate reduction in the water column or at the sediment-water interface (Schoepfer *et al.*, 2013). $\delta^{34}\text{S}$ values in the pyrite bed are dissimilar to typical hydrothermal pyrites (Seal, 2006). It is thus likely that stage II marks a brief episode during which coastal upwelling and the supply of sulfate continued to be high while productivity increased, thus resulting in bottom water euxinia and rapid precipitation of sulfide minerals. Water-column euxinia is thought to have developed globally along ocean margins shortly before the mass extinction event (Brennecka *et al.*, 2011), and the short interval of intense pyrite formation in this section is plausibly a local manifestation of this phenomenon.

The positive excursion in $\delta^{82/78}\text{Se}$ to around +0.5‰ during stage II is consistent with anoxic conditions in which Se oxyanions were quantitatively consumed by assimilation in the photic zone and/or reduction below, similar to modern anoxic basins (Cutter, 1982; Cutter, 1992). A large fraction of total Se in these samples is probably in the form of inorganic $\text{Se}^{-\text{II}}$, as

suggested by the high concentrations of both Se and S (Fig. 7.6b). Bulk sedimentary $\delta^{82/78}\text{Se}$ values should thus capture the composition of seawater Se^{VI} in the late Permian, as sediments from restricted anoxic basins do today (Chapter 6). By mass balance, the small positive excursion in $\delta^{82/78}\text{Se}$ at this locality implies an isotopically light selenium sink elsewhere. If euxinia was localized to oxygen minimum zones along continental margins (Algeo *et al.*, 2010; Brennecka *et al.*, 2011; Proemse *et al.*, 2013), then, as in the modern open ocean, the isotopically light sink may have been partial diagenetic reduction in deep marine sediments (Chapter 6). To achieve an isotopic enrichment in residual dissolved Se^{VI} of +0.5‰ by partial reduction, according to our fractionation model (Section 3.5) only 3.5% to 26% of the total Se^{VI} reservoir needs to be reduced (which is $1-f$, expressed as a percentage, in the calculations Fig. 7.4). This relatively small fraction supports the hypothesis that the deep ocean was oxic during this interval and that euxinia and the positive excursion in $\delta^{82/78}\text{Se}$ are a localized feature that would probably not be encountered in the deep ocean (Algeo *et al.*, 2010; Brennecka *et al.*, 2011; Proemse *et al.*, 2013). The high Se/TOC ratios (Fig. 7.6a) also support the conclusion that Se deposition was enhanced by local processes at this site, because if euxinia and Se drawdown had been an ocean-wide phenomenon, then the total marine Se reservoir should have become so small that total concentrations at individual localities should have been minimal. Our isotope and abundance data from stage II thus support the view that euxinia prior to the mass extinction was not widespread (Brennecka *et al.*, 2011).

7.5.3. Stage III: extinction

Above the pyrite interval, $\delta^{13}\text{C}$ begins to decrease and $\delta^{15}\text{N}$ drops off sharply from +9‰ to values around +2-3‰, which has been interpreted as indicating the cessation of coastal upwelling and a decline in productivity (Schoepfer *et al.*, 2012). High TOC/S ratios and the lack

of trace metal enrichment are most consistent with suboxic to oxic conditions in the water column, *i.e.* more oxidized than in the preceding euxinic interval (Schoepfer *et al.*, 2013). The decline in $\delta^{34}\text{S}$ and the occurrence of framboidal pyrite with diagenetic sulfide overgrowth and interstitial carbonate indicates microbial sulfate reduction close to the sediment-water interface at a relatively slower rate of sulfate consumption than during stage II (Schoepfer *et al.*, 2013). Hence sediments were probably anoxic. Negative excursions in carbon and sulfur isotopes are observed globally at this time (Erwin *et al.*, 2002; White, 2002), suggesting that this interval marks a worldwide perturbation in major biogeochemical cycles.

Sedimentary $\delta^{82/78}\text{Se}$ decreases to a minimum of -1.8‰, which is lower than anything reported from other Phanerozoic marine sediments (Chapter 6). It is unlikely that this excursion reflects volcanic input of Se from the Siberian Traps (Campbell *et al.*, 1992) or enhanced erosion rates due to loss of vegetation on land (Ward *et al.*, 2000), because both of those additional selenium sources would have had an isotopic composition near the crustal average of 0‰. Phanerozoic marine sediments are on average not fractionated relative to the crust (Chapter 6), indicating that fractionation during weathering is negligible. The only other type of geological samples known to be isotopically depleted by 2‰ or more relative to the crust are hydrothermal precipitates or highly altered sediments (Rouxel *et al.*, 2004; Wen & Carignan, 2011; Layton-Matthews *et al.*, 2013; Zhu *et al.*, 2014). However, it is unlikely that enhanced hydrothermal fluid input or erosion of hydrothermal deposits caused this excursion, because other elements such as Cu, with short ocean residence times and commonly associated with hydrothermal activity, are close to crustal background levels during stage III and into stage IV (Schoepfer *et al.*, 2013). Supergene alteration (Wen & Carignan, 2011; Zhu *et al.*, 2014) can be ruled out because the selenium isotope excursion correlates well with global excursions in $\delta^{34}\text{S}$ and $\delta^{13}\text{C}$,

and this part of the section does not show any evidence for an unusually high degree of alteration. Below a weathering rind, which was removed during sample preparation, pyrite is well preserved without any sign of oxidation. It is also unlikely that the light $\delta^{82/78}\text{Se}$ values were caused by weathering of altered rocks (cf. Zhu *et al.*, 2014), because then similarly light values should be common throughout Earth's history. The most plausible explanation for a negative excursion of this magnitude in marine sediments is thus partial reduction of Se oxyanions to Se^0 and/or inorganic $\text{Se}^{-\text{II}}$ at the site of deposition.

Preservation of $\delta^{82/78}\text{Se}$ values significantly below the crustal average and the composition of seawater (Section 7.5.4) can only occur if dissolved Se oxyanions are not quantitatively consumed. Given the high uncertainty in natural fractionation factors, the amount of reduction required to explain a value of -1.8‰ may be anywhere between 9% and 96% of the oceanic Se^{VI} reservoir according to our fractionation model (Fig. 7.4). But if the fractionation factor is small (Fig. 7.4a,c), *i.e.* close to the range of $\delta^{82/78}\text{Se}$ values observed in marine sediments, a smaller percentage is more likely. A large fraction of residual Se^{VI} implies that the water column must have been sufficiently oxygenated for dissolved Se^{VI} (and probably Se^{IV}) to be stable in excess concentrations relative to biological demand, which also explains the relatively high Se/TOC ratios in the sediments (Fig. 7.6a). This interpretation is consistent with other geochemical evidence indicating oxic bottom waters across the extinction even (Algeo *et al.*, 2010; Brennecka *et al.*, 2011; Proemse *et al.*, 2013). Sulfur concentrations are not particularly high during this interval (Fig. 7.6b), so Se oxyanion reduction probably occurred independently from sulfate reduction, as in stage I, perhaps at the oxic-suboxic interface in sediments or in bottom waters. A small negative isotope excursion with a minimum of -0.22‰ has been reported by Mitchell *et al.* (2012) for the late Cretaceous Ocean Anoxic Event 2 when

volcanic activity may have increased the supply of nutrients, including selenium (Mitchell *et al.*, 2012). They argue that high nutrient input stimulated productivity, but that Se oxyanions were supplied in amounts beyond the capacity for complete biological reduction. In the Opal Creek section, however, productivity evidently declined during stage III (Schoepfer *et al.*, 2012; Schoepfer *et al.*, 2013), trace metals are not enriched with respect to crustal compositions (Schoepfer *et al.*, 2013) and TOC concentrations are 1-2 orders of magnitude lower than in the late Cretaceous samples studied by Mitchell *et al.* (2012). It is thus more likely that at Opal Creek dissolved Se^{VI/IV} excess resulted not from a high Se supply but instead from a relatively low demand. Because biological assimilation and reduction are the major sinks of Se from the ocean, this decrease in the consumption rate could well have been caused by a decline in biological activity. In other words, Se isotopes probably responded to the worldwide collapse in biological productivity associated with the latest Permian mass extinction. Assuming a small isotopic fractionation factor between 2 and 2.5‰, the isotopic composition of residual dissolved Se^{VI} during the peak of the negative $\delta^{82/78}\text{Se}$ excursion would have been between +0.2‰ and +1.6‰, depending on whether partial reduction occurred under open- or closed-system conditions (Section 7.3.5). The complementary sink of this isotopically enriched dissolved Se may have been in restricted basins or in localized euxinic parts of the global ocean (Algeo *et al.*, 2010; Brenneka *et al.*, 2011), similar to today (Chapter 6).

The offset between the minimum in $\delta^{82/78}\text{Se}$ and the major paleontological extinction horizon defined by a change in conodont genera and the disappearance of bioturbation (Schoepfer *et al.*, 2012) is probably due to further shifts in ocean circulation that led to a decrease in the dissolved Se oxyanion supply. Consequently, Se reduction or assimilation became more quantitative, resulting in overall less negative $\delta^{82/78}\text{Se}$ values, even when biological

productivity was very low. If so, then the main extinction at this site was perhaps influenced by a limiting supply of nutrients, including Se. Alternatively, it is possible that total biological productivity was indeed at its minimum prior to the main extinction boundary, due to reasons other than nutrient supply, but microbial productivity resumed quickly and already dominated Se consumption by the time major groups of metazoans died out. However, Se/TOC ratios decline steadily throughout stage III (Table 7.2), supporting the first scenario of dwindling Se input. In either case, our data suggest that total biological productivity collapsed over the course of ~1kyr (from ~10cm to 12cm, assuming 0.5kyr cm^{-1} (Farley *et al.*, 2005)) under relatively oxygenated conditions.

7.5.4. Stage IV: stagnation

During stage IV (Fig. 7.1), sulfur and carbon isotopes change little compared to the end of stage III, indicating that the ocean probably continued to be oxic to suboxic and productivity remained low (Schoepfer *et al.*, 2012). Bottom-water suboxia likely limited organic matter re-oxidation, leading to the high TOC content of these samples. It is also possible that the relatively high TOC values reflect a recovery of microbial life on the shelf, whereas the carbon isotope record is mostly sensitive to global productivity, which continued to be suppressed.

$\delta^{82/78}\text{Se}$ is the only tracer that returns to values similar to stage I (average $-0.05 \pm 0.42 \text{‰}$, $n = 14$, Fig. 7.1), probably because Se is a much rarer element than C and S with a shorter residence time in the ocean and so is perhaps more sensitive to environmental changes and ocean circulation. The return to slightly heavier values could have resulted from two processes: (i) consumption of a relatively higher proportion of Se oxyanions by partial reduction than during stage III, leading to a smaller net fractionation in the reduced phase compared to the starting composition (as modeled in Fig. 7.4 for large values of f), or (ii) isotopically heavy organic $\text{Se}^{-\text{II}}$

becoming the major component in marine sediments, leading to dilution of isotopically light Se^0 and/or inorganic $\text{Se}^{-\text{II}}$ produced from oxyanion reduction. Both processes would have been facilitated by a lower supply of Se oxyanions to the shelf, *i.e.* a continuation of the second half of stage III, but also by local recovery of biological activity. The first possibility is supported by Se/TOC ratios, which are distinctly lower in stage IV than in other parts of the section (Fig. 7.6a). Hence low nutrient supply under oxic to suboxic conditions perhaps continued to suppress biological recovery until the early Triassic.

Combined with data from stage III, we observe an inverse relationship between $\delta^{82/78}\text{Se}$ values and the logarithm of Se/TOC ratios ($R^2 = 0.57$). Low Se/TOC ratios paired with high $\delta^{82/78}\text{Se}$ values may reflect a situation in which the supply of Se was locally limited and only organic $\text{Se}^{-\text{II}}$ was preserved; high Se/TOC ratios paired with low $\delta^{82/78}\text{Se}$ values likely indicate increased availability of Se oxyanions, which were then subject to partial reduction. If the sample with highest $\delta^{82/78}\text{Se}$ and lowest Se/TOC (Fig. 7.6a, circle A) represents nearly pure biomass with no addition of Se^0 and/or inorganic $\text{Se}^{-\text{II}}$ to the sediment, then it may capture the composition of seawater Se^{VI} in the early Triassic.

During stage IV, the $\delta^{82/78}\text{Se}$ record diverges most strongly from the $\delta^{34}\text{S}$ record, which only shows a comparatively small recovery (Fig. 7.1). The sulfur system is sensitive to profound redox changes, which, as discussed above and elsewhere (Algeo *et al.*, 2010; Schoepfer *et al.*, 2012; Proemse *et al.*, 2013), did not occur between the onset of the extinction (stage III) and the subsequent stagnation. The ocean was probably mostly oxic with suboxic bottom waters. Even though the dissolved sulfate reservoir may have contracted (Luo *et al.*, 2010), sulfate was likely a conservative ion before, during and after the latest Permian extinction event. Se, however, being a trace element in the ocean, is more sensitive to subtle redox and productivity changes. In this

case, our Se data indicate more clearly than the S record alone that ocean circulation was sluggish, though not absent, across the Permian-Triassic boundary.

7.6. Conclusion

At Opal Creek, Se isotopes display the largest negative excursion so far recorded in marine sediments, coincident with the largest mass extinction of the Phanerozoic eon. The preservation of such low $\delta^{82/78}\text{Se}$ values in bulk sediments is interpreted to result from a unique decline of biological activity, leading to excess Se oxyanion concentrations in the water column, which were then subject to partial reduction in suboxic bottom waters or at the sediment-water interface. The event is preceded by a small positive excursion, which was likely caused by locally euxinic conditions due to an increase in upwelling and productivity, and hence quantitative consumption of isotopically heavy Se in the water column. However, euxinia was likely limited to ocean margins, consistent with recent evidence from Mo and U isotopes and metal abundances (Algeo *et al.*, 2010; Algeo *et al.*, 2011; Brennecka *et al.*, 2011; Proemse *et al.*, 2013), and thus probably not responsible for the mass extinction. Instead, our data suggest that the ocean was oxic at the onset of the productivity decline, because otherwise Se oxyanions would not have been stable in the water column. Productivity appears to have collapsed relatively quickly over $\sim 1\text{kyr}$, and it is likely that this also caused perturbations in the carbon isotope record. The globally observed negative excursion in $\delta^{13}\text{C}$ is thus probably not due to CH_4 injections alone. During the peak extinction in the late Permian and continuing into the early Triassic, ocean circulation probably slowed down and decreased the supply of nutrients, leading to more quantitative Se consumption even under oxic to suboxic conditions. Hence nutrient

limitation probably did not cause the collapse of the marine biosphere but it may have inhibited its recovery.

Lastly, this study shows that Se isotopes can be a valuable proxy for geobiological changes in deep time. As demonstrated with one sample, the sequential extraction and isotopic analysis of different Se phases may help disentangle some of the complexity of this new isotopic system and should be pursued in future studies.

Acknowledgements

This study was funded by National Science Foundation grant EAR-0921580 and a University of Washington Royalty Research Fund grant to RB. We thank Joy Laydbak and Scott Kuehner at the University of Washington for technical support.

Tables

Table 7.1: Method comparison. Selenium isotope results, given in ‰, for four samples processed with two different protocols (E) and (D). M = number of replicate analyses. Differences between protocols are not systematic.

[cm]	protocol I							protocol II						
	M	$\delta^{82/78}\text{Se}$	1 σ	$\delta^{76/78}\text{Se}$	1 σ	$\delta^{77/78}\text{Se}$	1 σ	M	$\delta^{82/78}\text{Se}$	1 σ	$\delta^{76/78}\text{Se}$	1 σ	$\delta^{77/78}\text{Se}$	1 σ
-4	5	-0.05	0.29	-0.04	0.16	0.05	0.12	4	-0.01	0.13	-0.01	0.11	0.01	0.04
22	8	-1.95	0.29	0.93	0.17	0.55	0.13	4	-1.58	0.05	0.84	0.24	0.43	0.01
49.5	2	-0.32	0.14	0.39	0.04	0.37	0.21	4	-0.60	0.07	0.37	0.17	0.18	0.02
159.5	3	-0.06	0.15	-0.77	0.60	-0.12	0.16	4	-0.08	0.10	0.04	0.04	0.09	0.04

Table 7.2: Data set. M(Se) = number of replicate Se measurements, using method D in Stüeken *et al.* (2013) unless noted otherwise; RE = relative error; blank = not determined; dashed lines = stages boundaries discussed in the text.

depth [cm]	M (Se)	Se [ppm]	RE [%]	$\delta^{82/78}\text{Se}$ [‰]	1 σ [‰]	$\delta^{77/78}\text{Se}$ [‰]	1 σ [‰]	$\delta^{76/78}\text{Se}$ [‰]	1 σ [‰]	S [%]	$\delta^{34}\text{S}$ [‰]	TOC [%]	$\delta^{13}\text{C}$ [‰]	log(Se/S) [mol/mol]	log(Se/TOC) [mol/mol]
-40	9	9.61	2.91	-0.17	0.11	0.06	0.07	0.07	0.10	0.65	-2.90	0.52	-29.77	-3.22	-3.55
-21	7	25.08	17.39	-0.09	0.25	0.02	0.11	0.00	0.07	0.86	-1.27	0.95	-29.66	-2.93	-3.40
-4	9	8.49	4.63	-0.03	0.22	-0.03	0.13	0.03	0.09	0.86	0.63	0.36	-28.90	-3.39	-3.45
1.5	3	9.40	1.35	0.68	0.13	-0.35	0.11	-0.15	0.04	1.74	-2.73	1.29	-29.68	-3.66	-3.95
3	2	8.52	4.07	0.00	0.01	-0.09	0.01	-0.11	0.16	4.37	-11.06	0.08	-27.00	-4.10	-2.80
3.5	3	12.50	1.79	-0.06	0.09	0.05	0.05	0.02	0.02	3.47	-7.47	1.24	-29.75	-3.84	-3.82
4	2	24.42	5.90	0.60	0.02	-0.24	0.01	-0.11	0.07	29.87	-8.99	0.13	-27.05	-4.48	-2.53
5	2	25.56	31.64	0.59	0.15	-0.33	0.07	-0.24	0.26	28.71	-7.73	0.12	-27.44	-4.44	-2.48
6	2	18.56	52.70	0.70	0.23	-0.31	0.03	-0.01	0.30	9.32	-8.48	0.32	-29.65	-4.09	-3.05
8	2	22.88	6.28	0.67	0.03	-0.35	0.03	-0.17	0.07	27.86	-8.38	0.12	-26.38	-4.48	-2.53
9	2	18.49	2.54	0.19	0.15	-0.16	0.07	0.01	0.04	26.35	-7.34	0.21	-25.68	-4.55	-2.87
10.5	7	8.31	3.96	-0.41	0.32	0.16	0.14	0.10	0.12	5.77	-11.85	0.10	-25.77	-4.23	-2.88
15	4	4.35	7.61	-1.08	0.27	0.52	0.16	0.26	0.13	1.76	-7.30	0.07	-26.69	-4.00	-3.02
17.5	2	3.94	0.22	-1.54	0.06	0.82	0.03	0.39	0.01	2.58	-17.73	0.08	-27.16	-4.21	-3.11
22	12	2.31	10.98	-1.83	0.30	0.90	0.19	0.51	0.12	2.96	-19.52	0.10	-27.06	-4.50	-3.46
24.25	2	2.30	0.47	-1.74	0.02	0.95	0.01	0.48	0.01	2.67	-21.50	0.00		-4.46	
29	5	2.06	5.61	-1.53	0.36	1.10	0.16	0.38	0.13	5.36	-30.90	0.29	-29.59	-4.81	-3.97
30.75	8	2.46	13.10	-1.22	0.17	0.84	0.11	0.40	0.09	3.74	-23.99	0.46	-30.76	-4.57	-4.09
36.5	2	2.48	0.19	-1.08	0.03	0.58	0.03	0.32	0.00	2.57	-23.34	0.62	-29.73	-4.41	-4.21
37.5	2	2.39	8.06	-1.06	0.06	0.59	0.01	0.37	0.03	3.93	-19.00	0.39	-30.37	-4.61	-4.03
40	2	2.82	0.57	-0.79	0.12	0.43	0.07	0.26	0.05		-22.59	0.48	-30.96		-4.04
43	2	5.14	6.67	-0.52	0.13	0.39	0.02	0.21	0.12	3.55	-23.58	0.66	-30.55	-4.23	-3.93
46	2	3.19	0.48	-1.28	0.06	0.71	0.00	0.40	0.01			0.89	-30.92		-4.27
49.5	6	2.53	4.22	-0.51	0.16	0.38	0.13	0.25	0.13	2.60	-25.96	0.40	-31.34	-4.40	-4.01
72	2	2.26	1.18	-0.54	0.13	0.38	0.07	0.31	0.11	3.31	-19.43	0.70	-31.04	-4.56	-4.31
90.15	5	1.64	5.47	-0.51	0.23	0.56	0.07	0.26	0.12	3.54	-19.99	0.75	-31.16	-4.73	-4.48
106.25	5	1.35	4.08	-0.57	0.25	0.31	0.12	0.29	0.10	2.80	-19.52	1.01	-30.70	-4.71	-4.69
116.75	4	1.16	8.45	-0.35	0.44	0.29	0.20	0.18	0.14	3.35	-16.77	1.45	-30.49	-4.85	-4.91
133.5	5	1.72	2.23	-0.19	0.20	0.13	0.09	0.11	0.12	2.65	-20.59	1.97	-31.64	-4.58	-4.88
159.5	6	0.58	7.08	-0.17	0.18	0.10	0.10	0.10	0.04	3.63	-9.79	0.62	-31.97	-5.19	-4.85
310.5	3	0.58	4.02	-0.02	0.22			0.17	0.17	1.89	-20.41	1.57	-31.62	-4.90	-5.25
386	5	0.90	4.36	0.59	0.28	-0.26	0.31	0.00	0.13	1.88	-20.42	1.66	-32.06	-4.71	-5.08
494.2	3	1.17	2.09	0.35	0.14	-0.21	0.06	-0.10	0.06	3.09	-13.70	2.01	-31.92	-4.81	-5.05
563	3	0.92	5.65	0.49	0.09	-0.32	0.43	0.17	0.22	1.62	-20.03	2.30	-31.90	-4.64	-5.22
850.5	4	1.35	6.53	0.35	0.19	-0.41	0.14	0.02	0.08	1.96	-10.89	2.26	-31.57	-4.55	-5.04
1237	2	0.96	1.82	-0.11	0.09	-0.35	0.02	0.09	0.02	1.47	-14.30	2.14	-30.97	-4.58	-5.16
1684	2	0.58	7.80	0.35	0.17	-0.63	0.33	0.18	0.11	1.25	-18.25	1.62	-30.57	-4.72	-5.26

- Prepared with both protocols D and E in Stüeken *et al.* (2013) See Table 1 for method comparison.
- Only prepared with protocol E in Stüeken *et al.* (2013).

Table 7.3: Selenium species in sample from -40 cm. Isotopic values are given in ‰, selenium concentrations in ppm. % tot. = fraction of bulk rock. Each fraction was prepared and analyzed in four replicates. SeX = uncertain contributions of reduced Se phases that were oxidized by O₂ dissolved in NaOH.

reagent	Se species	[Se]	1σ	% tot.	1σ	δ ^{82/78} Se	1σ	δ ^{76/78} Se	1σ	δ ^{77/78} Se	1σ
NaOH	Se ^{IV} _{ads} ± SeX	0.62	0.02	6.4%	0.2%	-0.93	0.23	0.47	0.12	0.29	0.24
CrCl ₂ + HCl	Se ^{II} _{pyr} ± Se ⁰	1.26	0.17	13.2%	1.7%	-0.90	0.23	0.47	0.14	0.20	0.15
HF+HClO ₄ +HNO ₃	Se ^{II} _{org} ± Se ⁰	6.93	0.63	72.2%	6.5%	0.03	0.07	-0.08	0.06	0.05	0.19
weighted average		8.82	0.92	91.7%	4.7%	-0.16	0.02	0.04	0.01	0.08	0.02
missing				8.3%	4.7%						
BULK		9.61	0.28			-0.17	0.11	0.06	0.07	0.07	0.10

Figures

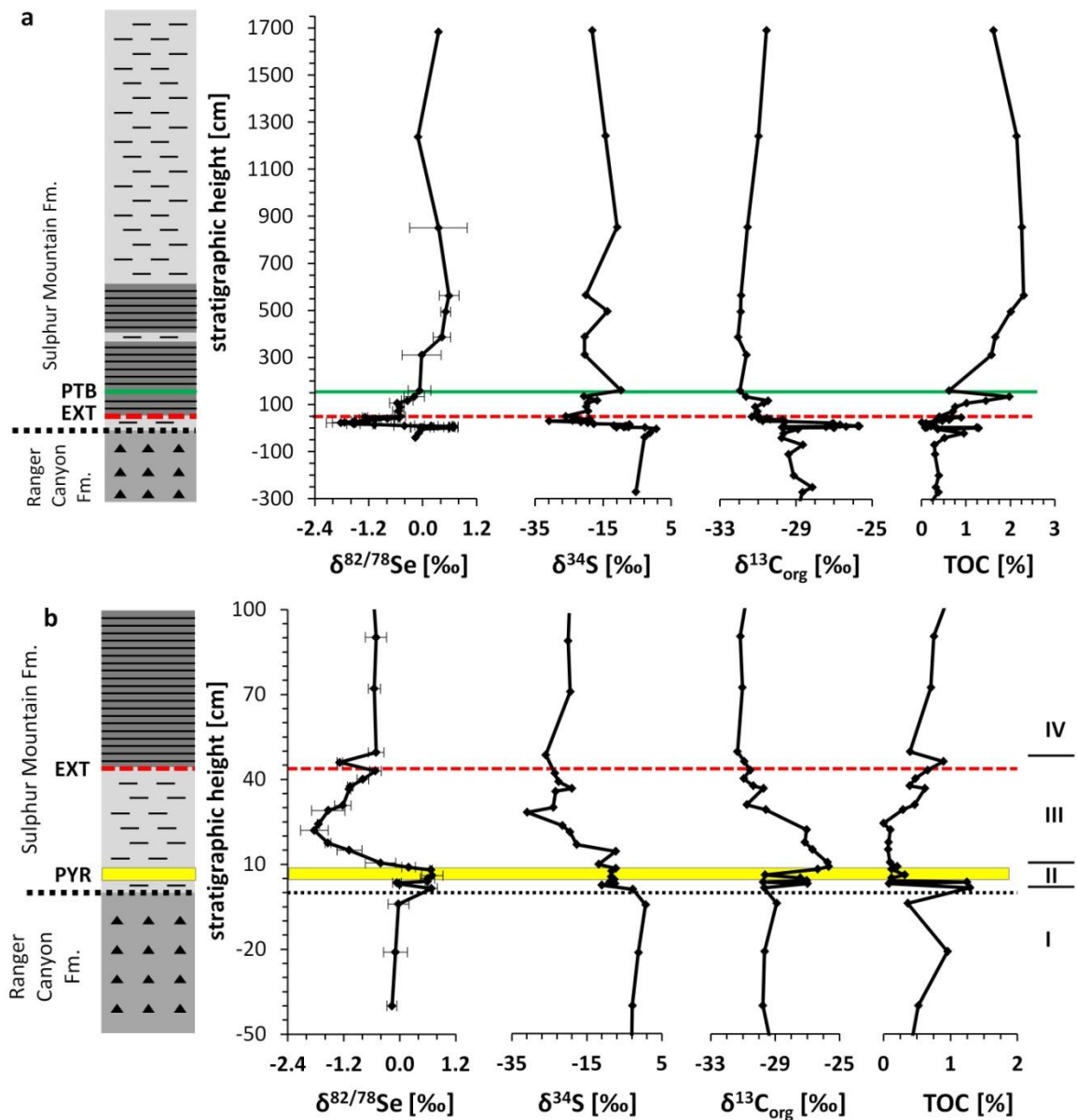


Figure 7.1: Stratigraphic section across the PT extinction event in the Western Canada Basin at Opal Creek. Sulfur data are from Schoepfer *et al.* (2013); carbon data and lithostratigraphy are from Schoepfer *et al.* (2012). Triangles = chert, broken lines = siltstone, solid lines = shale, dotted black line = unconformity, PYR and yellow bar = pyrite-rich bed, EXT and dashed red line = main extinction horizon, PTB and solid green line = Permian-Triassic boundary. $\delta^{82/78}\text{S}$ data show one-sigma error bars. Roman numerals refer to stages described in the text. **A:** complete section. **B:** detail of the section between -0.5 and +1.0 m.

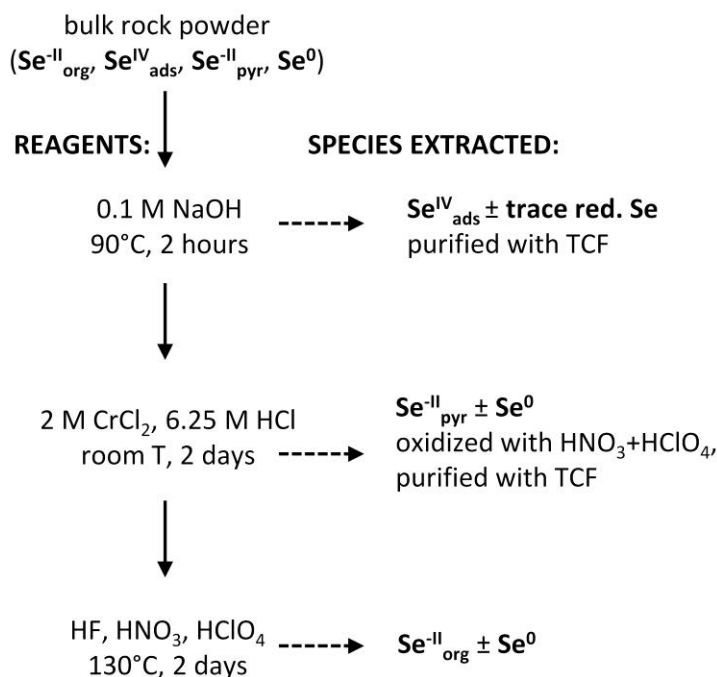


Figure 7.2: Sequential extraction protocol. Solid arrows mark transfer of rock powder; dashed arrows mark separation and removal of selenium species from rock powder. See Section 7.3.2 for detailed descriptions of each step.

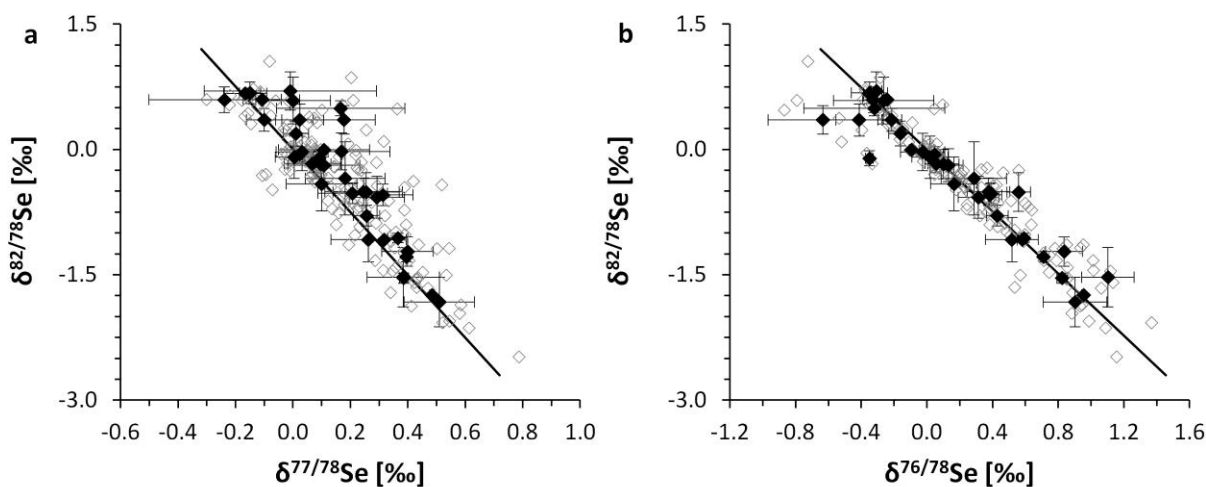


Figure 7.3: Mass-dependent fractionation and interference correction. Empty diamonds are individual measurements, filled diamonds are averages $\pm 1\sigma$ (Table 2). **a:** $\delta^{77/78}\text{Se}$ versus $\delta^{82/78}\text{Se}$. **b:** $\delta^{76/78}\text{Se}$ versus $\delta^{82/78}\text{Se}$. Line marks the theoretical relationship of mass-dependent fractionation. Within 2σ , almost all samples fall along the mass-dependent fractionation line, indicating that natural mass-independent mass fractionation is absent and that major isobaric interferences have been corrected.

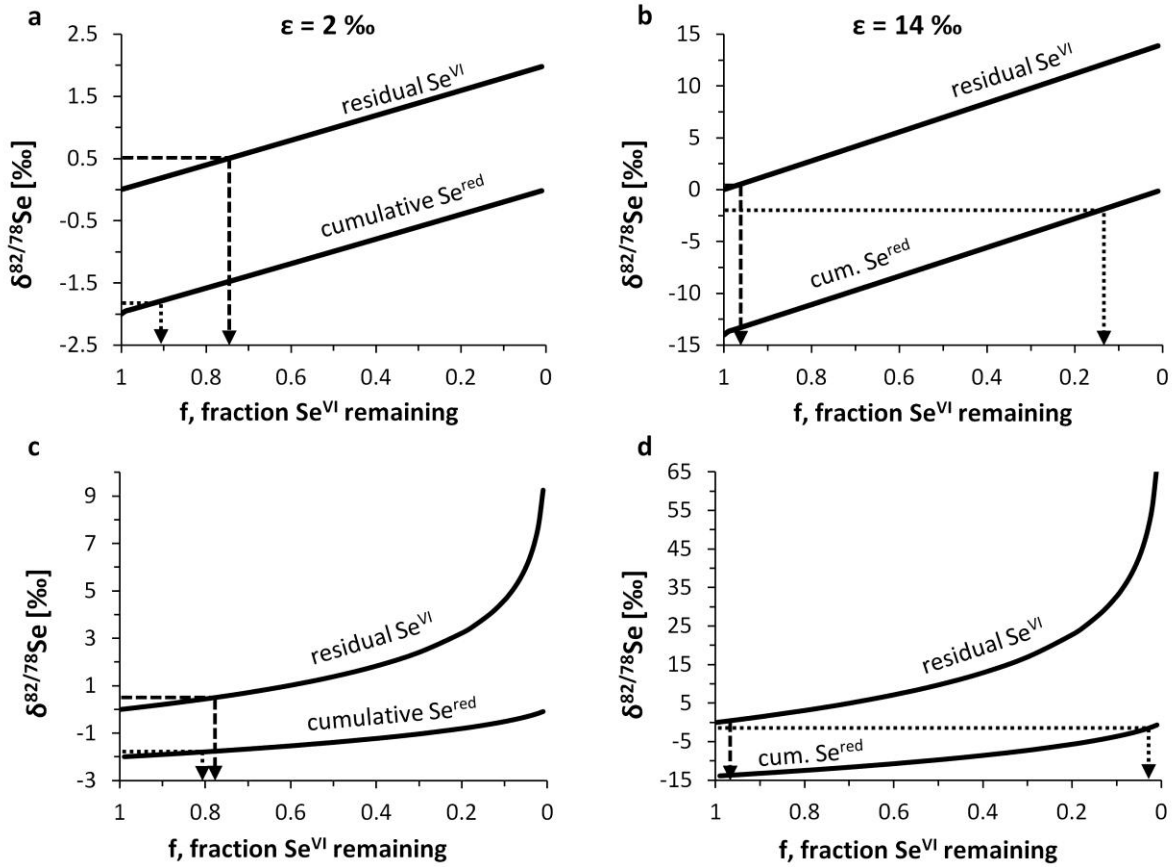


Figure 7.4: Possible solutions for Se isotope mass balance. a, b: Open system fractionation with a maximum fractionation of $\epsilon = 2\text{‰}$ (a) or 14‰ (b). **c, d:** Closed system Rayleigh fractionation with a maximum fractionation of $\epsilon = 2\text{‰}$ (c) or 14‰ (d). Dashed arrows point to values of f needed to obtain $\delta^{82/78}\text{Se}^{\text{VI}} = +0.5\text{‰}$, dotted arrows point to values of f needed to obtain $\delta^{82/78}\text{Se}^{\text{red}} = -1.8\text{‰}$. Model calculations are explained in Section 7.3.5.

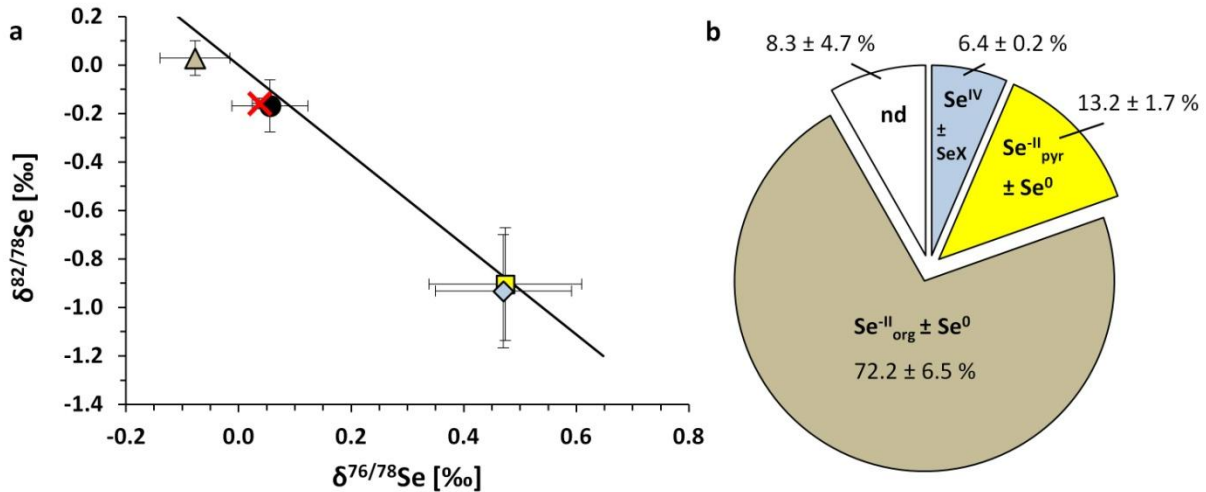


Figure 7.5: Sequential extraction of Se phases in sample -40 cm. a: isotopic compositions. Blue diamond = adsorbed Se^{IV} with potential traces of reduced Se phases (SeX) oxidized by O_2 dissolved in NaOH ; yellow square = inorganic $\text{Se}^{\text{II}} \pm \text{Se}^0$; brown triangle = refractory organic $\text{Se}^{\text{II}} \pm \text{Se}^0$; black circle = bulk sample; red x = weighted average of extracted fractions; solid line = theoretical mass-dependent fractionation line. b: Relative proportions of Se phases in bulk sample, using the same color scheme as in panel a. nd = not determined (missing fraction). All errors are 1σ and listed in Table 7.3.

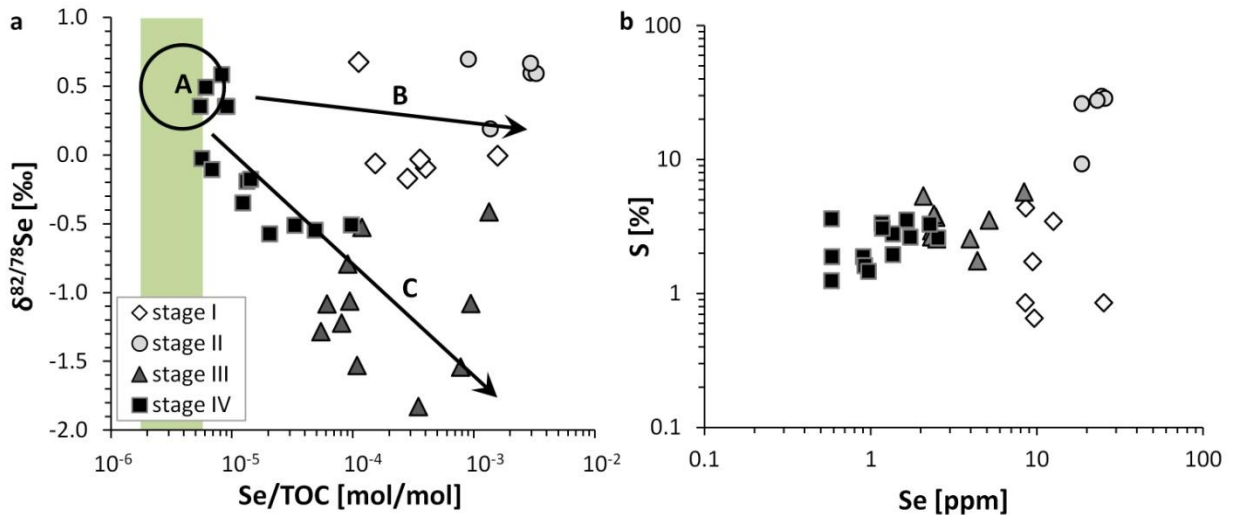


Figure 7.6: $\delta^{82/78}\text{Se}$ versus Se/TOC (a) and total Se versus total S (b). In panel a, green bar marks Se/TOC ratio of modern phytoplankton ($1.7 \cdot 10^{-6}$ to $5.7 \cdot 10^{-6}$, Mitchell *et al.*, 2012). A: a circle that represents the range for a putative biomass end-member that may capture the isotopic composition of early Triassic seawater. B: Effects of Se addition to sediments by reductive scavenging in oxygen-minimum zone (stage I) or local euxinia (stage II). C: Effects of Se addition by partial (diagenetic) reduction in suboxic bottom water or sediment (stages III and IV).

References

- Algeo TJ, Henderson CM, Tong J, Feng Q, Yin H, Tyson RV (2013) Plankton and productivity during the Permian–Triassic boundary crisis: An analysis of organic carbon fluxes. *Global and Planetary Change*, **105**, 52-67.
- Algeo TJ, Hinnov L, Moser J, Maynard B, Elswick E, Kuwahara K, Sano H (2010) Changes in productivity and redox conditions in the Panthalassic Ocean during the latest Permian. *Geology*, **38**, 187-190.
- Algeo TJ, Kuwahara K, Sano H, Bates S, Lyons TW, Elswick E, Hinnov L, Ellwood B, Moser J, Maynard B (2011) Spatial variation in sediment fluxes, redox conditions, and productivity in the Permian–Triassic Panthalassic Ocean. *Palaeogeography, Palaeoclimatology, Palaeoecology*, **308**, 65-83.
- Brennecke GA, Herrmann AD, Algeo TJ, Anbar AD (2011) Rapid expansion of oceanic anoxia immediately before the end-Permian mass extinction. *Proceedings of the National Academy of Sciences*, **108**, 17631-17634.
- Broecker WS, Peng TH (1982) *Tracers in the Sea*, Eldigio Press Lamont-Doherty Geological Survey, New York.
- Burton ED, Sullivan LA, Bush RT, Johnston SG, Keene AF (2008) A simple and inexpensive chromium-reducible sulfur method for acid-sulfate soils. *Applied Geochemistry*, **23**, 2759-2766.
- Campbell IH, Czamanske GK, Fedorenko VA, Hill RI, Stepanov V (1992) Synchronism of the Siberian traps and the Permian-Triassic boundary. *Science*, **258**, 1760-1763.
- Canfield DE (2001) Biogeochemistry of sulfur isotopes. *Reviews in Mineralogy and Geochemistry*, **43**, 607-636.
- Canfield DE, Raiswell R, Westrich JT, Reaves CM, Berner RA (1986) The use of chromium reduction in the analysis of reduced inorganic sulfur in sediments and shales. *Chemical Geology*, **54**, 149-155.
- Carignan J, Wen H (2007) Scaling NIST SRM 3149 for Se isotope analysis and isotopic variations of natural samples. *Chemical Geology*, **242**, 347-350.
- Clark SK, Johnson TM (2010) Selenium stable isotope investigation into selenium biogeochemical cycling in a lacustrine environment: Sweitzer Lake, Colorado. *Journal of Environmental Quality*, **39**, 2200-2210.
- Cutter GA (1982) Selenium in reducing waters. *Science*, **217**, 829-831.
- Cutter GA (1992) Kinetic controls on metalloid speciation in seawater. *Marine Chemistry*, **40**, 65-80.
- Cutter GA, Bruland KW (1984) The marine biogeochemistry of selenium: a re-evaluation. *Limnology and Oceanography*, **29**, 1179-1192.
- Cutter GA, Cutter LS (2001) Sources and cycling of selenium in the western and equatorial Atlantic Ocean. *Deep-Sea Research II*, **48**, 2917-2931.
- Ellis AS, Johnson TM, Herbel MJ, Bullen T (2003) Stable isotope fractionation of selenium by natural microbial consortia. *Chemical Geology*, **195**, 119-129.
- Erwin DH, Bowring SA, Yugan J (2002) End-Permian mass extinction: a review. In: *Catastrophic events and mass extinctions: impacts and beyond* (eds Koeberl C, MacLeod KG). Geological Society of America Special Paper, Boulder, Colorado, pp. 363-383.

- Fan HF, Wen H, Hu M, Zhao H (2011) Selenium speciation in Lower Cambrian Se-enriched strata in South China and its geological implications. *Geochimica et Cosmochimica Acta*, **75**, 7725-7740.
- Farley KA, Ward PD, Garrison GH, Mukhopadhyay S (2005) Absence of extraterrestrial ³He in Permian-Triassic age sedimentary rocks. *Earth and Planetary Science Letters*, **240**, 265-275.
- Grice K, Cao C, Love GD, Boettcher ME, Twitchett RJ, Grosjean E, Summons RE, Turgeon SC, Dunning W, Jin Y (2005) Photic Zone Euxinia During the Permian-Triassic Superanoxic Event. *Science*, **307**, 706-709.
- Gröger J, Franke J, Hamer K, Schulz HD (2009) Quantitative recovery of elemental sulfur and improved selectivity in a chromium-reducible sulfur-distillation. *Geostandards and Geoanalytical Research*, **33**, 17-27.
- Henderson CM (1997) Uppermost Permian conodonts and the Permian–Triassic boundary in the Western Canada Sedimentary Basin. *Bulletin of Canadian Petroleum Geology*, **45**, 693-707.
- Herbel MJ, Johnson TM, Oremland RS, Bullen T (2000) Fractionation of selenium isotopes during bacterial respiratory reduction of selenium oxyanions. *Geochimica et Cosmochimica Acta*, **64**, 3701-3709.
- Hsieh YP, Shieh YN (1997) Analysis of reduced inorganic sulfur by diffusion methods: improved apparatus and evaluation for sulfur isotopic studies. *Chemical Geology*, **137**, 255-261.
- Hsieh YP, Yang CH (1989) Diffusion methods for the determination of reduced inorganic sulfur species in sediments. *Limnology and Oceanography*, **34**, 1126-1130.
- Johnson TM, Bullen T (2003) Selenium isotope fractionation during reduction by Fe(II)-Fe(III) hydroxide-sulfate (green rust). *Geochimica et Cosmochimica Acta*, **67**, 413-419.
- Johnson TM, Bullen T (2004) Mass-dependent fractionation of selenium and chromium isotopes in low-temperature environments. *Reviews in Mineralogy and Geochemistry*, **55**, 289-317.
- Johnson TM, Herbel MJ, Bullen TD, Zawislanski PT (1999) Selenium isotope ratios as indicators of selenium sources and oxyanion reduction. *Geochimica et Cosmochimica Acta*, **63**, 2775-2783.
- Kajiwara Y, Yamakita S, Ishida K, Ishiga H, Imai A (1994) Development of a largely anoxic stratified ocean and its temporary massive mixing at the Permian/Triassic boundary supported by the sulfur isotopic record. *Palaeogeography, Palaeoclimatology, Palaeoecology*, **111**, 367-379.
- Korte C, Kozur HW (2010) Carbon-isotope stratigraphy across the Permian–Triassic boundary: A review. *Journal of Asian Earth Sciences*, **39**, 215-235.
- Kulp TR, Pratt LM (2004) Speciation and weathering of selenium in Upper Cretaceous chalk and shale from South Dakota and Wyoming, USA. *Geochimica et Cosmochimica Acta*, **68**, 3687-3701.
- Kump LR, Pavlov AA, Arthur MA (2005) Massive release of hydrogen sulfide to the surface ocean and atmosphere during intervals of oceanic anoxia. *Geology*, **33**, 397-400.
- Layton-Matthews D, Leybourne MI, Peter JM, Scott SD, Cousens B, Eglington B (2013) Multiple sources of selenium in ancient seafloor hydrothermal systems: compositional and Se, S and Pb isotopic evidence from volcanic-hosted and volcanic-sediment-hosted

- massive sulfide deposits of the Finlayson Lake District, Yukon, Canada. *Geochimica et Cosmochimica Acta*, **117**, 313-331.
- Luo G, Kump LR, Wang Y, Tong J, Arthur MA, Yang H, Huang J, Yin H, Xie S (2010) Isotopic evidence for an anomalously low oceanic sulfate concentration following end-Permian mass extinction. *Earth and Planetary Science Letters*, **300**, 101-111.
- Martens DA, Suarez DL (1997) Selenium speciation of soil/sediment determined with sequential extractions and hydride generation atomic absorption spectrophotometry. *Environmental Science and Technology*, **31**, 133-139.
- Mitchell K, Mason PRD, Van Cappellen P, Johnson TM, Gill BC, Owens JD, Ingall ED, Reichart G-J, Lyons TW (2012) Selenium as paleo-oceanographic proxy: A first assessment. *Geochimica et Cosmochimica Acta*, **89**, 302-317.
- Proemse BC, Grasby SE, Wieser ME, Mayer B, Beauchamp B (2013) Molybdenum isotopic evidence for oxic marine conditions during the latest Permian extinction. *Geology*, **41**, 967-970.
- Rouxel O, Fouquet Y, Ludden JN (2004) Subsurface processes at the Lucky Strike hydrothermal field, Mid-Atlantic Ridge: evidence from sulfur, selenium, and iron isotopes. *Geochimica et Cosmochimica Acta*, **68**, 2295-2311.
- Rouxel O, Ludden J, Carignan J, Marin L, Fouquet Y (2002) Natural variations of Se isotopic composition determined by hydride generation multiple collector inductively coupled plasma mass spectrometry. *Geochimica et Cosmochimica Acta*, **66**, 3191-3199.
- Schoepfer SD, Henderson CM, Garrison GH, Foriel J, Ward PD, Selby D, Hower JC, Algeo TJ, Shen Y (2013) Termination of a continent-margin upwelling system at the Permian–Triassic boundary (Opal Creek, Alberta, Canada). *Global and Planetary Change*, **105**, 21-35.
- Schoepfer SD, Henderson CM, Garrison GH, Ward PD (2012) Cessation of a productive coastal upwelling system in the Panthalassic Ocean at the Permian–Triassic Boundary. *Palaeogeography, Palaeoclimatology, Palaeoecology*, **313-314**, 181-188.
- Seal RR (2006) Sulfur isotope geochemistry of sulfide minerals. *Reviews in Mineralogy and Geochemistry*, **61**, 633-677.
- Shore AJT (2010) Selenium geochemistry and isotopic composition of sediments from the Cariaco Basin and the Bermuda Rise: a comparison between a restricted basin and the open ocean over the last 500 ka. In: *Department of Geology*. University of Leicester, Leicester, pp. 307.
- Stüeken EE (2013) A test of the nitrogen-limitation hypothesis for retarded eukaryote radiation: Nitrogen isotopes across a Mesoproterozoic basinal profile. *Geochimica et Cosmochimica Acta*, **120**, 121-139.
- Stüeken EE, Foriel J, Nelson BK, Buick R, Catling DC (2013) Selenium isotope analysis of organic-rich shales: advances in sample preparation and isobaric interference correction. *Journal of Analytical Atomic Spectrometry*, **28**, 1734-1749.
- Ulrich GA, Krumholz LR, Suflita JM (1997) A rapid and simple method for estimating sulfate reduction activity and quantifying inorganic sulfides. *Applied and Environmental Microbiology*, **63**, 1627-1630.
- Ward PD, Montgomery DR, Smith R (2000) Altered river morphology in South Africa related to the Permian-Triassic extinction. *Science*, **289**, 1740-1743.

- Wen H, Carignan J (2011) Selenium isotopes trace the source and redox processes in the black shale-hosted Se-rich deposits in China. *Geochimica et Cosmochimica Acta*, **75**, 1411-1427.
- White RV (2002) Earth's biggest 'whodunnit': unravelling the clues in the case of the end-Permian mass extinction. *Philosophical Transactions of the Royal Society of London B*, **360**, 2963-2985.
- Wright MT, Parker dR, Amrhein C (2003) Critical evaluation of the ability of sequential extraction procedures to quantify discrete forms of selenium in sediments and soils. *Environmental Science and Technology*, **37**, 4709-4716.
- Yu M, Sun D, Tian W, Wang G, Shen W, Xu N (2002) Systematic studies on adsorption of trace elements Pt, Pd, Au, Se, Te, As, Hg, Sb on thiol cotton fiber. *Analytica Chimica Acta*, **456**, 147-155.
- Zhu JM, Johnson TM, Clark SK, Zhu XK, Wang XL (2014) Selenium redox cycling during weathering of Se-rich shales: A selenium isotope study. *Geochimica et Cosmochimica Acta*, **126**, 228-249.

Chapter 8: A test of the nitrogen-limitation hypothesis for retarded eukaryote radiation: nitrogen isotopes across a Mesoproterozoic basinal profile⁴

Abstract

Nitrogen limitation caused by trace metal scarcity under euxinic ocean conditions has been proposed as an explanation for the delayed the radiation of eukaryotes until at least the late Mesoproterozoic. However, evidence for how the nitrogen cycle was operating during the middle Precambrian is, so far, rare. More specifically, it is unknown which steps in the biogeochemical nitrogen cycle, *e.g.* nitrogen fixation, nitrification or ammonification, were rate-limiting and thus controlling microbial community structures. The Mesoproterozoic Belt Supergroup in western Montana hosts a variety of facies ranging from shallow to deep water and thus offers the opportunity to address this issue. Bulk $\delta^{15}\text{N}$ values show a clear trend from -1 ‰ in the deepest part of the basin to +5 ‰ along basin margins, which suggests that coastal areas were sufficiently oxygenated for aerobic nitrogen cycling. The total fractionation of carbon isotopes between carbonate and organic carbon ($\Delta^{13}\text{C}$) increases from 20 ‰ to 32 ‰ in the same direction, possibly indicating an ecological response to redox stratification and nitrogen speciation. Evidence from the Belt Supergroup is thus consistent with the idea that nutrient availability may have restricted early eukaryotic organisms to a narrow range of habitats, which thus prevented a global rise to ecological dominance until concentrations of fixed nitrogen increased in the global open ocean.

⁴ Published in *Geochimica et Cosmochimica Acta* (2013), v. 120, pp. 121-139.

8.1. Introduction

Nitrogen is one of the essential elements of life and a major nutrient that controls biological activity (e.g. Falkowski, 1997; Tyrrell, 1999; Arrigo, 2005; Canfield *et al.*, 2010). The major nitrogen reservoir at the Earth's surface and the ultimate source of nitrogen for the biosphere is atmospheric N₂. However, the fixation of N₂ gas into biomass is an energetically costly process that can only be performed by certain groups of prokaryotes (e.g. Karl *et al.*, 2002; Raymond *et al.*, 2004). Once fixed, nitrogen can participate in a number of biogeochemical processes, primarily depending on the availability of oxygen in the system (Canfield *et al.*, 2004, Figure 8.1). When nitrogen is released as ammonium during degradation of organic matter, it can either be reassimilated into biomass, taken up into clay particles, or become oxidized to nitrite and nitrate during nitrification. The latter is the major source of nitrate in the modern ocean and supplies nitrogen to many non-nitrogen fixing organisms, especially eukaryotic algae, in oxic environments. The largest sinks of nitrogen from the ocean are denitrification and anaerobic ammonia oxidation that ultimately release nitrogen as N₂ back to the atmosphere. Both of these processes are carried out under suboxic conditions in oxygen minimum zones or sediments (Prokopenko *et al.*, 2006; Lam *et al.*, 2009; Sigman *et al.*, 2009a).

Because atmospheric oxygen levels have changed markedly over time (Canfield, 2005; Catling & Claire, 2005; Kah & Bartley, 2011), it is almost certain that the nitrogen cycle has evolved since the early Archean (Beaumont & Robert, 1999; Fennel *et al.*, 2005), with important ramifications for organisms that depend on fixed nitrogen. N₂ fixation is most efficient if it is catalyzed by Mo-bearing enzymatic cofactors (reviewed in Glass *et al.*, 2009, Figure 8.1). Although some evidence is consistent with an early evolution of N₂ fixation (Beaumont & Robert, 1999; Raymond *et al.*, 2004; Schoepp-Cothenet *et al.*, 2011), it may have been limited

until after the Great Oxidation Event around 2.4 Gyr when Mo was finally mobilized by oxidative weathering of Mo-bearing sulfide minerals (Scott *et al.*, 2008; Boyd *et al.*, 2011). Similarly, nitrification and denitrification, which require Fe, Mo and Cu, had already evolved by the late Archean (Garvin *et al.*, 2009; Godfrey & Falkowski, 2009). But in the absence of oxidative weathering, or in the presence high seawater sulfide concentrations that scavenged the trace metals required for nitrifying metalloenzymes from the ocean (Saito *et al.*, 2003; Poulton *et al.*, 2010; Scott *et al.*, 2011), the availability of nitrate may have been localized to coastal environments until deep-ocean oxygenation in the Neoproterozoic (Sahoo *et al.*, 2012).

This scenario has led to the hypothesis that throughout the Proterozoic the availability of fixed nitrogen, in particular nitrate, limited the proliferation of eukaryotic life (Anbar & Knoll, 2002). Eukaryotic algae may thus have been restricted to oxygenated coastal habitats during most of the Precambrian, which may in turn explain the apparent retardation in eukaryotic radiation in the fossil record until the Neoproterozoic (Anbar & Knoll, 2002). This line of thought is consistent with subsequent findings about Precambrian ocean chemistry (Scott *et al.*, 2008; Planavsky *et al.*, 2011; Poulton & Canfield, 2011; Sahoo *et al.*, 2012), but it has never been tested directly. Nitrogen isotopes as a proxy for biogeochemical nitrogen cycling may help fill this gap.

Nitrogen has two stable isotopes (^{15}N , 0.3663 %, and ^{14}N , 99.6337%) that are fractionated during most biogeochemical transformations (reviewed in Robinson, 2001, Figure 8.1; Casciotti, 2009; Pinti & Hashizume, 2011). While nitrogen fixation only imparts a very small fractionation of -2 to +2 ‰ (average -1‰), the isotopic fractionation associated with denitrification (and probably anammox) ranges from 20 to 30 ‰, rendering residual nitrate isotopically enriched in the modern ocean (Sigman *et al.*, 2009b). This fractionation is not

expressed if denitrification occurs in the sediment (Sigman et al., 2009a). From an average composition of $+5.0 \pm 0.5$ ‰ for nitrate in the modern open ocean it follows that today approximately 20 % of global denitrification occurs in suboxic water columns and 80 % in sediments where the reaction goes to completion (Sigman et al., 2000; Sigman et al., 2009a) (but see Granger *et al.* (2011) for recent evidence that the modern nitrogen cycle may be out of balance). Residual nitrate that escapes denitrification is assimilated quantitatively in the photic zone, such that the isotopic composition of biomass preserved in sediments can serve as a proxy for the availability and isotopic composition of seawater nitrate (Altabet & Francois, 1994). The other two processes that impart large isotopic fractionations, partial assimilation of NH_4^+ and partial nitrification (Figure 8.1), by themselves do not necessarily lead to a separation of the isotopically enriched and depleted phase over geologic time scales or if integrated over a whole basin (further discussed below). It is therefore the balance of nitrogen fixation and denitrification that typically controls the isotopic composition of geological samples (reviewed in Pinti & Hashizume, 2011). Hence if nitrate were present in significantly large quantities in at least parts of the mid-Proterozoic ocean, then that may be reflected in the isotopic composition of marine sedimentary rocks, provided that the nitrate pool was affected by partial denitrification in the water column (Altabet & Francois, 1994).

This hypothesis is tested using shales and siltstones from the Mesoproterozoic Belt Supergroup in western Montana, USA. Drill core samples from this succession have been used in previous studies to corroborate models of Proterozoic iron, sulfur and molybdenum chemistry (Lyons *et al.*, 2006; Scott *et al.*, 2008; Planavsky *et al.*, 2011). Furthermore, the Belt Supergroup has the advantage that a variety of different facies representing different depositional environments are preserved. This study is therefore designed to test if nitrogen speciation

changed as a function of water depth, and if nitrate may have been stable and bioavailable in shallow water. Carbon isotopes have been analyzed in addition to nitrogen to further constrain potential differences in microbial ecology.

8.2. Geological setting

The Belt Supergroup extends from western Montana to eastern Washington in the USA and northward into British Columbia, Canada (Figure 8.2). It comprises thick sequences of variably metamorphosed siliciclastic and carbonate sedimentary rocks, that have, in places, been intruded or covered by igneous rocks (Harrison, 1972; Chandler, 2000). Because the intrusions likely occurred prior to lithification (Sears *et al.*, 1998), their age constrains the time of sedimentation to approximately 1470-1400 Ma (Sears *et al.*, 1998; Evans *et al.*, 2000).

The Belt basin is generally divided into the main branch, represented by rocks along the north-south axis of the present outcrop extent, and the Helena embayment, which projects eastward from the southern tip of the main branch (Figure 8.2). The basin is thought to have formed during continental rifting as a result of lithospheric extension (reviewed in Lydon, 2007). After continental break-up in the Neoproterozoic, the western part of the basin drifted away and may now be preserved in Siberia (Sears & Price, 2000), eastern Australia (Ross & Villeneuve, 2003) or Antarctica (Moores, 1991).

The environmental setting is still debated. Sedimentological evidence has been interpreted to suggest it was lacustrine (Winston, 1986; Winston, 1990), whereas some geochemical and mineralogical data are more consistent with a marine influence for at least part of the depositional time (Hall & Veizer, 1996; Frank *et al.*, 1997; Schieber, 1998b; Chandler, 2000; Lyons *et al.*, 2000; Luepke & Lyons, 2001; Pratt, 2001; Lyons *et al.*, 2006). The two

models may not be mutually exclusive if the basin was an epeiric sea that was intermittently restricted and periodically dominated by freshwater input (Cressman, 1989; Pratt, 2001).

The sedimentary succession in the main branch reaches a much greater thickness (max. ~16 km) than in the Helena embayment (max. ~4 km) (Harrison, 1972; Chandler, 2000); however, metamorphism generally increases from east to west as well as with depth (reviewed in Lydon, 2007), which may compromise analyses of nitrogen isotopes in rocks from the western, main branch, part of the basin. This study therefore focuses on samples of the Lower Belt Group (~1.47 Gyr, Sears et al., 1998) from the Helena embayment, which are the least metamorphosed and generally below greenschist facies (Schieber, 1989).

The base of the succession in the Helena embayment is represented by the Neihart Formation, which has been interpreted as the shallow-water and fan-delta facies that would have been deposited at the margins of the rift basin (Lydon, 2007). It is a mature quartz arenite that may already have covered the craton prior to basin subsidence (Ross & Villeneuve, 2003), but was probably reworked by stream and wave activity in the developing near-shore setting (Schieber, 1986). Mud-chips and shale beds become increasingly more abundant as the Neihart Fm. grades into the Chamberlain Fm. (Schieber, 1986). This transition likely indicates continuing transgression and flooding of the Helena embayment (Schieber, 1986; Horodyski, 1993). Horodyski (1993) noted the absence in the Chamberlain Fm. of desiccation cracks, ripple marks, cross bedding and other sedimentary features typically associated with very shallow water environments. However, careful examination during this study has revealed that such features are present in some beds (discussed below), suggesting that the Chamberlain was deposited above wave base. In contrast, the conformably overlying Newland Fm. is composed of mostly plane-laminated calcareous shale at the base grading into alternating beds of nearly pure

carbonate and variably calcareous shale at the top (Schieber, 1986; Zieg, 1986). Hence most of the Newland Formation was probably deposited in a low-energy environment below fairweather wave base (Zieg, 1986; Schieber, 1990; Lydon, 2007). Iron speciation indicates ferruginous conditions, which, when compared with other Mesoproterozoic marine basins, supports a moderately deep-water environment (Poulton *et al.*, 2010; Planavsky *et al.*, 2011; Poulton & Canfield, 2011). Sulphur isotopes are consistent with input of marine water during this time (Lyons *et al.*, 2000; Lyons *et al.*, 2006). The transition into the Greyson Formation, a silty shale to sandy siliciclastic deposit, probably marks a period of basin shallowing and return to higher energy regimes (Zieg, 1986; Lydon, 2007).

8.3. Sampling

Samples were collected along three outcrop sections and from one drill core (SC11-009) that was obtained during the Sheep exploration project carried out by Tintina Alaska Exploration Inc. (Figure 8.2). Where possible, samples for nitrogen and organic carbon analyses were selected from particularly dark-colored, fine-grained shale horizons.

The eastern-most section along Jefferson Creek in the northern Little Belt Mountains (N 46.908609°, W -110.684244° to N 46.913532°, W -110.650073°) extends from the upper Neihart Fm. through the Chamberlain Fm. to the base of the Newland Fm. (Reynolds & Brandt, 2007). Beds dip between 8° and 17° to the east over a distance of around 2 km. The Newland Formation is unconformably overlain by the Cambrian Flathead sandstone.

The second section begins in Miller Gulch in the southern Little Belt Mountains and is exposed along Newlan Creek towards Newlan Creek Reservoir (N 46.731289°, W -110.849097° to N 46.659044°, W -110.898558°). This section comprises parts of the Newland and Greyson

fms (Reynolds & Brandt, 2007). Dip angles are mostly between 12° and 18° to the southwest, but some outcrops along the 10 km section display local deformation. Exposures are less continuous than in Jefferson Creek. The upper Greyson Fm. was not sampled because it is cut by local intrusions which could have compromised isotopic analyses by contact metamorphism. The Sheep Creek drill core (N 46.780955°, W-110.907483°) connects the lower Newland Fm. from section 2 with the underlying Chamberlain Fm., which is not exposed in the southern Little Belt Mountains.

The third outcrop section, along Deep Creek, cuts through the western limb of the Big Belt Mountain anticline, nearly perpendicular to the fold axis (N 46.333904°, W -111.226685° to N 46.328566°, W -111.274581°). Beds dip steeply between 60° and 85° to the west over 3.5 km and display more evidence for cleavage and local shear than strata in the Little Belt Mountains. Samples were taken from undeformed layers. The section comprises parts of the Newland and lower Greysen fms (Reynolds & Brandt, 2006). It ends west of the mountain range where outcrops are less accessible due to private ownership.

8.4. Analytical methods

All analyses were carried out in the University of Washington Isolab facilities. Prior to analysis, samples were washed in DI-H₂O, and weathering surfaces were cut or polished off. Clean and dry samples were then pre-crushed into sub-cm sized chips that were sequentially sonicated in hexane, methanol and DI-H₂O (18 MΩ) for several minutes each to remove any modern organic contaminants. After drying in a ventilated fume hood, the rock chips were finely powdered in an aluminum oxide ceramic puck mill. The mill was cleaned with DI-H₂O,

methanol and pre-combusted silica sand (500°C overnight) in between samples. The resulting powder was stored in pre-combusted pyrex vials.

Nitrogen and organic carbon analyses were carried out on decarbonated powder aliquots. Carbonate was removed by acidification in centrifuge tubes with 20 % HCl (assay) at 65°C for three days, and the acid was refreshed after the first day. The decarbonated samples were washed three times with DI-H₂O to remove any residual acid and left to dry for three days in a 65°C oven. For the analysis, 50-120 mg of powder were weighed into a 9x5 mm tin capsule, which was then flash-combusted in a Costech ECS 4010 Elemental Analyzer coupled to a continuous flow isotope-ratio mass spectrometer (Finnigan MAT253) via a ThermoFinnigan Conflo III (Garvin et al., 2009; Schoepfer et al., 2012).

Measured $\delta^{15}\text{N}$ values can be elevated by trace amounts of CO in the sample gas stream, produced by incomplete combustion of organic carbon (Beaumont et al., 1994). Contributions of CO were monitored by observing the peak shape of the $^{15}\text{N}/^{14}\text{N}$ ratio. Because CO is released from the gas chromatograph of the EA slightly later than N₂, significant contributions of CO result in an irregularity in the $^{15}\text{N}/^{14}\text{N}$ peak (Garvin et al., 2009). However, no such signals were observed in any of the samples. The absence of CO interferences was further verified by analyzing one sample mixed with varying amounts of V₂O₅ (Acros Organics, containing trace nitrogen: [N] = 0.0035 ± 0.0002%, $\delta^{15}\text{N}$ 29.27 ± 1.16 ‰, n = 7), which is a strong oxidizing agent and improves combustion of organic carbon to CO₂ (Papineau et al., 2009). Furthermore, V₂O₅ can improve the extraction of silicate-bound NH₄⁺ (Bräuer & Hahne, 2005). The chosen sample (+186.8 m, Jefferson Creek) has one of the highest $\delta^{15}\text{N}$ values, a relatively high TOC content, and no carbonate. If CO were produced by incomplete combustion, then it should be most apparent in this sample. However, no trend is observed over a range of V₂O₅/sample ratios

from 0.1 to 1.7, where sample amount ranged from 50 to 60 mg and nitrogen contributions from V_2O_5 were subtracted. These results indicate that CO is not produced and no isotopically distinct nitrogen phase is missed during combustion without addition of V_2O_5 .

Isotope and abundance measurements were calibrated against three in-house standards (two glutamic acids, GA-1 and GA-2, and dried salmon, SA), which were analyzed after each set of six samples. In-house standards were calibrated against the international reference materials USGS40 and USGS41 (Qi et al., 2003). The average analytical accuracy in individual runs based on the calibrated in-house standards was -0.02 ± 0.07 ‰ (1σ) for $\delta^{15}N$, -0.08 ± 0.14 ‰ (1σ) for $\delta^{13}C$, -1.1 ± 1.3 % (relative error, RE) for total nitrogen, and -0.2 ± 0.5 % (RE) for total carbon. The average analytical precision was 0.08 ± 0.07 ‰ for $\delta^{15}N$, 0.04 ± 0.02 ‰ for $\delta^{13}C_{org}$, 1.7 ± 1.4 % (RE) for total nitrogen, and 1.0 ± 0.8 % (RE) for total carbon. Sample replicates were measured to achieve a standard deviation of 0.5 ‰ or better for $\delta^{15}N$. The average difference between replicate acidifications, tested with 12 samples, was 0.36 ± 0.28 ‰ for $\delta^{15}N$ and 0.13 ± 0.24 ‰ for $\delta^{13}C$. Total nitrogen varied on average by 21 ± 17 % (1σ) and total carbon by 2 ± 2 % (1σ). Some of this difference is likely due to sample heterogeneity, because the total nitrogen and carbon quantities were relatively small.

Carbon and oxygen isotopes in carbonates were analyzed on untreated powders with a third generation Kiel Carbonate Device (Thermo Scientific) coupled to a dual-inlet isotope-ratio mass spectrometer (Delta-Plus Thermo Scientific). Aliquots of 0.1 to 1.5 mg of powder were reacted with 10 drops of concentrated anhydrous phosphoric acid at $80^\circ C$ for 12 minutes. Generated CO_2 gas was trapped and purified cryogenically before analysis in the mass spectrometer. Measurements were calibrated against three in-house calcite standards (C-1, C-2 and CQS-1, calibrated against the international standards NBS19 and L-SVEC, Coplen, 1994;

Coplen et al., 2006, and references therein) that were analyzed after a set of eight samples. The carbonate mineral in the samples was assumed to be calcite because it reacted readily with 1M HCl (cf. Hall & Veizer, 1996). Therefore no additional correction was applied during data processing (Kim et al., 2007). The average analytical accuracy based on calibrated standards was 0.04 ± 0.02 ‰ for $\delta^{18}\text{O}$, 0.01 ± 0.03 ‰ for $\delta^{13}\text{C}_{\text{carb}}$, and 7.6 ± 9.0 % (RE) for total carbonate. The average analytical precision was 0.07 ± 0.03 ‰ for $\delta^{18}\text{O}$, 0.05 ± 0.05 ‰ for $\delta^{13}\text{C}_{\text{carb}}$, and 3.5 ± 11.4 % (RE) for total carbonate. Results are reported in standard delta notation relative to air for nitrogen and relative to Vienna PeeDee Belemnite (VPDB) for carbon and oxygen (Table 8.1).

While sedimentary characteristics of the Newland Fm. have been described and discussed in great detail (Zieg, 1986; Schieber, 1989), small-scale sedimentological features of the Neihart, Chamberlain, and Greyson fms are not well documented. Some samples of typical lithologies from each facies were therefore examined by optical microscopy to further constrain relative changes in depositional environments, especially along the Jefferson Creek transect.

8.5. Results

8.5.1. Petrography

The upper Neihart Fm. has been described as a fine-grained orthoquartzite with lenses and laminae of interbedded shale (Zieg, 1986; Schieber, 1989; Ross & Villeneuve, 2003). Cross-stratification is visible at sub-cm to dm-scale within the sand beds, and the silty shale lenses are frequently wavy-laminated at mm-scale. Detailed examination of the sandstone reveals that the grain size is bimodal (Figure 8.3A), containing well-rounded, sub-spherical, medium to coarse-grained sand particles embedded in a matrix of close-packed, angular, fine sand grains. Some

laminae are matrix-supported, whereas in others the larger grains are in point-contact. Minerals other than quartz, most importantly K-spar, make up less than 10 % of both grain-size populations. Grains are mostly cemented by silica, but some beds contain interstitial iron oxides. The silty shale lenses, one of which was sampled for this study, are medium grey in color and range in thickness from less than one cm to several cm.

The Chamberlain Fm. is significantly more diverse in its lithology than the Neihart Fm. In the lower part of the Chamberlain, three different lithologies are interbedded at scales ranging from a few mm to several dm. The most abundant lithology is poorly-sorted coarse siltstone to very fine sandstone (Figure 8.3C top) composed of angular quartz grains (~70%), muscovite flakes (~20%) and K-spar (~10%). Interstitial spaces are filled with a matrix of fine clay and irregularly shaped opaque particles, some of which may be organic matter, giving the rock its overall dark gray appearance. In hand-samples, fine wavy and cross-lamination can be seen at mm-scale in some beds (Zieg, 1986). The second rock type in the lower Chamberlain is plane-laminated black silty shale (Figure 8.3C bottom). It rarely forms beds thicker than a few cm, but is frequently present as thin laminae between thick packages of the coarser sandstone components. The silt grains suspended within the clay laminae are typically finer in size with a higher ratio of muscovite to quartz than those in preceding lithology. Some laminae within the shale are opaque and wrinkly, suggesting that they may be remnants of microbial mats (cf. Schieber, 1998a). Mud cracks are rare (Horodyski, 1993), but well developed on some surfaces (Figure 8.3G). The third lithology (Figure 8.3B) is fine sandstone composed mostly of quartz, K-spar (~10%) and a small amount of muscovite. Laminae alternate between grain-supported, with clay particles filling the few interstitial spaces, and matrix-supported, where the matrix is dark gray and contains abundant opaque particles, probably including organic matter. The sandstone

laminae are typically wavy laminated and rarely cross-bedded. Some sand beds contain randomly oriented mm to cm-long fragments of laminated black shale. The sandstone facies is most common just above the Neihart-Chamberlain contact, but is present in every outcrop throughout the lower Chamberlain.

The upper Chamberlain differs from the lower Chamberlain in that the sandstone facies is absent, and the coarse-siltstone to fine-sandstone facies contains a higher proportion of clay matrix (~40%) and muscovite among the particles (~30%). The shale facies is more abundant, now forming dm-thick platy packages. So, overall, the average grain size decreases up-section and muscovite becomes relatively more abundant in the silt-sized component. Furthermore, calcareous cement starts to appear in some beds in the upper-most part of the Chamberlain (Zieg, 1986).

The Newland Fm. at the end of the Jefferson Creek section is composed of m-thick beds of calcareous massive shale, interbedded with dm-thick beds of nearly non-calcareous plane-laminated shale. The latter is identical to the shale facies of the Chamberlain Fm. The carbonate-rich facies contains abundant black laminae and vuggy porosity filled with microspar (Figure 8.3D). These vugs are frequently associated with fluid escape structures. Sedimentary features of the Newland Fm. sampled in the Sheep Creek drill core and from outcrops along Newlan Creek and Deep Creek are broadly similar to the partially calcareous shale of the Jefferson Creek section (see Zieg, 1986, and Schieber, 1989a, for more detailed descriptions). Sandstone beds are very rare, and the most common rock type is calcareous shale with small proportions of silt (Figure 8.3E). Beds are mostly planar but sometimes wavy laminated.

The Greyson Fm. has been described as a silty shale with scattered sandstone (Zieg, 1986; Horodyski, 1993). The principal difference to the Chamberlain Fm. is the near absence of

cm-thick beds of plane-laminated black shale. Instead, shale laminae occur mostly at mm-scale, are typically greenish-gray in color and always closely interlaminated with silt and sometimes sand layers. Wavy lamination and cross-bedding are ubiquitous at sub-cm scale (Figure 8.3F). Mud cracks were not observed.

8.5.2. Nitrogen isotopes

$\delta^{15}\text{N}$ values show consistent stratigraphic and lateral trends across the four sampling sites (Figure 8.4A-D). In the eastern-most section at Jefferson Creek, values are generally highest, but decrease towards the west and stratigraphically upwards. From the top of the Neihart quartzite to upper Chamberlain Formation at Jefferson Creek (Figure 8.4D), $\delta^{15}\text{N}$ stays relatively constant around $+4.5 \pm 0.8$ ‰ (n = 9), before it declines to a minimum of $+0.7$ ‰ and a lower average of $+2.3 \pm 1.1$ ‰ (n = 5) in the upper part of the section. This lower average is similar to that of the Sheep Creek drill core ($+2.5 \pm 0.6$ ‰, n = 11, Figure 8.4C), which captures the Chamberlain-to-Newland transition further to the west, and it also overlaps with values measured at the base of the Newland Fm. sampled along Newlan Creek (Figure 8.4B). Above the lowest two measurements at the base of the Newlan Creek section, $\delta^{15}\text{N}$ declines further to an average of $+1.3 \pm 0.5$ ‰ (n = 12) which persists up into the Greyson Fm. Here $\delta^{15}\text{N}$ decreases again to -0.1 ± 0.5 ‰ (n = 5). In the Deep Creek section (Figure 8.4A) that is furthest to the west, nitrogen isotopes generally show much greater variability. The total average of this section is $+0.1 \pm 0.9$ ‰ (n = 25), but ranges from -1 ‰ to $+1.9$ ‰.

8.5.3. Organic carbon isotopes

$\delta^{13}\text{C}_{\text{org}}$ values show large variations within a range from -19 ‰ to -34‰ throughout the four sections but record consistent stratigraphic trends (Figure 8.4). In the eastern-most section in Jefferson Creek (Figure 8.4D), organic carbon isotopes start out at -30.7 ± 0.3 ‰ ($n = 2$) at the Neihart-to-Chamberlain contact, but then decline to a minimum of -34.2 ‰ in the middle of the Chamberlain Fm. After this negative excursion, values return to around -31 ‰ at the base of the Newland Fm. As for $\delta^{15}\text{N}$, $\delta^{13}\text{C}_{\text{org}}$ measurements at the top of the Jefferson Creek section overlap with the average composition of the Sheep Creek drill core (-32.0 ± 0.4 ‰, $n = 11$, Figure 8.4C), and are similar, albeit slightly more negative, to the basal values of the Newlan Creek section (Figure 8.4B). For the rest of the Newland Fm. along Newlan Creek, values average around -28.3 ± 0.9 ‰ ($n = 11$), but then decline steadily in the Greyson Fm., reaching a minimum of -32.8 ‰ at the top of the section. Throughout the first 1.2 km of the Deep Creek section in the western part of the embayment (Figure 8.4A), $\delta^{13}\text{C}_{\text{org}}$ averages around -20.1 ± 0.8 ‰ ($n = 10$), but then steadily declines to -29 ‰ at the end of the section in the lower Greyson Fm.

8.5.4. Carbon and oxygen isotopes in carbonates

Carbonate is abundant in the Newland Fm., but scarce to absent in the Neihart, Chamberlain and Greyson fms. In the Jefferson Creek section (Figure 8.4D), $\delta^{13}\text{C}_{\text{carb}}$ values increase over a stratigraphic distance of 80 m from a minimum of -2 ‰ at the top of the Chamberlain Fm. to -0.1 ‰ at the base of the Newland Fm. $\Delta^{13}\text{C}$ ($= \delta^{13}\text{C}_{\text{carb}} - \delta^{13}\text{C}_{\text{org}}$) has an average of 30.2 ± 0.9 ‰ ($n = 5$) but does not show a similar trend. $\delta^{18}\text{O}$ is highly variable around an average of -9.5 ± 1.9 ‰ ($n = 6$) (Table 8.1). The carbonate content of all analyzed samples lies mostly between 28 and 44 wt%, with one outlier at 5.5 wt%.

Of the Sheep Creek drill core (Figure 8.4C), only three samples contained enough carbonate (8-22 wt%) for isotopic analyses. $\delta^{13}\text{C}_{\text{carb}}$ and $\delta^{18}\text{O}$ values range from -1.8 ‰ to +0.8 ‰ and from -7.8 ‰ to -6.5 ‰, respectively, with no stratigraphic trend. The average $\Delta^{13}\text{C}$ is 31.5 ± 1.0 ‰.

In the Newlan Creek section (Figure 8.4B), which is fairly carbonate rich (range 5-94 %, average 29 %), $\delta^{13}\text{C}_{\text{carb}}$ starts out at around +0.5 ‰, *i.e.* within the range of values found in the drill core and the lower Newland Formation from Jefferson Creek. About 700 m above the base of the section, $\delta^{13}\text{C}_{\text{carb}}$ increases sharply to an average of $+1.8 \pm 0.4$ ‰ ($n = 7$), which persists into the lowest Greyson Fm. Then values decrease again to around -0.3 ± 0.4 ‰ ($n = 3$). $\Delta^{13}\text{C}$ increases steadily up section from approximately 28 ‰ at the bottom to nearly 32 ‰ at the top. $\delta^{18}\text{O}$ fluctuates around -9.8 ± 1.9 ‰ throughout the section.

In Deep Creek (Figure 8.4A), carbonate is similarly abundant as in Newlan Creek. Above the lowest two samples, where $\delta^{13}\text{C}_{\text{carb}}$ is around +0.5 ‰, $\delta^{13}\text{C}_{\text{carb}}$ increases to an average of $+1.3 \pm 0.2$ ‰ ($n = 8$) for about 1 km. Values then decrease to $+0.8 \pm 0.2$ ‰ (after removing one outlier at 537 m below the contact to the Greyson Fm.). $\Delta^{13}\text{C}$ stays low for the first 800 m (20.8 ± 0.6 ‰, $n = 7$), then increases up section to a new plateau around 26.4 ± 0.8 ‰ ($n = 8$). $\delta^{18}\text{O}$ increases from an average of -8.1 ± 0.4 ‰ ($n = 9$) in the lower Newland Fm. to a brief maximum of -4.5 ‰. Values then generally decrease again towards -9.2 ‰ at the top of the Newland (and one extreme outlier at -13.2 ‰), but are overall more variable than before. No carbonate was detected in the Greyson Fm. in this section.

8.6. Discussion

8.6.1. Preservation of primary isotopic signatures

Both organic and inorganic carbon and nitrogen can be mobilized and isotopically fractionated during diagenesis or metamorphism. It is therefore essential to evaluate all possibilities for alteration before making any biogeochemical interpretations.

8.6.1.1. Diagenesis

During early diagenesis under oxic conditions, partial oxidation of refractory components of fresh biomass can lead to an isotopic enrichment in $\delta^{15}\text{N}$ by up to +4‰ and a depletion in $\delta^{13}\text{C}_{\text{org}}$ by -1.6‰ (Freudenthal et al., 2001; Lehman et al., 2002). The TOC/N ratio increases because organic nitrogen is more readily oxidized than carbon. Under anoxic conditions, both $\delta^{15}\text{N}$ and $\delta^{13}\text{C}_{\text{org}}$ can become depleted by -3 ‰ and -1.6 ‰, respectively, while the TOC/N ratio remains nearly constant (Freudenthal et al., 2001; Lehman et al., 2002). Diagenetic effects may thus contribute to isotopic fluctuations seen within each of the four sections (Figure 8.4), but they are probably too small to explain the large-scale variation of up to 6 and 16 ‰, respectively, in either $\delta^{15}\text{N}$ or $\delta^{13}\text{C}_{\text{org}}$ (Robinson, 2012). If oxic degradation were responsible for the positive $\delta^{15}\text{N}$ excursion found in the Chamberlain Fm., then the excursion should correlate with high TOC/N ratios, which is not observed ($R^2 = 0.04$; Figure 8.5A). Furthermore, the shale beds sampled in the Chamberlain Fm. are black in appearance (in contrast to the highly oxidized redbeds found, for example, in the Spokane Fm. or the upper Belt Supergroup) and not depleted in organic carbon relative to other parts of the sections, which suggests that these sediments were anoxic or suboxic during the time of deposition. This makes it unlikely that oxic diagenesis is the reason for elevated $\delta^{15}\text{N}$ values in the Chamberlain Fm. or elsewhere.

Oxygen and carbon isotopes in carbonates can be reset during late diagenesis by infiltration of fluids with a different isotopic composition (Banner & Hanson, 1990). However, in

this dataset $\delta^{18}\text{O}$ and $\delta^{13}\text{C}_{\text{carb}}$ do not correlate with each other ($R^2 = 0.03$; Figure 8.5B), which would be the case if measured variations in both systems were entirely due to alteration (Banner & Hanson, 1990). Furthermore, there is no consistent difference in the isotopic composition between carbonate-poor and carbonate-rich samples (Table 8.1), as one might expect if samples with a low carbonate content were more readily altered than pure carbonates. It is therefore likely that $\delta^{13}\text{C}_{\text{carb}}$ values are primary. Oxygen, however, is generally more susceptible to isotopic exchange than carbon (Banner & Hanson, 1990). Furthermore, measured $\delta^{18}\text{O}$ values could be affected by mineralogical differences that were not accounted for during data processing. It is therefore possible that measured $\delta^{18}\text{O}$ data do not record primary compositions.

8.6.1.2. Metamorphism

Nitrogen is generally more mobile than organic carbon during metamorphic alteration above greenschist facies, resulting in increasing TOC/N ratios and $\delta^{15}\text{N}$ values (Haendel *et al.*, 1986; Bebout & Fogel, 1992; Ader *et al.*, 1998; Jia, 2006). However, the metamorphic grade of rocks in the Helena embayment is generally low, below greenschist facies (Schieber, 1989). Furthermore, it increases with depth and towards the west (Lydon, 2007), and so, if metamorphism were playing a role, the heaviest $\delta^{15}\text{N}$ values would be expected in the lower part of the Deep Creek section rather than in Jefferson Creek at the eastern edge of the basin. Lastly, $\delta^{15}\text{N}$ and TOC/N ratio do not show any correlation, neither within individual sections ($R^2_{\text{DeepCreek}} = 0.07$, $R^2_{\text{NewlanCreek}} = 0.25$, $R^2_{\text{SheepCreek}} = 0.26$, $R^2_{\text{JeffersonCreek}} = 0.02$) nor over the entire dataset ($R^2_{\text{total}} = 0.04$; Figure 8.5A). The nitrogen data are therefore most likely unaffected by metamorphism. Organic carbon isotopes also tend to become more positive with increasing metamorphic grade (Hayes *et al.*, 1983), while inorganic carbon isotopes in carbonate can

become lighter by equilibration with organic matter (Schidlowski et al., 1983). However under sub-greenschist facies conditions, the effect is only a few permil and cannot explain the 12 ‰ variation in $\Delta^{13}\text{C}$ within this dataset. Given the east-west metamorphic trend and the correlative increase in thickness of the rock formations, the greatest metamorphic effect would be expected for the lower Newland Fm. along Deep Creek, which displays the heaviest $\delta^{13}\text{C}_{\text{org}}$ values (Figure 8.4A). However, if this isotopic enrichment were due to metamorphism, then $\delta^{13}\text{C}_{\text{carb}}$ values should be relatively depleted, which is not the case. Furthermore, the heavy $\delta^{13}\text{C}_{\text{org}}$ values found in these samples have among the lowest $\delta^{15}\text{N}$ values (Figure 8.5C) and TOC/N ratios (Figure 8.5D), which is inconsistent with metamorphic overprinting.

8.6.2. Depositional environment

Zieg (1986) and Schieber (1986) concluded from field observations that the Neihart and Chamberlain fms represent a transgressive stage when the Helena embayment was flooded from the west. The Newland Fm. thus captures maximum flooding, and the Greyson Fm. marks a time of regression. Results presented in this study are consistent with this model.

The high maturity of the Neihart sandstone, the abundant cross-bedding and the bimodal distribution in grain size and angularity are indicative of a high-energy littoral setting. The larger well-rounded grains were probably reworked and mixed with the finer population by wave activity. Shale lenses and laminae could have been incorporated during intermittent low-energy periods. The subsequent transitions into the Chamberlain and finally the Newland Fm. are most plausibly explained by progressive deepening, indicated by several lines of evidence: (i) The contacts between the three formations are conformable and gradual at outcrop-scale, showing that environmental conditions must have changed progressively from the beach environment of

the Neihart Fm. (ii) The scarcity (though not absence, Figure 8.3G), of mudcracks, occasional occurrences of wave-cross-lamination, and the appearance of carbonate at the top of the section imply that both the Chamberlain and Newland Fm. were mostly deposited subaqueously. (iii) The overall decrease in average grain size along the Jefferson Creek section suggests a decrease in water energy from high in the Neihart to moderate in the Chamberlain, to low in the Newland. (iv) The change in mineralogy in the silt and very fine sand facies towards a higher proportion of muscovite is consistent with a decrease in depositional energy (Schieber, 1998a). Mica-rich beds do not show enhanced cleavage or any other evidence of stronger metamorphic overprint compared to mica-poor beds. Therefore, a metamorphic origin for these mica grains can be ruled out. (v) The appearance of substantial amounts of microcrystalline carbonate in the Newland Fm. may suggest that the terrigenous sediment influx was reduced, which is consistent with a relatively deep-water setting.

Although it is difficult to determine absolute water depth from any of the features (except mud-cracks) described in this study, it is likely that the Newland Fm. in each of the four sections represents a lower-energy, deeper water regime further offshore than the Neihart and Chamberlain fms., consistent with previous models (Schieber, 1986; Zieg, 1986). The deepest part of the embayment is probably captured by the western exposures of the lower Newland Fm. along Deep Creek, where wave or storm activity seems to have had little to no effect on sedimentation (Schieber, 1989).

Grain-size coarsening, frequent cross-stratification and the slow disappearance of carbonate in the Greyson Fm. is best explained by a return to a shallower-water environment, perhaps similar to that represented by the Chamberlain Fm. or slightly deeper (Zieg, 1986). The

absence of black shales, however, might reflect more open water circulation at this time in this part of the Helena embayment, which lies closer to the western opening of the basin.

8.6.3. Carbon cycling in the Belt basin

8.6.3.1. Diversity in carbon fixation pathways

Carbon isotopes are fractionated primarily during CO₂ fixation by autotrophic organisms. Depending on which carbon fixation pathway is dominating and under which conditions it is operating, the isotopic difference between contemporary carbonate and total organic carbon can vary by several permil (Schidlowski et al., 1983). The lowest fractionation with a minimum of 20 ‰ occurs in the lower Newland Fm. along the Deep Creek section. In the upper Newland Fm., which is preserved in both the Deep Creek and Newlan Creek section, fractionations are larger closer to the margin of the Helena embayment (~30 ‰, Newlan Creek) than towards the main branch of the basin (~27 ‰, Deep Creek). $\delta^{13}\text{C}_{\text{carb}}$ could not be measured in the lower Chamberlain Fm. where $\delta^{13}\text{C}_{\text{org}}$ is lowest, but assuming a value between -2 and + 2 ‰, *i.e.* within the observed range of carbonate-bearing samples higher up in the stratigraphy, $\Delta^{13}\text{C}$ values in the Chamberlain Fm. were probably between 32 and 36 ‰. This range overlaps with values of up to 32 ‰ found in the Greyson Fm. along Newlan Creek. Combined with the facies analysis, carbon isotopes are thus more strongly fractionated in onshore environments and relatively shallow water throughout the Helena embayment.

Both extremes in $\Delta^{13}\text{C}$ may result from cyanobacteria alone, fixing CO₂ under different environmental conditions or nutrient supplies, but it is also conceivable that this large isotopic gradient is a manifestation of diverse metabolic strategies. Larger fractionations may reflect a higher proportion of methanogenesis and methanotrophy, which together can fractionate carbon

isotopes by as much as 85 ‰ (Schidlowski, 2001). Such organisms could have thrived at and below the sediment-water interface in microbial mats such as those found in the Chamberlain Fm. (Figure 8.3B). Fractionations of 30 ‰ in the upper Newland Fm. along Newlan Creek probably indicate a small contribution of this metabolism to the total biomass. Slightly smaller $\Delta^{13}\text{C}$ values in the stratigraphically analogous upper Newland Fm. along Deep Creek could be the result of metamorphic alteration. Alternatively, they may indicate a geographic gradient in methanogenic contributions from the basin margin to the opening. The upper Deep Creek section shows a greater abundance of silty intervals compared to its stratigraphic equivalent along Newland Creek, suggesting that the Deep Creek sediments were deposited under relatively higher energy. This difference could be due to stronger wave mixing closer to the less restricted main branch of the basin (Irwin, 1965). Consequently, microbial mats and methanogens were perhaps less pervasive in the more turbulent regimes of the western part of the embayment, leading to comparatively smaller carbon isotope fractionations of 27 ‰ in bulk organic matter.

The lowest fractionations associated with deep water in the lower Newland Fm., which was anoxic and ferruginous (Planavsky et al., 2011), may have been induced by a large population of anoxygenic photosynthetic bacteria. Green sulphur and green non-sulphur bacteria, for example, typically fractionate carbon isotopes in the range of 9 ‰ to 21 ‰ (Schidlowski, 1987). Although the water column was probably not euxinic (Planavsky et al., 2011), pyrite is present in the Newland Fm. (Strauss & Schieber, 1990, personal observations; Lyons *et al.*, 2000; Luepke & Lyons, 2001), and hence sulfide as well as Fe^{2+} may have been available substrates for anoxygenic phototrophs, which have previously been identified as possibly significant contributors to the mid-Proterozoic biosphere (Brocks et al., 2005; Johnston et al., 2009). The absence of small $\Delta^{13}\text{C}$ values in the lower part of the Newlan Creek section is

probably a reflection of a shallower water column with a relatively larger oxygenated surface layer and perhaps less efficient entrainment of anoxic deep waters from the main branch of the basin compared to the Deep Creek locality. Even though neither of the two endmembers in $\Delta^{13}\text{C}$ are absolutely diagnostic of a particular metabolism, the data are thus at least consistent with a gradient in microbial community structures between onshore and offshore settings, perhaps in response to other geochemical parameters, including nitrogen speciation.

8.6.3.2. Isotopic variability in dissolved inorganic carbon (DIC)

Inorganic carbon isotope values from the Helena embayment (range -2.0 to +2.3 ‰, grand mean +0.6 ‰) overlap widely with those of other early Mesoproterozoic marine carbonates (Buick *et al.*, 1995; Frank *et al.*, 1997; Kah *et al.*, 1999; Shields & Veizer, 2002; Frank *et al.*, 2003), consistent with – though not indicative of – a marine influence on water chemistry inferred during previous geochemical studies (Hall & Veizer, 1996; Frank *et al.*, 1997; Lyons *et al.*, 2000; Luepke & Lyons, 2001; Pratt, 2001; Lyons *et al.*, 2006).

As DIC concentrations were probably high during the early Proterozoic, it is unlikely that excursions in $\delta^{13}\text{C}_{\text{carb}}$ were caused by short-term perturbations of the carbon cycle (Bartley & Kah, 2004), but lateral variations may have persisted at steady state, especially in an epicratonic sea such as the Belt basin (Kah *et al.*, 2012; Gilleaudeau & Kah, 2013). Hence the comparatively low values in $\delta^{13}\text{C}_{\text{carb}}$ in the Greyson Fm. (Newlan Creek) and the lower Newland Fm. (Jefferson Creek) may have resulted from locally enhanced methanogenic recycling of organic matter in microbial mats (Gilleaudeau & Kah, 2013, and references therein), which is supported by the large $\Delta^{13}\text{C}$ values in these samples. Overall, however, $\Delta^{13}\text{C}$ and $\delta^{13}\text{C}_{\text{carb}}$ are not strongly correlated ($R^2 = 0.11$ for all data; $R^2 = 0.05$ if Jefferson Creek data are excluded), indicating that

metabolic diversity is not the principal driver of variation in $\delta^{13}\text{C}_{\text{carb}}$ (cf. Ripperdan, 2001). An additional factor may have been the ‘biological pump’ (Kroopnick, 1995), *i.e.* differences in productivity affecting both the consumption and recycling of DIC. The biological pump may have been weaker in the Precambrian than it is today (Fischer et al., 2009), but it could still have been significant in the Belt sea, given that the effects are severe in modern restricted basins (Song et al., 2013). It may thus be possible to reconstruct the $\delta^{13}\text{C}_{\text{DIC}}$ -profile of the Helena embayment from the four sections (cf. Song et al., 2013, and references therein). The positive $\delta^{13}\text{C}_{\text{carb}}$ excursion to +2 ‰ in the Newlan Creek transect, for example, may reflect a peak in productivity at mid-water depth, possibly triggered by upwelling of nutrients into the photic zone. Unfortunately, accurate reconstruction of the isotopic profile is complicated because the carbonates may have precipitated higher up in the water column rather than *in situ* (e.g. Higgins et al., 2009). Petrographic observations of predominantly microcrystalline carbonate are not necessarily indicative of but consistent with water-column precipitation. Furthermore, $\delta^{13}\text{C}_{\text{DIC}}$ may also have varied laterally due to upwelling of $\delta^{13}\text{C}$ -depleted DIC from the main branch or freshwater input along the coast, similar to other epicratonic basins (Patterson & Walter, 1994; Holmden *et al.*, 1998; Freeman, 2001; Panchuk *et al.*, 2005). The positive excursion from the Newlan Creek section (Figure 8.4B), for example, is only represented by a single data point in the Deep Creek section (Figure 8.4A), although both sections capture the transition from the Newland into the Greyson Fm.

8.6.4. Nitrogen cycling in the Belt basin

$\delta^{15}\text{N}$ shows a general trend from most positive values along the shallow basin margin to most negative values offshore. Most biological activity and hence production of organic

nitrogen probably occurred in the photic zone. The observed trend is therefore a reflection of lateral variation in dissolved nitrogen speciation and availability near the sea surface. However, the speciation of nitrogen in the photic zone is heavily influenced by the degree of biomass remineralization and/or denitrification in deeper waters. The lateral gradient in $\delta^{15}\text{N}$ is thus most likely due to lateral variation in the redox-state of water column.

8.6.4.1. Offshore anaerobic nitrogen cycling

Assuming that the nitrogen isotopic composition of the atmosphere has not changed markedly over time (Sano & Pillinger, 1990), values within a range from -2 ‰ to +2‰ as observed in the offshore sections can result from one of three possible scenarios: (i) N_2 fixation as the principle nitrogen source for the local biota and without any further processing prior to or during sedimentation. This would be the case especially under anoxic conditions that inhibit nitrification, which is strictly dependent on O_2 (Stenstrom & Poduska, 1980; Klotz & Stein, 2008); (ii) Rapid nitrification followed by quantitative denitrification across a redox gradient in the water column, such that very little NO_3^- is available for uptake and its isotopic composition does not contribute significantly to bulk samples; (iii) Fixed nitrogen is readily nitrified, but the water column is so pervasively oxidized that denitrification is restricted to sediments. In this case, the isotopic composition of dissolved nitrate is identical to that of the fixed nitrogen from which it formed, and the biomass of nitrate-consuming organisms is indistinguishable from that of nitrogen fixers.

The third scenario is unlikely in the case of the Newland Fm., because iron speciation indicates that deeper water in this part of the basin was anoxic and ferruginous (Planavsky et al., 2011). In the absence of oxygen, organic-bound nitrogen sinking below the photic zone or

produced by N_2 -fixation at depth could not have been nitrified. Hence, even though rapid aerobic turnover of nitrogen compounds may have occurred in the photic zone (scenario (ii); Figure 8.6), nitrate was probably scarce such that the relative contribution of residual nitrate to biomass would have been limited. Therefore, the offshore parts of the Belt basin were likely dominated by an anaerobic nitrogen cycle that was isotopically controlled by nitrogen fixation (scenario (i)). Small fluctuations around 0 ‰ may thus result from minor contributions of isotopically enriched nitrate, but also from anoxic diagenetic processes (Freudenthal et al., 2001; Lehman et al., 2002), or from variations in the availability of dissolved iron, which can affect the fractionation imparted during N_2 fixation (Zerkle et al., 2008). It has recently been proposed that during ocean anoxic events in the mid-Cretaceous, dissolved NH_4^+ served as a major source of fixed nitrogen for eukaryotes (Higgins et al., 2012). In that case, NH_4^+ -replete conditions were inferred from bulk sedimentary $\delta^{15}N$ values < -2 ‰ resulting from partial NH_4^+ -assimilation. In the Mesoproterozoic Belt basin, however, such light values are not observed, suggesting that NH_4^+ did not build up to high concentrations. Furthermore, eukaryotes are usually outcompeted by prokaryotes in assimilation of NH_4^+ (Anbar & Knoll, 2002 and references therein). Offshore regions in the Belt basin were therefore likely inhospitable environments for eukaryotic organisms.

8.6.4.2. Aerobic nitrogen cycling in shallow waters

Values of up to +5 ‰ in the Chamberlain Fm. (Figure 8.4D) are outside the realm of typical fractionations associated with nitrogen fixation (Figure 8.1) and, as discussed above, cannot be explained by post-depositional alteration. Hence these values imply loss of isotopically light nitrogen from the water column. Three pathways in the biogeochemical nitrogen cycle

(Figure 8.1) can result in fractionations of this magnitude: partial assimilation of NH_4^+ advected from different parts of the basin (Papineau et al., 2009), partial nitrification followed by complete denitrification (Thomazo et al., 2011), and partial denitrification (Garvin *et al.*, 2009; Godfrey & Falkowski, 2009) or perhaps anammox. Each of these has previously been invoked to explain isotopic enrichments in other Precambrian formations and will be discussed in turn.

8.6.4.2.1. *Assimilation of NH_4^+* favors isotopically light nitrogen, rendering the residual $\text{NH}_4^+_{(\text{aq})}$ enriched in ^{15}N (e.g. Papineau et al., 2009 and references therein). $\delta^{15}\text{N}$ values of +5 ‰ in the Chamberlain Fm. would thus require that $\text{NH}_4^+_{(\text{aq})}$ was partially consumed elsewhere, before the enriched residue reached shallow waters in the eastern part of the basin where it could then serve as a major nitrogen source. This explanation is improbable because none of the other facies sampled in this study has preserved the complementary light phase, although the three outcrop sections probably span most environmental sub-settings that existed within the Helena embayment. Indeed, the lightest $\delta^{15}\text{N}$ value obtained in this study is -1 ‰, consistent with N_2 -fixation alone (see above) and far different from the very negative values required in a complementary light reservoir. If partial consumption of $\text{NH}_4^+_{(\text{aq})}$ were occurring offshore, it would have to go to near completion to be concealed by a bulk isotopic value of -1 ‰. If the isotopic fractionation associated with NH_4^+ -assimilation was perhaps much smaller than the maximum 27 ‰ (Waser et al., 1998), a large fraction of isotopically light NH_4^+ would have to be sequestered elsewhere to render the residual as heavy as +5 ‰. Consequently, the total amount of isotopically enriched residue would be very small. However, it is unlikely that such a small amount of isotopically enriched NH_4^+ could supply enough organisms to leave a detectable isotopic signal in the Chamberlain samples. The relatively high organic matter content in the

Chamberlain Fm. does not indicate that productivity and nitrogen demand were significantly smaller than in deeper parts of the basin. Partial assimilation of NH_4^+ can therefore not explain the observed pattern in $\delta^{15}\text{N}$.

8.6.4.2.2. *Partial nitrification of NH_4^+* leads to the production of isotopically light NO_2^- , while residual NH_4^+ becomes enriched (Figure 8.1). For the light isotope to be removed from the system, partial nitrification thus has to be followed by complete denitrification of NO_2^- to $\text{N}_{2(\text{g})}$. A positive $\delta^{15}\text{N}$ excursion can then result from quantitative assimilation of residual enriched NH_4^+ into biomass (Thomazo et al., 2011). If NH_4^+ is the major nitrogen source, then a bulk value of +5 ‰ as observed in the Chamberlain Fm. would require that 17 % of the dissolved NH_4^+ was nitrified, assuming a fractionation of 30 ‰ during nitrification. In the modern Black Sea, nitrification rapidly proceeds to completion and does not impart a net isotopic fractionation (Fuchsman et al., 2008), but it is conceivable that nitrification was less efficient in a Mesoproterozoic epeiric sea when atmospheric oxygen levels were lower than today. However it is important to note that so far, a mechanism like this has only been demonstrated for water bodies that undergo strong seasonal variation in oxygen concentrations due to overturn of a stratified water column (Hadas *et al.*, 2009; Granger *et al.*, 2011), but not for equilibrated systems over long geologic timescales. Thus, this scenario lacks a pathway by which isotopically enriched nitrogen is removed over the long term from the shallow ocean, other than by assimilation and burial of NH_4^+ . Remineralization of biomass, however, would have returned isotopically enriched NH_4^+ to the water column, which, after another cycle of partial nitrification, could have become progressively enriched in ^{15}N . One would therefore expect a larger range in

sedimentary $\delta^{15}\text{N}$ than what is observed in the Chamberlain Fm. Hence, overall this mechanism is an unlikely explanation for the prolonged and stable $\delta^{15}\text{N}$ enrichment in the Chamberlain Fm.

8.6.4.2.3. *Isotopic fractionation during water-column denitrification* renders the residual NO_3^- isotopically heavy (Figure 8.1). This enrichment can be preserved in biomass that quantitatively assimilates NO_3^- as a nutrient (Altabet & Francois, 1994).

A fundamental requirement for a model where water-column denitrification is the main driver of isotopic variations in sediments is quantitative nitrification and nitrate stability in most of the water column. Denitrification occurs under suboxic conditions, whereas nitrification is strictly dependent on O_2 (Stenstrom & Poduska, 1980; Klotz & Stein, 2008). Hence, for water-column denitrification to be a viable explanation for basin-scale differences in sedimentary $\delta^{15}\text{N}$, the basin has to be heterogeneous in its oxidation state. So far, independent redox analyses have only been conducted on samples from the Newland Fm., which was deposited under anoxic ferruginous conditions (Planavsky et al., 2011). But if the basin was significantly shallower during deposition of the Chamberlain Fm., and if atmospheric oxygen had already built up to a few percent of modern levels by the Mesoproterozoic (Canfield, 2005; Catling & Claire, 2005), then it seems plausible that the sediments of the Chamberlain Fm. could have formed under a mildly oxygenated water column. Even though sediments may have been anoxic where they were covered by microbial mats (Schieber, 1998a, Figure 8.3B), sedimentological evidence for wave and storm activity (Figure 8.3B) suggests that oxygen dissolved in the overlying water column may have been moderately well equilibrated with the atmosphere, which at the time contained enough oxygen to oxidize terrestrial environments (reviewed in Canfield, 2005; Catling & Claire, 2005). It is therefore conceivable that free NH_4^+ was oxidized quickly to NO_3^-

with no net isotopic fractionation, similar to the modern ocean. Subsequent denitrification would probably have occurred along the chemocline (Figure 8.6), and quantitative uptake of the residual enriched nitrate would have rendered biomass forming in shallow water isotopically heavy. In other words, nitrate was stable in the oxic shallow parts of the Belt basin, represented by the Chamberlain Fm. in the east. The general decline in $\delta^{15}\text{N}$ up section and towards the west (Figure 8.4) is consistent with progressive deepening and transition into anoxic conditions. During the regressive stage and deposition of the Greyson Fm., however, $\delta^{15}\text{N}$ remains low despite a return to somewhat shallower water regimes. This could be due to nearly quantitative denitrification by entrainment of anoxic deep waters from the proximal main branch of the basin. In this case, NO_3^- levels in the water column would have become so low that the isotopic signature of N_2 fixation dominated. Similar situations have been recorded during numerous anoxic events in the Phanerozoic ocean (Rau *et al.*, 1987; Sephton *et al.*, 2002; Ohkouchi *et al.*, 2006; Junium & Arthur, 2007; LaPorte *et al.*, 2009; Schoepfer *et al.*, 2012).

8.7. Conclusion

Nitrogen and carbon isotope data from the Lower Belt Supergroup indicate significant differences in nitrogen speciation and microbial communities between anoxic deep water and oxic basin margins. After exploring multiple possible scenarios, it seems most plausible that coastal waters were dominated by aerobic nitrogen cycling and organic matter remineralization by methanogenesis and methanotrophy in microbial mats, whereas offshore environments were predominantly anaerobic, perhaps fostering growth of anoxygenic phototrophs (Johnston *et al.*, 2009). The preservation of isotopic evidence for denitrification in the Chamberlain Fm. would imply that dissolved NO_3^- was abundant enough along basin margins to serve as the major

nitrogen source for living organisms. If fixed nitrogen, including NH_4^+ , were scarce in other parts of the basin (Section 8.6.4.1), and if eukaryotes were outcompeted by cyanobacteria in the acquisition of NH_4^+ (Anbar & Knoll, 2002), then aerobic nitrogen cycling may indeed have restricted favorable habitats for eukaryotic organisms to coastal areas (Anbar & Knoll, 2002; Buick, 2007; Johnston *et al.*, 2009). This interpretation is consistent with the occurrence of eukaryotic acritarchs in both the Greyson and the Chamberlain shale facies (Horodyski, 1980). If the Belt basin, and the Helena embayment in particular, was restricted, then water column stagnation and stratification may have been more severe than in the open ocean. The extreme difference in $\Delta^{13}\text{C}$ between onshore and offshore settings perhaps attests to this conclusion. Regions of aerobic nitrogen cycling may thus have been more extensive along the margins of the open ocean; however, the global predominance of ferruginous conditions at depth (Kendall *et al.*, 2010; Poulton *et al.*, 2010; Planavsky *et al.*, 2011; Poulton & Canfield, 2011), wide-spread scavenging of Mo from seawater by expansion of euxinia (Arnold *et al.*, 2004), and the scarcity of eukaryotic microfossils in deep-water successions from other basins (e.g. Buick & Knoll, 1999; Javaux *et al.*, 2001) support the conclusion that throughout most of the Proterozoic and perhaps the Archean nitrate-consuming organisms, especially eukaryotic algae, may have been globally restricted to shallow waters where dissolved nitrate was stable (Blumenberg *et al.*, 2012). The original hypothesis formulated by Anbar and Knoll (2002) that habitats for eukaryotes were spatially restricted to marine margins or estuaries therefore seems plausible, but it remains to be tested to what degree trace metal limitation played an active role in this pattern. Furthermore, the scarcity of rocks preserved from truly non-marine environments throughout the Precambrian makes it difficult to assess whether or not the exclusion of eukaryotes from the deep ocean did indeed result in global evolutionary retardation. It is possible that fluvial, lacustrine

and estuarine environments harbored greater eukaryotic diversity than what has been inferred from the Mesoproterozoic ocean.

Acknowledgments

This work was financially supported by NASA Exobiology/Astrobiology grant NNX08AP56G, the NAI Virtual Planetary Laboratory at the University of Washington, and the Robert and Nadine Bassett Fund of the Department of Earth & Space Sciences. Constructive criticism from the editor and three reviewers greatly improved the manuscript. I further thank Zach Adam for guidance in the field, Gerald Zieg and colleagues for access to drill core material, the UW Isolab staff for technical assistance, and Roger Buick for valuable discussion.

Tables

Table 8.1: Data set. Concentrations are in weight percent. Clastic N and TOC content are not corrected for carbonate contribution. Nitrogen isotopes are relative to air, carbon and oxygen isotopes are relative to VPDB. $\Delta^{13}\text{C}$ is calculated as $\delta^{13}\text{C}_{\text{carb}} - \delta^{13}\text{C}_{\text{org}}$. Chamberl. = Chamberlain.

Formation	[m]	$\text{N}_{\text{clastic}}$ [%]	σ [%]	$\delta^{15}\text{N}$ [‰]	σ [‰]	$\text{TOC}_{\text{clastic}}$ [%]	σ [%]	$\delta^{13}\text{C}_{\text{org}}$ [‰]	σ [‰]	TOC/N atom.	σ	CaCO_3 [%]	σ [%]	$\delta^{13}\text{C}_{\text{carb}}$ [‰]	σ [‰]	$\delta^{18}\text{O}_{\text{carb}}$ [‰]	σ [‰]	$\Delta^{13}\text{C}$ [‰]	σ [‰]
Deep Creek																			
Greyson	276.8	0.024	0.003	0.70	0.36	0.34	0.01	-28.97	0.11	16.75	1.69								
Greyson	226.1	0.031	0.003	0.03	0.04	0.82	0.02	-28.04	0.09	30.53	1.90								
Greyson	149.9	0.058	0.003	-0.58	0.24	0.21	0.00	-27.93	0.02	4.22	0.25								
Greyson	105.9	0.058	0.005	0.04	0.10	0.40	0.01	-27.31	0.11	8.08	0.68								
Newland	-42.4	0.008	0.001	0.28	0.09	0.07	0.00	-26.26	0.14	10.64	0.91	4.71	0.05	0.65	0.01	-13.22	0.01	26.91	0.14
Newland	-185.3	0.072	0.000	0.53	0.20	3.67	0.03	-28.07	0.10	59.45	0.82								
Newland	-426.3	0.026	0.004	-0.66	0.47	1.07	0.02	-25.03	0.11	48.28	7.59	60.47	2.12	1.16	0.02	-9.23	0.02	26.19	0.11
Newland	-491.6	0.039	0.003	0.11	0.01	1.68	0.01	-27.42	0.09	49.97	4.27	1.28	0.99	0.65	0.54	-4.64	0.03	28.07	0.55
Newland	-536.5	0.017	0.004	1.60	0.37	0.70	0.03	-23.34	0.06	51.02	12.06	73.76	0.93	2.34	0.01	-8.55	0.02	25.67	0.06
Newland	-780.6	0.086	0.013	1.13	0.15	0.18	0.00	-25.39	0.07	2.51	0.41	3.70	0.62	0.77	0.02	-5.83	0.08	26.16	0.08
Newland	-890.6	0.031	0.001	-0.52	0.43	0.17	0.00	-25.17	0.02	6.40	0.20	2.52	0.50	0.73	0.05	-7.58	0.10	25.89	0.06
Newland	-1001.2	0.032	0.005	-0.95	0.39	0.31	0.00	-25.31	0.07	11.79	2.01	30.64	0.15	0.61	0.01	-6.02	0.00	25.91	0.07
Newland	-1085.9	0.023	0.002	-1.02	0.12	0.67	0.01	-25.44	0.03	34.74	2.59	31.64	0.98	0.76	0.02	-5.58	0.02	26.20	0.04
Newland	-1228.9	0.018	0.000	-0.82	0.06	0.50	0.01	-24.44	0.01	32.41	0.68	11.64	0.87	0.98	0.01	-5.42	0.12	25.42	0.01
Newland	-1326.8	0.019	0.002	-0.65	0.15	1.38	0.01	-23.61	0.05	85.01	11.44	12.92	0.15	1.10	0.00	-4.53	0.05	24.71	0.05
Newland	-1532.3	0.023	0.000	-0.36	0.00	0.11	0.00	-20.97	0.01	5.51	0.02	29.71	0.02	1.64	0.07	-6.13	0.05	22.62	0.07
Newland	-1667.0	0.014	0.002	1.39	0.37	0.11	0.00	-20.64	0.17	9.74	1.10	24.3	0.58	1.40	0.02	-7.93	0.07	22.04	0.17
Newland	-1808.5	0.037	0.002	1.95	0.17	0.12	0.00	-20.85	0.17	3.70	0.11	10.0	0.00	1.29	0.00	-8.38	0.04	22.14	0.17
Newland	-1928.2	0.021	0.000	0.41	0.35	0.09	0.00	-20.01	0.13	5.10	0.01	12.81	0.37	1.13	0.00	-7.74	0.02	21.14	0.13
Newland	-1996.8	0.025	0.002	1.02	0.42	0.12	0.00	-19.74	0.08	5.38	0.55	17.63	1.82	1.24	0.02	-7.46	0.03	20.98	0.09
Newland	-2119.9	0.031	0.002	0.49	0.36	0.21	0.06	-20.09	0.03	7.78	1.77	14.70	5.01	1.12	0.30	-8.00	0.09	21.21	0.30
Newland	-2465.2	0.024	0.001	-0.32	0.45	0.06	0.00	-18.56	0.01	2.87	0.11	6.98	1.32	1.15	0.06	-7.87	0.02	19.71	0.06
Newland	-2543.2	0.020	0.000	-0.40	0.41	0.15	0.00	-19.50	0.04	8.65	0.29	28.84	3.30	1.18	0.04	-8.79	0.01	20.67	0.06

Newland	-2696.4	0.043	0.002	0.60	0.44	0.32	0.01	-19.82	0.05	8.71	0.63	5.40	0.10	0.60	0.02	-8.14	0.03	20.42	0.05
Newland	-2745.2	0.013	0.002	-1.05	0.38	0.65	0.01	-20.96	0.01	60.49	8.61	26.32	2.93	0.53	0.02	-8.28	0.12	21.49	0.03
Jefferson Creek																			
Newland	347.1	0.015	0.001	2.25	0.41	0.14	0.00	-31.31	0.17	11.61	0.50								
Newland	328.7	0.006	0.001	3.17	0.35	0.08	0.00	-31.04	0.28	17.69	4.02	44.2	0.16	-0.53	0.00	-8.05	0.03	30.51	0.28
Newland	322.6	0.010	0.000	3.41	0.08	0.12	0.00	-30.99	0.06	15.15	0.34	34.7	3.06	-0.10	0.05	-11.90	0.07	30.89	0.08
Newland	298.0	0.015	0.000	1.88	0.08	0.18	0.00	-32.40	0.12	13.88	0.34	5.5	0.71	-1.29	0.04	-7.68	0.07	31.11	0.12
Newland	296.0											28.0	2.00	-1.03	0.03	-10.64	0.01		
Chamberl.	279.6	0.009	0.001	0.67	0.05	0.15	0.00	-32.38	0.21	19.98	2.11								
Chamberl.	270.0	0.005	0.001	3.42	0.25	0.10	0.00	-30.89	0.23	22.68	2.10	37.0	4.60	-2.02	0.04	-10.98	0.06	28.87	0.24
Chamberl.	268.2	0.007	0.000	2.99	0.21	0.09	0.00	-31.08	0.21	13.91	0.09	29.9	1.12	-1.47	0.02	-7.67	0.05	29.61	0.21
Chamberl.	254.2	0.020	0.002	4.23	0.12	0.19	0.01	-32.73	0.49	11.15	1.26								
Chamberl.	186.8	0.044	0.001	5.00	0.18	1.10	0.01	-33.13	0.06	29.30	0.28								
Chamberl.	153.5	0.049	0.003	4.90	0.33	0.43	0.02	-34.09	0.21	10.27	0.39								
Chamberl.	98.9	0.042	0.002	5.02	0.33	0.58	0.02	-34.22	0.14	16.14	0.81								
Chamberl.	47.5	0.045	0.002	5.19	0.34	0.45	0.01	-33.46	0.17	11.67	0.49								
Chamberl.	3.1	0.029	0.002	5.07	0.48	0.25	0.02	-30.87	0.14	10.14	0.54								
Neihart	-94.3	0.007	0.001	4.20	0.41	0.04	0.00	-30.60	0.24	6.36	0.80								
Newlan Creek																			
Greyson	760.8	0.007	0.001	-0.34	0.49	0.13	0.00	-32.80	0.28	22.10	4.36								
Greyson	558.6	0.012	0.002	0.79	0.18	0.16	0.00	-32.56	0.25	15.72	2.58								
Greyson	356.4	0.007	0.000	-1.06	0.19	0.30	0.01	-32.00	0.19	49.13	1.44	5.55	0.40	-0.26	0.03	-10.69	0.02	31.75	0.19
Greyson	198.8	0.016	0.002	0.06	0.23	0.18	0.00	-31.27	0.21	13.54	1.64	5.64	0.49	0.05	0.00	-13.04	0.04	31.32	0.21
Greyson	137.1	0.012	0.000	0.05	0.25	0.09	0.00	-30.59	0.07	9.05	0.23	7.93	0.28	-0.76	0.04	-12.34	0.04	29.84	0.08
Greyson	12.0	0.034	0.001	1.59	0.08	0.42	0.02	-29.71	0.09	14.46	0.31	25.39	0.43	1.97	0.01	-9.98	0.03	31.68	0.09
Newland	-62.7	0.010	0.001	1.04	0.18	0.19	0.00	-28.84	0.09	21.79	2.20	8.79	0.28	1.29	0.02	-9.57	0.03	30.13	0.10
Newland	-120.2	0.011	0.002	0.60	0.23	0.27	0.00	-28.57	0.18	29.81	5.17	46.63	1.73	2.26	0.01	-10.90	0.02	30.83	0.18
Newland	-223.7	0.083	0.004	2.30	0.06	0.35	0.01	-30.00	0.13	4.91	0.09								
Newland	-266.5	0.060	0.009	1.14	0.48	1.47	0.06	-26.33	0.04	29.07	5.50	94.18	2.41	1.41	0.03	-11.19	0.03	27.74	0.05
Newland	-271.5	0.021	0.002	1.67	0.18	0.65	0.03	-28.46	0.14	36.77	1.85	80.39	3.90	2.09	0.03	-10.49	0.00	30.54	0.14
Newland	-715.9	0.012	0.001	0.61	0.44	0.10	0.00	-27.69	0.25	9.49	1.05	15.72	2.32	1.69	0.05	-7.05	0.10	29.38	0.26

Newland	-794.3	0.016	0.001	0.71	0.19	0.21	0.00	-28.28	0.13	15.45	1.25	34.36	2.62	1.92	0.03	-6.83	0.06	30.19	0.13
Newland	-867.4	0.016	0.007	1.30	0.42	0.11	0.00	-28.75	0.40	9.79	0.92	18.38	1.23	-0.30	0.03	-8.82	0.02	28.46	0.40
Newland	-1007.5	0.021	0.001	1.71	0.45	0.06	0.00	-27.62	0.11	3.54	0.14	19.36	0.45	-0.08	0.02	-8.78	0.02	27.54	0.11
Newland	-1092.1	0.009	0.000	1.33	0.44	0.23	0.00	-27.72	0.15	31.23	1.04	29.85	1.71	0.42	0.04	-10.31	0.00	28.15	0.16
Newland	-1139.2	0.014	0.002	1.83	0.18	0.10	0.00	-27.62	0.23	8.35	0.79	20.01	1.72	0.55	0.01	-7.68	0.08	28.17	0.23
Newland	-1309.0	0.044	0.001	3.47	0.16	0.30	0.00	-30.69	0.03	7.78	0.12								
Newland	-1504.9	0.036	0.001	2.78	0.25	0.26	0.01	-29.73	0.17	8.32	0.32								
Sheep Creek																			
Newland	364.3	0.025	0.001	1.52	0.16	0.65	0.03	-32.23	0.05	30.19	0.22								
Newland	335.7	0.022	0.003	2.72	0.25	0.83	0.01	-32.21	0.06	44.67	4.42	22.42	0.12	-0.44	0.03	-6.89	0.02	31.77	0.06
Newland	289.1	0.025	0.003	1.84	0.38	1.23	0.04	-31.58	0.07	57.43	6.06	17.02	0.10	0.83	0.05	-6.54	0.06	32.41	0.09
Newland	233.5	0.013	0.001	2.79	0.23	0.13	0.00	-32.00	0.07	11.90	1.27								
Newland	204.4	0.014	0.000	2.63	0.18	0.13	0.00	-32.48	0.09	11.06	0.21								
Newland	128.4	0.017	0.002	2.19	0.16	0.19	0.00	-32.24	0.13	13.28	1.22	8.07	0.84	-1.80	0.11	-7.82	0.08	30.44	0.17
Newland	77.1	0.014	0.000	3.42	0.10	0.20	0.00	-32.05	0.02	16.85	0.43								
Newland	44.2	0.008	0.000	2.48	0.28	0.43	0.02	-32.21	0.09	61.37	2.66								
Chamberl.	-0.6	0.012	0.002	2.02	0.45	0.63	0.01	-31.45	0.07	62.71	9.82								
Chamberl.	-7.9	0.044	0.002	2.52	0.00	0.96	0.06	-31.61	0.06	25.41	0.92								
Chamberl.	-22.0	0.031	0.004	3.31	0.31	0.22	0.01	-32.48	0.13	8.66	1.15								

Figures

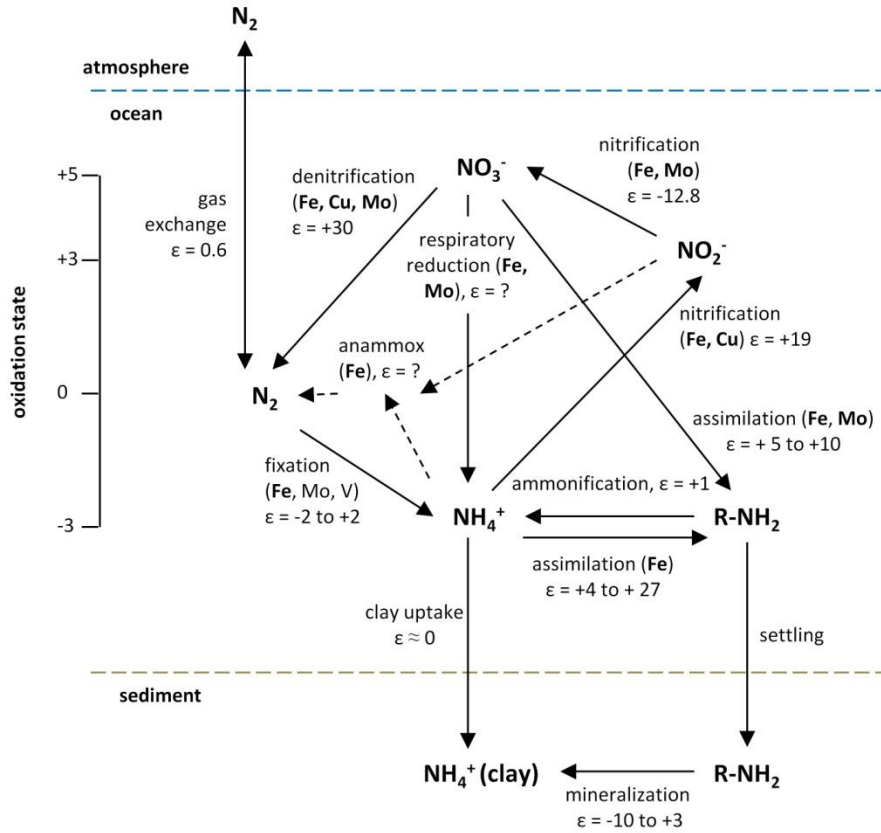


Fig. 8.1: The biogeochemical nitrogen cycle. Elements in parentheses are used as co-factors in enzymes. Bolded elements are essential. Intermediate species during the reduction of NO_3^- to N_2 or NH_4^+ are left out for simplicity. Dashed arrows indicate anammox pathway. Isotopic fractionation associated with anammox and respiratory reduction are probably similar to that of denitrification to N_2 (Quan & Falkowski, 2009). $\epsilon \approx \delta_{\text{reactant}} - \delta_{\text{product}}$. Adapted from Thomazo et al. (2011), Godfrey & Glass (2011), and Buick (2007).

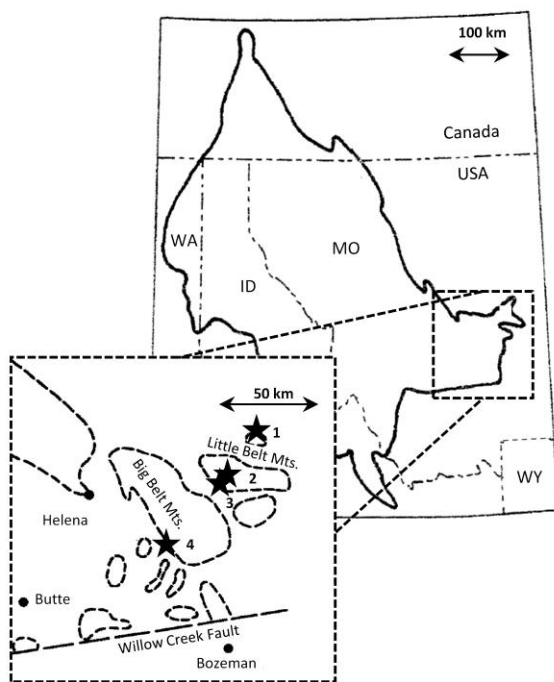


Fig. 8.2: Sample sites in the Belt Supergroup. Outline in large map shows rough extent of Belt Spgp. exposures in Montana, Idaho, Washington and British Columbia (adapted from Horodyski, 1993). Dashed outlines in blow-up mark outcrops of the lower Belt Supergroup in the Helena embayment (adapted from Strauss & Schieber, 1990). Asterics indicate section localities: 1. Jefferson Creek, 2. Newlan Creek and Sheep Creek, 3. Deep Creek.

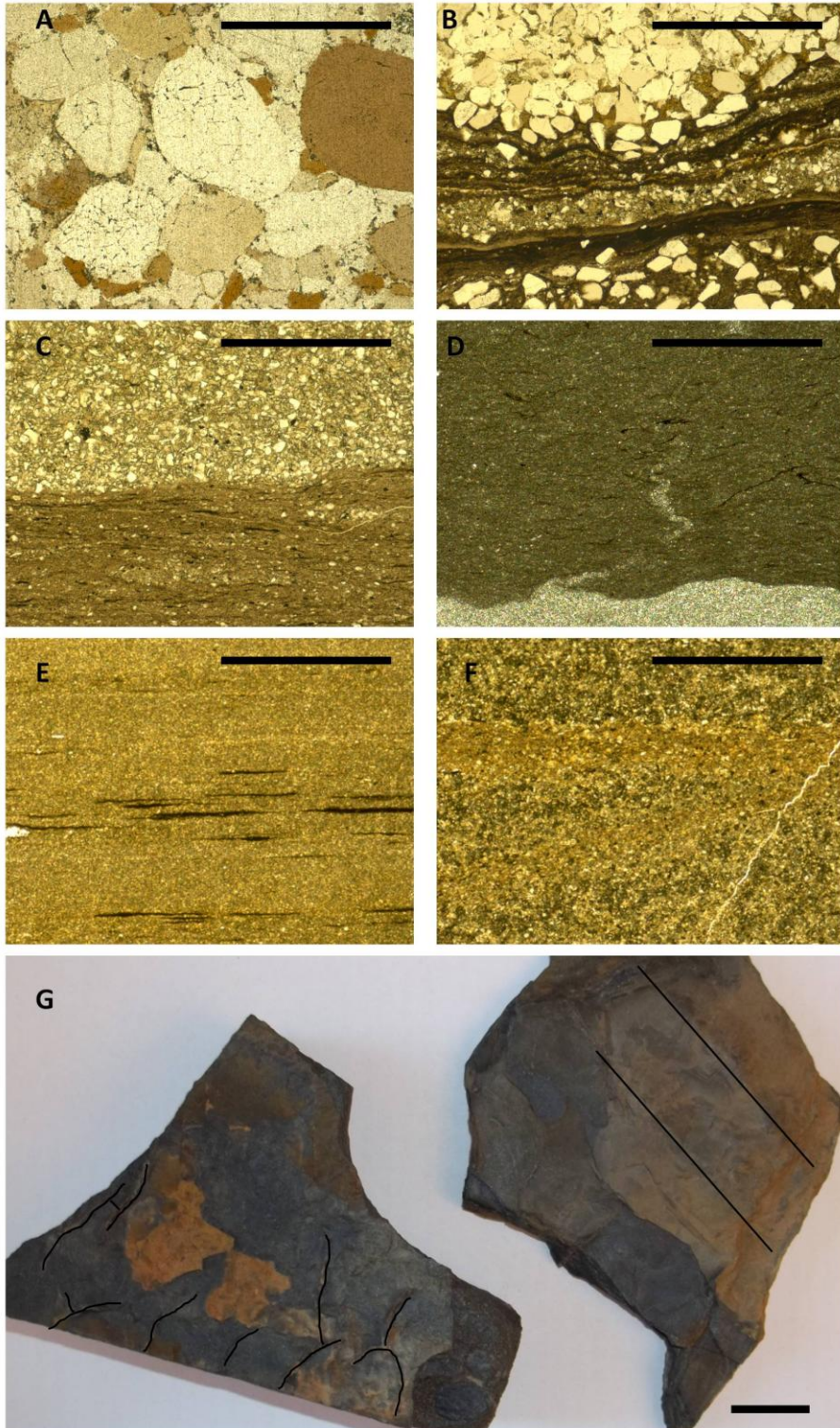


Fig. 8.3: Characteristic sedimentary features. **A.** Upper Neihart Fm. (crossed polars). **B.** fine sandstone facies of Chamberlain Fm. containing fragments of microbial mats (plane-polarized light). **C.** silt to very fine sandstone facies of Chamberlain Fm. (top part) in direct contact with laminated silty shale (lower part) (plane-polarized light) **D.** calcareous shale with micro-spar filled vugs and fluid-escape structures in lower Newland Fm., Jefferson Creek (crossed polars). **E.** calcareous plane laminated shale with carbonaceous laminae, Newland Fm., Deep Creek (plane-polarized light). **F.** silty shale displaying cross-bedding, Greyson Fm., Newlan Creek (plane-polarized light). **G.** mud-cracks (left) and wave ripples (right, marked with black lines), from the Chamberlain shale facies. Scale bar in A-D is 1 mm, scale bar in E is 2 cm.

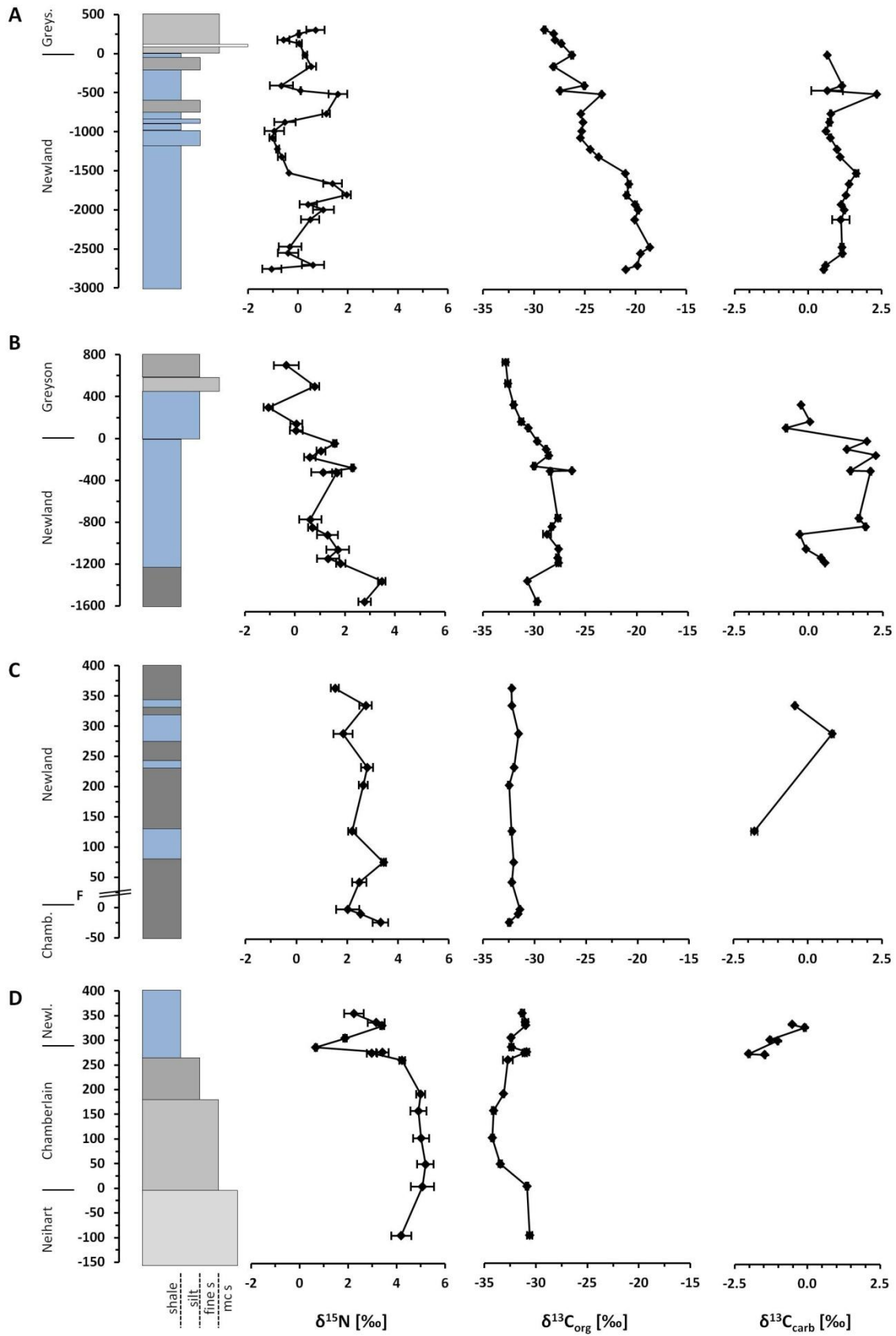


Fig. 8.4: Nitrogen and carbon isotopes the four sampled sections. A: Deep Creek, nearest to basin main branch. **B:** Newlan Creek. **C:** Sheep Creek; 'F' marks a reverse fault, but offset is unknown. **D:** Jefferson Creek, nearest to basin margin. fine s = fine-grained sandstone, mc s = medium to coarse-grained sandstone. Blue indicates presence of carbonate; The scale of the y-axis in all plots is in meters. Error bars are $\pm 1 \sigma$.

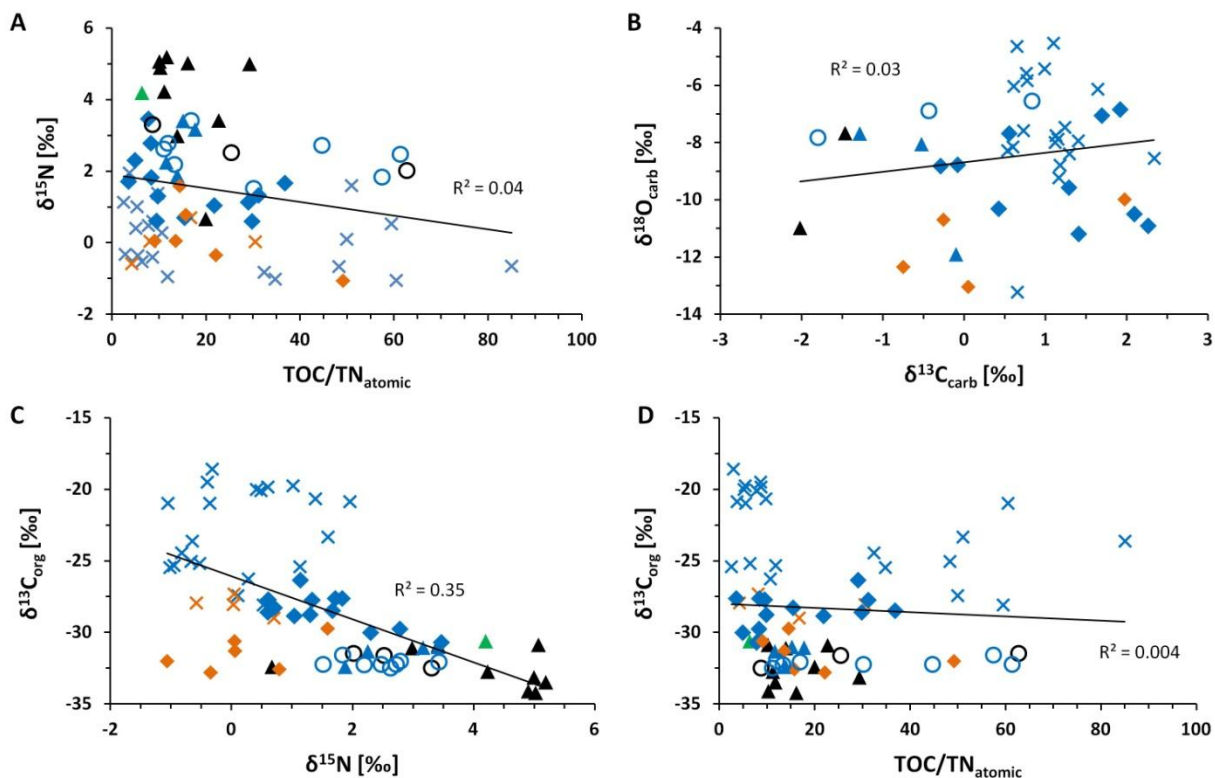


Fig. 8.5: Scatter plots of all data. A: Total $\delta^{15}\text{N}$ versus atomic TOC/N ratio. **B:** $\delta^{18}\text{O}$ versus $\delta^{13}\text{C}$ of carbonates. **C:** $\delta^{15}\text{N}$ versus organic $\delta^{13}\text{C}$. **D:** Organic $\delta^{13}\text{C}$ versus atomic TOC/N ratio.

Squares = Deep Creek, diamonds = Newlan Creek, circles = Sheep Creek, triangles = Jefferson Creek. Green = Neihart Fm., black = Chamberlain Fm., blue = Newland Fm., orange = Greyson Fm. Trend lines (black lines) and correlation coefficients represent all data points.

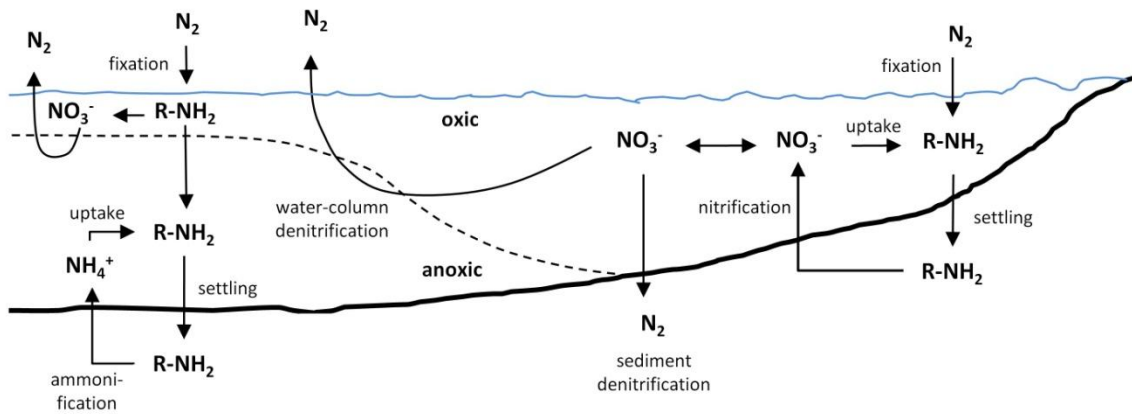


Fig. 8.6: Proposed model of nitrogen cycling in the Helena embayment. Stippled line indicates chemocline separating oxic from anoxic conditions. Aerobic pathways are restricted to the oxic basin margins or the photic zone. The deep basin is dominated by anaerobic processes.

References

- Ader M, Boudou J-P, Javoy M, Goffe B, Daniels E (1998) Isotope study on organic nitrogen of Westphalian anthracites from the Western Middle field of Pennsylvania (USA) and from the Bramsche Massif (Germany). *Organic Geochemistry*, **29**, 315-323.
- Altabet MA, Francois R (1994) Sedimentary nitrogen isotopic ratio as a recorder for surface ocean nitrate utilization. *Global Biogeochemical Cycles*, **8**, 103-116.
- Anbar AD, Knoll AH (2002) Proterozoic ocean chemistry and evolution: a bioinorganic bridge? *Science*, **297**, 1137-1142.
- Arnold GL, Anbar AD, Barling J, Lyons TW (2004) Molybdenum isotope evidence for widespread anoxia in Mid-Proterozoic oceans. *Science*, **304**, 87-90.
- Arrigo KR (2005) Marine microorganisms and global nutrient cycles. *Nature*, **437**, 349-355.
- Banner JL, Hanson GN (1990) Calculations of simultaneous isotopic and trace element variations during water-rock interaction with applications to carbonate diagenesis. *Geochimica et Cosmochimica Acta*, **54**.
- Bartley JK, Kah LC (2004) Marine carbon reservoir, C_{org} - C_{carb} coupling, and the evolution of the Proterozoic carbon cycle. *Geology*, **32**, 129-132.
- Beaumont V, Agrinier P, Javoy M, Robert F (1994) Determination of the CO contribution to the $^{15}N/^{14}N$ ratio measured by mass spectrometry. *Analytical Chemistry*, **66**, 2187-2189.
- Beaumont V, Robert F (1999) Nitrogen isotope ratios of kerogens in Precambrian cherts: a record of the evolution of atmosphere chemistry? *Precambrian Research*, **96**, 63-82.
- Bebout GE, Fogel ML (1992) Nitrogen-isotopic composition of metasedimentary rocks in the Catalina Schist, California: implications for metamorphic devolatilization history. *Geochimica et Cosmochimica Acta*, **56**, 2839-2849.
- Blumenberg M, Thiel V, Riegel W, Kah LC, Reitner J (2012) Biomarkers of black shales formed by microbial mats, Late Mesoproterozoic (1.1 Ga) Taoudeni Basin, Mauritania. *Precambrian Research*, **196-197**, 113-127.
- Boyd ES, Anbar AD, Miller S, Hamilton TL, Lavin M, Peters JW (2011) A late methanogen origin for molybdenum-dependent nitrogenase. *Geobiology*, **9**, 221-232.
- Bräuer K, Hahne K (2005) Methodical aspects of ^{15}N -analysis of Precambrian and Paleozoic sediments rich in organic matter. *Chemical Geology*, **218**, 361-368.
- Brocks JJ, Love GD, Summons RE, Knoll AH, Logan GA, Bowden SA (2005) Biomarker evidence for green and purple sulphur bacteria in a stratified Palaeoproterozoic sea. *Nature*, **437**, 866-870.
- Buick R (2007) Did the Proterozoic 'Canfield Ocean' cause a laughing gas greenhouse? *Geobiology*, **5**, 97-100.
- Buick R, Des Marais DJ, Knoll AH (1995) Stable isotopic compositions of carbonates from the Mesoproterozoic Bangemall Group, northwestern Australia. *Chemical Geology*, **123**, 153-171.
- Buick R, Knoll AH (1999) Acritarchs and microfossils from the Mesoproterozoic Bangemall Group, northwestern Australia. *Journal of Paleontology*, **73**, 744-764.
- Canfield DE (2005) The early history of atmospheric oxygen: homage to Robert M. Garrels. *Annual Review of Earth and Planetary Sciences*, **33**, 1-36.
- Canfield DE, Glazer AN, Falkowski PG (2010) The evolution and future of Earth's nitrogen cycle. *Science*, **330**, 192-196.

- Canfield DE, Kristensen E, Thamdrup B (2004) *Aquatic Geomicrobiology*, Academic Press, San Diego, CA.
- Casciotti KL (2009) Inverse kinetic isotope fractionation during bacterial nitrite oxidation. *Geochimica et Cosmochimica Acta*, **73**, 2061-2076.
- Catling DC, Claire MW (2005) How Earth's atmosphere evolved to an oxic state: a status report. *Earth and Planetary Science Letters*, **237**, 1-20.
- Chandler FW (2000) The Belt-Purcell basin as a low-latitude passive rift: implications for the geological environment of Sullivan type deposits. In: *The geological environment of the Sullivan deposit, British Columbia* (eds Lydon JW, Hoey T, Slack JF, Knapp M). Geological Association of Canada, Mineral Deposits Division, Special Publication, pp. 82-112.
- Coplen TB (1994) Reporting of stable hydrogen, carbon, and oxygen isotopic abundances. *Pure and Applied Chemistry*, **66**, 273-276.
- Coplen TB, Brand WA, Gehre M, Groening M, Meijer HAJ, Toman B, Verkouteren RM (2006) After two decades a second anchor for the VPDB $\delta^{13}\text{C}$ scale. *Rapid Communications in Mass Spectrometry*, **20**, 3165-3166.
- Cressman ER (1989) Reconnaissance stratigraphy of the Prichard Formation (middle Proterozoic) and the early development of the Belt basin, Washington, Idaho, and Montana. *US Geological Survey Professional Papers*, **1490**.
- Evans Kv, Aleinikoff JN, Obradovich JD, Fanning CM (2000) SHRIMP U-Pb geochronology of volcanic rocks, Belt Supergroup, western Montana: evidence for rapid deposition of sedimentary strata. *Canadian Journal of Earth Sciences*, **37**, 1287-1300.
- Falkowski PG (1997) Evolution of the nitrogen cycle and its influence on the biological sequestration of CO_2 in the ocean. *Nature*, **387**, 272-275.
- Fennel K, Follows M, Falkowski PG (2005) The co-evolution of the nitrogen, carbon and oxygen cycles in the Proterozoic ocean. *American Journal of Science*, **305**, 526-545.
- Fischer WW, Schroeder S, Lacassie JP, Beukes NJ, Goldberg T, Strauss H, Horstmann UE, Schrag DP, Knoll AH (2009) Isotopic constraints on the late Archean carbon cycle from the Transvaal Supergroup along the western margin of the Kaapvaal craton, South Africa. *Precambrian Research*, **169**, 15-27.
- Frank TD, Kah LC, Lyons TW (2003) Changes in organic matter production and accumulation as a mechanism for isotopic evolution in the Mesoproterozoic ocean. *Geological Magazine*, **140**, 397-420.
- Frank TD, Lyons TW, Lohmann KC (1997) Isotopic evidence for the paleoenvironmental evolution of the Mesoproterozoic Helena Formation, Belt Supergroup, Montana, USA. *Geochimica et Cosmochimica Acta*, **61**, 5023-5041.
- Freeman KH (2001) Isotopic biogeochemistry of marine organic carbon. *Reviews in Mineralogy and Geochemistry*, **43**, 579-605.
- Freudenthal T, Wagner T, Wenzhoefer F, Zabel M, Wefer G (2001) Early diagenesis of organic matter from sediments of the eastern subtropical Atlantic: evidence from stable nitrogen and carbon isotopes. *Geochimica et Cosmochimica Acta*, **65**, 1795-1808.
- Fuchsman CA, Murray J, Konovalov SK (2008) Concentration and natural stable isotope profiles of nitrogen species in the Black Sea. *Marine Chemistry*, **111**, 90-105.
- Garvin J, Buick R, Anbar AD, Arnold GL, Kaufman AJ (2009) Isotopic evidence for an aerobic nitrogen cycle in the latest Archean. *Science*, **323**, 1045-1048.

- Gilleaudeau GJ, Kah LC (2013) Carbon isotope records in a Mesoproterozoic epicratonic sea: Carbon cycling in a low-oxygen world. *Precambrian Research*, **228**, 85-101.
- Glass JB, Wolfe-Simon F, Anbar AD (2009) Coevolution of metal availability and nitrogen assimilation in cyanobacteria and algae. *Geobiology*, **7**, 100-123.
- Godfrey LV, Falkowski PG (2009) The cycling and redox state of nitrogen in the Archaean ocean. *Nature Geoscience*, **2**, 725-729.
- Godfrey LV, Glass JB (2011) The geochemical record of the ancient nitrogen cycle, nitrogen isotopes, and metal cofactors. *Methods in Enzymology*, **486**, 483-506.
- Granger J, Prokopenko MG, Sigman DM, Mordy CW, Morse ZM, Morales LV, Sambrotto RN, Plessen B (2011) Coupled nitrification-denitrification in sediment of the eastern Bering Sea shelf leads to ¹⁵N enrichment of fixed N in shelf waters. *Journal of Geophysical Research*, **116**, doi: 10.1029/2010JC006751.
- Hadas O, Altabet MA, Agnihotri R (2009) Seasonally varying nitrogen isotope biogeochemistry of particulate organic matter (POM) in Lake Kinneret, Israel. *Limnology and Oceanography*, **54**, 75-85.
- Haendel D, Muehle K, Nitzsche H-M, Stiehl g, Wand U (1986) Isotopic variations of the fixed nitrogen in metamorphic rocks. *Geochimica et Cosmochimica Acta*, **50**, 749-758.
- Hall SM, Veizer J (1996) Geochemistry of Precambrian carbonates: VII. Belt Supergroup, Montana and Idaho, USA. *Geochimica et Cosmochimica Acta*, **60**, 667-677.
- Harrison JE (1972) Precambrian Belt basin of northwestern United States: its geometry, sedimentation, and copper occurrences. *Geological Society of America Bulletin*, **83**, 1215-1240.
- Hayes JM, Kaplan IR, Wedeking KW (1983) Precambrian organic geochemistry, preservation of the record. In: *Earth's earliest biosphere - its origin and evolution* (ed Schopf JW). Princeton University Press, Princeton, NJ.
- Higgins JA, Fischer WW, Schrag DP (2009) Oxygenation of the ocean and sediments: consequences for the seafloor carbonate factory. *Earth and Planetary Science Letters*, **284**, 25-33.
- Higgins MB, Robinson RS, Husson JM, Carter SJ, Pearson A (2012) Dominant eukaryotic export production during ocean anoxic events reflects the importance of recycled NH₄⁺. *Proceedings of the National Academy of Sciences*, **109**, 2269-2274.
- Holmden C, Creaser RA, Muehlenbachs K, Leslie SA, Bergstroem SM (1998) Isotopic evidence for geochemical decoupling between ancient epeiric seas and bordering oceans: implications for secular curves. *Geology*, **26**, 567-570.
- Horodyski RJ (1980) Middle Proterozoic shale-facies microbiota from the lower Belt Supergroup, Little Belt Mountains, Montana. *Journal of Paleontology*, **54**, 649-663.
- Horodyski RJ (1993) Paleontology of Proterozoic shales and mudstones: examples from the Belt Supergroup, Chuar Group and Pahrump Group, western USA. *Precambrian Research*, **61**, 241-278.
- Irwin ML (1965) General theory of epeiric clear water sedimentation. *American Association of Petroleum Geologists Bulletin*, **49**, 445-459.
- Javaux EJ, Knoll AH, Walter MR (2001) Morphological and ecological complexity in early eukaryotic ecosystems. *Nature*, **412**, 66-69.
- Jia Y (2006) Nitrogen isotope fractionations during progressive metamorphism: a case study from the Paleozoic Cooma metasedimentary complex, southeastern Australia. *Geochimica et Cosmochimica Acta*, **70**, 5201-5214.

- Johnston DT, Wolfe-Simon F, Pearson A, Knoll AH (2009) Anoxygenic photosynthesis modulated Proterozoic oxygen and sustained Earth's middle age. *Proceedings of the National Academy of Sciences*, **106**, 16925-16929.
- Junium CK, Arthur MA (2007) Nitrogen cycling during the Cretaceous, Cenomanian-Turonian Oceanic Anoxic Event II. *Geochemistry Geophysics Geosystems*, **8**, doi: 10.1029/2006GC001328.
- Kah LC, Bartley JK (2011) Protracted oxygenation of the Proterozoic biosphere. *International Geology Review*, **53**, 1424-1442.
- Kah LC, Bartley JK, Teal DA (2012) Chemostratigraphy of the late Mesoproterozoic Atar Group, Taoudeni basin, Mauritania: muted isotopic variability, facies correlation, and global isotopic trends. *Precambrian Research*, **200-203**, 82-103.
- Kah LC, Sherman AG, Narbonne GM, Knoll AH, Kaufman AJ (1999) $\delta^{13}\text{C}$ stratigraphy of the Proterozoic Bylot Supergroup, Baffin Island, Canada: implications for regional lithostratigraphic correlations. *Canadian Journal of Earth Sciences*, **36**, 313-332.
- Karl D, Michaels A, Bergman B, Capone D, Carpenter E, Letelier R, Lipschultz F, Paerl H, Sigman D, Stal L (2002) Dinitrogen fixation in the world's oceans. *Biogeochemistry*, **57/58**, 47-98.
- Kendall B, Reinhard CT, Lyons TW, Kaufman AJ, Poulton SW, Anbar AD (2010) Pervasive oxygenation along late Archaean ocean margins. *Nature Geoscience*, **3**, 647-652.
- Kim S-T, Mucci A, Taylor BE (2007) Phosphoric acid fractionation factors for calcite and aragonite between 25 and 75 C: revisited. *Chemical Geology*, **246**, 135-146.
- Klotz MG, Stein LY (2008) Nitrifier genomics and evolution of the nitrogen cycle. *FEMS Microbiology Letters*, **278**, 146-156.
- Kroopnick PM (1995) The distribution of ^{13}C of ΣCO_2 in the world oceans. *Deep Sea Research Part A. Oceanographic Research Papers*, **32**, 57-84.
- Lam P, Lavik G, Jensen MM, van de Vossenberg J, Schmid M, Woebken D, Gutierrez D, Amann R, Jetten MSM, Kuypers MMM (2009) Revising the nitrogen cycle in the Peruvian oxygen minimum zone. *Proceedings of the National Academy of Sciences*, **106**, 4752-4757.
- LaPorte DF, Holmden C, Patterson WP, Loxton JD, Melchin MJ, Mitchell CE, Finney SC, Sheets HD (2009) Local and global perspectives on carbon and nitrogen cycling during the Hirnantian glaciation. *Palaeogeography Palaeoclimatology Palaeoecology*, **276**, 182-195.
- Lehman MR, Bernasconi SM, Barbieri A, McKenzie JA (2002) Preservation of organic matter and alteration of its carbon and nitrogen isotope composition during simulated and in situ early sedimentary diagenesis. *Geochimica et Cosmochimica Acta*, **66**, 3573-3584.
- Luepke JJ, Lyons TW (2001) Pre-Rodinian (Mesoproterozoic) supercontinental rifting along the western margin of Laurentia: geochemical evidence from the Belt-Purcell Supergroup. *Precambrian Research*, **111**, 79-90.
- Lydon JW (2007) Geology and metallogeny of the Belt-Purcell basin. In: *Mineral deposits of Canada: a synthesis of major deposit-types, district metallogeny, the evolution of geological provinces, and exploration methods* (ed Goodfellow WD). Geological Association of Canada, Mineral Deposits Division, Special Publication, pp. 581-607.
- Lyons TW, Gellatly AM, McGoldrick PJ, Kah LC (2006) Proterozoic sedimentary exhalative (SEDEX) deposits and links to evolving global ocean chemistry. In: *Evolution of early*

- Earth's atmosphere, hydrosphere, and biosphere - constraints from ore deposits* (eds Kesler SE, Ohmoto H). Geological Society of America Memoir.
- Lyons TW, Luepke JJ, Schreiber ME, Zieg GA (2000) Sulfur geochemical constraints on Mesoproterozoic restricted marine deposition: lower Belt Supergroup, northwestern United States. *Geochimica et Cosmochimica Acta*, **64**, 427-437.
- Moore EM (1991) Southwest US - East Antarctica (SWEAT) connection: a hypothesis. *Geology*, **19**, 425-428.
- Ohkouchi N, Kashiyama Y, Kuroda J, Ogawa NO, Kitazato H (2006) The importance of diazotrophic cyanobacteria as primary producers during Cretaceous Oceanic Anoxic Event 2. *Biogeosciences*, **3**, 467-478.
- Panchuk KM, Holmden C, Kump LR (2005) Sensitivity of the epeiric sea carbon isotope record to local-scale carbon cycle processes: tales from the Mohawkian Sea. *Palaeogeography Palaeoclimatology Palaeoecology*, **228**, 320-337.
- Papineau D, Purohit R, Goldberg T, Pi D, Shields GA, Bhu H, Steele A, Fogel ML (2009) High primary productivity and nitrogen cycling after the Paleoproterozoic phosphogenic event in the Aravalli Supergroup, India. *Precambrian Research*, **171**, 37-56.
- Patterson WP, Walter LM (1994) Depletion of ^{13}C in seawater CO_2 on modern carbonate platforms: significance for the carbon isotopic record of carbonates. *Geology*, **22**, 885-888.
- Pinti DL, Hashizume K (2011) Early life record from nitrogen isotopes. In: *Earliest life on Earth: habitats, environments and methods of detection* (eds Golding SD, Glikson M). Springer.
- Planavsky NJ, McGoldrick PJ, Scott C, Li C, Reinhard CT, Kelly AE, Chu X, Bekker A, Love GD, Lyons TW (2011) Widespread iron-rich conditions in the mid-Proterozoic ocean. *Nature*, **477**, 448-451.
- Poulton SW, Canfield DE (2011) Ferruginous conditions: a dominant feature of the ocean through Earth's history. *Elements*, **7**, 107-112.
- Poulton SW, Fralick PW, Canfield DE (2010) Spatial variability in oceanic redox structure 1.8 billion years ago. *Nature Geoscience*, **3**, 486-490.
- Pratt BR (2001) Oceanography, bathymetry and syndepositional tectonics of a Precambrian intracratonic basin: integrating sediments, storms, earthquakes and tsunamis in the Belt Supergroup (Helena Formation, ca. 1.45 Ga), western North America. *Sedimentary Geology*, **141-142**, 371-394.
- Prokopenko MG, Hammond DE, Berelson WM, Bernhard JM, Scott L, Douglas R (2006) Nitrogen cycling in the sediments of Santa Barbara basin and eastern subtropical North Pacific: nitrogen isotopes, diagenesis, and possible chemosymbiosis between two lithotrophs (*Thioploca* and *Anammox*) - "riding on a glider". *Earth and Planetary Science Letters*, **242**, 186-204.
- Qi H, Coplen TB, Geilmann H, Brand WA, Boehlke JK (2003) Two new organic reference materials for d^{13}C and d^{15}N measurements and a new value for the d^{13}C of NBS 22 oil. *Rapid Communications in Mass Spectrometry*, **17**.
- Quan TM, Falkowski PG (2009) Redox control of N:P ratios in aquatic ecosystems. *Geobiology*, **7**, 124-139.
- Rau GH, Arthur MA, Dean WE (1987) $^{15}\text{N}/^{14}\text{N}$ variations in Cretaceous Atlantic sedimentary sequences: implications for past changes in marine nitrogen biogeochemistry. *Earth and Planetary Science Letters*, **82**, 269-279.

- Raymond J, Siefert JL, Staples CR, Blankenship RE (2004) The natural history of nitrogen fixation. *Molecular Biology and Evolution*, **21**, 541-554.
- Reynolds MW, Brandt TR (2006) Preliminary geologic map of the Townsend 30' x 60' quadrangle, Montana. US Geological Survey.
- Reynolds MW, Brandt TR (2007) Preliminary geologic map of the White Sulphur Springs 30' x 60' quadrangle, Montana. US Geological Survey.
- Ripperdan RL (2001) Stratigraphic variation in marine carbonate carbon isotope ratios. *Reviews in Mineralogy and Geochemistry*, **43**, 637-662.
- Robinson D (2001) $\delta^{15}\text{N}$ as an integrator of the nitrogen cycle. *TRENDS in Ecology & Evolution*, **16**, 153-162.
- Robinson RS (2012) A review of nitrogen isotopic alteration in marine sediments. *Paleoceanography*, **27**, doi: 10.1029/2012PA002321.
- Ross GM, Villeneuve M (2003) Provenance of the Mesoproterozoic (1.45 Ga) Belt basin (western North America): another piece in the pre-Rodinia paleogeographic puzzle. *Geological Society of America Bulletin*, **115**, 1191-1217.
- Sahoo SK, Planavsky NJ, Kendall B, Wang X, Shi X, Scott C, Anbar AD, Lyons TW, Jiang G (2012) Ocean oxygenation in the wake of the Marinoan glaciation. *Nature*, **489**, 546-549.
- Saito MA, Sigman DM, Morel FMM (2003) The bioinorganic chemistry of the ancient ocean: the co-evolution of cyanobacterial metal requirements and biogeochemical cycles at the Archean-Proterozoic boundary? *Inorganica Chimica Acta*, **356**, 308-318.
- Sano Y, Pillinger CT (1990) Nitrogen isotopes and N_2/Ar ratios in cherts: an attempt to measure time evolution of atmospheric $\delta^{15}\text{N}$ value. *Geochemical Journal*, **24**, 315-325.
- Schidlowski M (1987) Application of stable carbon isotopes to early biochemical evolution on Earth. *Annual Review of Earth and Planetary Sciences*, **15**, 47-72.
- Schidlowski M (2001) Carbon isotopes as biogeochemical recorders of life over 3.8 Ga of Earth history: evolution of a concept. *Precambrian Research*, **106**, 117-134.
- Schidlowski M, Hayes JM, Kaplan IR (1983) Isotopic interferences of ancient biochemistries: carbon, sulfur, hydrogen, and nitrogen. In: *Earth's earliest biosphere - its origin and evolution* (ed Schopf JW). Princeton University Press, Princeton, NJ.
- Schieber J (1986) Stratigraphic control of rare-earth pattern types in mid-Proterozoic sediments of the Belt Supergroup, Montana, USA: implications for basin analysis. *Chemical Geology*, **54**, 135-148.
- Schieber J (1989) Facies and origin of shales from the mid-Proterozoic Newland Formation, Belt basin, Montana, USA. *Sedimentology*, **36**, 203-219.
- Schieber J (1990) Significance of styles of epicontinental shale sedimentation in the Belt basin, mid-Proterozoic of Montana, USA. *Sedimentary Geology*, **69**, 297-312.
- Schieber J (1998a) Possible indicators of microbial mat deposits in shales and sandstones: examples from the mid-Proterozoic Belt Supergroup, Montana, USA. *Sedimentary Geology*, **120**, 105-124.
- Schieber J (1998b) Sedimentologic, geochemical, and mineralogical features of the Belt Supergroup and their bearing on the lacustrine versus marine debate. Montana Bureau of Mines Special Publication.
- Schoepfer SD, C.M. H, Garrison GH, Ward PD (2012) Cessation of a productive coastal upwelling system in the Panthalassic Ocean at the Permian-Triassic boundary. *Palaeogeography Palaeoclimatology Palaeoecology*, **313-314**, 181-188.

- Schoepp-Cothenet B, van Lis R, Phillippot P, Magalon A, Russell MJ, Nitschke W (2011) The ineluctable requirement for the trans-iron elements molybdenum and/or tungsten in the origin of life. *Scientific Reports*, **2**, doi: 10.1038/srep00263.
- Scott C, Bekker A, Reinhard CT, Schnetger B, Krapez B, Rumble III D, Lyons TW (2011) Late Archean euxinic conditions before the rise of atmospheric oxygen. *Geology*, **39**, 119-122.
- Scott C, Lyons TW, Bekker A, Shen Y, Poulton SW, Chu X, Anbar AD (2008) Tracing the stepwise oxygenation of the Proterozoic ocean. *Nature*, **452**, 456-459.
- Sears JW, Chamberlain KR, Buckley SN (1998) Structural and U-Pb geochronological evidence for 1.47 Ga rifting in the Belt basin, western Montana. *Canadian Journal of Earth Sciences*, **35**, 467-475.
- Sears JW, Price RA (2000) New look at the Siberian connection: no SWEAT. *Geology*, **28**, 423-426.
- Sephton MA, Amor K, Franchi IA, Wignall PB, Newton R, Zonneveld J-P (2002) Carbon and nitrogen isotope disturbances and an end-Norian (Late Triassic) extinction event. *Geology*, **30**, 1119-1122.
- Shields G, Veizer J (2002) Precambrian marine carbonate isotope database: Version 1.1. *Geochemistry Geophysics Geosystems*, **3**, doi: 10.1029/2001GC000266.
- Sigman DM, Altabet MA, McCorkle DC, Francois R, Fischer G (2000) The $\delta^{15}\text{N}$ of nitrate in the southern ocean: nitrogen cycling and circulation in the ocean interior. *Journal of Geophysical Research*, **105**, doi: 10.1029/2000JC000265.
- Sigman DM, DiFiore PJ, Hain MP, Deutsch C, Wang Y, Karl DM, Knappe AN, Lehman MF, Pantoja S (2009a) The dual isotope of deep nitrate as a constraint on the cycle and budget of oceanic fixed nitrogen. *Deep Sea Research Part I*, **56**, 1419-1439.
- Sigman DM, Karsh KL, Casciotti KL (2009b) Ocean process tracers: nitrogen isotopes in the ocean. In: *Encyclopedia of ocean science*. Elsevier, Amsterdam.
- Song H, Tong J, Algeo TJ, Horacek M, Qiu H, Song H, Tian L, Chen Z-Q (2013) Large vertical $\delta^{13}\text{C}_{\text{DIC}}$ gradients in Early Triassic seas of the South China craton: Implications for oceanographic changes related to Siberian Traps volcanism. *Global and Planetary Change*, **105**, 7-20.
- Stenstrom MK, Poduska RA (1980) The effect of dissolved oxygen concentration on nitrification. *Water Research*, **14**, 643-649.
- Strauss H, Schieber J (1990) A sulfur isotope study of pyrite genesis: the mid-Proterozoic Newland Formation, Belt Supergroup, Montana. *Geochimica et Cosmochimica Acta*, **54**, 197-204.
- Thomazo C, Ader M, Phillippot P (2011) Extreme ^{15}N -enrichment in 2.72-Gyr-old sediments: evidence for a turning point in the nitrogen cycle. *Geobiology*, **9**, 107-120.
- Tyrrell T (1999) The relative influences of nitrogen and phosphorus on oceanic primary production. *Nature*, **400**, 525-531.
- Waser NA, Yin K, Yu Z, Tada K, Harrison PJ, Turpin DH, Calvert SE (1998) Nitrogen isotope fractionation during nitrate, ammonium and urea uptake by marine diatoms and coccolithophores under various conditions of N availability. *Marine Ecology Progress Series*, **169**, 29-41.
- Winston D (1986) Sedimentology of the Ravalli Group, middle Belt carbonate and Missoula Group, middle Proterozoic Belt Supergroup, Montana, Idaho and Washington. In: *Belt Supergroup* (ed Roberts SM). Montana Bureau of Mines and Geology, Special Publication, pp. 85-124.

- Winston D (1990) Evidence for intracratonic, fluvial and lacustrine settings of middle to late Proterozoic basins of western USA. In: *Mid-Proterozoic Laurentia-Baltica* (eds Gower CF, Rivers T, Ryan B). Geological Association Canada, Special Papers, pp. 535-564.
- Zerkle A, Junium CK, Canfield DE, House CH (2008) Production of ¹⁵N-depleted biomass during cyanobacterial N₂-fixation at high Fe concentrations. *Journal of Geophysical Research*, **113**, doi: 10.1029/2007JG000651.
- Zieg GA (1986) Stratigraphy and sedimentology of the middle Proterozoic upper Newland limestone. In: *Belt Supergroup - A guide to Proterozoic rocks of western Montana and adjacent areas* (ed Roberts SM). Montana Bureau of Mines and Geology, Special Publication, pp. 125-142.

Chapter 9: Isotopic evidence for biological N₂ fixation by Mo-nitrogenase since 3.2 Gyr

Abstract

Nitrogen is an essential nutrient for all organisms that must have been bioavailable since the origin of life. Abiotic processes including hydrothermal reduction (Brandes *et al.*, 1998), photochemical reactions (Tian *et al.*, 2011) or lightning discharge (Navarro-Gonzalez *et al.*, 2001) could have converted atmospheric N₂ into bioavailable NH₄⁺, HCN, or NO_x species, collectively termed fixed nitrogen. But these sources should have been scarce on the early Earth, severely limiting the size of the primordial biosphere (Kasting & Siefert, 2001). The evolution of the N₂-fixing enzyme nitrogenase, which reduces atmospheric N₂ to organic NH₄⁺, thus represented a major breakthrough in the radiation of life but its timing is uncertain (Raymond *et al.*, 2004; Boyd *et al.*, 2011a). Here we present tightly clustered nitrogen isotope ratios near 0‰ from slightly metamorphosed marine and fluvial sedimentary rocks between 3.2 and 2.75 Gyr. These are strongly indicative of biological N₂ fixation using Mo-based nitrogenase rather than the alternative V and Fe isozymes which impart significant negative fractionations (Zhang *et al.*, 2014). Our data place a minimum age constraint of 3.2 Gyr on the origin of this enzyme, the most ancient record of a specific biomolecule, implying that Mo was bioavailable in the mid-Archean ocean long before Great Oxidation Event (GOE). The early origin of biological nitrogen sequestration in an anoxic environment could have significantly affected the atmospheric N₂ budget over geologic timescales (Som *et al.*, 2012).

9.1. Introduction

Nitrogenase is present in ~15% of all sequenced prokaryotic genomes, including several phyla of Bacteria and one phylum of Archaea, but it is absent in Eukaryotes (Dos Santos *et al.*, 2012). The most common form contains Mo in the catalytically active site (Nif), but a subset of diazotrophic (N₂-fixing) organisms also produce ‘alternative nitrogenases’ containing V (Vnf) or Fe (Anf) (Boyd *et al.*, 2011b; McGlynn *et al.*, 2012). It was once thought that Vnf and Anf evolved earlier than Nif, possibly in the Archean when seawater was enriched in Fe and depleted in Mo (Anbar & Knoll, 2002; Raymond *et al.*, 2004), but more recent phylogenetic evidence indicates that Nif is ancestral to the alternative isozymes (Boyd *et al.*, 2011a; Boyd *et al.*, 2011b). Protein substitution rates (Boyd *et al.*, 2011a), combined with the conventional view that Mo was scarce in the ocean prior to ~2.5 Gyr (Scott *et al.*, 2008), have been interpreted as pointing to a relatively late origin of Mo-nitrogenase around 1.5-2.2 Gyr (Boyd *et al.*, 2011a). However, other Mo-based enzymes, in particular the molybdopterin cofactor, have been traced back phylogenetically to the last universal common ancestor (Schoepp-Cothenet *et al.*, 2012), implying that some Mo was bioavailable in the early Archean. Furthermore, abiotic nitrogen sources may have become limiting long before the GOE (Kasting & Siefert, 2001), making it conceivable that Nif is much more ancient than new models suggest.

Nitrogen isotopes of sedimentary rocks can resolve this issue because metabolic nitrogen pathways exert characteristic fractionations that can be preserved in kerogen over geologic time. Generally positive $\delta^{15}\text{N}$ values from the late Archean (2.7-2.5 Gyr) indicate an aerobic nitrogen cycle involving nitrification and denitrification (Garvin *et al.*, 2009; Godfrey & Falkowski, 2009). It is widely assumed that prior to ~2.7 Gyr, before the onset of oxidative weathering on land (Stüeken *et al.*, 2012), the nitrogen cycle was anaerobic (Thomazo & Papineau, 2013). An

isotopic signature of biological nitrogen fixation, if present, should therefore be discernible from the Archean rock record. Nif imparts a fractionation of -2 to +1‰ (average -1‰) relative to atmospheric N₂, while Vnf and Anf fractionate δ¹⁵N by -6 to -8‰ (Zhang *et al.*, 2014). The composition of the atmosphere has probably been between -2 and +2‰ since the early Archean (Sano & Pillinger, 1990 ; Marty *et al.*, 2013). Therefore δ¹⁵N values of Archean sediments should reveal if nitrogenase had evolved and which of the three isozymes was ecologically dominating. However, all published nitrogen isotope data from early and mid-Archean rocks are compromised by metamorphic alteration to above greenschist facies, by metasomatism with ammoniated brines, by hydrothermal input at the time of deposition, or by high analytical uncertainty (Thomazo & Papineau, 2013, Appendix A9.1). Existing δ¹⁵N data from the earlier Archean are thus extremely scattered, unrepresentative of normal marine conditions, and inconclusive as to the presence of microbial nitrogen fixation (McGlynn *et al.*, 2012).

To address this problem and to place a better constraint of the origin of nitrogenase, we analyzed nitrogen as well as organic carbon isotope ratios in shales and siltstones of very low metamorphic grade from various marine and non-marine environments between 3.2 and 2.75 Gyr (Table 9.1, Appendix A9.2). Analyses were carried out by EA-IRMS on decarbonated whole-rock powder aliquots and a few kerogen isolates (Stüeken, 2013) (Appendix A9.3). Unlike cherts, which were commonly used in previous studies, mudrocks are relatively kerogen-rich and widespread, making them ideal for obtaining accurate data that are comparable over long geological timescales. Phyllosilicate minerals in shales can further accumulate NH₄⁺ released from organic matter during diagenesis, so whole-rock samples containing both organic and inorganic ammonium should therefore come closest to preserving the original isotopic composition of biomass (Appendix A9.4.1), if infiltration of fluids from other sources can be

ruled out. To detect possible alteration, as well as to quantify the availability of Mo, V, and Fe in the depositional environments, we also obtained major and minor element abundance data by ICP-AES and ICP-MS (Table A9.4 and A9.5).

9.2. Results

Our results showed a narrow range (-2.8 to $+3.9\text{‰}$, Fig. 9.1) for mid-Archean $\delta^{15}\text{N}_{\text{bulk}}$ with a total average of $0.0 \pm 1.3\text{‰}$. Samples from the Witwatersrand basin (2.96-2.87Gyr) showed a weak negative gradient in $\delta^{15}\text{N}$ from $1.0 \pm 1.5\text{‰}$ in fluvial and very shallow marine samples to $-1.6 \pm 0.8\text{‰}$ on the proximal marine shelf, roughly correlating with the previously reported strong positive gradient in $\delta^{13}\text{C}$ (Guy *et al.*, 2012). This $\delta^{15}\text{N}$ gradient is similar in sign and direction to that in the Mesoproterozoic Belt Supergroup (Stüeken, 2013) but much smaller in magnitude. Data from offshore environments, in particular from the Soanesville Group ($\delta^{15}\text{N} = +0.4 \pm 0.4\text{‰}$, 3.19Gyr), tend to be more tightly clustered than data from fluvial settings in the Fortescue Group (2.77-2.75Gyr) and the Witwatersrand Supergroup, probably reflecting environmental homogeneity. Kerogen isolates are slightly lighter than whole rocks (by -1.39‰ to -4.12‰), consistent with diagenetic alteration under anoxic conditions (Appendix A9.4.1). Elemental abundances in the Soanesville Group and the Witwatersrand Supergroup, including concentrations of Mo and V, are generally close to the crustal average (Fig. 9.2 and A9.2). This pattern argues against any significant metasomatic overprint.

9.3. Discussion

The narrow range in $\delta^{15}\text{N}_{\text{bulk}}$ close to the presumed composition of the atmosphere is inconsistent with an excess supply of fixed nitrogen from abiotic sources, because partial

assimilation of either NH_4^+ or NO_x species would have resulted in substantial fractionations of several permil (reviewed by Casciotti, 2009). External sources of fixed nitrogen can therefore only be reconciled with our data if assimilation was quantitative, and if those fixed nitrogen species had an initial $\delta^{15}\text{N}$ composition near 0‰. Isotopic fractionations associated with abiotic nitrogen fixation have not yet been thoroughly investigated, but recent experimental evidence has shown that organic nitrogen compounds formed during electric discharge are fractionated relative to N_2 by -15‰ to -25‰ (Kuga *et al.*, 2014). It is conceivable that other atmospherically produced NO_x species would have been similarly fractionated, making them incompatible with our data. A significant hydrothermal NH_4^+ flux can also be ruled out, because it would not have been accessible in fluvial settings like those of the Fortescue and Witwatersrand rocks, and the similarity in $\delta^{15}\text{N}_{\text{bulk}}$ values between fluvial and marine samples suggests that nitrogen was generally supplied by the same mechanism.

Another possible explanation for the $\delta^{15}\text{N}_{\text{bulk}}$ values could be nitrogen fixation by Vnf and/or Anf to -6‰, followed by a scenario similar to the modern ocean, *i.e.* quantitative nitrification, followed by partial denitrification in the water column imparting a positive fractionation to residual nitrate, and then nearly quantitative assimilation of that nitrate into biomass. Today, this process leads to a positive fractionation to the resulting biomass of around 5‰ to 7‰ compared to the initial fixed nitrogen. This could conceivably result in $\delta^{15}\text{N}_{\text{bulk}}$ values around 0‰ if Vnf and/or Anf were the dominant nitrogenases. However, because of the varying magnitudes of fractionation imparted by denitrification, a tight cluster of values right at 0‰ would not be expected; instead a spread between the composition of newly fixed N (*i.e.* -6‰ in this hypothetical scenario) and dissolved nitrate (*i.e.* 0‰ in this case), as seen in the modern ocean in response to varying climate (Galbraith *et al.*, 2013) and ocean circulation (Straub *et al.*,

2013), should be evident. Thus, given the small variance around 0‰ shown by samples from different environments over 450 million years and in particular by the Soanesville Group, this explanation seems unlikely.

Overall, our data point to an ecosystem where the supply of nitrogen was limited. The most likely explanation for nitrogen acquisition is therefore biological N₂ fixation, specifically using Mo-based nitrogenase. Alternative nitrogenases employing V or Fe may have been minor contributors of light nitrogen on the shelf of the Witwatersrand basin, thus explaining the subtle basinal gradient. However, Mo was evidently the dominant catalyst of N₂ fixation in fluvial and offshore marine environments throughout the mid-Archean, indicated by the very small variance of $\delta^{15}\text{N}_{\text{bulk}}$ values around 0‰ that is especially noticeable in the Soanesville Group.

Modern Mo-dependent diazotrophs are capable of fixing N₂ down to ~1nM [Mo], or ~1% of modern marine concentrations (Glass *et al.*, 2010). These low levels may have been supplied to the mid-Archean ocean by hydrothermal fluids or localized oxidative weathering (Crowe *et al.*, 2013; Planavsky *et al.*, 2014). If combined with very low concentrations of dissolved sulfide in the water column, such that Mo was not be scavenged quantitatively by sulfide sequestration, sufficient Mo concentrations may have been sustained to support the considerable biomass evident in the Soanesville Group, where post-metamorphic TOC levels of up to 2% are recorded (Table A9.2). Mo uptake may have been further enhanced by molybdophores (Liermann *et al.*, 2005), if they had already evolved at this time. Thus, the absence of Mo enrichments in these sediments (Fig. 9.2) does not preclude Mo bioavailability (Appendix A9.4.2). The slightly heavy $\delta^{15}\text{N}_{\text{bulk}}$ values in some fluvial samples from the Witwatersand Supergroup could reflect aerobic nitrogen cycling, especially if Mo was delivered by localized oxidative weathering on land (Guy *et al.*, 2012; Crowe *et al.*, 2013).

9.4. Conclusion

Our results have several important implications for the early evolution of life and environments. First, the nitrogen cycle was predominantly anaerobic prior to 2.7 Gyr. Any biologically produced O₂ (Planavsky *et al.*, 2014) must therefore have had a very short lifetime and oxidative weathering (Crowe *et al.*, 2013) was probably restricted to environments where oxygen was actively being produced. Second, nitrogenase is a much more ancient enzyme than recent models suggest (Boyd *et al.*, 2011a). Our data from the Soanesville Group constrain the minimum age for Mo-nitrogenase evolution to ~3.2 Gyr (Fig. 9.3), the most ancient evidence for the existence of a specific enzyme. If the subtle basinal gradient in the Witwatersrand basin reflects contributions of Anf or Vnf, then nitrogenase diversification dates back to at least 2.9 Gyr. Third, Mo must have been sufficiently bioavailable in the mid-Archean to serve as an enzymatic catalyst. This supports phylogenetic evidence for the early evolution of other Mo-containing enzymes (Schoepp-Cothenet *et al.*, 2012). Lastly, the early origin of nitrogenase before environmental oxygenation could have enhanced Archean sequestration of atmospheric nitrogen by organic burial in the mantle or continental crust, consistent with relatively low atmospheric pressure at 2.7 Gyr (Som *et al.*, 2012).

Acknowledgments

This work was funded by a GSA graduate student research grant to EES and by an Agouron Institute grant to RB. We thank N. Beukes for access to the Witwatersrand samples and the UW Isolab for technical support.

Author contributions

R. Buick collected samples from the Soanesville Group; B. M. Guy collected samples from the Witwatersrand Supergroup; R. Buick and E. E. Stüeken collected samples from the Fortescue Group and Nullagine Group; E. E. Stüeken performed the analyses and drafted the manuscript with advice and contributions from R. Buick; B. M. Guy commented on the draft.

Tables

Table 9.1: Sample localities and depositional environments. Metamorphic grade: PP = prehnite-pumpellyite, GR = greenschist; n = number of samples. Isotopic uncertainties are reported as 1σ . * For the Nullagine sample, the reported standard deviation is equal to the analytical uncertainty of triplicate analyses.

Unit	Age [Gyr]	Depositional setting	Metam. grade	n	$\delta^{15}\text{N}_{\text{bulk}}$ [‰]	TOC [%]	TN [ppm]
Soanesville Group	3.19	upper continental slope	PP	11	$+0.4 \pm 0.4$	1.3 ± 0.4	353 ± 99
Nullagine Group	2.98	outer shelf	GR	1*	$+0.1 \pm 0.4$	0.2 ± 0.0	42 ± 3
Witwatersrand	2.92	fluvial	GR	8	$+0.9 \pm 1.9$	0.2 ± 0.2	65 ± 63
Supergroup	2.87	shallow marine, near rivers	GR	5	$+1.2 \pm 1.0$	0.5 ± 0.2	47 ± 18
	2.96	marine shelf	GR	5	-1.6 ± 0.8	0.5 ± 0.5	105 ± 48
Fortescue Group	2.76	fluvio-lacustrine	PP	13	-0.7 ± 0.8	0.1 ± 0.1	22 ± 7

Figures

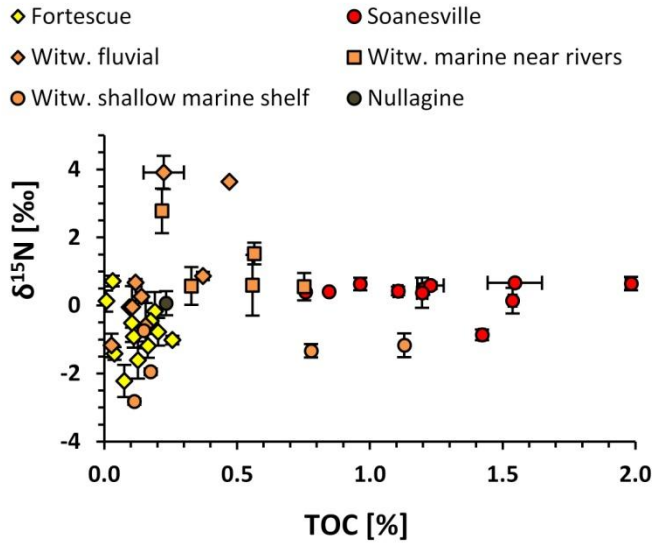


Fig. 9.1: Whole-rock $\delta^{15}\text{N}$ versus TOC. Error bars are 1σ . Nitrogen isotopic composition is independent from total biomass.

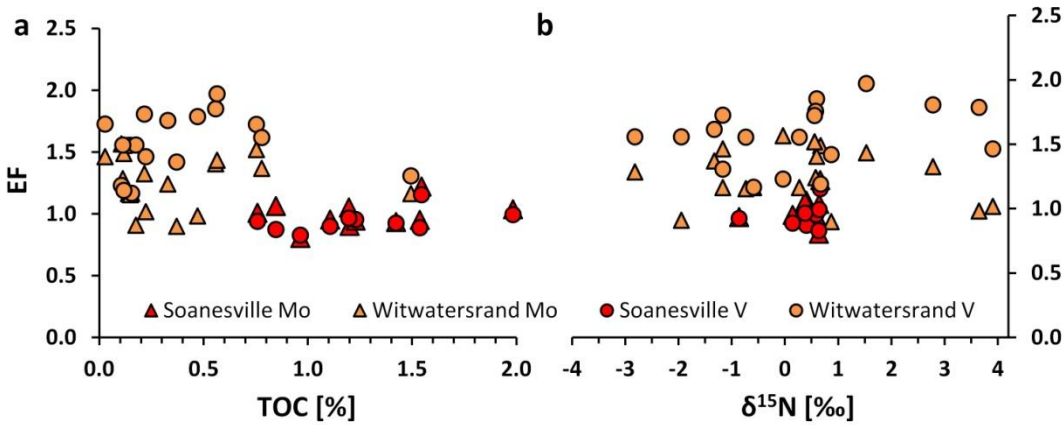


Fig. 9.2: TOC (panel A) and $\delta^{15}\text{N}$ (panel B) versus Mo and V enrichment factors (EF). EF are calculated relative to average upper continental crust (Appendix A9.3.3). No trends are observed, indicating that availability of Mo and V did not influence either TOC or $\delta^{15}\text{N}$.

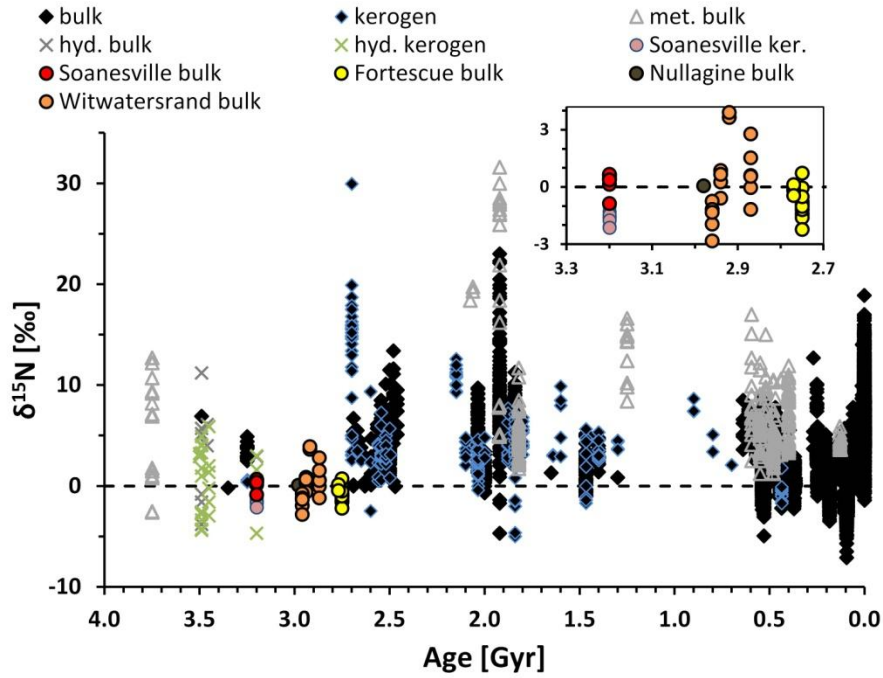


Fig. 9.3: Sedimentary $\delta^{15}\text{N}$ through time. Hyd. = samples from hydrothermal veins, met. = metamorphosed above greenschist facies. Insert shows data from this study at higher resolution. See Appendix A9.1 for references.

References

- Anbar AD, Knoll AH (2002) Proterozoic ocean chemistry and evolution: a bioinorganic bridge? *Science*, **297**, 1137-1142.
- Boyd ES, Anbar AD, Miller S, Hamilton TL, Lavin M, Peters JW (2011a) A late methanogen origin for molybdenum-dependent nitrogenase. *Geobiology*, **9**, 221-232.
- Boyd ES, Hamilton TL, Peters JW (2011b) An alternative path for the evolution of biological nitrogen fixation. *Frontiers in Microbiology*, **2**, doi: 10.3389/fmicb.2011.00205.
- Brandes JA, Boctor NZ, Cody GD, Cooper BA, Hazen RM, Yoder Jr HS (1998) Abiotic nitrogen reduction on the early Earth. *Nature*, **395**, 365-367.
- Casciotti KL (2009) Inverse kinetic isotope fractionation during bacterial nitrite oxidation. *Geochimica et Cosmochimica Acta*, **73**, 2061-2076.
- Crowe SA, Døssing LN, Beukes NJ, Bau M, Kruger SJ, Frei R, Canfield DE (2013) Atmospheric oxygenation three billion years ago. *Nature*, **501**, 535-538.
- Dos Santos PC, Fang Z, Mason SW, Setubal JC, Dixon R (2012) Distribution of nitrogen fixation and nitrogenase-like sequences amongst microbial genomes. *BMC genomics*, **13**, 162.
- Galbraith E, Kienast M, NICOPP (2013) The acceleration of oceanic denitrification during deglacial warming. *Nature Geoscience*, **6**, 579-584.
- Garvin J, Buick R, Anbar AD, Arnold GL, Kaufman AJ (2009) Isotopic evidence for an aerobic nitrogen cycle in the latest Archean. *Science*, **323**, 1045-1048.
- Glass JB, Wolfe-Simon F, Elser JJ, Anbar AD (2010) Molybdenum-nitrogen co-limitation in freshwater and coastal heterocystous cyanobacteria. *Limnology and Oceanography*, **55**, 667-676.
- Godfrey LV, Falkowski PG (2009) The cycling and redox state of nitrogen in the Archean ocean. *Nature Geoscience*, **2**, 725-729.
- Guy BM, Ono S, Gutzmer J, Kaufman AJ, Lin Y, Fogel ML, Beukes NJ (2012) A multiple sulfur and organic carbon isotope record from non-conglomeratic sedimentary rocks of the Mesoarchean Witwatersrand Supergroup, South Africa. *Precambrian Research*, **216-219**, 208-231.
- Kasting JF, Siefert JL (2001) Biogeochemistry: the nitrogen fix. *Nature*, **412**, 26-27.
- Kuga M, Carrasco N, Marty B, Marrocchi Y, Bernard S, Rigaudier T, Fleury B, Tissandier L (2014) Nitrogen isotopic fractionation during abiotic synthesis of organic solid particles. *Earth and Planetary Science Letters*, **393**, 2-13.
- Liermann LJ, Guynn RL, Anbar A, Brantley SL (2005) Production of a molybdophore during metal-targeted dissolution of silicates by soil bacteria. *Chemical Geology*, **220**, 285-302.
- Marty B, Zimmermann L, Pujol M, Burgess R, Philippot P (2013) Nitrogen isotopic composition and density of the Archean atmosphere. *Science*, **342**, 101-104.
- McGlynn SE, Boyd ES, Peters JW, Orphan VJ (2012) Classifying the metal dependence of uncharacterized nitrogenases. *Frontiers in microbiology*, **3**, doi:10.3389/fmicb.2012.00419.
- Navarro-Gonzalez R, McKay CP, Nna Mvondo D (2001) A possible nitrogen crisis for Archean life due to reduced nitrogen fixation by lightning. *Nature*, **412**, 61-64.
- Planavsky NJ, Asael D, Hofmann A, Reinhard CT, Lalonde SV, Knudsen A, Wang X, Ossa Ossa F, Pecoits E, Smith AJB, Beukes NJ, Bekker A, Johnson TM, Konhauser K, Lyons TW,

- Rouxel OJ (2014) Evidence for oxygenic photosynthesis half a billion years before the Great Oxidation Event. *Nature Geoscience*.
- Raymond J, Siefert JL, Staples CR, Blankenship RE (2004) The natural history of nitrogen fixation. *Molecular Biology and Evolution*, **21**, 541-554.
- Sano Y, Pillinger CT (1990) Nitrogen isotopes and N₂/Ar ratios in cherts: an attempt to measure time evolution of atmospheric $\delta^{15}\text{N}$ value. *Geochemical Journal*, **24**, 315-325.
- Schoepp-Cothenet B, van Lis R, Philippot P, Magalon A, Russell MJ, Nitschke W (2012) The ineluctable requirement for the trans-iron elements molybdenum and/or tungsten in the origin of life. *Scientific Reports*, **2**, 1-5.
- Scott C, Lyons TW, Bekker A, Shen Y, Poulton SW, Chu X, Anbar AD (2008) Tracing the stepwise oxygenation of the Proterozoic ocean. *Nature*, **452**, 456-459.
- Som SM, Catling DC, Harnmeijer JP, Polivka PM, Buick R (2012) Air density 2.7 billion years ago limited to less than twice modern levels by fossil raindrop imprints. *Nature*, **484**, 359-362.
- Straub M, Sigman DM, Ren H, Martinez-Garcia A, Meckler AN, Hain MP, Haug GH (2013) Changes in North Atlantic nitrogen fixation controlled by ocean circulation. *Nature*, **501**, 200-203.
- Stüeken EE (2013) A test of the nitrogen-limitation hypothesis for retarded eukaryote radiation: nitrogen isotopes across a Mesoproterozoic basal profile. *Geochimica et Cosmochimica Acta*, **120**, 121-139.
- Stüeken EE, Catling DC, Buick R (2012) Contributions to late Archaean sulphur cycling by life on land. *Nature Geoscience*, **5**, 722-725.
- Thomazo C, Papineau D (2013) Biogeochemical cycling of nitrogen on the early Earth. *Elements*, **9**, 345-351.
- Tian F, Kasting JF, Zahnle K (2011) Revisiting HCN formation in Earth's early atmosphere. *Earth and Planetary Science Letters*, **308**, 417-423.
- Zhang X, Sigman DM, Morel FM, Kraepiel AM (2014) Nitrogen isotope fractionation by alternative nitrogenases and past ocean anoxia. *Proceedings of the National Academy of Sciences*, **111**, 4782-4787.

Appendix to Chapter 9

A9.1. Nitrogen isotope database

A9.1.1. Critical review of existing Archaean (pre-2.7 Gyr) nitrogen isotope data

Almost all rocks of early and mid-Archaean age (> 2.7 Gyr) that have previously been analyzed for nitrogen isotopes have been altered by metamorphism or geothermal fluids. Several studies have documented that metamorphism leads to preferential volatilization of isotopically light nitrogen (Haendel *et al.*, 1986; Bebout & Fogel, 1992; Boyd & Philippot, 1998; Bebout *et al.*, 1999; Mingram & Bräuer, 2001; Jia, 2006; Bauersachs *et al.*, 2009; Palya *et al.*, 2011), although to varying degrees and not under all circumstances (Busigny *et al.*, 2003; Yui *et al.*, 2009; Plessen *et al.*, 2010). Nitrogen isotope ratios from rocks of amphibolite grade may therefore have been raised by several permil, but it is not possible to unambiguously back-calculate the primary composition. Metasomatic and hydrothermal fluids can further alter primary $\delta^{15}\text{N}$ values by addition of nitrogen derived from either mantle fluids (van Zuilen *et al.*, 2005) or possibly from younger sedimentary rocks (Svensen *et al.*, 2008). Experimental evidence has shown that kerogen-bound nitrogen equilibrates with ammonium from exogenous fluids (Schimmelmann & Lis, 2010), hence even nitrogen analyses of kerogen isolates may not necessarily be pristine (cf. Beaumont & Robert, 1999). These two factors probably explain most of the spread in sedimentary $\delta^{15}\text{N}$ in samples older than 2.7Gyr. More specifically:

- Samples from the Isua Greenstone Belt (Pinti *et al.*, 2001; Nishizawa *et al.*, 2005; Papineau *et al.*, 2005; van Zuilen *et al.*, 2005) are highly metamorphosed or metasomatically overprinted and therefore not useful as metabolic proxies.

- Pinti *et al.*(2001; 2009) and Ueno *et al.*(2004) analyzed low-grade cherts from the Pilbara Craton, but essentially all of them were sampled from hydrothermal veins. Only two stromatolitic cherts from the Dresser Fm and the Strelley Pool Chert may be representative of normal marine conditions, but their $\delta^{15}\text{N}$ values differ significantly (+6.9‰ and -0.2‰) and are thus inconclusive regarding the presence of biological nitrogen fixation. Moreover, the fact that both were originally carbonates but have undergone siliceous metasomatism to chert suggests that neither may be a primary value.
- Yamaguchi (2002) analyzed 15 drill core samples from the Sheba Fm (3.25Gyr, greenschist facies) and found an average $\delta^{15}\text{N}_{\text{bulk}}$ composition of $+3.4 \pm 0.7\text{‰}$; the composition of three kerogen isolates was $\delta^{15}\text{N}_{\text{ker}} = +0.5 \pm 0.1\text{‰}$. The bulk composition was originally interpreted as a signal of aerobic nitrogen cycling, but it is possible that metamorphic alteration has elevated the bulk value by 1-2‰. Hence these data may be consistent with biological nitrogen fixation, but uncertainties in reconstructing primary $\delta^{15}\text{N}$ from altered samples make this interpretation speculative.

The third major issue with some published data is low reproducibility or analytical uncertainty. Data reported by Hayes *et al.*(1983) from greenschist-grade cherts and shales have an analytical uncertainty of 2‰ at a 95% confidence level. Their four mid-Archaean data points ranging from 1.6 to 3.2‰ may thus reflect nitrogen fixation, but this is uncertain. Beaumont & Robert (1999) reported $\delta^{15}\text{N}$ values of kerogen isolates from cherts of various ages and metamorphic grades (Table A9.1), but results for replicate extractions from the same sample differ by up to 19.2‰. Even replicate analyses of the same kerogen isolates show differences of up to 5.8‰. The authors attribute this to sample heterogeneity, but as pointed out by Yamaguchi

(2002) such extreme variability is very unusual and cannot easily explained by any primary process. Furthermore, sample pulverization and kerogen extraction should have homogenized the sample. It is therefore conceivable that these samples were contaminated in the laboratory. Pure natural organic matter was used to track contamination, but because Archaean kerogen contains much less nitrogen than fresh organic matter, this comparison is invalid (Yamaguchi, 2002). But even if the data are primary, the vast spread makes it impossible to discern any particular metabolic pathway.

Table A1: Published early and mid-Archaean nitrogen isotope data. Metamorphic grades (as specified by the authors): PP = prehnite-pumpellyite, GR = greenschist, l = lower, AMPH = amphibolite; lithologies: CH = chert, STCH = stromatolitic chert, SH = shale/metapelite, CARB = carbonate; notes: A = high analytical uncertainty, H = hydrothermal contributions during time of deposition, M = metamorphic/metasomatic alteration. C/N = atomic ratios of organic carbon to total nitrogen (C/N_{bulk}) or to kerogen-bound nitrogen (C/N_{ker}). References: 1 = Nishizawa *et al.* (2005), 2 = Papineau *et al.* (2005), 3 = van Zuilen *et al.* (2005), 4 = Pinti *et al.* (2001), 5 = Beaumont & Robert (1999), 6 = Pinti *et al.* (2009), 7 = Ueno *et al.* (2004), 8 = Hayes *et al.* (1983), 9 = Yamaguchi (2002)

[Gyr]	unit	$\delta^{15}\text{N}_{\text{bulk}}$	$\delta^{15}\text{N}_{\text{ker}}$	$\delta^{13}\text{C}_{\text{org}}$	C/N_{bulk}	C/N_{ker}	metam.	lith.	ref.	notes
3.75	Isua Supracrustal Belt	6.9			210		AMPH	BIF	1	M
3.75	Isua Supracrustal Belt	1.0			72		AMPH	BIF	1	M
3.75	Isua Supracrustal Belt	10.7					AMPH	SH	2	M
3.75	Isua Supracrustal Belt	12.7					AMPH	SH	2	M
3.75	Isua Supracrustal Belt	12.7					AMPH	SH	2	M
3.75	Isua Supracrustal Belt	1.5					AMPH	CARB	3	M
3.75	Isua Supracrustal Belt	1.8					AMPH	CARB	3	M
3.75	Isua Supracrustal Belt	-2.6					AMPH	CARB	3	M
3.75	Isua Supracrustal Belt	-2.5					AMPH	SH	3	M
3.75	Isua Supracrustal Belt	9.2			5000		AMPH	CH	4	M
3.75	Isua Supracrustal Belt	8.2			746		AMPH	BIF	4	M
3.75	Isua Supracrustal Belt	0.8			585		AMPH	BIF	4	M
3.75	Isua Supracrustal Belt	12.2			2728		AMPH	CH	4	M
3.75	Isua Supracrustal Belt	7.1			585		AMPH	SH	4	M
3.75	Isua Supracrustal Belt	9.4			28		AMPH	SH	4	M
3.75	Isua Supracrustal Belt	10.7					AMPH	SH	4	M
3.49	Dresser Fm, Warrawoona Gp		3.3	-35.2		150	PP to l-GR	CH	5	A, H(?)
3.49	Dresser Fm, Warrawoona Gp		-2.6	-35.7		137	PP to l-GR	CH	5	A, H(?)
3.49	Dresser Fm, Warrawoona Gp		-4.4	-32.7		77	PP to l-GR	CH	5	A, H(?)
3.49	Dresser Fm, Warrawoona Gp		-4.3	-32.4		54	PP to l-GR	STCH	5	A, H(?)
3.49	Dresser Fm, Warrawoona Gp		4.9	-33.7		309	PP to l-GR	STCH	5	A, H(?)
3.49	Dresser Fm, Warrawoona Gp	-3.8			201		PP to l-GR	CH	4	H
3.49	Dresser Fm, Warrawoona Gp	6.9			442		PP to l-GR	STCH	4	
3.49	Dresser Fm, Warrawoona Gp	5.2					PP to l-GR	CH	4	H
3.49	Dresser Fm, Warrawoona Gp	5.7			18		PP to l-GR	CH	6	H
3.49	Dresser Fm, Warrawoona Gp	-0.8					PP to l-GR	CH	6	H
3.49	Dresser Fm, Warrawoona Gp	11.2			58		PP to l-GR	CH	6	H
3.49	Dresser Fm, Warrawoona Gp	-1.6					PP to l-GR	CH	6	H
3.49	Dresser Fm, Warrawoona Gp		4.0	-35.9			PP to l-GR	CH	7	H

3.49	Dresser Fm, Warrawoona Gp		-2.8	-34.2	200	PP to I-GR	CH	7	H	
3.49	Dresser Fm, Warrawoona Gp		1.0	-37.2		PP to I-GR	CH	7	H	
3.49	Dresser Fm, Warrawoona Gp		-3.4	-33.1	250	PP to I-GR	CH	7	H	
3.49	Dresser Fm, Warrawoona Gp		1.8	-34.6	250	PP to I-GR	CH	7	H	
3.49	Dresser Fm, Warrawoona Gp		4.1	-34.8	200	PP to I-GR	CH	7	H	
3.46	Apex chert, Warrawoona Gp	4.0				I-GR	CH	6	H	
3.46	Marble Bar, Warrawoona Gp	6.1		221		PP	CH	4	H	
3.45	Onverwacht Gp		-0.2	-27.8	247	I-GR to AMPH	CH	5	A, H(?), M(?)	
3.45	Onverwacht Gp		5.9	-35.2	320	I-GR to AMPH	CH	5	A, H(?), M(?)	
3.45	Onverwacht Gp		-1.6	-29.9	181	I-GR to AMPH	CH	5	A, H(?), M(?)	
3.45	Onverwacht Gp		2.0	-27.8	135	I-GR to AMPH	CH	5	A, H(?), M(?)	
3.45	Onverwacht Gp		1.4	-25.3	291	I-GR to AMPH	CH	5	A, H(?), M(?)	
3.45	Onverwacht Gp		-3.0	-31.7	239	I-GR to AMPH	CH	5	A, H(?), M(?)	
3.45	Hooggenoeg Fm, Onverwacht Gp		2.9		250	GR	CH	8	A, H(?)	
3.35	Strelley Pool chert, Kelly Gp	-0.2		2071		I-GR	STCH	6		
3.25	Fig Tree Gp		3.2		167	GR	CH	8	A, H(?)	
3.25	Sheba Fm, Fig Tree Gp	2.9		49		GR	SH	9	M(?)	
3.25	Sheba Fm, Fig Tree Gp	2.9		36		GR	SH	9	M(?)	
3.25	Sheba Fm, Fig Tree Gp	2.7		57		GR	SH	9	M(?)	
3.25	Sheba Fm, Fig Tree Gp	2.5		42		GR	SH	9	M(?)	
3.25	Sheba Fm, Fig Tree Gp	3.8		27		GR	SH	9	M(?)	
3.25	Sheba Fm, Fig Tree Gp	2.9		38		GR	SH	9	M(?)	
3.25	Sheba Fm, Fig Tree Gp	2.8		3		GR	SH	9	M(?)	
3.25	Sheba Fm, Fig Tree Gp	3.3		22		GR	SH	9	M(?)	
3.25	Sheba Fm, Fig Tree Gp	4.0		43		GR	SH	9	M(?)	
3.25	Sheba Fm, Fig Tree Gp	4.9		42	133	GR	SH	9	M(?)	
3.25	Sheba Fm, Fig Tree Gp	3.7		50		GR	SH	9	M(?)	
3.25	Sheba Fm, Fig Tree Gp	4.4		59		GR	SH	9	M(?)	
3.25	Sheba Fm, Fig Tree Gp	3.8	0.4	-29.9	37	110	GR	SH	9	M(?)
3.25	Sheba Fm, Fig Tree Gp	3.9	0.6	-28.6	37	150	GR	SH	9	M(?)
3.25	Sheba Fm, Fig Tree Gp	3.0	0.4	-29.3	40	110	GR	SH	9	M(?)
3.2	Gorge Creek Gp		-4.7	-28.3	106	GR	CH	5	A, H(?)	
3.2	Gorge Creek Gp		1.6		91	GR	SH	8	A, H(?)	
3.2	Gorge Creek Gp		3.0		100	GR	SH	8	A, H(?)	
3.2	Dixon Island Fm, Clearville Gp	-0.5		36		I-GR	CH	6	H	
3.2	Dixon Island Fm, Clearville Gp	2.9				I-GR	CH	6	H	

A9.1.2. Sources of late Archean and post-Archean nitrogen data

From the late Archean onwards, the nitrogen isotope record is mostly based on siliclastic rocks, many of which are unaltered or only mildly metamorphosed. Observed fractionations are therefore likely primary. The literature data plotted in Figure 3 in the main text represents a combination of previous compilations by Papineau *et al.* (2005), Godfrey & Falkowski (2009), and Algeo *et al.* (2013) with additional recently published data (Papineau *et al.*, 2009; Kump *et al.*, 2011; Palya *et al.*, 2011; Schoepfer *et al.*, 2012; Busigny *et al.*, 2013; Cremonese *et al.*, 2013; Godfrey *et al.*, 2013; Papineau *et al.*, 2013; Stüeken, 2013; Cremonese *et al.*, 2014; Kikumoto *et al.*, 2014).

A9.2: Sample description and geologic background

A9.2.1. Soanesville Group, Paddy Market Formation

The Soanesville Group in Western Australia, formerly part of the Gorge Creek Group (Horwitz, 1990), is a predominantly sedimentary sequence that was deposited along the Pilbara craton ~3.2 Gyr (Van Kranendonk *et al.*, 2010). The Paddy Market Formation is a unit of black shale that probably represents the distal part of turbidity flows in a fault-bounded, open marine basin (Thomas, 1997; Buick *et al.*, 2002). The metamorphic grade is very low (prehnite-pumpellyite facies). We obtained 11 shale samples from two different drill cores near Sulphur Springs.

A9.2.2. Nullagine Group, Mosquito Creek Formation

The Nullagine Group represents a turbidite unit that was deposited on the Pilbara craton, Western Australia, around 2.98Gyr (Van Kranendonk *et al.*, 2010). The rocks have been metamorphosed to greenschist facies. We collected one sample of shale from an outcrop near the town of Nullagine, a few meters below the unconformity with the late Archaean Fortescue Group. The sediments in this area are graded at cm-scale, thus probably from a slightly more proximal setting than the black shales of the Soanesville Group.

A9.2.3. Witwatersrand Supergroup

The mostly sedimentary Witwatersrand Supergroup was deposited over the central Kaapvaal craton between 3.0 and 2.8 Gyr. The older West Rand Group marks an interval of sealevel highstand with mostly marine sedimentary facies, while the younger Central Rand

Group mainly contains fluvial and very shallow marine sediments (reviewed by Bumby *et al.*, 2012). The metamorphic grade is low (greenschist facies) (Guy *et al.*, 2012). We obtained samples representing marine to fluvial environments from drill cores BAB1 (Rietkuil, Promise and Coronation Formations), DK12 (Booysens Formation), TW6 (Booysens Formation) and TF1 (Parktown and Brixton Formations), most of which were previously analyzed for carbon and sulfur isotopes (Guy *et al.*, 2012). We specifically focused on samples where the sulfide grains were identified as mostly diagenetic (Guy *et al.*, 2012) to minimize the potential impacts of metasomatic alteration.

A9.2.4. Fortescue Group, Hardey Formation and Bellary Formation

The Hardey Formation is a fluvio-lacustrine unit deposited over parts of the eastern Pilbara craton ~2.77-2.75 Gyr (Blake *et al.*, 2004; Hall, 2005). It unconformably overlies the mostly subaerial Mt. Roe basalt and has been intruded by a felsic porphyry (packages 2-4 in Blake *et al.* (2004). We collected 10 samples of shales and siltstones from outcrops of both units above and below the porphyry. Furthermore, we obtained 3 samples from the Bellary Formation, a fluvio-lacustrine clastic sedimentary unit that underlies the Mt. Roe basalt. The metamorphic grade of all Fortescue samples is very low (prehnite-pumpellyite facies) (Smith *et al.*, 1982). Fluvial sandstones in the Hardey Formation contain detrital uraninite, siderite and pyrite, indicative of very low levels of atmospheric and dissolved oxygen at this time (Rasmussen & Buick, 1999). Total sulfur and carbon content are generally low in the Hardey Fm (Watanabe *et al.*, 2004; Ohmoto *et al.*, 2006), arguing against significant metasomatic fluid infiltration.

A9.3: Analytical method

A9.3.1. Sample preparation

Sample preparation followed established protocols (Stüeken, 2013). First all outer surfaces were cut or polished off, then the rocks were crushed into sub-cm chips and sonicated sequentially in hexane, methanol and DI-H₂O (18M Ω) for a few minutes each to remove any modern contaminants. The chips were dried at 60°C in an oven overnight and then pulverized in an aluminum oxide ceramic puck mill. The mill was cleaned with pre-combusted sand, DI-H₂O and methanol in between samples. Rock powders were de-carbonated with 6N HCl for three days at 60°C, where the acid was refreshed after one day and stirred after two days. The de-carbonated samples were washed with DI-H₂O three times to remove residual acid and dried at 60°C. All glassware used during sample preparation and storage was combusted in a muffle-furnace at 500°C overnight.

Kerogen isolates were prepared following the HF-BF₃ maceration protocol of Robl & Davis (1993). Five to six grams of untreated rock powder were weighed into a 250ml Teflon bottle, mixed with 100ml DI-H₂O (18M Ω) and 100ml concentrated HF (reagent grade), and placed into a heated shaking water bath at 55°C overnight. The next day, the HF was decanted after centrifugation for 45min. Then a mixture of 62.5g H₃BO₃ (reagent grade), 100ml H₂O and 100ml HF was added to each sample and placed back into the heated shaking water bath overnight. This mixture results in the formation of BF₃, which efficiently dissolves fluoride precipitates (Robl & Davis, 1993). The BF₃ was decanted the following day after centrifugation, the sample was washed three times with DI-H₂O, and then transferred with ~10ml of water into a scintillation vial. The vials were then placed in a freezer and finally desiccated with a freeze-drier. Freezing the liquid first minimizes loss of kerogen by splashing during evacuation in the

freeze-drier. Reproducibility of kerogen extraction was tested with an in-house rock standard from the 2.5Gyr Mt. McRae Shale (UW-McRae) and was around 0.1‰ for $\delta^{15}\text{N}_{\text{ker}}$.

A9.3.2. Isotopic analyses

All analyses were carried out with an elemental analyzer (Costech ECS 4010) coupled to a continuous-flow isotope-ratio mass spectrometer (Finnigan MAT253) via a ThermoFinnigan ConFlo III (Garvin *et al.*, 2009; Schoepfer *et al.*, 2012; Stüeken, 2013). Powders were weighed into 9x5mm tin capsules (Costech) and flash-combusted with 10ml O₂ (“macro” setting) at 1bar and 1000°C. Resulting N₂ and CO₂ gas were purified with Cr₂O₃ (conversion of trace CO to CO₂) and silvered Co₃O₄ (capture of sulfur gases and halogens) at 1000°C and with Cu (conversion of trace NO_x to N₂) at 650°C. Traces of H₂O were scrubbed with Mg(ClO₄)₂ at room temperature. N₂ and CO₂ were then separated chromatographically at 40°C and analyzed sequentially. For analyses of kerogen isolates, CO₂ gas was scrubbed from the samples with soda lime at room temperature, which allows combustion of larger amounts of kerogen without any risk of saturating the detector cups in the mass spectrometer. Kerogen was mixed with V₂O₅ in a 1:1 ratio to enhance combustion efficiency, although subsequent tests shows that samples also combust well without an additional combustion aid (see below).

All measurements were corrected for instrumental mass bias with two previously calibrated in-house standards (glutamic acid GA-2 and dried salmon SA, calibrated against USGS41 and USGS40, Qi *et al.*, 2003), which were analyzed after each set of 5 samples. Accuracy and long-term reproducibility were monitored with a second glutamic acid standard (GA-1) and the UW-McRae rock standard. In all runs, accuracy for $\delta^{15}\text{N}$ was better than 0.3‰ (average absolute value 0.1‰) and average long-term precision over 12 months was 0.27‰.

Results are expressed in standard delta notation relative to air. For $\delta^{13}\text{C}_{\text{org}}$, the average long-term accuracy was 0.08‰ and average precision was 0.07‰. Results are expressed relative to VPDB. N and C concentrations were reproducible with average precision of 1.7 and 1.2%, respectively. All whole-rock samples and kerogen isolates were analyzed in duplicates or triplicates.

A9.3.3. Combustion efficiency

It has been noted that flash combustion may be inefficient in oxidizing organic carbon quantitatively to CO_2 such that any residual CO may interfere with N_2 in the mass spectrometer and increase the measured ratio of mass 29 to 28, leading to artificially higher $\delta^{15}\text{N}$ values (Beaumont *et al.*, 1994; Papineau *et al.*, 2009). Furthermore, NH_4^+ bound to phyllosilicate minerals may not be quantitatively released from the sample (Bräuer & Hahne, 2005). In both cases V_2O_5 has been proposed as a combustion aid; however, it can contain traces of nitrogen itself that needs to be subtracted.

In a previous study (Stüeken, 2013) using the same analytical protocol and facilities, we demonstrated that we could achieve good reproducibility in $\delta^{15}\text{N}$ ($1\sigma = 0.11\%$) over a range of V_2O_5 /sample ratios from 0 to 1.7 for a shale sample from the 1.5 Gyr Belt Supergroup. Also the measured total nitrogen concentrations showed no correlation with the V_2O_5 /sample ratio ($r^2 = 0.008$) and had a high precision (relative error 0.96%). Kerogen extraction and mass balance shows that 25% of all nitrogen in this sample is organic-bound (with $\delta^{15}\text{N} = +4.7 \pm 0.3\%$) and 75% is silicate-bound (with $\delta^{15}\text{N} = +5.1 \pm 0.4\%$). The good reproducibility of both isotopic ratio and total nitrogen abundance over a range of sample quantities from 50 to 150mg implies that even in the absence of V_2O_5 the flash combustion technique quantitatively oxidizes all organic- and silicate-bound nitrogen in this type of sample, where the majority of nitrogen is silicate-

bound. Furthermore, the data suggests that CO interferences are insignificant for up to 1.66mg organic carbon, which was the highest amount combusted with this sample (TOC = 1.1%, molar C/N_{bulk} ratio = 29).

In the course of this study, we conducted a second test with the UW-McRae standard (TOC = 7.7%, TN = 0.11%) to verify that this conclusion holds at high organic carbon abundances. We analyzed aliquots of powder ranging from 1.6 to 61.2mg, equivalent to 0.1-4.7mg organic carbon, and achieved good reproducibility for both $\delta^{15}\text{N}$ ($1\sigma = 0.19\text{‰}$) and total nitrogen (relative error 5.8%), without addition of V_2O_5 and at constant O_2 supply during flash combustion. If traces of CO were produced, it would be most significant at large sample sizes, *i.e.* at small O_2/sample ratios. However, the absence of any significant trend in the data (Figure A9.1) indicates that up to at least 4.7mg organic carbon, interferences with CO can be disregarded.

A9.3.3. Elemental analyses

We submitted aliquots of powder to ALS for major, minor and trace element analyses (method ME-MS61). Samples were digested with HF, HNO_3 and HClO_4 , and then analyzed in dilute HCl with ICP-AES and ICP-MS. We calculated enrichment factors for Mo and V ($\text{EF} = ([X]/[Al])_{\text{sample}}/([X]/[Al])_{\text{reference}}$, where [X] is the concentration of either Mo or V) with reference to average upper continental crust (Rudnick & Gao, 2014) and average Archean crust (Taylor & McLennan, 2001).

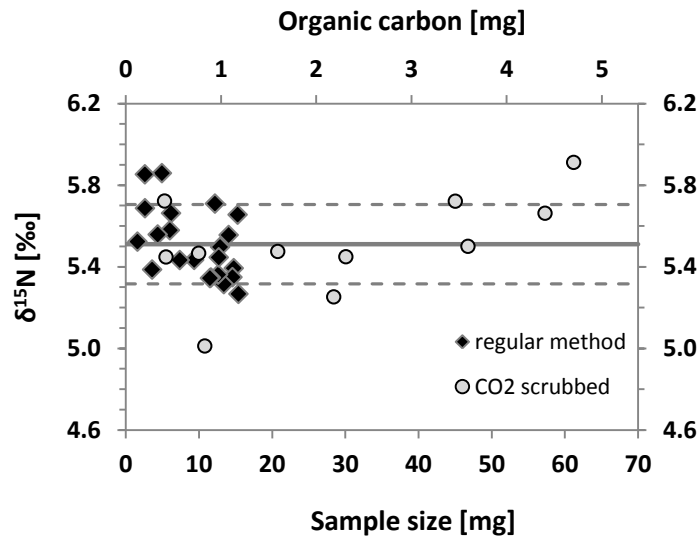


Figure A9.1: Reproducibility of the UW-McRae in-house standard over a range of sample sizes. Filled diamonds = analyzed with regular CN method; grey circles = analyzed with a soda-lime column to scrub CO₂ from the gas stream; horizontal lines = total average (solid) ± one standard deviation (dashed).

A9.4. Supplementary discussion

A9.4.1. Validity of whole-rock nitrogen analyses

There is some disagreement in the literature about whether kerogen isolates or whole rocks are better recorders of primary nitrogen isotope compositions. In studies of Precambrian rocks where both fractions were analyzed, $\delta^{15}\text{N}_{\text{ker}}$ tends to be systematically depleted by a few permil relative to $\delta^{15}\text{N}_{\text{bulk}}$ (Yamaguchi, 2002; Godfrey & Falkowski, 2009; Kump *et al.*, 2011; Godfrey *et al.*, 2013; this study, also reviewed by Ader *et al.*, 2014). This offset is consistent with anoxic incubation experiments and analyses of fresh anoxic sediments where organic matter becomes depleted by up to 3‰ during early diagenesis (Lehman *et al.*, 2002). This depletion may be due to (1) addition of isotopically light nitrogen by anaerobic microbes (Lehman *et al.*, 2002), (2) preferential removal of isotopically enriched proteins (Macko *et al.*, 1987; Altabet *et al.*, 1991), or (3) preferential preservation of isotopically depleted porphyrins such as bacteriochlorophyll (Chicarelli *et al.*, 1993; Beaumont *et al.*, 2000; Kashiyama *et al.*, 2008). In

the second and third case, clay minerals would incorporate isotopically enriched nitrogen compounds, consistent with observations from whole-rock data. The offset between $\delta^{15}\text{N}_{\text{ker}}$ and $\delta^{15}\text{N}_{\text{bulk}}$ may therefore be a result of early diagenetic degradation of organic matter, and hence, as argued by Godfrey & Glass (2011) and demonstrated by Busigny *et al.* (2013), $\delta^{15}\text{N}_{\text{bulk}}$ should be closest to the primary composition of biomass.

Large offsets of up to 13‰ have only been observed in Paleoproterozoic sediments proximal to an igneous intrusion that were likely metasomatically altered (Godfrey *et al.*, 2013). Here, $\delta^{15}\text{N}_{\text{bulk}}$ was found to be enriched by $\sim+4\%$ compared to surrounding unperturbed rocks, while $\delta^{15}\text{N}_{\text{ker}}$ was depleted by $\sim-7\%$. Hence kerogen isolates are not necessarily a better proxy for primary compositions, consistent with experimental evidence for isotopic equilibration between kerogen-bound nitrogen and NH_4^+ -bearing fluids (Schimmelmann & Lis, 2010). Instead, whole rocks of low metamorphic grade, that show no evidence of metasomatic input, and where the composition of kerogen isolates is within a few permil, *i.e.* explicable by the diagenetic processes described above, are probably the most accurate recorders of ancient metabolic nitrogen pathways.

We see no indication of metasomatic alteration in our samples. First, hand specimens do not contain any fractures or veins allowing fluid infiltration. Second, major and minor elements show no significant deviations from average upper crust (Figure A9.2), except for Ca and Na which show the standard weathering-related depletion (Nesbitt & Young, 1982) also noted in other Archaean mudrocks (Fedó *et al.*, 1996; Hessler & Lowe, 2006). Notably, there is no evidence of any significant enrichment of K relative to either average continental upper crust or Archaean upper crust, so post-depositional processes have added no new substitution sites for late ammonium addition. And lastly, the $\delta^{15}\text{N}$ offsets between whole rocks and kerogen isolates

from a subset of samples are small ($-2.29 \pm 0.77\%$, $n = 17$, Table A9.3), within the range of other unaltered shales (Yamaguchi, 2002; Godfrey & Falkowski, 2009; Godfrey *et al.*, 2013). We therefore conclude that our whole rock data accurately reflect the original isotopic composition of the Archaean biomass.

A9.4.2. Molybdenum bioavailability in the mid-Archaean

Mo concentrations in seawater are commonly approximated by measuring concentrations in sediments that were deposited under euxinic conditions, where dissolved MoO_4^{2-} is quantitatively scavenged by sulfidization (Gordon *et al.*, 2009). High sedimentary Mo enrichments relative to average continental crust thus indicate that dissolved MoO_4^{2-} was present and bioavailable in other, non-euxinic parts of the water body. This approach has been used to propose that Mo was scarce in the Archaean ocean, but became more abundant across the Paleoproterozoic and Neoproterozoic oxidation events (Anbar, 2008; Scott *et al.*, 2008). However, this technique becomes inaccurate in sediments that were not deposited under a euxinic water column, where some MoO_4^{2-} could have stayed in solution (e.g. Sekine *et al.*, 2011; Canfield *et al.*, 2013). Hence, although our samples display low Mo enrichment factors around 1 (Figure 9.3, Table A9.4 and A9.5), the scarcity of sulfide implies that bioavailable concentrations of dissolved Mo in mid-Archaean seawater and rivers cannot be ruled out from these data.

Mo-dependent organisms are extremely efficient in Mo-assimilation (Wang, 2012) and can fix nitrogen with Mo-based nitrogenase down to nanomolar Mo concentrations (Glass *et al.*, 2010). Thermodynamic models of Archaean seawater chemistry suggest dissolved Mo concentrations of $\sim 1\text{nM}$ compared to 105nM in the modern ocean (Saito *et al.*, 2003; Zerkle *et*

al., 2005). Given the uncertainty in such calculations, the minimum requirements for diazotrophy could thus easily have been met. Riverine Mo input from oxidative weathering was probably low (though not necessarily absent (Crowe *et al.*, 2013)) in the mid-Archaeon before the GOE; however, low-temperature hydrothermal fluids contribute up to 10% of the total marine Mo budget today (Poulson Brucker *et al.*, 2009; Reinhard *et al.*, 2013), and this flux probably persisted throughout Earth's history. Mo isotope fractionation in banded iron formation around 3.0 Gyr indeed suggests that some form of dissolved Mo was present in the water column at that time (Planavsky *et al.*, 2014). It is therefore unlikely that biological N₂-fixation was Mo-limited, even in offshore habitats (cf. Sánchez-Baracaldo *et al.*, 2014).

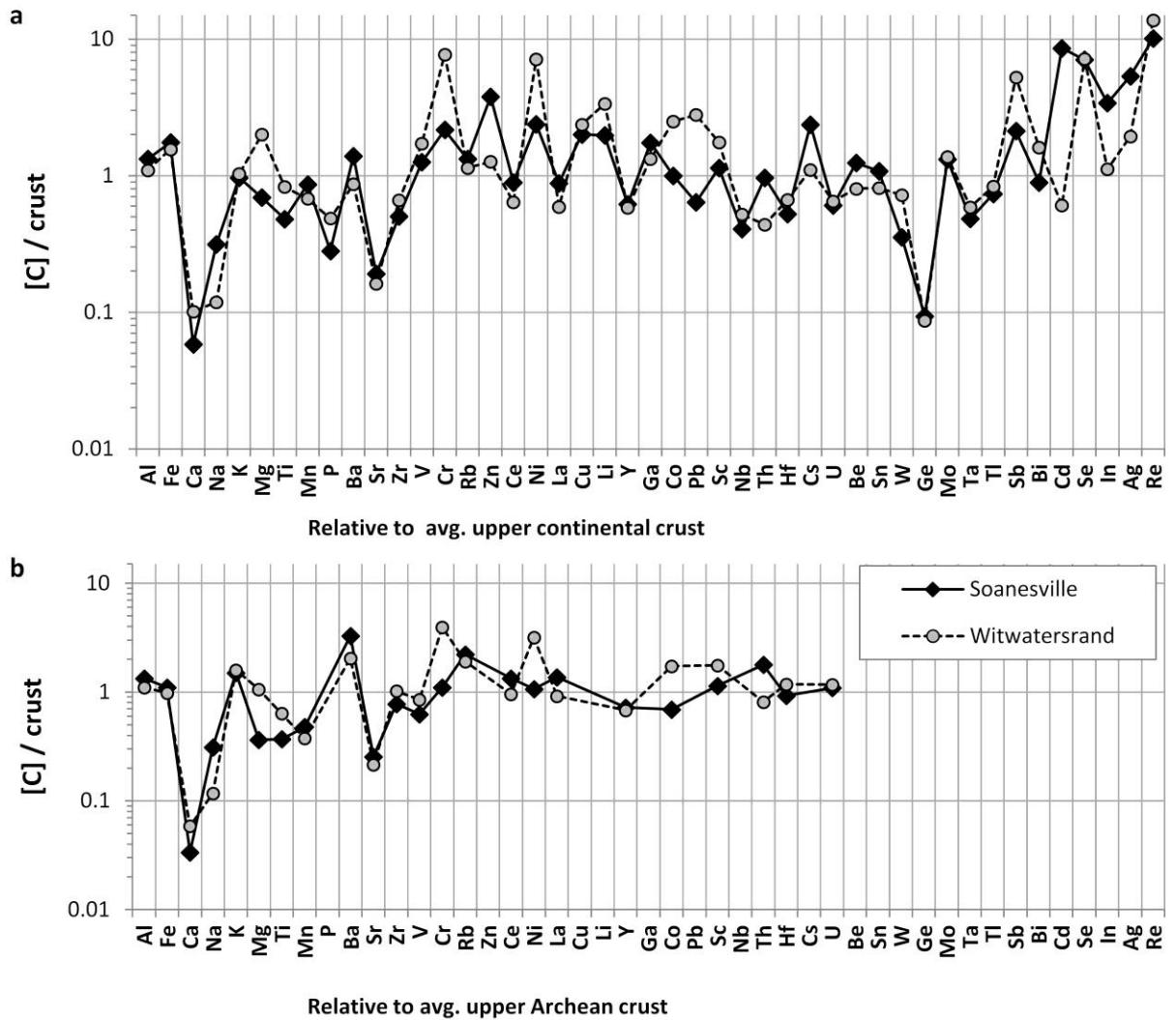


Figure A9.2: Crust-normalized elemental abundances. A: normalized relative to average upper continental crust (Rudnick & Gao, 2014), B: normalized relative to average upper Archean crust (Taylor & McLennan, 2001). Some data points in panel B are missing because concentrations for those elements in average upper Archean crust were not provided. In both panels, elements are sorted by relative abundance in upper continental crust (Rudnick & Gao, 2014).

Table A9.2: Whole-rock data for nitrogen isotopes, total nitrogen abundances (TN), organic carbon isotopes and total organic carbon (TOC) abundances.

Sample	$\delta^{15}\text{N}$ [‰]	σ [‰]	TN [ppm]	σ [ppm]	$\delta^{13}\text{C}$ [‰]	σ [‰]	TOC [%]	σ [%]	C/N [atom]	σ [atom]	Age [Gyr]	Setting
Fortescue Group:												
<i>Hardey Formation</i>												
130708-1	-1.41	0.19	25	0.14	-33.20	0.01	0.04	0.00	17.65	0.09	2.75	fluvio-lacustrine
130708-2	-1.60	0.55	24	5.22	-39.80	0.03	0.13	0.00	64.76	16.31	2.75	fluvio-lacustrine
130708-3	-0.05	0.03	16	0.70	-37.69	0.04	0.09	0.00	68.93	2.82	2.75	fluvio-lacustrine
130708-4	-0.91	0.33	15	0.20	-34.73	0.06	0.11	0.00	84.89	0.64	2.75	fluvio-lacustrine
130711-1	0.72	0.16	10	0.02	-24.85	0.08	0.03	0.00	36.43	0.21	2.75	fluvio-lacustrine
130711-2	-1.18	0.35	15	1.21	-37.97	0.01	0.16	0.00	131.34	11.59	2.75	fluvio-lacustrine
130711-3	-2.22	0.47	16	2.97	-30.96	0.06	0.08	0.00	56.66	10.64	2.75	fluvio-lacustrine
96039	-0.77	0.41	31	5.74	-39.90	0.19	0.20	0.00	78.79	15.69	2.75	fluvio-lacustrine
96041	-1.01	0.13	35	3.31	-41.18	0.19	0.26	0.00	86.41	8.69	2.75	fluvio-lacustrine
96042	-0.51	0.56	30	4.95	-38.48	0.18	0.10	0.00	41.48	7.25	2.75	fluvio-lacustrine
<i>Bellary Formation</i>												
21003	-0.17	0.57	25	0.32	-39.14	0.06	0.19	0.00	87.84	1.41	2.77	fluvio-lacustrine
21004	0.13	0.31	19	0.53	-27.93	0.23	0.01	0.00	4.62	0.47	2.77	fluvio-lacustrine
96038	-0.45	0.03	23	0.50	-41.71	0.00	0.17	0.00	89.28	1.30	2.77	fluvio-lacustrine
Soanesville Group:												
<i>Paddy Market Formation</i>												
96049	0.48	0.16	359	15.90	-31.39	0.10	1.20	0.01	39.02	2.05	3.19	upper slope
96050	0.40	0.02	348	0.57	-31.29	0.13	0.76	0.01	25.40	0.27	3.19	upper slope
96051	0.42	0.13	423	8.34	-31.10	0.00	1.11	0.02	30.52	0.14	3.19	upper slope
96052	0.40	0.02	325	10.86	-30.84	0.04	0.85	0.01	30.43	0.75	3.19	upper slope
96053	0.58	0.10	405	18.67	-30.69	0.14	1.23	0.05	35.41	0.19	3.19	upper slope
96054	0.14	0.38	392	11.81	-30.78	0.09	1.54	0.01	45.78	0.95	3.19	upper slope
96055	0.64	0.20	503	35.04	-30.58	0.08	1.98	0.02	46.09	2.73	3.19	upper slope
96056	0.63	0.18	360	9.71	-30.84	0.01	0.96	0.01	31.25	0.47	3.19	upper slope

97SSD32-06	0.66	0.00	292	11.77	-30.72	0.02	1.55	0.10	61.68	1.60	3.19	upper slope
97SSD32-21	0.37	0.44	107	16.00	-31.39	0.01	1.20	0.02	131.97	21.83	3.19	upper slope
97SSD51-03	-0.86	0.16	371	2.02	-30.58	0.04	1.42	0.01	44.68	0.59	3.19	upper slope
Witwatersrand Supergroup:												
<i>Coronation Formation</i>												
BABI_1013m	0.87	0.13	33	1.10	-47.06	0.14	0.37	0.00	131.54	4.53	2.94	fluvial
BABI_934m	0.27	0.13	33	0.40	-40.46	0.10	0.14	0.00	49.18	0.42	2.94	fluvial
<i>Promise Formation</i>												
BABI_1119m	-0.59	0.67	37	2.15	-45.84	0.02	0.16	0.00	49.01	2.63	2.94	fluvial
BABI_1157m	0.67	0.11	51	1.12	-45.66	0.06	0.12	0.00	26.98	0.79	2.94	fluvial
<i>Rietkuil Formation</i>												
BABI_115m	3.64	0.02	135	0.82	-47.37	0.03	0.47	0.00	40.67	0.37	2.92	fluvial
BABI_125m	3.91	0.49	191	23.46	-45.98	0.27	0.22	0.08	13.50	2.98	2.92	fluvial
<i>Booyens Formation</i>												
DK12_3325m	-0.04	0.61	17	0.16	-33.16	0.00	0.10	0.00	69.90	0.45	2.87	fluvial
DK12_3377.8m	-1.17	0.35	23	9.92	-28.80	0.08	0.03	0.01	14.28	3.55	2.87	fluvial
TW6_1746.4m	0.60	0.89	24	0.09	-37.43	0.05	0.56	0.00	268.94	0.08	2.87	shallow marine near rivers
TW6_1749.9m	0.57	0.55	39	4.40	-37.88	0.07	0.33	0.00	102.43	11.79	2.87	shallow marine near rivers
TW6_1750.9m	0.55	0.41	43	2.38	-39.11	0.08	0.75	0.00	202.62	13.83	2.87	shallow marine near rivers
TW6_1750.2m	1.53	0.32	64	0.28	-38.71	0.07	0.56	0.00	103.67	0.78	2.87	shallow marine near rivers
TW6_1758.2m	2.78	0.66	67	8.94	-35.92	0.02	0.22	0.00	38.49	5.78	2.87	shallow marine near rivers
<i>Brixton Formation</i>												
TF1_3035m	-2.82	0.09	188	4.90	-27.28	0.01	0.11	0.00	7.03	0.19	2.96	inner shelf marine
TF1_3065m	-1.95	0.10	85	1.99	-29.62	0.01	0.17	0.00	23.94	1.04	2.96	inner shelf marine
<i>Parktown Formation</i>												
TF1_3525m	-0.74	0.04	72	1.30	-28.32	0.03	0.15	0.00	24.14	0.41	2.96	inner shelf marine
TF1_4400m	-1.17	0.35	74	3.01	-27.77	0.39	1.13	0.00	171.28	12.93	2.96	inner shelf marine
TF1_4440m	-1.33	0.20	106	0.83	-28.24	0.01	0.78	0.00	85.71	0.39	2.96	inner shelf marine
Nullagine Group:												
<i>Mosquito Creek Formation</i>												
130711-4	0.06	0.35	42	3.00	-40.67	0.04	0.23	0.01	64.47	2.42	2.98	outer shelf

Table A9.3: Comparison of kerogen and whole-rock data for samples with sufficient material from the Soanesville Group and the Witwatersrand Supergroup. Whole-rock data are repeated from Table A2.

Sample	$\delta^{15}\text{N}_{\text{bulk}}$ [‰]	TN [ppm]	TOC [%]	C/N _{bulk} [atom.]	$\delta^{15}\text{N}_{\text{ker}}$ [‰]	σ [‰]	C/N _{ker} [atom.]	f (N _{ker}) [%]	f (N _{sil}) [%]
Soanesville Group:									
96049	0.48	359	1.20	39	-1.29	0.10	274	14	86
96050	0.40	348	0.76	25	-0.99	0.07	252	10	90
96051	0.42	423	1.11	31	-1.63	0.10	278	11	89
96052	0.40	325	0.85	30	-1.57	0.01	266	11	89
96053	0.58	405	1.23	35	-1.47	0.31	267	13	87
96054	0.14	392	1.54	46	-2.08	0.02	282	16	84
96055	0.64	503	1.98	46	-1.75	0.01	289	16	84
96056	0.63	360	0.96	31	-2.12	0.16	287	11	89
97SSD32-06	0.66	292	1.55	62	-1.40	0.01	297	21	79
97SSD32-21	0.37	107	1.20	132	-2.24	0.23	302	43	57
97SSD51-03	-0.86	371	1.42	45	-2.25	0.06	267	17	83
Witwatersrand Supergroup:									
BABI_1119	-0.59	37	0.16	49	-2.40	0.01	673	7	93
BABI_115	3.64	135	0.47	41	-0.48	0.30	394	10	90
TW6_1749.9	0.57	39	0.33	102	-2.17	0.72	1279	8	92
TW6_1750.2	1.53	64	0.56	104	-1.79	0.05	1251	8	92
TF1_4400	-1.17	74	1.13	171	-2.28	0.64	1910	9	91
TF1_4440	-1.33	106	0.78	86	-4.44	0.28	1781	5	95

Table A9.4: Elemental abundances in drill-core samples from the Soanesville Group

Sample	96049	96050	96051	96052	96053	96054	96055	96056	97SSD32-06	97SSD32-21	97SSD51-03
Mo [EF]	0.90	1.01	0.95	1.06	0.94	0.95	1.04	0.80	1.22	1.05	0.93
V [EF]	0.96	0.94	0.90	0.87	0.95	0.89	0.99	0.83	1.16	0.96	0.92
Al [%]	11.25	11.1	12.5	11.65	11.45	9.74	11.5	11.05	13.6	5.14	10
Fe [%]	4.49	5.9	5.87	6.17	5.93	12.1	5.75	8.41	4.13	6.6	10.15
Ca [%]	0.05	0.06	0.06	0.07	0.08	0.36	0.08	0.33	0.04	0.26	0.25
Na [%]	0.95	0.98	1.07	1.02	1.12	0.62	0.92	0.96	0.08	0.02	0.65
K [%]	2.11	1.84	2.26	1.77	1.96	1.55	2.25	1.76	6.18	1.72	1.36
Mg [%]	0.83	0.9	0.88	0.94	0.83	1.43	0.78	1.04	0.9	1.5	1.35
Ti [%]	0.315	0.204	0.196	0.184	0.151	0.124	0.171	0.123	0.284	0.147	0.133
Mn [ppm]	338	309	267	290	226	2500	222	937	77	489	1700
P [ppm]	130	150	160	190	170	240	190	200	190	210	200
Ba [ppm]	730	630	760	570	560	460	650	500	2450	1860	410
Sr [ppm]	72.1	66	80.2	76.1	87.1	57.2	80	79.5	14.4	3.5	56.3
Zr [ppm]	90.7	93.2	95.9	103	89.8	90.7	103	83.3	177	68.9	75.6
V [ppm]	129	124	134	121	130	103	136	109	187	59	110
Cr [ppm]	216	187	207	198	208	172	227	162	312	119	181
Rb [ppm]	112	86.1	126	103	107	107	145	111	199	65.8	63.4
Zn [ppm]	112	137	189	177	180	256	259	551	205	451	285
Ce [ppm]	58.1	40.3	59.6	73.2	44.5	70.3	65.3	62.8	50.1	43.4	51.8
Ni [ppm]	79.4	88.5	91.4	88.5	94.5	120.5	104.5	118.5	214	104.5	128.5
La [ppm]	28.3	16.4	28.7	35.2	18.4	39	33.6	31.7	23.2	23.4	23.1
Cu [ppm]	22.1	98.2	54	36.7	34.3	22.9	59.8	72.2	95.1	97.8	25.1
Li [ppm]	40.5	45.2	45.7	50.8	47.7	49.5	39	45.7	15.9	14	61.9
Y [ppm]	14.3	11.9	14.4	16.2	10.9	15.2	13.3	12.7	13.2	8.9	11.9
Ga [ppm]	32.6	30.7	33.9	31.6	32.9	28.1	32.7	30.4	42.1	13.7	27.7
Co [ppm]	14.6	15	15.8	16.2	14.2	20.4	14.8	18.9	26.6	10.4	23.6
Pb [ppm]	11.2	9.3	16.8	13.1	10.1	8.5	14.1	11.8	6.6	8.6	9.2
Sc [ppm]	17.9	16.9	18	16.5	15.5	13.3	16.8	15.5	23.1	6.8	15.5

Nb [ppm]	8.4	5.4	5.5	5.4	4.3	3.4	4.5	3.6	6.8	2.8	3.6
Th [ppm]	9.9	8.6	11.3	12.6	9.3	11	11.8	10.7	13.3	4.9	8.4
Hf [ppm]	2.6	2.7	2.8	2.9	2.6	2.5	3.1	2.3	5	1.9	2.2
Cs [ppm]	21.4	14.25	14.75	13.9	13	8.69	12.55	9.97	9.15	1.45	8.43
U [ppm]	1.5	1.4	1.6	1.5	1.7	1.5	1.8	1.4	3.2	1	1.4
Be [ppm]	2.16	2.3	2.82	2.76	3.02	2.01	3.12	2.87	4.18	1.5	1.91
Sn [ppm]	2.5	2.1	2.5	2.2	2.1	1.8	2.3	1.8	5	1.2	1.5
W [ppm]	1	0.7	0.8	0.7	0.7	0.5	0.7	0.5	0.8	0.5	0.5
Ge [ppm]	0.14	0.11	0.13	0.13	0.13	0.11	0.14	0.14	0.16	0.13	0.12
Mo [ppm]	1.37	1.51	1.61	1.67	1.46	1.25	1.61	1.2	2.24	0.73	1.26
Ta [ppm]	0.71	0.48	0.49	0.47	0.4	0.31	0.43	0.3	0.62	0.26	0.32
Tl [ppm]	0.66	0.61	0.74	0.58	0.67	0.53	0.83	0.55	1.06	0.55	0.5
Sb [ppm]	0.56	0.4	0.55	0.56	0.69	0.7	1.16	1.23	2.06	0.84	0.58
Bi [ppm]	0.14	0.16	0.24	0.16	0.13	0.13	0.17	0.15	0.13	0.05	0.11
Cd [ppm]	<0.02	<0.02	2.29	0.02	0.38	0.52	0.71	1.36	0.49	0.95	0.23
Se [ppm]	0.2	0.2	0.2	1	1	1	1	0.2	1	0.2	1
In [ppm]	0.083	0.499	0.524	0.187	0.098	0.15	0.16	0.19	0.091	0.078	0.039
Ag [ppm]	0.2	0.36	0.61	0.23	0.21	0.18	0.31	0.39	0.37	0.1	0.17
Re [ppm]	0.002	<0.002	0.002	0.002	<0.002	0.002	0.002	<0.002	0.002	<0.002	<0.002
Te [ppm]	0.1	<0.05	0.06	<0.05	<0.05	0.05	0.1	0.07	0.15	0.05	0.08

Table A9.5: Elemental abundances in drill-core samples from the Witwatersrand Supergroup

Core	TW6	TW6	TW6	TW6	TW6	DK12	DK12	BABI	BABI	BABI	BABI	BABI	BABI	TF1	TF1	TF1	TF1	TF1
Sample	1746.4	1749.9	1750.2	1750.9	1758.2	3325	3377.8	115	125	934	1013	1119	1157	3035	3065	3525	4400	4440
Mo [EF]	1.41	1.24	1.43	1.52	1.33	1.57	1.46	0.98	1.02	1.16	0.90	1.16	1.49	1.28	0.91	1.16	1.16	1.37
V [EF]	1.85	1.76	1.97	1.72	1.81	1.23	1.73	1.79	1.46	1.56	1.42	1.17	1.19	1.56	1.56	1.56	1.31	1.62
Al [%]	8.17	7.7	8.99	8.87	11.35	8.89	8.66	8.98	9.76	7.83	9.64	9.86	9.81	9.87	8.31	7.24	7.9	9.2
Fe [%]	6.05	4.15	4.24	5.67	1.37	4.46	5.52	12.1	6.73	6.56	7.54	5.33	5.65	3.29	7.91	5.33	10.4	7.8
Ca [%]	0.12	0.07	0.1	0.12	0.1	0.86	0.92	0.19	0.36	0.82	0.04	0.05	0.22	0.04	0.02	0.26	0.31	0.07
Na [%]	0.03	0.11	0.16	0.11	0.29	1.02	1	0.08	0.14	0.12	0.21	0.22	0.22	0.14	0.04	0.55	0.34	0.4
K [%]	0.6	1.37	1.88	1.33	2.89	2.98	1.84	1.56	2.89	1.61	2.63	3.3	3.34	4.46	2.26	2.23	2.31	3.58
Mg [%]	6.42	3.45	3.72	4.33	0.87	3.37	6.06	2.89	2.45	2.82	1.87	1.94	1.58	1.73	2.29	3.23	2.01	2.92
Ti [%]	0.369	0.272	0.323	0.303	0.331	0.372	0.338	0.301	0.363	0.287	0.311	0.256	0.259	0.284	0.24	0.284	0.326	0.489
Mn [ppm]	1100	340	376	419	77	492	613	388	289	664	506	308	288	382	1160	394	1220	447
P [ppm]	470	220	360	460	530	410	310	260	430	420	140	70	800	160	110	220	150	210
Ba [ppm]	230	470	670	460	930	730	560	310	560	400	570	690	750	740	410	390	370	490
Sr [ppm]	10.3	34.5	48.7	38.6	59.7	143	166.5	20.6	40.3	40.3	47.3	54.7	60.6	29.1	11	40.1	51.4	33.5
Zr [ppm]	98	150.5	123	93.4	153	109.5	74.3	119.5	123	112	148	131	198.5	164.5	107	121.5	102	167.5
V [ppm]	180	161	211	182	244	130	178	191	170	145	163	137	139	183	154	134	123	177
Cr [ppm]	941	869	763	1040	1300	540	988	621	608	480	539	437	464	783	583	787	422	602
Rb [ppm]	32.9	72.7	82.3	42.4	150	99.4	82.4	49.5	129	68.8	77.8	120	143	136.5	65.9	118.5	145.5	110.5
Zn [ppm]	152	81	84	93	27	101	87	102	98	94	130	94	73	31	41	66	76	98
Ce [ppm]	5.13	36.3	49.9	45.7	63.8	49.2	29.8	37.4	47.5	37	20.1	37.6	52.3	9.69	21.6	35.7	53.2	94
Ni [ppm]	505	411	544	661	189.5	308	468	357	355	254	330	251	304	213	214	298	171	192
La [ppm]	2.6	16	21.8	19.6	27.6	22.4	13.1	16.8	22.1	18.2	8.1	15.9	24.6	4.1	9.9	18.2	27.1	42.5
Cu [ppm]	125.5	81.4	89.4	98.3	60.3	58.2	18.5	57.2	68	58.3	45.1	59.3	161.5	28	26.7	60.7	15.9	82.7
Li [ppm]	105	60.1	65.7	74	22.6	98.2	129.5	111	61.9	99.1	74	71	55.6	37.1	32.4	57.7	54	61.7
Y [ppm]	14	14.9	13.5	12.7	16	16.6	16	13.7	15.8	12.6	9	11.7	18.7	5.4	5	10.1	6.3	8.8
Ga [ppm]	19.55	19.15	23.7	21.3	32.2	25.9	24.1	22.4	23	19.65	24.5	27.6	24.3	27.4	20.2	17.8	20.3	25.2
Co [ppm]	21.4	51.4	48.4	99.2	11.3	39.5	48.3	56	53.3	33.9	59.3	42.3	73.4	38.1	16.9	34.4	29.3	22.2
Pb [ppm]	26.3	5.5	7.2	10	5.1	223	55.1	75.3	339	10.1	15	27.4	37.4	2.5	1.5	2.1	4.3	4.9

Sc [ppm]	30.3	24.9	29.2	27.6	42.7	19.2	27.7	28.8	22.9	21.1	21.2	19.4	19.3	25.2	22.7	22.5	18.2	20.6
Nb [ppm]	5.1	4.2	4.8	4.6	6.1	9.1	6.2	5.3	6.9	4.8	6.6	7.3	6.2	5.5	2.6	4.7	10.7	11.7
Th [ppm]	4.1	4.4	4.2	3.4	5.8	4.9	3.5	4	4.4	4.1	4.2	4.9	8	2.4	3.1	4.5	6.4	6.8
Hf [ppm]	2.7	4.1	3.4	2.7	4.5	3.1	2.2	3.5	3.4	2.9	4.1	3.7	5.5	4.5	2.9	3.2	2.7	4.6
Cs [ppm]	2.95	6.23	7.67	6.92	11.2	7.37	4.79	2.5	4.68	4.51	4.2	5.68	5.2	6.52	2.88	6.41	3.39	4.18
U [ppm]	1.1	1.4	1.2	1.2	2	2.2	1.1	1.5	1.4	1.4	2.2	2.2	3.2	2.6	1.3	1.7	1.7	2.2
Be [ppm]	1.13	2.08	2.31	1.97	1.79	1.94	1.74	1.58	1.87	1.29	0.74	1.32	1.85	1.82	1.71	1.29	2	1.97
Sn [ppm]	1.2	1.1	1.4	1.3	1.6	2.2	1.6	1.5	1.8	1.2	1.4	2	1.9	1.9	1.5	1.3	2.9	3
W [ppm]	1.9	1.2	1.7	1.6	1.5	1.9	1.5	1.2	1.3	1.4	1.1	1.2	1.2	0.9	0.9	0.9	1.5	1.7
Ge [ppm]	0.08	0.09	0.11	0.12	0.14	0.12	0.1	0.14	0.12	0.11	0.1	0.12	0.12	0.18	<0.05	0.11	0.14	0.17
Mo [ppm]	1.55	1.29	1.74	1.82	2.03	1.88	1.71	1.19	1.34	1.23	1.17	1.55	1.97	1.71	1.02	1.13	1.24	1.7
Ta [ppm]	0.4	0.34	0.4	0.37	0.53	0.79	0.5	0.46	0.59	0.41	0.59	0.72	0.62	0.41	0.19	0.34	0.86	1
Tl [ppm]	0.31	0.71	1.06	0.73	1.44	1.12	0.67	0.52	0.84	0.46	0.77	0.98	0.9	0.93	0.4	0.42	0.48	0.74
Sb [ppm]	2.75	1.8	3.1	5.21	0.67	0.73	0.51	3.22	3.95	2.25	3.95	2.29	3.23	0.46	0.61	0.54	1.61	0.9
Bi [ppm]	0.09	0.09	0.25	0.6	0.17	0.43	0.14	0.31	0.25	0.21	0.34	0.26	0.67	0.21	0.1	0.05	0.37	0.1
Cd [ppm]	<0.02	0.02	0.03	0.09	0.05	0.09	<0.02	0.03	0.1	0.04	0.03	<0.02	0.09	<0.02	<0.02	0.03	<0.02	<0.02
Se [ppm]	0.2	1	1	1	1	1	0.2	1	0.2	0.2	1	0.2	1	0.2	0.2	1	0.2	1
In [ppm]	0.076	0.061	0.08	0.066	0.074	0.054	0.068	0.07	0.057	0.053	0.039	0.049	0.07	0.047	0.049	0.05	0.067	0.094
Ag [ppm]	0.18	0.1	0.15	0.4	0.05	0.09	0.02	0.1	0.12	0.07	0.15	0.08	0.17	0.03	0.02	0.04	0.03	0.05
Re [ppm]	0.003	0.002	0.004	0.002	0.003	<0.002	<0.002	<0.002	<0.002	0.002	<0.002	<0.002	<0.002	0.003	<0.002	<0.002	<0.002	<0.002
Te [ppm]	0.05	<0.05	<0.05	0.09	<0.05	<0.05	<0.05	0.05	0.06	0.08	0.05	<0.05	0.07	0.06	<0.05	<0.05	0.06	<0.05

Supplementary references

- Ader M, Sansjofre P, Halverson GP, Busigny V, Trindade RI, Kunzmann M, Nogueira AC (2014) Ocean redox structure across the Late Neoproterozoic oxygenation event: A nitrogen isotope perspective. *Earth and Planetary Science Letters*, **396**, 1-13.
- Algeo TJ, Meyers PA, Robinson RS, Rowe H, Jiang GQ (2013) Icehouse-greenhouse variations in marine denitrification. *Biogeosciences Discussions*, **10**, 14769-14813.
- Altabet MA, Deuser WG, Honjo S, Stienen C (1991) Seasonal and depth-related changes in the source of sinking particles in the North Atlantic. *Nature*, **354**, 136-139.
- Anbar A (2008) Elements and evolution. *Science*, **322**, 1481-1483.
- Bauersachs T, Kremer B, Schouten S, Sinninghe Damsté JS (2009) A biomarker and $\delta^{15}\text{N}$ study of thermally altered Silurian cyanobacterial mats. *Organic Geochemistry*, **40**, 2
- Beaumont V, Agrinier P, Javoy M, Robert F (1994) Determination of the CO contribution to the $^{15}\text{N}/^{14}\text{N}$ ratio measured by mass spectrometry. *Analytical Chemistry*, **66**, 2187-2189.
- Beaumont V, Robert F (1999) Nitrogen isotope ratios of kerogens in Precambrian cherts: a record of the evolution of atmosphere chemistry? *Precambrian Research*, **96**, 63-82.
- Beaumont VI, Jahnke LL, Des Marais DJ (2000) Nitrogen isotopic fractionation in the synthesis of photosynthetic pigments in *Rhodobacter capsulatus* and *Anabaena cylindrica*. *Organic Geochemistry*, **31**, 1075-1085.
- Bebout GE, Cooper DC, Bradley AD, Sadofsky SJ (1999) Nitrogen-isotope record of fluid-rock interactions in the Skiddaw Aureole and granite, English Lake District. *American Mineralogist*, **84**, 1495-1505.
- Bebout GE, Fogel ML (1992) Nitrogen-isotopic composition of metasedimentary rocks in the Catalina Schist, California: implications for metamorphic devolatilization history. *Geochimica et Cosmochimica Acta*, **56**, 2839-2849.
- Blake TS, Buick R, Brown SJA, Barley ME (2004) Geochronology of a late Archaean flood basalt province in the Pilbara craton, Australia: constraints on basin evolution, volcanic and sedimentary accumulation, and continental drift rates. *Precambrian Research*, **133**, 143-173.
- Boyd SR, Phillippot P (1998) Precambrian ammonium biogeochemistry: a study of the Moine metasediments, Scotland. *Chemical Geology*, **144**, 257-268.
- Bräuer K, Hahne K (2005) Methodical aspects of the ^{15}N -analysis of Precambrian and Palaeozoic sediments rich in organic matter. *Chemical Geology*, **218**, 361-368.
- Buick R, Brauhart CW, Morant P, Thornett JR, Maniw JG, Archibald NJ, Doepel MG, Fletcher IR, Pickard AL, Smith JB, Barley ME, McNaughton NJ, Groves DI (2002) Geochronology and stratigraphic relationships of the Sulphur Springs Group and Strelley Granite: a temporally distinct igneous province in the Archaean Pilbara Craton, Australia. *Precambrian Research*, **114**, 87-120.
- Bumby AJ, Eriksson KA, Catuneanu O, Nelson DR, Rigby MJ (2012) Meso-Archaean and Palaeo-Proterozoic sedimentary sequence stratigraphy of the Kaapvaal Craton. *Marine and Petroleum Geology*, **33**, 92-116.
- Busigny V, Cartigny P, Philippot P, Ader M, Javoy M (2003) Massive recycling of nitrogen and other fluid-mobile elements (K, Rb, Cs, H) in a cold slab environment: evidence from HP to UHP oceanic metasediments of the Schistes Lustrés nappe (western Alps, Europe). *Earth and Planetary Science Letters*, **215**, 27-42.

- Busigny V, Lebeau O, Ader M, Krapež B, Bekker A (2013) Nitrogen cycle in the Late Archean ferruginous ocean. *Chemical Geology*, **362**, 115-130.
- Canfield DE, Ngombi-Pemba L, Hammarlund EU, Bengtson S, Chaussidon M, Gauthier-Lafaye F, Meunier A, Riboulleau A, Rollion-Bard C, Rouxel O, Asael D, Pierson-Wickmann A-C, El Albani A (2013) Oxygen dynamics in the aftermath of the Great Oxidation of Earth's atmosphere. *Proceedings of the National Academy of Sciences*, **110**, 16736-16741.
- Chicarelli MI, Hayes JM, Popp BN, Eckardt CB, Maxwell JR (1993) Carbon and nitrogen isotopic compositions of alkyl porphyrins from the Triassic Serpiano oil shale. *Geochimica et Cosmochimica Acta*, **57**, 1307-1311.
- Cremonese L, Shields-Zhou G, Struck U, Ling H-F, Och L, Chen X, Li D (2013) Marine biogeochemical cycling during the early Cambrian constrained by a nitrogen and organic carbon isotope study of the Xiaotan section, South China. *Precambrian Research*, **225**, 148-165.
- Cremonese L, Shields-Zhou GA, Struck U, Ling HF, Och LM (2014) Nitrogen and organic carbon isotope stratigraphy of the Yangtze Platform during the Ediacaran-Cambrian transition in South China. *Palaeogeography, Palaeoclimatology, Palaeoecology*, **398**, 165-186.
- Crowe SA, Døssing LN, Beukes NJ, Bau M, Kruger SJ, Frei R, Canfield DE (2013) Atmospheric oxygenation three billion years ago. *Nature*, **501**, 535-538.
- Fedo CM, Eriksson KA, Krogstad EJ (1996) Geochemistry of shales from the Archean (~3.0 Ga) Buhwa Greenstone Belt, Zimbabwe: implications for provenance and source-area weathering. *Geochimica et Cosmochimica Acta*, **60**, 1751-1763.
- Garvin J, Buick R, Anbar AD, Arnold GL, Kaufman AJ (2009) Isotopic evidence for an aerobic nitrogen cycle in the latest Archean. *Science*, **323**, 1045-1048.
- Glass JB, Wolfe-Simon F, Elser JJ, Anbar AD (2010) Molybdenum-nitrogen co-limitation in freshwater and coastal heterocystous cyanobacteria. *Limnology and Oceanography*, **55**, 667-676.
- Godfrey LV, Falkowski PG (2009) The cycling and redox state of nitrogen in the Archaean ocean. *Nature Geoscience*, **2**, 725-729.
- Godfrey LV, Glass JB (2011) The geochemical record of the ancient nitrogen cycle, nitrogen isotopes, and metal cofactors. *Methods in Enzymology*, **486**, 483-506.
- Godfrey LV, Poulton SW, Bebout GE, Fralick PW (2013) Stability of the nitrogen cycle during development of sulfidic water in the redox-stratified late Paleoproterozoic ocean. *Geology*, **41**, 655-658.
- Gordon GW, Lyons TW, Arnold GL, Roe J, Sageman BB, Anbar AD (2009) When do black shales tell molybdenum isotope tales? *Geology*, **37**, 535-538.
- Guy BM, Ono S, Gutzmer J, Kaufman AJ, Lin Y, Fogel ML, Beukes NJ (2012) A multiple sulfur and organic carbon isotope record from non-conglomeratic sedimentary rocks of the Mesoarchean Witwatersrand Supergroup, South Africa. *Precambrian Research*, **216-219**, 208-231.
- Haendel D, Muehle K, Nitzsche H-M, Stiehl G, Wand U (1986) Isotopic variations of the fixed nitrogen in metamorphic rocks. *Geochimica et Cosmochimica Acta*, **50**, 749-758.
- Hall CE (2005) SHRIMP U-Pb depositional age for the lower Hardey Formation: evidence for diachronous deposition of the lower Fortescue Group in the southern Pilbara region, Western Australia. *Australian Journal of Earth Sciences*, **52**, 403-410.

- Hayes JM, Kaplan IR, Wedeking KW (1983) Precambrian organic geochemistry, preservation of the record. In: *Earth's earliest biosphere - its origin and evolution* (ed Schopf JW). Princeton University Press, Princeton, NJ.
- Hessler AM, Lowe DR (2006) Weathering and sediment generation in the Archean: an integrated study of the evolution of siliciclastic sedimentary rocks of the 3.2 Ga Moodies Group, Barberton Greenstone Belt, South Africa. *Precambrian Research*, **151**, 185-210.
- Horwitz RC (1990) Palaeogeographic and tectonic evolution of the Pilbara Craton, Northwestern Australia. *Precambrian Research*, **48**, 327-340.
- Jia Y (2006) Nitrogen isotope fractionations during progressive metamorphism: a case study from the Paleozoic Cooma metasedimentary complex, southeastern Australia. *Geochimica et Cosmochimica Acta*, **70**, 5201-5214.
- Kashiyama Y, Ogawa NO, Kuroda J, Shiro M, Nomoto S, Tada R, Kitazato H, Ohkouchi N (2008) Diazotrophic cyanobacteria as the major photoautotrophs during mid-Cretaceous oceanic anoxic events: Nitrogen and carbon isotopic evidence from sedimentary porphyrin. *Organic Geochemistry*, **39**, 532-549.
- Kikumoto R, Tahata M, Nishizawa M, Sawaki Y, Maruyama S, Shu D, Han J, Komiya T, Takai K, Ueno Y (2014) Nitrogen isotope chemostratigraphy of the Ediacaran and Early Cambrian platform sequence at Three Gorges, South China. *Gondwana Research*, **25**, 1057-1069.
- Kump LR, Junium C, Arthur MA, Brasier A, Fallick A, Melezhik V, Lepland A, Črncić AE, Luo G (2011) Isotopic evidence for massive oxidation of organic matter following the Great Oxidation Event. *Science*, **334**, 1694-1696.
- Lehman MR, Bernasconi SM, Barbieri A, McKenzie JA (2002) Preservation of organic matter and alteration of its carbon and nitrogen isotope composition during simulated and in situ early sedimentary diagenesis. *Geochimica et Cosmochimica Acta*, **66**, 3573-3584.
- Macko SA, Fogel ML, Hare PE, Hoering TC (1987) Isotopic fractionation of nitrogen and carbon in the synthesis of amino acids by microorganisms. *Chemical Geology*, **65**, 79-92.
- Mingram B, Bräuer K (2001) Ammonium concentration and nitrogen isotope composition in metasedimentary rocks from different tectonometamorphic units of the European Variscan Belt. *Geochimica et Cosmochimica Acta*, **65**, 273-287.
- Nesbitt HW, Young GM (1982) Early Proterozoic climates and plate motions inferred from major element chemistry of lutites. *Nature*, **299**, 715-717.
- Nishizawa M, Takahata N, Terada K, Komiya T, Ueno Y, Sano Y (2005) Rare-earth element, lead, carbon, and nitrogen geochemistry of apatite-bearing metasediments from the ~3.8 Ga Isua Supracrustal Belt, West Greenland. *International Geology Review*, **47**, 952-970.
- Ohmoto H, Watanabe Y, Ikemi H, Poulson SR, Taylor BE (2006) Sulphur isotope evidence for an oxic Archean atmosphere. *Nature*, **442**, 908-911.
- Palya AP, Buick IS, Bebout GE (2011) Storage and mobility of nitrogen in the continental crust: Evidence from partially melted metasedimentary rocks, Mt. Stafford, Australia. *Chemical Geology*, **281**, 211-226.
- Papineau D, Mojzsis SJ, Karhu JA, Marty B (2005) Nitrogen isotopic composition of ammoniated phyllosilicates: case studies from Precambrian metamorphosed sedimentary rocks. *Chemical Geology*, **216**, 37-58.
- Papineau D, Purohit R, Fogel ML, Shields-Zhou GA (2013) High phosphate availability as a possible cause for massive cyanobacterial production of oxygen in the Paleoproterozoic atmosphere. *Earth and Planetary Science Letters*, **362**, 225-236.

- Papineau D, Purohit R, Goldberg T, Pi D, Shields GA, Bhu H, Steele A, Fogel ML (2009) High primary productivity and nitrogen cycling after the Paleoproterozoic phosphogenic event in the Aravalli Supergroup, India. *Precambrian Research*, **171**, 37-56.
- Pinti DL, Hashizume K, Matsuda JI (2001) Nitrogen and argon signatures in 3.8 to 2.8 Ga metasediments: Clues on the chemical state of the Archean ocean and the deep biosphere. *Geochimica et Cosmochimica Acta*, **65**, 2301-2315.
- Pinti DL, Hashizume K, Sugihara A, Massault M, Philippot P (2009) Isotopic fractionation of nitrogen and carbon in Paleoproterozoic cherts from Pilbara craton, Western Australia: Origin of ^{15}N -depleted nitrogen. *Geochimica et Cosmochimica Acta*, **2009**, 3819-3848.
- Planavsky NJ, Asael D, Hofmann A, Reinhard CT, Lalonde SV, Knudsen A, Wang X, Ossa Ossa F, Pecoits E, Smith AJB, Beukes NJ, Bekker A, Johnson TM, Konhauser K, Lyons TW, Rouxel OJ (2014) Evidence for oxygenic photosynthesis half a billion years before the Great Oxidation Event. *Nature Geoscience*.
- Plessen B, Harlov DE, Henry D, Guidotti CV (2010) Ammonium loss and nitrogen isotopic fractionation in biotite as a function of metamorphic grade in metapelites from western Maine, USA. *Geochimica et Cosmochimica Acta*, **74**, 4759-4771.
- Poulson Brucker RL, McManus J, Severmann S, Berelson WM (2009) Molybdenum behavior during early diagenesis: Insights from Mo isotopes. *Geochemistry, Geophysics, Geosystems*, **10**.
- Qi H, Coplen TB, Geilmann H, Brand WA, Böhlke JK (2003) Two new organic reference materials for $\delta^{13}\text{C}$ and $\delta^{15}\text{N}$ measurements and a new value for the $\delta^{13}\text{C}$ of NBS 22 oil. *Rapid Communications in Mass Spectrometry*, **17**, 2483-2487.
- Rasmussen B, Buick R (1999) Redox state of the Archean atmosphere: Evidence from detrital heavy minerals in ca. 3250-2750 Ma sandstones from the Pilbara Craton, Australia. *Geology*, **27**, 115-118.
- Reinhard CT, Planavsky NJ, Robbins LJ, Partin CA, Gill BC, Lalonde SV, Bekker A, Konhauser KO, Lyons TW (2013) Proterozoic ocean redox and biogeochemical stasis. *Proceedings of the National Academy of Sciences*, **110**, 5357-5362.
- Robl TL, Davis BH (1993) Comparison of the HF-HCl and HF-BF₃ maceration techniques and the chemistry of resultant organic concentrates. *Organic Geochemistry*, **20**, 249-255.
- Rudnick RL, Gao S (2014) Composition of the continental crust. *Treatise on Geochemistry*, **4**, 1-51.
- Saito MA, Sigman DM, Morel FMM (2003) The bioinorganic chemistry of the ancient ocean: the co-evolution of cyanobacterial metal requirements and biogeochemical cycles at the Archean-Proterozoic boundary? *Inorganica Chimica Acta*, **356**, 308-318.
- Sánchez-Baracaldo P, Ridgwell A, Raven JA (2014) A Neoproterozoic transition in the marine nitrogen cycle. *Current Biology*, **24**, 652-657.
- Schimmelmann A, Lis GP (2010) Nitrogen isotopic exchange during maturation of organic matter. *Organic Geochemistry*, **41**, 63-70.
- Schoepfer SD, Henderson CM, Garrison GH, Ward PD (2012) Cessation of a productive coastal upwelling system in the Panthalassic Ocean at the Permian–Triassic Boundary. *Palaeogeography, Palaeoclimatology, Palaeoecology*, **313-314**, 181-188.
- Scott C, Lyons TW, Bekker A, Shen Y, Poulton SW, Chu X, Anbar AD (2008) Tracing the stepwise oxygenation of the Proterozoic ocean. *Nature*, **452**, 456-459.
- Sekine Y, Suzuki K, Senda R, Goto KT, Tajika E, Tada R, Goto K, Yamamoto S, Ohkouchi N, Ogawa NO, Maruoka T (2011) Osmium evidence for synchronicity between a rise in

- atmospheric oxygen and Palaeoproterozoic deglaciation. *Nature Communications*, **2**, DOI: 10.1038/ncomms1507
- Smith RE, Perdrix JL, Parks TC (1982) Burial metamorphism in the Hamersley Basin, Western Australia. *Australian Journal of Petrology*, **23**, 75-102.
- Stüeken EE (2013) A test of the nitrogen-limitation hypothesis for retarded eukaryote radiation: nitrogen isotopes across a Mesoproterozoic basinal profile. *Geochimica et Cosmochimica Acta*, **120**, 121-139.
- Svensen H, Bebout G, Kronz A, Li L, Planke S, Chevallier L, Jamtveit B (2008) Nitrogen geochemistry as a tracer of fluid flow in a hydrothermal vent complex in the Karoo Basin, South Africa. *Geochimica et Cosmochimica Acta*, **72**, 4929-4947.
- Taylor SR, McLennan SM (2001) Chemical composition and element distribution in the Earth's crust. *Encyclopedia of Physical Science and Technology*, 697-719.
- Thomas OD (1997) Mid-Archaean environments: The sedimentology, stratigraphy and biogeochemistry of the Gorge Creek Group in the Strelley Domain, Pilbara Craton, Western Australia. In: *Geology*. University of Sidney, Sidney, pp. 75.
- Ueno Y, Yoshioka H, Maruyama S, Isozaki Y (2004) Carbon isotopes and petrography of kerogens in ~3.5-Ga hydrothermal silica dikes in the North Pole area, Western Australia. *Geochimica et Cosmochimica Acta*, **68**, 573-589.
- Van Kranendonk MJ, Smithies RH, Hickman AH, Wingate MTD, Bodorkos S (2010) Evidence for Mesoarchean (~3.2 Ga) rifting of the Pilbara Craton: The missing link in an early Precambrian Wilson cycle. *Precambrian Research*, **177**, 145-161.
- van Zuilen MA, Mathew K, Wopenka B, Lepland A, Marti K, Arrhenius G (2005) Nitrogen and argon isotopic signatures in graphite from the 3.8-Ga-old Isua Supracrustal Belt, Southern West Greenland. *Geochimica et Cosmochimica Acta*, **69**, 1241-1252.
- Wang D (2012) Redox chemistry of molybdenum in natural waters and its involvement in biological evolution. *Frontiers in microbiology*, **3**, doi:10.3389/fmicb.2012.00427.
- Watanabe Y, Bevacqua DC, Ohmoto H (2004) Microbial ecosystem in the oldest freshwater lake revealed from a drill core of the 2.76 Ga Hardey Formation, Pilbara District, Western Australia. *AGU Fall Meeting Abstracts*, **1**, 0996.
- Yamaguchi KE (2002) Geochemistry of Archean-Paleoproterozoic black shales: the early evolution of the atmosphere, oceans, and biosphere. In: *Department of Geosciences*. Pennsylvania State University, pp. 485.
- Yui T-F, Kao S-J, Wu T-W (2009) Nitrogen and N-isotope variation during low-grade metamorphism of the Taiwan mountain belt. *Geochemical Journal*, **43**, 15-27.
- Zerkle AL, House CH, Brantley SL (2005) Biogeochemical signatures through time as inferred from whole microbial genomes. *American Journal of Science*, **305**, 467-502.

Chapter 10: Nitrogen isotope evidence for alkaline lakes on late Archean continents

Abstract

Nitrogen isotope ratios in ancient sedimentary rocks are generally interpreted as a proxy for metabolic nitrogen pathways and the redox state of the water column. Fractionation processes occurring under anoxic, alkaline conditions during the dissociation of NH_4^+ to H^+ and volatile NH_3 are frequently overlooked, although this mechanism imparts large isotopic fractionations. Here we propose that NH_3 volatilization is largely responsible for $\delta^{15}\text{N}$ values of up to +50‰ at extremely high C/N ratios in the late Archean Tumbiana Formation. This sequence of sedimentary rocks represents a system of lakes that formed on subaerial flood basalts and were partly filled by basaltic volcanic ash. Aqueous alteration of volcanic glass followed by evaporative concentration of ions should have led to the development of high alkalinity with a pH of 9 or higher, as in modern analogues. In this sedimentologically unusual setting, nitrogen isotope ratios thus provide indirect evidence for the oldest alkaline lake system in the rock record. These very heavy lacustrine $\delta^{15}\text{N}$ values contrast markedly with those of Archean marine sedimentary rocks, making an Archean “soda ocean” unlikely. Today, alkaline lakes are among the most productive ecosystems on Earth. Some nutrients, in particular molybdenum, are more soluble at high pH, and certain prebiotic reactions would likely have been favored under alkaline conditions in similar settings earlier in Earth’s history. Hence alkaline lakes in the Archean could have been significant for the origin and early evolution of life.

10.1. Introduction

Since ~2.7 Gyr, isotope fractionation in the marine nitrogen cycle has probably been dominated by redox reactions, in particular the large fractionation of up to 30‰ imparted during denitrification and/or anammox in the water column (Garvin *et al.*, 2009; Godfrey & Falkowski, 2009; Brunner *et al.*, 2013). In the modern ocean, these processes render residual NO_3^- , the major dissolved nitrogen species, isotopically enriched to ~+5‰, and this enrichment is passed on to biomass that incorporates NO_3^- as a nitrogen source (Sigman *et al.*, 2009). In the early and mid-Archean, prior to the onset of oxidative weathering on land (Stüeken *et al.*, 2012), the nitrogen cycle was evidently anaerobic, marine nitrate was scarce, and N_2 -fixation was dominant (Stüeken *et al.*, in prep.), leading to $\delta^{15}\text{N}$ values near 0‰, *i.e.* close to the composition of the atmosphere (Marty *et al.*, 2013). The time around 2.7 Gyr has been proposed as a transition from nitrate-depleted to nitrate-rich conditions in surface environments (Thomazo *et al.*, 2011). More specifically, $\delta^{15}\text{N}$ values of up to +50.4‰ from the 2.72 Gyr lacustrine Tumbiana Formation (Figure 10.1) in the Fortescue Group, Western Australia, were interpreted as evidence of partial nitrification of NH_4^+ under low ambient oxygen levels to isotopically light NO_2^- or N_2O , which were then lost from the system by either complete denitrification (NO_2^-) or direct escape into the atmosphere (N_2O) (Thomazo *et al.*, 2011). The residual heavy NH_4^+ would then have served as the major nitrogen source for living organisms such that its isotopic composition was preserved in the rock record. This process is not implausible, but it may not necessarily have been the major contributor to the observed fractionations in the Tumbiana Formation. First, N_2O is only a byproduct of nitrification with nearly 90% of initial NH_4^+ going to NO_2^- (Stein *et al.*, 2012). While some methanotrophic bacteria can fractionate nitrogen isotopes by up to 55‰ during the conversion of NH_4^+ to N_2O (Mandernack *et al.*, 2009), nitrification to NO_2^- usually imparts

fractionations of up to 38‰ (reviewed by Casciotti, 2009). Therefore, a large fraction of NH_4^+ would have to be oxidized to NO_2^- and subsequently lost from the system in order to explain $\delta^{15}\text{N}$ values of up to +50‰. Assuming a starting composition of 0‰, over 72% would have to be lost, combined with Rayleigh fractionation. This may not be fully compatible with the proposal that the residual NH_4^+ supply was large enough to sustain the vigorous ecosystem recorded in the Tumbiana rocks and leave an isotopic imprint on the biomass. Second, as also noted by Farquhar *et al.* (2014), it is difficult to explain why little of the isotopically light NO_2^- would have been re-assimilated rather than denitrified, if NH_4^+ became limiting due to partial oxidation. Lastly, the Tumbiana Formation not only stands out because of its uniquely heavy isotopic composition (Figure 10.2), but also because of its remarkably high $\text{C}_{\text{org}}/\text{N}_{\text{bulk}}$ ratios (485 ± 327 , 1σ ; Figure 10.3) (Thomazo *et al.*, 2011, this study). This results from nitrogen concentrations that are unusually low (< 21 ppm, this study), despite the moderately high total organic carbon (TOC) concentrations (up to 0.76%, this study) and the very low metamorphic grade (prehnite-pumpellyite, Smith *et al.*, 1982) of these rocks. For these three reasons, we propose that an additional mechanism with a marked preference for ^{14}N over ^{15}N must have contributed to nitrogen loss from the water column and perhaps during diagenesis. Volatilization of NH_3 under alkaline conditions would fulfill this condition and is consistent with the tuffaceous, carbonate-rich composition of Tumbiana sediments (discussed below).

NH_4^+ produced from degradation of organic matter dissociates to H^+ and volatile NH_3 with a pKa of 9.24 at standard conditions (Figure 10.4a). This dissociation imparts a large isotopic fractionation with residual NH_4^+ becoming increasingly heavy (Figure 10.4b). Li *et al.* (2012) observed an equilibrium fractionation of 45.4‰ between $\text{NH}_4^+_{(\text{aq})}$ and $\text{NH}_3_{(\text{aq})}$ (solid black line in Figure 10.4b), while the isotopic effect of $\text{NH}_3_{(\text{aq})} \leftrightarrow \text{NH}_3_{(\text{g})}$ transformation was negligible.

However, NH_4^+ was supplied in excess in their experiments and $\text{NH}_{3(g)}$ volatilization proceeded under an oxic atmosphere. It is conceivable that a kinetic path (dashed black line in Figure 10.4b) would result during diagenesis where NH_4^+ release from organic matter is rate-limiting, or under anoxic conditions where $\text{NH}_{3(g)}$ escapes more rapidly from the solution. Furthermore, higher net fractionations could also be achieved if $\delta^{15}\text{N}$ of initial NH_4^+ from biomass were $> 0\text{‰}$ due to additional redox processes such as those described by Thomazo *et al.* (2011). But intense NH_3 volatilization under anoxic alkaline conditions could probably by itself explain net $\delta^{15}\text{N}$ values of up to 50‰ and relatively low nitrogen concentrations in these rocks.

To explore this hypothesis, we analyzed nitrogen and organic carbon isotopes in bulk samples and a few kerogen isolates from three lake sub-basins of the 2.72 Gyr Tumbiana Formation near Billadunna (drill core SV-1), Beabea Creek (outcrop locality) and in drill core WRL-1 where the Tumbiana Formation does not crop out at the surface (Figure 10.1). These three sites are distinct from the sub-basin near Meentheena that was previously sampled by Thomazo *et al.* (2011). Additionally, we collected four samples from an outcrop of the lacustrine Mopoke carbonate member of the underlying Kylena Formation (2.74 Gyr), which is sedimentologically comparable to the Tumbiana Formation. These samples should display similarly large isotopic fractionations to those previously reported from the Tumbiana Formation (Thomazo *et al.*, 2011) if their analogous environment caused identical water chemistry. However, they should be systematically different from nearly contemporaneous marine sediments as well as from fluvio-lacustrine shales of the underlying siliciclastic Hardey Formation (~2.76 Gyr) (Stüeken *et al.*, in prep.), where carbonate and volcanic ash are scarce. To add to the late Archean marine database, we also analyzed five samples from the 2.71 Gyr Kidd Creek deposits in the Abitibi Greenstone Belt, Canada, and four samples from the 2.66 Gyr

Jeerinah Formation in Fortescue Group, Western Australia. Samples were prepared by either off-line (low $[N_{\text{bulk}}] < 100\text{ppm}$) or on-line (high $[N_{\text{bulk}}] > 100\text{ppm}$) combustion and analyzed with a continuous-flow isotope-ratio mass-spectrometer (Appendix A10). Results are reported relative to atmospheric air for $\delta^{15}\text{N}$ and relative to VPDB for $\delta^{13}\text{C}$.

10.2. Results

Our isotopic results (Table 10.1) from the Tumbiana and Kylena Formations are in good agreement with those of Thomazo *et al.* (2011), confirming that they are not analytical artifacts resulting from abnormally low TN concentrations but are instead characteristic of these stratigraphic units. $\delta^{15}\text{N}_{\text{bulk}}$ values in our Tumbiana samples display a similar mean value ($+31.9 \pm 6.8\text{‰}$ compared to $+29.5 \pm 10.1\text{‰}$) but slightly smaller range ($+22.9\text{‰}$ to $+44.0\text{‰}$ compared to $+8.6\text{‰}$ to $+50.4\text{‰}$), which may be due to our smaller sample set (17 compared to 30). Samples from the Kylena Formation are also isotopically enriched ($+24.0 \pm 6.5\text{‰}$, $n = 4$). With some exceptions (#130707-3, #130707-2b), very fine mudrocks that lack an internal fabric (Section A10.2.1) tend to be relatively more enriched ($+36.1 \pm 6.1\text{‰}$, $n = 6$), while samples with slightly coarser grain size (carbonate as well as siliciclastic composition), more common carbonate fenestrae, and relatively more wrinkled laminae deposited by microbial mats (Section A10.2.2) usually have lower $\delta^{15}\text{N}_{\text{bulk}}$ values ($+29.0 \pm 6.0\text{‰}$, $n = 10$). Similarly, mudrocks analysed by Thomazo *et al.* (2011) ($+35.6 \pm 11.2$, $n = 11$) were on average 10‰ heavier than siltstone and stromatolites ($+26.0 \pm 7.6\text{‰}$, $n = 19$). Kerogen isolates are relatively more uniform ($\delta^{15}\text{N}_{\text{org}} = 40.0 \pm 7.3\text{‰}$, $n = 15$) and don't correlate with bulk compositions ($r^2 = 0.20$).

The total N content in decarbonated aliquots of our samples was slightly higher than in those of Thomazo *et al.* (2011) ($11.9 \pm 7.1\text{ppm}$, compared to $4.7 \pm 3.0\text{ppm}$), probably because

we analyzed relatively more black shales (average $\text{TOC}_{\text{decarbonated}} = 0.4 \pm 0.3\%$, compared to $0.2 \pm 0.1\%$). Here, ‘decarbonated’ denotes the siliciclastic fraction remaining after treatment with HCl, as reported by Thomazo *et al.* (2011). The Kylenea Fm is as similarly nitrogen-poor as the Tumbiana Fm ($\text{TN}_{\text{decarbonated}} = 12.6 \pm 6.3\text{ppm}$, $\text{TOC} = 0.2 \pm 0.0\%$). TN and TOC, both decarbonated, are strongly correlated in the Tumbiana samples ($r^2 = 0.89$, Figure 10.5a), with a y-axis (TN) intercept of 2.3ppm TN, which may represent the average detrital background of silicate-bound nitrogen (N_{sil}).

Our $\text{C}_{\text{org}}/\text{N}_{\text{bulk}}$ ratios in the Tumbiana Fm (412 ± 103 , compared to 527 ± 399 from Thomazo *et al.*, 2011), are on average higher than in the Kylenea Fm (173 ± 87). We find no correlation between $\delta^{15}\text{N}_{\text{bulk}}$ and $\text{C}_{\text{org}}/\text{N}_{\text{bulk}}$ ($r^2 = 0.0001$, Figure 10.5b) or $\text{C}_{\text{org}}/\text{N}_{\text{bulk}}$ and $\text{C}_{\text{org}}/\text{N}_{\text{org}}$ ($r^2 = 0.11$, Figure 10.5c) in the Tumbiana samples, but a strong positive correlation between $\delta^{15}\text{N}_{\text{bulk}}$ and $\text{C}_{\text{org}}/\text{N}_{\text{org}}$ ($r^2 = 0.52$, Figure 10.5d). Because of the relatively invariable $\delta^{15}\text{N}_{\text{org}}$ (Figure 10.5e), this correlation is driven primarily by changes in the composition of silicate-bound nitrogen ($\delta^{15}\text{N}_{\text{sil}}$), *i.e.* $\text{C}_{\text{org}}/\text{N}_{\text{org}}$ is correlated with $\delta^{15}\text{N}_{\text{sil}}$ ($r^2 = 0.43$, Figure 10.5f), which ranges from +1.3‰ to +43.7‰. N_{sil} includes NH_4^+ added to clay minerals during diagenesis in the Tumbiana lakes and detrital N_{sil} that was already present in terrigenous siliciclastic minerals that were transported into the basin. We will further discuss this below.

Organic carbon isotopes ($-48.5 \pm 3.1\text{‰}$) are slightly lighter than those of Thomazo *et al.* (2011) ($-39.5 \pm 8.7\text{‰}$) but are in good agreement with their mudrock values ($-45.5 \pm 6.6\text{‰}$). However, we do not see any significant correlation between $\delta^{13}\text{C}_{\text{org}}$ and $\delta^{15}\text{N}_{\text{bulk}}$ ($r^2 = 0.01$) or $\delta^{15}\text{N}_{\text{org}}$ ($r^2 = 0.25$). The Kylenea data ($\delta^{13}\text{C}_{\text{org}} = -45.9 \pm 9.4\text{‰}$) are on average similar to the Tumbiana values.

Nitrogen isotope ratios in the roughly contemporaneous marine samples (Table 10.2) are consistently much lower in $\delta^{15}\text{N}_{\text{bulk}}$ and $\text{C}_{\text{org}}/\text{N}_{\text{bulk}}$ (Kidd Creek: $\delta^{15}\text{N}_{\text{bulk}} = +7.6 \pm 1.2\text{‰}$, $\text{C}_{\text{org}}/\text{N}_{\text{bulk}} = 130 \pm 109$, $n = 5$; Jeerinah: $\delta^{15}\text{N}_{\text{bulk}} = +2.3 \pm 1.8\text{‰}$, $\text{C}_{\text{org}}/\text{N}_{\text{bulk}} = 137 \pm 127$, $n = 4$) and agree well with published data of similar age from the Fortescue Group (Yamaguchi, 2002) and the Transvaal Supergroup (Godfrey & Falkowski, 2009) (Figure 10.2). This indicates that the relatively high $\delta^{15}\text{N}_{\text{org}}$ values of up to +20‰ that were previously reported from substantially metamorphosed rocks in the Abitibi Greenstone Belt and localities in Botswana and India (Jia & Kerrich, 2004; Kerrich *et al.*, 2006) are not globally representative of marine sediments from this time period.

10.3. Discussion

10.3.1. Preservation of primary compositions

The very low metamorphic grade and the consistency of results between sub-basins that are several hundred km apart (Figure 10.1) strongly argues against significant isotopic resetting as a result of metamorphic or metasomatic alteration. Indeed, even the most metamorphosed samples in the entire geological record (Figure 10.3), which have been subjected to amphibolite facies conditions at temperatures several hundred degrees higher than the sub-greenschist Tumbiana rocks, are not nearly as enriched in $\delta^{15}\text{N}$. We therefore conclude that the Tumbiana results reflect unique primary or early diagenetic processes and not later overprinting.

10.3.2. A unique nitrogen isotope signal

Nitrogen isotope ratios in the Tumbiana Formation (and the underlying Kylenea Formation) are clearly distinct from those from other non-marine (Stüeken *et al.*, in prep.) and marine environments of similar age (this study, Figure 10.2, 10.3), being much heavier with

much higher $C_{\text{org}}/N_{\text{bulk}}$ ratios based on much lower $N_{\text{bulk}}\%$. This makes it highly unlikely that the Tumbiana $\delta^{15}\text{N}$ enrichments were caused by a small but global increase in $p\text{O}_2$ (cf. Thomazo *et al.*, 2011). If micro-aerobic conditions always led to large fractionations, then extremely heavy $\delta^{15}\text{N}$ values should be common in micro-aerobic environments today and in the Precambrian rock record. For example, in the Belt Supergroup of Mesoproterozoic age, when atmospheric oxygen levels may have been less than 1% of present atmospheric levels (Lyons *et al.*, 2014), nitrogen isotopes display a basinal gradient from +5‰ in shallow water, indicative of aerobic nitrogen cycling, to ~0‰ offshore, where anaerobic N_2 -fixation was dominating (Stüeken, 2013); the data do not show any evidence of an intermediate micro-aerobic site where fractionations were unusually high. Similarly, $\delta^{15}\text{N}_{\text{bulk}}$ values during the end-Archean “whiff of oxygen” range from +1‰ to +8‰, representing anaerobic and aerobic end-members (Garvin *et al.*, 2009) with no extreme fractionations like those in the Tumbiana Formation representing intermediate micro-aerobic conditions. However, we stress that redox reactions including partial nitrification and denitrification or anammox could have occurred locally and contributed to the overall fractionations observed in the Tumbiana lakes, because these process were likely operating in the ocean at this time (Godfrey & Falkowski, 2009). The prevalence of stromatolites and tufted mats of cyanobacterial origin (Buick, 1992; Flannery & Walter, 2012) make it likely that nitrogen was redox-active in the Tumbiana lakes. However, net fractionations resulting from redox processes are mostly below 10‰ and rarely as large as 20‰ at any other time in Earth’s history (Figure 10.2). It is thus likely that an additional mechanism such as NH_3 volatilization at high pH played a significant role during Tumbiana deposition. This process operates in alkaline lakes today (Collister & Hayes, 1973; Talbot & Johannessen, 1992; Lent *et al.*, 1995; Menzel *et al.*, 2013), which are enriched in $\delta^{15}\text{N}_{\text{bulk}}$ (up to +28.0‰, mean $+13.7 \pm 2.5\%$) compared to

Holocene freshwater lakes (mean $+2.2 \pm 0.7\%$, McLauchlan *et al.*, 2013) (Figure 10.3). The enrichment is not as extreme as in the Tumbiana Formation, but in the late Archean, NH_3 loss could have been more severe than today, because the atmosphere was anoxic, locally-produced O_2 would have had a short residence time in the upper water column and it probably disappeared quickly at nightfall when photosynthesis halted. Hence NH_3 could probably have escaped more readily than today, leading to larger isotopic effects. In modern redox-stratified lakes such as Mono Lake in California (pH ~ 10), NH_3 builds up at depth in the anoxic zone and is released during seasonal water-column overturn (Jellison *et al.*, 1993). Prior to the oxygenation of the atmosphere, NH_3 loss could thus have occurred more frequently, perhaps during diurnal redox cycles. The observed anti-correlation between $\delta^{15}\text{N}$ and microbial lamination (Section A10.2.1, Figures A10.4-6) supports this interpretation, if the microbial mats were mostly composed of cyanobacteria and thus relatively more oxic (Buick, 1992; Flannery & Walter, 2012) whereas the massive black shales represent the most anoxic part of the lakes where NH_3 was produced and released in larger quantities.

The absence of a correlation between $\text{C}_{\text{org}}/\text{N}_{\text{org}}$ and $\delta^{15}\text{N}_{\text{org}}$ does not argue against alkaline NH_3 removal and may in fact be evidence that the water column as well as sedimentary pore waters were alkaline. Living organisms likely assimilated some isotopically enriched NH_4^+ as a nitrogen source (in addition to N_2 -fixation, Stüeken *et al.*, in prep.), and hence the isotopic composition of biomass ($\delta^{15}\text{N}_{\text{org}}$) was probably largely set when $\text{C}_{\text{org}}/\text{N}_{\text{org}}$ was still the same as that of living microbes ($\sim 4-7$, Godfrey & Glass, 2011), whereas further enrichments in $\text{C}_{\text{org}}/\text{N}_{\text{org}}$ beyond 4-7 occurred during biomass degradation in sediments and during later low-grade metamorphism. Ammonification, *i.e.* conversion of N_{org} to NH_4^+ during diagenesis, may have been enhanced under alkaline equilibrium conditions where NH_4^+ was constantly removed by

conversion to volatile NH_3 . However, ammonification itself does not impart any significant isotopic fractionation ($\epsilon = 1\text{‰}$, reviewed by Quan & Falkowski, 2009). It is conceivable that residual isotopically heavy NH_4^+ (aq) in pore waters would have back-reacted and re-equilibrated to some extent with N_{org} . But to first order, the two processes that led to enrichments in $\delta^{15}\text{N}_{\text{org}}$ (assimilation of heavy NH_4^+ (aq) by living biomass in the water column) and $\text{C}_{\text{org}}/\text{N}_{\text{org}}$ (ammonification in alkaline sediments) were probably largely separated in space and time and therefore not directly correlated

The occurrences of fairly light $\delta^{15}\text{N}_{\text{sil}}$ values down to $+1.3\text{‰}$ suggests that siliciclastic minerals, including basaltic ash, already contained isotopically light background levels of N_{sil} . The concentrations of N_{sil} down to 0.3ppm and its isotopic composition down to $+1.3\text{‰}$ are consistent with contributions from an end-member of basaltic glass (0.01-23.6ppm, geometric mean 0.4ppm, $\delta^{15}\text{N} = -1.4 \pm 2.7\text{‰}$, Marty & Humbert, 1997). In sediments where ammonification of organic matter was more efficient (high $\text{C}_{\text{org}}/\text{N}_{\text{org}}$), this background reservoir of detrital N_{sil} would have become most diluted with new, isotopically enriched NH_4^+ produced from degradation of organic matter. This would explain the weak correlation between $\text{C}_{\text{org}}/\text{N}_{\text{org}}$ and $\delta^{15}\text{N}_{\text{sil}}$ ($r^2 = 0.43$, Figure 10.5d).

10.3.3. Development of alkaline conditions

Apart from its high nitrogen isotope and C/N ratios, the Tumbiana Formation also stands out because of its high basaltic ash content. Tuff laminae drape over almost every sedimentary feature, including wave ripples and stromatolites (Figure 10.6). In some parts, tuff is present as reworked arenites, in others as massive airfall deposits with accretionary lapilli. The blocky morphology of individual glass shards and their metamorphic alteration to chlorite indicate that

they are of mafic composition. Mafic igneous rocks, and fine-grained basaltic glass in particular, act as a strong bases, *i.e.* they consume protons and release cations during aqueous alteration (Abelson, 1966; Gislason & Eugster, 1987; Kempe & Kazmierczak, 2002; Gysi & Stefansson, 2008). In a confined lacustrine basin with persistent tuffaceous rainout, this process should have significantly increased the pH of the water column. In most cases, pore spaces within tuff beds in the Tumbiana Formation are filled with early diagenetic carbonate (*e.g.* Figure 10.6a), consistent with an alkaline fluid composition. The pH could have increased further during evaporative concentration of cations (Garrels & Mackenzie, 1967; Eugster, 1980), for which there is evidence in the form of desiccation cracks (Figure 10.6d) and halite pseudomorphs (Buick, 1992). Evaporation increases the pH if $[Na^+] + [K^+] > [Cl^-] + [SO_4^{2-}]$ and $[HCO_3^-] + [CO_3^{2-}] > [Mg^{2+}] + [Ca^{2+}]$ in solution (Garrels & Mackenzie, 1967). Ca^{2+} , Mg^{2+} , SO_4^{2-} and Cl^- are consumed by precipitation of $CaCO_3$, $MgCO_3$, $CaSO_4$ and $NaCl$. SO_4^{2-} , if present, could also be consumed by microbial reduction. The charge of residual dissolved Na^+ and K^+ then has to be balanced by HCO_3^- or CO_3^{2-} . These species are produced from CO_2 by consumption of H^+ , which leads to an increase in pH. The relative scarcity of SO_4^{2-} in the late Archean could further have facilitated this process. Lastly, also CO_2 consumption by cyanobacteria has been shown to increase the pH of the surrounding waters to >10 (Lopez-Archilla *et al.*, 2004), and as mentioned above, stromatolites and tufted mats provide strong evidence for cyanobacterial activity in the Tumbiana lakes (Buick, 1992; Flannery & Walter, 2012). Although none of these features can provide an absolute pH constraint, the combination of tuff, carbonate, cyanobacteria and evaporation makes it likely that the Tumbiana lakes were alkaline and that the pH could have exceeded values around 9, such that a large proportion of NH_4^+ dissociated to NH_3 and H^+

(Figure 10.4). The abundance of carbonate could have further facilitated NH_3 volatilization, because it can act as a buffer for the released H^+ (Avnimelech & Laher, 1977).

Alkaline conditions can also be reconciled with the unusually low organic carbon isotope ratios characteristic of the Tumbiana Formation, which are on average several permil lighter ($-47.3 \pm 3.1\text{‰}$, Eigenbrode & Freeman, 2006) than the already light contemporaneous marine values ($-42.5 \pm 1.9\text{‰}$ in the slightly younger Jeerinah Formation in the Fortescue Group, Eigenbrode & Freeman, 2006). These light values are generally interpreted as indicating widespread methanogenesis in the late Archean, but it is so far unclear why the Tumbiana Formation is the most extreme. Several studies show that in high-pH saline environments, methylotrophic methanogens dominate methane production while acetate-dependent methanogens are rare (Oremland *et al.*, 1982; Nolla-Ardèvol *et al.*, 2012), and methylotrophic methanogens generally impart larger carbon isotope fractionations ($\epsilon = 74 \pm 13\text{‰}$) than acetoclastic organisms ($\epsilon = 21 \pm 19\text{‰}$) (Conrad, 2005). Hence if alkaline conditions in the Tumbiana Formation favored methylotrophy, whereas the more neutral ocean favored acetoclastic methanogenesis with CO_2 -dependent hydrogenotrophic methanogenesis (the third type) relatively the same in both environments, then this could explain the observed patterns in organic $\delta^{13}\text{C}$ values.

Lastly, high alkalinity could be the reason why Mg-carbonate as well as Fe-carbonate and Fe-oxide minerals are rare in the Tumbiana Formation, whereas the marine Carawine and Wittenoom Formations higher up in the local Archean stratigraphy are largely dolomitized (Buick, 1992). Basaltic ash should have delivered lots of Mg and Fe, and O_2 produced by cyanobacteria (Buick, 1992; Flannery & Walter, 2012) could have oxidized Fe^{2+} to Fe^{3+} . However, Mg- and Fe-silicates are much less soluble than Ca-silicates at high pH (Gudbrandsson

et al., 2011). Hence if the Tumbiana lakes were alkaline, then the flux of Ca^{2+} into solution was probably dominating, while Fe^{2+} and Mg^{2+} were relatively immobile.

10.3.4. Implications

It has been proposed before that alkaline lakes should have been common on Archean continents if the upper crust was basalt-dominated (Jones *et al.*, 1998; Nisbet *et al.*, 2007). However, the only piece of tentative evidence for their existence are occurrences of bedded cherts in the late Archean Rietgat Formation, Ventersdorp Supergroup, South Africa which sedimentologically resemble cherts found in the modern alkaline Lake Magadi in Kenya (Karpeta, 1989). The extreme enrichments in nitrogen isotope ratios in the Tumbiana Formation thus represent an independent confirmation that alkaline lakes likely existed. As discussed in Appendix A10.3, it is conceivable that rare earth element patterns of Tumbiana sediments can provide additional independent evidence in future studies.

If mafic terrains were more abundant than today (Taylor & McLennan, 1995) and volcanic activity relative high, then alkaline lakes could have been a common feature on early Precambrian land masses. They are among the most productive ecosystems on the modern Earth (Jones *et al.*, 1998) and may have also been so in the past. For instance, Helz *et al.* (2011) demonstrated that Mo is more soluble at high pH, even in the presence of significant H_2S concentrations as found, for example, in the Black Sea. Mo is a constituent of many important metalloenzymes, including nitrogenase used for N_2 fixation. High Mo solubility combined with nitrogen scarcity due to NH_3 loss in alkaline lakes could thus perhaps have created an ideal environment for the origin or radiation of the Mo-nitrogenase enzyme earlier in the Archean (cf. Stüeken *et al.*, in prep.). Further, the most dominant organisms in modern alkaline lakes are

cyanobacteria (Zavarzin, 1993; Lopez-Archilla *et al.*, 2004). Their diversity is significantly higher than in the ocean, which has led to the proposal that this phylum originated in alkaline habitats (Zavarzin, 1993). If so, then occurrences of alkaline lakes in the Archean further support a relatively early origin of oxygenic photosynthesis, long before the GOE (Crowe *et al.*, 2013; Planavsky *et al.*, 2014). Moreover, if alkaline lakes were common in the Archean, and if, as today and in the Tumbiana Formation (Buick, 1992; Flannery & Walter, 2012) they hosted large populations of cyanobacteria, then this could have led to local hotspots of oxidative weathering over a significant expanse of continental crust. These settings could thus have contributed to pre-GOE accumulation of sulfate-derived sulfur in late Archean marine sediments (Stüeken *et al.*, 2012).

Alkaline lakes could also have been important much earlier in Earth's history, during the origin of life itself. Due to rapid precipitation of CaCO_3 , the solubility of Ca^{2+} is up to five orders of magnitude lower in alkaline lakes than in seawater, which limits Ca^{2+} binding to phosphate and favors the formation of phosphatic biopolymers (Kempe & Kazmierczak, 1994). Furthermore, high pH is required for abiotic formation of carbohydrates through the formose reaction (Kim *et al.*, 2011), and it also enhances the polymerization of HCN, thus facilitating abiotic synthesis of amino acids and nucleobases (Ferris & Hagan Jr., 1984) and ultimately polypeptides (Kempe & Kazmierczak, 2011). Hence, if basaltic Archean and Hadean crust favored the formation of alkaline lakes, then those settings could have made significant contributions to the global geochemical network of prebiotic reactions (Stüeken *et al.*, 2013)

Lastly, the disparity in $\delta^{15}\text{N}$ between ancient marine settings and the Tumbiana alkaline lake system should disprove the "Archean alkaline soda ocean" hypothesis of Kempe & Degens (1985) and others (Kempe & Kazmierczak, 1994; Kempe & Kazmierczak, 2002; Kempe &

Kazmierczak, 2003; Kempe & Kazmierczak, 2011). The concept has already been discredited by rare-earth-element geochemical data (Bau & Dulski, 1996), but the emergence of a second line of contradictory evidence, one that has quantitative predictions that are unfulfilled in Archean marine sediments, makes it almost untenable. If highly alkaline, as would be the case for a “soda ocean”, the Archean marine $\delta^{15}\text{N}$ record should show comparably large positive fractionations to the Tumbiana Formation, outside the 0‰ to +20‰ range attributable to redox processing without alkaline ammonia volatilization. Indeed, as the “soda ocean” concept predicts Archean marine pH levels above 9.5 (Kempe & Degens, 1985), by analogy to most modern soda lakes, Archean marine $\delta^{15}\text{N}$ should have always been extremely fractionated everywhere as volatile ammonia is strongly favored in such highly alkaline conditions (Figure 10.4a). But, as Figure 10.2 shows, this was not the case, except in moderately to highly metamorphosed rocks also exposed to hydrothermal alteration. So, in the light of alkaline lake $\delta^{15}\text{N}$ values, the “Archean alkaline soda ocean” hypothesis should be discarded.

10.4. Conclusion

The unusually heavy nitrogen isotope ratios of the Tumbiana Formation (Thomazo *et al.*, 2011, this study), combined with the high abundance of basaltic ash and carbonate, are plausibly explained by NH_3 volatilization at high pH, *i.e.* the same mechanism that contributes to $\delta^{15}\text{N}$ enrichments in modern alkaline lakes. Redox reactions may have contributed to the overall nitrogen isotope fractionation, such that values of up to 50‰ could be achieved, but they are not discernible without ambiguity. Therefore, these $\delta^{15}\text{N}$ data cannot be used to draw inferences about global atmospheric or marine oxygen levels (*cf.* Thomazo *et al.*, 2011). Instead, these

results reveal the presence of a potentially important environmental niche for prebiotic chemistry and early evolution.

Acknowledgements

The analytical work was funded by a GSA graduate student research grant to EES and an Agouron Institute grant to RB. Field work was supported by the Virtual Planetary Laboratory at the University of Washington. We thank Boswell Wing for providing samples from the Kidd Creek deposit.

Author contributions

R. Buick supervised the project and provided drill core samples, R. Buick and E. E. Stüeken collected additional samples in the field, A. J. Schauer and E. E. Stüeken developed the offline combustion technique, E. E. Stüeken carried out the analyses and wrote the manuscript with advice and contributions from R. Buick.

Tables

Table 10.1: New Tumbiana and Kylena data presented in this study. Carb. = carbonate content; fN = fraction of total nitrogen (TN) present as organic (org) or silicate-bound (sil) nitrogen. All concentrations are by weight, C/N ratios are in units of mol/mol. Sample 99024 is from drill core WRL-1, samples 99037 through 99046 are from drill core SV-1, all others are outcrop samples from Beabea Creek. The Kylena samples are from an outcrop near Meentheena (Figure 10.1).

	$\delta^{15}\text{N}$ bulk	σ	TN bulk	σ	TOC bulk	σ	$\delta^{13}\text{C}$ org	σ	C/N bulk	σ	C/N org	σ	$\delta^{15}\text{N}$ org	σ	fN org	σ	fN sil	σ	carb	σ	$\delta^{15}\text{N}$ sil	σ	
	[‰]	[‰]	[ppm]	[ppm]	[%]	[%]	[‰]	[‰]					[‰]	[‰]	[%]	[%]	[%]	[%]	[%]	[%]	[%]	[%]	[%]
Tumbiana:																							
99024	25.39	0.54	9.4	0.3	0.23	0.01	-43.99	0.10	281	12									26.0	0.1			
99037	38.36	0.03	12.5	0.4	0.34	0.01	-49.56	0.02	319	12	1120	21	32.02	0.22	28	1	72	1	14.9	0.1	40.9	4.8	
99038	37.91	0.08	15.0	1.5	0.44	0.00	-49.26	0.02	339	33	1243	88	39.26	0.64	27	3	73	3	24.0	0.0	37.4	6.0	
99039	30.62	1.23	8.2	0.6	0.25	0.00	-47.57	0.01	351	26	1351	5	34.07	0.16	26	2	74	2	22.2	0.0	29.4	5.7	
99040	36.98	1.33	20.6	0.9	0.76	0.00	-47.77	0.05	431	19	1455	9	49.96	0.70	30	1	70	1	26.1	0.1	31.5	5.5	
99042	37.70	0.77	14.1	0.9	0.60	0.01	-46.41	0.01	499	32	1044	42	48.06	0.46	48	4	52	4	30.4	0.0	28.2	4.9	
99043	36.23	0.96	12.4	0.1	0.54	0.00	-45.90	0.07	506	2	878	39	42.85	0.51	58	3	42	3	30.1	0.1	27.2	4.5	
99044	28.79	1.55	7.0	0.2	0.28	0.00	-45.41	0.10	464	16	868	37	45.72	0.68	53	3	47	3	28.1	0.0	9.4	1.9	
99045	30.32	1.28	8.0	0.7	0.40	0.00	-44.94	0.14	589	52	846	28	42.96	0.52	70	7	30	7	43.8	0.2	1.3	0.4	
99046	29.35	0.29	9.5	0.3	0.35	0.00	-46.30	0.04	426	16	920	51	38.28	0.61	46	3	54	3	44.5	0.3	21.7	3.6	
130707-2B	22.86	0.71	5.2	0.0	0.14	0.00	-51.43	0.16	327	9	852	60	42.72	0.79	38	3	62	3	23.5	0.2	10.5	2.0	
130707-3	43.95	0.93	2.2	0.1	0.08	0.00	-51.54	0.13	433	21	1161		44.45		37		63		56.7	0.2	43.7		
130707-4	23.76	0.76	3.8	0.5	0.08	0.00	-49.40	0.12	256	33	920	217	41.13	0.67	28	7	72	7	37.4	0.3	17.1	4.4	
130707-5	24.47	1.34	0.8	0.1	0.03	0.00	-49.52	1.67	462	59	677		31.18		68	9	32	9	47.2	0.2	10.0	3.5	
130707-7	29.86	0.89	1.4	0.2	0.04	0.00	-51.39	0.24	343	47									85.0	0.1			
130707-8	42.28	0.21	6.2	0.1	0.17	0.01	-53.65	0.06	324	12	1526	97	44.89	0.70	21	2	79	2	16.0	0.4	41.6	5.4	
130707-9	23.52	0.49	0.7	0.0	0.03	0.00	-57.06	0.36	539	24	629		22.56		86	4	14	4	59.3	1.0	29.3	9.6	
Kylena:																							
130708-5	14.97	0.88	3.7	0.1	0.09	0.01	-54.49	0.21	286	18	753	50	18.46	0.43	38	4	62	4	48.9	0.2	12.8	3.1	
130708-6	25.79	0.13	3.2	0.3	0.05	0.00	-51.13	0.08	170	14	350	9	32.00	0.40	48	4	52	4	56.7	0.7	20.0	3.8	
130708-7	24.80	0.21	5.9	0.2	0.04	0.00	-46.57	0.10	78	4	204	4	31.47	0.21	38	2	62	2	70.2	1.1	20.7	3.2	
130708-8	30.45	0.30	1.8	0.1	0.02	0.00	-32.42	0.75	152	6									88.5	0.7			

Table 10.2: New marine nitrogen data. All samples are from drill cores. Jeerinah samples (Roy Hill Shale Member) are from drill core WRL-1. Nitrogen isotope data are for bulk samples.

	$\delta^{15}\text{N}$	TN	TOC	C/N	Age
	[‰]	[%]	[%]		[Gyr]
Kidd Creek:					
KL0039_119.5	8.83	0.12	29.91	285	2.71
Z-80-2_107.1	7.18	0.10	14.70	175	2.71
Z-80-2_68.5	7.59	0.11	2.33	24	2.71
Z-80-2_84.7	5.69	0.03	3.33	135	2.71
Z-80-2_94.4	8.47	0.14	3.48	29	2.71
Jeerinah:					
99018	-0.28	0.02	7.01	328	2.67
99019	2.47	0.07	3.87	67	2.67
99021	3.38	0.10	7.22	84	2.67
99022	3.69	0.08	5.04	70	2.67

Figures

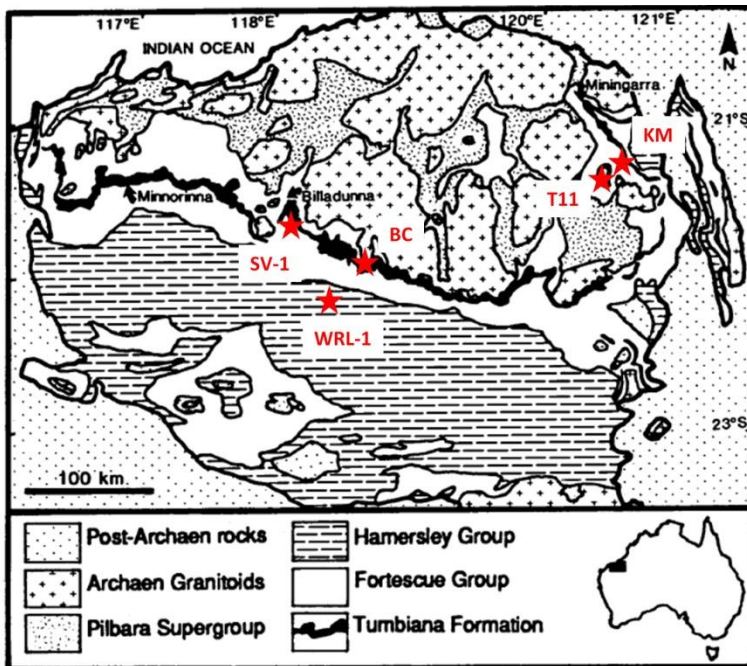


Figure 10.1. Geographic sample locations in the Fortescue Group, Western Australia. SV-1, WRL-1 = locations of drill cores used in this study; T11 = location of the drill core studied by Thomazo *et al.* (2011); BC = outcrop locality in Beabea Creek; KM = outcrop locality of the Kylene Formation, Mopoke Member. Adapted from Buick (1992)

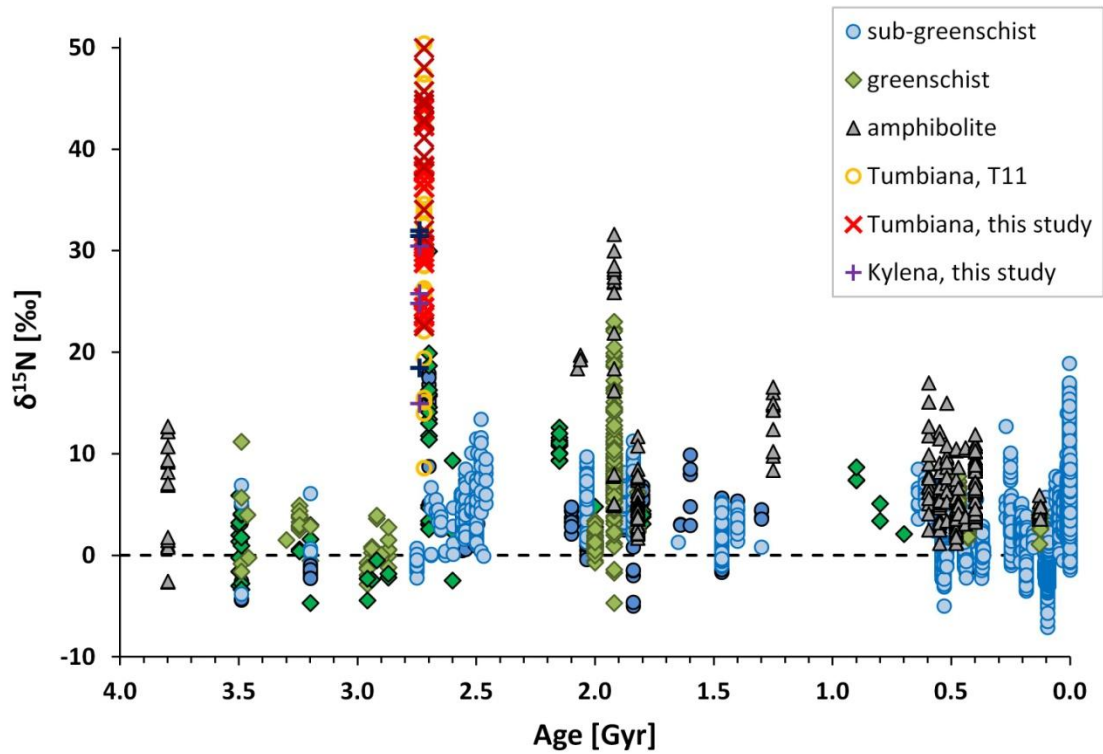


Figure 10.2: Nitrogen isotope ratios through time. ‘T11’ = data from Thomazo *et al.* (2011). Light symbols are bulk samples, dark symbols of same color are kerogen isolates. Most samples older than 3.2 Gyr are associated with hydrothermal deposits and thus not representative of normal marine conditions (see Stüeken *et al.*, in prep. for discussion and references).

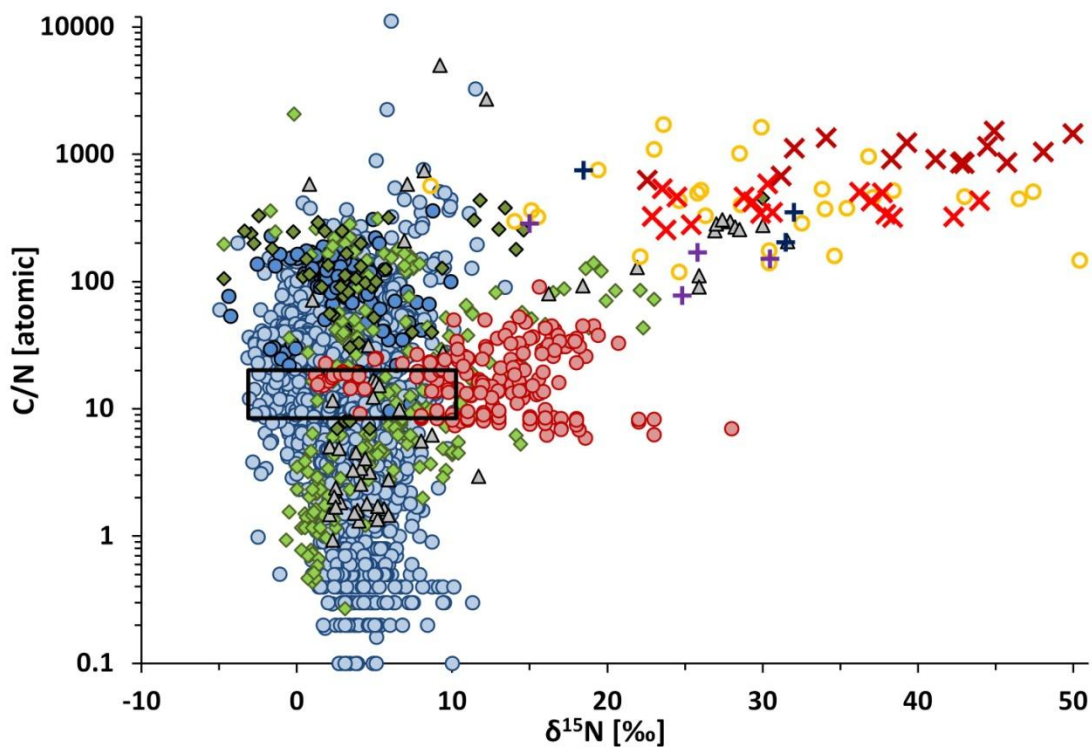


Figure 10.3: $\delta^{15}\text{N}$ versus $\text{C}_{\text{org}}/\text{N}$ ratios. N is organic for kerogen isolates (darker symbols) and bulk for all others (lighter symbols). Red circles = bulk sediment data from modern and Eocene alkaline lakes (see text for references). Black open rectangle = bulk sediments from Holocene freshwater lakes (taken from Figure S4c in McLauchlan *et al.*, 2013). Symbols are the same as in Figure 10.2.

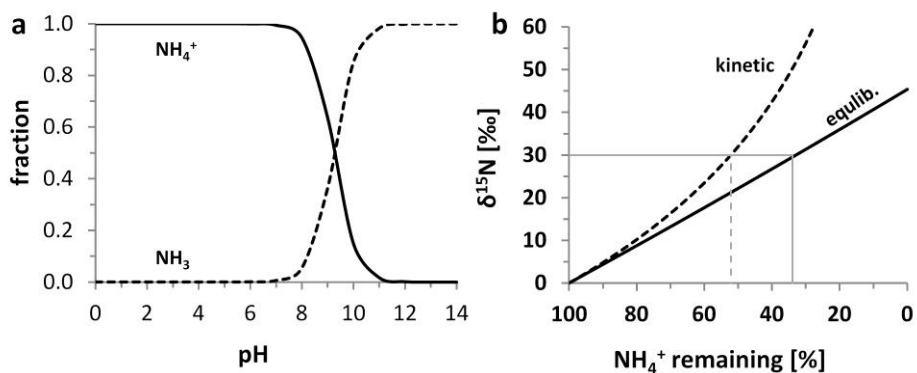


Figure 10.4: pH effects on nitrogen isotopes. (a) relative proportions of volatile ammonia (NH_3) and aqueous ammonium (NH_4^+) as a function of pH at 25°C . (b) isotopic composition of NH_4^+ remaining in solution with progressive conversion to volatile NH_3 . Grey lines mark average $\delta^{15}\text{N}_{\text{bulk}}$ seen in the Tumbiana samples.

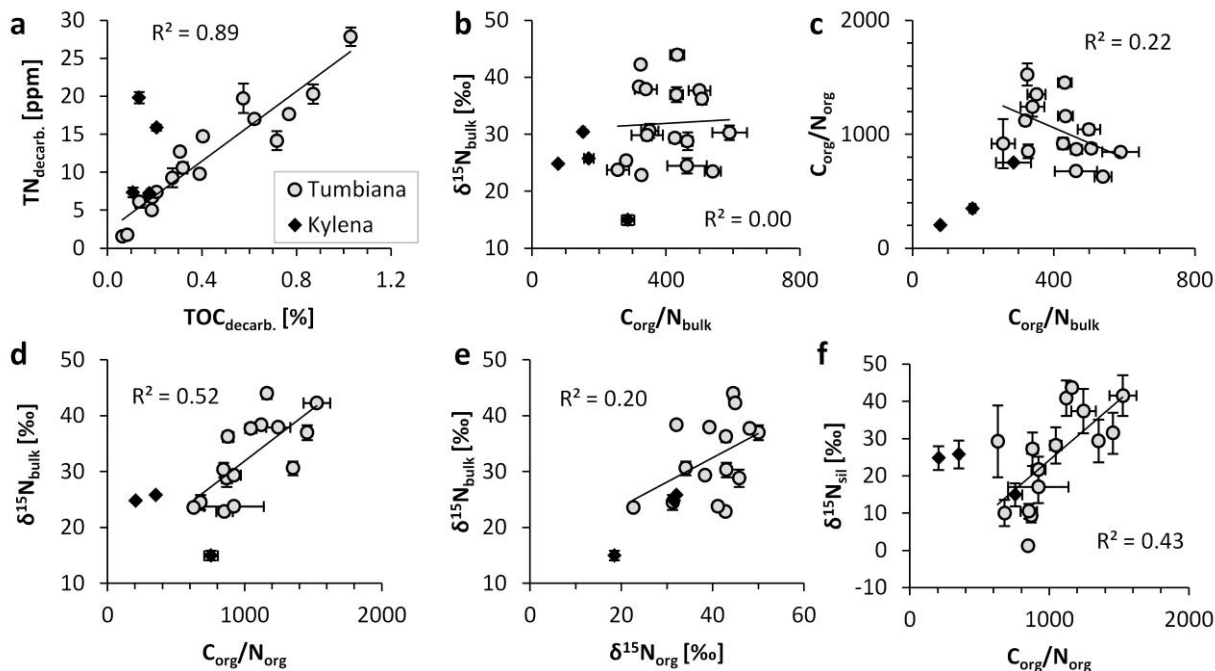


Figure 10.5: Cross-plots. C/N ratios are in units of mol/mol. Regression lines always refer to Tumbiana data only. Error bars are $\pm 1\sigma$.

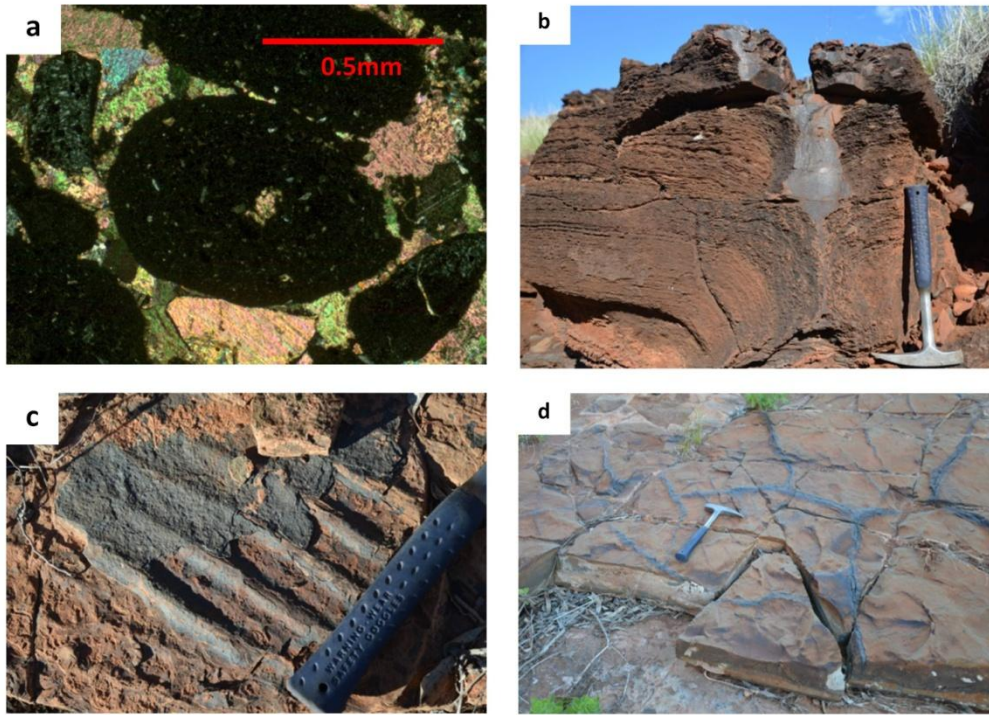


Figure 10.6: Common sedimentary features in the Tumbiana Formation. a: photomicrograph (crossed polarizers) of accretionary lapilli once composed of glassy basaltic ash (black spheroids), surrounded by sparry calcite cement. b: turbinated stromatolites where individual laminae are defined by fine tuff that is more resistant to weathering than carbonate. Spaces between stromatolites are filled with fine air-fall tuff. c: medium-grained tuff draped over symmetric wave ripples composed of fine tuff and carbonate. d: polygonal desiccation cracks, filled with fine tuff. Desiccation cracks are also visible at much smaller scale on many other bedding surfaces that are not depicted. All photos were taken at Beabea Creek (Figure 10.1).

References

- Abelson PH (1966) Chemical events on the primitive Earth. *Proceedings of the National Academy of Sciences of the United States of America*, **55**, 1365-1372.
- Avnimelech Y, Laher M (1977) Ammonia volatilization from soils: Equilibrium considerations. *Soil Science Society of America Journal*, **41**, 1080-1084.
- Bau M, Dulski P (1996) Distribution of yttrium and rare-earth elements in the Penge and Kuruman iron-formations, Transvaal Supergroup, South Africa. *Precambrian Research*, **79**, 37-55.
- Brunner B, Contreras S, Lehmann MF, Matantseva O, Rollog M, Kalvelage T, Klockgether G, Lavik G, Jetten MSM, Kartal B, Kuypers MM (2013) Nitrogen isotope effects induced by anammox bacteria. *Proceedings of the National Academy of Sciences*, **110**, 18994-18999.
- Buick R (1992) The antiquity of oxygenic photosynthesis: evidence from stromatolites in sulphate-deficient Archaean lakes. *Science*, **255**, 74-77.
- Casciotti KL (2009) Inverse kinetic isotope fractionation during bacterial nitrite oxidation. *Geochimica et Cosmochimica Acta*, **73**, 2061-2076.
- Collister JW, Hayes JM (1973) A preliminary study of carbon and nitrogen isotopic biogeochemistry of lacustrine sedimentary rocks from the Green River Formation, Wyoming, Utah, and Colorado. In: *Geochemical, biogeochemical, and sedimentological studies of the Green River formation, Wyoming, Utah, and Colorado* (ed Tuttle ML). U.S. Geological Survey, Denver, CO.
- Conrad R (2005) Quantification of methanogenic pathways using stable carbon isotopic signatures: a review and a proposal. *Organic Geochemistry*, **36**, 739-752.
- Crowe SA, Døssing LN, Beukes NJ, Bau M, Kruger SJ, Frei R, Canfield DE (2013) Atmospheric oxygenation three billion years ago. *Nature*, **501**, 535-538.
- Eigenbrode JL, Freeman KH (2006) Late Archean rise of aerobic microbial ecosystems. *Proceedings of the National Academy of Sciences*, **103**, 15759-15764.
- Eugster HP (1980) Geochemistry of evaporitic lacustrine deposits. *Annual Reviews in Earth and Planetary Sciences*, **8**, 35-63.
- Farquhar J, Zerkle A, Bekker A (2014) Geologic and geochemical constraints on Earth's early atmosphere. *Treatise on Geochemistry*, **6**, 91-138.
- Ferris JP, Hagan Jr. WJ (1984) HCN and chemical evolution: the possible role of cyano compounds in prebiotic synthesis. *Tetrahedron*, **40**, 1093-1120.
- Flannery DT, Walter MR (2012) Archean tufted microbial mats and the Great Oxidation Event: new insights into an ancient problem. *Australian Journal of Earth Sciences*, **59**, 1-11.
- Garrels RM, Mackenzie FT (1967) Origin of the chemical composition of some springs and lakes. In: *Equilibrium concepts in natural water systems* (ed Stumm W). American Chemical Society, Washington, D.C., pp. 222-242.
- Garvin J, Buick R, Anbar AD, Arnold GL, Kaufman AJ (2009) Isotopic evidence for an aerobic nitrogen cycle in the latest Archean. *Science*, **323**, 1045-1048.
- Gislason SR, Eugster HP (1987) Meteoric water-basalt interaction. I: A laboratory study. *Geochimica et Cosmochimica Acta*, **51**, 2827-2840.
- Godfrey LV, Falkowski PG (2009) The cycling and redox state of nitrogen in the Archaean ocean. *Nature Geoscience*, **2**, 725-729.
- Godfrey LV, Glass JB (2011) The geochemical record of the ancient nitrogen cycle, nitrogen isotopes, and metal cofactors. *Methods in Enzymology*, **486**, 483-506.

- Gudbrandsson S, Wolff-Boenisch D, Gislason SR, Oelkers EH (2011) An experimental study of crystalline basalt dissolution from $2 \leq \text{pH} \leq 11$ and temperatures from 5 to 75 °C. *Geochimica et Cosmochimica Acta*, **75**, 5496-5509.
- Gysi AP, Stefansson A (2008) Numerical modelling of CO₂-water-basalt interaction. *Mineralogical Magazine*, **72**, 55-59.
- Helz GR, Bura-Nakic E, Mikac N, Ciglenecki I (2011) New model for molybdenum behavior in euxinic waters. *Chemical Geology*, **284**, 323-332.
- Jellison R, Miller LG, Melack JM, Dana GL (1993) Meromixis in hypersaline Mono Lake, California. II: Nitrogen fluxes. *Limnology and Oceanography*, **38**, 1020-1039.
- Jia Y, Kerrich R (2004) Nitrogen 15-enriched Precambrian kerogen and hydrothermal systems. *Geochemistry Geophysics Geosystems*, **5**, doi: 10.1029/2004GC000716.
- Jones BE, Grant WD, Duckworth AW, Owenson GG (1998) Microbial diversity of soda lakes. *Extremophiles*, **2**, 191-200.
- Karpeta WP (1989) Bedded cherts in the Rietgat Formation, Hartbeesfontein, South Africa: a late Archaean to early Proterozoic magadiite alkaline playa lake deposit? *South African Journal of Geology*, **92**, 29-36.
- Kempe S, Degens ET (1985) An early soda ocean? *Chemical Geology*, **53**, 95-108.
- Kempe S, Kazmierczak J (1994) The role of alkalinity in the evolution of ocean chemistry, organization of living systems, and biocalcification processes. *Bulletin de l'Institut océanographique*, 61-117.
- Kempe S, Kazmierczak J (2002) Biogenesis and early life on Earth and Europa: favored by an alkaline ocean? . *Astrobiology*, **2**, 123-130.
- Kempe S, Kazmierczak J (2003) Modern soda lakes - model environments for an early alkaline ocean. In: *Modelling in natural sciences* (eds Mueller T, Mueller H). Springer Verlag, Heidelberg, pp. 309-322.
- Kempe S, Kazmierczak J (2011) Soda ocean hypothesis. In: *Encyclopedia of Geobiology* (eds Reitner J, Thiel V). Springer.
- Kerrich R, Jia Y, Manikyamba C, Naqvi SM (2006) Secular variations of N-isotopes in terrestrial reservoirs and ore deposits. *Geological Society of America Memoir*, **198**, 81-104.
- Kim HJ, Ricardo A, Illangkoon HI, Kim MJ, Carrigan MA, Frye F, Benner SA (2011) Synthesis of carbohydrates in mineral-guided prebiotic cycles. *Journal of the American Chemical Society*, **133**, 9457- 9468.
- Lent RM, Lyons WB, Showers WJ, Johannesson KH (1995) Late Holocene paleoclimatic and paleobiologic records from sediments of Devils Lake, North Dakota. *Journal of Paleolimnology*, **13**, 193-207.
- Li L, Sherwood Lollar B, Li H, Wortmann UG, Lacrampe-Couloume G (2012) Ammonium stability and nitrogen isotope fractionations for NH₄⁺-NH_{3(aq)}-NH_{3(gas)} systems at 20-70°C and pH of 2-13: applications to habitability and nitrogen cycling in low-temperature hydrothermal systems. *Geochimica et Cosmochimica Acta*, **84**, 280-296.
- Lopez-Archilla AI, Moreira D, Lopez-Garcia P, Guerrero C (2004) Phytoplankton diversity and cyanobacterial dominance in a hypereutrophic shallow lake with biologically produced alkaline pH. *Extremophiles*, **8**, 109-115.
- Lyons TW, Reinhard CT, Planavsky NJ (2014) The rise of oxygen in Earth's early ocean and atmosphere. *Nature*, **506**, 307-315.

- Mandernack KW, Mills CT, Johnson CA, Rahn T, Kinney C (2009) The $\delta^{15}\text{N}$ and $\delta^{18}\text{O}$ values of N_2O produced during the co-oxidation of ammonia by methanotrophic bacteria. *Chemical Geology*, **267**, 96-107.
- Marty B, Humbert F (1997) Nitrogen and argon isotopes in oceanic basalts. *Earth and Planetary Science Letters*, **152**, 101-112.
- Marty B, Zimmermann L, Pujol M, Burgess R, Philippot P (2013) Nitrogen isotopic composition and density of the Archean atmosphere. *Science*, **342**, 101-104.
- McLauchlan KK, Williams JJ, Craine JM, Jeffers ES (2013) Changes in global nitrogen cycling during the Holocene epoch. *Nature*, **495**, 352-355.
- Menzel P, Gaye B, Wiesner MG, Prasad S, Stebich M, Krishna Das B, Anoop A, Riedel N, Basavaiah N (2013) Influence of bottom water anoxia on nitrogen isotopic ratios and amino acid contributions of recent sediments from small eutrophic Lonar Lake, central India. *Limnology and Oceanography*, **58**, 1061-1074.
- Nisbet EG, Grassineau NV, Howe CJ, Abell PI, Regelous M, Nisbet RER (2007) The age of Rubisco: the evolution of oxygenic photosynthesis. *Geobiology*, **5**, 311-335.
- Nolla-Ardèvol V, Strous M, Sorokin DY, Merkel AY, Tegetmeyer HE (2012) Activity and diversity of haloalkaliphilic methanogens in Central Asian soda lakes. *Journal of Biotechnology*, **161**, 167-173.
- Oremland RS, Marsh L, Des Marais DJ (1982) Methanogenesis in Big Soda Lake, Nevada: an alkaline, moderately hypersaline desert lake. *Applied and environmental microbiology*, **43**, 462-468.
- Planavsky NJ, Asael D, Hofmann A, Reinhard CT, Lalonde SV, Knudsen A, Wang X, Ossa Ossa F, Pecoits E, Smith AJB, Beukes NJ, Bekker A, Johnson TM, Konhauser K, Lyons TW, Rouxel OJ (2014) Evidence for oxygenic photosynthesis half a billion years before the Great Oxidation Event. *Nature Geoscience*.
- Quan TM, Falkowski PG (2009) Redox control of N:P ratios in aquatic ecosystems. *Geobiology*, **7**, 124-139.
- Sigman DM, Karsh KL, Casciotti KL (2009) Ocean process tracers: nitrogen isotopes in the ocean. In: *Encyclopedia of ocean science*. Elsevier, Amsterdam.
- Smith RE, Perdrix JL, Parks TC (1982) Burial metamorphism in the Hamersley Basin, Western Australia. *Australian Journal of Petrology*, **23**, 75-102.
- Stein LY, Roy R, Dunfield PF (2012) Aerobic methanotrophy and nitrification: processes and connections. *eLS*, DOI: 10.1002/9780470015902.a9780470022213.
- Stüeken EE (2013) A test of the nitrogen-limitation hypothesis for retarded eukaryote radiation: nitrogen isotopes across a Mesoproterozoic basinal profile. *Geochimica et Cosmochimica Acta*, **120**, 121-139.
- Stüeken EE, Anderson RE, Bowman JS, Brazelton WJ, Colangelo-Lillis J, Goldman AD, Som SM, Baross JA (2013) Did life originate from a global chemical reactor? *Geobiology*, **11**, 101-126.
- Stüeken EE, Buick R, Guy BM (in prep.) Isotopic evidence for biological nitrogen fixation by Mo-nitrogenase at 3.2 Gyr.
- Stüeken EE, Catling DC, Buick R (2012) Contributions to late Archean sulphur cycling by life on land. *Nature Geoscience*, **5**, 722-725.
- Talbot MR, Johannessen T (1992) A high resolution palaeoclimatic record for the last 27,500 years in tropical west Africa from the carbon and nitrogen isotopic composition of lacustrine organic matter. *Earth and Planetary Science Letters*, **110**, 23-37.

- Taylor SR, McLennan SM (1995) The geochemical evolution of continental crust. *Reviews of Geophysics*, **33**, 241-265.
- Thomazo C, Ader M, Phillippot P (2011) Extreme ^{15}N -enrichment in 2.72-Gyr-old sediments: evidence for a turning point in the nitrogen cycle. *Geobiology*, **9**, 107-120.
- Yamaguchi KE (2002) Geochemistry of Archean-Paleoproterozoic black shales: the early evolution of the atmosphere, oceans, and biosphere. In: *Department of Geosciences*. Pennsylvania State University, pp. 485.
- Zavarzin GA (1993) Epicontinental soda lakes as probable relict biotopes of terrestrial biota formation. *Microbiology*, **62**, 473-479.

Appendix to Chapter 10

A10.1: Methods

For total nitrogen content and nitrogen isotopes in whole-rocks, samples were prepared by off-line combustion, and the resulting N₂ gas was introduced into the He stream of a continuous-flow isotope-ratio mass spectrometer (CF-IR-MS; Finnigan MAT253) with a newly-designed tube-cracker system. Kerogen isolates of a subset of samples, as well as total organic carbon (TOC) and carbon isotopes of decarbonated samples were determined by conventional on-line combustion with an elemental analyzer (Costech ECS 4010) coupled to the CF-IR-MS (e.g. Stüeken, 2013). Both systems included a ThermoFinnigan Conflo III. Isotopic data are reported in standard delta notation relative to atmospheric air for $\delta^{15}\text{N}$ and relative to VPDB for $\delta^{13}\text{C}$.

A10.1.1. Sample preparation

Sample preparation followed established protocols (Stüeken, 2013; Stüeken *et al.*, in prep.) and is summarized briefly. Weathering surfaces present on outcrop samples were sawed off, rocks were crushed into <0.5cm-sized chips, and then sonicated sequentially in hexane, methanol, and DI-H₂O (18M Ω MilliQ) to remove any modern organic contaminants. The rock chips were dried in a closed oven at 60°C, and then pulverized in an aluminum oxide ceramic puck mill. The mill was cleaned between samples by pulverizing pre-combusted (500°C overnight) silica sand and rinsing with hexane, methanol and DI-H₂O. Powders were stored in pre-combusted scintillation vials.

Samples with less than 0.1% TOC and significant carbonate contents were decarbonated with acid to concentrate the nitrogen content. We used ~15ml of 6N HCl per 1g sample, (ACS grade, EMD) for three days at 60°C, where the acid was refreshed after one day and stirred after two days. The acid was decanted after centrifugation and the samples were washed three times with DI-H₂O. This method was also used to determine the carbonate content of all samples by weighing the material before and after acid treatment.

Kerogen isolates were prepared with a protocol adapted from Robl & Davis (1993) as described by Stüeken *et al.* (in prep.). Approximately 5-6g of rock powder were weighed into a 250ml Teflon bottle, and carbonate was removed with 100ml of 6N HCl at 55°C in a shaking water bath overnight. The HCl was decanted after centrifugation, the sample washed once with 200ml DI-H₂O, and then silicates were removed with concentrated HF (ACS grade, EMD) in the heated shaking water bath overnight. Fluoride precipitates were re-dissolved with a mixture of H₃BO₃ (62.5g, ACS grade, Macron), HF (100ml), and DI-H₂O (100ml) overnight in the water bath at 55°C. The kerogen was washed three times with DI-H₂O, poured into a scintillation vial with ~10ml of water, placed into a freezer overnight, and then desiccated with a freeze-drier.

A10.1.2. Off-line combustion

A10.1.2.1. Materials

We used the Dumas combustion technique with a mixture of CuO and Cu in quartz tubes (e.g. Strauss *et al.*, 1992). CaO was added to trap H₂O and CO₂ (Kendall & Grim, 1990). The tubes were prepared with a metal vacuum line connected to a turbo pump (Figure A10.1).

- *Quartz tubes:* We used 30cm long tubes (O.D. = 9.5mm, I.D. = 7mm; Technical Quartz Products) compatible with 3/8" Ultra-Torr fittings (Swagelok) that connected the tubes to the metal vacuum line. The tubes were baked at 1100°C in a muffle oven overnight to anneal the sealed end and to remove contaminants.
- *Copper oxide wire for sample oxidation via O₂ release at high temperature:* CuO wire (Ø = 0.5mm, length ~2-5mm, PerkinElmer) was first sieved to >200µm to remove CuO dust, which can stick electrostatically to the walls of the quartz tube and make it more difficult to melt the quartz. The wires were then placed into a ceramic crucible and baked at 800°C in atmospheric air overnight to remove contaminants. On the following day, they were cooled to 600°C and kept at that temperature in the muffle oven for 2h to allow recombination of O₂ and Cu that may have formed from CuO at high temperature.
- *Calcium oxide granules for trapping H₂O and CO₂:* The CaO granules were prepared following a protocol adapted from Boyd *et al.* (1994). First, 10g of CaO powder (ACS grade, J.T.Baker) were mixed with 20ml DI-H₂O (18MΩ MilliQ) in a glass beaker and stirred thoroughly for ~15minutes with a glass rod until the mixture became noticeably viscous and the heat released by the dissolution reaction dropped. The beaker was then covered with Al foil and placed into an oven at 60°C for three days. The dry product was crushed with a spatula and sieved to ~0.5-2mm granules, which were transferred into a ceramic crucible and baked at 1100°C in the muffle oven overnight to remove H₂O, CO₂ and any organic contaminants. The granules were stored in a desiccator.
- *Copper wire for trapping excess of O₂ and conversion of trace NO_x to N₂:* We used untreated Cu wire recommended for CNS analyses with the EA (Ø = 0.5mm, length ~2-5mm, Costech),

but tried to minimize contamination introduced by this reagent through a pre-combustion step in sealed tubes (Section A10.1.2.2).

- *Silver capsules as sample holders*: Samples were introduced into the tubes in silver capsules (9x5mm, Costech), which have the additional advantage that the silver reacts with halogens and sulfur gases produced during the combustion (e.g. Therion *et al.*, 1986). The capsules were baked out at 800°C in atmospheric air in the muffle oven overnight for decontamination.

Bebout *et al.* (2007) avoided the use of CaO to reduce blank size and instead used cold-traps (discussed below) to remove H₂O and CO₂ liberated from their samples. Although we used a similar trap in our analytical setup (Section A10.1.3.1), we decided to use CaO, because our shales were significantly more carbon- and water-rich than the igneous rocks and mineral separates analyzed by Bebout *et al.* (2007). Excess amounts of H₂O and CO₂ not removed by CaO could potentially have clogged the cold trap and reduced the flow rate in the analytical setup (Section A10.1.3.1). CO₂ can also prevent NO_x conversion to N₂ in the combustion tube (Boyd *et al.*, 1994).

Ader *et al.* (2006) and Bebout *et al.* (2007) did not add Cu to their combustion tubes, because (a) it was found to contaminate the samples, and (b) sufficient amounts of Cu were contained in their (self-made) CuO or produced from it during the combustion process. However, we decided to use Cu, because our commercial CuO may have been too pure to achieve the same effect. Addition of Cu thus ensured that enough reductant was available for conversion of NO_x to N₂.

A10.1.2.2. Combustion procedure

We used 0.45-0.55g Cu wire, 0.15-0.17g CaO granules and 1.0-1.1g CuO wire, all prepared as described above. The amount of CuO, the most important reagent, was scaled up from 120mg used by Thomazo *et al.* (2011) for Tumbiana samples in proportion to larger sample quantities. The CuO was dark grey after the sample combustion in all cases, indicating that it never got completely spent and O₂ was supplied in excess.

- *Pre-combustion:* After adding the reagents to the tubes through a glass funnel, the tubes were evacuated with a Turbo pump overnight to a vacuum of <0.3μtorr. Throughout the evacuation, the lower part of the tubes containing the reagents was heated to 550°C with heat tape (maximum achievable temperature) and the upper part was flamed twice with a torch to just below the quartz melting point. On the following day, the tubes were sealed with the torch, and then placed into a muffle oven at 850°C overnight to pre-combust the reagents and remove contaminants. The tubes were then cooled over 1h to 600°C and kept at that temperature for 2h to allow recombination of Cu with O₂ released during the combustion. After cooling to room temperature, the tubes were opened by breaking off the top 2cm, sharp edges were smoothed by flaming for a few seconds, and the tubes were quickly reattached to the vacuum line. The reagents were again evacuated for one night at 550°C to remove H₂O and CO₂ trapped by the CaO.

- *Sample evacuation and combustion:* The next day, the vacuum pump was closed off and the tubes were filled to just below atmospheric pressure with a stream of He gas, which was passed through a cold-trap filled with molecular sieve (pore size 5Å) at liquid nitrogen temperature to remove trace N₂ and other volatiles. The tubes were then briefly detached from the vacuum line, 200-400mg of sample powder was added in silver capsules, and the tubes were re-attached

quickly. The addition of He to the tubes was meant to minimize air intake during sample addition, but we have so far not tested this effect quantitatively. Once re-attached, the tubes were evacuated to $\sim 1\mu\text{torr}$ overnight at 200°C . This temperature was lower than the temperature reached during metamorphism of these rocks (prehnite-pumpellyite facies, Smith *et al.*, 1982) and should therefore not have affected the nitrogen content. Glutamic acid standards were evacuated at 100°C to prevent melting. On the next day, the tubes were purged 30 times with clean He, *i.e.* they were filled to just below atmospheric pressure and immediately re-evacuated to remove traces of air from pore spaces. The tubes were tapped gently with a plastic rod at maximum and minimum pressure. Then evacuation was continued for two more nights (120°C for samples; room temperature for glutamic acid standards) to a final vacuum of $<0.3\mu\text{torr}$. After three days of evacuation, the tubes were sealed and combusted overnight at 850°C , followed by 2h at 600°C , and slow cooling ($\sim 4\text{h}$) to $<100^\circ\text{C}$. We chose a lower combustion temperature than the $950\text{--}1100^\circ\text{C}$ used by, for example, Busigny *et al.* (2005) or Bebout *et al.* (2007), but in agreement with previous methods (Strauss *et al.*, 1992), because otherwise the Ag capsules began to react with the quartz tubes during the combustion. Our relatively long combustion time likely compensated for the lower temperature (Bebout *et al.*, 2007). The 600°C combustion temperature was adopted from Thomazo *et al.* (2011).

A10.1.3. Isotopic analyses of pre-combusted N_2

A10.1.3.1. Analytical protocol

We built an analytical setup similar to that described by Bebout *et al.* (2007), *i.e.* a tube cracker attached to a continuous-flow isotope ratio mass spectrometer, but with several simplifications (Figure A10.2). The advantage of this setup is that it can be assembled from

available parts at relatively low cost, and it can easily be closed off to switch between the tube cracker and the conventional EA mode. In brief, the He stream, which usually flows through the EA, was diverted with a three-way valve through a metal line towards a tube cracker where it picked up N₂ gas from the sample, which was then carried to the mass spectrometer with additional purification and cryo-focusing during transport. Detailed steps were as follows:

1. *He purification:* Before entering the tube cracker, traces of N₂, CO₂, H₂O, Ar and other volatiles were removed from the He stream (flow rate ~35ml/min) with a cold trap (1/4" tubing) containing 5Å-molecular sieve cooled to liquid nitrogen temperature. This trap was kept frozen throughout the day. To minimize backflow of air when the tube cracker was opened, the cold trap was followed by an empty coil of 1/16" tubing (~1m long).
2. *Sample uptake in tube cracker:* The clean He then flowed through a section of corrugated 1/2" tubing which held the sample quartz tube. The tubing was flexible and could be bent manually to crack the quartz tube inside and release N₂ gas into the He stream. To ensure quantitative N₂ extraction, the quartz tube was scored and cracked twice, at ~2cm distance from each end. The tube cracker was connected to the He line with gas-tight metal washers on each end that were exchanged daily.
3. *H₂O and CO₂ removal:* Traces of H₂O and CO₂ contained in the quartz tube that had not been captured by the CaO were removed from the He stream with a second cold trap (1/8" tubing) at liquid nitrogen temperature but without molecular sieve. This trap was thawed after each sample.
4. *Optional venting:* The H₂O/CO₂ trap was followed by a three-way valve that could be turned towards the atmosphere for purging the tube cracker after exchanging tubes. When

the He stream was carrying N₂ gas from the sample, the valve was pointed towards the next cold trap.

5. *Cryo-focusing of N₂*: The N₂ gas was extracted from the He with a third cold-trap (1/8" tubing) containing 5Å-molecular sieve at liquid nitrogen temperature. This step focused the sample and led to a sharper peak in the mass spectrometer. The N₂ gas was collected for 30 minutes after cracking the tube to ensure complete extraction, but shorter durations may be possible. After 30min, the trap was thawed quickly with hot water, releasing the N₂ gas as a pulse back into the He stream. This cold trap also collected any traces of Ar and CO contained in the sample.
6. *Chromatographic purification*: N₂ was then separated chromatographically from Ar and CO with a gas chromatograph (GC) column (Restek) packed with 5Å-molecular sieve at room temperature. The GC was baked out with a heater at 300°C every 2-3 weeks.
7. *Mass spectrometry*: The He stream then entered the mass spectrometer through the Conflo. Ar arrived first, separated from N₂ by 4min, and was analyzed as m/z 40. We used the area of the Ar peak to monitor air contamination in the samples. Rock samples can contain significant amounts of radiogenic ⁴⁰Ar from ⁴⁰K decay, and hence this method can only be used quantitatively for synthetic or biological samples. However, it provides a means of qualitatively monitoring sample consistency. N₂ was analyzed as m/z 28 and 29, calibrated against a reference gas that was injected into the Conflo ~4min after the sample peak had passed. The N₂ peak area was used to measure total nitrogen in the sample. If CO has been present, then, according to the manufacturer's specifications for the GC column, it would have entered the mass spectrometer ~2min after N₂ and well

before the reference peak, without any risk of interference. However, no CO signal was visible in the m/z 28 trace in this position.

A10.1.3.2. Data correction

Samples and standards were corrected for blanks by mass balance, using blank signals and isotopic ratios measured from quartz tubes that were filled with the same amount of reagents and combusted and analyzed in the same way as sample tubes. Our average blank size was 10.27 ± 1.79 nmol with $\delta^{15}\text{N} = -5.18 \pm 1.61\text{‰}$ (1σ), which is comparable to that of Bebout *et al.* (2007) (3.8 ± 0.2 nmol N_2 , or 7.4 ± 0.4 nmol N; $\delta^{15}\text{N} = -7.3 \pm 0.4\text{‰}$). The contribution of atmospheric leaks in the He line, as determined by cryo-focusing the He stream for 30 min without cracking a tube, was 2.52 ± 1.16 nmol, $\delta^{15}\text{N} = -2.72 \pm 6.55\text{‰}$, and cracking an empty, combusted tube had no detectable impact. Most of the nitrogen contained in the blank was likely derived from residual contaminants in the reagents. As suggested by Bebout *et al.* (2007) and Ader *et al.* (2006), eliminating CaO and Cu would probably decrease the blank size significantly. Using CuO and CaO but no Cu, Ader *et al.* (2006) obtained blanks of 1-3 nmol for sealed-tube combustion, but they also evacuated their samples at higher temperature (450°C versus $100\text{--}200^\circ\text{C}$). Thomazo *et al.* (2011) obtained blanks of 2.4 ± 0.8 nmol with smaller quantities of all three reagents, but also with evacuation at 450°C . Hence it is likely that our method would be suitable for samples such as organic-lean igneous rocks or mineral separates, for which CaO and/or Cu can be reduced or eliminated and which can safely be evacuated at 450°C .

Following the blank correction, we corrected our data for mass bias by calibration against in-house standard GA2 (glutamic acid, $\delta^{15}\text{N} = -5.7\text{‰}$) and the international reference standard

USGS41 (glutamic acid, $\delta^{15}\text{N} = +47.57\text{‰}$), which cover the isotopic range encountered in our samples.

A10.1.3.3. Method validation

Accuracy was monitored with rock standard SGR-1 over a range of sample sizes. Above ~50nmol N (Figure A10.3), equivalent to 0.12mg decarbonated rock powder, we obtained a consistent value of $+17.83 \pm 0.42\text{‰}$ (1σ , $n=10$). This is slightly lighter than our average result obtained with the conventional method ($+18.24 \pm 0.53\text{‰}$, $n=27$, see below), but they agree within error. Both values are close to the nominal value of $+17.4\text{‰}$ (Dennen *et al.*, 2006). Dennen *et al.* (2006) chose an uncertainty of 0.2‰ , but the true measured uncertainty was 0.9‰ if all data in their study are included. It is possible that this rock standard is slightly heterogeneous. Below 50nmol, precision decreased for SGR-1 (Figure A10.3). We were able to avoid this range, except for two samples (130707-5 with ~33nmol and 130707-9 with ~38nmol). The precision (1σ) of blank-corrected values for GA2 and USGS41 was 0.50‰ and 0.31‰ , respectively. For Tumbiana samples we measured an average standard deviation of 0.71‰ , which compares well with the average standard deviation of 2‰ obtained by Thomazo *et al.* (2011). Total nitrogen quantity in all reference standards showed good linearity with N_2 peak area ($R^2 = 0.93$). The average relative standard deviation for samples was 5.5% .

A10.1.4. Conventional method for TOC and kerogen

For conventional EA-IR-MS measurements of kerogen isolates (N_{ker} , $\delta^{15}\text{N}_{\text{ker}}$) and organic carbon in decarbonated powders (TOC, $\delta^{13}\text{C}_{\text{org}}$), samples were weighed into untreated 9.x5mm untreated tin capsules (Costech) and analyzed by flash combustion with 10ml O_2 gas at 1000°C

(e.g. Stüeken, 2013; Stüeken *et al.*, in prep.). Kerogen isolates were mixed with V₂O₅ (Acros Organics) in a 1:1 ratio to avoid isobaric interferences between N₂ and CO (Beaumont *et al.*, 1994; Papineau *et al.*, 2009). Results were corrected for instrumental mass bias with two glutamic acid standards (USGS41 (Qi *et al.*, 2003) and an in-house standard, GA1). Long-term accuracy (-0.28‰ for δ¹⁵N and 0.08‰ for δ¹³C) and precision (0.40‰ for δ¹⁵N and 0.12‰ for δ¹³C) were monitored with an in-house standard of dried salmon (SA). Relative precision for N and C concentrations were 1.6% and 1.5%, respectively. For the USGS rock standard SGR-1 we obtained a value of +18.24 ± 0.53‰ (n=27). As discussed above, this is within error of the measured value reported by Dennen *et al.* (2006).

A10.1.5: Rare earth element and aluminum concentrations

We submitted the drill core samples from the Tumbiana Formation to ALS Global for analyses of trace and major elements (method MEMS-61). In brief, samples were powdered, dissolved in HNO₃, HF, and HClO₄, then evaporated to dryness, and analyzed in HCl by ICP-MS and ICP-AES.

A10.2: Sample description

Photomicrographs of each Tumbiana and Kylene sample analyzed in this study are shown in Figures A10.4-7. Significant features are briefly described here, in order from low to high δ¹⁵N_{bulk}. Samples categorized as relatively featureless mudrocks in the main text are 130707-2b, 99043, 99042, 99040, 99038, 99037 and 130707-8.

A10.2.1. Tumbiana samples:

- 130707-2b: This sample is predominantly composed of clay and silt-sized basaltic ash particles as shown in the upper part of Figure A10.4a. Rare angular quartz grains (~2%) with varying sizes up to very fine sand, as well as silt-sized euhedral pyrite grains (<0.1%) are randomly dispersed in the tuff matrix. The cement is composed of carbonate (high birefringence) and probably chlorite. Fragments of wrinkled black laminae (up to 0.1mm amplitude), a few mm in length and less than 0.05mm thick, are present in some parts of the sample (5%), as shown in the lower part of Figure A10.4a. The fragments are parallel to bedding. In some, but not all cases, these are associated with accumulations of several quartz grains. In outcrop, these rocks appear massive with few internal features, but display wave ripples at cm-scale on some bedding surfaces. Interpretation: This sediment probably represents an airfall tuff into a stagnant water body with minor aqueous reworking by wind-waves. The wrinkled laminae are likely microbial mats that developed between ash fall events. The fact that they are bedding-parallel suggests that they grew in-situ and are not reworked fragments.

- 130707-9: This sample displays cross-bedding in hand specimens and is very heterogeneous in grain size. Around 30% of the rock is made up of laminated silt-sized well-rounded particles of chloritized tuff, suspended in a tuff matrix of clay-sized particles with carbonate cement (lower part in Figure A10.4d). In some cases the rounded grains reach the size of fine sand size. A few grains have a chlorite crystal in their core but whose margin is replaced by sparry carbonate (Figure A10.4c). The other 70% are made up of fine tuff and micritic carbonate, alternating and interfingering at sub-mm scale. Both components contain ~10% angular tuff particles. Black wrinkled laminae are present between some laminae (Figure A10.4d), but unlike in sample 130707-2b, they are frequently wrapped around silt particles. Interpretation: The cross-

bedding, the high degree of rounding and moderate sorting indicate current reworking. The micritic carbonate may also have precipitated directly from the water column. Most of the kerogen extracted from this sample is probably derived from the crinkled laminae; however, the inclusion of silt particles within many of these laminae suggest that they may be stylolitic concentrations of kerogen rather than primary microbial mats. The biomass may thus originally have been detrital or planktonic.

- 130707-4: The source rock of this sample was fairly massive in outcrop and it contains laminae of clayey tuff similar to sample 130707-2b, but it differs from that sample because it contains abundant (~20%) mm-sized fenestrae filled with sparry carbonate (Figure A10.4b) and up to 5% angular silt-sized glass shards, now chloritized. Furthermore, it is over- and underlain within 1-2 meters by abundant stromatolites. Wrinkled laminae of possibly microbial mats are also present, at a similar scale as in sample 130707-2b but in a slightly larger proportion of the rock (15% vs 5%). Interpretation: Like sample 130707-2b, this probably represents an airfall tuff with little reworking, but the high frequency of gas holes (*i.e.* fenestrae) may indicate a relatively lower sedimentation rate. The gas holes could have been created by biogenic gases such as CO₂ or CH₄.

- 130707-5: This sample is a heterogeneous composite of beds with poorly-sorted angular and rounded silt-sized particles of quartz and tuff with either a fine tuff or sparry carbonate matrix (60%; upper part in Figure A10.4e) and beds in which the fine tuff is dominating and silt grains are rare (40%; lower part in Figure A10.4e). The fine tuff beds frequently contain fragmented and continuous black wrinkled laminae (~50%). Carbonate is present as a cement throughout the

sample. The hand specimen further shows that the fine tuff layers are frequently underlain by carbonate fenestrae of up to 2cm in diameter. Interpretation: The layers of rounded silt grains were probably deposited by infrequent water currents that perhaps transported these grains away from better-sorted deposits, such as sample 130707-9, to this locality and entrained angular grains, coherent mud flakes and ash particles in the process. The continuous finer layers that lack silt grains may represent episodes where airfall sedimentation into a stagnant water column was dominating. These layers were probably colonized rapidly by microbial mats, which would explain the black wrinkled laminae and the associated fenestrae after possibly biogenic gases.

- 99024: This sample is an outlier in the set, because it contains ~50% micro-crystalline chert (Figure A10.4f). Chert occurs frequently as a secondary replacement in outcrops, but this is the only drill core sample (from 1297.4m depth in core WRL-1) in which chert is a dominant component. The chert is homogeneously mixed with very fine crystals of carbonate, recognizable by their high birefringence. Carbonate-rich tuff laminae and lenses are interbedded at sub-mm scale. Interpretation: In the absence of an outcrop perspective or additional samples from the same drill core, the depositional setting of this sample is difficult to assess. The absence of silt or sand grains indicates a low-energy environment, but the wavy appearance of tuffaceous laminae may reflect very mild wave activity. The chert may be a primary precipitate, an early replacement of sodium silicate (*i.e.* Magadi-type chert) or a late replacement of carbonate. As reviewed by Kerrich *et al.*(2002), textural distinction can be ambiguous. If it is a Magadi-type chert, then it may preserve evidence thereof in its trace element composition (Section A10.3).

- 99044: This sample is composed of alternating mm to cm-thick laminae of clay- and silt-sized tuff particles. Figure A10.5a shows a silt-dominated portion. The cement is carbonate-rich. Wrinkled black laminae are common at sub-mm intervals and show doming with wavelength of up to 1mm and ~0.2mm amplitude. The hand specimen further shows doming of laminae at cm-scale, as well as cm-sized carbonate fenestrae and carbonate-filled fluid or gas escape structures (together ~10%). Parts of the clay-rich portion contain isolated grains of subhedral to euhedral pyrite (<0.5%). Interpretation: The crinkled laminae are most likely remnants of microbial mats; the domical morphology further suggests that they may have been part of a stromatolite, but without an outcrop view this is difficult to verify. If so, then the silt-sized grains may have been trapped by adhesion. The pyrite probably formed from sulfate reduction during diagenesis, as suggested by its morphology. This may indicate a redox gradient from anoxic conditions in the sediments to suboxic or oxic conditions at the sediment-water interface. Parts of the sample appear to have been reworked, possibly during a storm event, because in some cases internally intact cm-sized blocks are clearly dislocated.

- 99046: This sample is dominated by sub-mm thin black wrinkled laminae, separated by clay- (50%) or silt-sized tuff (50%) with carbonate cement. Particles of angular quartz or tuff of coarse silt size are rare (<2%) (Figure A10.5b). Some laminae display doming and strong cohesion across micro-faults, but are mostly plane-parallel. In a ~2cm-thick bed in the hand specimen, black clay fragments of a few mm in length are chaotically interspersed with coarser tuff particles. Carbonate-filled fenestrae make up ~5% of the rock. Interpretation: The wrinkled laminae are likely microbial mat remnants, partly stromatolitic, that may have trapped coarser siliciclastic particles by adhesion. The fine tuff probably settled from the water column under

low-energy conditions. The chaotic bed likely represents a short storm interval of sediment reworking.

- 130707-7: This sample is mostly composed of micritic carbonate (Figure A10.5c) interspersed with very thin (<0.05mm) laminae of tuff. The hand specimen shows that the micrite is wavy laminated by wave ripples of ~5mm amplitude and ~1cm wavelength. In some cases, domical stromatolites developed on the crests of the wave ripples. Thin black laminae are also present (~2%) (Figure A10.5c), but as evident from the hand specimen, they are often perfectly parallel and thus likely stylolitic concentrations of kerogen and/or silicate minerals rather than microbial mats. Interpretation: The micron-sized carbonate crystals may have precipitated in the water column and subsequently settled, together with fine suspended ash particles. The overall very small grain size throughout this sample indicates a very low-energy environment

- 99045: This sample is dominated by clay-sized, moderately dense, kerogenous tuff (Figure A10.5d). The hand specimen shows that the tuff is mostly plane-laminated, but frequently (~10%) interrupted by large carbonate fenestrae of several cm in length. Sub-mm fenestral carbonate is also visible throughout the sample (Figure A10.5d). Silt-sized sub-angular quartz grains (~2%) and flakes of chlorite (~3%) are randomly interspersed in the tuff matrix. Chlorite flakes are oriented parallel to bedding. Interpretation: The dark laminae are probably kerogen-rich remnants of microbial mats. This interpretation is supported by the carbonate fenestrae that may have formed from voids produced by biogenic gases. The infrequent silt-sized particles were likely trapped by adhesion and may originally have blown into the basin by wind.

- 99039: The hand specimen shows that this sample is entirely composed of stacked domical and turbinated stromatolites. At microscopic scale (Figure A10.5e), these are composed of laminae with clay- and rare silt-sized particles of tuff (~60%), micritic carbonate (~40%) and occasional (<1%) quartz. The cement is carbonate-rich. Carbonate is also present in large cm-sized fenestrae (10%) in the hand sample. Subhedral-to-euhedral pyrite grains (<0.1mm, <0.1%) occur in both coarser and finer layers. Interpretation: These stromatolites probably formed in a low-energy environment and grew by trapping of ash particles and precipitation of carbonate. Some carbonate may also have rained down from the water column. The angular pyrite grains are likely diagenetic, and the carbonate fenestrae may have formed after biogenic gas holes, as indicated by the association with microbial mats, here and in other samples.

- 99043: This sample is a plane-laminated relatively dense mudrock. In many cases, the laminae are fining upwards from fine silt to clay. Most of the particles are probably tuff, given their nearly opaque appearance in thin section (Figure A10.5f). At mm to sub-mm scale, the mud laminae are separated by thin layers or lenses of silt-sized sub-angular quartz grains in a matrix of clay and carbonate. Interpretation: This sediment was probably deposited in stagnant water under low-energy conditions, perhaps from air-fall ash deposition. If so, then the fining-upward cycles may represent individual volcanic eruptions. Silt particles could have been blown in by wind. The dark mud layers may be kerogenous after microbial mats, but crinkled lamination is not as evident as in other samples.

- 99042: This is a nearly featureless dense mudrock (Figure A10.6a). The hand specimen shows plane lamination in some sections, where laminae are defined by rare, cm-long, sub-mm thin

lenses of pyrite (1%) or micritic carbonate (3%). Very fine silt particles of quartz (<0.5%) are interspersed within the mud matrix. Interpretation: Unlike sample 99043, this sample does not show any cyclicity and may instead represent a more distal environment that was only accumulated the finest ash particles. It has a strong resemblance to sample 130707-2b, which showed wave lamination at outcrop scale. In the absence of outcrop evidence, the depositional environment of this sample is more difficult to determine, but if wave lamination is indeed absent, then unlike sample 130707-2b, it perhaps represents relatively deeper water conditions.

- 99040: This sample (Figure A10.6b) is very similar in appearance to sample 99042, except that in the hand specimen, some laminae are clearly wrinkled. It also contains occasional (<0.5%) mm-sized pyrite nodules as well as finely dispersed sub-mm pyrite grains (1%). Interpretation: The depositional environment is likely the same as of 99042. The crinkled laminae are likely microbial mats and the reason for their more frequent occurrence in this sample compared to 99042 may be a relatively slower sedimentation rate.

- 99038: Like the previous two samples, this is a dense mudrock with few internal features (Figure A10.6c). Plane lamination and lenses of carbonate (5%) and rare subhedral pyrite (<0.5%) are visible in the hand specimen. Interpretation: The depositional setting was probably the same as that of sample 99040 and 99042, *i.e.* under stagnant water and low-energy conditions with a constant rain out of volcanic ash, either from the air or from aqueous suspension.

- 99037: This is also a dark, plane-laminated mudrock lacking internal features (Figure A10.6d) besides occasional carbonate (5%, 1-5mm thickness) and thin pyrite (0.5%, 0.1-1mm thickness) lenses visible in the hand specimen. Interpretation: see 99038.

- 130707-3: This sample is similar to sample 130707-5. It is a composite of dense laminae of clay-sized tuff (30%, 0.1-10mm thick) and coarser laminae (70%, 1-10mm thick) of micritic carbonate (50%) and fine-silt-sized tuff (50%). (Figure A10.6e). Unlike 130707-5, silt-sized quartz particles are rarer (5%). Silty tuff grains are sub-rounded. The dense clayey tuff laminae are often wrinkled a sub-mm scale and frequently domed (5mm amplitude, 5-20mm wavelength). The hand-specimen further shows large cm-sized carbonate fenestrae (10%), present in both the coarser micritic part of the sample and the dense wrinkled laminae.

Interpretation: The wrinkled laminae are likely microbial mats that developed in a low-energy environment, probably on airfall tuff deposits. The micritic carbonate may have precipitated from the water column. The relative abundance of sub-rounded silt grains within much of the micrite suggests input of reworked material by current activity. Fluctuations between the two regimes may be the result of changing water level in the lake or varying ash rainout.

- 130707-8: This is another massive dark mudrock (Figure A10.6f), plane-laminated in hand specimen, with occasional sub-mm pyrite crystals (<0.5%). Interpretation: see 99038.

A10.2.2: Kylena samples

- 130708-5: This sample is composed of alternating laminae of dense clay-sized tuff particles (0.1-3mm thickness) and fine silt-sized tuff and micrite particles (0.5-2mm thickness) (Figure

A10.7a). The laminae are nearly perfectly parallel, but slightly wavy at 5-10mm wavelengths. Wave ripples can also be seen in hand specimens. Carbonate cement is present throughout the sample. At outcrop scale, the rocks exhibit a weak slaty cleavage. Interpretation: This was probably a wave-dominated environment of low-to-moderate energy that was frequently inundated with fine airfall tuff. The micritic carbonate crystals may be water column precipitates or reworked carbonate grains.

- 130708-7: The hand specimen of this sample shows that it is composed of stacked domical and conical stromatolites of up to 2cm in height. The stromatolites are composed of micritic carbonate and fine silt-sized particles of tuff, surrounded by carbonate cement (Figure A10.7b). They are draped by irregular layers of fine tuff (<0.5cm) with interspersed silt-sized particles of quartz, tuff and carbonate. The fine tuff also fills spaces in between individual stromatolites. Anhydral pyrite (0.5%) is present in some stromatolitic and tuffaceous laminae. Interpretation: The stromatolites probably grew predominantly by carbonate precipitation and occasional trapping of particles. Growth appears to have been interrupted at fairly regular intervals (~every 2-3cm in hand specimens) by airfall tuff, probably deposited concurrently with volcanic eruptions.

- 130708-6: This sample (Figure A10.7c) is very similar to 130708-7, except that the stromatolites are larger but much less well defined. Also the fine tuff coatings are significantly thicker, up to ~2cm. Interpretation: Like 130708-7, this probably represents frequently recurring events of stromatolite burial by volcanic ash. The irregularity compared to 130708-7 may be a result of soft-sediment deformation in response to a thicker, heavier ash load.

- 130708-8: This sample is almost entirely composed of sparry carbonate grains (Figure A10.7d) that have inclusions of nearly opaque particles, which may be ash and possibly kerogen. Black particles also become concentrated in stylolites. Interpretation: The sparry carbonate is probably a secondary feature, possibly a recrystallization of micrite, as indicated by the tuff inclusions. If this sample started out as a micrite, then it may have formed from water-column precipitates of carbonate. The hand specimen shows faint domical lamination in parts of the sample, which may be remnant features of a stromatolite. If so, then carbonate could originally also have been precipitated in response to microbial activity.

A10.3: Rare-earth elements

The lanthanides (Ln), or rare-earth elements (REE), have the potential to provide independent evidence for alkaline conditions in ancient water bodies. REE are trace elements in aqueous environments, with concentrations of less than 0.1nM in seawater (Elderfield *et al.*, 1988). The major sink from the ocean is adsorption of free Ln^{3+} ions onto clay minerals and oxides (Elderfield *et al.*, 1988). At high alkalinity, more than 99% of dissolved lanthanides are stabilized in solution as $[\text{Ln}(\text{CO}_3^{2-})_2]^-$ complexes (Johannesson & Lyons, 1994), with a strong preference for heavy over light REE (Moeller & Bau, 1993; Johannesson & Lyons, 1994). Light REE thus have a relatively shorter residence time in alkaline waters and are lost more rapidly by adsorption of Ln^{3+} to particles than heavy REE. Residual dissolved REE in alkaline lakes therefore show strongly increasing concentrations with increasing atomic number (Figure A10.8a).

REE patterns in chemical sediments, including cherts and carbonates, are commonly used as recorders of REE patterns in the overlying water column. In a study of cherts from alkaline Lake Magadi in Kenya, Kerrich *et al.* (2002) reported light-REE depletions (Figure A10.8b), which are much less extreme than those observed in alkaline waters (Figure A10.8a), but attributed to the same carbonate-complexation process. Kerrich *et al.* (2002) therefore concluded that such patterns could be used as an indicator of alkaline conditions in the past. Cherts in Lake Magadi formed as a replacement of magadiite ($\text{NaSi}_7\text{O}_{13}(\text{OH})_3 \cdot 3\text{H}_2\text{O}$) or kenyaite ($\text{NaSi}_{11}\text{O}_{20.5}(\text{OH})_4 \cdot 3\text{H}_2\text{O}$), minerals characteristic of alkaline conditions (Eugster, 1967). The light-REE depletion was only observed in cherts where the replacement was nearly complete, with less than 10% magadiite remaining (Kerrich *et al.*, 2002).

Bolhar & van Kranendonk (2007) analyzed REE in stromatolitic carbonates from the Tumbiana Formation and did not find any significant depletions in light REE. However, they also analyzed a sample from the Green River Formation, which was an alkaline lake in the Eocene, and found lower REE concentrations but a nearly flat pattern, essentially indistinguishable from the Tumbiana data. Hence it is conceivable that carbonate minerals from alkaline lakes do not preserve the steep REE gradient observed in alkaline waters, perhaps because they are the major REE sink. For example, in carbon isotopes, the larger sink (carbonate, 80%, $\delta^{13}\text{C} \approx 0\text{‰}$) is much less fractionated relative to the source ($\delta^{13}\text{C} \approx -5\text{‰}$) than the smaller sink (organic carbon, 20%, $\delta^{13}\text{C} \approx -25\text{‰}$). If the bulk of dissolved REE eventually end up in carbonate minerals, regardless of the strength of the $\text{Ln}(\text{CO}_3)_2^-$ complex, then chemical sediments other than carbonates, *i.e.* the smaller sinks such as chert, may be more sensitive to aqueous fractionation processes. We stress that this remains speculative in the absence of more data, but we will use it as an assumption in the following discussion.

Cherts are extremely rare in the Tumbiana Formation. In outcrop, they are mostly present as late secondary replacements of carbonate. However, one of our drill-core samples (99024) is largely composed of chert with minor carbonate and fine tuff (Figure A10.4f). Its REE pattern is distinct, with a marked depletion in light REE increasing in magnitude towards lighter elements (Figure A10.9a). Some other samples, in particular 99045 and 99046, also exhibit light REE depletions, but in a much more step-wise fashion. The REE pattern of 99024 thus has a close resemblance to that of alkaline waters (Figure A10.8a). As discussed in Section A10.2, we are not absolutely certain that this chert is primary. Furthermore, it is the only sample from this drill core (WRL-1) and from this particular sub-basin of the Tumbiana Formation, making any comparisons to other samples speculative. However, it is at least possible that sample 99024 represents a mixture of two end-members, a siliciclastic end-member with a flat REE pattern, and a chert end-member with a Magadi-type fractionation.

To assess if this is possible, we constructed a simple mixing model. We used sample 99037 as a proxy for the siliciclastic end-member, because it has the highest Al content (8.57%, Table A10.1), within the range of average Archean clastic sediments ($7.88 \pm 0.69\%$, McLennan, 1982). Assuming that Al is proportional to the abundance of siliciclastic minerals, the siliciclastic REE end-member of sample 99024 (2.18% Al) should make up ~25%. The residual 75% should be carbonate or chert. We measured a carbonate content of 26% (Table 10.1) by treatment with HCl, leaving 49% chert. Assuming that, as discussed above, the carbonate fraction has the same REE pattern as the siliciclastic fraction, we calculated a theoretical mixture between average Magadi chert and the siliciclastic end-member represented by sample 99037, shown in Figure A10.9b (“mixture 51/49”). In this calculation, Ce and Eu anomalies present in the Magadi chert (Kerrick *et al.*, 2002) were removed and scaled to values found in 99037, because

they are likely caused by unique redox processes or source rock compositions that would not have been relevant to the late Archean Tumbiana Formation. Furthermore, two of the eight Magadi chert samples presented by Kerrich *et al.* (2002) had four times higher La enrichments than the other six samples and were therefore removed from the average. The result of this 51/49 mixture is not a good match with the actually observed REE pattern in 99024. Slightly better agreement is achieved if we assume that the carbonate fraction has a similar REE pattern as the chert, *i.e.* if the proportions of the two end-members are shifted to 25% and 75%, respectively (Figure A10.9b, “mixture 27/75”). Perhaps the carbonate of this sample differs from the stromatolitic carbonate analyzed by Bolhar & van Kranendonk (2007), because it precipitated during a stage of extreme evaporation and concentration of REE in solution, *i.e.* during rare conditions that also led to the precipitation of Magadi-chert precursors. The calculated mixture would match sample 99024 more closely if the Magadi chert were more depleted in light REE, *i.e.* if it had stronger resemblance with alkaline waters. It is conceivable that the actual chert component of 99024 does show that degree of depletion.

Overall, this exercise does not prove that the unique REE pattern of sample 99024 is the result of alkaline water chemistry. First, the origin of the chert is uncertain; second, the fact that this sample comes from a different sub-basin could imply that the source composition of REE was different and hence 99037 cannot be used as a representative of the siliciclastic end-member; third, the composition of the carbonate fraction is unknown. However, our results at least suggest that this approach may be worth pursuing if new, chert-rich Tumbiana samples become available.

Table A10.1. Rare earth element and Al data of some Tumbiana samples. REE concentrations are in ppm, Al is in %.

	La	Ce	Pr	Nd	Sm	Eu	Gd	Tb	Dy	Ho	Er	Tm	Yb	Lu	Al
99024	5.5	13.85	1.69	7.1	1.48	0.62	2.03	0.32	1.85	0.41	1.27	0.18	1.21	0.18	2.18
99037	33.3	67.5	7.06	27.4	5.15	1.48	5.58	0.9	5.01	1.06	3.26	0.48	3.25	0.49	8.57
99038	31.6	63.8	6.77	26.4	5.04	1.4	5.7	0.89	4.8	1.01	3.05	0.45	3.1	0.46	8.12
99039	14.7	29.5	3.19	12.6	2.45	0.81	3.06	0.47	2.54	0.55	1.67	0.24	1.64	0.25	4.76
99040	25.3	54.2	6	24.1	4.72	1.16	5.25	0.78	4.18	0.91	2.84	0.44	3.06	0.46	6.82
99042	21.4	45	4.91	19.3	3.69	0.95	4.16	0.61	3.24	0.67	2.06	0.3	2.08	0.31	5.69
99043	24.7	47	5.13	19.8	4.05	0.75	3.1	0.48	2.69	0.55	1.75	0.26	1.8	0.27	5.59
99044	16	32.8	3.58	14.3	2.83	0.65	3.13	0.44	2.29	0.48	1.45	0.21	1.4	0.21	3.27
99045	16.8	34.5	3.77	14.8	3.02	0.98	4.39	0.72	3.94	0.84	2.55	0.38	2.51	0.37	6.64
99046	22.8	46.3	4.95	18.7	3.47	1.07	4.25	0.67	4.02	0.94	3.05	0.47	3.17	0.49	5.03

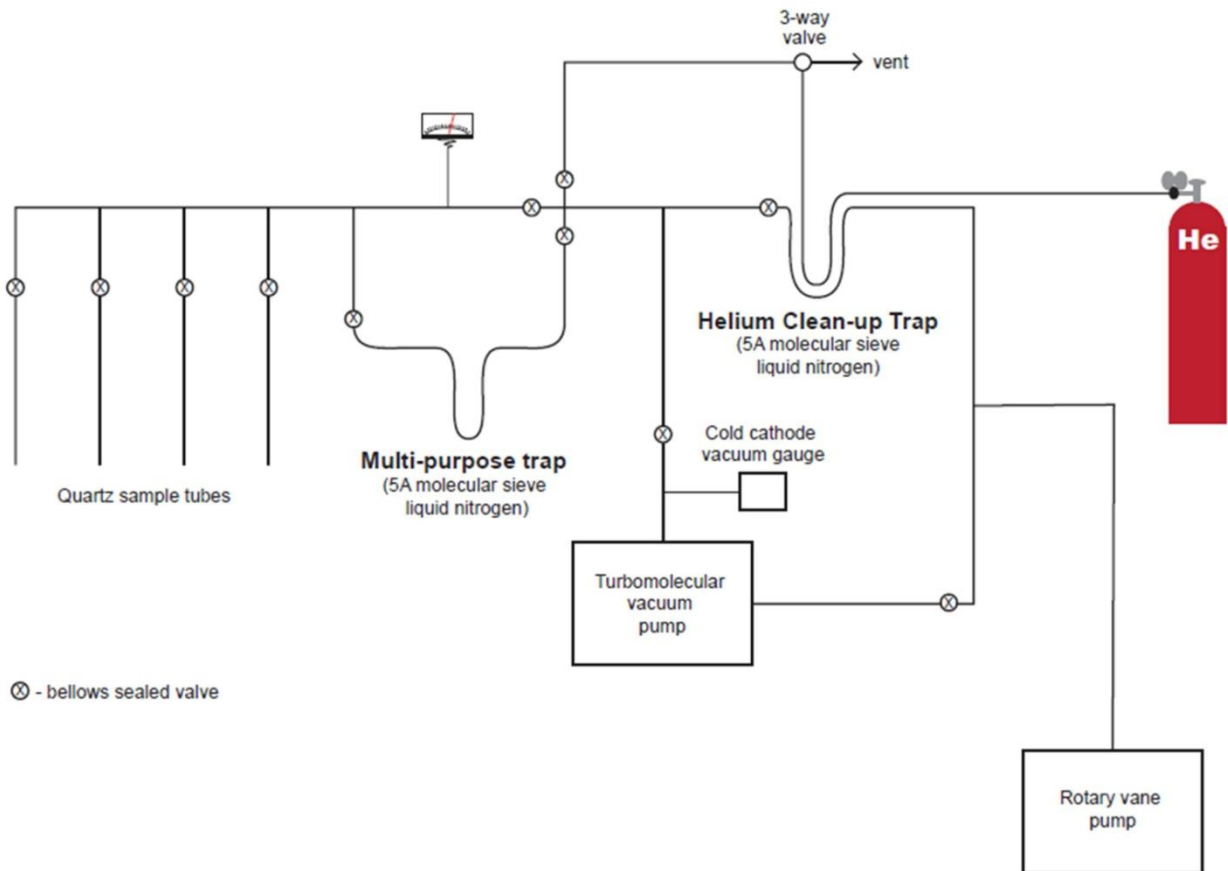


Figure A10.1: Vacuum preparation line. Rotary vane pump serves for initial evacuation and subsequently to back up the Turbomolecular pump. The multi-purpose trap removes traces of N₂ contained in the He stream used for purging the sample tubes.

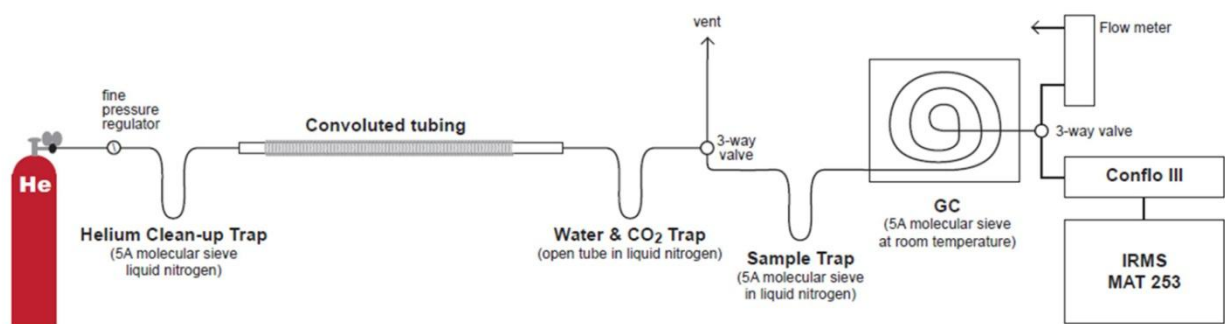


Figure A10.2: Tube-cracker line for sample analysis. The first three-way valve is used for purging air out of the tube cracker (convoluted tubing) after exchanging sample tubes. The second three-way valve is used to measure the flow rate of the He stream.

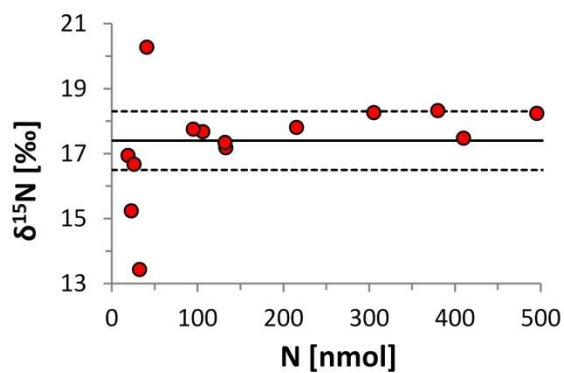


Figure A10.3: Reproducibility of SGR-1. Horizontal lines = average (solid) \pm 1 measured standard deviation (dashed) of SGR-1 data reported by Dennen *et al.* (2006).

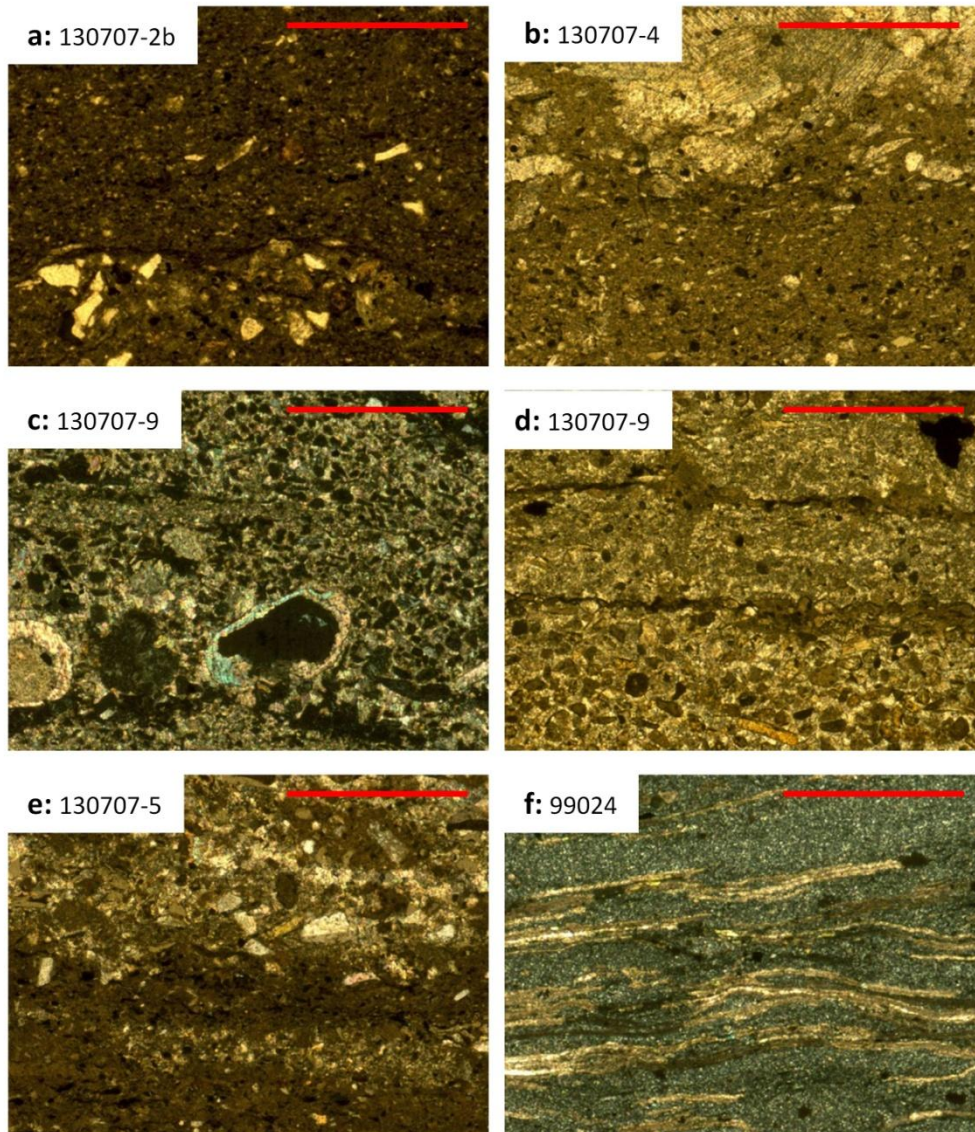


Figure A10.4: Photomicrographs, Tumbiana. Scale bar is 0.5mm in all panels. Photo in panel c was taken under crossed polarizers, all others were uncrossed.

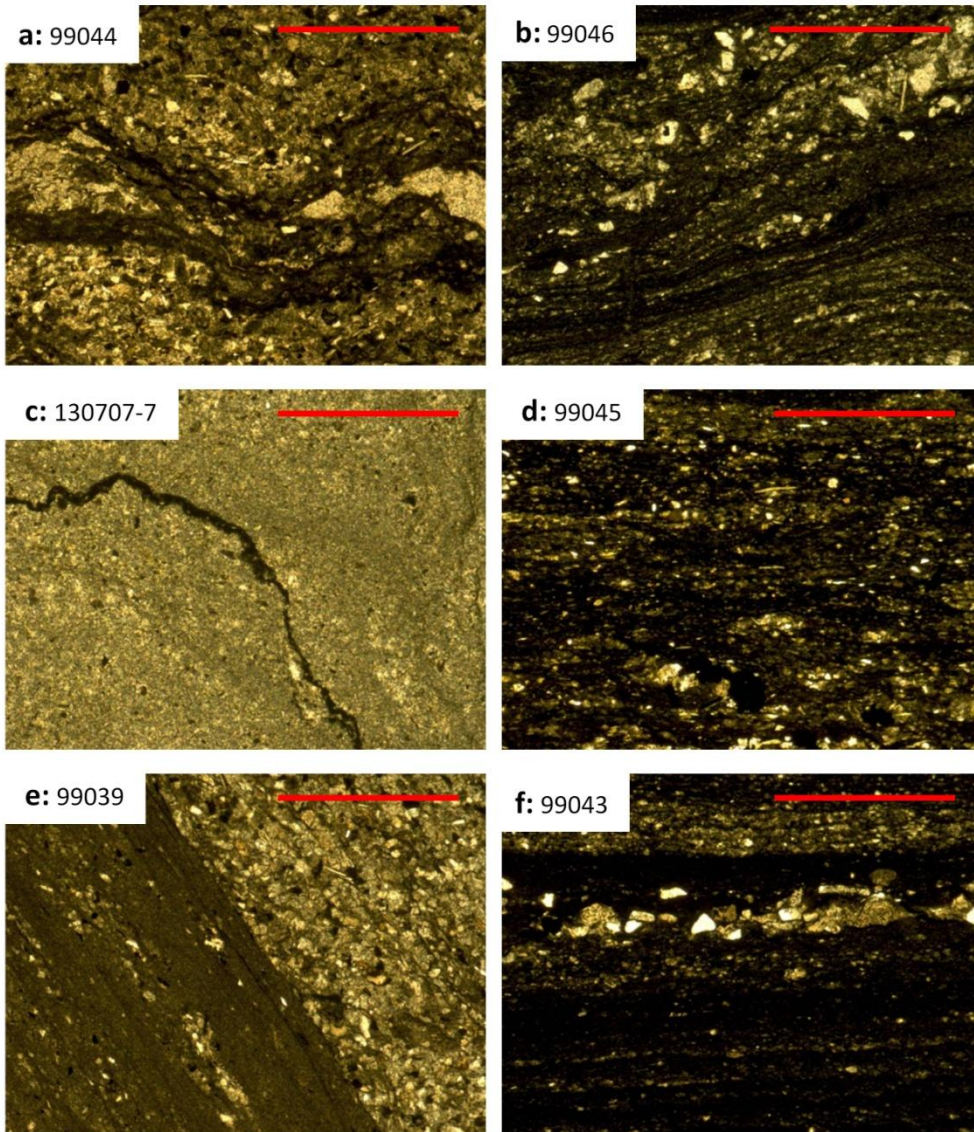


Figure A10.5: Photomicrographs, Tumbiana. Scale bar is 0.5mm in all panels. All photos were taken under uncrossed polarizers.

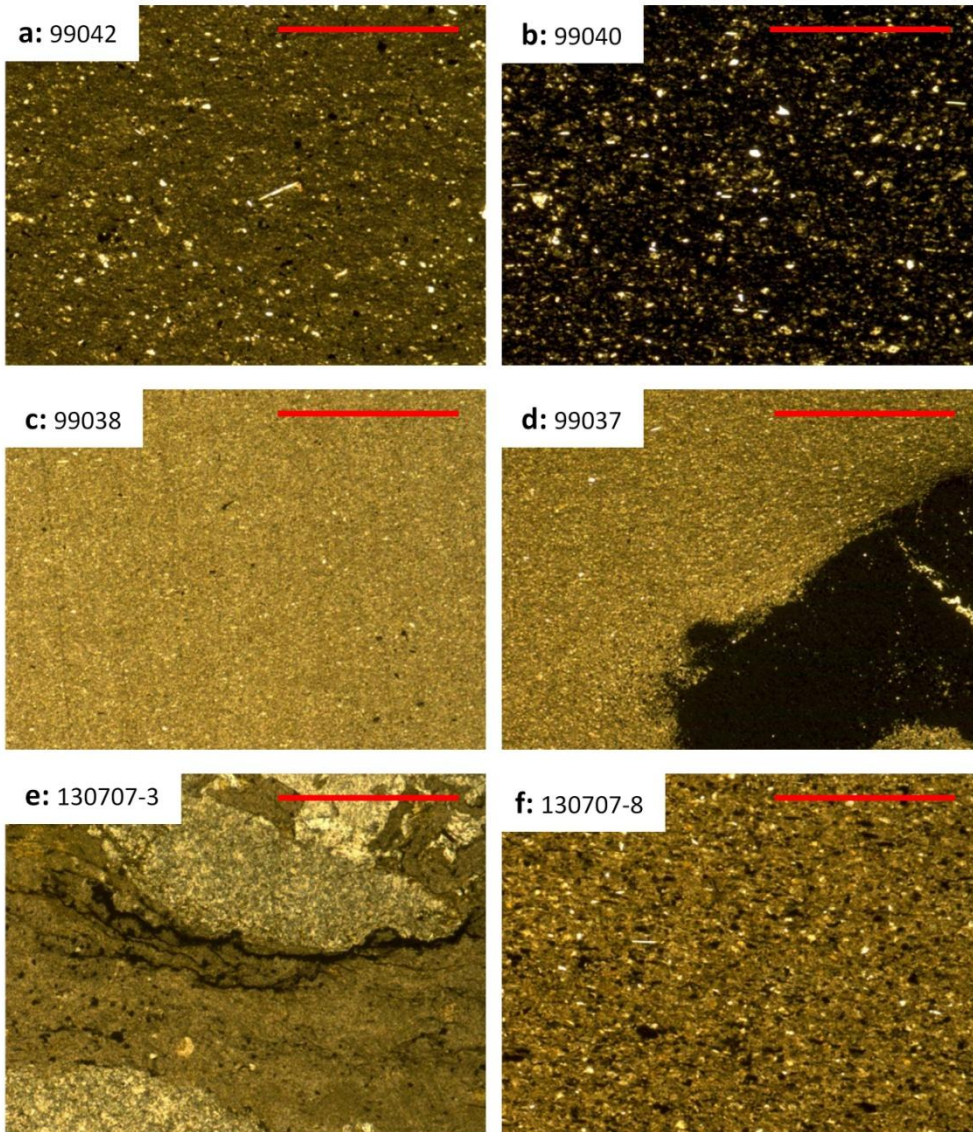


Figure A10.6: Photomicrographs, Tumbiana. Scale bar is 0.5mm in all panels. All photos were taken under uncrossed polarizers.

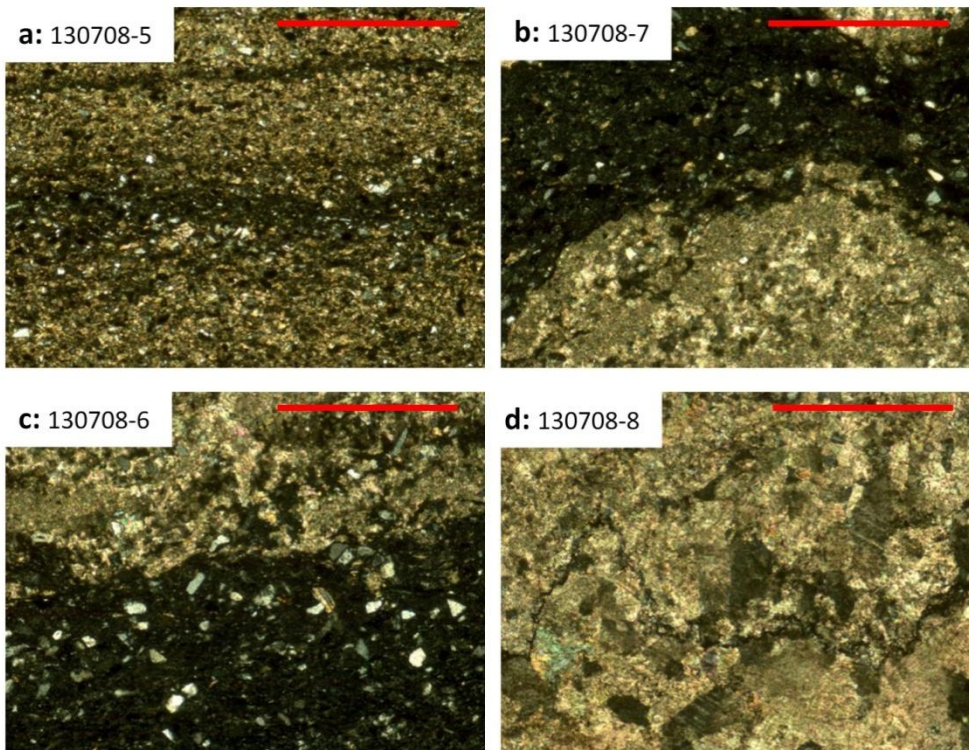


Figure A10.7: Photomicrographs, Kylene. Scale bar is 0.5mm in all panels. All photos were taken under crossed polarizers.

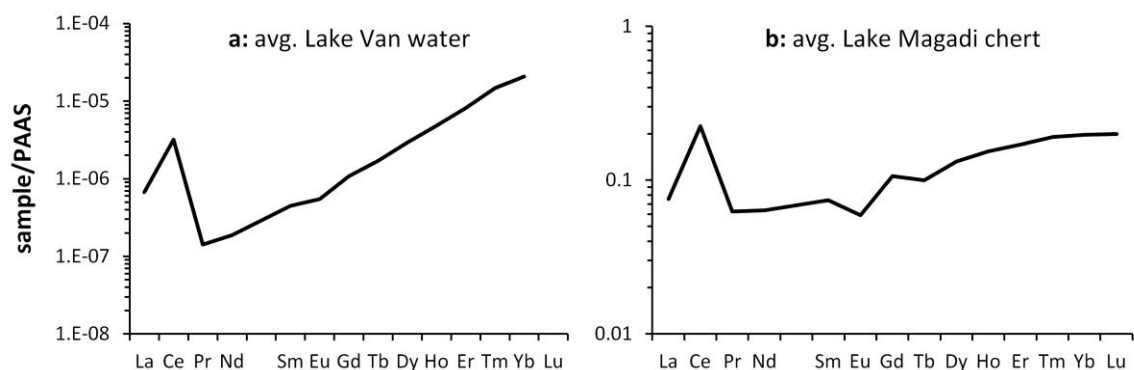


Figure A10.8: REE patterns in Lake Van waters (a) and Lake Magadi cherts (b). Concentrations are normalized to post-Archean average shale (PAAS, McLennan, 1989)). Data are taken from Moeller & Bau (1993) (panel a) and Kerrich *et al.* (2002) (panel b). The Magadi chert average only includes data for pure cherts in which magadiite has almost entirely recrystallized and is only present in concentrations of less than 10%.

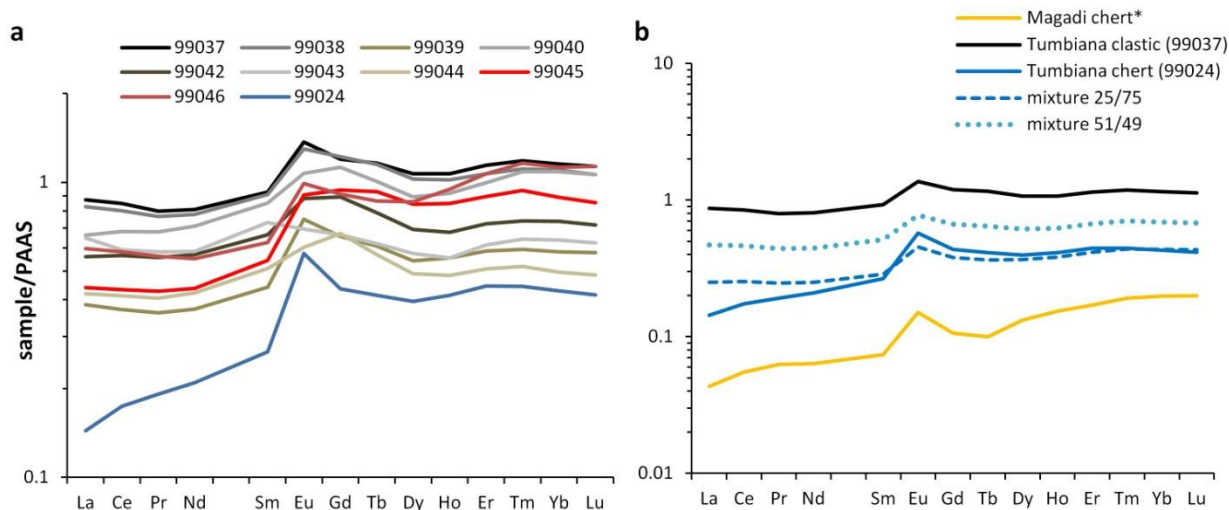


Figure A10.9: REE patterns in the Tumbiana Formation (a) and possible mixing model (b). Concentrations are normalized to PAAS (McLennan, 1989). a: sample 99024 (blue) shows an anomalous depletion in light REE relative to heavy REE, similar to Lake Van waters. Samples 99045 (light red) and 99046 (dark red) also show significant but less continuous differences. b: The pattern of sample 99024 (solid blue) shows some resemblance with a 25%/75% mixture (dashed blue) of clastic material (black) and Magadi chert* (yellow). A 51%/49% mixture (dotted blue) is not sufficient. *Note that La, Ce, and Eu anomalies in the Magadi chert average have been adjusted.

Supplementary references

- Ader M, Cartigny P, Boudou J-P, Oh J-H, Petit E, Javoy M (2006) Nitrogen isotopic evolution of carbonaceous matter during metamorphism: methodology and preliminary results. *Chemical Geology*, **232**, 152-169.
- Beaumont V, Agrinier P, Javoy M, Robert F (1994) Determination of the CO contribution to the $^{15}\text{N}/^{14}\text{N}$ ratio measured by mass spectrometry. *Analytical Chemistry*, **66**, 2187-2189.
- Bebout GE, Idleman BD, Li L, Hilkert A (2007) Isotope-ratio-monitoring gas chromatography methods for high-precision isotopic analysis of nanomole quantities of silicate nitrogen. *Chemical Geology*, **240**, 1-10.
- Bolhar R, van Kranendonk MJ (2007) A non-marine depositional setting for the northern Fortescue Group, Pilbara Craton, inferred from trace element geochemistry of stromatolitic carbonates. *Precambrian Research*, **155**, 229-250.
- Boyd SR, Rejou-Michel A, Javoy M (1994) Noncryogenic purification of nanomole quantities of nitrogen gas for isotopic analysis. *Analytical Chemistry*, **66**, 1396-1402.
- Busigny V, Ader M, Cartigny P (2005) Quantification and isotopic analysis of nitrogen in rocks at the ppm level using sealed tube combustion technique: a prelude to the study of altered oceanic crust. *Chemical Geology*, **223**, 249-258.
- Dennen KO, Johnson CA, Otter ML, Silva SR, Wandless GA (2006) $\delta^{15}\text{N}$ and non-carbonate $\delta^{13}\text{C}$ values for two petroleum source rock reference materials and a marine sediment reference material. *U.S. Geological Survey Open-File Report 2006-1071*.
- Elderfield H, Whitfield M, Burton JD, Bacon MP, Liss PS (1988) The oceanic chemistry of the rare-earth elements. *Philosophical Transactions of the Royal Society*, **325**, 105-126.
- Eugster HP (1967) Hydrous sodium silicates from Lake Magadi, Kenya: precursors of bedded chert. *Science*, **157**, 1177-1180.
- Johannesson KH, Lyons WB (1994) The rare earth element geochemistry of Mono Lake water and the importance of carbonate complexing. *Limnology and Oceanography*, **39**, 1141-1154.
- Kendall C, Grim E (1990) Combustion tube method for measurement of nitrogen isotope ratios using calcium oxide for total removal of carbon dioxide and water. *Analytical Chemistry*, **62**, 526-529.
- Kerrich R, Renaut RW, Bonli T (2002) Trace-element composition of cherts from alkaline lakes in the East African Rift: a probe for ancient counterparts. *Society of Sedimentary Geology Special Publications*, **73**, 275-294.
- McLennan SM (1982) On the geochemical evolution of sedimentary rocks. *Chemical Geology*, **37**, 335-350.
- McLennan SM (1989) Rare earth elements in sedimentary rocks; influence of provenance and sedimentary processes. *Reviews in Mineralogy and Geochemistry*, **21**, 169-200.
- Moeller P, Bau M (1993) Rare-earth patterns with positive cerium anomaly in alkaline waters from Lake Van, Turkey. *Earth and Planetary Science Letters*, **117**, 671-676.
- Papineau D, Purohit R, Goldberg T, Pi D, Shields GA, Bhu H, Steele A, Fogel ML (2009) High primary productivity and nitrogen cycling after the Paleoproterozoic phosphogenic event in the Aravalli Supergroup, India. *Precambrian Research*, **171**, 37-56.
- Qi H, Coplen TB, Geilmann H, Brand WA, Böhlke JK (2003) Two new organic reference materials for $\delta^{13}\text{C}$ and $\delta^{15}\text{N}$ measurements and a new value for the $\delta^{13}\text{C}$ of NBS 22 oil. *Rapid Communications in Mass Spectrometry*, **17**, 2483-2487.

- Robl TL, Davis BH (1993) Comparison of the HF-HCl and HF-BF₃ maceration techniques and the chemistry of resultant organic concentrates. *Organic Geochemistry*, **20**, 249-255.
- Smith RE, Perdrix JL, Parks TC (1982) Burial metamorphism in the Hamersley Basin, Western Australia. *Australian Journal of Petrology*, **23**, 75-102.
- Strauss H, Des Marais DJ, Hayes JM, Lambert IB, Summons R (1992) Procedures of whole rock and kerogen analysis. In: *The Proterozoic Biosphere - A Multidisciplinary Study* (eds Schopf JW, Klein C). Cambridge University Press, Cambridge.
- Stüeken EE (2013) A test of the nitrogen-limitation hypothesis for retarded eukaryote radiation: nitrogen isotopes across a Mesoproterozoic basinal profile. *Geochimica et Cosmochimica Acta*, **120**, 121-139.
- Stüeken EE, Buick R, Guy BM (in prep.) Isotopic evidence for biological nitrogen fixation by Mo-nitrogenase at 3.2 Gyr.
- Therion JJ, Human HGC, Claase C, Mackie RI, Kistner A (1986) Automatic nitrogen-15 analyser for use in biological research. *Analyst*, **111**, 1017-1021.
- Thomazo C, Ader M, Phillippot P (2011) Extreme ¹⁵N-enrichment in 2.72-Gyr-old sediments: evidence for a turning point in the nitrogen cycle. *Geobiology*, **9**, 107-120.

Conclusion

Redox chemistry is fundamental to all life on Earth and as discussed in Chapter 1, gradients in redox potential and other physicochemical parameters may also have been important in prebiotic chemistry. In an astrobiological context, this implies that planets with active geological cycles that create such gradients may not only be more likely to sustain a biosphere over long timescales but they are perhaps also more conducive to an independent origin of life. The new geochemical analyses presented in this work address the early evolution of metabolism in its planetary context and support three general conclusions.

1. Major metabolic strategies evolved very early in Earth's history.

Sulfur, nitrogen and selenium isotope data from Archean sedimentary rocks support previous studies invoking an early origin of microbial sulfate reduction (Shen *et al.*, 2001, Chapter 3), N₂ fixation (Kasting & Siefert, 2001, Chapter 9), and oxygenic photosynthesis (Crowe *et al.*, 2013; Planavsky *et al.*, 2014, Chapters 2, 5, 6) long before the Paleoproterozoic Great Oxidation Event (Lyons *et al.*, 2014). In other words, microbial life evidently evolved to access major planetary reservoirs of metabolic energy and substrates at a very early stage. One could speculate that perhaps some these reactions already occurred on the prebiotic Earth and were incorporated into early biochemistry as it transitioned towards living cells. This idea is commonly raised in the context of CO₂-fixation pathways (e.g. Russell & Martin, 2004), but if multiple environments were involved in the origin of life (Chapter 1), then precursors of other reactions that are seen in modern metabolism and that were perhaps favored in certain prebiotic settings could also have been part of early proto-metabolic networks.

2. Non-marine environments were colonized by the late Archean and may have provided unique conditions for early evolution.

Most of the preserved sedimentary record represents marine environments, in particular continental shelves and epeiric seas. This preservational bias, combined with strong evidence that O₂ and hence UV-protection by O₃ were essentially absent from the Archean atmosphere, has generally led to the potential importance of non-marine habitats for early life being underestimated. Sulfur and selenium data from this study (Chapters 2, 6) suggest that continents have been inhabited by diverse microbial communities since at least 2.75 billion years ago and that the metabolic activity of these microbes may have greatly affected nutrient fluxes into the ocean (Chapters 2, 3). This represents another example of how life can transform geochemical cycles on a global scale. As shown by nitrogen isotope data, non-marine habitats could have differed from the ocean in chemical composition, including pH and nutrient supply (Chapter 10), which could have made them favorable niches for the origin and diversification of certain organisms.

3. Ocean anoxia may have limited the radiation of complex life in the mid-Proterozoic, possibly until the mid-Paleozoic, but it was perhaps not the sole cause of the late Permian mass extinction.

While prokaryotic organisms have evidently been widespread since the Archean, thriving in many different environments under many different redox conditions, the fossil record of eukaryotes suggests that this domain was environmentally restricted to near-shore environments until the end of the Precambrian, likely because of anoxia in the deep ocean (reviewed by Knoll *et al.*, 2006). Nitrogen isotope data from this study (Chapter 8) show that anoxic conditions may have limited the supply of nitrate in deeper waters, which may have placed an additional

constraint on the radiation of eukaryotes that cannot fix N₂ themselves. The selenium isotope data through time (Chapter 6) further suggest that the deep ocean may not have become fully oxygenated until the mid-Paleozoic. The low temporal resolution of this record makes this conclusion tentative, but if correct, then it may support the idea that the evolution of vascular plants on land in the Devonian was critical for increasing the marine redox state (Dahl *et al.*, 2010). But although ocean anoxia can evidently restrict the habitats of eukaryotes, in particular of large complex multicellular organisms, selenium data across the late Permian mass extinction horizon suggest that anoxia cannot have been the direct cause of the extinction event (Chapter 7).

In summary, this work has shown that prokaryotes had few boundaries in the early Precambrian whereas eukaryotes did, that lakes and rivers may be good targets for future investigations of evolutionary innovations, and that selenium isotopes can be a useful biogeochemical proxy but they are not the most informative key to Earth's redox history. From an astrobiological perspective, these results are encouraging for searches of microbial life even in harsh environments, but selenium isotopes are not the best tool to look for it.

References

- Crowe SA, Døssing LN, Beukes NJ, Bau M, Kruger SJ, Frei R, Canfield DE (2013) Atmospheric oxygenation three billion years ago. *Nature*, **501**, 535-538.
- Dahl TW, Anbar AD, Gordon GW, Rosing MT, Frei R, Canfield DE (2010) The behavior of molybdenum and its isotopes across the chemocline and in the sediments of sulfidic Lake Cadagno, Switzerland. *Geochimica et Cosmochimica Acta*, **74**, 144-163.
- Kasting JF, Siefert JL (2001) Biogeochemistry: the nitrogen fix. *Nature*, **412**, 26-27.
- Knoll AH, Javaux EJ, Hewitt D, Cohen P (2006) Eukaryotic organisms in Proterozoic oceans. *Philosophical Transactions of the Royal Society of London B*, **361**, 1023-1038.
- Lyons TW, Reinhard CT, Planavsky NJ (2014) The rise of oxygen in Earth's early ocean and atmosphere. *Nature*, **506**, 307-315.
- Planavsky NJ, Asael D, Hofmann A, Reinhard CT, Lalonde SV, Knudsen A, Wang X, Ossa Ossa F, Pecoits E, Smith AJB, Beukes NJ, Bekker A, Johnson TM, Konhauser K, Lyons TW, Rouxel OJ (2014) Evidence for oxygenic photosynthesis half a billion years before the Great Oxidation Event. *Nature Geoscience*.
- Russell MJ, Martin W (2004) The rocky roots of the acetyl-CoA pathway. *Trends in biochemical sciences*, **29**, 358-363.
- Shen Y, Buick R, Canfield DE (2001) Isotopic evidence for microbial sulphate reduction in the early Archaean era. *Nature*, **410**, 77-81.